Wideband 1.55 μm Waveguide Photodiodes Employing Planar Resonant Circuits for E-band (60–90 GHz) Operation

Vitaly Rymanov[1], **Sascha Lutzmann**[2], **Merih Palandöken**[2], **Tolga Tekin**[2], **and Andreas Stöhr**[1]

[1]Universität Duisburg-Essen, Lotharstraße 55, Duisburg 47057, Germany
[2]Technische Universität Berlin, Gustav-Meyer-Allee 25, Berlin 13355, Germany

Abstract— The recently regulated 10 GHz bandwidth (71–76 GHz and 81–86 GHz) within the E-band (60–90 GHz) is of particular interest for fixed wireless systems. Since radio-over-fiber (RoF) techniques have opened up the possibility to transmit up to 100 Gb/s in such a wide bandwidth, it is one of the most interesting technologies for ultra-broadband wireless link.

In this work, we present E-band waveguide photodiodes (PDs) with high external quantum efficiency, which are required for such ultra-broadband RoF links. In detail, we demonstrate advanced partially p-doped, partially non-intentionally doped (PDPN) absorbing 1.55 μm waveguide PDs implemented in a mushroom-type layer structure primarily approaching 71–76 GHz operation within the E-band. Furthermore, a passive optical waveguide (POW) is monolithically integrated in the layer structure and is used for efficient optical coupling. As a result, an extremely flat frequency response with a deviation of less than ±1 dB in the complete E-band is experimentally achieved. Moreover, an output radio frequency (RF) power level exceeding 0 dBm at a photocurrent in the order of ∼ 15 mA is obtained, e.g., at a frequency of 72 GHz. Since no 1 dB compression point is adumbrated, maximum safely working photocurrent levels of ∼ 20 mA are expected for cooled operation. For superlative devices, a DC responsivity of up to 0.5 A/W was actually found even without additional anti-reflection (AR) coating.

For hybrid integration in a wireless E-band transmitter module, the PDs comprise a grounded coplanar waveguide (GCPW) output circuitry employing linearly tapered feeds. Thus, a matched GCPW circuitry with a 50 Ω output impedance is realized. To ensure a return loss exceeding 20 dB for the 70 GHz band operation, additional LC resonant GCPW circuits were studied and modeled using the method of moments (MoM). Applying the designed GCPW circuitries to the devices, the resulting return loss was optimized about 10–20 dB in the frequency range of 70–90 GHz.

1. INTRODUCTION

Photonic high-capacity wireless systems exploiting manifold millimeter wave (mmW) and RoF techniques are taken into account as a disruptive technology, e.g., for expansion in optical access and metro networks and in mobile backhauling [1–5]. Here, leadoff E-band (60–90 GHz) regulations were constituted by the Federal Communications Commission (FCC) in the United States allocating frequency bands within 71–76 GHz, 81–86 GHz and 92–95 GHz with the exception of the 94–94.1 GHz portion. Europe and other countries such as Canada and Australia quickly adopted these regulations [2].

In the recent past, we already demonstrated 60 GHz photonic wireless systems with record data rates up to 27 Gb/s [3]. Due to the oxygen absorption at 60 GHz, it is more beneficial for fixed wireless systems with spans of > 1 km to operate at even higher frequencies. For this reason, concentrated attention is paid to the 10 GHz bandwidth within the 71–76 GHz and 81–86 GHz frequency bands. Additionally, these allocations enable full duplex multi-gigabit wireless transmission with bandwidths up to 10 GHz [4].

For ultra-wideband wireless RoF system operation, photonic transmitter and receiver modules are required. It is certain that the expensive and time-consuming realization of a module like, e.g., a photonic transmitter exploits discrete components such as coaxial cables or bulky rectangular waveguides for connection between the PD and the antenna. Furthermore, additionally implemented transitions and connectors are needed and result in additional losses, oversized module dimensions and once more lead to higher costs.

Thus, a particular focus is put on an integrated photonic solution to reduce costs and device dimensions. This means that the PD as well as the antenna would be monolithically or hybrid integrated on one die [6] or a RF subcarrier [7]. For this purpose, wideband waveguide PDs with high bandwidth as well as high external quantum efficiency are essential.

In this work, wideband 1.55 µm waveguide PDs featuring a monolithically integrated shallow ridge-type POW for efficient lateral fiber-chip coupling are introduced for hybrid integration in a wireless E-band transmitter module as part of an ultra-broadband RoF link. Thoroughly, the active PD section takes advantage of a PDPN absorbing layer centered in a mushroom-type optical waveguide to ensure wideband operation. Besides technological achievements, we present the experimental characterization and study resonant GCPW circuits enabling optimized impedance matching within the E-band.

2. WIDEBAND 1.55 µm WAVEGUIDE PHOTODIODES

For ultra-broadband RoF applications, an InP-based double-waveguide PD operating at the optical wavelengths around 1.55 µm is designed primarily approaching 71–76 GHz operation and fabricated by means of conventional photolithography, selective etching and metal evaporation. More precisely, a monolithically integrated shallow ridge-type InGaAsP/InP POW for efficient lateral fiber-chip coupling is introduced below the active PD section. A view on the model of the developed device is given in Figure 1. Here, a fiber-chip coupling loss of ~ 1 dB is determined at the facet of the POW. Furthermore, maximum coupling efficiencies between the POW and the active waveguide section and an absorption within a PD's length of < 20 µm are achieved in exceed of 90% and 70%, respectively [8]. Experimentally, DC responsivities up to 0.5 A/W were found for superlative devices even without additional AR coating.

The active PD section benefits from a PDPN absorbing InGaAs layer centered in a mushroom-type optical waveguide [9]. Thoroughly, a highly p-doped InP upper cladding layer balances the trade-off between the active optical waveguide losses and the series resistance. The absorber consists of a graded p-doped InGaAs layer in combination with a non-intentionally doped InGaAs layer to enhance the transit times of the photo-generated carriers. Further weakly n-doped InGaAsP layers are introduced as spacer layers between the InGaAs layer and the weakly n-doped guiding InP stripe layer (POW) to overcome the band discontinuity.

For RF characterization, a coplanar ground-signal-ground probe ($\sim 50\,\Omega$) was applied to measure the output power RF levels of the PD. In Figure 2, the fabricated PD and the corresponding frequency response are presented. As can be seen from the measured response, a flatness of < 2 dB within the 60–90 GHz frequency band is achieved. The PD was operated without additional cooling at a photocurrent of 1 mA and a drive voltage of -8 V. Moreover, an output power level exceeding 0 dBm (1 mW) at a photocurrent of approx. 15 mA is obtained, e.g., at 72 GHz. Since no 1 dB compression point is adumbrated, maximum safely working photocurrent levels of ~ 20 mA are expected for cooled operation.

3. PLANAR RESONANT GCPW CIRCUITS

For hybrid integration in a wireless photonic 71–76 GHz transmitter module such as presented in [10], the PDs feature a GCPW output circuitry employing linearly tapered feeds followed by implemented output pads ($\sim 50\,\Omega$) for bonding. A detailed illustration of the fabricated PD is given in Figure 2(a). In Figure 3(b), results of measured S_{22} are presented. Here, S_{22} of the device integrated solely with a GCPW output circuitry decreases from about -6 dB at 60 GHz to < -8.5 dB at 90 GHz. Maximum return loss exceeding 9 dB is identified within 71–76 GHz and 81–86 GHz.

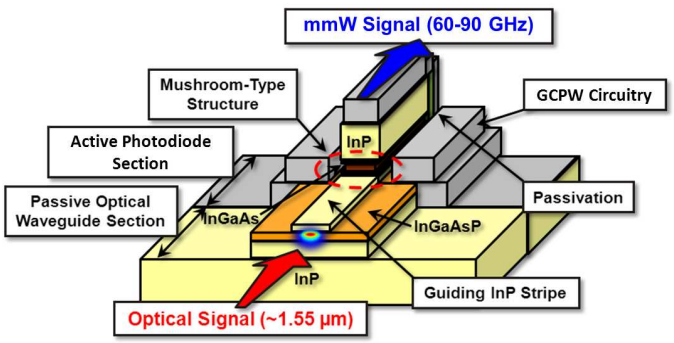

Figure 1: Schematic of the developed double-waveguide 1.55 µm PD (without output GCPW circuitry).

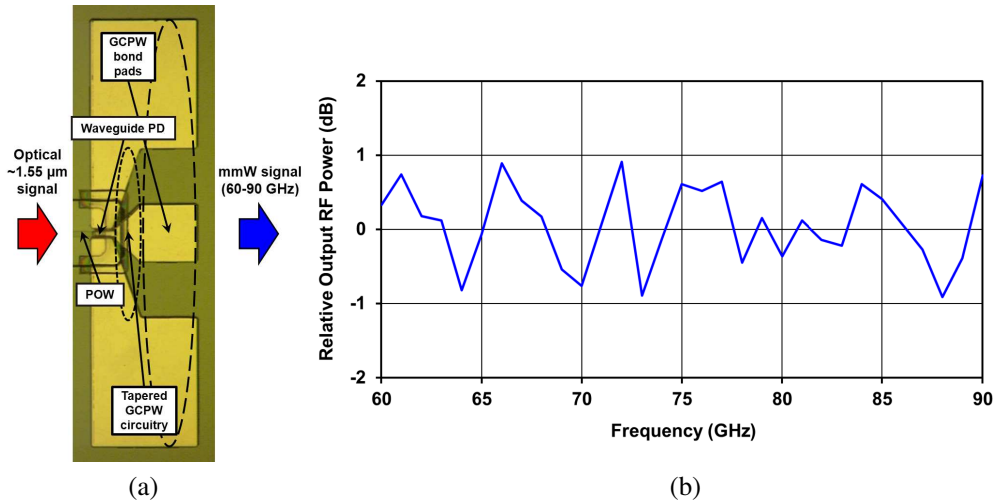

(a) (b)

Figure 2: (b) Relative frequency response of (a) the fabricated waveguide PD for the 60–90 GHz frequency range.

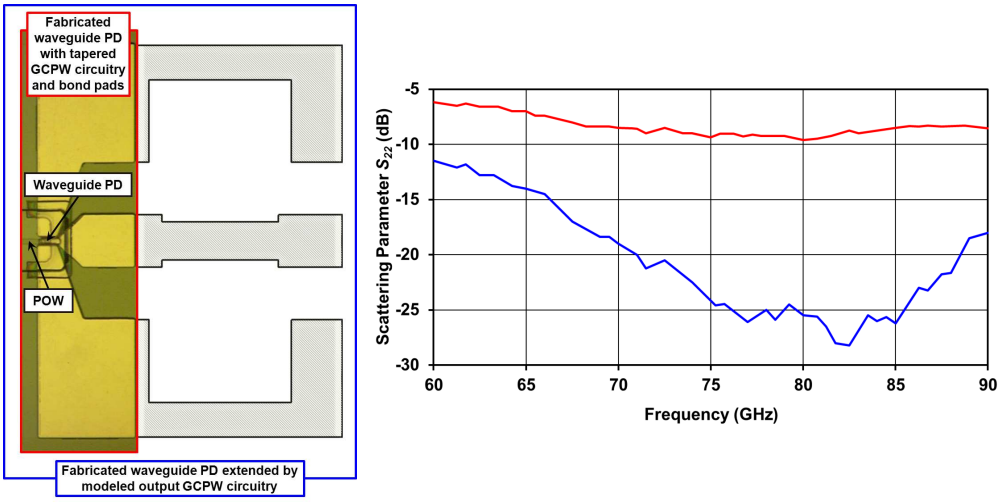

(a) (b)

Figure 3: (b) Upper red curve: measured scattering parameter S_{22} of a fabricated waveguide PD with a linearly tapered GCPW circuitry and bond pads, and lower blue curve: calculated S_{22} of the same device extended by the modeled GCPW matching circuitry shown in (a).

To ensure a return loss of > 20 dB at least for the 70 GHz band operation, resonant LC circuits employing the GCPW approach were designed utilizing the analytic model presented in [11] and simulated based upon MoM analyses. As an example, a fabricated PD combined with modeled GCPW matching circuitry is shown in Figure 3(a). For compensation of identified capacitive behavior dominating on S_{22} of the fabricated device, inductance is implemented by the narrowed center conductor and additional cavities in the ground planes. When the PD is extended by the matching circuitry, an overall optimization of S_{22} in the order of 10–20 dB is achieved within 70–90 GHz as presented in Figure 3(b). Consequentially, a return loss exceeding 20 dB is realized within the 71–76 GHz and 81–86 GHz frequency bands. Moreover, a minimum S_{22} of -28 dB is obtained at a frequency of 82 GHz, which results actually in an optimization of around 20 dB.

4. CONCLUSIONS

In this paper, we demonstrated wideband double-waveguide PDPN absorbing 1.55 μm mushroom-type PDs studied in conjunction with modeled GCPW matching circuitries for optimized operation within the E-band. Experimentally, fabricated PDs comprise an extremely flat frequency response of $< \pm 1$ dB for the entire 60–90 GHz range. Due to the high linearity measured without additional

cooling, output RF power levels of > 0 dBm are achieved at photocurrents in the region of 15 mA within 71–76 GHz. Furthermore, an output return loss of up to 28 dB is obtained, when the designed planar LC matching circuit is applied to the PD resulting in an overall optimization of S_{22} in the order of 10–20 dB for the 70 GHz and 80 GHz bands. Details relating to the hybrid integration in a wireless E-band transmitter module can be found in further contributions presented within the conference [12, 13].

ACKNOWLEDGMENT

The authors wish to acknowledge the contributions of Alex Zhebraytys and Melanie Wachholz for device simulation and fabrication. This work was supported by the European STReP iPHOS under the grant No. 257539.

REFERENCES

1. www.iphos-project.eu.
2. Stöhr, A., "Photonic millimeter-wave generation and its applications in high data rate wireless access," *Proceedings of IEEE International Topical Meeting on Microwave Photonics (MWP 2010)*, 7–10, Montreal, Canada, Oct. 2010, Plenary Paper.
3. Weiß, M., A. Stöhr, F. Lecoche, and B. Charbonnier, "27 Gbit/s photonic wireless 60 GHz transmission system using 16-QAM OFDM," *Proceedings of IEEE International Topical Meeting on Microwave Photonics (MWP 2009)*, 1–3, Valencia, Spain, Oct. 2009, Post Deadline Paper.
4. Stöhr, A. and D. Jäger, "High data rate radio over fiber technologies," *Proceedings of IEEE Photonics Conference (PHO 2011)*, 192–193, Arlington, Virginia, USA, Oct. 2011, Invited Paper.
5. Stöhr, A., S. Babiel, P. J. Cannard, B. Charbonnier, F. van Dijk, S. Fedderwitz, D. Moodie, L. Pavlovic, L. Ponnampalam, C. C. Renaud, D. Rogers, V. Rymanov, A. J. Seeds, A. G. Steffan, A. Umbach, and M. Weiß, "Millimeter-wave photonic components for broadband wireless systems," *IEEE Trans. Microw. Theory Tech.*, Vol. 58, No. 11, 3071–3082, 2010, Invited Paper.
6. Rymanov, V. and A. Stöhr, "Semicircular bow-tie antenna-integrated double waveguide 1.55 µm mushroom photodetectors for CW photonic millimeter wave transmitter modules," *Proceedings of 7th German Microwave Conference (GeMiC 2012)*, 1–4, Ilmenau, Germany, Mar. 2012.
7. Rymanov, V., S. Babiel, A. Stöhr, S. Lutzmann, M. Palandöken, B. Bouhlal, and T. Tekin, "Integrated E-band photoreceiver module for wideband (71–76 GHz) wireless transmission," *Proceedings of European Microwave Week 2012, European Microwave Conference (EuMC 2012)*, Amsterdam, The Netherlands, Oct./Nov. 2012, in Press.
8. Rymanov, V., S. Babiel, and A. Stöhr, "Monolithically integrated photonic transmitters employing double waveguide 1.55 µm photodetectors for compact continuous-wave photonic millimeter wave (30–300 GHz) transmitter modules," *Proceedings of Asia-Pacific Microwave Photonics Conference (APMP 2012)*, Kyoto, Japan, Apr. 2012.
9. Rymanov, V., T. Tekin, and A. Stöhr, "Double mushroom 1.55 µm waveguide photodetectors for integrated E-band (60–90 GHz) wireless transmitter modules," *Proceedings of SPIE Photonics West Conference (SPIE OPTO 2012)*, Vol. 8259, 82590E, San Francisco, California, USA, Jan. 2012.
10. Rymanov, V., M. Palandöken, S. Lutzmann, B. Bouhlal, T. Tekin, and A. Stöhr, "Integrated photonic 71–76 GHz transmitter module employing high linearity double mushroom-type 1.55 µm waveguide photodiodes," *Proceedings of IEEE International Topical Meeting on Microwave Photonics (MWP 2012)*, Noordwijk, The Netherlands, Sep. 2012, in Press.
11. Madjar, A., N. Koka, J. Bloch, P. K. L. Yu, A. Stöhr, and D. Jäger, "A novel analytical model as a design tool for uni-traveling-carrier traveling wave photo detectors approaching 1 THz," *IEEE Trans. Microw. Theory Tech.*, Vol. 57, No. 1, 223–230, 2009.
12. Palandöken, M., V. Rymanov, A. Stöhr, and T. Tekin, "Compact metamaterial-based bias tee design for 1.55 µm waveguide-photodiode based 71–76 GHz wireless transmitter," *PIERS Proceedings*, Moscow, Russia, Aug. 2012, in Press.
13. Palandöken, M., S. Lutzmann, V. Rymanov, A. Stöhr, and T. Tekin, "Grounded CPW-WR12 transition design for 1.55 µm photodiode based E-band transmitter," *PIERS Proceedings*, Moscow, Russia, Aug. 2012, in Press.

Analysis and Design of Ferroelectric Phase Shifters Appropriate for Printed Phased Arrays

A. S. Paraskevopoulos, **C. I. Kolitsidas**, **F. E. Fakoukakis**, **and G. A. Kyriacou**
Microwaves Laboratoty, Department of Electrical and Computer Engineering
Democritus University of Thrace, Xanthi 67100, Greece

Abstract— Electronically controllable phase shifters exploiting thin layers (films) of BSTO ferroelectric are elaborated. Their basic advantage over ferrite phase shifters is their convenient control from a DC biasing voltage which can be implemented even within integrated circuits, in contrary to bulky electromagnets required by ferrite technology. However, this convenience is offered at the expense of much higher losses. Printed line technologies operating at a differential (odd) transverse electromagnetic (TEM) mode like Coplanar Strips (CPS), coplanar waveguide (CPW) and grounded CPS excited at their odd mode are found more appropriate. These lines yield the necessary field confinement within the BSTO thin layer which maximizes its interaction with the electromagnetic field to yield the highest possible phase shift.

1. INTRODUCTION

The trend for mobile communications is clearly moving toward increasing number of communication standards and services which occupy increasingly wide frequency ranges. In order to meet these rapidly increasing demands, the need for directional antennas with different functionalities arises. Such antennas could be implemented in base stations and work together with analogue phase shifters in order to electronically control their performance without changing the geometrical characteristics of the antenna. Herein we focus our effort on phased arrays providing radiation pattern that is electronically controlled allowing tunable beam steering or scanning. Recent applications of phased array antennas are encountered in smart base station antennas for WLAN and cellular communications, in traffic control and collision-avoidance radars, wireless sensor networks, environmental monitoring and RFID tags. This work mainly aims at investigating analogue phase shifters based on ferroelectric materials that control the excitation's phase sequence of a phased array with the objective of achieving wideband operation, large phase shifts and a corresponding wide beam steering. After concluding to the suitable phase shifter, we will implement it in a 4-element phased array operating at 2.4 GHz Wi-Fi band.

A general architecture of a phased array is presented in Fig. 1, which is comprised of power dividers, electronically controllable (possibly analogue) phase shifters and appropriate antenna elements. Normally phase shifters are the devices in a phased array antenna that allow the radiated beam to be steered in direction. Depending on the manufacturing method, phase shifters can be classified into the following categories; MEMS phase shifters, ferrite phase shifters, MMIC phase shifters and ferroelectric phase shifters. Various types of antenna elements that include wire antenna, microstrip patches, horn antenna and waveguide are used. Power dividers are used for splitting microwave signals to feed the radiating elements.

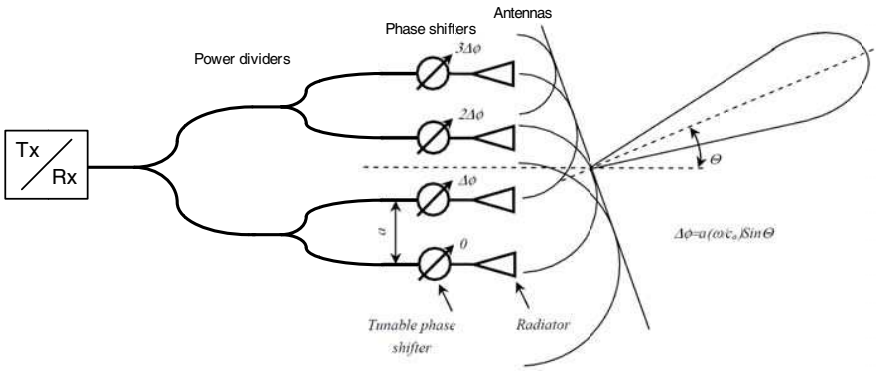

Figure 1: Four element phased array based on electronically controllable phase shifters.

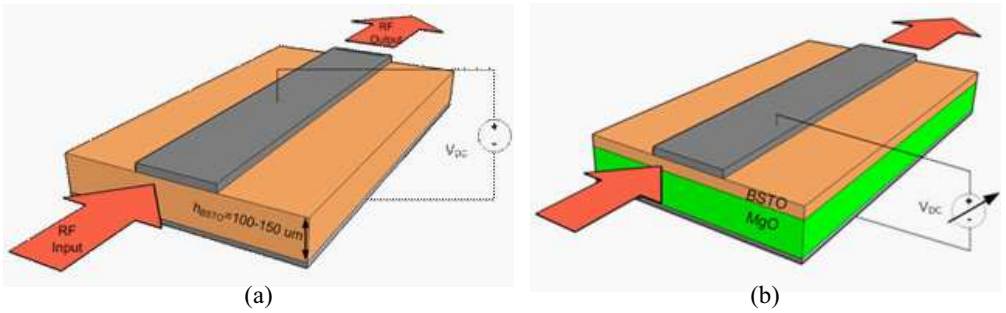

(a) (b)

Figure 2: A structure of microstrip-based ferroelectric phase shifter: (a) Bulk ($\sim 100\,\mu$m) BSTO substrate, and (b) thick film ($\sim 25\,\mu$m) BSTO.

2. FERROELECTRIC PHASE SHIFTER

Ferroelectric materials have the potential to overcome the limitations of MEMS, ferrite and MMIC phase shifters but at the expense of their high insertion loss [1]. Several groups have investigated the possibility of implementing phase shifter circuits using barium strontium titanate (BSTO), which has an electric field tunable dielectric constant at room temperature. In these circuits the ferroelectric material $BaSrTiO_3$ (BSTO) either forms the entire microwave substrate (Fig. 2(a)) on which the conductors are deposited or a fraction of the substrate with thick BSTO film sandwiched between the substrate and the conductors (Fig. 2(b)). Bulk or thick film circuits rely on the principle that because a large part or all of the microwave fields pass through the ferroelectric layer, the phase velocity of waves propagating in these structures can be altered by changing the permittivity of the ferroelectric layer, with the aid of a DC-voltage control. The voltage controllability constitutes actually their main advantage over ferrite phase shifters which require heavy electromagnets to create the DC biasing magnetic field.

Particularly if the DC electric field is applied perpendicular to the direction of propagation of the electromagnetic signal, as shown in Fig. 2, the propagation constant ($\beta = 2\pi/\lambda$) of the signal will depend upon the DC biasing electric field since ($\beta = 2\pi\sqrt{\varepsilon_{r,eff}}/\lambda$) and ($\varepsilon_{r,eff} \propto \varepsilon_r(V_{bias})$). The total wave delay will become a function of the DC biasing field, and, therefore, will produce a phase shift ($\Delta\varphi = l \cdot \Delta\beta$), where l is the length of the line. As a result, the associated differential phase shift can be written in terms of effective dielectric permittivity:

$$\Delta\varphi(V_{bias}) = \frac{l \cdot 2\pi f}{c}\left[\sqrt{\varepsilon_{r,eff}(0)} - \sqrt{\varepsilon_{r,eff}(V_{bias})}\right] \tag{1}$$

The strong dependence of the dielectric permittivity of the ferroelectric material on the applied bias electric field can be derived from the Vendik formula, [4]:

$$\varepsilon_r(T, E_0) = \frac{\varepsilon_{00}}{\left[(\xi^2+\eta^3)^{1/2}+\xi\right]^{2/3} + \left[(\xi^2+\eta^3)^{1/2}-\xi\right]^{2/3} - \eta} \tag{2}$$

where ε_{00}, ξ, η are parameters derived from the same Vendik analysis [4].

The above analytical expression is programmed in Matlab. For the ferroelectric material $Ba_xSr_{1-x}TiO_3$ with barium concentration of $x = 0.5$ and in room temperature $T = 300\,\mathrm{K}$ at paraelectric state the ε_r shows a continuous decrease from $\varepsilon_r(E_0 = 0) = 650$ to about $\varepsilon_r(E_0 = 200\,\mathrm{kV/cm}) = 268$.

Because of the handling and fabrication difficulty in using a single bulk ferroelectric layer, most of the phase shifter designs are based on multilayer microstriplines and preferably coplanar strips (CPS) or coplanar waveguide (CPW) technologies, where a thin layer of BSTO is utilized. The requirement for CPS or CPW geometries is satisfied by the fact that when BSTO is formed into a very thin layer its interaction with the electromagnetic field below the microstrip line becomes minimal, since the electric field is perpendicular to the strip conductor. Hence, a printed line where the electromagnetic energy will be concentrated within the thin BSTO layer should be employed. Thus CPS or CPW operating at the appropriate differential mode should be adopted.

3. DESIGN OF CPS FERROELECTRIC PHASE SHIFTER

Coplanar-Strips (CPS) on multilayer substrates including a ferroelectric layer are considered. The simple analytic formulas obtained by Gevorgian [1] are utilized herein. These are based on a conformal mapping technique and assume uniform dielectric permittivity distribution in the ferroelectric layer. So, the basic parameters of the ferroelectric transmission lines, such as capacitance, impedance and effective dielectric constant are computed using Matlab and exploited for device design and optimization. In coplanar-strip (CPS) lines, in contrast to microstrips, the desired impedance may be achieved by appropriate selection of the strip width (s) and gap ($2g$) regardless the thickness of the substrate (Fig. 3(a)). Besides that, the important feature of CPS is their inherent ability to operate in the "odd" mode. Operating in the odd mode the electromagnetic energy is concentrated between the two strips and thus within the BSTO film. Hence the interaction is maximized and similarly the resulting controllable phase shift. Likewise the CPW geometry (Fig. 3(b)) operates in a differential mode, since it can be obtained from three coplanar strips with the signal conductor in the middle. In contrary the grounded coplanar strips or coupled microstrip lines which could be another possibility may operate in either the desired "odd mode" as Fig. 3(c) or at an "even" mode (Fig. 3(d)). In this case the appropriate excitation of the odd mode should be ensured. For the three-layer CPS shown in Fig. 3, we assume that the permittivity of the layers is decreasing going away from the strips: $\varepsilon_{r1} > \varepsilon_{r2}$ so that the electric field streamlines are predominantly parallel to the dielectric/dielectric interfaces and concentrated within the BSTO layer, thus maximizing the interaction in the odd mode.

4. NUMERICAL RESULTS

Using the analytical formulas [1], the geometrical characteristics of a multilayer ferroelectric CPS line (Fig. 3(c)) are optimized aiming at a well matched transmission line with $Z_0 = 50\,\Omega$, to yield the parameters of Table 1.

In order to reveal the impact of the ferroelectric film on the phase shifter tunability, grounded CPS lines loaded with different BSTO thickness $h_1 = 0.5$, 1, 2 and 5 μm for an operation frequency at 2.45 GHz is examined. The corresponding characteristic impedance with zero bias was found $Z_0 = 52.89\,\Omega$, while the resulting phase shift is presented in Fig. 4(a). The dependence of the characteristic impedance on the biasing DC electric field (E_0) is shown in Fig. 4(b). The Z_0 variation is exactly due to the corresponding changes in the BSTO dielectric constant and consequently to

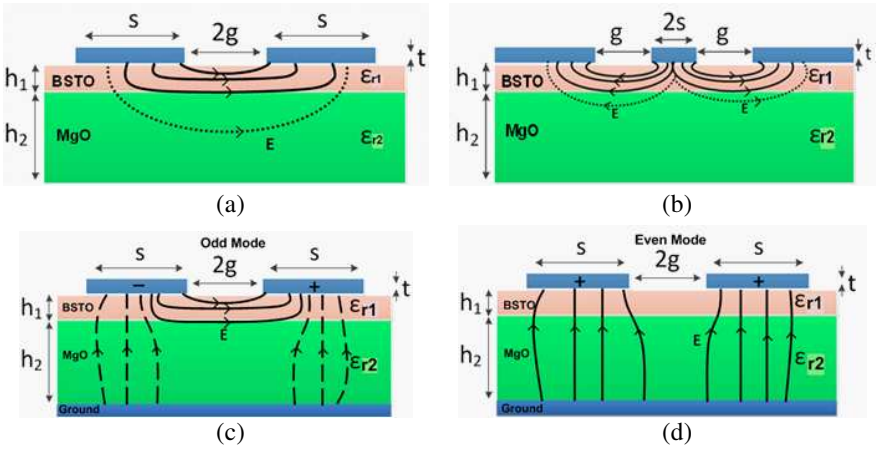

Figure 3: Ferroelectric phase shifter based on (a) CPS line technology, (b) CPW technology and coupled microstrip lines or grounded CPS geometry operating at (c) "odd mode" or (d) "even mode".

Table 1: Design parameters of the grounded CPS ferroelectric phase shifter with $Z_0 = 50\,\Omega$ operating in its "odd mode".

		$\mathbf{Ba_{0.5}Sr_{0.5}TiO_3}$		**MgO**	
s	$2g$	h_1	ε_{r1}	h_2	ε_{r2}
320 μm	48 μm	0.5 μm	650	500 μm	9.7

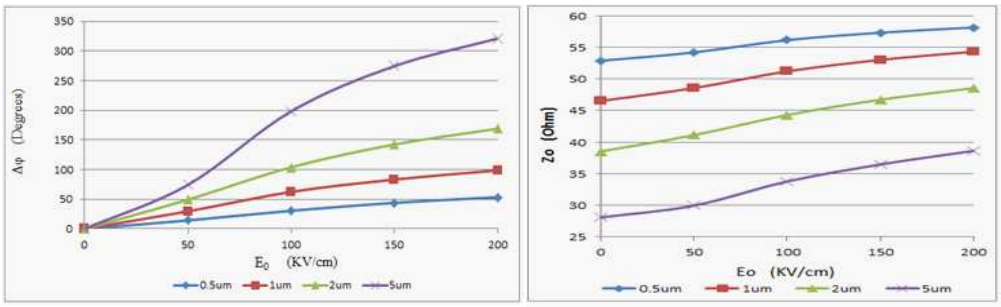

(a) (b)

Figure 4: (a) Simulated results of CPS phase shifter showing increasing phase shift with increased BSTO ferroelectric thickness ($h_1 = 0.5$, 1, 2 and 5 μm), (b) the corresponding characteristic impedance Z_0.

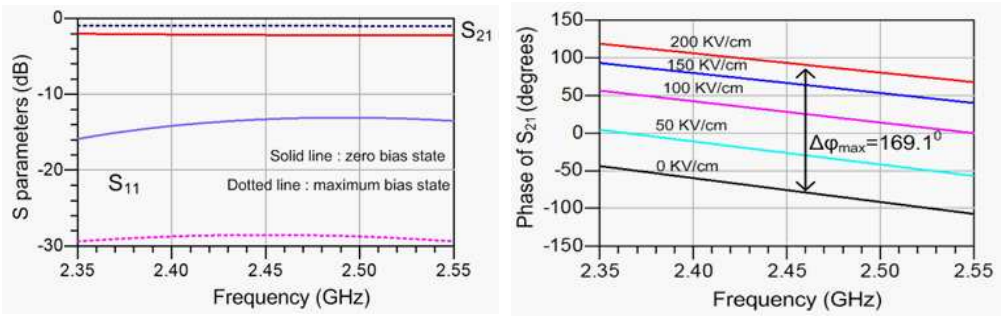

(a) (b)

Figure 5: S-parameters of the grounded CPS ferroelectric phase shifter obtained with the aid of ADS momentum: (a) Insertion and return loss and (b) phase shift versus frequency for different DC-bias.

$\varepsilon_{r,eff}$ dependence on E_0. This dependence is approximately of the form $Z_0 \approx 1/(U_p \cdot C)$ where $C =$ the capacitance per unit length and U_p the phase velocity $U_p = \omega/\beta = c_{light}/\sqrt{\varepsilon_{r,eff}}$. This Z_0 variation reveals another important requirement for the impedance matching for the ferroelectric phase shifter to the 50 Ω lines connected at its input and output ports. In general such a wideband matching can be achieved by utilizing radial stubs.

Observing the phase shifts, one may conclude that the CPS line with a 2 μm ferroelectric substrate provides 3 times higher tunability compared to its 0.5 μm counterpart, while 5 μm substrate gives 6 times improved phase difference. This behavior can be justified by the relatively low microwave frequency (2.45 GHz) where larger dielectric (BSTO) thickness is required to confine most of the electromagnetic energy within that layer. On the other hand, it should be noted that the larger the thickness of the ferroelectric substrate, the more deteriorates the corresponding dissipated power due to its high loss tangent.

The designed phase shifter is based on a grounded CPS (Fig. 4(c)) loaded with $Ba_{0.5}Sr_{0.5}TiO_3$ thin film of 2 μm thickness, dielectric constant ranging from $\varepsilon_{r1} = 650$ at zero bias to $\varepsilon_{r1} = 268$ when applying a DC electric field of $E_0 = 200$ kV/cm and a loss tangent of 0.05. The ferroelectric thin film is usually grown by chemical vapor deposition (CCVD) on 0.5 mm MgO [3]. The phase shifter results are shown in Fig. 5, where both the magnitudes of S_{11} and S_{21} (Fig. 5(a)) and the phase of S_{21} (Fig. 5(b)) are depicted. The phase shifter exhibits an insertion loss of $|S_{21}| \approx -2.2$ dB and a return loss of $|S_{11}| \approx -13.3$ dB at zero DC bias state. The phase shifting ability of the ferroelectric phase shifter can be proven from the response of the phase of S_{21}. The maximum phase difference can be obtained by biasing the ferroelectric film with a DC electric field of 200 kV/cm, resulting to a phase difference of 169.1°.

5. CONCLUSIONS

This paper demonstrates the possibility for integration of electrostatically actuated multilayer CPS phase shifters to be exploited in a phased array antenna system. Additional phase shifter designs based on CPW technologies will be presented at the symposium. The next step is the design of the feed network and antenna patches based on microstrip technology in order to complete the whole phased array and present the beam steering capability.

ACKNOWLEDGMENT

This work was financially supported by the Greek Ministry of Education, Lifelong Learning and Religious Affairs through the research project THALIS Design Techniques for Digitally Controlled RF-Microwave Structures Appropriate for Software Defined-Cognitive Radio (RF-EIGEN-SDR).

REFERENCES

1. Gevorgian, S., *Ferroelectrics in Microwave Devices, Circuits and Systems*, 1st Edition, Springer-Verlag, 2009.
2. Tagantsev, A. K., "Ferroelectric materials for microwave tunable applications," *J. of Electroceramics*, 2003.
3. Miranda, F. A., et al., "Design and development of ferroelectric tunable microwave components for ku- and K-band satellite communication systems," *IEEE Transactions on Microwave Theory and Techniques*, Vol. 48, July 2000.
4. Vendik, O. G., et al., "Microwave loss-factor of $Ba_xSr_{1-x}TiO_3$ as a function of temperature, biasing field, barium concentration, and frequency," *J. of Superconductivity*, Vol. 12, 325, 1999.

General Ray Method for Solution of Direct and Inverse Problems of Electromagnetism

Alexandre Grebennikov
Facultad de Ciencias Físico Matemáticas, Benemérita Universidad Autónoma de Puebla
Av. San Claudio y Río Verde, Ciudad Universitaria, CP 72570, Puebla, Pue., México

Abstract— A new approach for the solution of direct and inverse problems of distribution of electric field is considered here on the base of the General Ray Principle (*GRP*). *GRP* leads to explicit analytical formulas (*GR*-method) for the direct boundary value problems and for the coefficient inverse problems for the Laplace type equations. Here we develop *GR*-method for some type of equations and domains. In the case of noised data we use regularization by spline approximation method. New variants of *GR*-method are realized by fast algorithms and MATLAB software, whose quality is justified by numerical experiments.

1. INTRODUCTION

We consider the Dirichlet boundary value problem for the Laplace equation written in the divergent form, namely

$$\nabla\left(\varepsilon\left(x,y\right)\nabla u\left(x,y\right)\right) = 0, \quad (x,y)\in\Omega; \tag{1}$$

$$u\left(x,y\right) = f, \quad (x,y)\in\Gamma; \tag{2}$$

The problem (1) describes the distribution of the potential function $u(x,y)$ for the electrostatic stationary field [1]. If functions $f(x,y)$ and permittivity function $\varepsilon(x,y)>0$ are given, then we have the Direct Problem with respect to the unknown function $u(x,y)$. If bought functions $u(x,y)$, $\varepsilon(x,y)$ in Equation (1) are unknown, function $f(x,y)$ and some additional data on normal derivative of $u(x,y)$ on the boundary are given, we have the inverse coefficient problem.

A new approach for the solution of direct and inverse problems on the base of the General Ray Principle (*GRP*) was proposed by the author in [1, 2] for the stationary waves field. *GRP* leads to explicit analytical formulas (*GR*-method) and fast algorithms for solution of considering problems. There are two versions of *GR*-method: τ-version [1, 2] and p-version [3]. Here we extend the proposed approach to more general class of coefficients $\varepsilon(x,y)$ in Equation (1) for direct problems. We present also application of the *GR*-method for solution of the coefficient inverse problems for the Laplace type equation.

2. τ-VERSION OF *GR*-METHOD

The *GRP* means to construct for considering PDE an analogue as family of ODE describing the distribution of the function $u(x,y)$ along of "General Rays", which are presented by a straight line l with the traditional Radon parameterization due a parameter τ: $x = p\cos\varphi - \tau\sin\varphi$, $y = p\sin\varphi + \tau\cos\varphi$. Here $|p|$ is a length of the perpendicular from the centre of coordinates to the line l, $\varphi\in[0,\pi]$ is the angle between the axis x and this perpendicular.

Using the mentioned above parameterization, we shall define functions $u(x,y)$, $\varepsilon(x,y)$, $f(x,y)$ at $(x,y)\in l$ for fixed p, φ as functions $u(\tau)$, $\varepsilon(\tau)$, $f(\tau)$ of variable τ. We suppose that the domain Ω is a convex one. Let us define for every fixed p and φ functions $u_0(p,\varphi)=u(\tau_0)$, $u_1(p,\varphi)=u(\tau_1)$, for parameters τ_0, τ_1, which correspond to the points of the intersection of the line l and boundary of the domain.

Hence, the *GR*-principle leads to the assemblage (depending of p, φ) of ordinary differential equations:

$$\left(\varepsilon\left(\tau\right)u_\tau\left(\tau\right)\right)_\tau = 0, \quad \tau\in\left[\tau_0,\tau_1\right]; \tag{3}$$

as the local analogy of the Equation (1). Boundary conditions lead to the corresponding local boundary conditions for $u(\tau)$ at points τ_0,τ_1. We will designate the solution of the local problem (3) with such boundary conditions as $\bar{u}(\tau)$. For standard domains such as a circle or rectangular $\bar{\Omega}$ it is simple to calculate τ_0, τ_1 and functions $u_0(p,\varphi)$, $u_1(p,\varphi)$, using boundary function f and then obtain the solution $\bar{u}(\tau)$ in explicit analytical or approximate form, using well known standard formulas and numerical methods for the solution of boundary value problems for ordinary differential equations.

Formulation of τ-version of the *GR*-method: *the following formula for the solution of problem (1)–(2) is proposed*

$$u(x,y) = R^{-1}\left[u_0(p,\varphi)(\tau_1-\tau_0) + \frac{u_1(p,\varphi)-u_0(p,\varphi)}{K_1(p,\varphi)}K_0(p,\varphi)\right], \tag{4}$$

where R^{-1} is inverse Radon transform, functions

$$\gamma(\tau) = 1/\varepsilon(\tau); \quad k_0(\tau) = \int\limits_{\tau_0}^{\tau_1}\gamma(\xi)\,d\xi; \quad K_0(p,\varphi) = \int\limits_{\tau_0}^{\tau_1}k_0(\xi)d\xi; \quad K_1(p,\varphi) = k_0(\tau_1).$$

3. *P*-VERSION OF *GR*-METHOD

We suppose that Ω is the simple connected star region with the centre at the coordinate origin. The p-version of the GR-method we explain as the consequence of the next steps: 1) reduce boundary condition to homogeneous one; 2) describe the distribution of the potential function along the general ray (a straight line l) by its direct Radon transform $u(p,\varphi)$; 3) construct the family of ODE on the variable p with respect the function $u(p,\varphi)$; 4) solution of the constructed ODE with the zero boundary conditions; 5) calculate the inverse Radon transform of the obtained solution; 6) regress to the initial boundary condition.

We consider the case of piecewise constant function $\varepsilon(x,y)$: $\varepsilon(x,y) = \varepsilon_i, (x,y) \in \Omega_i,\ i = 1,\ 2;\ \Omega_1 \cup \Omega_2 = \Omega$. Let us define as Γ_1 a boundary curve of the contact of subdomaines Ω_1 and Ω_2, $u_1(x,y)$ and $u_2(x,y)$ — parts of the solution of the problem that corresponds to subdomaines Ω_1 and Ω_2. These functions must satisfy to conditions of continuity and continuity of the normal component of induction at the curve Γ_1. The realization of the p-version scheme for this case leads to consideration of additional condition for points 3) and 4). Then we get for the solution of the direct problem under consideration the explicit final formula, which can be written in the form similar to the case of constant function $\varepsilon(x,y)$ [3]. Implementation of this formula as algorithm and MATLAB programs gives possibility to make numerical solution of this class of problems. The result of one model numerical experiment is presented below.

4. SOLUTION OF INVERSE COEFFICIENT PROBLEM BY τ-VERSION OF *GR*-METHOD

The mentioned above additional boundary conditions for inverse problem with respect the function $\varepsilon(x,y)$ in Equation (3), can be presented by function $v(p,\varphi)$ and $J(p,\varphi)$ and relations for $u(\tau)$ at points $\tau_0,\ \tau_1$: $u(\tau_1) - u(\tau_0) = v(p,\varphi)$; $\varepsilon(\tau_0)u_\tau(\tau_0) = J(p,\varphi)$. The main formula for $\varepsilon(x,y)$:

$$\varepsilon(x,y) = 1/R^{-1}\left[\frac{v(p,\varphi)}{J(p,\varphi)}\right], \tag{5}$$

Formula (5) represents the General Ray method for the inverse problem [4]. This formula can be applied also for space structures. This is approved by numerical experiments, one of which is presented below.

5. REGULARIZATION OF GR-MRTHOD WITH RECURSIVE SMOOTHING BY SPLINES

Analysis of formulas for inverse Radon transformation shows that its instability for discrete noised data is equivalent to the instability of the problem of the numerical differentiation of the noised function $\bar{v}(p,\varphi)$ with respect to the variable p. The regularization of the inversion of Radon transform was constructed by author in [5] on the base of the Recursive Spline Smoothing (RSS).

RSS uses the explicit formulas for two-dimensional spline on the regular uniform grid $\{p_i', \varphi_j\}$, $p_i = -1 + h(i-1)$, $i = -2, \ldots, n+2$; $\varphi_j = -1 + h_\varphi(j-1)$, $j = -2, \ldots, n+2$; $h = 2/(n-1)$, $h_\varphi = \pi/(n-1)$. Let $s_i(u)$ be a local basic cubic spline, constructed on the units $w_{i-2}, \ldots, w_{i+2}$; $i = 0, \ldots, n+1$; where w is p, or w is φ. Mentioned formulas are the next ones:

$$S_k(p,\varphi) = \sum_{i=1}^{n}\sum_{j=1}^{n} S_{k-1}(p_i,\varphi_i)\,s_i(p)\,s_j(\varphi), \quad k = 1,\ 2, \ldots, \bar{K}; \quad S_0(p_i,\varphi_j) = \bar{\nu}(p_i,\varphi_j) \tag{6}$$

The number of smoothes $\bar{K}$ is the regularization parameter, which can be chosen here in accordance with residual (discrepancy) principle, using the discrete estimation δ of the errors. Theoretical and

numerical justifications of the regularization properties of this type of smoothing are presented in [6].

6. RESULTS OF NUMERICAL EXPERIMENTS

We consider the example for solution of direct problem with piecewise constant function $\varepsilon(x, y) = 2,\ -x < y$, $\varepsilon(x, y) = 1,\ y < -x$, and boundary condition function $\bar{f}(\alpha) = r_0(\alpha)\cos\alpha + r_0(\alpha)\sin\alpha$, $-\pi/4 < \alpha < 3\pi/4$, $\bar{f}(\alpha) = 2(r_0(\alpha)\cos\alpha + r_0(\alpha)\sin\alpha)$, $3\pi/4 < \alpha < 7\pi/4$.

At Figure 1, it is presented the result of application τ-version of GR-method with formula (5) for domain as unit circle, i.e., $r_0(\alpha) = 1$. At Figure 2, we can see the result of application p-version of GR-method for the same example with $r_0(\alpha) = 0.8 + 0.2\sin(3\alpha)$. At Figure 3, we present reconstruction of space structure by formula (5) which applied for slices at some fixed values of coordinate z. For this problem it is better to us RSS even for exact data.

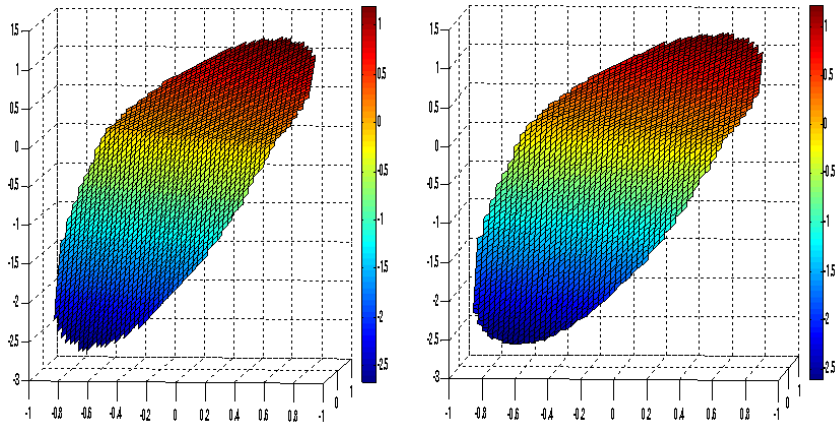

Figure 1: (a) Exact solution; (b) Approximate solution, reconstructed on exact data.

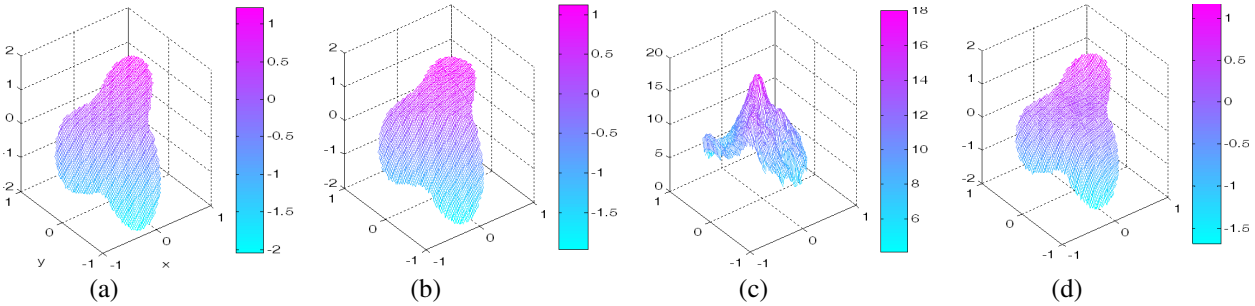

Figure 2: (a) Exact solution; (b) Approximate solution, reconstructed on exact data; (c) Approximate solution, reconstructed on noised data without regularization; (d) Approximate solution, reconstructed on noised data with RSS.

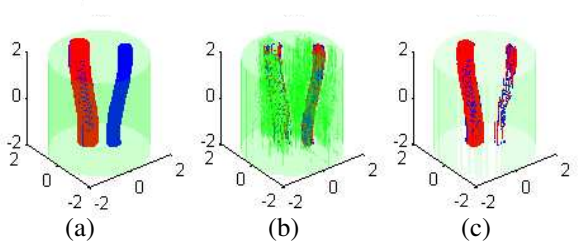

Figure 3: (a) Exact solution; (b) Approximate solution, reconstructed on exact data without RSS; (c) Approximate solution, reconstructed on exact data with RSS.

7. CONCLUSIONS

The approach based on the *GRP* is extended to direct boundary value problems for the Laplace type equation with piecewise constant coefficients. τ-version and p-version of *GR*-method are adapted to the class of such problems.

The plane τ-version of *GR*-method for solution of inverse problems is applied to the space structures. The approximation properties of the constructed algorithms are illustrated by numerical experiments.

ACKNOWLEDGMENT

The author acknowledges to VIEP of Merited Autonomous University of Puebla, Mexico for the support of the part of this investigation in the frame of the Project No. GRA-EXC12-I.

REFERENCES

1. Grebennikov, A. I., "Fast algorithm for solution of dirichlet problem for laplace equation," *WSEAS Transaction on Computers Journal*, Vol. 2, No. 4, 1039–1043, 2003.
2. Grebennikov, A. I., "The study of the approximation quality of *GR*-method for solution of dirichlet problem for Laplace equation," *WSEAS Transaction on Mathematics Journal*, Vol. 2, No. 4, 312–317, 2003.
3. Grebennikov, A., "Fast algorithms and MATLAB software for solution of the dirichlet boundary value problems for elliptic partial differential equations in domains with complicated geometry," *WSEAS Transaction on Mathematics Journal*, Vol. 7, No. 4, 173–182, 2008.
4. Grebennikov, A. I., "A novel approach for the solution of direct and inverse problems of some equations of mathematical physics," *Proceedings of the 5th International Conference on Inverse Problems in Engineering: Theory and Practice*, D. Lesnic, Ed., Vol. II, Chapter G04, 1–10, Leeds University Press, Leeds, UK, 2005.
5. Grebennikov, A. and C. Gamio, "Fast post-processing algorithm for improving electrical capacitance tomography image reconstruction," *Inverse Problems in Science and Engineering*, Vol. 14, No. 1, Jan. 64–74, 2006.
6. Morozov, V. A. and A. I. Grebennikov, *Methods for Solution of Ill-posed Problems: Algorithmic Aspects*, Moscow University Press, Moscow, 1992 (English Edition in 2005).

Inverse Problems to Determine Constant Permittivity and Coefficient of Nonlinearity in the Problem of TE Wave Propagation in a Layer with Kerr Nonlinearity

D. V. Valovik
Penza State University, 40 Krasnaya Street, Penza 440026, Russia

Abstract— We consider a plane one-layer waveguide structure. The layer is located between two half-spaces with constant permittivities. The permittivity inside the layer is described by Kerr law: $\varepsilon = \varepsilon_2 + \alpha|\mathbf{E}|^2$, where ε_2 is a constant part of the permittivity, α is a coefficient of nonlinearity and $\mathbf{E} = (E_x, E_y, E_z)^T$ is the electric field. We suppose that ε_2 and α are unknown constants. The problem is to find these unknown constants. To solve this problem we can use amplitudes I, R, and T of the incident, reflected, and transmitted waves respectively. Amplitude I is supposed to be prescribed and amplitudes R, T are supposed to be measured.

1. INTRODUCTION

Here we consider inverse problems to determine parameters of Kerr law. We use simple geometry, namely, isotropic dielectric layer, which is infinite in two directions and special type of electromagnetic field (plane monochromatic polarized waves). In spite of the fact that often inverse problems are very difficult to solve in this case we managed to find simple explicit formulae for sought for parameters. For inverse problems to determine complex permittivity for isotropic homogeneous diaphragm placed in a rectangular waveguide see [1] and for anisotropic nonhomogeneous body placed in a rectangular waveguide see [2].

2. STATEMENT OF THE PROBLEM

Consider electromagnetic waves propagating through homogeneous isotropic nonmagnetic dielectric layer. The permittivity in the layer is described by Kerr law. The layer is located between two half-spaces $x < 0$ and $x > h$ in Cartesian coordinate system $Oxyz$. The half-spaces are filled with homogeneous isotropic nonmagnetic media without any sources and have constant permittivities ε_1 and ε_3, respectively (ε_1 and ε_3 are arbitrary real values). Suppose that everywhere $\mu = \mu_0$ is the permeability of free space.

The fields depend harmonically on time

$$\tilde{\mathbf{E}}(x,y,z,t) = \mathbf{E}_+(x,y,z)\cos\omega t + \mathbf{E}_-(x,y,z)\sin\omega t,$$
$$\tilde{\mathbf{H}}(x,y,z,t) = \mathbf{H}_+(x,y,z)\cos\omega t + \mathbf{H}_-(x,y,z)\sin\omega t,$$

where ω is the circular frequency; $\tilde{\mathbf{E}}$, $\mathbf{E}_+$, $\mathbf{E}_-$, $\tilde{\mathbf{H}}$, $\mathbf{H}_+$, $\mathbf{H}_-$ are real functions. Below the time multipliers $\cos\omega t$, $\sin\omega t$ are omitted.

Form complex amplitudes $\mathbf{E} = \mathbf{E}_+ + i\mathbf{E}_-$, $\mathbf{H} = \mathbf{H}_+ + i\mathbf{H}_-$, where $\mathbf{E} = (E_x, E_y, E_z)^T$, $\mathbf{H} = (H_x, H_y, H_z)^T$; $(\,\cdot\,)^T$ is the transposition operation, and

$$E_x = E_x(x,y,z), \quad E_y = E_y(x,y,z), \quad E_z = E_z(x,y,z),$$
$$H_x = H_x(x,y,z), \quad H_y = H_y(x,y,z), \quad H_z = H_z(x,y,z).$$

The electromagnetic field $\mathbf{E}$, $\mathbf{H}$ satisfies the Maxwell equations

$$\begin{aligned} \mathrm{rot}\mathbf{H} &= -i\omega\varepsilon\mathbf{E}, \\ \mathrm{rot}\mathbf{E} &= i\omega\mu\mathbf{H}, \end{aligned} \tag{1}$$

the continuity condition for the tangential field components on the boundaries $x = 0$, $x = h$ and the radiation condition at infinity: the electromagnetic field exponentially decays as $|x| \to \infty$ in the domains $x < 0$ and $x > h$.

The permittivity inside the layer is described by Kerr law

$$\varepsilon = \varepsilon_2 + \alpha\,|\mathbf{E}|^2,$$

where ε_2 is a constant part of the permittivity, α is the coefficient of nonlinearity.

We look for solutions to Maxwell's equations in the entire space.

Geometry of the problem is shown in Fig. 1.

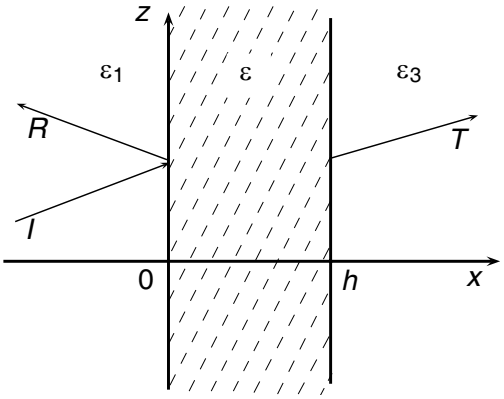

Figure 1.

3. TE WAVES

Consider TE waves $\mathbf{E} = (0, E_y, 0)^T$, $\mathbf{H} = (H_x, 0, H_z)^T$. It is easy to show that for considered geometry the fields components do not depend on y. Waves propagating along z depend on z harmonically. So the fields components have the form

$$E_y = \mathrm{E}_y(x)e^{i\gamma z}, \quad H_x = \mathrm{H}_x(x)e^{i\gamma z}, \quad H_z = \mathrm{H}_z(x)e^{i\gamma z}, \tag{2}$$

where γ is supposed to be known.

Substituting components (2) into (1), normalizing accordingly with the formulae $\tilde{x} = kx$, $\frac{d}{dx} = k\frac{d}{d\tilde{x}}$, $\tilde{\gamma} = \frac{\gamma}{k}$, $\tilde{\varepsilon}_j = \frac{\varepsilon_j}{\varepsilon_0}$, $j = 1, 2, 3$, where $k^2 = \omega^2\mu_0\varepsilon_0$, denoting by $Y(\tilde{x}) := \mathrm{E}_y(\tilde{x})$ and omitting the tilde, we obtain the equation [3]

$$Y''(x) = \gamma^2 Y(x) - \varepsilon Y(x), \tag{3}$$

where

$$\varepsilon = \begin{cases} \varepsilon_1, & x < 0 \\ \varepsilon_2 + \alpha Y^2, & 0 < x < h \\ \varepsilon_3, & x > h \end{cases}$$

4. SOLUTIONS TO DIFFERENTIAL EQUATIONS IN HALF-SPACES

For $x < 0$ we have $\varepsilon = \varepsilon_1$. From Equation (3), we obtain the equation

$$Y''(x) = \left(\gamma^2 - \varepsilon_1\right) Y(x).$$

Its general solution is

$$Y(x) = C_1 e^{-\sqrt{\gamma^2-\varepsilon_1}x} + C_2 e^{\sqrt{\gamma^2-\varepsilon_1}x}.$$

Introduce the notation $k_1^2 := \gamma^2 - \varepsilon_1$, $I := C_1$, and $R := C_2$. Then we obtain

$$Y(x) = Ie^{-k_1 x} + Re^{k_1 x}. \tag{4}$$

It is supposed that $\gamma^2 - \varepsilon_1 > 0$. Otherwise it will be impossible to satisfy the radiation condition.
For $x > h$ we have $\varepsilon = \varepsilon_3$. From Equation (3) we obtain the equation

$$Y''(x) = \left(\gamma^2 - \varepsilon_3\right) Y(x).$$

Its general solution is

$$Y(x) = C_3 e^{-(x-h)\sqrt{\gamma^2-\varepsilon_3}} + C_4 e^{(x-h)\sqrt{\gamma^2-\varepsilon_3}}.$$

Taking into account the radiation condition at infinity we obtain $C_4 = 0$.
Introduce the notation $k_3^2 := \gamma^2 - \varepsilon_3$, $T := C_3$. Then we obtain

$$Y(x) = Te^{-(x-h)k_3} \tag{5}$$

It is supposed that $\gamma^2-\varepsilon_3>0$. Otherwise it will be impossible to satisfy the radiation condition. It follows from formulae (4), (5) that $\gamma^2>\max(\varepsilon_1,\varepsilon_3)$.

Inside the layer we obtain

$$Y''(x)=-\left(\varepsilon_2-\gamma^2+\alpha Y^2(x)\right)Y(x). \tag{6}$$

5. TRANSMISSION CONDITIONS AND FORMULATION OF THE PROBLEM

Tangential components of an electromagnetic field are known to be continuous at the interfaces.

In this case the tangential components are $E_y\ \ H_z$. Since $\frac{\partial E_y}{\partial x}=i\omega\mu H_z$; then the function $\frac{\partial E_y}{\partial x}$ is also continuous at the interfaces.

The continuity conditions imply the following conditions for functions Y and Y'

$$[Y]_{x=0}=0,\quad [Y]_{x=h}=0,\quad [Y']_{x=0}=0,\quad [Y']_{x=h}=0, \tag{7}$$

where $[f]_{x=x_0}=\lim\limits_{x\to x_0-0}f(x)-\lim\limits_{x\to x_0+0}f(x)$.

Then we obtain

$$Y(0-0)=I+R,\quad Y(h+0)=T,\quad Y'(0-0)=(-I+R)k_1,\quad Y'(h+0)=-Tk_3 \tag{8}$$

Inverse problem IP: *find (real) constant part ε_2 of permittivity ε and (real) coefficient of nonlinearity α from the known amplitudes I, R, and T of the incident, reflected, and transmitted waves respectively.*

6. SOLUTION TO THE INVERSE PROBLEM

Assuming that the permittivity inside the layer is described by Kerr law: $\varepsilon=\varepsilon_2+\alpha Y^2$ and consider nonlinear Equation (6).

There are at least two ways to solve problem IP. The first way requires to carry out two measurements (R and T at one frequency ω of the incident wave). In addition in this case it is necessary to have explicit solution of Equation (6). The second way implies to carry out four measurements (R_1 and T_1 at frequency ω_1 and R_2 and T_2 at frequency ω_2). In this case it is not necessary to get explicit solution of Equation (6) as opposed to the first way. However it is necessary to have first integral of Equation (6). In spite of the fact that Equation (6) is integrable in Weierstrass elliptic functions we prefer to investigate the second way to solve considered problem.

The first integral of Equation (6) has the form

$$Y'^2(x)=-k_2^2Y^2(x)-\frac{\alpha}{2}Y^4(x)+c, \tag{9}$$

where $k_2^2=\varepsilon_2-\gamma^2$ and C is the constant of integration.

Let γ_1, k_1^2, k_2^2, k_3^2, I_1, R_1, T_1 correspond to ω_1 and γ_2, $\tilde{k}_1^2$, $\tilde{k}_2^2$, $\tilde{k}_3^2$, I_2, R_2, T_2 correspond to ω_2.

Setting $x=0$ and $x=h$ in (9), from transmission conditions (7) we obtain

$$\begin{cases} Y'^2(0-0)=-k_2^2Y^2(0-0)-\frac{\alpha}{2}Y^4(0-0)+c_1,\\ Y'^2(h+0)=-k_2^2Y^2(h+0)-\frac{\alpha}{2}Y^4(h+0)+c_1, \end{cases}$$

and

$$\begin{cases} Y'^2(0-0)=-\tilde{k}_2^2Y^2(0-0)-\frac{\alpha}{2}Y^4(0-0)+c_2,\\ Y'^2(h+0)=-\tilde{k}_2^2Y^2(h+0)-\frac{\alpha}{2}Y^4(h+0)+c_2 \end{cases}$$

for ω_1 and ω_2 respectively.

Using formulae (8) we find from the latter systems

$$\begin{cases} k_1^2(-I_1+R_1)^2=-k_2^2(I_1+R_1)^2-\frac{\alpha}{2}(I_1+R_1)^4+c_1,\\ k_3^2T_1^2=-k_2^2T_1^2-\frac{\alpha}{2}T_1^4+c_1, \end{cases}$$

and

$$\begin{cases} \tilde{k}_1^2(-I_2+R_2)^2=-\tilde{k}_2^2(I_2+R_2)^2-\frac{\alpha}{2}(I_2+R_2)^4+c_2,\\ \tilde{k}_3^2T_2^2=-\tilde{k}_2^2T_2^2-\frac{\alpha}{2}T_2^4+c_2. \end{cases}$$

From this systems we obtain

$$\begin{cases} \varepsilon_2 \left(T_1^2-(I_1+R_1)^2\right)+\alpha\frac{1}{2}\left(T_1^4-(I_1+R_1)^4\right)=\gamma_1^2\left(T_1^2-(I_1+R_1)^2\right)+k_1^2(I_1-R_1)^2-k_3^2T_1^2, \\ \varepsilon_2 \left(T_2^2-(I_2+R_2)^2\right)+\alpha\frac{1}{2}\left(T_2^4-(I_2+R_2)^4\right)=\gamma_2^2\left(T_2^2-(I_2+R_2)^2\right)+\tilde{k}_1^2(I_2-R_2)^2-\tilde{k}_3^2T_2^2. \end{cases} \tag{10}$$

This is a linear system w.r.t to ε_2, α. We rewrite it in a more convenient form

$$\begin{cases} \varepsilon_2 A_1 + \alpha B_1 = C_1, \\ \varepsilon_2 A_2 + \alpha B_2 = C_2. \end{cases}$$

where $A_1,\ A_2,\ B_1,\ B_2,\ C_1,\ C_2$ are defined by system (10).

Solve this system we obtain

$$\begin{aligned} \varepsilon_2 &= \frac{B_2C_1 - B_1C_2}{A_1B_2 - A_2B_1}, \\ \alpha &= \frac{A_1C_2 - A_2C_1}{A_1B_2 - A_2B_1}. \end{aligned} \tag{11}$$

As it is seen from formula (11) values ε_2 and α are uniquely expressed through amplitudes I, R, and T.

7. CONCLUSION

In this study, we suggest an approach to determine constant part ε_2 and coefficient of nonlinearity α in Kerr law: $\varepsilon = \varepsilon_2 + \alpha|\mathbf{E}|^2$. This approach allows to us uniquely determine ε_2 and α by means of two known amplitudes I_1 and I_2 and four measured amplitudes R_1, R_2, and T_1, T_2 at frequencies ω_1 and ω_2 respectively. Amplitudes I, R, and T correspond to the incident, reflected, and transmitted waves respectively (see Fig. 1). It is well known that the nonlinear susceptibility in Kerr law can be expressed through α. This means that if it is possible to measure R and T then it is easy to determine the nonlinear susceptibility.

We would like to pay reader's attention to the fact that it is possible to decrease a number of measurement if we can find explicit solution of Equation (6). However in this case we can not find explicit expression for ε_2 and α but we can find transcendental equations for them. If we consider a linear case only, that is $\varepsilon = \varepsilon_2$, then this transcendental equation can be transformed into the form, which contains amplitudes I, R only (or I, T only). You can see [3] for details of the linear case.

ACKNOWLEDGMENT

I should like to thank Prof. Yu. G. Smirnov for fruitful discussions. The work is supported by Russian Federation President Grant (MK-2074.211.1) and the Russian Foundation for Basic Research, project No. 11-07-00330-A.

REFERENCES

1. Smirnov, Y. G., Y. V. Shestopalov, and E. D. Derevyanchuk, "Permittivity reconstruction of layered dielectrics in a rectangular waveguide from the transmission coefficients at different frequencies," *Proceedings of the Annual Workshop on Inverse Problems within the Visby Program*, 2012 (approved).
2. Smirnov, Y. G. and Y. V. Shestopalov, "Existence and uniqueness of a solution to the inverse problem of the complex permittivity reconstruction of a dielectric body in a waveguide," *Inverse Problems*, Vol. 26, No. 10, 105002–105005, 2010.
3. Schürmann, H. W., V. S. Serov, and Y. V. Shestopalov, "Reflection and transmission of a plane TE-wave at a lossless nonlinear dielectric film," *Physica D*, Vol. 158, 197–215, 2001.

Reconstruction of Complex Permittivity of a Nonhomogeneous Body of Arbitrary Shape in a Rectangular Waveguide

Yury G. Smirnov, **Mikhail Yu. Medvedik**, **and Elena E. Grishina**
Penza State University, 40 Krasnaya Street, Penza 440026, Russia

Abstract— We present statement of uniqueness and solution techniques for inverse problem of the electromagnetic wave scattering from a dielectric inclusion in a 3D waveguide. The inverse problem consists in reconstructing the permittivity from the reflection characteristics. The approach employs a volume singular integral equation (VSIE). The inverse problem is solved by the method of iterations applied to VSIE. Numerical results for the determination of permittivity of parallelepiped-shaped dielectric bodies are presented.

1. STATEMENT OF INVERSE PROBLEMS

Determination of electric and magnetic parameters of dielectric materials of complicated structure and geometry is an urgent task finding numerous applications [1–3]. We consider the VSIE-based method of finding permittivity of inhomogeneous dielectric samples of materials having arbitrary geometric shape placed in a rectangular waveguide with perfectly conducting walls.

Assume that a waveguide

$$P = \{x\colon 0 < x_1 < a,\ 0 < x_2 < b,\ -\infty < x_3 < \infty\}$$

with the perfectly conducting boundary surface ∂P is given in the Cartesian coordinate system. A three-dimensional body Q ($Q \subset P$ is a domain) with a constant magnetic permeability μ_0 and variable permittivity $\varepsilon(x)$ is placed in the waveguide. Function $\varepsilon(x)$ is bounded in $\bar{Q}$, $\varepsilon \in L_\infty(Q)$, and $\varepsilon^{-1} \in L_\infty(Q)$. The boundary ∂Q of domain Q is piecewise smooth. The case of variable permeability (when the permittivity is a constant equal to ε_0) is considered in a similar manner by performing an appropriate replacement of notations.

We assume that the electromagnetic field $\mathbf{E},\ \mathbf{H} \in L_{2,loc}(P)$ in the waveguide is excited by an external field with the time dependence $e^{-i\omega t}$; the source of the external field is the electric current $\mathbf{j}^0 \in L_{2,loc}(P)$. In the domain $P \subset R^3$ the standard differential operators grad, div, rot are understood in the sense of distributions.

Choose the waveguide parameters so that $\pi/a < k_0 < \pi/b$, where k_0 is the free-space wave number, $k_0^2 = \omega^2\varepsilon_0\mu_0$, and ω is the circular frequency. In this case, only one mode propagates in the waveguide (namely, the principal $\mathbf{H}_{10}$ mode), and all other modes are evanescent (decaying). Next, let $\mathbf{E}^0(x) = \mathbf{e_2} A^{(+)} i\omega\mu_0 \frac{\pi}{a} \sin\frac{\pi x_1}{a} e^{-i\gamma_1^{(2)} x_3}$, $\mathbf{H}^0 = (i\omega\mu_0)^{-1}\,\mathrm{rot}\mathbf{E}^0$ be the given incident field (a waveguide mode), where $A^{(+)}$ is the known amplitude of the incident wave, $\gamma_1^{(2)} = \sqrt{k_0^2 - \frac{\pi^2}{a^2}}$, and $\mathbf{e_2}$ is the second Cartesian ort-vector; the current $\mathbf{j}_E^0 = \mathrm{rot}\mathbf{H}^0 + i\omega\varepsilon_0\mathbf{E}^0$.

We will seek weak (generalized) solutions to Maxwell's system of equations

$$\begin{aligned} \mathrm{rot}\mathbf{H} &= -i\omega\varepsilon\mathbf{E} + \mathbf{j}_E^0 \\ \mathrm{rot}\mathbf{E} &= i\omega\mu_0\mathbf{H}. \end{aligned} \tag{1}$$

The tangential components of field $\mathbf{E}$ satisfy the boundary conditions on the waveguide walls

$$\mathbf{E}_\tau|_{\partial P} = 0.$$

Solutions to (1) satisfy the conditions at infinity: fields $\mathbf{E}$ and $\mathbf{H}$ admit for $x_3 > C$ and sufficiently large $C > 0$ the representations

$$\begin{pmatrix} \mathbf{E} \\ \mathbf{H} \end{pmatrix} = \sum_p R_p^{(+)} e^{i\gamma_p^{(1)}|x_3|} \begin{pmatrix} \lambda_p^{(1)}\Pi_p e_3 - i\gamma_p^{(1)}\nabla_2\Pi_p \\ -i\omega\varepsilon_0\,(\nabla_2\Pi_p)\times e_3 \end{pmatrix} + \sum_p Q_p^{(+)} e^{i\gamma_p^{(2)}|x_3|} \begin{pmatrix} i\omega\mu_0\,(\nabla_2\psi_p)\times e_3 \\ \lambda_p^{(2)}\Psi_p e_3 - i\gamma_p^{(2)}\nabla_2\Psi_p \end{pmatrix},$$

and for $x_3 < -C$

$$\begin{pmatrix} \mathbf{E} \\ \mathbf{H} \end{pmatrix} = \begin{pmatrix} \mathbf{E}^0 \\ \mathbf{H}^0 \end{pmatrix} + \sum_p R_p^{(-)} e^{i\gamma_p^{(1)}|x_3|} \begin{pmatrix} \lambda_p^{(1)} \Pi_p e_3 - i\gamma_p^{(1)} \nabla_2 \Pi_p \\ -i\omega\varepsilon_0 \left(\nabla_2 \Pi_p\right) \times e_3 \end{pmatrix} + \sum_p Q_p^{(-)} e^{i\gamma_p^{(2)}|x_3|} \begin{pmatrix} i\omega\mu_0 \left(\nabla_2 \psi_p\right) \times e_3 \\ \lambda_p^{(2)} \Psi_p e_3 - i\gamma_p^{(2)} \nabla_2 \Psi_p \end{pmatrix}, \tag{2}$$

where

$$\gamma_p^{(j)} = \sqrt{k_0^2 - \lambda_p^{(j)}}, \quad \mathrm{Im}\gamma_p^{(j)} > 0 \ \text{ or } \ \mathrm{Im}\gamma_p^{(j)} = 0, \ \ k\gamma_p^{(j)} \geq 0, \tag{3}$$

$\lambda_p^{(1)}$, $\Pi_p(x_1, x_2)$ and $\lambda_p^{(2)}$, $\Psi_p(x_1, x_2)$ are the complete system of eigenvalues and orthogonal and normalized in $L_2(\Pi)$ eigenfunctions of the two-dimensional Laplace operator $-\Delta$ in the rectangle

$$\Pi := \{(x_1, x_2): 0 < x_1 < a, \ 0 < x_2 < b\}$$

with the Dirichlet and the Neumann conditions, respectively; and $\nabla_2 \equiv e_1 \partial/\partial x_1 + e_2 \partial/\partial x_2$.

The inverse problem that we address consists in the determination of $\varepsilon(x)$ from the given reflection, $R = Q_1^{(-)}/A^{(+)}$, coefficients. The 'given' here means that these quantities are measured at one or several frequencies of the incident field.

The simplest case here is when inclusion Q is an isotropic dielectric body and (effective) permittivity $\varepsilon(x)$ of the medium filling the body is an unknown constant to be determined. When the inclusion is situated in a guide that supports only *one* principal guided mode, then we prove that the data in the inverse problem that provide uniqueness of reconstructing effective permittivity can be taken as two (known) complex numbers, the transmission and reflection coefficients, measured at one frequency.

2. VSIE METHOD

It is shown that the considered inverse problem can be reduced to the solution of a VSIE

$$\left[\frac{\varepsilon(x)}{\varepsilon_0} - 1\right]^{-1} \mathbf{J}(x) = \mathbf{E}^0(x) + k_0^2 \int\limits_Q \tilde{G}_E(x, y) \mathbf{J}(y)\, dy + \mathrm{grad}\,\mathrm{div} \int\limits_Q \tilde{G}_E(x, y) \mathbf{J}(y)\, dy, \quad x \in Q.$$

where the current $\mathbf{J}(x) = \left[\frac{\varepsilon(x)}{\varepsilon_0} - 1\right] \mathbf{E}(x)$, and $\tilde{G}_E(x, y)$ is the diagonal Green tensor [2] with the components

$$\begin{aligned} G_E^1 &= \frac{2}{ab} \sum_{n=0}^{\infty} \sum_{m=1}^{\infty} \frac{e^{-\gamma_{nm}|x_3 - y_3|}}{\gamma_{nm}(1 + \delta_{0n})} \cos\frac{\pi n}{a} x_1 \sin\frac{\pi m}{b} x_2 \cos\frac{\pi n}{a} y_1 \sin\frac{\pi m}{b} y_2, \\ G_E^2 &= \frac{2}{ab} \sum_{n=1}^{\infty} \sum_{m=0}^{\infty} \frac{e^{-\gamma_{nm}|x_3 - y_3|}}{\gamma_{nm}(1 + \delta_{0m})} \sin\frac{\pi n}{a} x_1 \cos\frac{\pi m}{b} x_2 \sin\frac{\pi n}{a} y_1 \cos\frac{\pi m}{b} y_2, \\ G_E^3 &= \frac{2}{ab} \sum_{n=1}^{\infty} \sum_{m=1}^{\infty} \frac{e^{-\gamma_{nm}|x_3 - y_3|}}{\gamma_{nm}} \sin\frac{\pi n}{a} x_1 \sin\frac{\pi m}{b} x_2 \sin\frac{\pi n}{a} y_1 \sin\frac{\pi m}{b} y_2. \end{aligned}$$

In these expressions, $\gamma_{nm} = \sqrt{\left(\frac{\pi n}{a}\right)^2 + \left(\frac{\pi m}{b}\right)^2 - k_0^2}$, where $\mathrm{Im}\gamma_{nm} \geq 0$ and if $\mathrm{Im}\gamma_{nm} = 0$.

We show that a relation between the transmission coefficient and permittivity can be written, using an asymptotic expression for the scattered field that follows from condition at infinity (2) and (3), in the form

$$Q_1^{(-)} = \frac{k_0^2}{b\gamma_{10} i\pi\omega\mu_0} \int\limits_Q \sin\frac{\pi y_1}{a} e^{-i\gamma_1^{(2)} y_3} \left[\frac{\varepsilon(y)}{\varepsilon_0} - 1\right] \mathbf{E}(y) \cdot \mathbf{e_2} dy, \tag{4}$$

where $\gamma_{10} = \sqrt{\frac{\pi^2}{a^2} - k_0^2}$. Coefficient $Q_1^{(-)}$ is assumed to be the known measured quantity. It is necessary to determine permittivity $\varepsilon(x)$, $x \in Q$ using generally a series of measurements.

When the inclusion is a homogeneous body and its permittivity is a constant to be determined, then it is sufficient to perform the measurement at *one* frequency. Finally, the constant permittivity can be efficiently calculated using an iteration procedure of the fixed-point method applied to (4) which is treated as a nonlinear operator equation.

The situation becomes essentially different when an inhomogeneous obstacle is considered. As the first natural step towards the solution technique that develops the VSIE method for this case we propose the following approach: it is assumed that the number of unknown parameters characterizing the inclusion is finite; consequently, the permittivity is given by a piecewise constant function of coordinates so that the inclusion is a piecewise homogeneous body. Then we justify the idea that in this case the number of measurements must be finite in order to uniquely determine all unknown permittivity values.

In more detail: assume that body (domain) Q consists of N subdomains Q_j such that $Q = \bigcup\limits_j Q_j$ and $Q_i \bigcap Q_j = \emptyset,\ i \neq j$. Moreover, $\varepsilon(x) = \varepsilon^{(j)}$ for $x \in Q_j$; that is, the permittivity is constant in every subdomain. Then the total number of unknown parameters will be N. The measurements are performed at several frequencies $\omega^{(1)}, \omega^{(2)}, \ldots, \omega^{(N)}$; the corresponding values of the wavenumber is calculated by the formula $k_0^{(i)} = \omega^{(i)}\sqrt{\varepsilon_0\mu_0}$.

3. PARALLELEPIPED-SHAPED INCLUSIONS

Generally the full computational scheme should be applied for the numerical solution to the inverse problem of reconstructing the permittivity. Following [2, 3] demonstrate how it works when the body is a parallelepiped

$$Q = \{x\colon a_1 < x_1 < a_2,\ b_1 < x_2 < b_2,\ c_1 < x_3 < c_2\}\,.$$

Choose a uniform rectangular grid in Q formed by a set of elementary parallelepipeds and describe a two-layer iteration scheme [3] for solving the inverse problem under study according to the formulas

$$\xi_n(x) = \left[\frac{\varepsilon_n(x)}{\varepsilon_0} - 1\right]^{-1}, \tag{5}$$

$$\xi_n(x)\mathbf{J}_n(x) - k_0^2 \int\limits_Q \tilde{G}(x,y)\mathbf{J}_n(y)dy - \operatorname{grad}\operatorname{div}\int\limits_Q \tilde{G}(x,y)\mathbf{J}_n(y)dy = \mathbf{E}^0(x),\quad x \in Q \tag{6}$$

$$\mathbf{E}_n(x) = \xi_n(x)\mathbf{J}_n(x), \tag{7}$$

$$F = k_0^2 \frac{1}{iab\gamma_1^{(2)}} \int\limits_Q \sin\left(\frac{\pi y_1}{a}\right) e^{-i\gamma_1^{(2)} y_3}\eta_{n+1}(x)\mathbf{E}_n(y)\cdot e_2 dy \tag{8}$$

where

$$F = \frac{i\pi\omega\mu_0}{a}Q_1^{(-)},\quad \eta_n(x) = \left[\frac{\varepsilon_n(x)}{\varepsilon_0} - 1\right],\quad \xi_n(x) = \eta_n^{-1}(x)\,. \tag{9}$$

The calculations by (5)–(9) are performed as follows. First, we choose an initial approximation $\varepsilon_0(x) = \varepsilon_e(n=0)$, where $\varepsilon_e = \varepsilon_{eff}$ and ε_{eff} is the effective permittivity of the body calculated from the solution to the inverse problem obtained in the case when the inclusion has the constant permittivity [2]. Note that one cannot set $\varepsilon_e = \varepsilon_0$ because it is not possible to find the electric field from (7). The value of $\xi_0(x)$ is calculated by formula (3). Next, we use (6) to determine current $\mathbf{J}_n(x)$ as a solution to the integro-differential equation by the collocation method. Then we find electric field $\mathbf{E}_n(x)$ on the grid points in terms of the current using (7). We repeat this procedure N times at different $k_0 = k_0^{(1)}$, $k_0 = k_0^{(2)}$, …, $k_0 = k_0^{(N)}$ obtaining N values $\mathbf{E}_n^{(1)}$, $\mathbf{E}_n^{(2)}$, …, $\mathbf{E}_n^{(N)}$ (calculated at different $k_0^{(1)}$, $k_0^{(2)}$, …, $k_0^{(N)}$). This terminates the 'first-layer' calculation stage.

At the 'second-layer' calculation stage, we use the known $\mathbf{E}_n^{(i)}(x)$ $(i = 1, \ldots, N)$ and calculate the next value $\eta_{n+1}(x)$ from formula (8). To this end, it is necessary to solve the system of linear algebraic equations (SLAE) composed from (8) with respect to the unknown parameters. The transmission coefficients $F_i = F(k_0^{(i)})$ are determined as a result of measurements, and it is assumed that $A^{(+)} = 1$.

We assumed that $\eta_n(x) = \eta_n^{(j)}$ at $x \in Q_j$. Also, let each subdomain Q_j be the union of the elementary grid parallelepipeds, $Q_j = \bigcup_l \Pi_l$. We also set $\mathbf{E}_n^{(i)}(x) = \mathbf{E}_n^{(i,l)}$ at $x \in \Pi_l$; this means that inside the elementary parallelepipeds, the field is approximated by a constant.

Formula (8) yields a finite-dimensional SLAE. Let us form the matrices $E = \{\mathbf{e}_2 \cdot \mathbf{E}_n^{(i,l)}\}_{i=1,\,l=1}^{N,N_0}$ and $H = \{H_{lj}\}_{l=1,j=1}^{N_0,N}$ of the size, respectively, $N \times N_0$ and $N_0 \times N$; here $H_{lj} = 0$ at the values of index l such that $\Pi_l \not\subset Q_j$. Finally we obtain a SLAE with the $N \times N$-matrix $A_N = EH$:

$$A_N \eta_{n+1} = B$$

with respect to the unknowns $\eta_{n+1} = (\eta_{n+1}^{(1)}, \ldots, \eta_{n+1}^{(N)})^T$. Here and below, we assume that the piecewise constant function $\eta_{n+1} = \eta_{n+1}(x) =$ and vector $(\eta_{n+1}^{(1)}, \ldots, \eta_{n+1}^{(N)})^T$ are identical because they uniquely determine each other.

Next, we verify the fulfillment of inequalities $|\eta_{n+1}^{(i)} - \eta_n^{(i)}| < \delta$ $(i = 1, \ldots, N)$ where $\delta(> 0)$ is the given tolerance (accuracy of calculations). If the required accuracy is attained for every $\eta_{n+1}^{(i)}$ $(i = 1, \ldots, N)$, the calculations are terminated. If the accuracy is not attained, then $\xi_{n+1}(x) := \eta_{n+1}^{-1}(x)$, $n := n + 1$, and calculations are repeated beginning from formula (6).

The sought-for quantity is the relative permittivity $\frac{\varepsilon_n(x)}{\varepsilon_0} = \eta_n(x) + 1$.

The key issue in this two-layer iteration scheme is the possibility of determination of $\varepsilon_{n+1}(x)$ from the known field $\mathbf{E}_n(x)$ by formula (7). If the sought-for function $\varepsilon(x)$ is characterized by N unknown parameters, then it is necessary to have the results of at least N different measurements.

Since the size of matrix A_N is comparatively small (of the order of several thousand) one can solve the corresponding system by relatively simple well-developed methods of numerical linear algebra, i.e. by the Gauss method with pivoting over the entire matrix. A more detailed description of the solution procedure can be found in [3].

Convergence of this iteration method is proved in [3]. This result gives a theoretical justification of the two-layer iteration method for the determination of function $\varepsilon(x)$. Note that the main difficulty of implementing this procedure is to provide the fulfillment of the condition that the solution to the inverse problem with "close" parameters must be known. As such a problem, one

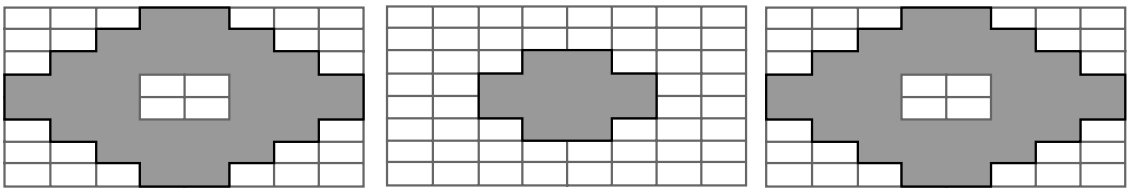

(a) (b) (c)

Figure 1.

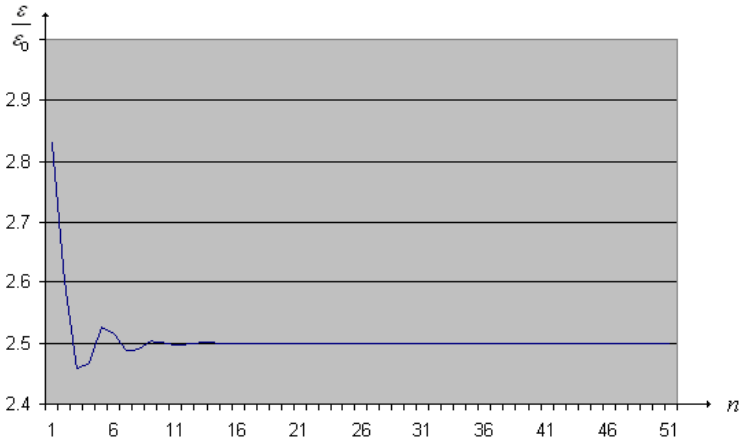

Figure 2.

can choose the determination of the permittivity for $\eta^{(1)} = \ldots = \eta^{(N)} = \eta_e$. This problem is studied in detail in [2] (where the existence conditions are also given).

4. NUMERICAL RESULTS

The problem parameters are

$$a = 2.274,\ b = 1.004,\ c = 0.982,\ c_1 = 0,\ c_2 = c,\ k_0 = 1.7;\ \text{mesh size is } 8 \times 8 \times 8.$$

Shape of the body is formed by layers. First, second and third layers are presented in Fig. 1(a), forth and fifth layers are presented in Fig. 1(b), sixes, seventh and eighth layers are presented in Fig. 1(c).

Figure 2 shows the convergence of the iteration process w.r.t number of iterations n. Exact value of relative permittivity is $\frac{\varepsilon}{\varepsilon_0} = 2.5$.

The VSIE-based method set forth in this paper can be also applied to numerical solution of the inverse problem of reconstructing permittivity of an inclusion of rather complicated shape. Fig. 2 demonstrates, as a typical example, the rate of convergence of iterations according to the computational procedure of numerical reconstruction of permittivity of the inclusion shown in Fig. 1.

ACKNOWLEDGMENT

This work was supported by Russian Foundation for Basic Research, project 11-07-00330-a.

REFERENCES

1. Smirnov, Y., "Inverse boundary value problem for determination of permittivity of a dielectric body in a waveguide using the method of volume singular integral equation," *IEEJ Fundamentals and Materials*, Vol. 129, 675–680, 2009.
2. Smirnov, Y. and Y. Shestopalov, "Existence and uniqueness of solution to the inverse problem of complex permittivity reconstruction of a dielectric body in a waveguide," *Inverse Problems*, Vol. 26, 105002, 2010.
3. Smirnov, Y. and Y. Shestopalov, "Determination of permittivity of an inhomogeneous dielectric body in a waveguide," *Inverse Problems*, Vol. 27, 095010, 2011.

Analysis of Electromagnetic Wave Propagation through a Layer with Graded-index Distribution of Refraction Index

N. B. Pleshchinskii and D. N. Tumakov
Kazan Federal University, Russia

Abstract— The problem of plane electromagnetic harmonic wave diffraction on a graded-refractive-index layer of some thickness is considered. It is assumed that refractive index of a layer monotonically increases and then monotonically decreases. Cases of the linear, parabolic, sinusoidal, exponential and logarithmic refractive index profiles of the layer are investigated. The diffraction problem is reduced to an ordinary differential equation with appropriate boundary conditions. The problem for the linear profile is solved analytically; for the other profiles it is investigated numerically. The method of approximating an integral identity is applied to increase accuracy of the grid solution of the boundary value problem. Emphasis is given to the cases, in which wave energy, either reflected or transited, reaches maxima.

1. INTRODUCTION

Refractive index gradients in the direction of light propagation have been theoretically studied for quite a long time. Physical implementation of this concept for using in antireflective applications has also been investigated based on evaporation of very thin alternating high/low index films that create an effective index gradient by varying the thickness ratios in these stacks [1, 2].

Applications for a thin film include dye-sensitized solar cells [3], optical waveguides [4], distributed Bragg reflectors, light-emitting diodes, and as potential replacements for SiO_2 in advanced gate stacks on metaloxide semiconductor field effect transistors. TiO_2 and SiO_2 have a high refractive index ($n \approx 2.5$) and a low refractive index ($n \approx 1.5$), respectively, and both are optically transparent in the visible and the near-IR region. Varying compositions of TiO_2 and SiO_2 can help to form thin films of any refractive index between those of TiO_2 and SiO_2. The volume ratio of TiO_2 and SiO_2 in a deposited dielectric film, defined as x in $(TiO_2)_x(SiO_2)_{1-x}$, determines the refractive index of the composite material [5]. Deposition of thin dielectric layers of different materials forms a stack of graded-refractive-index layers, which have been used as antireflection coatings for applications such as solar cells [6] and optical interference filters.

In this article, the diffraction problem is reduced to an ordinary differential equation with appropriate boundary conditions. These conditions are formed by elimination of two semi-infinite domains from the waveguide structure. We consider the case in which refractive index (wave number) of a layer monotonically increases and then monotonically decreases. As refractive index varies from one layer to another unissentially, we neglected a graded structure of the layer and adopted a continuous function for the refractive index distribution. Furthermore, we assume that the refractive index is independent of wave frequency ω.

We studied the cases of the linear, parabolic, sinusoidal, exponential and logarithmic refractive index profiles of the layer. The characteristic resemblance and peculiarities of influence of each of the profiles on wave propagation through the graded-index layer are presented.

The problem of diffraction on the layer for the linear profile is solved analytically; for the other profiles it is investigated numerically. The method of approximating a n integral identity is applied to increase the accuracy of the grid solution of the boundary value problem.

In the case of elastic waves, the problem of wave propagation through a non-homogeneous layer can be considered by the same method but this case is more complicated for performing calculations.

2. PROBLEM STATEMENT

Let the plane electromagnetic harmonic wave of type $u_0(x) = A_0 e^{-ik_1 \cdot x}$ fall on a layer of thickness L having refractive index $n_2(x)$ from a homogenous isotropic medium (see Fig. 1). It is necessary to find the diffracted field or, more precisely, the reflected, transited waves and a field in a layer $u_2(x)$.

The function $u(x)$, which is continuous everywhere as its derivative, satisfies the equation

$$u''(x) + k^2(x)u(x) = 0, \quad x \in \mathbf{R}$$

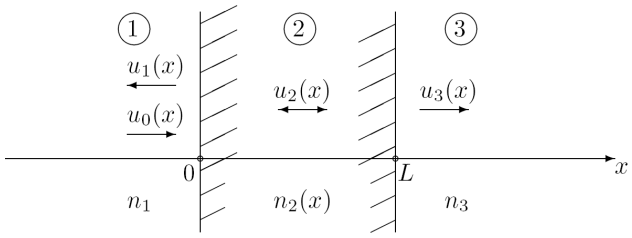

Figure 1: Geometry of the problem.

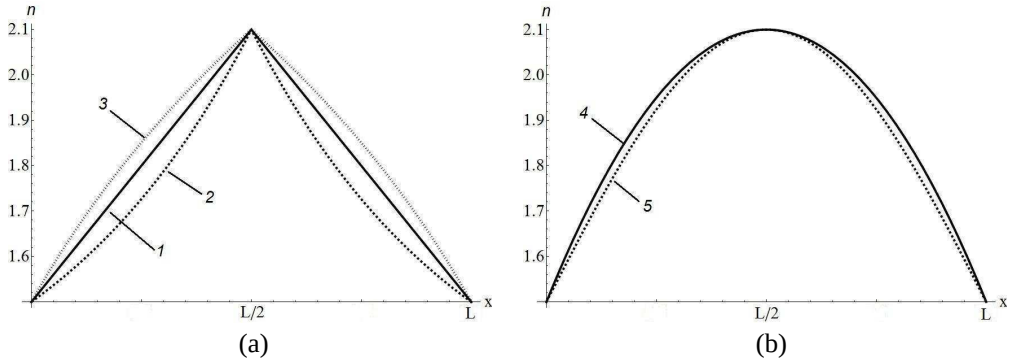

Figure 2: The distribution of refractive index in the gradient layer: 1 — linear, 2 — exponential, 3 — log, 4 — parabolic, 5 — sine.

with a given piecewise function $k(x)$. For regions 1 and 3 of the medium, function $k(x)$ is constant and the equation for these cases is solved explicitly.

Thus, the diffraction problem is reduced to an ordinary differential equation

$$u_2''(x) + k_2^2(x)u_2(x) = 0, \quad 0 < x < L, \tag{1}$$

with boundary conditions

$$u_2'(0) - ik_1u_2(0) = -2ik_1A_0, \quad u_2'(L) + ik_3u_2(L) = 0, \tag{2}$$

where $k_j = k_0n_j$ are wavenumbers of the media. We considered the case in which refractive index (wavenumber) of a layer monotonically increases and then monotonically decreases. Cases of the linear, parabolic, sinusoidal, exponential and logarithmic refractive index profiles are investigated.

The problem of diffraction on a layer is solved for the linear profile analytically. For the remaining profiles we studied the problem numerically. The method of approximating an integral identity is applied to increase accuracy of the grid solution to the obtained boundary problem.

3. TYPES OF GRADED-REFRACTIVE-INDEX LAYERS

Changes in the refractive index in the layer will be considered in the range from $n_0 = 1.5$ to $n_M = 2.1$, which is a somewhat narrower range, and typical for industrial optical glasses. We consider the refractive index distribution in the layer as monotonically increasing up to the layer center, and then decreasing up to the end of the layer (Fig. 2). We select the five distributions $n_2(x)$. Let us consider, first, the refractive indices with a piecewise-smooth distribution with a break in smoothness in the middle layer: linear, exponential, logarithmic, as well as two smooth distributions: parabolic, and sinusoidal.

3.1. Linear Distribution of the Refractive Index

First, we consider the simplest case of refractive index distribution: piecewise-linear. Thus, the function is defined on each interval as $n(x) = ax + b$. Equation (1) in this case becomes the Weber equation and can be solved in each interval explicitly:

$$u_2(x) = A \cdot D_{-\frac{1}{2}}\left(-\frac{(1-i)(b+ax)\sqrt{k_0}}{\sqrt{a}}\right) + B \cdot D_{-\frac{1}{2}}\left(\frac{(1+i)(b+ax)\sqrt{k_0}}{\sqrt{a}}\right),$$

where A and B are arbitrary constants which vary from interval to interval, $D_\nu(x)$ are parabolic cylindrical functions. If one satisfies the conditions of continuity of the potential function, continuity of its derivative at the point $L/2$ as well as boundary values, the unknown constants will be determined.

For determining a and b, we use the condition that $n(x)$ takes the minimum value n_0 at the ends and the maximum value n_M in the middle (see Fig. 2). Once a and b are determined, $n(x)$ for the layer is found.

3.2. Other Distributions of the Refractive Index

Just as in the linear case, we assume that the minimum and maximum values of $n(x)$ are n_0 and n_M, respectively. Refractive index distributions for all cases are given in Table 1.

4. THE METHOD OF APPROXIMATING AN INTEGRAL IDENTITY

The Equation (1) can be written as

$$u''(x) + q(x)u(x) = 0, \quad 0 \le x \le L, \tag{3}$$

with boundary conditions

$$u'(0) - \zeta_1 u(0) = \mu_1, \quad u'(L) - \zeta_2 u(L) = 0. \tag{4}$$

Let us introduce the following notation $q(x) = k_2^2(x)$, $\zeta_1 = ik_1$, $\zeta_2 = ik_3$ and $\mu_1 = -i2k_1A_0$.

We will consider continuous functions $n_2(x)$, which implies continuity of $q(x)$. From the physical point of view, namely, continuity of the tangential components of the electromagnetic field, it is reasonable to require continuity of $u(x)$ and $u'(x)$. Therefore, we will assume that $u(x) \in C^1[0, L]$.

Table 1: Distributions of refractive index for all five considered profiles.

profile type	**distribution of refractive index**
linear	$n(x) = \begin{cases} \dfrac{2(n_M - n_0)}{L}x + n_0, & 0 < x < \dfrac{L}{2}, \\ -\dfrac{2(n_M - n_0)}{L}x + 2n_M - n_0, & \dfrac{L}{2} < x < L. \end{cases}$
exponential	$n(x) = \begin{cases} \dfrac{e\,n_0 - n_M}{-1+e} - \dfrac{n_0 - n_M}{-1+e}e^{2x/L}, & 0 < x < \dfrac{L}{2}, \\ \dfrac{e\,n_0 - n_M}{-1+e} - \dfrac{e^2(n_0 - n_M)}{-1+e}e^{-2x/L}, & \dfrac{L}{2} < x < L. \end{cases}$
logarithmic	$n(x) = \begin{cases} n_0 + \dfrac{n_M - n_0}{\ln 2}\ln\left(1 + \dfrac{2x}{L}\right), & 0 < x < \dfrac{L}{2}, \\ n_0 + \dfrac{n_M - n_0}{\ln 2}\ln\left(3 - \dfrac{2x}{L}\right), & \dfrac{L}{2} < x < L. \end{cases}$
parabolic	$n(x) = -\dfrac{4(n_M - n_0)}{L^2}\left(x - \dfrac{L}{2}\right)^2 + n_M.$
sinusoidal	$n(x) = n_0 + (n_M - n_0)\sin x.$

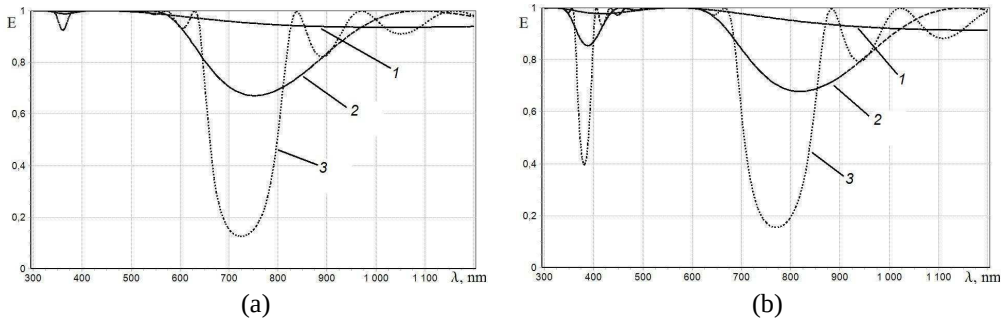

Figure 3: Dependence of the transited energy on wavelength: 1 — one layer, 2 — three layers, 3 — eight layers. (a) Is for linear profile, (b) is for the parabolic profile.

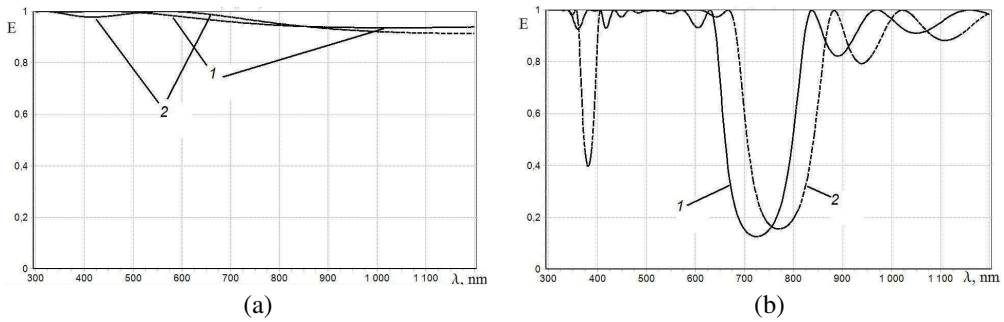

Figure 4: Dependence of the transited energy on wavelength: 1 — linear, 2 — parabolic. (a) Is for one layer, (b) is for eight layers.

(Note that the fact that $q(x)$ are continuous function and from the Equation (3), it should be $u(x) \in C^2[0, L]$.)

Using the method of approximating an integral identity [7, p. 228], Equations (3), (4) for step $h = L/N$ can be reduced to

$$-u_{i-1} + (2 - q_i h^2)u_i - u_{i+1} = 0, \quad i = 1, \ldots, N-1, \tag{5}$$

$$(1 - q_0 h^2/2 + \zeta_1 h)u_0 - u_1 = -\mu_1 h, \qquad -(1 - q_N h^2/2 - \zeta_2 h)u_N + u_{N-1} = 0. \tag{6}$$

The finite-difference analog (5), (6) represents approximation of the system (3), (4) for accuracy $O(h^2)$. The obtained system (5), (6) can be solved using the Thomas algorithm. Note that the solution accuracy can be increased by "deterioration" of the system's matrix (matrix will no longer be tridiagonal).

5. RESULTS AND CONCLUSIONS

Numerical analysis was performed for the layer of glass made of mixture of oxides: TiO_2 and SiO_2, in which refractive index varies from $n_0 = 1.5$ to $n_M = 2.1$. Thickness of one layer was taken as $L = 200$ nm.

Let us consider how the amount of energy of transited field varies with an increase in the number of layers. Fig. 3 shows plots for the magnitude of the energy for one, three and eight layers ((a) is for the linear profile, (b) is for the parabolic profile). It can be seen that the increase in the number of layers raises reflectivity of the stack.

It can be seen that the transited energy in the cases of the linear and parabolic profiles has a sharp minimum in the region of 700–800 nm. The approximate expression for determining the frequency of the n-th minimum for the linear profile is following:

$$\omega_n \approx \frac{\sqrt{3}\, c}{2\pi L} n,$$

where c is speed of light. The splash of reflected energy at the wavelength of 400 nm is characteristic for the parabolic profile only.

Note that the graphs of the values of transited energy for all considered refractive index profiles are very similar in shape and have prominent minima at the wavelength of 700–800 nm. In the two smooth functions, parabolic and sine, the minimum occurs near 400 nm (see Fig. 4).

ACKNOWLEDGMENT

This work was supported by RFBR 12-01-97012-r_povolzh′e_a.

REFERENCES

1. Southwell, W. H., "Gradient-index antireflection coatings," *Optics Letters*, Vol. 8, No. 11, 584–586, 1983.
2. Berning, P. H., "Use of equivalent films in the design of infrared multilayer antireflection coatings," *J. Opt. Soc. Am.*, Vol. 52, 431–436, 1962.
3. O'Regan, B. and M. Gratzel, "A low-cost, high-efficiency solar cell based on dye-sensitized colloidal TiO_2 films," *Nature*, Vol. 353, 737–740, 1991.
4. Guglielmi, M., P. Colombo, L. M. D. Esposti, G. C. Righini, S. Pellic, and V. Rigato, "Characterization of laser-densified sol-gel films for the fabrication o f planar and strip optical waveguides," *J. Non-Cryst. Solids*, Vol. 147–148, 641–645, 1992.
5. Noemaun, A. N., F. W. Mont, J. Cho, and E. F. Schubert, "Inductively coupled plasma etching of graded-refractive-index layers of TiO_2 and SiO_2 using an ITO hard mask," *J. Vac. Sci. Technol. A*, Vol. 29, 051302, 2011.
6. Chhajed, S., M. F. Schubert, J. K. Kim, and E. F. Schubert, "Nanostructured multilayer graded-index antireflection coating for Si solar cells with broadband and omnidirectional characteristics," *Appl. Phys. Lett.*, Vol. 93, No. 25, 251108, 2008.
7. Samarskii, A. A., *The Theory of Difference Schemes*, Marcel Dekker, New York, 2001.

Reconstruction of Heterogeneity Parameters by Reflected Field in the Wave Guided Structure

I. L. Aleksandrova, S. V. Baranov, and N. B. Pleshchinskii
Kazan Federal University, Russia

Abstract— Heterogeneity in plane wave guide sets a connection between traces of potential functions of coming and of reflected waves on a section. It is possible to apply the scanning screen method to reconstruct kernel of the reflection operator in the case when possibilities of measuring equipment are limited. The influence of transversal screen in the wave guided structure on the reflection operator is investigated. It is proposed to use a solution of the auxiliary transmission problem for recalculation of data obtained by measuring characteristics of reflected field.

It is shown on simple examples how information on heterogeneity in plane waveguide can be restored by the reflection matrix. The possibility of applying method of neural networks for solving the inverse problem is investigated. Some results of numerical experiment are presented.

1. INTRODUCTION

As it is known, information on heterogeneity parameters in the wave guided structure can be obtained by measuring characteristics of electromagnetic field reflected from heterogeneity. As a rule, in practice the limited set of values characterizing the reflected field can be measured. It is not sufficient for complete reconstruction of the reflection operator.

In the work [1] to get an additional information on the reflected field it was proposed to place an ideally conducting infinitely thin screen (in the plane $z = 0$) which can move along axis z. Such screen was called a scanning screen. If we measure the reflected field for different positions of screen, then we can obtain the additional information on the reflection operator.

In the work [2] it was investigated how the reflection operator changes when a scanning screen is added. This investigation is based on reducing the electromagnetic wave diffraction problem on a conducting screen in the cross-section of the plane wave guide to integral equation of special form.

In the present work it is proposed to use solution of the auxiliary transmission problem for recalculation of results of measuring the reflected field.

By reconstructing the heterogeneity parameters in the plane waveguide two methods are used: minimal squares method in the case when the heterogeneity type is known beforehand and method of neural networks which is more universal but can be applied by some additional conditions also.

2. THE PROBLEM STATEMENT

Assume the plane wave guide with metallic walls $x = 0$ and $x = a$ contains in the right side $z > d$ heterogeneity — the conducting or dielectric inclusions. Suppose that the source of electromagnetic waves spreading along wave guide to the right is placed in the left side of the waveguide $z < 0$. It is necessary to reconstruct information on heterogeneity by the field reflected to the left.

We will consider harmonically dependent on time two-dimensional TE-polarized electromagnetic field ($e^{i\omega t}$). In this case field is determined in a unique fashion by potential function $u(x, z)$ being a solution of Helmholtz equation. Denote by $\overrightarrow{u}(x, z)$ and $\overleftarrow{u}(x, z)$ potentials of electromagnetic waves moving along waveguide to the right ant to the left. Let $\overrightarrow{u}_0(x)$ and $\overleftarrow{u}_0(x)$ be traces of these functions on a cross-section of waveguide $z = 0$. Heterogeneity in the right side of waveguide sets a connection between these traces of the form

$$\overleftarrow{u}_0(x) = \int_0^a M(t, x)\overrightarrow{u}_0(t)\, dt \tag{1}$$

or in the operator form

$$\overleftarrow{u}_0 = M\overrightarrow{u}_0, \tag{2}$$

where M is an integral reflection operator which kernel $M(t, x)$ contains information on heterogeneity.

As it is known, field in wave guide can be represented as an imposition of eigen waves. Let $\overrightarrow{u} = (\overrightarrow{u}_1, \overrightarrow{u}_2, \ldots)$ and $\overleftarrow{u} = (\overleftarrow{u}_1, \overleftarrow{u}_2, \ldots)$ be coefficients of waves decomposition into series by

eigen waves. Then it is possible to pass from Equation (1) to vector equation $\overleftarrow{u} = M\overrightarrow{u}$, here M is an infinite matrix, called a reflection matrix.

3. THE RECONSTRUCTION OF REFLECTION OPERATOR KERNEL

We use some results of the work [2]. Denote by $\mathcal{M} = (\alpha, \beta)$ a metallic screen and by $\mathcal{N}$ a complement of set $\mathcal{M}$ to a section of wave guide S. Assume that waveguide is filled by homogeneous isotropic dielectric with dielectric constant ε_- for $z < 0$ and ε_+ for $z > 0$ on the left and on the right of screen.

Denote $\overrightarrow{u}_0(x) = \overrightarrow{u}(x, 0-0)$ and $\overrightarrow{u}_1(x) = \frac{\partial \overrightarrow{u}}{\partial z}(x, 0-0)$ traces of potential function $\overrightarrow{u}(x,z)$ on a section $z = 0$. By analogy, denote $\overleftarrow{u}_0(x) = \overleftarrow{u}(x, 0-0)$ and $\overleftarrow{u}_1(x) = \frac{\partial \overleftarrow{u}}{\partial z}(x, 0-0)$; $\overrightarrow{v}_0(x) = \overrightarrow{v}(x, 0+0)$ and $\overrightarrow{v}_1(x) = \frac{\partial \overrightarrow{v}}{\partial z}(x, 0+0)$; $\overleftarrow{v}_0(x) = \overleftarrow{v}(x, 0+0)$ and $\overleftarrow{v}_1(x) = \frac{\partial \overleftarrow{v}}{\partial z}(x, 0+0)$.

Assume

$$s_n(x) = \sqrt{\frac{2}{a}} \sin \frac{\pi n x}{a}, \qquad \gamma_n^{\pm} = \sqrt{k_{\pm}^2 - \left(\frac{\pi n}{a}\right)^2}, \quad n = 1, 2, \ldots,$$

here $k_{\pm}^2 = \omega^2 \mu_0 \mu \varepsilon_0 \varepsilon_{\pm}$ are wave numbers on the left and on the right of wave guide section $z = 0$. Suppose that $\mathrm{Re}\gamma_n^{\pm} > 0$ or $\mathrm{Im}\gamma_n^{\pm} < 0$. Then potential functions of waves spreading to the right and to the left can be represented in the form

$$\overrightarrow{u}(x,z) = \sum_{n=1}^{+\infty} \overrightarrow{u}_n s_n(x) e^{-i\gamma_n^{\pm} z}, \qquad \overleftarrow{u}(x,z) = \sum_{n=1}^{+\infty} \overleftarrow{u}_n s_n(x) e^{i\gamma_n^{\pm} z}.$$

In *the diffraction problem* of electromagnetic wave on a screen $\mathcal{M}$ by potential functions $\overrightarrow{u}(x,z)$ and $\overleftarrow{v}(x,z)$ of waves, running into screen, it is necessary to seek such potential functions $\overleftarrow{u}(x,z)$ and $\overrightarrow{v}(x,z)$ of dissipated field that boundary conditions and conjugation conditions should fulfill for $z = 0$:

$$\begin{aligned} &\overleftarrow{u}_0(x) + \overrightarrow{u}_0(x) = 0, \quad x \in \mathcal{M}, \quad \overleftarrow{u}_0(x) + \overrightarrow{u}_0(x) = \overleftarrow{v}_0(x) + \overrightarrow{v}_0(x), \quad x \in \mathcal{N}, \\ &\overleftarrow{v}_0(x) + \overrightarrow{v}_0(x) = 0, \quad x \in \mathcal{M}, \quad \overleftarrow{u}_1(x) + \overrightarrow{u}_1(x) = \overleftarrow{v}_1(x) + \overrightarrow{v}_1(x), \quad x \in \mathcal{N}. \end{aligned} \tag{3}$$

Assume

$$K_0^{\pm}(t,x) = -i \sum_{m=1}^{+\infty} \gamma_m^{\pm} s_m(t) s_m(x), \qquad K_1(t_1, x) = -i \sum_{m=1}^{+\infty} \frac{2}{\gamma_m^- + \gamma_m^+} s_m(t_1) s_m(x).$$

It can be shown that the electromagnetic wave diffraction problem on the cross-section screen in the plane waveguide is equivalent to the integral equation

$$\begin{aligned} \overleftarrow{u}_0(x) + \overrightarrow{v}_0(x) &= -\overrightarrow{u}_0(x) - \overleftarrow{v}_0(x), \quad x \in \mathcal{M}, \\ \overleftarrow{u}_0(x) + \overrightarrow{v}_0(x) &= \int_0^a [\overleftarrow{u}_0(t) + \overrightarrow{v}_0(t)] \left(\int_{\mathcal{M}} \frac{K_0^-(t,t_1) + K_0^+(t,t_1)}{2} K_1(t_1, x) dt_1 \right) dt \\ &\quad + \int_0^a \left(\overrightarrow{u}_0(t) \int_{\mathcal{N}} \frac{3K_0^-(t,t_1) - K_0^+(t,t_1)}{2} K_1(t_1, x) dt_1 \right. \\ &\quad \left. + \overleftarrow{v}_0(t) \int_{\mathcal{N}} \frac{3K_0^+(t,t_1) - K_0^-(t,t_1)}{2} K_1(t_1, x) dt_1 \right) dt, \quad x \in \mathcal{N}. \end{aligned} \tag{4}$$

Let's copy the Equation (4) and first three conditions from (3) in the operator form:

$$\overleftarrow{u}_0 + \overrightarrow{v}_0 = C(\overleftarrow{u}_0 + \overrightarrow{v}_0) + A\overrightarrow{u}_0 + B\overleftarrow{v}_0, \quad \overleftarrow{u}_0 - \overrightarrow{v}_0 = -\overrightarrow{u}_0 + \overleftarrow{v}_0, \tag{5}$$

where A, B, C are integral operators which kernels are present in formulas (4). Assume

$$\begin{aligned} P &= \frac{1}{2}(-I + (I-C)^{-1}A), \quad Q = \frac{1}{2}(I + (I-C)^{-1}B), \\ R &= \frac{1}{2}(I + (I-C)^{-1}A), \quad S = \frac{1}{2}(-I + (I-C)^{-1}B). \end{aligned}$$

Let us add to a set of Equations (5) the equality $\overleftarrow{v}_0 = M\overrightarrow{v}_0$ and obtain

$$\overleftarrow{u}_0 = \left[P + QM(I - SM)^{-1}R\right]\overrightarrow{u}_0. \tag{6}$$

Kernel of the reflection operator can be found by solving the minimization problem

$$\sum_{\nu} \| \left[P_\nu + Q_\nu M(I - S_\nu M)^{-1}R_\nu\right]\overrightarrow{u}_0 - \overleftarrow{u}^{\nu}_0\|^2 \to \min, \tag{7}$$

here parameter ν determines position of scanning screen.

The calculating experiment has been carried out. To solve the problem (7) numerically the method of coordinates descent was applied. The matrix which left block was determined by Equation (2) was chosen as an initial approximation in the case when scanning screen was absent. The recent matrix elements were assumed to be equal to zero. It is proved that if we give a simple construction as a heterogeneity for $z > d$ with known solution of the diffraction problem and use this solution as initial data for the minimization problem (7), then the refraction matrix is restored with sufficient accuracy.

4. THE TRANSMISSION PROBLEM

The reflection operator kernel search by condition (7) is rather difficult problem. To simplify algorithm it is expedient to use an auxiliary *transmission problem*. In this problem by field from one side of screen — by potential functions $\overrightarrow{u}(x,z)$ and $\overleftarrow{u}(x,z)$ — field from another side of screen is being reconstructed-functions $\overrightarrow{v}(x,z)$ and $\overleftarrow{v}(x,z)$ are determined. After this, when $\overrightarrow{v}(x,z)$ and $\overleftarrow{v}(x,z)$ are known, it is possible to seek the reflection operator by equalities of the form $\overleftarrow{v}_0 = M\overrightarrow{v}_0$.

Suppose

$$K_1^+(t,x) = i\sum_{m=1}^{+\infty}\frac{1}{\gamma_m^+}s_m(t)s_m(x).$$

By formulas (5) and conjugation conditions (3) the integral equation follows

$$\begin{aligned}\overleftarrow{v}_0(x) - \overrightarrow{v}_0(x) \;=\; & \int_0^a [\overleftarrow{v}_0(t) - \overrightarrow{v}_0(t)]\left(\int_{\mathcal{M}} K_0^+(t,t_1)K_1^+(t_1,x)dt_1\right)dt \\ & + \int_0^a [\overleftarrow{u}_0(t) - \overrightarrow{u}_0(t)]\left(\int_{\mathcal{N}} K_0^-(t,t_1)K_1^+(t_1,x)dt_1\right)dt.\end{aligned} \tag{8}$$

This equation is equivalent to the transmission problem of the electromagnetic wave on a cross-section screen in the plane wave guide.

Equation (8) can be solved by Galerkin method with decomposition of unknown function into Fourier series by functions $s_n(x)$. The numerical experiment has shown that if we take the approximate solution of the diffraction problem as the initial data in the transmission problem, then functions $\overrightarrow{v}_0(x)$ and $\overleftarrow{v}_0(x)$ can be reconstructed with enough accuracy for rather small sizes of scanning screen. The solution of the transmission problem is steady with respect to small perturbations of initial data.

5. THE RECONSTRUCTION OF INFORMATION ON HETEROGENEITY BY A REFLECTION MATRIX

Let us consider on an example of two simple problems how it is possible to reconstruct information on heterogeneity in wave guide by a reflection matrix.

Problem 1. Let the right side $z > l$ of a plane wave guide be filled by homogeneous isotropic dielectric, by this let a wave number be equal to k (Fig. 2). In this case heterogeneity represents a semi-infinite dielectric inclusion.

We will seek distance l to a heterogeneity and wave number k by a reflection matrix M.

By solving the direct diffraction problem, it is possible to calculate matrix M elements explicitly:

$$M_{lj} = \frac{\gamma_j^+ - \gamma_j(k)}{\gamma_j^+ + \gamma_j(k)}e^{-2i(l-d)\gamma_j^+}\delta_{lj},$$

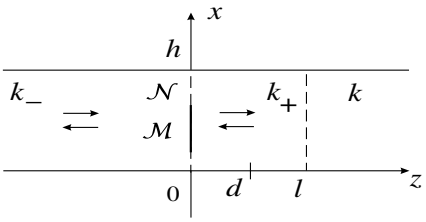

Figure 1: Semi-infinite dielectric inclusion.

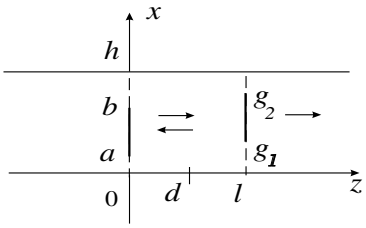

Figure 2: Thin conducting screen.

here δ_{lj} is a Kronecker symbol.

Let $\tilde{M}$ be a given reflection matrix. Corresponding to it heterogeneity parameters l and k can be found by conditions

$$\sum_{j=1}^{N} \left\| \tilde{M}_{jj} - \frac{\gamma_j^+ - \gamma_j(k)}{\gamma_j^+ + \gamma_j(k)} e^{-2i(l-d)\gamma_j^+} \right\|^2 \to \min . \tag{9}$$

Problem (9) is to be solved under natural restrictions $l > d,\ k > 0$. A sequence of random numbers from a set $\{(x, y)\colon d < x < d_1,\ 0 < y < k_m\}$ is chosen as an initial approximation for l and k. Constants d_1 and k_m are set artificially. For every point of initial approximation the problem (9) is being solved and the local minimum point is being found. Point in which function will have it's minimal value is being sought among all points of local minimum. Pair which was found in this way is taken as a solution of problem. The relative error of the solution is approximately from 1% to 5%.

Problem 2. Let us consider now as a heterogeneity in a plane wave guide a thin metallic screen $\mathcal{E} = (g_1, g_2)$ placed in a plane $z = l\ \ (l > d)$ (Fig. 2).

We will seek a distance l to a screen and screen boundaries g_1 and g_2 by given reflection matrix.

To find a reflection matrix describing the heterogeneity, it is necessary preliminary to solve the auxiliary electromagnetic wave diffraction problem on a screen $\mathcal{E}$: from the left on a screen $\mathcal{E}$ falls down the electromagnetic wave $\overrightarrow{v}(x, z)$, it is necessary to find scattering field — functions $\overleftarrow{v}(x, z)$ and $\overrightarrow{w}(x, z)$.

We can say that electromagnetic wave diffraction problem on a screen $\mathcal{E}$ is equivalent to equation of the form

$$D^{-1} F \overleftarrow{v} = G D \overrightarrow{v}.$$

Here F and G are matrices depending on position of a screen $\mathcal{E}$ (on parameters l, g_1, g_2). Elements of matrices F and G can be found analytically. Matrix $D = \mathrm{diag}\{e^{i(l-d)\gamma_n^+}\}$ is used to recalculate coefficients of field decomposition from section $z = l$ to section $z = 0$. By this a reflection matrix has the form $M = DF^{-1}GD$.

Let $\tilde{M}$ be given reflection matrix, then heterogeneity parameters l, g_1 and g_2 can be found by condition

$$\left\| \tilde{M} - DF^{-1}GD \right\|^2 \to \min . \tag{10}$$

This problem is a problem of a search of global minimum with linear restrictions $l > d,\ 0 \le g_1 \le a,\ d0 \le g_2 \le a$. As an initial approximation for l we take $l_0 = d$, as an initial approximation for screen boundaries g_1, g_2 a sequence of points $\{g_{1j}^0\}$, $\{g_{2j}^0\}$ randomly distributed on an interval $(0, a)$ was chosen. For every point of initial approximation $(l^0,\ g_{1j}^0,\ g_{2j}^0)$ the problem (10) was solved and a point of local minimum was determined. Among all points of local minimum the point was found in which function has its minimal value.

The calculating experiment has shown that position of a screen is reconstructed rather precisely.

6. NEURAL NETWORKS METHOD

To solve the heterogeneity reconstruction problem the artificial neural network method was used also. The inverse problem consists of the following. It is necessary to find a period and other geometric parameters of the diffraction grating by given characteristics of the falling down and being reflected from the grating waves. To solve this problem the neural networks method is used.

The model of the multilayer perceptron with one hidden layer consisting of forty neurons was developed. The error of the network response was minimized by Levenberg-Marquardt method. The training set was constructed on the base of numerical solutions of the different variants of diffraction problems. The trained neural network was tested on the set of examples that were not included in the training sample. By reconstructing the grating parameters the maximal value of error did not exceed 2.5%.

ACKNOWLEDGMENT

Supported by RFBR 12-01-97012-r-povolzh'e-a.

REFERENCES

1. Pleshchinskii, N. B., "On reconstruction of reflection matrix in the plane waveguide by scanning screen method," *Issledovaniya po Prikladnoi Matematike i Informatike*, No. 24, 115–121, 2003 (in Russian).
2. Aleksandrova, I. L. and N. B. Pleshchinskii, "On information restoring of heterogeneity in the plane wavegude," *Issledovaniya po Prikladnoi Matematike i Informatike*, No. 27, 11–17, 2011 (in Russian).
3. Baranov, S. V. and N. B. Pleshchinskii, "On reconstruction of parameters of diffraction grating by neuron web method using the reflected field," *XI Mezhdunarodnyj Seminar Supervychisleniya i Matematicheskoe Modelirovanie*, Vol. 21, Sarov, Russia, October 2009.

Wave Diffraction Problems on Periodical Sets of Heterogeneities in the Stratified Media

I. L. Aleksandrova, E. A. Osipov, N. B. Pleshchinskii, and P. A. Rogozhin
Kazan Federal University, Russia

Abstract—The universal approach to solving the diffraction problems on the periodical set of heterogeneities in the stratified media is proposed. The infinite periodic grating consisting of thin conducting bands embedded into a dielectric plate is considered as an example. The boundary value problem for the quasi-periodic potential functions is equivalent to the pair summatorial functional equation for the Floquet coefficients.

At first, it is advisable to solve the auxiliary diffraction problem for the stratified medium in the case when the heterogeneities are moved off. The heterogeneities generate the field perturbation; it is a solution of a similar pair equation. Secondly, we need to define new unknown variables in such way that the pair equation should have the standard form. To get this result we propose to use the boundary value conditions on the heterogeneities. Then the other conditions on the media interface can be transformed to standard form. The dual equation is equivalent to regular infinite set of linear algebraic equations for the coefficients of decomposition of the electromagnetic field by Floquet harmonics.

In the case of elastic waves the wave diffraction problems on the periodical sets of heterogeneities can be reduced to vector dual summatorial functional equations. The electromagnetic wave diffraction problems on the periodical knife grating was investigated by analogous scheme.

1. INTRODUCTION

The electromagnetic and elastic wave diffraction problems on the periodical sets of heterogeneities drew attention of many scientists. The important stage of development of methods of solving electromagnetic wave diffraction problems on the periodical gratings, including the multilayered ones, is connected with appearance of Riemann-Hilbert method [1]. Good results are provided by the integral equations method but it is connected with difficult calculations generated by increasing of number of grating elements in the strip of period. Method of regularization of pair functional equations of the diffraction problem based on integral identities obtained by solving an auxiliary over-determined boundary value problem in the partial domains [2, 3] is free from restrictions of such type.

In the present work general rules are stated permitting to reduce the diffraction wave problem on the periodical set of heterogeneities to a standard form of pair summatorial equation relative to Floquet coefficients of field potential function. These rules are illustrated on example of several two-dimensional problems. Such pair equation is equivalent to regular infinite set of linear algebraic equations.

First rule. If set of heterogeneities is placed on the media interface, then it is necessary at first to solve an auxiliary wave reflection and refraction problem at this boundary without heterogeneities.

Second rule. Let $\mathcal{M}$ be periodical set of heterogeneities and $\mathcal{N}$ be the remaining part of the media interface. In order to get pair equation in standard form it is necessary to introduce new variables on the basis of equalities in the boundary conditions of the diffraction problem on $\mathcal{M}$.

Third rule. Second part of pair equation should be deduced by the equalities which are given in the conjugation conditions only on $\mathcal{N}$.

2. DIFFRACTION OF TE-WAVE ON A SIMPLE PERIODIC GRATING

Suppose that electromagnetic field does not depend on coordinate y of Cartesian system of coordinates. Let the Floquet wave with potential function

$$u^0(x,z) = e^{i\alpha x} \sum_{n=-\infty}^{+\infty} b_n^0 \, e^{-i\gamma_n z} \, e^{idnx} \tag{1}$$

run from above on the p-periodical grating of ideally conducting infinitely thin ribbons in the plane $z = 0$ (Fig. 1). Here α is some number (Floquet parameter), $d = 2\pi/p$, $\gamma_n = \sqrt{k^2 - (\alpha + dn)^2}$, or $\mathrm{Re}\gamma_n \geq 0$ or $\mathrm{Im}\gamma_n > 0$.

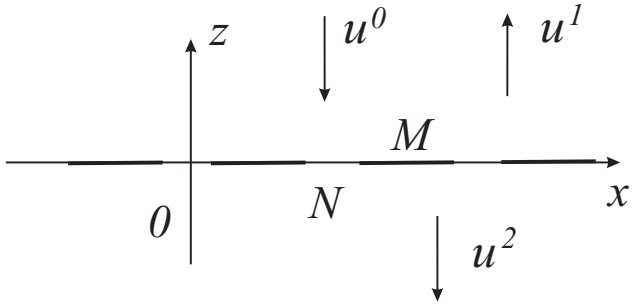

Figure 1: Periodic grating in the homogeneous space.

We will seek potential functions of outgoing from grating waves in the form

$$u^1(x,z) = e^{i\alpha x}\sum_{n=-\infty}^{+\infty} a_n\, e^{i\gamma_n z}\, e^{idnx}, \qquad u^2(x,z) = e^{i\alpha x}\sum_{n=-\infty}^{+\infty} b_n\, e^{-i\gamma_n z}\, e^{idnx}. \tag{2}$$

The meaning of α is just the same in all decompositions.

Suppose that the whole space is filled by homogeneous isotropic medium. Let the initial wave be given both for $z > 0$ and for $z < 0$. Therefore we will seek in practice at once field perturbation from grating (rule 1).

Boundary conditions on a metal $\mathcal{M}$ have the form

$$\sum_{n=-\infty}^{+\infty} b_n^0\, e^{idnx} + \sum_{n=-\infty}^{+\infty} a_n\, e^{idnx} = 0, \qquad \sum_{n=-\infty}^{+\infty} b_n^0\, e^{idnx} + \sum_{n=-\infty}^{+\infty} b_n\, e^{idnx} = 0. \tag{3}$$

Conjugation conditions on $\mathcal{N}$ are reduced to equalities

$$\sum_{n=-\infty}^{+\infty} a_n\, e^{idnx} = \sum_{n=-\infty}^{+\infty} b_n\, e^{idnx}, \qquad \sum_{n=-\infty}^{+\infty} \gamma_n\, a_n\, e^{idnx} = \sum_{n=-\infty}^{+\infty} (-\gamma_n)\, b_n\, e^{idnx}.$$

Consequently, the first conjugation condition is fulfilled everywhere. By this

$$a_n = b_n = c_n,$$

here c_n are new unknown coefficients (rule 2).

Equalities (3) give the first half of pair summatorial equation

$$\sum_{n=-\infty}^{+\infty} c_n\, e^{idnx} = -\sum_{n=-\infty}^{+\infty} b_n^0\, e^{idnx} \qquad \mathcal{M}.$$

The second half of pair equation is deduced from the second conjugation condition (rule 3):

$$\sum_{n=-\infty}^{+\infty} \gamma_n\, c_n\, e^{idnx} = 0 \qquad \mathcal{N}. \tag{4}$$

Denote

$$I_n = \int_{\mathcal{M}} e^{idnt}\, dt, \qquad J_n = \int_{\mathcal{N}} e^{idnt}\, dt.$$

By integral-summatorial identity

$$\sum_{n=-\infty}^{+\infty} c_n\, e^{idnx} = \int_0^p \Big(\sum_{n=-\infty}^{+\infty} \gamma_n\, c_n\, e^{idnt}\Big)\Big(\frac{1}{p}\sum_{m=-\infty}^{+\infty} \frac{1}{\gamma_m}\, e^{idm(x-t)}\Big)\, dt.$$

Let us pass from (4) to equation on $\mathcal{N}$

$$\sum_{n=-\infty}^{+\infty} c_n\, e^{idnx} = \int_{\mathcal{M}} \Big(\sum_{n=-\infty}^{+\infty} \gamma_n\, c_n\, e^{idnt} \Big) \Big(\frac{1}{p} \sum_{m=-\infty}^{+\infty} \frac{1}{\gamma_m}\, e^{idm(x-t)} \Big)\, dt$$

$$= \frac{1}{p} \sum_{n=-\infty}^{+\infty} \gamma_n\, c_n \sum_{m=-\infty}^{+\infty} \frac{1}{\gamma_m}\, e^{idmx}\, I_{n-m}. \tag{5}$$

Let us project (4) and (5) on functions e^{idkx} and obtain infinite SLAE

$$p\, c_k - \frac{1}{p} \sum_{n=-\infty}^{+\infty} \gamma_n\, c_n \sum_{m=-\infty}^{+\infty} \frac{1}{\gamma_m}\, I_{n-m}\, J_{m-k} = - \sum_{n=-\infty}^{+\infty} b_n^0\, I_{n-k}, \quad k = 0, \pm 1, \ldots \tag{6}$$

It can be shown that it's approximate solution can be found by truncation method.

3. ELECTROMAGNETIC WAVE DIFFRACTION ON THE PERIODIC GRATING IN THE LAYERED MEDIUM

What will change if media above grating and under grating are different?

It is necessary to substitute numbers γ_n^1 and γ_n^2 in decompositions (1) and (2) instead of γ_n. At first we consider an auxiliary problem of reflection and refraction on the media interface without grating (rule 1). By conjugation conditions

$$u^0(x,0) + u^1(x,0) = u^2(x,0), \qquad \frac{\partial u^0}{\partial z}(x,0) + \frac{\partial u^1}{\partial z}(x,0) = \frac{\partial u^2}{\partial z}(x,0)$$

It follows that for any n $b_n^0 + a_n = b_n$, $-\gamma_n^1\, b_n^0 + \gamma_n^1\, a_n = -\gamma_n^2\, b_n$. Denote by $\underline{a}_n$, $\underline{b}_n$ solution of this set of equations.

Now we will seek perturbation of grating. In representations (2) we write down $\underline{a}_n + a_n$ and $\underline{b}_n + b_n$ instead of a_n and b_n. Then it follows by boundary conditions on $\mathcal{M}$ and conjugation conditions on $\mathcal{N}$, that new unknown coefficients, as before, $c_n = a_n = b_n$ (rule 2), and pair equation has the form

$$\sum_{n=-\infty}^{+\infty} c_n\, e^{idnx} = - \sum_{n=-\infty}^{+\infty} \frac{2\gamma_n^1}{\gamma_n^1 + \gamma_n^2}\, b_n^0\, e^{idnx} \quad \text{on} \quad \mathcal{M}, \quad \sum_{n=-\infty}^{+\infty} (\gamma_n^1 + \gamma_n^2)\, c_n\, e^{idnx} = 0 \quad \text{on} \quad \mathcal{N}.$$

So it is necessary to replace at the left γ_n by $\gamma_n^1 + \gamma_n^2$ and at the right replace b_n^0 by $\dfrac{2\gamma_n^1}{\gamma_n^1 + \gamma_n^2}\, b_n^0$ in SLAE of the form (6) of the wave diffraction problem on a simple grating at the media interface.

In the work [4] more general case is considered when periodic grating is placed at one of media interface in the multilayered structure. In the work [5] it is shown that periodic grating in the multilayered dielectric can be used as a scanning screen.

4. THE DIFFRACTION OF ELASTIC WAVE ON THE PERIODIC SET OF CRACKS

The elastic wave diffraction problems on the heterogeneities in the layered media are in many respects close to the electromagnetic waves diffraction problems. But in some cases infinite sets of linear equations relative to Floquet coefficients of elastic field can has vector form.

In the work [6] it is shown how it is possible to reduce the elastic wave diffraction problem on a set of cracks in the layered medium to regular set of linear algebraic equations by listed above rules.

Consider a structure of three elastic layers lying on the hard basis. In general case quasi-periodic complex tension amplitudes in every layer have the form

$$u_x(x,y) = \sum_{n=-\infty}^{+\infty} \Big[d_n\, a_{1n} e^{i\beta_{1n} y} + \beta_{2n}\, a_{2n} e^{i\beta_{2n} y} - d_n\, b_{1n} e^{-i\beta_{1n} y} + \beta_{2n}\, b_{2n} e^{-i\beta_{2n} y} \Big]\, e^{id_n x},$$

$$u_y(x,y) = \sum_{n=-\infty}^{+\infty} \Big[\beta_{1n}\, a_{1n} e^{i\beta_{1n} y} - d_n\, a_{2n} e^{i\beta_{2n} y} + \beta_{1n}\, b_{1n} e^{-i\beta_{1n} y} + d_n\, b_{2n} e^{-i\beta_{2n} y} \Big]\, e^{id_n x},$$

$$\beta_{in} = \sqrt{k_i^2 - d_n^2}, \quad \mathrm{Re}\beta_{in} \geq 0 \quad \text{or} \quad \mathrm{Im}\beta_{in} > 0, \quad k_1^2 = \frac{\rho\omega^2}{\lambda + 2\mu}, \quad k_2^2 = \frac{\rho\omega^2}{\mu},$$

ρ, λ, μ are medium density and Lame constants, $d_n = \alpha + dn$, α is Floquet parameter, $d = 2\pi/p$, p is a set of cracks period.

In the vector-matrix form

$$u(x,y) = \sum_{n=-\infty}^{+\infty} \left[A_n\, Y_n^+(y)\, a_n + B_n\, Y_n^-(y)\, b_n\right] e^{id_n x},$$

here A_n B_n are 42-matrices, which coefficients are contained in formulas (1), $Y_n^{\pm}(y)$ are diagonal 22-matrices with functions $e^{\pm i\beta_{1n}y}$, $e^{\pm i\beta_{2n}y}$ at the main (general) diagonal, $u = (u_x,\, u_y,\, \sigma_y,\, \tau)$ and $a_n = (a_{n1},\, a_{n2})$, $b_n = (b_{n1},\, b_{n2})$. Vectors a_n are coefficients at negatively oriented Floquet harmonics, and b_n are coefficients at positively oriented Floquet harmonics.

We have for running from above plane wave (one Floquet harmonic with number s)

$$u^+(x,y) = A_s^{(0)}\, Y_s^{(0)+}(y - h_1)\, a_s^{(0)}\, e^{id_s x},$$

and for for a Floquet wave leaving up in a layer 0 we have

$$u^-(x,y) = \sum_{n=-\infty}^{+\infty} B_n^{(0)}\, Y_n^{(0)-}(y - h_1)\, b_n^{(0)}\, e^{id_n x}.$$

Set of equations for coefficients $b_s^{(0)}$, a_s, b_s has the form

$$\begin{aligned} &A_s^{(0)}\, a_s^{(0)} + B_s^{(0)}\, b_s^{(0)} = A_s\, Y_s^+(h_1)\, a_s + B_s\, Y_s^-(h_1)\, b_s, \\ &P_s\, Y_s^+(-h_2)\, a_s + Q_s\, Y_s^-(-h_2)\, b_s = 0. \end{aligned}$$

Here P_s Q_s are 22-submatrices of matrices A_s and B_s, composed of lines of coefficients relating to components u_x, u_y. After the solution $\underline{b}_s^{(0)}$, $\underline{a}_s$, $\underline{b}_s$ of this set is obtained, in a layer from $-h_2$ to h_1

$$\underline{\tau}(x,y) = \left[C_s\, Y_s^+(y)\, \underline{a}_s + D_s\, Y_s^-(y)\, \underline{b}_s\right] e^{id_s x},$$

where C_s D_s are 12-submatrices of matrices A_s and B_s, composed of lines of coefficients relating to components τ.

Let us pass to the problem on perturbation of elastic field by set of cracks. Component τ is continuous both on $\mathcal{N}$ and on $\mathcal{M}$, if equalities

$$C_n\, a_n^{(1)} + D_n\, b_n^{(1)} = C_n\, a_n^{(2)} + D_n\, b_n^{(2)} = c_n,$$

are fulfilled, here c_n are new unknown variables. By this first part of pair equation

$$\sum_{n=-\infty}^{+\infty} c_n\, e^{id_n x} = -\left[C_s\, \underline{a}_s + D_s\, \underline{b}_s\right] e^{id_s x} \quad \text{on} \quad \mathcal{M}.$$

It can be shown that second part of pair equation will have the form

$$\sum_{n=-\infty}^{+\infty} \chi_n\, c_n\, e^{id_n x} = 0 \quad \text{on} \quad \mathcal{N},$$

where coefficients χ_n should be found by some auxiliary set of equations.

Pair equation is transformed into infinite set of linear equations by the same methodic than in the case of electromagnetic waves.

5. DIFFRACTION OF THE PLANE WAVE ON PERIODIC KNIFE GRATING

Let plane wave of unit amplitude $e^{-ik\sin\theta\cdot x - ik\cos\theta\cdot z}$ fall down on a-periodic grating of parallel strips of width b. In three parts of wave guided structure we will seek potential functions of TE-polarized field in the form

$$u^-(x,z) = e^{i\alpha x} \sum_{n=-\infty}^{+\infty} u_n^-\, e^{i\gamma_n z}\, e^{idnx}, \qquad u^+(x,z) = e^{i\alpha x} \sum_{n=-\infty}^{+\infty} u_n^+\, e^{-i\gamma_n (z-b)}\, e^{idnx},$$

$$u(x,z) = e^{i\alpha x} \sum_{n=1}^{+\infty} \left[\overrightarrow{u}_n \, e^{-i\overline{\gamma}_n z} + \overleftarrow{u}_n \, e^{i\overline{\gamma}_n (z-b)} \right] \sin \frac{\pi n x}{a},$$

here $d = 2\pi/a$, $\alpha = -k \sin\theta$.

Denote

$$I_{m,n} = \int_0^a e^{-i(\alpha+dm)x} \sin \frac{\pi n x}{a} \, dx, \quad J_{m,k} = \int_0^a e^{i(\alpha+dm)x} \sin \frac{\pi k x}{a} \, dx.$$

Exclude u_n^- from the conjugation conditions for $z = 0$. Then we get

$$\left(\overrightarrow{u}_k + \overleftarrow{u}_k \, e^{-i\overline{\gamma}_k b} \right) \frac{a}{2} = 2J_{0,k} + \frac{1}{a} \sum_{n=-\infty}^{+\infty} \left(-\overrightarrow{u}_n + \overleftarrow{u}_n \, e^{-i\overline{\gamma}_n b} \right) \overline{\gamma}_n \sum_{m=-\infty}^{+\infty} \frac{1}{\gamma_m} \, I_{m,n} \, J_{m,k}, \quad k = 0, \pm 1, \ldots$$

By the conjugation conditions for $z = b$ second group of equations follows

$$\left(\overrightarrow{u}_k \, e^{-i\overline{\gamma}_k b} + \overleftarrow{u}_k \right) \frac{a}{2} = \frac{1}{a} \sum_{n=-\infty}^{+\infty} \left(\overrightarrow{u}_n \, e^{-i\overline{\gamma}_n b} - \overleftarrow{u}_n \right) \overline{\gamma}_n \sum_{m=-\infty}^{+\infty} \frac{1}{\gamma_m} \, I_{m,n} \, J_{m,k}, \quad k = 0, \pm 1, \ldots$$

Thus, the plane wave diffraction problem on knife grating is equivalent to regular infinite set of linear algebraic equations.

ACKNOWLEDGMENT

Supported by RFBR 12-01-97012-r-povolzh'e-a.

REFERENCES

1. Shestopalov, V. P., *Method of Riemann-Hilbert Problem in the Theory of Electromagnetic Waves Diffraction and Propagation*, Kharkov University Press, Kharkov, 1971.
2. Pleshchinskaya, I. E. and N. B. Pleshchinskii, "The over-determined Cauchy problems for the Maxwell equations set and electromagnetic waves diffraction on the metallic screens," *Conf. Proc. 11th Int. Conf. Mathematical Methods in Electromagnetic Theory MMET*06*, 255–257, Kharkov, Ukraine, June 2006.
3. Pleshchinskii, N. B., I. E. Pleshchinskaya, and E. M. Karchevskiy, "The over-determined boundary value problem method in the electromagnetic waves propagation and diffraction theory," *PIERS Online*, Vol. 5, No. 5, 441–445, 2009.
4. Pleshchinskaya, I. E. and N. B. Pleshchinskii, "Transformation of the electromagnetic radiation by the layered composite with thin conducting periodical inclusions," *Vestnik KGTU*, No. 11, 147–153, 2010 (in Russian).
5. Aleksandrova, I. L., I. E. Pleshchinskaya, and N. B. Pleshchinskii, "On use of the layered composite reinforced by thin conducting plates as a scanning screen," *Vestnik KGTU*, No. 7, 37–40, 2012 (in Russian).
6. Pleshchinskaya, I. E., N. B. Pleshchinskii, and E. A. Osipov, "Elastic properties of the layered composite weakened by periodic system of cracks," *Vestnik KGTU*, No. 3, 82–85, 2012 (in Russian).

Mid-range Wireless Power Transmission System Using Real-time Complex Impedance Control

K. Takei
Hitachi Research Laboratory, Hitachi, Ltd., Japan

Abstract— A power transmission system that uses both electric and magnetic fields is proposed. The equivalent circuit of a pair of transmitting and receiving antennas is expressed by the 2-port circuit, of which mutual impedance has both imaginary and real parts. Precise calculation of the power transmission efficiency using this 2-port circuit and generating and loading circuit with complex impedances indicates that very high efficiency can be obtained due to their special complex values. Because their real values are very small and limited within a narrow range, the transmitting energy must be stored in a rechargeable battery to activate active devices and the real-time control of these values is necessary to stabilize high-efficient power transmission against changes in propagation environment.

1. INTRODUCTION

In 2008 the MIT group proposed technology that enables efficient power transmission for a distance of a few meters using a frequency of several tens of megahertz [1]. This technology, called "magnetic resonance" uses not only the magnetic field as well as the conventional near-range wireless power transmission technology but also the magnetic resonance, which is caused by the capacitance of the RF circuit and, the transmitting and receiving antennas. This technology efficiently transmits power when the mutual impedance between the transmitting and receiving antennas is large and imaginary. Effective power transmission for a distance of a few meters with this technology requires large three dimensional inductors, which are several tens of centimeters in diameter and a few centimeters in height, and a higher operation frequency, several tens of megahertz, than that of the conventional near-range power transmission technology [2]. The power transmission system using magnetic resonance that uses antennas of similar size to the distance enables high transmission efficiency, which exceeds ninety percent. When the distance between these antennas is so large that a part of the transmitting magnetic field is dispersed, another method that uses both electric and magnetic fields is expected to provide higher efficiency of the power transmission than that of magnetic resonance. In this case, the mutual impedance between transmitting and receiving antennas does not have a small enough real part to be negligible compared with its imaginary part.

I propose a power transmission system that consists of RF circuits, transmitting and receiving antennas, the size of which is of the same order as the distance between the two antennas and allows the provision of not that high of efficiency, e.g., a few tens of percent The electric characteristics are calculated by the equivalent circuit which consists of RF circuits, i.e., the power generating and loading circuits, and the transmitting and receiving antennas, which are expressed by the 2-port circuit [3]. This equivalent circuit enables precise calculation of the power transmission efficiency. The special values of the complex impedances in the equivalent circuit provide high power transmission efficiency. The sensitivity of these values to efficiency requires an algorithm for controlling such values to stabilize power transmission. The actual structures of the transmitting and receiving antennas that obtain the complex impedance of the 2-port circuit can be constructed using a special planar structure and its design algorithm. An antenna loaded by a lumped reactance enables this sensitivity: therefore it not only improves power transmission efficiency but also determined the transmission direction.

2. CIRCUIT ANALYSIS OF POWER TRANSMISSION

The equivalent circuit of a power transmission system consisting of a power generating circuit, loading circuit, and 2-port circuit, which expresses the transmitting and receiving antennas is shown in Fig. 1.

The self and mutual impedances of the 2-port circuit in Fig. 1 are the self and mutual impedances of the two antennas. The power generating circuit is represented by the voltage source and the inner complex impedance. Similarly, the loading circuit is expressed by the simple complex impedance. The parameters in Fig. 1 derive power that is consumed in the loading resistance. Power transmission efficiency is defined by this consuming power normalized by the maximum supplying power as

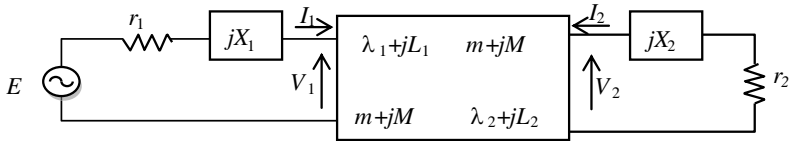

Figure 1: Equivalent circuit of power transmission system.

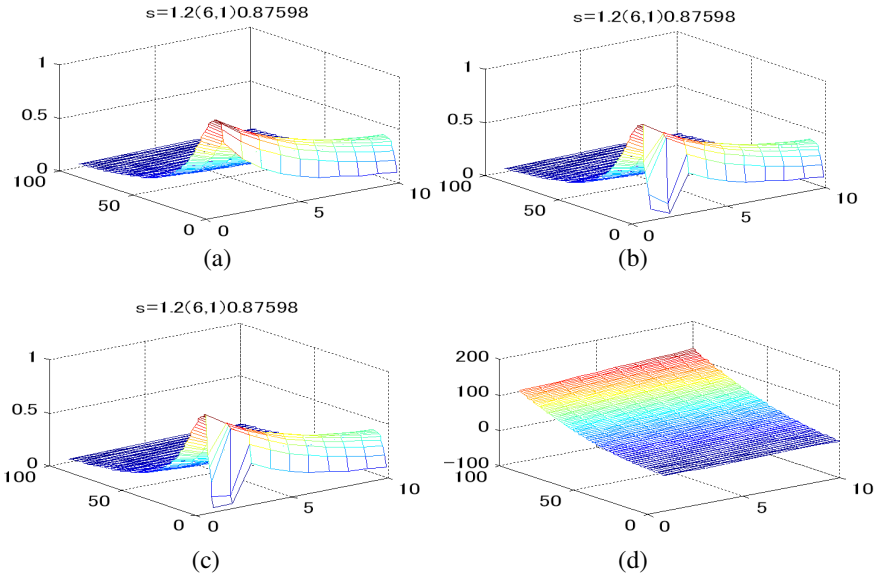

Figure 2: Efficiency for symmetric power transmission system.

follows.

$$\eta \equiv \frac{P_2}{P_0} = \frac{r_2 r_1 \left(m^2 + M^2\right)}{\left\{m^2 - M^2 - (r_1 + \lambda_1)(r_2 + \lambda_2) + (X_1 + L_1)(X_2 + L_2)\right\}^2 + \left\{(r_1 + \lambda_1)(X_2 + L_2) + (X_1 + L_1)(r_2 + \lambda_2) - 2mM\right\}^2} \tag{1}$$

The parameters that are controllable using conventional valuable elements are r_1, r_2, X_1, and X_2. The following derivatives of Eq. (1) with respect to these four parameters determine optimum values for achieving maximum efficiency.

$$\begin{aligned} 0 &= (X_1 + L_1)^3 \frac{r_2 + \lambda_2}{r_1 + \lambda_1} + (X_1 + L_1)\left\{m^2 - M^2 + (r_1 + \lambda_1)(r_2 + \lambda_2)\right\} - 2(r_1 + \lambda_1)mM, \\ 0 &= (X_2 + L_2)^3 \frac{r_1 + \lambda_1}{r_2 + \lambda_2} + (X_2 + L_2)\left\{m^2 - M^2 + (r_1 + \lambda_1)(r_2 + \lambda_2)\right\} - 2(r_2 + \lambda_2)mM \end{aligned} \tag{2}$$

Each equation is of third degree with respect to the sum of the self reactances of the antenna and RF circuit: therefore it is solved analytically. The parameters in Eq. (1) are divided into the two types. The first type, which consists of the self and mutual complex impedances of the two antennas cannot be changed during power transmission. On the other hand, the second type, which consists of the real and imaginary parts of both the power generating and loading circuits can be controlled to achieve maximum power transmission efficiency. The optimum values of the real parts of these circuits are numerically determined using their imaginary parts which are the solution to the equation of third degree. Example results of the parameters of the optimum values to achieve maximum power transmission efficiency are shown in Fig. 2. Since the symmetric circuit can transmit maximum power from the generating circuit to the loading one, the equivalent circuit is determined to be symmetric: therefore the suffixes of the parameters can be omitted. The conditions for determining the parameters are summarized in Table 1. The self reactance of each antenna is included in the reactance of each RF circuit. The first three graphs in Fig. 2 show efficiency along the vertical axis vs. the first and second parameters along the two horizontal axes. Each graph is related to a different solution of the equation of third degree. The fourth graph shows

Table 1: Parameters conditions for maximum power transmission.

Mutual resistance of Ant.: M	Mutual reactance of Ant.: m	Self resistance of Ant.: λ	Resistance of RF circuit: r
1 (normalized fixed value)	$0.1 * M - M$ (first parameter)	$1.2 * m$ (example fixed value)	$0.1 - 10$ (second parameter)

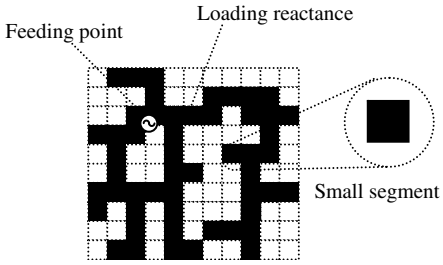

Figure 3: Planer antenna with loading reactance.

the determined value of the RF-circuit reactance along the vertical axis vs. the same horizontal axes as the previous ones.

It is obvious that the lager mutual reactance between the two antennas by comparing the mutual resistance provides higher efficiency power transmission efficiency. The optimum value of the resistance of the RF circuit is very small and is more sensitive to efficiency than its reactance. This fact indicates that a real-time control of the resistance of the RF circuit is important to achieve maximum power transmission efficiency.

3. ANTENNA DESIGN FOR EFFICIENT POWER TRANSMISSION

The results discussed in the previous section suggests that an antenna system consisting of transmission and receiving antenna is necessary to provide a higher ratio of mutual reactance to mutual resistance to achieve higher efficiency. I propose a design method to develop such an antenna system. The antennas, which are applied to the antenna system, are comprised of small square conductive segments and loading lamped reactance manufactured by chip inductors and capacitors. This planar-structure antenna is shown in Fig. 3.

The special structure occupying the entire area, which encompasses every available structure of the antenna, is called the "mother structure". All the available antenna structures were made from the mother structure by substituting the appropriate small segments. These segments were selected using a suitable process, for example, a random process [4].

3.1. Two-port Circuit Expression of Antenna System

The method of moments provides the 2-port circuit expression of this antenna system. The two feeding points of the two antennas become the two ports of this 2-port circuit. In accordance with the reciprocity between the transmission and reception of the antenna, the transmitting and receiving antennas with the same shape achieved highest power transmission efficiency. The induced currents on the small segments, of which the size is less than one-tenth of the operation wavelength, provided the impedance matrix that represents the electromagnetic characteristics of the antenna system. By introducing the induced currents and occurring voltages on the "n-th" segments belonging to the transmitting antenna i_n^t and v_n^t and the similar induced currents and occurring voltages on the "m-th" segments belonging to the transmitting antenna i_m^r and v_m^r, the matrix equation for the antenna system is expressed as follows.

Because v_n^t and v_m^r are diminished on the conductive segments except both the feeding and loading points of each antenna, Eq. (3) is rewritten in the following 4×4 form by components of the admittance matrix, which is the inverse of the impedance matrix [5].

Since the voltage was equal to the products of the current and loading reactance at the loading point, Eq. (4) is transformed into the 2×2 form: therefore the matrix of rank 2 in this 2×2 form

is equal to the 2-port circuit expression of the antenna system with the loading reactance.

$$\begin{bmatrix} z_{11}^{tt} & \cdots & z_{11}^{tt} & z_{11}^{tr} & \cdots & z_{11}^{tr} \\ \vdots & \ddots & \vdots & \vdots & \ddots & \vdots \\ z_{11}^{tt} & \cdots & z_{11}^{tt} & z_{11}^{tr} & \cdots & z_{11}^{tr} \\ z_{11}^{rt} & \cdots & z_{11}^{rt} & z_{11}^{rr} & \cdots & z_{11}^{rr} \\ \vdots & \ddots & \vdots & \vdots & \ddots & \vdots \\ z_{11}^{rt} & \cdots & z_{11}^{rt} & z_{11}^{rr} & \cdots & z_{11}^{rr} \end{bmatrix} \begin{bmatrix} i_1^t \\ \vdots \\ i_N^t \\ i_1^r \\ \vdots \\ i_N^r \end{bmatrix} = \begin{bmatrix} v_1^t \\ \vdots \\ v_N^t \\ v_1^r \\ \vdots \\ v_N^r \end{bmatrix} \tag{3}$$

$$\begin{bmatrix} y_{ee}^{tt} & y_{ea}^{tt} & y_{ee}^{tr} & y_{ea}^{tr} \\ y_{ae}^{tt} & y_{aa}^{tt} & y_{ae}^{tr} & y_{aa}^{tr} \\ y_{ee}^{rt} & y_{ea}^{rt} & y_{ee}^{tt} & y_{ea}^{tt} \\ y_{ae}^{rt} & y_{aa}^{rt} & y_{ae}^{tt} & y_{aa}^{tt} \end{bmatrix} \begin{bmatrix} v_e^t \\ v_a^t \\ v_e^r \\ v_a^r \end{bmatrix} = \begin{bmatrix} i_e^t \\ i_a^t \\ i_e^r \\ i_a^r \end{bmatrix} \tag{4}$$

3.2. Design Algorithm

The design of algorithm started from Eq. (1), which represents power transmission efficiency. The derivatives of Eq. (1) with respect to both the resistances and reactances of both the generating and loading circuits provide the following two equations of second degree that are independent with respects to the reactances of these circuits.

$$\begin{aligned} 0 &= -\left(m^2 - M^2\right)(r_2 + \lambda_2) - (r_1 - \lambda_1)(r_2 + \lambda_2)^2 - (X_2 + L_2)^2 (r_1 - \lambda_1) - 2mM(X_2 + L_2), \\ 0 &= -\left(m^2 - M^2\right)(r_1 + \lambda_1) - (r_2 - \lambda_2)(r_1 + \lambda_1)^2 - (X_1 + L_1)^2 (r_2 - \lambda_2) - 2mM(X_1 + L_1). \end{aligned} \tag{5}$$

Because the reactances are real, the discriminants of these equations are definitely positive. By introducing a new parameter "a", which is the ratio of the resistance of the loading circuit to that of the generating one, these conditions lead the following new inequality expressions using the energy conservation law $\lambda_1\lambda_2 - m^2 > 0$.

$$B \equiv 2\lambda_1\lambda_2 + M^2 - m^2 > 0, \tag{6}$$

$$\begin{aligned} &\frac{4\lambda_1\lambda_2 B + \left(M^2 + m^2\right)^2 - \left(M^2 + m^2\right)\sqrt{8\lambda_1\lambda_2 B + (M^2 + m^2)^2}}{4\lambda_1^2 B} < a \\ &= \frac{r_1}{r_2} < \frac{4\lambda_1\lambda_2 B + \left(M^2 + m^2\right)^2 + \left(M^2 + m^2\right)\sqrt{8\lambda_1\lambda_2 B + (M^2 + m^2)^2}}{4\lambda_1^2 B} \end{aligned}$$

$$\frac{|a\lambda_1 - \lambda_2| + \sqrt{(a\lambda_1 - \lambda_2)^2 + 4a(\lambda_1\lambda_2 - m^2)}}{2a} < r_1 < \frac{-|a\lambda_1 - \lambda_2| + \sqrt{(a\lambda_1 - \lambda_2)^2 + 4a(\lambda_1\lambda_2 + M^2)}}{2a}. \tag{7}$$

According to Eqs. (6) and (7), the ranges in r_1 and r_2 are finite. Hence the optimum values of the complex impedances of both the generating and loading circuits for achieving maximum power transmission efficiency found using a suitable numerical analysis, e.g., the bisection method.

3.3. Example Antenna Design

Maximum power transmission is possible by transmitting and receiving antennas with the same shape. Such antennas were designed using the specifications summarized in Table 2. The same shape of these antennas calculated values of the power transmission efficiency, and the 2-port parameter of the antenna system consisting of these antennas with respect to the loading reactances on these antennas are shown in Fig. 4.

Maximum efficiency was obtained when the small inducutances with the same value were loaded at the same points on both the transmitting and receiving antennas. High power transmission efficiency was possible within the very narrow ranges of the values of the two loading reactances.

Table 2: Specifications of antenna design.

Segment size	Max. antenna size	Distance between antennas	Frequency	Value of loading reactance
30 mm	150 mm	150 mm	950 MHz	−j200–j200 ohm

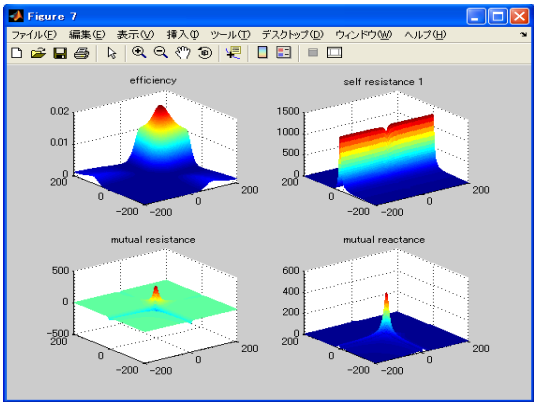

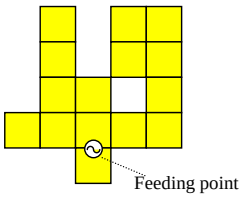

Structure of transmitting and receiving antennas with loading reactances, which are not-shown

Figure 4: Antenna structure, 2-port parameters, and power transmission efficiency via antenna loading reactances.

4. CONCLUSIONS

Under the condition of the 2-port parameters, determined by the same structure of both the transmission and receiving antennas and their loading reactances, maximum power transmission efficiency is possible when the reactance of both the generating and loading circuit are conjugate to the self impedances of these antennas and the resistances both of them are very small within a very narrow range. These characteristics indicate that the transmitting energy must be stored in a rechargeable battery to be useful for active devices and a real-time control of this value is necessary to stabilize power transmission against changes in propagation environments. The transmission and receiving antennas with loaded reactances can drastically affect power transmission efficiency by changing these reactances: therefore antenna system consisting of several antennas with valuable loading reactances can sequentially provide high power transmitting efficiency from one adjacent pair to the next by changing their reactances.

REFERENCES

1. Karalis, A., J. D. Joannopoulos, and M. Soljacic, "Efficient wireless non-radiative mid-range energy transfer," *Ann. Phys.*, Vol. 323, No. 1, 34–48, 2008.
2. Ahn, S. and J. Kim, "Magnetic field design for high efficient and low EMF wireless power transfer in on-line electric vehicle," *Proc. of EuCAP2011*, 4148–4151, 2011.
3. Takei, K., "Use of adaptive reactance control in optimum antenna design for transmitting power in near-mid ranges," *Proceedings of Asia Pacific Microwave Conference*, 1829–1832, Singapore, Dec. 2009.
4. Takei, K. and T. Ogawa, "Increment-decrement algorithm for compact circularly polarized antenna," *Proceedings of ICEcom*, 525–528, Dubrovnic, Croatia, Oct. 2005.
5. Takei, K., "Auto design tool for multimode antenna using method of moments and genetic algorithm with novel matrix equation," *Proceedings of PIERS*, 154, Singapore, Jan. 2003.

Wireless Power System for Implantable Heart Pumps Based on Energy Injection Control

H. Y. Leung[1], **D. M. Budgett**[1], **D. McCormick**[1], **and A. P. Hu**[2]

[1]Auckland Bioengineering Institute, University of Auckland
Auckland 1142, New Zealand
[2]Department of Electrical and Computer Engineering
University of Auckland, Auckland 1142, New Zealand

Abstract— Inductive power transfer (IPT) for powering high power implantable devices, such as total artificial hearts and heart assist devices, greatly reduces the risk of infection by eliminating the driveline cable which otherwise needs to puncture the skin to provide power. The operating conditions are demanding in terms of the power level, a wide range of coupling variations, restrictions on heat generated and resultant temperature rise in the surrounding tissue. This paper presents a wireless power transfer system which satisfies the requirements for powering a high power implant. The system consists of a half-bridge energy injection circuit which is fully soft-switched. No extra switching or power components are required to regulate the power flow. This is achieved by injecting energy into the tank when required, and allowing the resonant tank to free oscillate when power is sufficient. Feedback from the implanted device is provided via a radio link completing the feedback control loop. The external and internal power transfer coils are air-cored and have a maximum diameter of 75 mm and thickness of 7 mm including the biocompatible encapsulation, making a light and compact transcutaneous energy transfer (TET) system. The presented system is capable of delivering over 15 W to the implanted load over a wide range of coupling variation (k = 0.15 to 0.3) which corresponds to 20 mm to 10 mm coil separation. The system has achieved an end to end power efficiency of 78.7% to 82.2%.

1. INTRODUCTION

This paper presents a standalone Transcutaneous Energy Transfer (TET) system for powering high power implantable medical devices such as artificial heart pumps. Current state-of-the-art heart pumps require a level of power consumption that ranges from 5 to 15 W [1]. Such power levels are too demanding for implantable batteries for a heart pump which must run continuously. Thus electric power must be externally provided either with a percutaneous cable (punctures through the skin) or via a transcutaneous (through unbroken skin) method. Inductive power transfer (IPT) is a well known technology and is also very promising for delivering power to implantable devices.

In this paper, a TET system based on a half-bridge energy injection resonant converter was designed for powering an implantable heart pump. A TET system, when used by a patient, must be able to adapt to the prevailing coupling conditions as the separation of the coils depends on the tissue thickness of the patient and surgical placement. In addition to this the system should be able to tolerate slight changes in coupling, due to movement from physical activity and repetitive activity such as respiration. Size and weight of the power transfer coils is another important factor, especially for the implanted coil which has to be thin enough in order for it to be placed just under the skin. Finally the heat generated by the power transfer coils must not cause damage to the surrounding tissue.

2. SYSTEM ARCHITECTURE

A high level block diagram of the TET system is shown in Figure 1. It consists of an external primary power converter with its power delivery coil L1 and an internal secondary power receiving coil L2 with its power conditioning circuit. Resistor R2 represents the load of the implantable device. Power regulation is performed on the primary side with an energy injection converter which drives the power delivery coil which is part of a series resonant tank.

2.1. Resonant System and Power Transfer Coils

The transfer of power is achieved through the use of two LC resonant circuits, where the coils are mutually coupled together via the interaction of oscillating magnetic fields. The strength of the coupling is determined by a coupling co-efficient k. In this particular application the coupling k may vary quite significantly during practical usage.

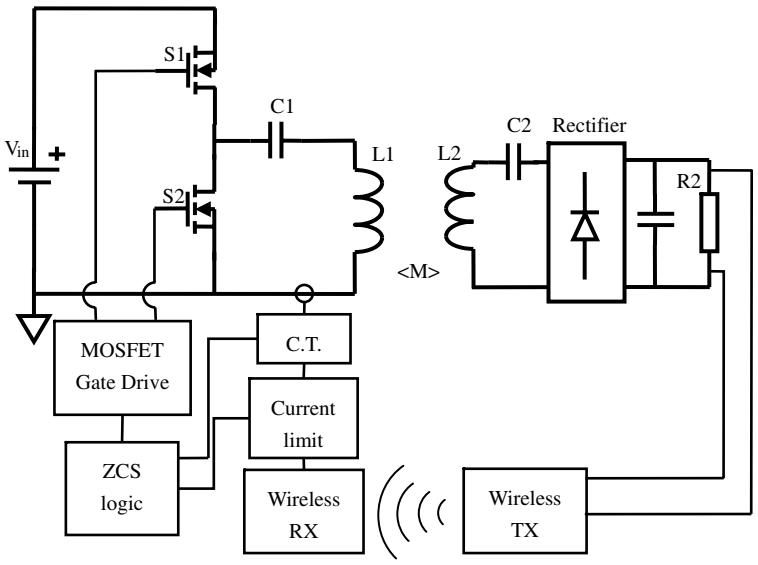

Figure 1: High level block diagram of presented TET system.

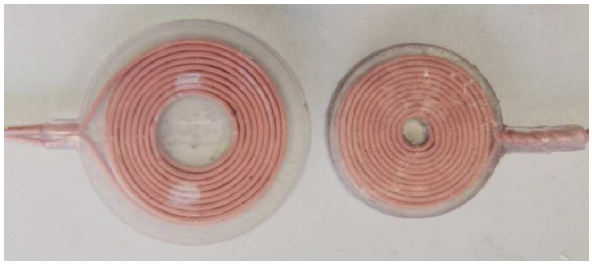

Figure 2: (a) Primary and (b) secondary power transfer coils.

Since the energy injection converter is essentially a voltage-fed half bridge converter the primary LC resonant tank topology must be a series tuned tank, as a parallel tuned tank has voltage source type characteristics and must be driven by a current-fed converter [2]. The configuration of the secondary resonant tank is also series tuned; this was chosen as this makes the secondary resonant current the same as the load current.

The most ideal shape of the power transfer coils is as flat and small as possible. The requirement of it being flat is because the secondary coil has to be implanted inside the body and near the surface of the skin, a flat coil allows the coil to be implanted just under the skin secured by nearby bone mass (such as on top of the rib cage), without creating a large extrusion. The coils used in the system are shown in Figure 2, they were made by winding 2 mm diameter Litz wire in a two layer pancake configuration creating a 4 mm thick coil, encapsulating the coils with biocompatible silicon brought the thickness to 6 mm. The diameter of the implanted coil including encapsulation is 55 mm and the external coil is 65 mm. The weight of the coil is also important, as a heavy coil would induce more discomfort, thus no ferrite core was used in our coils and the primary and secondary coils weighed 60 g and 45 g respectively. The size of the coils were designed so a maximum displacement of 20 mm of the coils either vertical or horizontally could be tolerated without their coupling co-efficient dropping below $k = 0.15$. The inductances of the primary and secondary coils were 14.2 µH and 11.45 µH respectively.

The tuning capacitors of the primary and secondary capacitors were not selected to make the individual primary and secondary tanks resonate at a nominal resonant frequency. As the coupling variation during operation is large ($k = 0.15$ to 0.3) it is important to analyze how the impedance of the system changes across all coupling conditions and select capacitor values which will minimize loss and avoids any frequency bifurcation behavior within the operating coupling range. The capacitor values were selected using an optimisation process previously described [3], the primary and secondary capacitances used in this setup are 12 nF and 16 nF respectively.

2.2. Energy Injection Converter

A half-bridge energy injection converter [4] was used in our TET system and is depicted in Figure 3. This converter was chosen due to a low component count, ability to implement soft-switching and it provides complete power flow control without additional power stage components. The half-bridge energy injection converter consists of two operating states; injection state and free oscillation state. During the injection state the high side switch is on while the low side switch is off, connecting the resonant tank to the DC input source, thus injecting energy into the tank. During the free oscillation state the low side switch is on while the high side switch is off, which connects the resonant tank together allowing it to free oscillate, damped by its own or any reflected impedance. In order for the system to be soft-switched the converter must change states during the zero crossings of the resonant current, this is achieved using a current transformer on the primary resonant track. The injection state can only occur during the positive phase of the resonant current as the power source is DC and can only provide power in one direction, but free oscillation state can occur in both phases of the resonant current.

2.3. Feedback and Control

A current limit controller was used to control power flow. The peak of the resonant current during the negative current phase is compared against a current limit. If the peak is below the limit, then an injection state will occur during the next positive current phase; else if the peak is above the limit, the converter will stay in free oscillation state during the next positive current phase. This current limit is the output of a proportional-integral controller which operates on the error of the output voltage with the desired output voltage. The output voltage at the secondary is received through a low power 2.4 GHz radio link. Control of the system is achieved completely onboard with discrete analog components and no external controllers were used, hence it is a standalone system.

3. RESULTS

The performance of the TET system was characterized at a load of 10 ohms. The control system was set to regulate the output voltage to 12.5 V corresponding to an output power of 15 W being available to drive the heart pump and charge any internal battery. Power measurements were recorded at different separations between the power transfer coils, this separation refers to the displacement of the coils with their centers concentric and radii parallel to each other. For this set of coils a 5 mm separation corresponds to a coupling co-efficient of $k = 0.41$ and a 20 mm separation corresponds to a coupling co-efficient of $k = 0.15$. Note that coupling is not linearly proportional to separation.

We have chosen 10 mm as a minimum coil separation to accommodate encapsulation, implantation, tissue, coil holder and clothing contributions. The output power vs. separation relationship is shown in Figure 4, it can be seen that the system is only able to reach desired output voltage when the separation is greater than 10 mm (or $k < 0.3$). It is unintuitive that output power decreases at close coupling. Figure 5 plots the injection percentage (power flow percentage) of the energy injection converter vs. vertical separation to help explain the effect of close coupling. Figure 5 shows that more energy injection is required when coupling is good than when coupling low, this

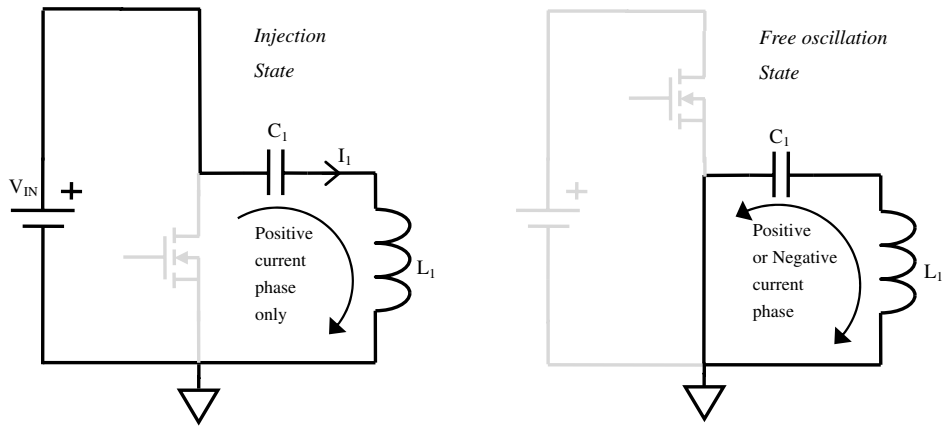

Figure 3: States of a half-bridge energy injection converter.

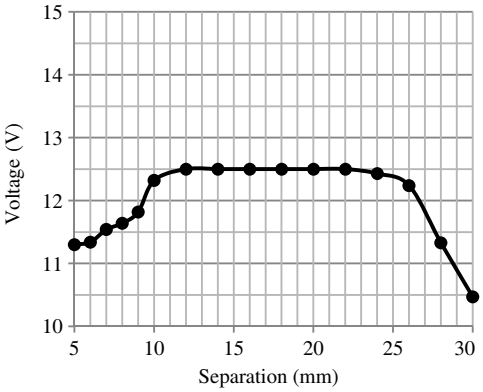

Figure 4: Output voltage vs. separation.

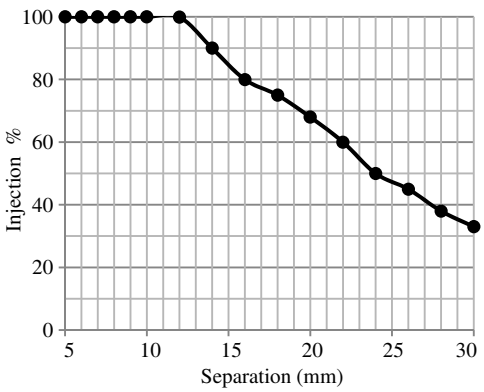

Figure 5: Injection percentage vs. separation.

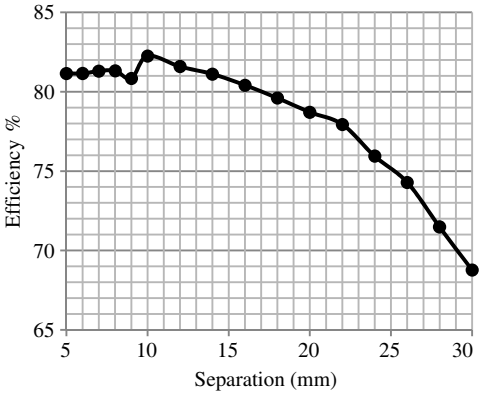

Figure 6: Efficiency vs. separation.

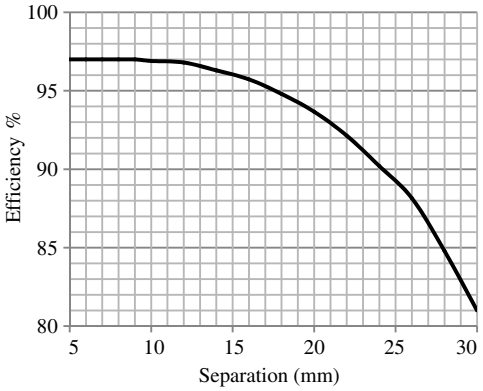

Figure 7: Theoretical maximum efficiency vs. separation.

is because the reflected impedance seen by the converter is greater when coupling is good. Thus it takes more energy injections to sustain the same resonant current. If operation at higher coupling levels is desired, different tuning capacitors would be selected to allow the desired output voltage to be reached at the cost of inferior efficiency at the low coupling end. A higher input voltage can also improve operation at high coupling, however high DC voltages come with safety issues and cause greater stress on the power components.

The end to end power efficiency vs. vertical separation is shown in Figure 6. Also a simulation of the resonant system was performed in order to find the theoretical maximum efficiency of the system when only the losses of the coils and resonant capacitors are taken into account; the result of this is shown in Figure 7. In Figure 6, it can be seen that for the designed separation range of 10 mm to 20 mm, the efficiency steadily decreases from 82.2% to 78.7%. This 3.5% decrease in efficiency across the coupling change of $k = 0.3$ to 0.15, is reflective of the theoretical maximum efficiency drop of 3.3% across the same coupling range. Thus the energy injection converter maintains almost constant efficiency throughout its control range.

4. CONCLUSION

This standalone TET system accommodates the power conditions applicable for an implantable heart pump. A half-bridge resonant converter was used to drive the power transfer coils, and power flow control was performed on the external primary side via feedback through wireless communication. The system was able to provide 15 W of power across a coil separation of 10 mm to 20 mm corresponding to a coupling change of $k = 0.3$ to 0.15; with a maximum end to end efficiency of 82.2% and a minimum efficiency of 78.7%. It has also been demonstrated that the energy injection converter retains it efficiency across a control range of 100% to 25% energy injection, making it ideal for TET systems which need to operate across a wide range of coupling. The presented power transfer coils and circuitry are also sufficiently compact for implantation.

REFERENCES

1. Strüber, M., A. L. Meyer, D. Malehsa, C. Kugler, A. R. Simon, and A. Haverich, "The current status of heart transplantation and the development of 'artificial heart systems'," *Dtsch Arztebl Int.*, Vol. 106, 471–478, 2009.
2. Hu, A. P., "Selected resonant converters for IPT power supplies," Ph.D. Dissertation, Department of Electrical and Electronic Engineeing, University of Auckland, Auckland, New Zealand, 2001.
3. Leung, H. Y., D. M. Budgett, and A. P. Hu, "Minimizing power loss in air-cored coils for TET heart pump systems," *IEEE Journal on Emerging and Selected Topics in Circuits and Systems*, Vol. 1, 8, 2011.
4. Li, H. L., A. Hu, and G. A. Covic, "Development of a discrete energy injection inverter for contactless power transfer," *3rd IEEE Conference on Industrial Electronics and Applications, ICIEA 2008*, Singapore, 2008.

Theory of the $\hat{L}_2(\hat{c},\hat{\rho},\hat{n})$ Numbers and Its Application to the Slow Wave Propagation in the Coaxial Ferrite Waveguide

Georgi Nikolov Georgiev[1] and Mariana Nikolova Georgieva-Grosse[2]

[1]Faculty of Mathematics and Informatics
University of Veliko Tirnovo "St. St. Cyril and Methodius"
BG-5000 Veliko Tirnovo, Bulgaria
[2]Consulting and Researcher in Physics and Computer Sciences
Meterstrasse 4, Gerlingen D-70839, Germany

Abstract— The core of the theory of $\hat{L}_2(\hat{c},\hat{\rho},\hat{n})$ numbers ($\hat{c}$, $\hat{\rho}$ — real, $0<\hat{\rho}<1$, $\hat{n}$ — a restricted positive integer) — the theorem for existence and for the basic characteristics of these new real positive quantities, is formulated by means of three lemmas and proved numerically. The first discovers the existence of the same and ascertains them, provided $\hat{c}\neq\hat{l}$, ($\hat{l}=0,-1,-2,\ldots$), as the common limits of definite couples of infinite sequences of real positive numbers, composed through the real positive zeros of a special function, devised, using real Kummer $\hat{\Phi}(\hat{a},\hat{c};\hat{x})$ and $\hat{\Phi}(\hat{a},\hat{c};\hat{\rho}\hat{x})$ and Tricomi $\hat{\Psi}(\hat{a},\hat{c};\hat{x})$ and $\hat{\Psi}(\hat{a},\hat{c};\hat{\rho}\hat{x})$ confluent hypergeometric ones of selected in an appropriate way real parameters $\hat{a}$ and $\hat{c}$, and a variable $\hat{x}$ (resp. $\hat{\rho}\hat{x}$). The second determines them for $\hat{c}=\hat{l}$ (when the Kummer function is not defined) with the help of the equality $\hat{L}_2(\hat{c},\hat{\rho},\hat{n})=\hat{L}_2(2-\hat{l},\hat{\rho},\hat{n})$. The third lemma says that for any admissible $\hat{c}$, $\hat{\rho}$ and $\hat{n}$, it is fulfilled: $\hat{L}_2(\hat{c},\hat{\rho},\hat{n})=\hat{L}_2(2-\hat{c},\hat{\rho},\hat{n})$ and $\hat{L}_2(1+\hat{h},\hat{\rho},\hat{n})=\hat{L}_2(1-\hat{h},\hat{\rho},\hat{n})$, ($\hat{h}=\pm(1-\hat{c})$). A problem for slow guided wave transmission is pointed out, in whose solution the outcomes obtained could be employed.

1. INTRODUCTION

The initiation of the L numbers (the common limits of certain infinite sequences of real positive numbers with terms, constructed by some zeros of transcendental functions, involving complex or real confluent hypergeometric [1] and eventually real cylindrical ones, too of expressly chosen parameters [2–15]) is a pioneering idea which originates a new branch of the theory of numbers. Its source are the problems for propagation of normal TE_{0n} or slow $\widehat{TE}_{0\hat{n}}$ modes in the azimuthally magnetized circular ferrite and ferrite-dielectric waveguides (configurations, suitable for the development of various microwave passive components), integrated in terms of the functions mentioned [2–15]. To distinguish the quantities and functions, connected with the second type of waves, all of which are real, it is accepted above the characters, standing for them, to put hats "$\widehat{\ }$" [4, 8, 10].

The fundamental result of this study is the numerical proof of the existence of finite real positive limits (named $\hat{L}_2(\hat{c},\hat{\rho},\hat{n})$ numbers) of the infinite sequences of real numbers $\hat{K}_{2-}(\hat{c},\hat{\rho},\hat{n},\hat{k}_-)=|\hat{k}_-|\hat{\chi}^{(\hat{c})}_{\hat{k}_-,\hat{n}}(\hat{\rho})$ and $\hat{M}_{2-}(\hat{c},\hat{\rho},\hat{n},\hat{k}_-)=|\hat{a}_-|\hat{\chi}^{(\hat{c})}_{\hat{k}_-,\hat{n}}(\hat{\rho})$, attained at $\hat{k}_-\to-\infty$, ($\hat{\chi}^{(\hat{c})}_{\hat{k}_-,\hat{n}}(\hat{\rho})$ — $\hat{n}$th real positive zero of the function $\hat{F}_2(\hat{a},\hat{c};\hat{x},\hat{\rho})=\hat{\Phi}(\hat{a},\hat{c};\hat{x})\hat{\Psi}(\hat{a},\hat{c};\hat{\rho}\hat{x})-\hat{\Phi}(\hat{a},\hat{c};\hat{\rho}\hat{x})\hat{\Psi}(\hat{a},\hat{c};\hat{\rho}\hat{x})$ in $\hat{x}$, $\hat{\Phi}(\hat{a},\hat{c};\hat{x})$ and $\hat{\Psi}(\hat{a},\hat{c};\hat{x})$ — Kummer and Tricomi confluent hypergeometric ones, resp. [1], $\hat{a}$, $\hat{c}$, $\hat{x}$, $\hat{\rho}$ — real, $\hat{a}<0$, $\hat{a}\neq-\hat{m}$, $\hat{m}=1,2,3,\ldots$, $\hat{a}=\hat{c}/2+\hat{k}_-$, $\hat{c}>0$ or $\hat{c}<0$, $\hat{c}\neq\hat{l}$, $\hat{l}=0,-1,-2,\ldots$, $\hat{a}<\hat{c}<0$ (in the two instances $\hat{a}<\hat{c}$), $\hat{x}>0$, $\hat{\rho}>0$, $0<\hat{\rho}<1$, $\hat{k}_-=\hat{a}-\hat{c}/2$ — real, $\hat{k}_-<0$, $\hat{a}_-\equiv\hat{a}$, $\hat{n}$ — a bounded positive integer, the maximum value which it might acquire depends on the parameters of $\hat{F}_2$). This fact constitutes the kernel of the enunciated Theorem for the $\hat{L}_2(\hat{c},\hat{\rho},\hat{n})$ numbers, whose object are the case $\hat{c}=\hat{l}$ and definite relations for the quantities, as well. The possibility to harness it in practice, is also debated.

2. THEOREM FOR EXISTENCE AND FOR THE MAIN PROPERTIES OF THE $\hat{L}_2(\hat{c},\hat{\rho},\hat{n})$ NUMBERS

2.1. Theorem 1

The statement of the theorem is expressed by the following three Lemmas:

Lemma 1: *If $\hat{\chi}^{(\hat{c})}_{\hat{k}_-,\hat{n}}(\hat{\rho})$ is the $\hat{n}$th real positive zero of the function $\hat{F}_2(\hat{a},\hat{c};\hat{x},\hat{\rho})=\hat{\Phi}(\hat{a},\hat{c};\hat{x})\times\hat{\Psi}(\hat{a},\hat{c};\hat{\rho}\hat{x})-\hat{\Phi}(\hat{a},\hat{c};\hat{\rho}\hat{x})\hat{\Psi}(\hat{a},\hat{c};\hat{x})$ in $\hat{x}$ in which $\hat{\Phi}(\hat{a},\hat{c};\hat{x})$ and $\hat{\Psi}(\hat{a},\hat{c};\hat{x})$ are the Kummer and Tricomi*

confluent hypergeometric functions with $\hat{a} = \hat{c}/2 + \hat{k}_-$ — *real, negative,* $(\hat{a} \neq -\hat{m},\ \hat{m} = 1, 2, 3, \ldots)$, $\hat{c}$ — *a restricted positive or negative real number, different from zero or a negative integer* $(\hat{c} \neq \hat{l},\ \hat{l} = 0, -1, -2, \ldots)$, (*in both cases* $\hat{a} < \hat{c}$), $\hat{x}$ — *real, positive,* $\hat{k}_- = \hat{a} - \hat{c}/2$ — *real, negative,* $\hat{\rho}$ — *real, positive,* $0 < \hat{\rho} < 1$, $\hat{n} = 1, 2, \ldots, \hat{t}$, $\hat{t}$ — *a finite positive integer, whose numerical equivalent is determined by the parameters of* $\hat{F}_2$, *and if* $\hat{K}_{2-}(\hat{c}, \hat{\rho}, \hat{n}, \hat{k}_-) = |\hat{k}_-|\hat{\chi}^{(\hat{c})}_{\hat{k}_-,\hat{n}}(\hat{\rho})$ *and* $\hat{M}_{2-}(\hat{c}, \hat{\rho}, \hat{n}, \hat{k}_-) = |\hat{a}_-|\hat{\chi}^{(\hat{c})}_{\hat{k}_-,\hat{n}}(\hat{\rho})$, $(\hat{a}_- \equiv \hat{a})$, *then the infinite sequences of real positive numbers* $\{\hat{\chi}^{(\hat{c})}_{\hat{k}_-,\hat{n}}(\hat{\rho})\}$, $\{\hat{K}_{2-}(\hat{c}, \hat{n}, \hat{\rho}, \hat{k}_-)\}$ *and* $\{\hat{M}_{2-}(\hat{c}, \hat{n}, \hat{\rho}, \hat{k}_-)\}$ *are convergent for* $\hat{k}_- \to -\infty$, $(\hat{c}, \hat{n}$ — *fixed*). *The limit of the first sequence is zero and the limit of the second and third ones is the same. It equals the finite real positive number* $\hat{L}_2$ *where* $\hat{L}_2 = \hat{L}_2(\hat{c}, \hat{\rho}, \hat{n})$. *It holds:*

$$\lim_{\hat{k}_- \to -\infty} \hat{K}_{2-}\left(\hat{c}, \hat{\rho}, \hat{n}, \hat{k}_-\right) = \lim_{\hat{k}_- \to -\infty} \hat{M}_{2-}\left(\hat{c}, \hat{\rho}, \hat{n}, \hat{k}_-\right) = \hat{L}_2\left(\hat{c}, \hat{\rho}, \hat{n}\right). \tag{1}$$

Lemma 2: *If* $\hat{L}_2(\hat{l} - \hat{\varepsilon}, \hat{\rho}, \hat{n})$ *and* $\hat{L}_2(\hat{l} + \hat{\varepsilon}, \hat{\rho}, \hat{n})$ *are finite real positive numbers in the sense of Lemma 1 in which* $\hat{l} = 0, -1, -2, \ldots$ *is zero or a negative integer,* $\hat{\varepsilon}$ *and* $\hat{\rho}$ *are real positive numbers, less than unity,* $(0 < \hat{\varepsilon} < 1,\ 0 < \hat{\rho} < 1)$ *and* $\hat{n} = 1, 2, \ldots, \hat{t}$ ($\hat{t}$ — *a finite positive integer, set in the Lemma in question and specified by the parameters of the function* $\hat{F}_2$, *defined in the same*), *then the infinite sequences of real positive numbers* $\{\hat{L}_2(\hat{l} - \hat{\varepsilon}, \hat{\rho}, \hat{n})\}$ *and* $\{\hat{L}_2(\hat{l} + \hat{\varepsilon}, \hat{\rho}, \hat{n})\}$ *are convergent for* $\hat{\varepsilon} \to 0$ *and possess a common limit. The sequence* $\{\hat{L}_2(\hat{l} - \hat{\varepsilon}, \hat{\rho}, \hat{n})\}$ ($\{\hat{L}_2(\hat{l} + \hat{\varepsilon}, \hat{\rho}, \hat{n})\}$) *tends to it from the left* (*right*). *The limit mentioned is accepted as a value of* $\hat{L}_2(\hat{c}, \hat{\rho}, \hat{n})$ *in case* $\hat{c} = \hat{l}$ ($\hat{c}$ —

Table 1: Real positive zeros $\hat{\chi}^{(\hat{c})}_{\hat{k}_-,\hat{n}}(\hat{\rho})$ of $\hat{F}_2(\hat{a}, \hat{c}; \hat{x}, \hat{\rho})$ and numbers $\hat{K}_{2-}(\hat{c}, \hat{\rho}, \hat{n}, \hat{k}_-)$ and $\hat{M}_{2-}(\hat{c}, \hat{\rho}, \hat{n}, \hat{k}_-)$ for large negative $\hat{k}_-$ in case $\hat{c} = 1,\ 3$; $\hat{n} = 1,\ 2$ and $\hat{\rho} = 0.1,\ 0.2$.

$\hat{k}_-$ \ $\hat{c}$	$\hat{\chi}_-$	$\hat{K}_{2-}$	$\hat{M}_{2-}$	$\hat{\chi}_-$	$\hat{K}_{2-}$	$\hat{M}_{2-}$	$\hat{\chi}_-$	$\hat{K}_{2-}$	$\hat{M}_{2-}$	$\hat{\chi}_-$	$\hat{K}_{2-}$	$\hat{M}_{2-}$
	1						3					
	$\hat{n}=1$			$\hat{n}=2$			$\hat{n}=1$			$\hat{n}=2$		
	$\hat{\rho}=0.1$											
−10	0.51445	**5.1**4449	4.88726	2.14626	**21**.46259	**20.**38946	0.77197	**7.7**1970	6.56174	2.45819	**24**.58191	**20**.89463
−20	0.25611	**5.12**225	4.99419	1.05270	**21**.05403	**20.**52768	0.38336	**7.66**729	**7.0**9224	1.20250	**24**.04991	**22**.24617
−30	0.17061	**5.11**817	**5.0**3286	0.69939	**20.9**8181	**20.**63211	0.25526	**7.65**773	**7.2**7485	0.79855	**23.**95648	**22**.75866
−40	0.12792	**5.11**674	**5.0**5278	0.52392	**20.9**5677	**20.**69481	0.19136	**7.65**440	**7.3**6736	0.59810	**23.**92413	**23.**02698
−50	0.10232	**5.11**608	**5.0**6492	0.41890	**20.9**4522	**20.**73577	0.15306	**7.65**286	**7.4**2327	0.47818	**23.**90922	**23.**19195
−60	0.08526	**5.11**573	**5.0**7310	0.34898	**20.9**3896	**20.**76447	0.12753	**7.65**202	**7.4**6072	0.39835	**23.**90114	**23.**30361
−70	0.07308	**5.11**551	**5.0**7897	0.29907	**20.9**3519	**20.**78565	0.10931	**7.65**152	**7.4**8756	0.34138	**23.8**9627	**23.**38420
−80	0.06394	**5.11**537	**5.0**8340	0.26166	**20.9**3274	**20.**80191	0.09564	**7.65**119	**7.5**0773	0.29866	**23.8**9311	**23.**44511
−90	0.05684	**5.11**528	**5.0**8686	0.23257	**20.9**3106	**20.**81478	0.08501	**7.650**97	**7.5**2345	0.26545	**23.8**9095	**23.**49276
−100	0.05115	**5.11**521	**5.0**8963	0.20930	**20.92**987	**20.**82522	0.07651	**7.650**81	**7.5**3604	0.23889	**23.88**940	**23.**53106
	$\hat{\rho}=0.2$											
−10	0.80339	8.03386	**7.6**3217	3.37146	**3**3.71462	**32.**02889	1.01016	10.10161	8.58637	3.61117	**3**6.11173	**3**0.69497
−20	0.39845	**7.96**901	**7.7**6979	1.62618	**32.**52359	**3**1.71050	0.49988	**9.99**765	**9.2**4783	1.73737	**3**4.74739	**3**2.14133
−30	0.26524	**7.95**723	**7.8**2461	1.07737	**32.**32123	**3**1.78254	0.33263	**9.97**886	**9.4**7992	1.15057	**3**4.51699	**3**2.79114
−40	0.19883	**7.95**312	**7.8**5371	0.80629	**32.**25160	**3**1.84845	0.24931	**9.97**232	**9.5**9836	0.86095	**3**4.43781	**3**3.14639
−50	0.15902	**7.95**122	**7.8**7171	0.64439	**32.**21958	**3**1.89738	0.19939	**9.96**929	**9.6**7022	0.68803	**3**4.40141	**3**3.36937
−60	0.13250	**7.95**019	**7.8**8394	0.53670	**32.**20224	**3**1.93388	0.16613	**9.96**765	**9.7**1846	0.57303	**3**4.38170	**3**3.52216
−70	0.11357	**7.94**957	**7.8**9279	0.45988	**32.1**9180	**3**1.96186	0.14238	**9.96**667	**9.7**5309	0.49100	**3**4.36984	**3**3.63334
−80	0.09936	**7.94**917	**7.8**9949	0.40231	**32.1**8503	**3**1.98387	0.12458	**9.96**602	**9.7**7916	0.42953	**3**4.36215	**3**3.71786
−90	0.08832	**7.94**889	**7.9**0473	0.35756	**32.1**8040	**32.**00162	0.11073	**9.96**558	**9.7**9949	0.38174	**3**4.35688	**3**3.78427
−100	0.07949	**7.94**870	**7.9**0895	0.32177	**32.1**7708	**32.**01620	0.09965	**9.96**527	**9.8**1579	0.34353	**3**4.35312	**3**3.83782

zero or a negative integer). *Thus, it is assumed that:*

$$\hat{L}_2\left(\hat{c},\hat{\rho},\hat{n}\right)=\lim_{\hat{\varepsilon}\to 0}\hat{L}_2\left(\hat{l}-\hat{\varepsilon},\hat{\rho},\hat{n}\right)=\lim_{\hat{\varepsilon}\to 0}\hat{L}_2\left(\hat{l}+\hat{\varepsilon},\hat{\rho},\hat{n}\right). \tag{2}$$

Lemma 3: *Under the conditions of Lemmas 1 and 2, it is true: i) Stipulating that* $\hat{c}\neq\hat{l}$, *it holds:* $\hat{L}_2(\hat{c},\hat{\rho},\hat{n})=\hat{L}_2(2-\hat{c},\hat{\rho},\hat{n})$; *ii) The requirement* $\hat{c}=\hat{l}$ *yields:* $\hat{L}_2(\hat{l},\hat{\rho},\hat{n})=\hat{L}_2(2-\hat{l},\hat{\rho},\hat{n})$; *iii) If* $\hat{c}=1\pm\hat{h}$, $\hat{h}\neq\hat{l}$, $(\hat{c}\neq 0,\pm1,\pm2,\ldots)$, *it is valid:* $\hat{L}_2(1+\hat{h},\hat{\rho},\hat{n})=\hat{L}_2(1-\hat{h},\hat{\rho},\hat{n})$; *iv) When* $\hat{c}=1\pm\hat{l}$, $(\hat{c}=0,\pm1,\pm2,\ldots)$, *it is fulfilled:* $\hat{L}_2(1+\hat{l},\hat{\rho},\hat{n})=\hat{L}_2(1-\hat{l},\hat{\rho},\hat{n})$.

2.2. Numerical Proof

The proof of Lemma 1 is illustrated in Tables 1 and 2 for $\hat{c}$ — positive integers, $\hat{n}=1$ and 2, and $\hat{c}$ — arbitrary real numbers, save for $\hat{c}=\hat{l}$; $\hat{n}=1$ and $\hat{\rho}=0.1$ and 0.2 (cf. the digits, marked by bold face type), and of Lemmas 2 and 3 — in Table 3 for $\hat{l}=0,-1,\ldots,-5$, $\hat{\varepsilon}=1.10^{-i}$, $i=1,2,\ldots,5$, $\hat{n}=1$, $\hat{\rho}=0.1$ and 0.2. Table 2 shows that $\hat{\chi}^{(\hat{c})}_{\hat{k}_-,\hat{n}}(\hat{\rho})=\hat{\chi}^{(2-\hat{c})}_{\hat{k}_-,\hat{n}}(\hat{\rho})$, $\hat{K}_{2-}(\hat{c},\hat{\rho},\hat{n},\hat{k}_-)=\hat{K}_{2-}(2-\hat{c},\hat{\rho},\hat{n},\hat{k}_-)$ and $\hat{M}_{2-}(\hat{c},\hat{\rho},\hat{n},\hat{k}_-)=\hat{M}_{2-}(2-\hat{c},\hat{\rho},\hat{n},\hat{k}_-)$, as well. The effect of $\hat{\rho}$ and $\hat{c}$ on $\hat{L}_2(\hat{c},\hat{\rho},\hat{n})$ at $\hat{n}=1$ is presented in Table 4. The blank spaces in the latter reflect the circumstance that the numbers studied do not exist in the meaning of Lemma 1, provided $\hat{c}=\hat{l}$.

3. APPLICATION

The zeros $\hat{\chi}^{(\hat{c})}_{\hat{k},\hat{n}}(\hat{\rho})$ of $\hat{F}_2(\hat{a},\hat{c};\hat{x},\hat{\rho})$ from Lemma 1 determine the eigenvalue spectrum $\bar{\hat{\beta}}_2=\chi^{(\hat{c})}_{\hat{k},\hat{n}}(\hat{\rho})/(2\bar{\hat{r}}_0)$ of the coaxial waveguide of outer and inner conductor radii $\hat{r}_0$ and $\hat{r}_1$, resp., filled with azimuthally magnetized ferrite of off-diagonal element of the Polder permeability tensor

Table 2: Real positive zeros $\hat{\chi}^{(\hat{c})}_{\hat{k}_-,\hat{n}}(\hat{\rho})$ of $\hat{F}_2(\hat{a},\hat{c};\hat{x},\hat{\rho})$ and numbers $\hat{K}_{2-}(\hat{c},\hat{\rho},\hat{n},\hat{k}_-)$ and $\hat{M}_{2-}(\hat{c},\hat{\rho},\hat{n},\hat{k}_-)$ for large negative $\hat{k}_-$ in case $\hat{c}=-8.0791324685$, 0.4157906328, 1.5842093672, 10.0791324685; $\hat{n}=1$ and $\hat{\rho}=0.1$, 0.2.

$\hat{k}_-$ \ $\hat{c}$	$\hat{\chi}_-$	$\hat{K}_{2-}$	$\hat{M}_{2-}$	$\hat{\chi}_-$	$\hat{K}_{2-}$	$\hat{M}_{2-}$	$\hat{\chi}_-$	$\hat{K}_{2-}$	$\hat{M}_{2-}$	$\hat{\chi}_-$	$\hat{K}_{2-}$	$\hat{M}_{2-}$
	−8.0791324685			0.4157906328			1.5842093672			10.0791324685		
	$\hat{\rho}=0.1$											
−10	4.89571	**4**8.95709	68.73362	0.53689	**5.3**6889	**5.**25727	0.53689	**5.3**6889	4.94361	4.89571	**4**8.95709	24.28484
−20	2.30094	**4**6.01878	55.31357	0.26723	**5.3**4456	**5.**28901	0.26723	**5.3**4456	**5.**13289	2.30094	**4**6.01878	34.42304
−30	1.51820	**45.**54598	51.67885	0.17800	**5.3**4010	**5.3**0310	0.17800	**5.3**4010	**5.**19911	1.51820	**45.**54598	37.89492
−40	1.13462	**45.**38490	**4**9.96828	0.13346	**5.33**855	**5.3**1080	0.13346	**5.33**855	**5.**23283	1.13462	**45.**38490	39.66689
−50	0.90622	**45.**31108	**4**8.97183	0.10676	**5.33**783	**5.3**1563	0.10676	**5.33**783	**5.**25327	0.90622	**45.**31108	**4**0.74412
−60	0.75452	**45.**27118	**4**8.31911	0.08896	**5.33**744	**5.3**1894	0.08896	**5.33**744	**5.**26697	0.75452	**45.**27118	**4**1.46873
−70	0.64639	**45.**24719	**4**7.85831	0.07625	**5.33**720	**5.3**2135	0.07625	**5.33**720	**5.**27681	0.64639	**45.**24719	**4**1.98967
−80	0.56540	**45.**23164	**4**7.51559	0.06671	**5.33**705	**5.3**2318	0.06671	**5.33**705	**5.**28420	0.56540	**45.**23164	**4**2.38229
−90	0.50246	**45.**22099	**4**7.25069	0.05930	**5.336**94	**5.3**2462	0.05930	**5.336**94	**5.**28997	0.50246	**45.**22099	**4**2.68883
−100	0.45213	**45.**21338	**4**7.03981	0.05337	**5.336**87	**5.3**2577	0.05337	**5.336**87	**5.**29459	0.45213	**45.**21338	**4**2.93482
	$\hat{\rho}=0.2$											
−10	4.90637	**4**9.06374	68.88336	0.82109	**8.**21090	**8.**04020	0.82109	**8.**21090	7.56051	4.90637	**4**9.06374	24.33774
−20	2.30496	**4**6.09910	55.41012	0.40715	**8.1**4308	**8.**05844	0.40715	**8.1**4308	7.82057	2.30496	**4**6.09910	34.48313
−30	1.52076	**45.**62273	51.76593	0.27103	**8.1**3076	**8.**07442	0.27103	**8.1**3076	7.91608	1.52076	**45.**62273	37.95877
−40	1.13651	**45.**46046	50.05147	0.20316	**8.12**647	**8.**08423	0.20316	**8.12**647	7.96554	1.13651	**45.**46046	39.73294
−50	0.90772	**45.**38611	**4**9.05291	0.16249	**8.12**449	**8.**09071	0.16249	**8.12**449	7.99578	0.90772	**45.**38611	**4**0.81158
−60	0.75577	**45.**34592	**4**8.39888	0.13539	**8.12**341	**8.**09526	0.13539	**8.12**341	**8.**01617	0.75577	**45.**34592	**4**1.53719
−70	0.64745	**45.**32175	**4**7.93718	0.11604	**8.12**276	**8.**09864	0.11604	**8.12**276	**8.**03084	0.64745	**45.**32175	**4**2.05886
−80	0.56633	**45.**30609	**4**7.59380	0.10153	**8.12**234	**8.1**0123	0.10153	**8.12**234	**8.**04192	0.56633	**45.**30609	**4**2.45205
−90	0.50328	**45.2**9537	**4**7.32841	0.09024	**8.12**205	**8.1**0329	0.09024	**8.12**205	**8.**05057	0.50328	**45.2**9537	**4**2.75905
−100	0.45288	**45.2**8770	**4**7.11713	0.08122	**8.12**184	**8.1**0496	0.08122	**8.12**184	**8.**05751	0.45288	**45.2**8770	**4**3.00540

Table 3: $\hat{L}_2(\hat{c},\hat{\rho},\hat{n})$ and $\hat{L}_2(2-\hat{c},\hat{\rho},\hat{n})$ numbers with $\hat{c}=\hat{l}-\hat{\varepsilon}$ and $\hat{c}=\hat{l}+\hat{\varepsilon}$ in case $\hat{l}=0,-1,\ldots,-5$; $\hat{\varepsilon}=1.10^{-i}$, $i=1,2,\ldots,5$; $\hat{n}=1$; $\hat{\rho}=0.1$ and 0.2.

$\hat{L}_2(\hat{c},\hat{\rho},\hat{n})$							$\hat{L}_2(2-\hat{c},\hat{\rho},\hat{n})$					
$\hat{\varepsilon}$ \ $\hat{l}$	−5	−4	−3	−2	−1	0	0	−1	−2	−3	−4	−5
$\hat{\rho}=0.1$												
$\hat{L}_2(\hat{l}-\hat{\varepsilon},\hat{\rho},\hat{n})$							$\hat{L}_2(2-(\hat{l}-\hat{\varepsilon}),\hat{\rho},\hat{n})$					
1.10^{-1}	**25**.27825	**19.8**1062	15.01917	11.00072	**7.9**0269	**5.8**9606	**5.8**9606	**7.9**0269	11.00072	15.01917	**19.8**1062	**25**.27825
1.10^{-2}	**24.76**007	**19.3**5063	**14.6**2399	**10.68**169	**7.67**491	**5.77**432	**5.77**432	**7.67**491	**10.68**169	**14.6**2399	**19.3**5063	**24.76**007
1.10^{-3}	**24.70**853	**19.3**0493	**14.58**482	**10.65**020	**7.65**263	**5.76**270	**5.76**270	**7.65**263	**10.65**020	**14.58**482	**19.3**0493	**24.70**853
1.10^{-4}	**24.70**338	**19.3**0037	**14.58**091	**10.64**706	**7.65**040	**5.76**154	**5.76**154	**7.65**040	**10.64**706	**14.58**091	**19.3**0037	**24.70**338
1.10^{-5}	**24.70**287	**19.299**91	**14.58**052	**10.64**674	**7.65**018	**5.76**142	**5.76**142	**7.65**018	**10.64**674	**14.58**052	**19.299**91	**24.70**287
$\hat{L}_2(2-\hat{l},\hat{\rho},\hat{n})$												
	24.70281	**19.299**86	**14.58**048	**10.64**671	**7.65**016	**5.76**141	**5.76**141	**7.65**016	**10.64**671	**14.58**048	**19.299**86	**24.70**281
$\hat{L}_2(\hat{l}+\hat{\varepsilon},\hat{\rho},\hat{n})$							$\hat{L}_2(2-(\hat{l}+\hat{\varepsilon}),\hat{\rho},\hat{n})$					
1.10^{-5}	**24.70**275	**19.299**81	**14.58**043	**10.64**667	**7.65**013	**5.76**140	**5.76**140	**7.65**013	**10.64**667	**14.58**043	**19.299**81	**24.70**275
1.10^{-4}	**24.70**224	**19.299**35	**14.58**004	**10.64**636	**7.6**4991	**5.76**128	**5.76**128	**7.6**4991	**10.64**636	**14.58**004	**19.299**35	**24.70**224
1.10^{-3}	**24.**69709	**19.29**479	**14.5**7613	**10.64**322	**7.6**4769	**5.76**013	**5.76**013	**7.6**4769	**10.64**322	**14.5**7613	**19.29**479	**24.**69709
1.10^{-2}	**24.**64561	**19.2**4916	**14.5**3703	**10.61**182	**7.6**2551	**5.7**4863	**5.7**4863	**7.6**2551	**10.61**182	**14.5**3703	**19.2**4916	**24.**64561
1.10^{-1}	**24.**13362	18.79589	**14.**14959	**10.**30205	**7.**40874	**5.**63925	**5.**63925	**7.**40874	**10.**30205	**14.**14959	18.79589	**24.**13362
$\hat{\rho}=0.2$												
$\hat{L}_2(\hat{l}-\hat{\varepsilon},\hat{\rho},\hat{n})$							$\hat{L}_2(2-(\hat{l}-\hat{\varepsilon}),\hat{\rho},\hat{n})$					
1.10^{-1}	**25.**75051	**20.**59882	16.24254	**12.**74596	10.16909	**8.**56070	**8.**56070	10.16909	**12.**74596	16.24254	**20.**59882	**25.**75051
1.10^{-2}	**25.2**5593	**20.1**7323	**15.8**9170	**12.4**7555	**9.9**8407	**8.4**6469	**8.4**6469	**9.9**8407	**12.4**7555	**15.8**9170	**20.1**7323	**25.2**5593
1.10^{-3}	**25.20**680	**20.1**3102	**15.85**700	**12.44**892	**9.96**600	**8.45**554	**8.45**554	**9.96**600	**12.44**892	**15.85**700	**20.1**3102	**25.20**680
1.10^{-4}	**25.20**189	**20.12**681	**15.85**353	**12.44**626	**9.96**420	**8.454**63	**8.454**63	**9.96**420	**12.44**626	**15.85**353	**20.12**681	**25.20**189
1.10^{-5}	**25.20**140	**20.12**639	**15.85**318	**12.44**600	**9.96**402	**8.454**54	**8.454**54	**9.96**402	**12.44**600	**15.85**318	**20.12**639	**25.20**140
$\hat{L}_2(2-\hat{l},\hat{\rho},\hat{n})$												
	25.20135	**20.12**634	**15.85**315	**12.44**597	**9.96**400	**8.454**53	**8.454**53	**9.96**400	**12.44**597	**15.85**315	**20.12**634	**25.20**135
$\hat{L}_2(\hat{l}+\hat{\varepsilon},\hat{\rho},\hat{n})$							$\hat{L}_2(2-(\hat{l}+\hat{\varepsilon}),\hat{\rho},\hat{n})$					
1.10^{-5}	**25.20**129	**20.12**629	**15.85**311	**12.44**594	**9.963**98	**8.454**52	**8.454**52	**9.963**98	**12.44**594	**15.85**311	**20.12**629	**25.20**129
1.10^{-4}	**25.20**080	**20.12**587	**15.85**276	**12.44**567	**9.963**80	**8.454**43	**8.454**43	**9.963**80	**12.44**567	**15.85**276	**20.12**587	**25.20**080
1.10^{-3}	**25.**19589	**20.12**165	**15.8**4929	**12.44**302	**9.96**199	**8.45**352	**8.45**352	**9.96**199	**12.44**302	**15.8**4929	**20.12**165	**25.**19589
1.10^{-2}	**25.**14684	**20.**07953	**15.8**1468	**12.4**1648	**9.9**4402	**8.4**4446	**8.4**4446	**9.9**4402	**12.4**1648	**15.8**1468	**20.**07953	**25.**14684
1.10^{-1}	24.65958	19.66187	**15.**47242	**12.**15524	**9.**76864	**8.**35840	**8.**35840	**9.**76864	**12.**15524	**15.**47242	19.66187	24.65958

$\hat{\alpha}=\gamma\hat{M}_r/\hat{\omega}$, ($\gamma$ — gyromagnetic ratio, $\hat{M}_r$ — remanent magnetization, $\hat{\omega}$ — angular frequency of the wave) and scalar permittivity $\hat{\varepsilon}=\varepsilon_0\hat{\varepsilon}_r$ for slow $\widehat{TE}_{0\hat{n}}$ modes of phase constant $\hat{\beta}$, if it holds $\hat{c}=3$, $\hat{k}=\hat{\alpha}\bar{\hat{\beta}}/(2\bar{\hat{\beta}}_2)$, $\bar{\hat{\beta}}_2=[\bar{\hat{\beta}}^2-(1-\hat{\alpha}^2)]^{1/2}$, $\hat{x}=\hat{x}_0$, $\hat{x}_0=2\bar{\hat{\beta}}_2\bar{\hat{r}}_0$, $\hat{\rho}=\bar{\hat{r}}_1/\bar{\hat{r}}_0$, $\bar{\hat{\beta}}=\hat{\beta}/(\beta_0\sqrt{\hat{\varepsilon}_r})$, $\bar{\hat{\beta}}_2=\hat{\beta}_2/(\beta_0\sqrt{\hat{\varepsilon}_r})$, $\bar{\hat{r}}_0=\beta_0\hat{r}_0\sqrt{\hat{\varepsilon}_r}$, $\bar{\hat{r}}_1=\beta_0\hat{r}_1\sqrt{\hat{\varepsilon}_r}$, $\beta_0=\hat{\omega}\sqrt{\varepsilon_0\mu_0}$, ($\hat{\beta}_2=[\hat{\beta}^2-\hat{\omega}^2\varepsilon_0\mu_0\hat{\varepsilon}_r(1-\hat{\alpha}^2)]^{1/2}$ — radial wavenumber) [4]. The numerical analysis reveals that the same exist only under the conditions of Lemma 1 ($\hat{a}<0$, $\hat{a}<\hat{c}$ and $\hat{k}_-<0$), i.e., it is fulfilled $\hat{\chi}^{(\hat{c})}_{\hat{k},\hat{n}}(\hat{\rho})\equiv\hat{\chi}^{(\hat{c})}_{\hat{k}_-,\hat{n}}(\hat{\rho})$ and $\hat{\chi}^{(\hat{c})}_{\hat{k}_+,\hat{n}}(\hat{\rho})$ have no sense. Accordingly, the structure referred to might propagate two sets of slow waves of the kind considered, exclusively in case of negative magnetization ($\hat{\alpha}_-<0$, $\hat{k}_-<0$), designated by the symbols $\widehat{TE}^{(1)}_{0\hat{n}}$ and $\widehat{TE}^{(2)}_{0\hat{n}}$. The first corresponds to $-1<\hat{\alpha}^{(1)}_-<0$ and the second one — to $-\infty<\hat{\alpha}^{(2)}_-<\hat{\alpha}^{(2)}_{-,\mathrm{lim}}$, where $\hat{\alpha}^{(2)}_{-,\mathrm{lim}}$ is a limiting value, depending on the parameters of configuration and the number of the mode, e.g., assuming $\hat{\rho}=0.2$, for the $\widehat{TE}^{(1)}_{01}$ wave $\hat{\alpha}^{(2)}_{-,\mathrm{lim}}=-4.5676$ [4].

Table 4: Values of $\hat{L}_2(\hat{c},\hat{\rho},\hat{n})$ as a function of $\hat{c}$ for $\hat{\rho}=0.1$ and 0.2 in case $\hat{n}=1$.

$\hat{c}$	$\hat{L}_2$	$\hat{c}$	$\hat{L}_2$	$\hat{c}$	$\hat{L}_2$	$\hat{c}$	$\hat{L}_2$	$\hat{c}$	$\hat{L}_2$	$\hat{c}$	$\hat{L}_2$	$\hat{c}$	$\hat{L}_2$	$\hat{c}$	$\hat{L}_2$
$\hat{\rho}=0.1$															
–4.0		–3.0		–2.0		–1.0		0.0		1.0	5.11493	2.0	5.76141	3.0	7.65016
–3.9	18.79589	–2.9	14.14959	–1.9	10.30205	–0.9	7.40874	0.1	5.63925	1.1	5.12144	2.1	5.89606	3.1	7.90269
–3.8	18.29880	–2.8	13.72665	–1.8	9.96692	–0.8	7.17859	0.2	5.52969	1.2	5.14096	2.2	6.04310	3.2	8.16615
–3.7	17.80866	–2.7	13.31179	–1.7	9.64149	–0.7	6.95988	0.3	5.43280	1.3	5.17347	2.3	6.20242	3.3	8.44039
–3.6	17.32556	–2.6	12.90516	–1.6	9.32595	–0.6	6.75276	0.4	5.34868	1.4	5.21896	2.4	6.37389	3.4	8.72522
–3.5	16.84960	–2.5	12.50690	–1.5	9.02047	–0.5	6.55738	0.5	5.27738	1.5	5.27738	2.5	6.55738	3.5	9.02047
–3.4	16.38088	–2.4	12.11717	–1.4	8.72522	–0.4	6.37389	0.6	5.21896	1.6	5.34868	2.6	6.75276	3.6	9.32595
–3.3	15.91949	–2.3	11.73612	–1.3	8.44039	–0.3	6.20242	0.7	5.17347	1.7	5.43280	2.7	6.95988	3.7	9.64149
–3.2	15.46555	–2.2	11.36391	–1.2	8.16615	–0.2	6.04310	0.8	5.14096	1.8	5.52969	2.8	7.17859	3.8	9.96692
–3.1	15.01917	–2.1	11.00072	–1.1	7.90269	–0.1	5.89606	0.9	5.12144	1.9	5.63925	2.9	7.40874	3.9	10.30205
–3.0		–2.0		–1.0		0.0		1.0	5.11493	2.0	5.76141	3.0	7.65016	4.0	10.64671
$\hat{\rho}=0.2$															
–4.0		–3.0		–2.0		–1.0		0.0		1.0	7.94790	2.0	8.45453	3.0	9.96400
–3.9	19.66187	–2.9	15.47242	–1.9	12.15524	–0.9	9.76864	0.1	8.35840	1.1	7.95297	2.1	8.56070	3.1	10.16909
–3.8	19.20549	–2.8	15.10041	–1.8	11.87383	–0.8	9.58306	0.2	8.27234	1.2	7.96819	2.2	8.67689	3.2	10.38389
–3.7	18.75725	–2.7	14.73720	–1.7	11.60179	–0.7	9.40730	0.3	8.19636	1.3	7.99356	2.3	8.80308	3.3	10.60834
–3.6	18.31722	–2.6	14.38285	–1.6	11.33918	–0.6	9.24139	0.4	8.13049	1.4	8.02908	2.4	8.93925	3.4	10.84240
–3.5	17.88547	–2.5	14.03740	–1.5	11.08603	–0.5	9.08536	0.5	8.07472	1.5	8.07472	2.5	9.08536	3.5	11.08603
–3.4	17.46206	–2.4	13.70093	–1.4	10.84240	–0.4	8.93925	0.6	8.02908	1.6	8.13049	2.6	9.24139	3.6	11.33918
–3.3	17.04706	–2.3	13.37349	–1.3	10.60834	–0.3	8.80308	0.7	7.99356	1.7	8.19636	2.7	9.40730	3.7	11.60179
–3.2	16.64053	–2.2	13.05515	–1.2	10.38389	–0.2	8.67689	0.8	7.96819	1.8	8.27234	2.8	9.58306	3.8	11.87383
–3.1	16.24254	–2.1	12.74596	–1.1	10.16909	–0.1	8.56070	0.9	7.95297	1.9	8.35840	2.9	9.76864	3.9	12.15524
–3.0		–2.0		–1.0		0.0		1.0	7.94790	2.0	8.45453	3.0	9.96400	4.0	12.44597

There is an envelope curve in the $\bar{\hat{\beta}}^{(1)}(\bar{\hat{r}}_0^{(1)})$ — phase diagram of each $\widehat{TE}_{0\hat{n}}^{(1)}$ mode, of equation $\bar{\hat{\beta}}_{en-}^{(1)}=\bar{\hat{\beta}}_{en-}^{(1)}(\bar{\hat{r}}_{0en-}^{(1)})$, written in parametric form as: $\bar{\hat{r}}_{0en-}^{(1)}=\hat{L}_2(\hat{c},\hat{\rho},\hat{n})/\{|\hat{\alpha}_{en-}^{(1)}|[1-(\hat{\alpha}_{en-}^{(1)})^2]^{1/2}\}$, $\bar{\hat{\beta}}_{en-}^{(1)}=[1-(\hat{\alpha}_{en-}^{(1)})^2]^{1/2}$, $(\hat{c}=3)$, restricting the phase characteristics for negative magnetization from the side of lower frequencies [4]. (The subscripts "$-$" and "$en-$" mark the quantities, relevant to $\hat{M}_r<0$ and to the envelope, and the superscripts "(1)" and "(2)" — the ones, describing the $\widehat{TE}_{0\hat{n}}^{(1)}$ and $\widehat{TE}_{0\hat{n}}^{(2)}$ sets of fields, resp. The envelope, pertinent to the $\widehat{TE}_{01}^{(1)}$ mode ($\hat{n}=1$) has been labeled earlier by the symbol $\hat{E}n_{1-}$. Furthermore, the notation $\hat{L}(\hat{c},\hat{\rho},\hat{n})$ has been used, instead of $\hat{L}_2(\hat{c},\hat{\rho},\hat{n})$ [4].

4. CONCLUSION

The real positive numbers $\hat{L}_2(\hat{c},\hat{\rho},\hat{n})$ are advanced for $\hat{c}$ — arbitrary, real, $\hat{\rho}$ — real, positive, less than unity and $\hat{n}$ — a natural number, not exceeding a certain finite one, as limits of special sequences of real numbers. Provided $\hat{c}\neq\hat{l}$, $\hat{l}=0,-1,-2,\ldots$, the terms of the latter are made up by specific zeros of a function, comprising real confluent ones of suitably picked out parameters, while if $\hat{c}=\hat{l}$ (for which the Kummer function, is not determined), as such serve the quantities $\hat{L}_2(\hat{l}\pm\hat{\varepsilon},\hat{\rho},\hat{n})$ with $\hat{\varepsilon}\to 0$. Moreover, a symmetry of the numbers with respect to the point $\hat{c}=1$ is established. The usage of some of their representatives is also considered.

ACKNOWLEDGMENT

We express our gratitude to our mother Trifonka Romanova Popnikolova and to our late father Nikola Georgiev Popnikolov for their self-denial and for their tremendous efforts to support all our undertakings.

REFERENCES

1. Tricomi, F. G., *Funzioni Ipergeometriche Confluenti*, Edizioni Cremonese, Rome, Italy, 1954.
2. Georgiev, G. N. and M. N. Georgieva-Grosse, "A new property of the complex Kummer function and its application to waveguide propagation," *IEEE Antennas Wireless Propagat. Lett.*, Vol. 2, 306–309, December 2003.
3. Georgiev, G. N. and M. N. Georgieva-Grosse, "The $L(c, n)$ numbers and their application in the theory of waveguides," *Proc. Int. Conf. Days Diffr. DD'08*, 44–56, St. Petersburg, Russia, June 3–6, 2008.
4. Georgiev, G. N. and M. N. Georgieva-Grosse, "A property of the $L(c, \rho, n)$ numbers and its application to waveguide propagation," *Proc. XXIX URSI General Assembly*, article ID BK.6(120), 4 pages, in CDROM, Chicago, IL, USA, August 7–16, 2008.
5. Georgiev, G. N. and M. N. Georgieva-Grosse, "Propagation in an azimuthally magnetized circular ferrite-dielectric waveguide," *Proc. 3rd Europ. Conf. Antennas Propagat. EuCAP 2009*, 345–349, in CDROM, Berlin, Germany, March 23–27, 2009.
6. Georgiev, G. N. and M. N. Georgieva-Grosse, "Theorem for the $L(c, \rho, n)$ numbers," *Progress In Electromagnetics Research Symposium Abstracts*, 743; *PIERS Proceedings*, 1478–1482, Moscow, Russia, August 18–21, 2009.
7. Georgiev, G. N. and M. N. Georgieva-Grosse, "Effect of the dielectric filling on the phase behaviour of the circular waveguide with azimuthally magnetized ferrite toroid and dielectric cylinder," *Proc. Asia-Pacific Microwave Conf. APMC-2009*, article ID WE4B-4, 870–873, in CDROM, Singapore, December 7–10, 2009.
8. Georgiev, G. N. and M. N. Georgieva-Grosse, "Theory of the $\hat{L}(\hat{c}, \hat{n})$ numbers and its application to the slow wave propagation in the circular ferrite waveguide," *Progress In Electromagnetics Research Symposium Abstracts*, 594; *PIERS Proceedings*, 976–980, Cambridge, USA, July 5–8, 2010.
9. Georgiev, G. N. and M. N. Georgieva-Grosse, "An application of the zeros of Laguerre polynomials," *Proc. Twelfth Int. Conf. Electromagn. Adv. Applicat. ICEAA'10 Offshore*, 637–640, Sydney, Australia, September 20–24, 2010.
10. Georgiev, G. N. and M. N. Georgieva-Grosse, "Theorem for the identity of the $L(c, n)$ and $\hat{L}(\hat{c}, \hat{n})$ numbers and its application in the theory of waveguides," *Progress In Electromagnetics Research Symposium Abstracts*, 259; *PIERS Proceedings*, 357–361, Marrakesh, Morocco, March 20–23, 2011.
11. Georgieva-Grosse, M. N. and G. N. Georgiev, "Transmission properties of the circular waveguide, containing an azimuthally magnetized ferrite toroid and a dielectric cylinder," *Proc. 5th Europ. Conf. Antennas Propagat. EuCAP 2011*, 1870–1874, Rome, Italy, April 11–15, 2011.
12. Georgiev, G. N. and M. N. Georgieva-Grosse, "Theory of the $\tilde{L}_4$ numbers: Existence theorem and physical interpretation," *Proc. XXX URSI General Assembly*, article ID DP1.7, 4 pages, in CDROM, Istanbul, Turkey, August 13–20, 2011.
13. Georgiev, G. N. and M. N. Georgieva-Grosse, "Theory of the L numbers: Definition, computational modeling, properties and application," *Proc. Thirteenth Int. Conf. Electromagn. Adv. Applicat. ICEAA'11*, 544–547, Turin, Italy, September 12–16, 2011, in CDROM, (Invited Paper in the Special Session: "Future challenges in mathematical and computational electromagnetics and its applications", organized by G. N. Georgiev and M. N. Georgieva-Grosse).
14. Georgiev, G. N. and M. N. Georgieva-Grosse, "On the L_4 numbers and their application," *Proc. XVIth Int. Sem./Worksh. Direct and Inverse Problems of Electromagn. and Acoustic Wave Theory DIPED-2011*, 228–236, Lviv, Ukraine, September 26–29, 2011.
15. Georgiev, G. N. and M. N. Georgieva-Grosse, "Propagation in the circular waveguide, containing an azimuthally magnetized ferrite cylinder and a dielectric toroid," *Proc. 6th Europ. Conf. Antennas Propagat. EuCAP 2012*, article ID P-75, 5 pages, Prague, Czech Republic, March 26–30, 2012.

Guided Modes of an Open Circular Magnetized Plasma Waveguide in the Resonant and Nonresonant Frequency Ranges

G. A. Markov, **M. G. Shkokov**, **and N. M. Shmeleva**
University of Nizhny Novgorod, Russia

Abstract— We consider axisymmetric and nonsymmetric guided modes of an open plasma waveguide in the form of a circular column placed in free space and aligned with an external magnetic field. It is assumed that the medium inside the column is a two-component cold plasma described by the general dielectric tensor. We calculate numerically the dispersion characteristics of the guided modes in a wide frequency band containing the Alfvén and whistler ranges and all basic resonant frequencies of a two-component magnetoplasma. Types of modes and their regions of existence have been determined. The emphasis has been placed on the behavior of the mode dispersion characteristics near the resonant frequencies. It is shown that to correctly describe the behavior of modes in these cases, minor collisional losses in the plasma should be taken into account. The results obtained are useful in interpreting the data of experiments on wideband excitation and propagation of electromagnetic waves in open magnetized plasma waveguides.

1. INTRODUCTION

Study of open plasma waveguides in an external dc magnetic field is of great importance for many applications including guiding structures in laboratory and ionospheric plasmas, as well as solid-state plasma devices. Although guided waves in such systems were discussed in many publications (see, e.g., [1, 2] and references therein), most works on the subject either deal with analyzing the dispersion properties and field structures of modes of such waveguides in rather limited spectral intervals not containing resonant frequencies or consider only the neighborhoods of these frequencies under some simplifying assumptions.

It is the purpose of the present work to study in a systematic manner the characteristics of modes guided by an open circular magnetized plasma waveguide in wide frequency intervals covering both the resonant and nonresonant frequency ranges of a magnetoplasma [2]. Note that by resonant ranges of a cold collisionless magnetoplasma, we mean the frequency intervals in which the refractive-index surface of one of the normal waves extends to infinity at a certain angle between the wave vector and the external dc magnetic field. In nonresonant ranges, on the contrary, the refractive-index surfaces have no such unbounded branches.

2. FORMULATION OF THE PROBLEM

Consider a system representing a cylindrical homogeneous plasma column with plasma density N_0. The column is located in free space and aligned with the external uniform magnetic field, which is directed along the z axis of a cylindrical coordinate system (ρ, ϕ, z). The plasma density profile in such a system can be written as

$$N(\rho) = N_0[1 - U(\rho - a)], \tag{1}$$

where U is a Heaviside function and a is the column radius. In the case of a time dependence $\exp(i\omega t)$, the plasma is described by the permittivity tensor

$$\boldsymbol{\varepsilon} = \begin{pmatrix} \varepsilon & -ig & 0 \\ ig & \varepsilon & 0 \\ 0 & 0 & \eta \end{pmatrix}, \tag{2}$$

the elements of which are given by the formulas

$$\begin{aligned} \varepsilon &= 1 - \frac{\omega_p^2(\omega - i\nu_e)}{\omega[(\omega - i\nu_e)^2 - \omega_H^2]} - \frac{\Omega_{p1}^2(\omega - i\nu_{i1})}{\omega[(\omega - i\nu_{i1})^2 - \Omega_{H1}^2]} - \frac{\Omega_{p2}^2(\omega - i\nu_{i2})}{\omega[(\omega - i\nu_{i2})^2 - \Omega_{H2}^2]}, \\ g &= \frac{\omega_p^2\omega_H}{\omega[(\omega - i\nu_e)^2 - \omega_H^2]} + \frac{\Omega_{p1}^2\Omega_{H1}}{\omega[(\omega - i\nu_{i1})^2 - \Omega_{H1}^2]} + \frac{\Omega_{p2}^2\Omega_{H2}}{\omega[(\omega - i\nu_{i2})^2 - \Omega_{H2}^2]}, \\ \eta &= 1 - \frac{\omega_p^2}{\omega(\omega - i\nu_e)} - \frac{\Omega_{p1}^2}{\omega(\omega - i\nu_{i1})} - \frac{\Omega_{p2}^2}{\omega(\omega - i\nu_{i2})}, \end{aligned} \tag{3}$$

where ω_p and $\Omega_{p1,2}$ are electron and ion plasma frequencies, respectively, ω_H is the electron gyrofrequency, $\Omega_{H1,2}$ are the gyrofrequencies of two species of ions, which are denoted by the subscript 1 or 2, ν_e is the effective electron collision frequency, and $\nu_{i1,2}$ are the effective ion collision frequencies.

Since the properties of guided modes in the frequency band containing the Alfvén and whistler ranges attract enhanced interest [1], in what follows we will focus on the behavior of the mode dispersion curves in these ranges.

3. BASIC EQUATIONS

To describe the properties of modes guided by an axially magnetized plasma column, we apply the approach developed in [1, 2] and seek the mode fields in the form

$$\mathbf{E} = \mathbf{E}(\rho)\exp(-im\phi - ik_0pz), \quad \mathbf{B} = \mathbf{B}(\rho)\exp(-im\phi - ik_0pz), \tag{4}$$

where m is the azimuthal number ($m = 0, \pm1, \pm2, \ldots$) and p is the propagation constant normalized to $k_0 = \omega/c$, the wave number in free space.

In the case of a uniform plasma column in free space, the vector wave functions $\mathbf{E}(\rho)$ and $\mathbf{B}(\rho)$ can be represented in explicit form. Inside the plasma column ($\rho < a$), the components of the vector functions $\mathbf{E}(\rho)$ and $\mathbf{B}(\rho)$ are written as follows:

$$\begin{aligned}
E_\rho &= -\sum_{k=1}^{2} B_k \left[\frac{n_k p + g}{\varepsilon} J_{m+1}(k_0 q_k \rho) + \alpha_k m \frac{J_m(k_0 q_k \rho)}{k_0 q_k \rho}\right], \\
E_\phi &= i\sum_{k=1}^{2} B_k \left[J_{m+1}(k_0 q_k \rho) + \alpha_k m \frac{J_m(k_0 q_k \rho)}{k_0 q_k \rho}\right], \\
E_z &= \frac{i}{\eta}\sum_{k=1}^{2} B_k n_k q_k J_m(k_0 q_k \rho), \\
B_\rho &= -i\sum_{k=1}^{2} B_k \left[pJ_{m+1}(k_0 q_k \rho) + n_k \beta_k m \frac{J_m(k_0 q_k \rho)}{k_0 q_k \rho}\right], \\
B_\phi &= -\sum_{k=1}^{2} B_k \left[n_k J_{m+1}(k_0 q_k \rho) + \beta_k m \frac{J_m(k_0 q_k \rho)}{k_0 q_k \rho}\right], \\
B_z &= -\sum_{k=1}^{2} B_k q_k J_m(k_0 q_k \rho).
\end{aligned} \tag{5}$$

Here, J_m is a Bessel function of the first kind of order m, $B_{1,2}$ are certain constants, and $q_{1,2}$ are the transverse wave numbers normalized to k_0. Other notations in (5) are given by the expressions

$$\begin{aligned}
\alpha_k(p) &= \frac{q_k^2(p)[1 + \eta^{-1} p n_k(p)]}{p^2 - P^2}, \quad \beta_k(p) = -q_k^2(p)\frac{p n_k^{-1}(p) + \eta^{-1}P^2}{p^2 - P^2}, \\
n_k(p) &= -\frac{\varepsilon}{pg}\left[p^2 + q_k^2(p) + \frac{g^2}{\varepsilon} - \varepsilon\right], \quad P = (\varepsilon - g)^{1/2}, \\
q_k(p) &= \frac{1}{\sqrt{2}}\left\{\varepsilon - \frac{g^2}{\varepsilon} + \eta - \left(\frac{\eta}{\varepsilon} + 1\right)p^2 - \left(\frac{\eta}{\varepsilon} - 1\right)(-1)^k \left[\left(p^2 - P_b^2\right)\left(p^2 - P_c^2\right)\right]^{1/2}\right\}^{1/2}, \\
P_{b,c} &= \left\{\varepsilon - (\eta + \varepsilon)\frac{g^2}{(\eta - \varepsilon)^2} + \frac{2\chi_{b,c}}{(\eta - \varepsilon)^2}\left[\varepsilon g^2 \eta\ \left(g^2 - (\eta - \varepsilon)^2\right)\right]^{1/2}\right\}^{1/2},
\end{aligned} \tag{6}$$

where $\chi_b = -\chi_c = -1$ and $k = 1, 2$.

The components of the field outside the plasma column ($\rho > a$) are given by

$$\begin{aligned}
E_\rho &= C_1 m \frac{K_m(k_0 s\rho)}{k_0 s\rho} - C_2 p \left[K_{m+1}(k_0 s\rho) - m \frac{K_m(k_0 s\rho)}{k_0 s\rho} \right], \\
E_\phi &= iC_1 \left[K_{m+1}(k_0 s\rho) - m \frac{K_m(k_0 s\rho)}{k_0 s\rho} \right] - iC_2 pm \frac{K_m(k_0 s\rho)}{k_0 s\rho}, \\
E_z &= -iC_2 s K_m(k_0 s\rho), \\
B_\rho &= -iC_1 p \left[K_{m+1}(k_0 s\rho) - m \frac{K_m(k_0 s\rho)}{k_0 s\rho} \right] + iC_2 m \frac{K_m(k_0 s\rho)}{k_0 s\rho}, \\
B_\phi &= C_1 pm \frac{K_m(k_0 s\rho)}{k_0 s\rho} - C_2 \left[K_{m+1}(k_0 s\rho) - m \frac{K_m(k_0 s\rho)}{k_0 s\rho} \right], \\
B_z &= C_1 s K_m(k_0 s\rho),
\end{aligned} \tag{7}$$

where K_m is a modified Bessel function of the second kind of order m, $C_{1,2}$ are constants, and $s = (p^2 - 1)^{1/2}$.

The condition of continuity of the tangential field components at $\rho = a$ yields a dispersion relation allowing one to obtain the axial wave numbers p of eigenmodes that are guided by the plasma waveguide considered. The dispersion relation can be represented as an equation in p. Roots of this equation, for which the required boundary conditions are ensured, are the propagation constants of the eigenmodes. Since the dispersion relation turns out to be very cumbersome, we do not present it here in the interests of brevity.

4. NUMERICAL RESULTS

For numerical calculations, we used the values of parameters which are typical of laboratory experiments with magnetized plasma waveguides. The induction of the external magnetic field was equal to 1000 G, the waveguide radius, to 1 cm, and the plasma density was assumed lying in the interval 10^{10}–10^{11} cm^{-3}. For proper passage through the resonant frequencies of a two-component magnetoplasma, the effective electron and ion collision frequencies were taken equal to 1% of the angular frequency.

We first examine axisymmetric eigenmodes that are of special interest because of the simplicity of their excitation under experimental conditions. Figure 1 shows the dispersion curves for three lower-order axisymmetric modes. The zeroth mode (black curves), also known as a fast magnetoacoustic mode, has a propagation constant p close to unity at almost all the considered frequencies. At the frequency $\omega_{uh}/\sqrt{2}$, where $\omega_{uh} = \sqrt{\omega_p^2 + \omega_H^2}$ is the upper hybrid frequency of a magnetoplasma, the real part of $p = p' - ip''$ for this mode turns out to be less than the attenuation constant p'', so that the mode becomes strongly damped. At the same time, this mode has a small attenuation constant at all frequencies that are lower than the frequency $\omega_{uh}/\sqrt{2}$, including both the resonant and nonresonant ranges.

The field of the zeroth mode is of surface type, but is only slightly bound to the waveguide boundary. In almost the whole frequency domain of existence of this mode, the field components E_ρ and B_ϕ are predominant, except for the neighborhood of the frequency $\omega_{uh}/\sqrt{2}$. Note that these field components exceed other components by several orders of magnitude. Thus, the zeroth-mode field resembles the field of a plane wave slightly perturbed by the presence of a plasma column. Near the frequency $\omega_{uh}/\sqrt{2}$, when a significant part of the electric field of the mode concentrates inside the waveguide, different field components of the mode become comparable.

Now discuss the dispersion curves of the first and second axisymmetric modes. The corresponding dependences are shown in Figure 1 by the red and blue lines, respectively. It follows from the figure that there are three frequency regions in which these modes can propagate with small attenuation. The first region is the Alfvén frequency range that is located below the first ion gyrofrequency corresponding to ions with a greater mass. The real part of the propagation constants of modes in the Alfvén range varies in the limits 10^3–10^4. Above this range, the modes become strongly damped. The field structures of these modes resemble those in a cylindrical waveguide with metal walls, because the fields of such modes are well localized inside the waveguide. In this case, the components E_ρ and B_ϕ are predominant.

The second characteristic region for axisymmetric modes is situated between the ion gyrofrequencies. It starts at a crossover frequency which depends on the ratio of the ion masses and the

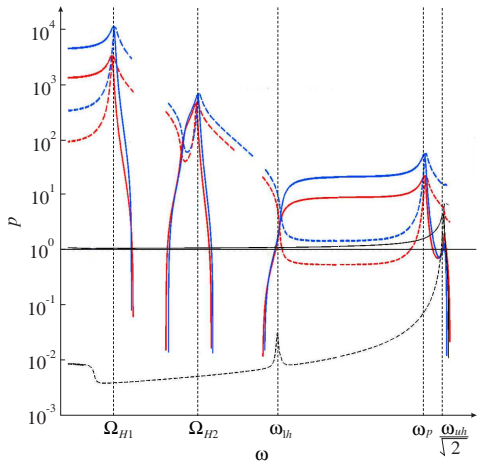

Figure 1: Propagation constants (solid lines) and attenuation constants (dashed lines) of axisymmetric modes as functions of frequency. The black, red, and blue lines refer to the zeroth, first, and second modes, respectively.

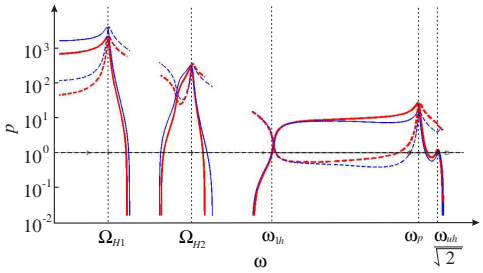

Figure 2: Propagation constants (solid lines) and attenuation constants (dashed line) of the $m = \pm 1$ modes as functions of frequency. The blue and red lines refer to the $m = 1$ and $m = -1$ modes, respectively.

ion number densities. Recall that the crossover frequency is a frequency at which two normal waves of a magnetoplasma have the same velocity and polarization.

The third region for axisymmetric modes in a plasma waveguide is the whistler range. It starts at the lower hybrid frequency $\omega_{lh} = \omega_H \sqrt{\frac{\Omega_{p1}^2+\Omega_{H1}^2}{\omega_p^2+\omega_H^2}}$ and terminates at the frequency $\min\{\omega_p, \omega_H\}$. All field components of the modes in the indicated frequency ranges should be taken into account, because none of them is predominant.

Now consider nonsymmetric modes of a cylindrical magnetoplasma waveguide. In this work, we examine the so-called dipole modes, i.e., nonsymmetric modes with the azimuthal indices $m = 1$ and $m = -1$. Figure 2 shows the dispersion curves of these modes. It follows from Figure 2 that the dispersion curves of these modes are close to those of axisymmetric modes. There are the same three characteristic frequency intervals in the chosen band, in which nonsymmetric modes have the same order of the propagation constant as axisymmetric modes. Moreover, the nonsymmetric modes demonstrate the same behavior at the resonant frequencies of a two-component magnetoplasma.

5. CONCLUSION

In this work, the dispersion properties of modes of a magnetoplasma waveguide located in free space were studied in a wide frequency band containing the Alfvén and whistler ranges, as well the resonant frequencies. The behavior of the dispersion curves when crossing the lower hybrid frequency, ion and electron gyrofrequencies, and other characteristic frequencies of a cold two-component magnetoplasma was analyzed. Types of modes and the frequency intervals of their existence were determined. It is shown that in the resonant frequency intervals of a magnetoplasma, all the considered waveguide modes have a small attenuation constant, whereas in nonresonant intervals, only the zeroth axisymmetric mode can propagate in a sufficiently narrow waveguide. The results obtained can be of interest for explaining the data of laboratory experiments and other applications related to using gyrotropic guiding systems in electronic devices.

ACKNOWLEDGMENT

This work was supported by the RFBR (project No. 12–02–00747-a), the Government of the Russian Federation (contract No. 11.G34.31.0048), and the Russian Federal Program "Scientific and Education Personnel of the Innovative Russia" (contract Nos. P313 and 02.740.11.0565).

REFERENCES

1. Kondrat'ev, I. G., A. V. Kudrin, and T. M. Zaboronkova, *Electrodynamics of Density Ducts in Magnetized Plasmas*, Gordon and Breach, Amsterdam, 1999.
2. Kondratenko, A. N., *Plasma Waveguides*, Atomizdat, Moscow, 1976 [in Russian].

Green's Function for Paraxial Equation

Alexander G. Nerukh[1], **D. A. Zolotariov**[1], **D. A. Nerukh**[2], **and Georgi N. Georgiev**[3]

[1]Kharkov National University of Radio Electronics, 14 Lenin Ave., Kharkov 61166, Ukraine
[2]Non-linearity and Complexity Research Group, Aston University, Birmingham B4 7ET, UK
[3]Faculty of Mathematics and Informatics, University of Veliko Tirnovo "St. St. Cyril and Methodius" BG-5000 Veliko Tirnovo, Bulgaria

Abstract— The theory and experimental applications of optical Airy beams are in active development recently. The Airy beams are characterised by very special properties: they are non-diffractive and propagate along parabolic trajectories. Among the striking applications of the optical Airy beams are optical micro-manipulation implemented as the transport of small particles along the parabolic trajectory, Airy-Bessel linear light bullets, electron acceleration by the Airy beams, plasmonic energy routing. The detailed analysis of the mathematical aspects as well as physical interpretation of the electromagnetic Airy beams was done by considering the wave as a function of spatial coordinates only, related by the parabolic dependence between the transverse and the longitudinal coordinates. Their time dependence is assumed to be harmonic. Only a few papers consider a more general temporal dependence where such a relationship exists between the temporal and the spatial variables. This relationship is derived mostly by applying the Fourier transform to the expressions obtained for the harmonic time dependence or by a Fourier synthesis using the specific modulated spectrum near some central frequency. Spatial-temporal Airy pulses in the form of contour integrals is analysed near the caustic and the numerical solution of the nonlinear paraxial equation in time domain shows soliton shedding from the Airy pulse in Kerr medium.

In this paper the explicitly time dependent solutions of the electromagnetic problem in the form of time-spatial pulses are derived in paraxial approximation through the Green's function for the paraxial equation. It is shown that a Gaussian and an Airy pulse can be obtained by applying the Green's function to a proper source current. We emphasize that the processes in time domain are directional, which leads to unexpected conclusions especially for the paraxial approximation.

1. INTRODUCTION

Intensive theoretical and experimental investigations of Airy beams are motivated by their unusual features (non-diffractive propagation, accelerating motion, and self-healing). A solution to the Schrodinger equation in the form of the non-spreading accelerating Airy wave function found by Berry and Balazs in 1979 [1] inspired Siviloglou and Christodoulides to put forward the concept of electromagnetic Airy beams to be spatial accelerated [2, 3]. These seminal publications with theoretical formulation and experimental confirmation were followed by many works on the Airy beam properties, for example [4–11] (and citations therein). These investigations generate very interesting applications, some of which are already realised [12–19]. Analogy with Schrodinger equation can be used if time is eliminated from a paraxial equation describing the beam propagation that holds for harmonic temporal dependence. In this case the parabolic relation exists between the transverse and longitudinal coordinates, and it is interpreted as accelerating movement of the beam. Accelerating movement in time is considered only in a few papers [20–28] where a more general temporal dependence exists. Therewith, the main attention of the recent publications on temporal Airy pulses is aimed at propagation in dispersive and nonlinear medium including such questions as causality effects and generation of solitons [26, 29]. We turn our attention to an inhomogeneous master equation containing a source and describing the electromagnetic field in a homogeneous linear non-dispersive medium. The solution to this equation is found by a rigorous method of the Green's function.

2. GREEN'S FUNCTION FOR PARAXIAL EQUATION IN TIME DOMAIN

We consider an electromagnetic field created by an extrinsic source given by a vector electric current $\mathbf{j} = (0, j, 0)$ located in a real non-dispersive dissipative medium with the permittivity ε, the permeability μ and the conductivity σ. In this case the electric field has the same orientation $\mathbf{E} = (0, E, 0)$ and is described by the wave equation

$$\left(\frac{\partial^2 E}{\partial x^2} + \frac{\partial^2 E}{\partial y^2} + \frac{\partial^2 E}{\partial z^2}\right) - \frac{1}{v^2}\frac{\partial^2 E}{\partial t^2} - \mu_0\mu\sigma\frac{\partial E}{\partial t} = \mu_0\mu\frac{\partial j}{\partial t} \tag{1}$$

where $v^2 = 1/(\varepsilon_0\varepsilon\mu_0\mu)$ is the velocity of light in this medium and ε_0 and μ_0 are the permittivity and permeability of vacuum. Assuming that the dependence of the field on the longitudinal coordinate x is dominant, $E = F(t,x,y,z)e^{-ikx}$, $k > 0$, such that the normal to a wave front makes a small angle with an average direction of wave propagation, $|F''_{xx}| \ll |2ik_xF'_x|$, the well known paraxial approximation of slow varying envelope we obtain from (1) the paraxial equation for the envelope

$$-2ik\frac{\partial F}{\partial x} - k^2F + \frac{\partial^2 F}{\partial y^2} + \frac{\partial^2 F}{\partial z^2} - \frac{1}{v^2}\frac{\partial^2 F}{\partial t^2} - \mu_0\mu\sigma\frac{\partial F}{\partial t} = \mu_0\mu\frac{\partial j}{\partial t}e^{ikx} \tag{2}$$

The Equation (2) is of the parabolic type and it is well known that such equations describe traditionally problems of thermal conductivity or diffusion. The solution to Equation (2) is convenient to construct by virtue of the fundamental solution to this equation, the Green's function G_p. Applying the Fourier transform to the equation for the Green's function

$$-2ik\frac{\partial G_p}{\partial x} - k^2G_p + \frac{\partial^2 G_p}{\partial y^2} + \frac{\partial^2 G_p}{\partial z^2} - \frac{1}{v^2}\frac{\partial^2 G_p}{\partial t^2} - \mu_0\mu\sigma\frac{\partial G_p}{\partial t} = \delta(t,x,y,z) \tag{3}$$

where $\delta(t,x,y,z)$ is the delta function and implementing the inverse transformation we obtain

$$G_p(t,x,y,z) = -\frac{(1-i)v\sqrt{k}\theta(x)}{8\pi x\sqrt{\pi x}}e^{i\frac{k}{2}x + i\frac{kv^2(t+i\frac{\mu_0\mu\sigma}{2k}x)^2}{2x} - i\frac{k^2y^2}{2kx} - i\frac{k^2z^2}{2kx}} \tag{4}$$

where $\theta(x)$ is the Heaviside unit function, which determines a definitional domain of a solution to Equation (2).

Convolution of the Green's function (4) with the right-hand side of Equation (2) gives the electric field radiated by the current j. We consider the current that is located in a plane $x = x_0$, which is transverse to a dominant direction of wave propagation, and is given by the spectral representation over plane waves running with the velocity v_1 along the transverse axis y

$$j = j_0\delta(x - x_0)\frac{1}{2\pi}\int\limits_{-\infty}^{\infty}\Phi(\omega)e^{\pm i\omega(t-qy)}d\omega \tag{5}$$

Convolution of (6) with (7) gives the spectral representation for the radiated field

$$E = j_0\frac{\mu_0\mu}{2ik}\theta(x-x_0)e^{i(x-x_0)\frac{q^2-k^2}{2k}}\frac{\partial}{\partial t}\frac{1}{2\pi}\int\limits_{-\infty}^{\infty}\Phi(\omega)d\omega e^{-i\omega^2\frac{(x-x_0)}{2kv^2}+i\omega^2\frac{q^2(x-x_0)}{2k}}e^{\pm i\omega(t+i\frac{\mu_0\mu\sigma}{2k}(x-x_0)-qy)} \tag{6}$$

Time-spatial structure of the field is determined by a spectral function for the current. It is very important that after the Green's function (4) Equation (6) does not contain retardation.

3. RADIATION OF A DECELERATING AIRY PULSE

To obtain an Airy pulse we take the source current in the form of the Airy function

$$j = \delta(x - x_0)\mathrm{Ai}\left(\pm(t-qy)/T\right)e^{\pm\alpha(t-qy)/T}/T, \tag{7}$$

that is provided by the spectrum function $\Phi(\omega) = \exp(i(\omega T + i\alpha)^3/3)$ in (7). Here, T is a dimensionless factor and the parameter α is introduced, which ensures energy finiteness of the source, the idea proposed in [2] for a problem with harmonic temporal dependence of the phenomenon.

Calculation of the integral in (6) gives the radiated wave with the envelope described by the Airy function but with more complex argument than in (7):

$$\begin{aligned} E(t,x) \;=\; & \frac{i\mu_0\mu}{2kT}j_0e^{-ik(x-x_0)/2}\theta(x-x_0)e^{i\frac{2}{3}\left(m\frac{x-x_0}{2kv^2T^2}\right)^3 - 2\alpha\left(m\frac{x-x_0}{2kv^2T^2}\right)^2 + i\alpha^2m\frac{x-x_0}{2kv^2T^2}} \\ & \times\frac{\partial}{\partial t}\left[e^{\pm i\left[(t+i\frac{\mu_0\mu\sigma}{2k}(x-x_0)) - qy\right]\frac{1}{T}\left(m\frac{x-x_0}{2kv^2T^2} - i\alpha\right)}\right. \\ & \left.\times\mathrm{Ai}\left(\pm\left[t + i\frac{\mu_0\mu\sigma}{2k}(x-x_0) - qy\right]\frac{1}{T} - \left(m\frac{x-x_0}{2kv^2T^2}\right)^2 + 2i\alpha m\frac{x-x_0}{2kv^2T^2}\right)\right] \end{aligned} \tag{8}$$

The coefficient $m = 1-q^2v^2$ takes into account a relation between a phase velocity v in a longitudinal direction and a velocity of a source current in a transverse direction. The velocity of the envelope movement in the longitudinal direction can be evaluated easily equating the Airy function argument in (8) to a constant value $\pm t/T-(m(x-x_0)/(2kv^2T^2))^2 = \text{const}$ where it is assumed for simplicity $\alpha = 0$, $\sigma = 0$ and $v_1 \to \infty$. This equation determines the parabolic trajectories of the field given value. Differentiation of this equality gives the envelope velocity $\dot{x} = \pm 2k^2v^4T^3m^{-2}/(x-x_0)$ as a function of a distance from the source or as a function of time $\dot{x} = \pm kv^2T^{3/2}m^{-1}/\sqrt{\pm t - \text{const}\,T}$. This velocity tends to zero with time as well as with the distance from the source. The acceleration of the movement $\ddot{x} = -\dot{x}^2/(x-x_0)$ is negative everywhere in the region of existence of the pulse, $x - x_0 > 0$, and it tends to zero also with the distance from the source confirming the decelerating character of the movement.

4. RADIATION OF A DECELERATING GAUSSIAN

Let consider the source with even spectrum $\Phi(\omega) = \exp(-(\omega T)^2/4w^2)$ where $w > 0$. This spectrum corresponds to running in the transverse plane the source current of the Gaussian form

$$j = j_0\delta(x-x_0)wT^{-1}\pi^{-1/2}e^{-w^2(t-qy)^2/T^2} \tag{9}$$

The field radiated by this source is well known the running Gaussian

$$E = \frac{1}{2ik}j_0\mu_0\mu e^{-ik(x-x_0)/2}\frac{w\theta(x-x_0)}{2T\sqrt{\pi}}\frac{1}{\sqrt[4]{1+r^2(x-x_0)^2}}\frac{\partial}{\partial t}AR \tag{10}$$

where

$$\begin{aligned}
A &= \exp\left(-\frac{w^2}{T^2}\frac{\tau^2-\left(\frac{\mu_0\mu\sigma}{2k}\right)^2(x-x_0)^2+\tau\frac{\mu_0\mu\sigma}{k}r(x-x_0)^2}{1+r^2(x-x_0)^2}\right),\\
R &= \exp\left(i\frac{rw^2(x-x_0)\left[\tau^2-\left(\frac{\mu_0\mu\sigma}{2k}\right)^2(x-x_0)^2-\tau\frac{\mu_0\mu\sigma}{rk}\right]}{T^2(1+r^2(x-x_0)^2)}-\frac{i}{2}\arctan r(x-x_0)\right),\\
r &= \frac{2w^2(1-q^2v^2)}{kv^2T^2} \quad \text{and} \quad \tau = t-qy.
\end{aligned}$$

If the medium is non-dissipative, $\sigma = 0$, then the expression is simplified sufficiently

$$\begin{aligned}
E &= \frac{1}{2ik}j_0\mu_0\mu e^{-ik(x-x_0)/2}\frac{w\theta(x-x_0)}{2T\sqrt{\pi}}\frac{1}{\sqrt[4]{1+r^2(x-x_0)^2}}\\
&\quad\times\frac{\partial}{\partial t}\exp\left(-\frac{w^2}{T^2}\frac{\tau^2}{1+r^2(x-x_0)^2}+i\frac{w^2}{T^2}\frac{r(x-x_0)\tau^2}{1+r^2(x-x_0)^2}\right)\exp\left(-\frac{i}{2}\arctan r(x-x_0)\right)
\end{aligned} \tag{11}$$

Evenness of the spectrum leads to that the radiated field does not depend on the sign in (5).

This pulse envelope moves also decelerating along the longitudinal axis x that is seen after differentiation of the equality $t^2/\left[1+\bar{r}^2(x-x_0)^2\right] = \text{const}$, $\bar{r} = 2w^2/(kv^2T^2)$:

$$\dot{x} = \frac{t}{\text{const}\;\bar{r}^2(x-x_0)} = \frac{\sqrt{1+\bar{r}^2(x-x_0)^2}}{\sqrt{\text{const}}\,\bar{r}^2(x-x_0)} = \frac{t}{\sqrt{\text{const}}\;\bar{r}\sqrt{t-\text{const}}} \tag{12}$$

The velocity tends to the asymptotic value of $\dot{x}_\infty = 1/\sqrt{\bar{r}^2\text{const}}$ with time as well as with the distant from the source. The trajectories for the field given values are hyperbolas $(t-qy)^2/\text{const} - r^2(x-x_0)^2 = \text{const}$.

5. CONCLUSIONS

It is shown that an electromagnetic field in paraxial approximation is described by a differential equation of a parabolic type that is attributable to processes of thermo conductivity and diffusion. For unambiguity of a problem solution an inhomogeneous paraxial equation in time domain with the right-hand side given by an electromagnetic field source is considered. Radiation of such a source in the form of Airy and Gaussian pulses is investigated. It is shown that these pulses propagate in time with deceleration.

REFERENCES

1. Berry, M. V. and N. L. Balazs, "Nonspreading wave packets," *Am. J. Phys.*, Vol. 47, 264, 1979.
2. Siviloglou, G. A. and D. N. Christodoulides, "Accelerating finite energy Airy beams," *Optics Letters*, Vol. 32, 979, 2007.
3. Siviloglou, G. A., J. Broky, A. Dogariu, and D. N. Christodoulides, "Observation of accelerating Airy beams," *Physical Review Letters*, Vol. 99, 213901, 2007.
4. Besieris, I. M. and A. M. Shaarawi, "A note on an accelerating finite energy Airy beams," *Optics Letters*, Vol. 32, 2447, 2007.
5. Saari, P., "Laterally accelerating airy pulses," *Optics Express*, Vol. 16, 10303–10308, 2008.
6. Carretero, L., P. Acebal, S. Blaya, C. García, A. Fimia, R. Madrigal, and A. Murciano, "Nonparaxial diffraction analysis of Airy and SAiry beams," *Optics Express*, Vol. 17, 22432–22441, 2009.
7. Bandres, M. A., "Accelerating beams," *Optics Letters*, Vol. 34, 3791, 2009.
8. Vo, S., K. Fuerschbach, K. P. Thompson, M. A. Alonso, and J. P. Rolland, "Airy beams: A geometric optics perspective," *J. Opt. Soc. Am. A*, Vol. 27, 2574–2582, 2010.
9. Kaganovsky, Y. and E. Heyman, "Wave analysis of Airy beams," *Optics Express*, Vol. 18, 8440, 2010.
10. Carvalho, M. I. and M. Facao, "Propagation of Airy related beams," *Optics Express*, Vol. 18, 21938, 2010.
11. Hwang, C.-Y., D. Choi, K.-Y. Kim, and B. Lee, "Dual Airy beam," *Optics Express*, Vol. 18, 23504–23516, 2010.
12. Baumgartl, J., M. Mazilu, and K. Dholakia, "Optically mediated particle clearing using Airy wavepackets," *Nature Photonics*, Vol. 2, 675, 2008.
13. Ellenbogen, T., N. Voloch-Bloch, A. Ganany-Padowicz, and A. Arie, "Nonlinear generation and manipulation of Airy beams," *Nature Photonics*, Vol. 3, 395, 2009.
14. Salandrino, A. and D. N. Christodoulides, "Airy plasmon: A nondiffracting surface wave," *Optics Letters*, Vol. 35, 2082–2084, 2010.
15. Salandrino, A. and D. N. Christodoulides, "Superresolution via enhanced evanescent tunneling," *Optics Letters*, Vol. 36, 487–489, 2011.
16. Cheng, H., W. Zang, W. Zhou, and J. Tian, "Analysis of optical trapping and propulsion of Rayleigh particles using Airy beam," *Optics Express*, Vol. 18, 20384–20394, 2010.
17. Li, J.-X., W.-P. Zang, and J.-G. Tian, "Vacuum laser-driven acceleration by Airy beams," *Optics Express*, Vol. 18, 7300–7306, 2010.
18. Zheng, Z., B.-F. Zhang, H. Chen, J. Ding, and H.-T. Wang, "Optical trapping with focused Airy beams," *Apl. Optics*, Vol. 50, 43–49, 2011.
19. Liu, W., D. N. Neshev, I. V. Shadrivov, A. E. Miroshnichenko, and Yu. S. Kivshar, "Plasmonic Airy beam manipulation in linear optical potentials," *Optics Letters*, Vol. 36, 1164–1166, 2011.
20. Christodoulides, D. N., N. K. Efremidis, P. D. Trapani, and B. A. Malomed, "Bessel X waves in two- and three-dimensional bidispersive optical system," *Optics Letters*, Vol. 29, 1446, 2004.
21. Abdollahpour, D., S. Suntsov, D. G. Papazoglou, and S. Tzortzaki, "Spatiotemporal Airy light bullets in the linear and nonlinear regimes," *Phys. Rev. Lett.*, Vol. 105, 253901–4, 2010.
22. Besieris, I. M. and A. M. Shaarawi, "Accelerating Airy wave packets in the presence of quadratic and cubic dispersion," *Phys. Rev. E*, Vol. 78, 046605(1–6), 2008.
23. Chong, A., W. H. Renninger, D. N. Christodoulides, and F. W. Wise, "Airy-Bessel wave packets as versatile linear light bullets," *Nature Photonics*, Vol. 4, 103–106, 2010.
24. Eichelkraut, T. J., G. A. Siviloglou, I. M. Besieris, and D. N. Christodoulides, "Oblique Airy wave packets in bidispersive optical media," *Optics Letters*, Vol. 35, 3655–3657, 2010.
25. Kaganovsky, Y. and E. Heyman, "Airy pulsed beams," *J. Opt. Soc. Am. A*, Vol. 28, 1243–1255, 2011.
26. Fattal, Y., A. Rudnick, and D. M. Marom, "Soliton shedding from Airy pulses in Kerr media," *Optics Express*, Vol. 19, No. 18, 17298–17307, 2011.
27. Papazoglou, D. G., N. K. Efremidis, D. N. Christodoulides, and S. Tzortzakis, "Observation of abruptly autofocusing waves," *Optics Letters*, Vol. 36, 1842–1844, 2011.
28. Ament, C., P. Polynkin, and J. V. Moloney, "Supercontinuum generation with self-healing Airy pulses," *CLEO 2011 — Laser Applications to Photonic Applications*, Paper PDPC9, OSA Technical Digest (CD), Optical Society of America, 2011.
29. Kaminer, I., Y. Lumer, M. Segev, and D. N. Christodoulides, "Causality effects on accelerating light pulses," *Optics Express*, Vol. 19, No. 23, 23132–23139, 2011.

A Simple Analytical Method for Describing Important Optical Beams Truncated by Finite Apertures

Michel Zamboni-Rached[1,*] , **Erasmo Recami**[2], **and Massimo Balma**[3]

[1]FEEC, Universidade Estadual de Campinas, Campinas, SP, Brazil
[2]Facoltà di Ingegneria, Università Statale di Bergamo, Bergamo, Italy
[3]SELEX Galileo, San Maurizio, Caselle, Torino, Italy

Abstract— In this paper, we present a simple and effective method, based on appropriate superpositions of Bessel-Gauss beams, which in the Fresnel regime is able to describe in *analytic* form the 3D evolution of important waves as Bessel beams, plane waves, Gaussian beams, Bessel-Gauss beams, when truncated by finite apertures.

1. INTRODUCTION

Notwithstanding the fact that some analytic solutions do exist for the Fresnel diffraction integral, they are rare, and normally it is necessary to have recourse to numerical simulations. This is particularly true when the mentioned integral is adopted for the description of beams generated by finite apertures, that is, of beams truncated in space.

Among the past attempts of an analytic description of truncated beams, probably the best known is the Wen and Breazele method [1, 2], which uses superpositions of Gaussian beams (with different waist sizes and positions) in order to describe *axially symmetrical* beams truncated by circular apertures. In that approach, those authors had to adopt a computational optimization process to get the superposition coefficients, and the beam waists and spot positions of the various Gaussian beams; actually, the necessity of a computational optimization to find out which beam superposition is adequate to describe a certain truncated beam is due to the simple fact that the Gaussian beams do not constitute an orthogonal basis.

In this paper, we are going to show that an *analytic* description of important truncated beams can be obtained by means of Bessel-Gauss beam superpositions, whose coefficients are obtained in a simple and direct way, without any need of numerical optimizations. Indeed, our method is capable of yielding analytic solutions for the 3D evolution of Bessel beams, plane waves, Gaussian beams, Bessel-Gauss beams, when truncated by finite apertures in the Fresnel regime [3]. In this paper, we are going to apply this method to the truncated Bessel beam.

2. THE METHOD

In this paper, for simplicity's sake, we shall leave understood in all solutions the harmonic time-dependence term $\exp(-i\omega t)$.

In the *paraxial approximation*, an axially symmetric monochromatic wave field can be evaluated, knowing its shape on the $z = 0$ plane, through the Fresnel diffraction integral in cylindrical coordinates [4]:

$$\Psi(\rho, z) = \frac{-ik}{z}\, e^{i\left(kz+\frac{k\rho^2}{2z}\right)} \int_0^\infty \Psi\left(\rho', 0\right)\, e^{ik\frac{\rho'^2}{2z}}\, J_0\left(k\frac{\rho\rho'}{z}\right) \rho' d\rho', \tag{1}$$

where $k = 2\pi/\lambda$ is the wavenumber, and λ the wavelength. In this equation, ρ' reminds us that the integration is being performed on the plane $z = 0$; thus, $\Psi(\rho', 0)$ does simply indicates the field value on $z = 0$.

An important solution is obtained by considering on the $z = 0$ plane the excitation given by

$$\Psi\left(\rho', 0\right) \;=\; \Psi_{BG}\left(\rho', 0\right) \;=\; AJ_0\left(k_\rho \rho'\right) \exp\left(-q\rho'^2\right), \tag{2}$$

which, according to Eq. (1), produces the so-called Bessel-Gauss beam [5]:

$$\Psi_{BG}(\rho, z) \;=\; -\frac{ikA}{2zQ}\, e^{ik\left(z+\frac{\rho^2}{2z}\right)} J_0\left(\frac{ikk_\rho\rho}{2zQ}\right) e^{-\frac{1}{4Q}\left(k_\rho^2+\frac{k^2\rho^2}{z^2}\right)}, \tag{3}$$

*Corresponding author: Michel Zamboni Rached (mzamboni@dmo.fee.unicamp.br).

where $Q = q - ik/2z$, and k_ρ being a constant[1]. When $k_\rho = 0$, the Bessel-Gauss beam results in the well known Gaussian beam.

The Gaussian beam, and the Bessel-Gauss, Eq. (3), solutions are among the few solutions to the Fresnel diffraction integral that can be got analytically. The situation gets much more complicated, however, when facing beams truncated in space by finite circular apertures: For instance, a Gaussian beam, or a Bessel beam, or a Bessel-Gauss beam, truncated via an aperture with radius R. In this case, the upper limit of the integral in Eq. (1) becomes the aperture radius, and the analytic integration becomes very difficult, requiring recourse to lengthy numerical calculations.

Now, we are going to propose a method, for the description of truncated beams, that appears to be noticeable for its simplicity and, in most cases, for its total analyticity.

Let us start with the Bessel-Gauss beam solution, Eq. (3), and consider the solution given by the following superposition of such beams:

$$\Psi(\rho, z) \;=\; -\frac{ik}{2\,z}\, e^{ik\left(z+\frac{\rho^2}{2\,z}\right)} \sum_{n=-N}^{N} \frac{A_n}{Q_n}\, J_0\left(\frac{i\,k\,k_\rho\,\rho}{2\,z\,Q_n}\right) e^{-\frac{1}{4Q_n}\left(k_\rho^2+\frac{k^2\rho^2}{z^2}\right)}, \tag{4}$$

quantities A_n being constants, and Q_n being given by

$$Q_n = q_n - \frac{ik}{2z}, \tag{5}$$

where q_n are constants that *can have complex values.* Notice that in this superposition all beams possess the same value of k_ρ.

Our purpose is that solution (4) be able to represent beams truncated by circular apertures: As announced, we are particularly interested in the analytic description of truncated beams of Bessel, Bessel-Gauss, Gaussian and plane wave types.

Given one of such beams truncated at $z = 0$ by an aperture with radius R, we have to determine the coefficients A_n and q_n in such a way that Eq. (4) represents with fidelity the resulting beam. If the truncated beam on the $z = 0$ plane is given by $V(\rho)$, we have to obtain $\Psi(\rho, 0) = V(\rho)$; that is to say:

$$V(\rho) \;=\; J_0(k_\rho\rho) \sum_{n=-N}^{N} A_n e^{-q_n\rho^2}. \tag{6}$$

The r.h.s. of this equation is nothing but a superposition of Bessel-Gauss beams, all with the same value k_ρ, at $z = 0$ [namely, each one of such beams is written at $z = 0$ according to Eq. (2)].

Equation (6) will provide us with the values of the A_n and q_n, as well as of N. Once these values have been obtained, the field emanated by the finite circular aperture located at $z = 0$ will be given by Eq. (4). Remembering that the q_n can be complex, let us make the following choices:

$$q_n \;=\; q_R + iq_{In}, \quad \text{with} \quad q_{In} \;=\; -\frac{2\pi}{L}\, n, \tag{7}$$

where $q_R > 0$ is the real part of q_n, having the *same value* for every n, q_{In} is the imaginary part of q_n, and L is a constant with the dimensions of a square length.

With such choices, and assuming $N \to \infty$, Eq. (6) gets written as

$$V(\rho) \;=\; J_0(k_\rho\rho)\, \exp\left(-q_R\rho^2\right) \sum_{n=-\infty}^{\infty} A_n\, \exp\left(i\frac{2\pi n}{L}\rho^2\right), \tag{8}$$

which has then to be exploited for obtaining the values of A_n, k_ρ, q_R and L.

In the cases of a truncated Bessel beam (TB) or of a truncated Bessel-Gauss beam (TBG), it seems natural to choose quantity k_ρ in Eq. (8) to be equal to the corresponding beam transverse wavenumber.

In the case of a truncated Gaussian beam (TG) or of a truncated plane wave (TP), by contrast, it is natural to choose $k_\rho = 0$ in Eq. (8).

[1] Quantity k_ρ is the transverse wavenumber associated with a Bessel beam transversally modulated by the Gaussian function.

In all cases, the product

$$\exp\left(-q_R\rho^2\right)\sum_{n=-\infty}^{\infty}A_n\,\exp\left(i\frac{2\pi n}{L}\rho^2\right), \tag{9}$$

in Eq. (8) must represent:

(i) a function $\mathrm{circ}(\rho/R)$, in the TB or TP cases;

(ii) a function $\exp\left(-q\,\rho^2\right)\mathrm{circ}(\rho/R)$, that is, a circ function multiplied by a Gaussian function, in the TBG or TG cases. Of course (i) is a particular case of (ii) with $q=0$. It may be useful to recall that the circ-function is the step-function in the cylindrically symmetrical case. Quantity R is still the aperture radius, and $\mathrm{circ}(\rho/R)=1$ when $0\le\rho\le R$, and equals 0 in the contrary case.

Let us now show how expression (9) can approximately represent the above functions, given in (i) and (ii).

Toward such an aim, let us consider a function $G(r)$ defined on an interval $|r|\le L/2$ and possessing the Fourier expansion:

$$G(r)\;=\;\sum_{n=-\infty}^{\infty}A_n\exp(i2\pi nr/L)\quad\text{for}\quad|r|\le L/2 \tag{10}$$

where r and L, having the dimensions of a square length, will be expressed in square meters (m^2).

Suppose now the function $G(r)$ to be given by

$$G(r)\;=\begin{cases}\exp\left(q_R\,r\right)\exp\left(-q\,r\right)\quad\text{for}\quad|r|\le R^2\\ 0\quad\text{for}\quad R^2<|r|<L/2\;,\end{cases} \tag{11}$$

where q is a given constant.

In this case, the coefficients A_n in the Fourier expansion of de $G(r)$ will be given by:

$$A_n=\frac{1}{L\left(q_R-q\right)-i2\pi n}\left(e^{(q_R-q-i\frac{2\pi}{L}n)R^2}-e^{-(q_R-q-i\frac{2\pi}{L}n)R^2}\right), \tag{12}$$

Writing now

$$r=\rho^2\;, \tag{13}$$

in Eqs. (10), (11) we shall have that Eq. (9) can be written as

$$e^{-q_R\rho^2}\sum_{n=-\infty}^{\infty}A_ne^{i2\pi n\rho^2/L}=\begin{cases}e^{-q\,\rho^2} & \text{for}\;\;0\le\rho\le R\\ 0 & \text{for}\;\;R<\rho\le\sqrt{L/2}\\ e^{-q_R\rho^2}\,f(\rho)\approx 0 & \text{for}\;\;\rho>\sqrt{L/2}\;,\end{cases} \tag{14}$$

where the coefficients A_n are still given by Eq. (12), and $f(\rho)$ is a function existing on decreasing space intervals, assuming $\exp[(q_R-q)R^2]$ (if $q_R>q$) or 1 (if $q_R\le q$) as its maximum values. Since $\sqrt{L/2}>R$, for suitable choices of q_R and L, we shall have that $\exp(-q_R\rho^2)\,f(\rho)\approx 0$ for $\rho\ge\sqrt{L/2}$.

Therefore, we get that

$$e^{-q_R\rho^2}\sum_{n=-\infty}^{\infty}A_ne^{i2\pi n\rho^2/L}\approx\;e^{-q\,\rho^2}\,\mathrm{circ}(\rho/R), \tag{15}$$

which corresponds to the case (i), when $q=0$, and to the case (ii).

Let us recall once more that the A_n are given by Eq. (12).

On the basis of what was shown before, we have now in our hands a very efficient method for describing important beams, truncated by finite apertures: Namely, the TB, TG, TBG, and TP beams. Indeed, it is enough to choose the desired field, truncated by a circular aperture with radius R, and describe it at $z=0$ by our Eq. (8). Precisely:

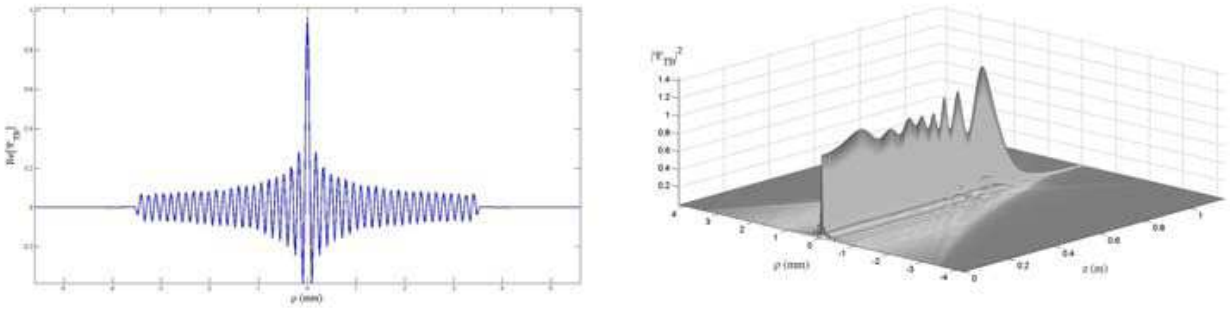

(a) (b)

Figure 1: (a) Field given by Eq. (8), representing a Bessel beam at $z = 0$, with $k_\rho = 4.07 \cdot 10^4\,\mathrm{m}^{-1}$ and truncated by a finite circular aperture with radius $R = 3.5\,\mathrm{mm}$. The coefficients A_n are given by Eq. (12), with $q = 0$, $L = 3R^2$, $q_R = 6/L$ and $N = 23$. (b) Intensity of a Bessel beam truncated by a finite aperture, as given by solution (4).

- In the TBG case: the value of k_ρ in Eq. (8) is the transverse wavenumber of the Bessel beam modulated by the Gaussian function; A_n is given in Eq. (12); q is related to the Gaussian function width at $z = 0$. The values L and q_R, and the number N of terms in the series (8), are chosen so as to guarantee a faithful description of the beam at $z = 0$ when truncated by a circular aperture with radius R.
- The TB, TG and TP are special cases of TBG: in TB, $q = 0$; in TG, $k_\rho = 0$; and in TP, $k_\rho = 0$ and $q = 0$.

Finally, *once the chosen beam is described on the truncation plane ($z = 0$), the beam emanated by the finite aperture will be given by solution (4).*

Let us go on to an important example.

3. APPLYING THE METHOD FOR DESCRIBING THE TRUNCATED BESSEL BEAM

In this section, we shall apply our method for describing an important truncated beam, namely, the Bessel beam.

Let us consider a Bessel beam, with wavelength of 632.8 nm, truncated at $z = 0$ by a circular aperture with radius R; that is to say, from $\Psi_{TB}(\rho, 0) = J_0(k_\rho \rho)\,\mathrm{circ}(\rho/R)$.

Let us choose $R = 3.5\,\mathrm{mm}$, and the transverse wavenumber $k_\rho = 4.07 \cdot 10^4\,\mathrm{m}^{-1}$, which corresponds to a beam spot with radius approximatively equal to $\Delta\rho = 59\,\mu\mathrm{m}$.

At $z = 0$ the field is described by Eq. (8), where the A_n are given by Eq. (12) and where $q = 0$. In this case, a quite good result can be obtained by the choice $L = 3R^2$, $q_R = 6/L$ and $N = 23$. Let us repeat that, since such a choice is not unique, very many alternative sets of values L and q_R exist, which yield as well excellent results.

Figure 1(a) shows the field given by Eq. (8): it represents with high fidelity the Bessel beam truncated at $z = 0$. The resulting field, emanated by the aperture, is given by solution (4), and its intensity is shown in Figure 1(b). One can see that the result really corresponds to a Bessel beam truncated by a finite aperture.

4. CONCLUSIONS

In this paper, starting from suitable superpositions of Bessel-Gauss beams [5], we have constructed a simple, effective method for the analytic description, in the Fresnel region, of important beams truncated by finite apertures.

ACKNOWLEDGMENT

The authors acknowledge partial support from FAPESP, CNPq and CAPES.

REFERENCES

1. Wen, J. J. and M. A. Breazele, "A diffraction beam field expressed as the superposition of Gaussian beams," *J. Acoust. Soc. Am.*, Vol. 83, 1752–1756, 1988.

2. Ding, D. and Y. Zhang, "Notes on the Gaussian beam expansion," *J. Acoust. Soc. Am.*, Vol. 116, 1401–1405, 2004.
3. Zamboni-Rached, M., E. Recami, and M. Balma, "Simple and effective method for the analytic description of important optical beams when truncated by finite apertures," *Appl. Opt.*, Vol. 51, 3370–3379, 2012.
4. Goodman, J. W., *Introduction to Fourier Optics*, McGraw-Hill, 1996.
5. Gori, F. and G. Guattari, "Bessel-Gauss beams," *Optics Communications*, Vol. 64, 491–495, 1987.

A Novel Interactive Approach for Modal Analysis of Nonlinear Waveguides Based on a Fully Hybrid Vectorial Finite Element Method

K. Z. Nóbrega[1] and A. M. F. Frasson[2]

[1]Departamento de Eletro-Eletrônica, Instituto Federal do Maranhão, São Luis, Ma, Brazil
[2]Departamento de Engenharia Elétrica, Universidade Federal do Espírito Santo, Vitória, Es, Brazil

Abstract— An interactive method for solving full anisotropic nonlinear wave guiding problems is presented. To do this, a vectorial finite element scheme using edge/nodal basis element with curved triangle is discussed. Actually, there are two methods commonly used to find the stationary solutions of nonlinear structures. The first one has already been realized using a vectorial formulation but that procedure only computes stable modes, which means that for those situations where bistability effects are present, the solution does not converge and such effects can not be properly discussed. Contrary to the former, the second one has the main characteristic of always reaching convergence, being very useful to describe bistable behaviour and nonlinear switching characteristics, but it has been implemented considering only scalar electromagnetic field modelling. Here, we will describe and present results of a new approach in which its main characteristics are the presence of all electric field components with no need of any adjust parameters, and the possibility to deal with a full nonlinear permittivity tensor.

1. INTRODUCTION

For many years, optical waveguides, including fibers, have been focus of many studies and much interest due to their potential to improve communication systems. As a matter of fact, they have also contributed to the popularization of nonlinear optical systems and all-optical applications, including optical bistability (OB) in such a way that to study stationary characteristic modes of optical waves guided by an arbitrary nonlinear dielectric distribution is widely necessary.

In a certain way, those kinds of analyses are abundant with both numerical and analytical tools in unidimensional waveguides but the waves are not confined in both transverse dimensions under low power regime so bidimensional guiding structures are important on practical applications.

On the other hand, nonlinear bidimensional guiding structures is anything arduously complex and, except for some cases that make use of perturbation's theory, they are normally developed through numerical methods like Finite Element Method (FEM) or Finite Difference (FD). Therefore, it is usual to share studies in two distinct classes: scalar and vectorial.

In particular, the scalar situation is useful in two basic situations. The former happens when nonlinear permittivity depends on electric field intensity rather than on each field component differently. The second one appears on analysis of linearly polarized modes in a certain transverse direction rather than as just one component of a multi-component vector field, once that scalar field can be interpreted as one component where the others are found starting from it. In practice, such conditions point that scalar theory could be initially considered but it should be used cautiously, specially for nonlinear waveguide's analysis.

On the other side, when someone considers vectorial FEM formulations with nodal basis functions he will deal with two magnetic field components only, and a convergent condition must be applied during the modeling to avoid spurious modes. For this reason, the analysis is limited to weak guiding condition in such a way that high contrast of dielectric permittivity is not allowed on the waveguide. Although there are hybrid vectorial FEM formulations where nodal and edge basic functions are applied on longitudinal and transverse electric (or magnetic) field components, respectively, they require a complex modeling of theory and demand much time on both computational implementation and simulation.

Probably, these are some of the reasons that explain why is rare on literature to find numerical tools applying hybrid FEM formulations with capability to analyse modes of nonlinear waveguides. To best of our knowledge, it is known only one group at United Kingdom [1] whose tools could be used on those kinds of problems even considering a vectorial FEM formulation purely nodal. Besides using nodal formulation, the tools developed by the United Kingdom's group has another particular characteristics that it does not make possible to study unstable nonlinear modes, i.e., on

those situations where bistability effects need to be deepened those modes do not even converge and they could be studied.

In this work, we present a new numerical tool able to study both stable and unstable modes in nonlinear waveguides through a hybrid and fully vectorial FEM formulation. Here, it was used the state of art at FEM, it means, using edge/nodal basis function with bent triangles applied on transverse and longitudinal electric field components, respectively, and which the three field components and anisotropy are already contemplated on its theoretical modeling. Moreover, the interative method turns out to be possible to visualize all modes (stable or not) and to clearly identify the well known "S"-bistability behaviour.

Following, it is briefly described the FEM formulation and its main characteristics as well as the procedure of convergence to find the modes. After that and with the only task to validate our program, some simulations of a typical nonlinear waveguide already published on literature are illustrated. Finally, some last considerations are done about the method and its capabilities.

2. FINITE ELEMENT METHOD FORMULATION

To full wave analysis of two-dimensional waveguides, the FEM formulation usually starts from the well known rot-rot equation that assumes the following equation:

$$\nabla \times ([\nu]\,\nabla \times \mathbf{E}) - k_0^2[\varepsilon_L + f(a|\mathbf{E}|^2)]\mathbf{E} = 0 \tag{1}$$

being $\mathbf{E}$ the electrical fied, k_0 the wavenumber at free space, $[\nu] = [\mu_r]^{-1}$ the inverse matrix of relative magnetic permeability and $[\varepsilon_L + f(a|\mathbf{E}|^2)]$ is the relative permittivity matrix where ε_L is the linear contribution while $f(a|E|^2)$ gives the nonlinear aspect. In optics, it is usual such function to depend on field's power intensity with a [m^2/V^2] being the nonlinear coefficient of the medium defined by $a = \varepsilon_L\varepsilon_0 n_2 c$ in terms of the usual nonlinear optical coefficient n_2 [m^2/W], the velocity of light in vacuum c, the vacuum permittivity ε_0 and the linear term of the relative permittivity ε_L. Broadly, the nonlinear function is modelled according to Kerr nonlinearity or two main saturation models illustrated on Table 1, where α is the saturation parameter. In this work, the third kind of nonlinearity will be used and although anisotropy is inherent to the theoretical modelling, only the isotropic case was studied for the sake of comparison with previous results already published.

Turning back to (1), it was rewritten using the typical FEM assumptions that include $\nabla = \nabla_T + \frac{\partial}{\partial z}\mathbf{a_z}$; expansion of electric field in terms of its transverse and longitudinal components to the xy plane, i.e., $\mathbf{E}$=$\mathbf{E}_t + E_z\mathbf{a}$ where edge and nodal basis functions are applied on $\mathbf{E}_t$ and E_z, respectively.

Beyond that, when someone also considers Galerkin's Method at transverse section of the optical structures with weight function given by $\mathbf{W} = \mathbf{W}_t + W_z\mathbf{a}_z$, the weak formulation form and the nonlinearity introduced at Table 1, Eq. (1) can be rewritten again as:

$$\iint \left(\nabla_T \times \mathbf{W_T} - \mathbf{W_T}\frac{\partial}{\partial z} - \nabla_T W_z\right) \cdot [P] \ldots \left\{\nabla_T \times \mathbf{E_T} - \left(\nabla_T E_z - \frac{\partial \mathbf{W_T}}{\partial z}\right)\right\} dS$$
$$-k_0^2 \iint (\mathbf{W_T} + W_z\mathbf{a_z}) \cdot \left[\varepsilon_i^L + f_i(a|\mathbf{E}|^2)\right] \begin{bmatrix} \mathbf{E_T} \\ E_z \end{bmatrix} dS = 0, \tag{2}$$

with $[P] = \begin{bmatrix} \nu_{22}- & \nu_{21} & \nu_{23} \\ -\nu_{12} & \nu_{11} & -\nu_{13} \\ \nu_{32} & -\nu_{31} & \nu_{33} \end{bmatrix}$ and the i-index describing the elements related to xx, yy, zz on the diagonal dielectric permittivity matrix. Clearly, one can notice that axial or biaxial anisotropy is already intrinsic on the formulation.

Concerning the FEM formulation, here succinctly described and implemented for us, surely it is the state of art related to FEM. One important aspect is the presence of all three electric

Table 1: Usual nonlinearities.

Model	**Saturability**
$\varepsilon = \varepsilon_L + a\|E\|^2$	Not
$\varepsilon = \varepsilon_L + \frac{a\|E\|^2}{1+\alpha\cdot a\|E\|^2}$	Yes
$\varepsilon = \varepsilon_L + \frac{1}{\alpha}\left[1 - \exp(-\alpha\cdot a\|E\|^2)\right]$	Yes

field components without necessity to add any conditions over them. Besides, it is also possible to consider high contrast of material's dielectric permittivity with no penalty on numerical simulations obtained. At last, once the formulation considers bent triangle, the results obtained are more accurate than the usual hybrid edge/nodal FEM.

In the usual modal analysis [2], the equivalent eigenvalue problem obtained from (2) would result on the effective refractive index and the mode as eigenvalue and eigenvector, respectively. This is a well known technique, stable for linear materials. On the other hand, for nonlinear cases one could believe that a pump power could be assumed and used to establish the refractive index changing and, after that, to find n_0. However, numerically speaking, this is not always a stable procedure due to optical bistability effects [8].

In fact, optical bistability is an effect inherent of nonlinear materials [3–7] and the modal analysis of nonlinear waveguides causes a dispersion curve ($P \times n_0$) where for a given power P it is possible to obtain one or more n_0 values. Therefore, for a possible adaptation from linear case, previously described and used on [1, 2], one would notice a numerical instability when tries to find n_0 as the eigenvalue, that turns such procedure stable only in some particular pump powers.

However, it is important to emphasize that in those few situations where modal analyses of nonlinear waveguides are discussed the method based on that previous adaptation is usual [1, 2, 8]. That seems intriguing because nonlinear simulations have to be more accurate by themselves once that nonlinear effects are dependent of electric field and consequently a better mesh of involved structures are necessary. Yet, one should never forget that nonlinear effects are so much present on actual systems of optical communications, integrated optics and photonic crystals.

By 90's decade, nonlinearities were poorly discussed due to computational and technological limitations, allegedly. Nowadays, it should not happen but it does. The present authors believe that curious fact is much more related to mathematic complexity on modelling and computational implementation of electromagnetic theory with accurate methods involving vectorial methodologies. Finally, a last aspect is related to the spent computational time when compared to linear cases once that a better mesh of at least one additional order of magnitude point is required what causes a higher computational demand.

After those tedious but necessary comments to a non expert reader, it is possible to get back to explanation of the approach here utilized. First, we point that the technique to find stable/unstable modes was first proposed by [9] and implemented later by K. Z. Nobrega also [10], where both works only discuss and model nonlinear structures using a scalar MEF, i.e., only one electric field component. Thinking about it, we have here adapted it to a modeling using hybrid and fully vectorial MEF formulation with bent triangles.

Contrary to what is seen on [1, 2], n_0 is not the eigenvalue anymore but the pump power, P, instead, while the modal field distribution remains to be the eigenvector. So, assuming usual conventions of MEF, it means, $\exp(-\gamma z)$ that results on $\partial/\partial z \Rightarrow -\gamma$, and transformations $W_z = \gamma w_z$, $E_z = \gamma e_z$, when someone uses Galerkin's Method with hybrid FEM, from (2) one could easily obtain:

$$\begin{bmatrix} \gamma^2(T_8 - T_{11}) & \gamma^2 T_5 \\ -\gamma^2 T_7 & -T_1 + \gamma^2 T_6 - T_{10} \end{bmatrix} \begin{bmatrix} \phi^z_{m+1} \\ \phi^t_{m+1} \end{bmatrix} = P_{m+1} \begin{bmatrix} \gamma^2 T^{NL}_{11} & 0 \\ 0 & T^{NL}_{10} \end{bmatrix} \begin{bmatrix} \phi^z_{m+1} \\ \phi^t_{m+1} \end{bmatrix} \tag{3}$$

where $\gamma = \alpha + j\beta$, with $\beta = k_0 n_0$, α representing a loss factor (not used here), P_{m+1} the eigenvalue to be found on next interaction and matrices T described on Table 2.

To solve (3), a linear modal analysis is initially done, i.e., the first β value and the modal field distribution are found ignoring any nonlinearity. At sequence, such field distribution is normalized, ϕ_0, so that $\int_{-\infty}^{+\infty}\int_{-\infty}^{+\infty} |\boldsymbol{\varphi}(x,y)|^2 dxdy = 1$. In a next step, it is assumed that previous normalized field, ϕ_0, is associated to a very small pump power (1 µW in our simulations), P_0, that is related to electric field as $\mathbf{E}_m = \sqrt{P_m}\boldsymbol{\varphi}_m$. Thus, the initial electric field distribution, $\mathbf{E}_0$, is already defined.

Starting from that point, the interactive scheme is started up considering a small increment, $\Delta\beta$, on the previous β. Once set that propagation constant and using the previous electric field's distribution, $\mathbf{E}_m$, associated to the previous power, P_m, all element matrices are evaluated and the eigenvalue problem is assembled. Once solved, the eigenvalue found would correspond to the new pump power, P_{m+1}, to that β used. Besides that, the eigenvector found (unnormalized electric field) must be normalized to generate, $\boldsymbol{\phi}_{m+1}$, in such a way that the appropriate electric field distribution is found, $\mathbf{E}_{m+1} = \sqrt{P_{m+1}}\boldsymbol{\varphi}_{m+1}$. Then, the scheme has just finished its first interaction. To go on,

everything should be repeated, in other words, an increment on the previous β is considered and those previous parameters obtained (E_{m+1} and P_{m+1} in the end of previous step) are now assumed to be E_m and P_m where they will be used to assemble elemental matrices of Table 2.

In Table 2, both weight and electric field functions must be substituted by shape functions usually established on edge/nodal formulation of MEF and inherent of Galerkin's Method.

3. NUMERICAL RESULTS

All simulations were done considering the same waveguide presented on [1, 10] because it was necessary to test and to validate the new computer programs here developed, especially with some well known results published on literature. Therefore, Fig. 1 illustrated that typical nonlinear waveguide used on integrated optics with width W and height H. On the schematics, core and cladding are assumed to be linear while substract is nonlinear.

The simulation parameters were $n_{ca} = n_{sb} = 1.55$ and $n_{nu} = 1.57$, being n the linear contribution of refractive index. Besides, on the nonlinear substract was considered $n_2 = 10^{-9}\,\mathrm{m}^2/\mathrm{W}$ with

Table 2: Constructive relationship of elemental matrices.

Nomenclature	**Mathematical Description**
T_1	$\iint (\nabla_T \times \mathbf{w_T}) \cdot [P] \{\nabla_T \times \mathbf{e_T}\}\, dS$
γT_2	$\gamma \iint \mathbf{w_T} \cdot [P] \{\nabla_T \times \mathbf{e_T}\}\, dS$
$-\gamma T_3$	$-\gamma \iint \nabla_T w_z \cdot [P] \{\nabla_T \times \mathbf{e_T}\}\, dS$
$-\gamma T_4$	$-\gamma \iint (\nabla_T \times \mathbf{w_T}) \cdot [P] \{\mathbf{e_T}\}\, dS$
$\gamma^2 T_5$	$\gamma^2 \iint \nabla_T w_z \cdot [P] \{\mathbf{e_T}\} dS$
$-\gamma^2 T_6$	$-\gamma^2 \iint \mathbf{w_T} \cdot [P] \{\mathbf{e_T}\}\, dS$
$-\gamma^2 T_7$	$-\gamma^2 \iint \mathbf{w_T} \cdot [P] \{\nabla_T e_z\}\, dS$
$\gamma^2 T_8$	$\gamma^2 \iint \nabla_T w_z \cdot [P] \{\nabla_T e_z\}\, dS$
$-\gamma T_9$	$-\gamma \iint (\nabla_T \times \mathbf{w_T}) \cdot [P] \{\nabla_T e_z\}\, dS$
$-T_{10}$	$-k_0^2 \iint \mathbf{w_T} \cdot \begin{bmatrix} \varepsilon_{xx}^L & 0 \\ 0 & \varepsilon_{yy}^L \end{bmatrix} \mathbf{e_T} dS$
$-T_{10}^{NL}$	$-k_0^2 \iint \mathbf{w_T} \cdot \begin{bmatrix} \frac{f_{xx}(a\lvert E_m\rvert^2)}{P_m} & 0 \\ 0 & \frac{f_{yy}(a\lvert E_m\rvert^2)}{P_m} \end{bmatrix} \mathbf{e_T} dS$
$-\gamma^2 T_{11}$	$-\gamma^2 k_0^2 \iint w_z \varepsilon_{zz}^L e_z dS$
$-\gamma^2 T_{11}^{NL}$	$-\gamma^2 k_0^2 \iint w_z \frac{f_{zz}(a\lvert E_m\rvert^2)}{P_m} e_z dS$

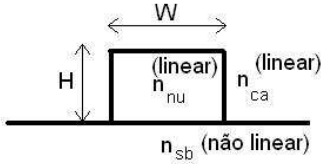

Figure 1: Schematics of a nonlinear waveguide.

saturable parameter $\Delta n_{sat} = 0.1$, so that $\alpha = 1/(2n_{sb}\Delta n_{sat})$ (to see Table 1). All simulations have been obtained considering $\lambda = 0.5\,\mu$m, an isotropy waveguide, about 70,000 points in the mesh and computational window of 3.5 times waveguide's dimension.

Figure 2 shows numerical results for a fixed width, $W = 2\,\mu$m, and two different heights, H. For $H = 0.4\,\mu$m, the field gradually moves toward outside core when pump power increases, while that for $H = 1.2\,\mu$m there is a switching and the bistability occurs.

In that simulation it was used 8,000 points to define dispersion curve and it demanded something about 6 hours of simulation using an 8 GB RAM memory PC, i7 as Intel processor, running FORTRAN in Linux. As can be seen on figure, n_0 gradually increases with the pump power but after a threshold value (P_{cr}), about 84 µW, there is a jump at n_0. Following, it is described step by step the dynamics of a system like that.

When pump power is small the refractive index changing on substract induced by nonlinearity is not big enough to support a mode in that region, i.e., the mode is still guided in the linear core. However, when P_{cr} is reach the self focusing effect caused by nonlinearity creates a region where refractive index is bigger than linear core, being able to guide a mode along substract. Besides that, in the "S" region, there is a transition zone that depending on initial operational conditions it turns possible the mode guiding either in the linear core or in nonlinear substract but in an unstable way.

The same "S" behaviour seen here was described on [9, 10] but through the scalar field's theory. If someone considers the adaptation from linear analysis [1], only envelope of such "S" is observed making difficult, sometimes, to visualize and to determine threshold power during simulation and, more important, only the stable modes are computed. Here all modes can be visualized.

Yet concerning bistability and initial operational conditions previously commented, they are related to pump power's regime, it means, when device is operating initially in a high power regime and such level is gradually reduced there will be a threshold power that below it the mode converges to the linear one. In face of that situation, when system initially operates under low power condition and its value increases and finds another threshold power is reach the mode clearly behaviours as if it would be in nonlinear regime. That is typical hysteresis behaviour.

Following, Fig. 3 presents all electromagnetic field components distributed along the waveguide in the low power regime, 36 µW. In that figure, it is important to emphasize the three electric fields are obtained using hybrid FEM formulation meanwhile magnetic field components are evaluated from the electric field.

All results presented in Fig. 3 are around core-substract of waveguide. The magnetic field components, H_x and H_y, were compared to those published in [1], showing to be in conformity to those ones.

Figures 4 and 5 show field distributions around $P_{cr} = 82\,\mu$W. At Fig. 4 it is illustrated the waveguide on its linear behaviour. Clearly, such distributions are similar to those already discussed

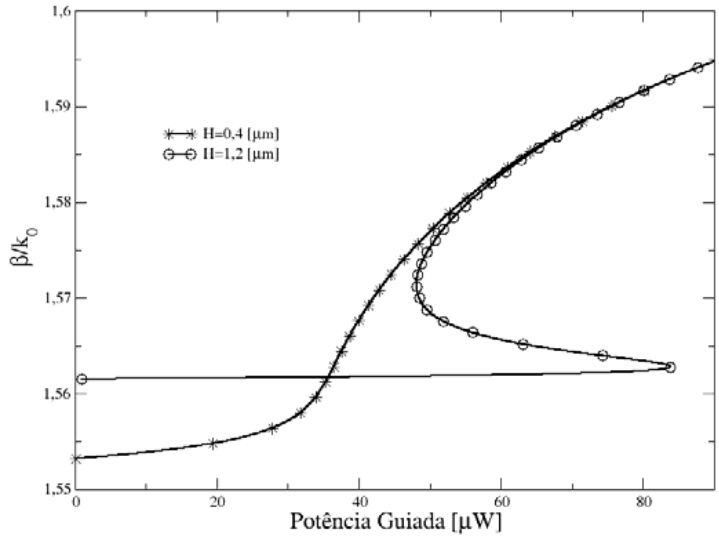

Figure 2: Effective index changing for different pump powers with $W = 2\,\mu$m and $H = 0.4$ and $1.2\,\mu$m.

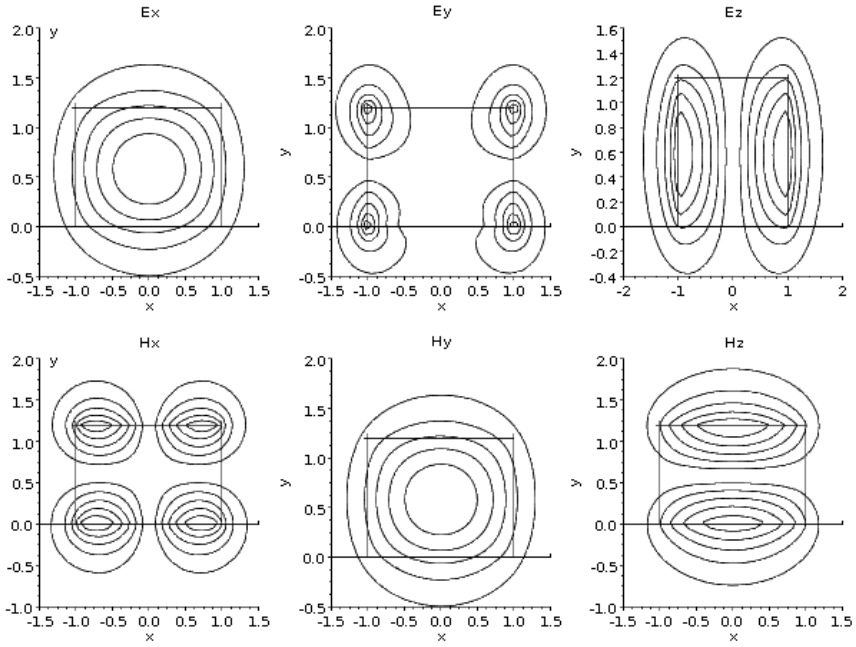

Figure 3: Electromagnetic field of fundamental mode in the region below threshold power in the dispersion curve with $H = 1.2\,\mu\text{m}$ and $P = 36\,\mu\text{W}$.

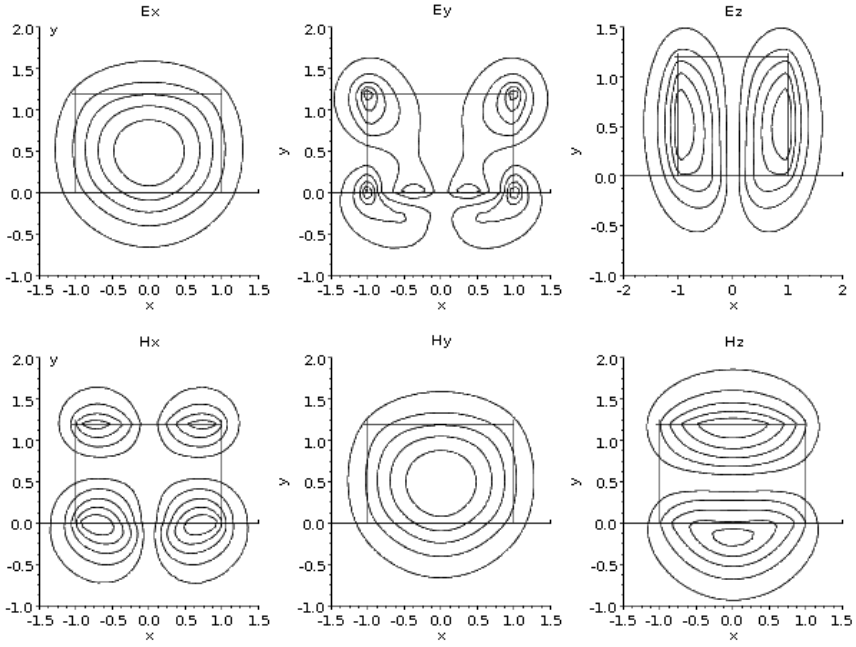

Figure 4: Electromagnetic field of fundamental mode at $P = 82\,\mu\text{W}$ (below threshold) considering $H = 1.2\,\mu\text{m}$.

in Fig. 3 once they are operating on linear regime. Contrary to that, on Fig. 5 the nonlinear effects are strong and the distributions are clearly different to those of Fig. 4.

At last, on Fig. 6 it is illustrated power's distribution along the three waveguide's layers, being possible to discuss numerically each different region and to understand then through the well established "S" of bistability. In fact, such characteristics are important because they could be suggested on conception of all optical gates using power to control swiching, for example.

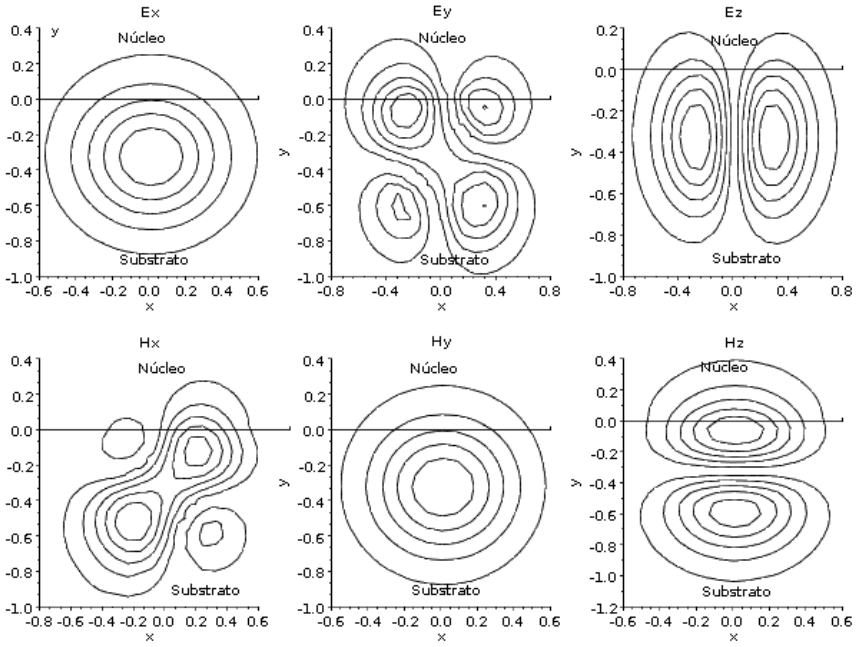

Figure 5: Electromagnetic field of fundamental mode at $P = 82\,\mu W$ (above threshold) considering $H = 1.2\,\mu m$.

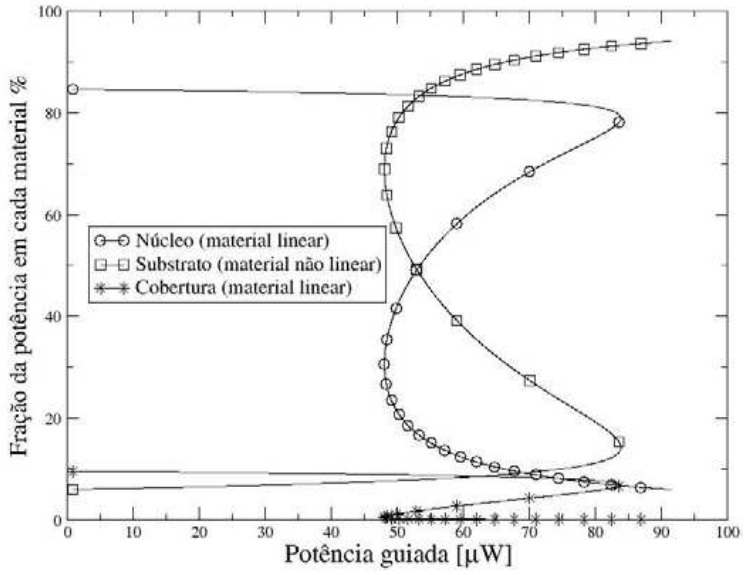

Figure 6: Power's distribution in all three regions of waveguide considering $H = 1.2\,\mu m$.

4. CONCLUSIONS

In this work, it was proposed a new approach of finding nonlinear modal analysis using a hybrid and vectorial FEM formulation when bistability effects are considered. For so, it was theoretically introduced the FEM with edge/nodal elements and all electric field components that implies on better numerical results no matter the structure design and the materials involved even those with high contrast of dielectric permittivity. Contrary to what it is seen on literature, it was also studied and discussed through examples a new interactive method with a fully vectorial FEM formulation which resulted on getting any kind of modes, fundamental to study properly bistability effects, for example.

ACKNOWLEDGMENT

Authors would like to gratefully thank FAPES and FAPEMA for the partial financial support, specially about technical visits between authors.

REFERENCES

1. Obayya, S. S. A., B. M. Azizur Rahman, K. T. V. Grattan, and H. A. El-Mikati, "Full vectorial finite-element solution of nonlinear bistable optical waveguides," *IEEE J. Quantum Electronics*, Vol. 38, 1120–1125, 2002.
2. Niiyama, A. and M. Koshiba, "Three dimensional beam propagation analysis of nonlinear optical fibers and optical logic gates," *IEEE J. Quantum Electronics*, Vol. 16, 162–168, 1998.
3. McCall, S. L., H. M. Gibbs, G. G. Churchil, and T. N. C. Venkatesan, "Optical transistor and bistability," *Bulletin of the American Physical Society*, Vol. 20, 636, 1975.
4. Nobrega, K. Z., M. G. da Silva, and A. S. B. Sombra, "Multistable alloptical switching behavior of the assymetric nonlinear directional coupler," *Optics Communications*, Vol. 173, 413–421, 2000.
5. Thirstrup, C., "Optical bistability in a nonlinear directional coupler," *IEEE J. Quantum Electronics*, Vol. 31, 2101–2106, 1995.
6. Yairi, M. B., H. V. Demir, and D. A. B. Miller, "Optically controlled optical gate with an optoelectronic dual diode structure-theory and experiment," *Opt. Quantum Electron.*, Vol. 33, 1035–1054, 2001.
7. Islam, M. N., C. E. Soccolich, and D. A. B. Miller, "Low-energy ultrafast fiber soliton logic gates," *Opt. Lett.*, Vol. 90, 909–911, 1990.
8. Obayya, S. S. A., B. M. A. Rahman, and K. T. V. Grattan, "Accurate finite element modal solution of photonic crystal fibres," *IEE Proceedings Optoelectronics*, Online No. 20045061, 2005, doi:10.1049/ip-opt:20045061.
9. Li, Q. Y., R. A. Sammut, and C. Pask, "Variational and finite element analyses of nonlinear strip optical waveguides," *Optics Communications*, Vol. 94, 37–43, 1992.
10. Nobrega, K. Z. and H. E. Hernandez-Figueroa, "Optical bistability in nonlinear waveguides with photonic crystals," *Microwave and Optical Technology Letters*, Vol. 41, 41–43, 2004.

Kummer Function Method for Analysis of the Azimuthally Magnetized Circular Ferrite Waveguides

Mariana Nikolova Georgieva-Grosse[1] **and Georgi Nikolov Georgiev**[2]

[1]Consulting and Researcher in Physics and Computer Sciences
Meterstrasse 4, D-70839 Gerlingen, Germany
[2]Faculty of Mathematics and Informatics, University of Veliko Tirnovo "St. St. Cyril and Methodius"
BG-5000 Veliko Tirnovo, Bulgaria

Abstract— The Kummer confluent hypergeometric function method for investigation of the circular waveguides, containing a co-axially positioned ferrite cylinder of single-connected cross-section, magnetized in azimuthal direction that sustain normal TE_{0n} or slow $\widehat{TE}_{0\hat{n}}$ modes, is considered and applied to the simplest case in which the anisotropic load fills entirely the transmission line. Its main points could be systemized as follows: *i*) The relevant wave equation is a form of the Kummer confluent hypergeometric equation; *ii*) The field components of the normal waves are expressed in terms of complex and of the slow ones — by real Kummer functions $\Phi(a, c; x)$ and $\hat{\Phi}(\hat{a}, \hat{c}; \hat{x})$, resp. where $a = c/2 - jk$ — complex, $c = 1$ or $c = 3$ (positive integers) and $x = jz$ — purely imaginary, k, z — real, $-\infty < k < +\infty$, $z > 0$ and $\hat{a}$ — real, $\hat{a} = \hat{c}/2 + \hat{k}$, $\hat{c} = 1$ or $\hat{c} = 3$ (positive integers), $\hat{k}$, $\hat{x}$ — real, $-\infty < \hat{k} < -\hat{c}/2$, $\hat{k} < 0$, $(\hat{a} < 0)$, $\hat{x} > 0$. [The characters without (with) hats "$\hat{}$" stand for both complex and real (only real) quantities and functions.]; *iii*) The solution of boundary-value problem needs a detailed examination of the behaviour of the functions in question and of their zeros in x ($\hat{x}$) in the complex (real) field. Here the discussion is restricted to the study of the zeros solely. It is established that the complex (real) function has an infinite (finite) number n ($\hat{n}$) of positive purely imaginary (real) zeros of the kind mentioned. The dependence of the first several of them on k ($\hat{k}$) is presented in a tabular and a graphical form at a relatively small in absolute value and at very large negative numerical equivalents of these parameters. The application of the results in the boundary-value analysis treated is talked over.

1. INTRODUCTION

The propagation problems of normal TE_{0n} or slow $\widehat{TE}_{0\hat{n}}$ modes in the circular waveguides with azimuthally magnetized concentric ferrite cylinder or toroid, are one of the challenges of the modern computational electromagnetics [1–5]. Though formulated years ago [6–9], due to their complexity, still they are not solved in sufficient depth. Different approaches have been suggested, aiming at clarifying the phenomena of anisotropic medium-microwave field interaction, based on: *i*) the Bolle-Heller functions [6]; *ii*) the transverse network representation [7]; *iii*) the perturbation techniques [8]; *iv*) the variational calculus [9]; *v*) the confluent hypergeometric functions [1–4]; *vi*) the Coulomb wave functions [5].

This work reveals the basic features of the Kummer confluent hypergeometric function method, employable to configurations in which the ferrite region is cylindrical. The ferrite is described by a Polder permeability tensor $\overleftrightarrow{\mu} = \mu_0[\mu_{ij}]$, i, j = 1, 2, 3, with non-zero components $\mu_{ii} = 1$ and $\mu_{13} = -\mu_{31} = -j\alpha$, $\alpha = \gamma M_r/\omega$, ($\gamma$ — gyromagnetic ratio, M_r — ferrite remanent magnetization, ω — angular frequency of the wave) and a scalar permittivity $\varepsilon = \varepsilon_0\varepsilon_r$. In the particular case it is thought that it fills-in completely the waveguide. Moreover, it is assumed that the latter is infinitely long, lossless and perfectly conducting and that its radius is r_0.

2. KUMMER FUNCTION METHOD

The solution of Maxwell equations in the anisotropic medium shows that the longitudinal component of the rotationally symmetric $TE(H_r, E_\theta, H_z)$ modes satisfies the following second-order ordinary differential equation [5]:

$$\left(r^{-1}D_r r D_r + \beta_f^2 - \beta^2 - \alpha\beta\, r^{-1}\right) H_z = 0 \tag{1}$$

in which $D_r = \partial/\partial r$ is a differential operator, $\beta_f^2 = \beta_0^2\varepsilon_r\mu_{eff}$, $\beta_0^2 = \omega^2\varepsilon_0\mu_0$ and β are the phase constants in the unlimited space, occupied by azimuthally magnetized ferrite, and the ones in

the free space and in the geometry examined, resp., and $\mu_{eff} = 1 - \alpha^2$ is the effective relative permeability of the load. If $\beta_f > \beta$ ($\hat{\beta}_f < \hat{\beta}$), it governs the propagation of normal TE_{0n} (slow $\widehat{TE}_{0\hat{n}}$) modes along the structure. It is accepted to denote the parameters of the second (first) of them by hats "$\widehat{\ }$" (without hats). It is easily shown that Eq. (1) is a form of the Kummer confluent hypergeometric equation [10]:

$$x\frac{d^2y}{dx^2} + (c - x)\frac{dy}{dx} - ay = 0. \tag{2}$$

Provided normal modes are argued out, this is done by means of the substitutions $x = jz$, $z = 2\beta_2 r$, $\beta_2 = (\beta_f^2 - \beta^2)^{1/2}$ — radial wavenumber and $H_z = y(x)e^{-x/2}$. In the instance regarded $c = 1$, $a = c/2 - jk$ and $k = \alpha\beta/(2\beta_2)$. As for the slow waves, the transformations are: $\hat{x} = 2\hat{\beta}_2\hat{r}$, $\hat{\beta}_2 = (\hat{\beta}^2 - \hat{\beta}_f^2)^{1/2}$ and $\hat{H}_z = \hat{y}(\hat{x})e^{-\hat{x}/2}$. Now, it is valid: $\hat{c} = 1$, $\hat{a} = \hat{c}/2 + \hat{k}$, $\hat{k} = \hat{\alpha}\hat{\beta}/(2\hat{\beta}_2)$. Obviously $\hat{\beta}_2 = j\beta_2$ and $\hat{k} = -jk$, (j — imaginary unit).

Accordingly, the field components and the characteristic equation of the normal modes are given

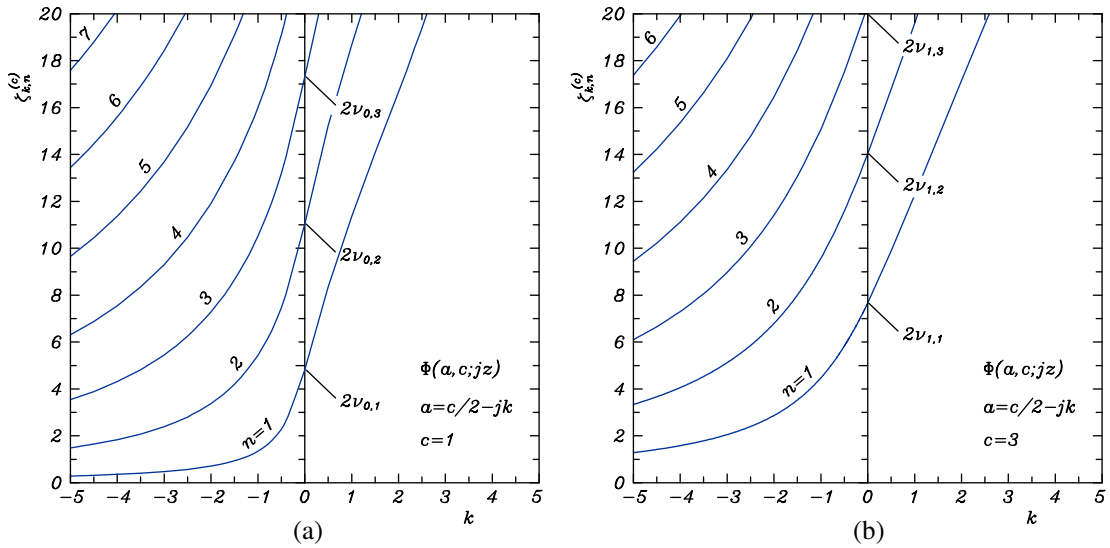

Figure 1: Positive purely imaginary zeros $\zeta_{k,n}^{(c)}$ in z of the complex Kummer confluent hypergeometric function $\Phi(a, c; jz)$ with $a = c/2 - jk$ vs. k in case: (a) $c = 1$, $n = 1(1)7$ and (b) $c = 3$, $n = 1(1)6$.

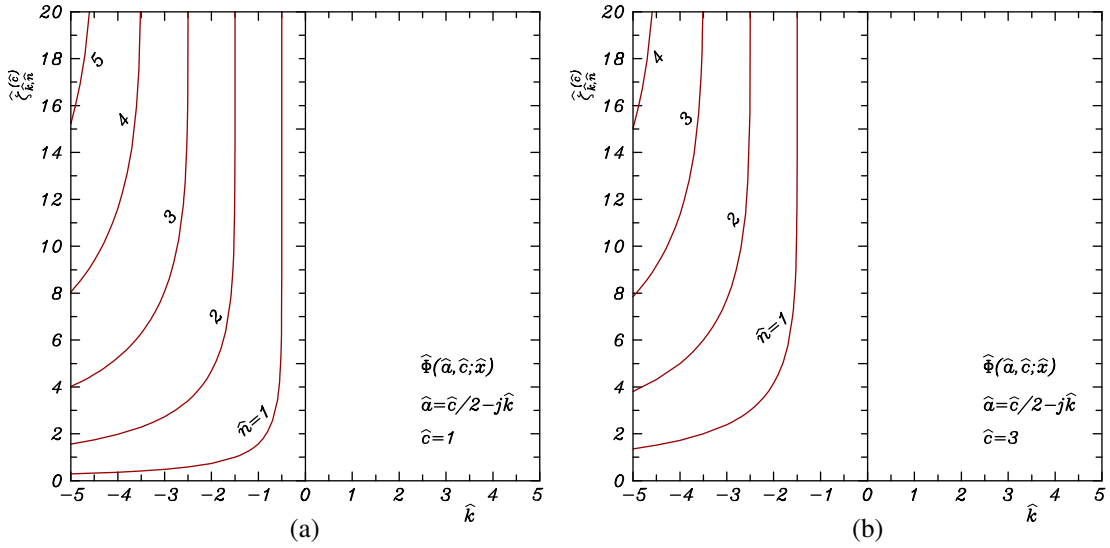

Figure 2: Real positive zeros $\hat{\zeta}_{\hat{k},\hat{n}}^{(\hat{c})}$ in $\hat{x}$ of the real Kummer confluent hypergeometric function $\hat{\Phi}(\hat{a}, \hat{c}; \hat{x})$ with $\hat{a} = \hat{c}/2 + \hat{k}$ vs. $\hat{k}$ in case: (a) $\hat{c} = 1$, $\hat{n} = 1(1)5$ and (b) $\hat{c} = 3$, $\hat{n} = 1(1)4$.

by the expressions:

$$H_r = jA\left[0.5\left(1-\alpha^2\right)\beta r\Phi\left(a+1,c+2;x\right)+\alpha\Phi\left(a,c;x\right)\right]e^{-x/2}, \tag{3}$$

$$E_\theta = -j0.5\omega\mu_0\left(1-\alpha^2\right)rA\Phi\left(a+1,c+2;x\right)e^{-x/2}, \tag{4}$$

$$H_z = A\Phi\left(a,c;x\right)e^{-x/2}, \tag{5}$$

$$\Phi\left(a+1,c+2;x_0\right)=0 \tag{6}$$

in which the parameters acquire the aforesaid values, A is an arbitrary constant and $x_0 = 2\beta_2 r_0$. It is worthwhile to introduce the normalized (barred) quantities: $\bar{\beta} = \beta/(\beta_0\sqrt{\varepsilon_r})$, $\bar{\beta}_2 = \beta_2/(\beta_0\sqrt{\varepsilon_r})$, $\bar{r}_0 = \beta_0 r_0\sqrt{\varepsilon_r}$ and $k = \alpha\bar{\beta}/(2\bar{\beta}_2)$, and to rewrite Eqs. (3)–(6) in terms of them. Then, if $\zeta_{k,n}^{(c)}$ stands for the nth ($n = 1, 2, 3, \ldots$) positive purely imaginary zero of $\Phi(a, c; x)$, Eq. (6) holds when $\bar{\beta}_2 = \zeta_{k,n}^{(c+2)}/(2\bar{r}_0)$ which yields the eigenvalue spectrum of the configuration. Putting hats "$\widehat{\ }$" above all the symbols in Eqs. (3)–(6) (giving them the relevant sense) and normalizing $\hat{\beta}$, $\hat{\beta}_2$, $\hat{r}_0$ and $\hat{k}$ as above, permits to describe the slow waves.

3. NUMERICAL STUDY OF THE ZEROS OF KUMMER FUNCTION

The solution of propagation problem considered: plotting the phase characteristics of the waveguide and the field distribution in it, needs a numerical investigation of the Kummer function and its zeros in the complex (real) area, corresponding to the normal TE_{0n} (slow $\widehat{TE}_{0\hat{n}}$) modes for the values of parameters, enumerated in the previous Section. This part of the research presents outcomes of the analysis of the zeros. The dependence of the first several positive purely imaginary zeros $\zeta_{k,n}^{(c)}$ in x (in z) of $\Phi(a, c; x)$ in case $a = c/2 - jk$ — complex, $c = 1$ or $c = 3$ (positive integers) and $x = jz$ — purely imaginary, k, z — real, $-\infty < k < +\infty$, $z > 0$ and of the first several real positive zeros $\hat{\zeta}_{\hat{k},\hat{n}}^{(\hat{c})}$ in $\hat{x}$ of $\hat{\Phi}(\hat{a}, \hat{c}; \hat{x})$, provided $\hat{a}$ — real, $\hat{a} = \hat{c}/2 + \hat{k}$, $\hat{c} = 1$ or $\hat{c} = 3$ (positive integers), $\hat{k}$, $\hat{x}$ — real, $-\infty < \hat{k} < -\hat{c}/2$, $\hat{k} < 0$, $(\hat{a} < 0)$, $\hat{x} > 0$ on k and $\hat{k}$, resp., is presented in Figs. 1, 2. (n and $\hat{n}$ are natural numbers which determine the number of zeros of the two functions.) [The characters without (with) hats "$\widehat{\ }$" stand for both complex and real (only real) quantities and functions. Accordingly, $\Phi(a, c; x)$ ($\hat{\Phi}(\hat{a}, \hat{c}; \hat{x})$) is complex (real).] The Figures mentioned illustrate the behaviour of $\zeta_{k,n}^{(c)}$ and $\hat{\zeta}_{\hat{k},\hat{n}}^{(\hat{c})}$ in a restricted interval of variation of k and $\hat{k}$, resp. in the vicinity of zero, while Table 1 — on condition that these parameters are large, negative. The symbols $2\nu_{0,n}$ and $2\nu_{1,n}$ in Figs. 1 (a), (b) stand for the nth zeros of the zeroth and first order Bessel functions $J_0(z/2)$ and $J_1(z/2)$, resp., (see the second Kummer theorem [10]). The analysis reveals that the complex (real) function has an infinite (finite) number n ($\hat{n}$) of zeros. Accordingly, $n = 1, 2, 3, \ldots$, irrespective of the particular values of a and c. $\hat{\Phi}(\hat{a}, \hat{c}; \hat{x})$, however, possesses zeros exclusively, if $\hat{a} < 0$ (if $-\infty < \hat{k} < -\hat{c}/2$, provided $\hat{c} > 0$, and if $-\infty < \hat{k} < \hat{c}/2$, on condition that $\hat{c} < 0$, i.e., in both instances $\hat{k} < 0$). On the understanding that $\hat{c} > 0$ their number $\hat{n}$ depends on $\hat{a}$ solely ($\hat{n} = 1, 2, \ldots, \hat{p}$, $\hat{p} = abs[\hat{a}]$), while stipulating that $\hat{c} < 0$ and $\hat{a} < \hat{c} < 0$, then it is specified by the two parameters of the function ($\hat{n} = 1, 2, \ldots, \hat{s}$, $\hat{s} = \hat{p} - \hat{q}$, $\hat{p} = abs[\hat{a}]$, $\hat{q} = abs[\hat{c}]$, $\hat{q} = 1, 2, \ldots, \hat{p} - 1$), ($[\hat{a}]$ denotes the largest integer less or equal to $\hat{a}$).

In addition, in case $c = \hat{c}$, $n = \hat{n}$ and $k = \hat{k}$ — large, negative, it holds: $\zeta_{k,n}^{(c)} \approx \hat{\zeta}_{\hat{k},\hat{n}}^{(\hat{c})}$, (see the underlined digits in the second and sixth columns of the Table). Besides, it is fulfilled:

$$\begin{aligned} L_1(c,n) &= \lim_{k_-\to-\infty} K_{1-}(c,n,k_-) = \lim_{k_-\to-\infty} M_{1-}(c,n,k_-) = \lim_{\hat{k}_-\to-\infty} \hat{K}_{1-n}(\hat{c},\hat{n},\hat{k}_-) \\ &= \lim_{\hat{k}_-\to-\infty} \hat{M}_{1-}(\hat{c},\hat{n},\hat{k}_-) = \hat{L}_1(\hat{c},\hat{n}) \end{aligned} \tag{7}$$

where $K_{1-}(c, n, k_-) = |k_-|\,\zeta_{k_-,n}^{(c)}$, $M_{1-}(c, n, k_-) = |a_-|\,\zeta_{k_-,n}^{(c)}$ and $\hat{K}_{1-}\left(\hat{c}, \hat{n}, \hat{k}_-\right) = \left|\hat{k}_-\right|\hat{\zeta}_{\hat{k}_-,\hat{n}}^{(\hat{c})}$, $\hat{M}_{1-}\left(\hat{c}, \hat{n}, \hat{k}_-\right) = |\hat{a}_-|\,\hat{\zeta}_{\hat{k}_-,\hat{n}}^{(\hat{c})}$ (cf. the marked by bold face type digits in the third, fourth, seventh and eighth columns of Table 1).

Table 1: Numbers $\zeta^{(c)}_{k_-,n}$, $K_{1-}(c,n,k_-)$, $M_{1-}(c,n,k_-)$, $\hat{\zeta}^{(\hat{c})}_{\hat{k}_-,\hat{n}}$, $\hat{K}_{1-}(\hat{c},\hat{n},\hat{k}_-)$ and $\hat{M}_{1-}(\hat{c},\hat{n},\hat{k}_-)$ for $c=\hat{c}=1$, $c=\hat{c}=3$, $n=\hat{n}=1$ and large negative $k_-=\hat{k}_-$.

k_-	$\zeta^{(c)}_{k_-,n}$	$K_{1-}(c,n,k_-)$	$M_{1-}(c,n,k_-)$	$\hat{k}_-$	$\hat{\zeta}^{(\hat{c})}_{\hat{k}_-,\hat{n}}$	$\hat{K}_{1-}(\hat{c},\hat{n},\hat{k}_-)$	$\hat{M}_{1-}(\hat{c},\hat{n},\hat{k}_-)$
$c=\hat{c}=1$							
-1.10^1	(–1) 1.44465 86233	**1.44**465 86233	**1.44**646 33194	-1.10^1	(–1) 1.44693 76779	**1.44**693 76779	**1.**37459 07940
-2.10^1	(–2) 7.22755 85667	**1.445**51 17133	**1.445**96 33652	-2.10^1	(–2) 7.23040 73781	**1.44**608 14756	**1.4**0992 94387
-4.10^1	(–2) 3.61431 31924	**1.4457**2 52769	**1.445**83 82198	-4.10^1	(–2) 3.61466 92937	**1.445**86 77175	**1.4**2779 43710
-6.10^1	(–2) 2.40960 80643	**1.4457**6 48386	**1.445**81 50379	-6.10^1	(–2) 2.40971 35758	**1.445**82 81455	**1.4**3377 95776
-8.10^1	(–2) 1.80722 33576	**1.4457**7 86861	**1.445**80 69237	-8.10^1	(–2) 1.80726 78703	**1.445**81 42962	**1.4**3677 79569
-1.10^2	(–2) 1.44578 50957	**1.4457**8 50957	**1.445**80 31679	-1.10^2	(–2) 1.44580 78861	**1.445**80 78861	**1.4**3857 88467
-2.10^2	(–3) 7.22896 82097	**1.44579** 36419	**1.44579** 81600	-2.10^2	(–3) 7.22899 66978	**1.44579** 93396	**1.44**218 48412
-4.10^2	(–3) 3.61448 94463	**1.44579** 57785	**1.44579 6**9081	-4.10^2	(–3) 3.61449 30074	**1.44579** 72029	**1.44**398 99564
-6.10^2	(–3) 2.40966 02903	**1.44579 6**1742	**1.44579 6**6762	-6.10^2	(–3) 2.40966 13455	**1.44579 6**8073	**1.44**459 19766
-8.10^2	(–3) 1.80724 53909	**1.44579 6**3127	**1.44579 6**5951	-8.10^2	(–3) 1.80724 58360	**1.44579 6**6688	**1.44**489 30459
-1.10^3	(–3) 1.44579 63768	**1.44579 6**3768	**1.44579 6**5575	-1.10^3	(–3) 1.44579 66047	**1.44579 6**6047	**1.445**07 37064
-2.10^3	(–4) 7.22898 23112	**1.44579 64**622	**1.44579 6**5074	-2.10^3	(–4) 7.22898 25961	**1.44579 6**5192	**1.445**43 50701
-4.10^3	(–4) 3.61449 12090	**1.44579 648**36	**1.44579 64**949	-4.10^3	(–4) 3.61449 12446	**1.44579 649**79	**1.445**61 57733
-6.10^3	(–4) 2.40966 08126	**1.44579 648**76	**1.44579 64**926	-6.10^3	(–4) 2.40966 08232	**1.44579 649**39	**1.445**67 60109
-8.10^3	(–4) 1.80724 56112	**1.44579 64**890	**1.44579 649**18	-8.10^3	(–4) 1.80724 56156	**1.44579 649**25	**1.4457**0 61302
-1.10^4	(–4) 1.44579 64896	**1.44579 64**896	**1.44579 649**14	-1.10^4	(–4) 1.44579 64919	**1.44579 649**19	**1.4457**2 42021
$c=\hat{c}=3$							
-1.10^1	(–1) 6.54973 98283	**6.5**4973 98283	**6.**62301 45239	-1.10^1	(–1) 6.63870 19591	**6.**63870 19591	5.64289 66652
-2.10^1	(–1) 3.29128 56556	**6.5**8257 13112	**6.**60105 88313	-2.10^1	(–1) 3.30240 38666	**6.**60480 77333	**6.**10944 71533
-4.10^1	(–1) 1.64771 91999	**6.59**087 67996	**6.59**550 93817	-4.10^1	(–1) 1.64910 89602	**6.59**643 58409	**6.**34906 94969
-6.10^1	(–1) 1.09873 65337	**6.59**241 92023	**6.59**447 90115	-6.10^1	(–1) 1.09914 83143	**6.59**488 98858	**6.**43001 76386
-8.10^1	(–2) 8.24119 92068	**6.59**295 93655	**6.59**411 81823	-8.10^1	(–2) 8.24293 64060	**6.59**434 91248	**6.**47070 50787
-1.10^2	(–2) 6.59320 94405	**6.593**20 94405	**6.593**95 11348	-1.10^2	(–2) 6.59409 88864	**6.59**409 88864	**6.**49518 74031
-2.10^2	(–2) 3.29677 14648	**6.593**54 29296	**6.593**72 83704	-2.10^2	(–2) 3.29688 26455	**6.593**76 52911	**6.5**4431 20514
-4.10^2	(–2) 1.64840 65780	**6.5936**2 63118	**6.5936**7 26731	-4.10^2	(–2) 1.64842 04755	**6.5936**8 19022	**6.5**6895 55951
-6.10^2	(–2) 1.09894 02922	**6.5936**4 17534	**6.5936**6 23585	-6.10^2	(–2) 1.09894 44100	**6.5936**6 64603	**6.5**7718 22941
-8.10^2	(–3) 8.24205 89475	**6.5936**4 71580	**6.59365** 87484	-8.10^2	(–3) 8.24207 63195	**6.5936**6 10556	**6.5**8129 79411
-1.10^3	(–3) 6.59364 96596	**6.5936**4 96596	**6.59365** 70774	-1.10^3	(–3) 6.59365 85540	**6.59365** 85540	**6.5**8376 80662
-2.10^3	(–3) 3.29682 64975	**6.59365** 29950	**6.59365 4**8494	-2.10^3	(–3) 3.29682 76093	**6.59365** 52186	**6.5**8870 99772
-4.10^3	(–3) 1.64841 34572	**6.59365** 38288	**6.59365 4**2925	-4.10^3	(–3) 1.64841 35962	**6.59365** 43847	**6.59**118 17643
-6.10^3	(–3) 1.09894 23305	**6.59365** 39833	**6.59365 4**1893	-6.10^3	(–3) 1.09894 23717	**6.59365** 42303	**6.59**200 58168
-8.10^3	(–4) 8.24206 75466	**6.59365 4**0373	**6.59365 4**1532	-8.10^3	(–4) 8.24206 77203	**6.59365 4**1763	**6.59**241 78661
-1.10^4	(–4) 6.59365 40623	**6.59365 4**0623	**6.59365 4**1365	-1.10^4	(–4) 6.59365 41513	**6.59365 4**1513	**6.59**266 51031

4. PHYSICAL INTERPRETATION OF THE OUTCOMES FOR THE ZEROS

The analysis of the results for the zeros of $\Phi(a,c;x)$ and $\hat{\Phi}(\hat{a},\hat{c};\hat{x})$ at $c=\hat{c}=3$, combined with that of the functions and with the peculiarities of the problem thrashed out, reveals the most important features of the phase behaviour of the circular waveguide, uniformly filled with azimuthally magnetized ferrite: *i*) An infinite (finite) number of normal TE_{0n} (slow $\widehat{TE}_{0\hat{n}}$) modes may be sustained in the structure, equal to the number of roots, resp. zeros of the concurring characteristic equation, resp. wave function n ($\hat{n}$) in case $c=3$ ($\hat{c}=3$). Obviously, in this instance $\hat{n}=1,2,\ldots,\hat{p}$, since $\hat{c}>0$; *ii*) The normal (slow) waves are observed both for positive and negative (exclusively for negative) magnetization of the ferrite filling; *iii*) There are two regions of propagation of the slow waves for different values of the off-diagonal element of ferrite permeability tensor element α [two slow waves $\widehat{TE}^{(1)}_{0\hat{n}}$ and $\widehat{TE}^{(2)}_{0\hat{n}}$ might exist for $-1<\hat{\alpha}^{(1)}<0$ and $-\infty<\hat{\alpha}^{(2)}<-(2\hat{n}+1)$, resp., cf.

the condition $\hat{\beta}_f < \hat{\beta}$]; *iv*) The zone of transmission of the normal waves, observed for $-1 < \alpha < 1$, assuming negative (positive) magnetization, is bilaterally restricted (is limited from below and unbounded from the side of higher frequencies); *v*) The area of propagation of slow $\widehat{TE}_{0\hat{n}}^{(1)}$ wave, conforming to $-1 < \hat{\alpha}^{(1)} < 0$, is bounded from the side of lower frequencies; *vi*) The upper limit of the domain in which the normal TE_{0n} mode may get excited coincides with the lower one of the area of existence of the slow $\widehat{TE}_{0\hat{n}}^{(1)}$ mode, when $n = \hat{n}$. (The outcomes for the zeros answering to $c = \hat{c} = 1$ are useful in the inspection of the field distribution.)

5. CONCLUSION

The method for examination of the circular waveguides, comprising a co-axial azimuthally magnetized ferrite cylinder which support normal TE_{0n} or slow $\widehat{TE}_{0\hat{n}}$ modes, based on the complex, resp. real Kummer confluent hypergeometric function of specially selected parameters, is regarded. The point at issue is the structure, completely filled with the anisotropic medium referred to. An analysis is performed on certain of the zeros of the functions in question, necessary for the solution of the task stated. The results are presented both in a graphical and a tabular form and discussed. The main characteristics of wave propagation are debated.

ACKNOWLEDGMENT

We express our gratitude to our mother Trifonka Romanova Popnikolova and to our late father Nikola Georgiev Popnikolov for their self-denial and for their tremendous efforts to support all our undertakings.

REFERENCES

1. Georgiev, G. N. and M. N. Georgieva-Grosse, "Effect of the dielectric filling on the phase behaviour of the circular waveguide with azimuthally magnetized ferrite toroid and dielectric cylinder," *Proc. Asia-Pacific Microwave Conf. APMC-2009*, WE4B-4, 870–873, in CDROM, Singapore, December 7–10, 2009.
2. Georgiev, G. N. and M. N. Georgieva-Grosse, "Theorem for the identity of the $L(c, n)$ and $\hat{L}(\hat{c}, \hat{n})$ numbers and its application in the theory of waveguides," *PIERS Proceedings*, 357–361, Marrakesh, Morocco, March 20–23, 2011.
3. Georgiev, G. N. and M. N. Georgieva-Grosse, "Theory of the $\hat{L}_2(\hat{c}, \hat{\rho}, \hat{n})$ numbers and its application to the slow wave propagation in the coaxial ferrite waveguide," *PIERS Proceedings*, Moscow, Russia, August 19–23, 2012, (in the Special Session: "Advanced mathematical and computational methods in the electromagnetic theory and their applications," organized by M. N. Georgieva-Grosse and G. N. Georgiev), in print.
4. Georgiev, G. N. and M. N. Georgieva-Grosse, "Advanced computational methods for analysis of the circular waveguide completely filled with azimuthally magnetized ferrite: Review of recent results," *Proc. Fourteenth Int. Conf. Electromagn. Adv. Applicat. ICEAA'12*, 62–65, in CDROM, Cape Town, South Africa, September 2–7, 2012, (Invited Paper in the Special Session "Modern problems of mathematical and computational electromagnetics and their advanced applications" organized by M. N. Georgieva-Grosse and G. N. Georgiev).
5. Georgiev, G. N. and M. N. Georgieva-Grosse, "Circular waveguide, completely filled with azimuthally magnetized ferrite," *Wave Propagation*, Academy Publish, Cheyenne, Wyoming, U.S.A., 2012, in print.
6. Bolle, D. M. and G. S. Heller, "Theoretical considerations on the use of circularly symmetric *TE* modes for digital ferrite phase shifters," *IEEE Trans. Microwave Theory Tech.*, Vol. 13, No. 4, 421–426, July 1965.
7. Clarricoats, P. J. B and A. D. Olver, "Propagation in anisotropic radially stratified circular waveguides," *Electron. Lett.*, Vol. 2, No. 1, 37–38, January 1966.
8. Eaves, R. E. and D. M. Bolle, "Perturbation theoretic calculations of differential phase shifts in ferrite-loaded circularly cylindrical waveguides in the TE_{01} mode," *Electron. Lett.*, Vol. 2, No. 7, 275–277, July 1966.
9. Lindell, I. V., "Variational methods for nonstandard eigenvalue problems in waveguide and resonator analysis," *IEEE Trans. Microwave Theory Tech.*, Vol. 30, No. 8, 1194–1204, August 1982.
10. Tricomi, F. G., *Funzioni Ipergeometriche Confluenti*, Edizioni Cremonese, Rome, Italy, 1954.

The Electrodynamics of the Induction Motor

Shayak Bhattacharjee
Department of Physics, Indian Institute of Technology Kanpur, Uttar Pradesh 208016, India

Abstract— In this work, we apply Maxwell's equations on the induction motor. A direct solution being unfeasible, we propose an iterative method. We test the method for the steady state behaviour of 2-pole motor with known stator current and we then use it to derive a dynamic motor model. We first examine the case where the magnetic coupling between the stator and rotor is weak. This case leads intuitively to the general case.

1. INTRODUCTION

Induction motors are the backbone of modern industry because of their high performance and low maintenance requirements. The standard procedure for analysing the steady state performance of these motors is the equivalent circuit method [1], in which the motor is modelled as a circuit where voltages are applied causing currents to flow. The dynamic model of the motor also follows from circuital considerations — the assumptions and approximations made vary slightly from model to model resulting in minor differences among the many models [2–4] existing in literature. In this work we propose an alternative model starting from Maxwell's equations for the motor.

2. MOTOR MODEL AND INFINITE-ORDER PERTURBATION TECHNIQUE

We first consider a three-phase 2-pole motor. Taking advantage of the fact that the height of a cylindrical motor is typically much greater than the radius, we use a two-dimensional model assuming the fields and currents to be invariant along the axial direction. We define the height of the motor as h, the radii of the cage rotor and the stator as r and R, the conductivities as σ and σ' and the depth of the conductor bars as b and b'. We treat the rotor and stator as continuous conducting cylinders since the narrow gaps between adjacent bars and wires merely serve to eliminate currents in undesirable directions. The thicknesses b and b' being much less than the radii r and R we work in terms of the surface currents flowing through the rotor and stator. Accordingly the final schematic of our model is as in Fig. 1.

The applied stator surface current for the nth phase ($n = 1, 2, 3$) is

$$K_n = K_{app} \cos\left(\Omega t + 2(n-1)\pi/3\right) \hat{z} \tag{1}$$

in a positive sector (shown in Fig. 1 as pure numbers) and the negative of that in a negative sector (shown with a bar above the number). This defines Ω as the excitation frequency. We will refer to the rotor rotation frequency as ω and the slip frequency $\Omega - \omega = \varepsilon$. Hereafter we assume the z directionality of the currents to be implicit. Using the angular extensions of the various sectors from Fig. 1, we now expand the applied stator surface current in a Fourier series. The constant term is the sum of the three-phase currents which is zero. The first angular harmonic can be written as

$$^1K_s = K_{\cos} \cos\theta + K_{\sin} \sin\theta, \tag{2}$$

where $K_{\cos}$ and $K_{\sin}$ are determined using the orthogonality of the sines and cosines. From Eq. (1), we readily find that the net first harmonic can be written as $K_0 \cos(\theta - \Omega t)$ for some K_0 which represents a current phasor rotating anticlockwise at frequency Ω. Since higher harmonics are undesirable we focus on this harmonic only. This automatically extends the following procedures to single, five, seven or other exotic phase motors. A direct solution of Maxwell's equations is rendered impossible by our ignorance of the constitutive relations between the electric fields and the surface currents in the stator and rotor. Our knowledge of the equivalent circuit model convinces us that the stator and rotor are like LR circuits — at present however there is no means of determining the inductances and resistances.

We now propose the following iterative method [5] for determining the empirical inductances and in the process solving the whole problem. We will first find the current per unit length *applied* to the stator (K_{s0}) and the rotor (K_{r0}, which in this case equals zero) and then find the magnetic field B_0 created by these currents. Since the tangential component of the magnetic field will not induce any current anywhere, we shall work only with the radial component which we shall denote

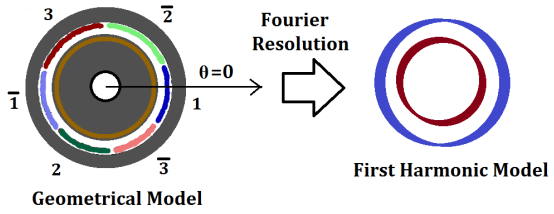

Figure 1.

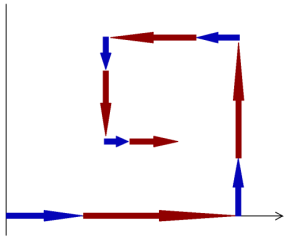

Figure 2.

as B but without the vector symbol. Subsequently we find the currents induced in the stator (ΔK_{s1}) and rotor (ΔK_{r1}) on account of this magnetic field. Again we calculate the magnetic field (ΔB_1) due to these induced currents, then again the currents induced by this field, and so on. In this way we generate a sequence of corrections to the basic stator and rotor currents and obtain successive approximations to these quantities by summing all the corrections.

It can be seen that all currents and magnetic fields will appear stationary in time if we transfer to a frame rotating anticlockwise at frequency Ω; this is called the synchronous reference frame. Because of this property, all quantities will be evaluated in this frame as functions of the angle (which we call θ') alone — the shift to the external frame will result in a replacement of θ' by $\theta - \Omega t$. The synchronous frame is suited for steady-state computations which shall be our focus in this section.

We first work assuming that the stator current is given. We temporarily ignore the processes by which the current came about a period. We just assume that its net value is known. Let the motor rotate counterclockwise and the stator current be $K_s = K_0 \sin(\theta - \Omega t)$. The cage is assumed to be a linear magnetic medium. Since the currents are in the stator which lies across the air gap, the effective permeability is that of the gap, which we call μ_g. Then a short calculation yields the magnetic field due to this current as $\frac{\mu_g}{2} K_0 \cos(\theta - \Omega t)$. In the synchronous frame the electric field will be obtained from Faraday's law. But since B is time-invariant, there will in fact be no electric field in this frame. From the theory of electromagnetic field transformations, there will be an electric field in the rotor frame. This can be obtained from $E = v \times B$. We now apply the real Ohm's law, i.e., $J = \sigma E$ with real conductivity to write the first round of rotor surface currents. These currents will again induce a magnetic field at the rotor surface; this time however the permeability will be that of the core, μ_c, and not of the air gap. It can be seen that on a phasor diagram with $(\theta - \Omega t)$ as the phasor argument, the successive fields and currents form a pattern as in Fig. 2. The currents will in fact form a geometric series, the ratio between successive terms being $\tau_r = \frac{1}{2}\mu_c \sigma r b$, and this series can be summed to infinity to obtain the following expression for the net rotor current,

$$K_r = \frac{K_0(\mu_g/\mu_c)\tau_r \varepsilon}{1 + \tau_r^2 \varepsilon^2} \left(\cos(\theta - \Omega t) - \tau_r \varepsilon \sin(\theta - \Omega t)\right). \tag{3}$$

This expression agrees with the prediction of the circuit model that the rotor is an inductor, τ_r being its time constant. Eq. (3) yields the magnetic field and the torque follows from Lorentz force law as

$$\Gamma = \frac{\pi}{2} \mu_g K_0^2 r^2 h \frac{\tau_r \varepsilon}{1 + \tau_r^2 \varepsilon^2}, \tag{4}$$

which is seen to be in agreement with the predictions of the equivalent circuit model.

3. DYNAMIC MODELING

The success of the preceding calculation encourages us to use infinite-order perturbation (IP) to derive the motor dynamics; this time however we use the stator frame. Let the kth order terms in the iterative developments of the rotor and stator surface currents be known. We then wish to find the $(k+1)$th order terms. For a $2n$-pole motor the first harmonic of the fields and currents takes the form $a\cos(n\theta) + b\sin(n\theta)$. Since the sines and cosines form a linearly independent basis we write this in complex notation as $a + jb$, with $j^2 = -1$. As such the real and imaginary parts of each field and current become the d and q components of a two-component vector. This motivates the vector signs on the fields and currents. This mirrors the standard space phasor approach. Each current produces a vector potential as well as a magnetic field at the surface of both the rotor and stator. The electric field is found from Faraday's law in its differential form. For the rotor

an additional electric field arises from the fact that it is moving through a magnetic field. The effect of the finite angular extension of the conductor bars of the rotor and stator can be factored in when we realize that it causes the currents $K\sin(n\theta)$ to get multiplied by a function which is unity in the angular intervals corresponding to the bars and zero in the intervals corresponding to the spaces. This function can be expanded in a Fourier series of which the leading term is the ratio of the angular extent of each bar to that of each bar-plus-space unit. Denoting this ratio by c for the rotor and c' for the stator, the complete transformation is found to be

$$\begin{bmatrix} \Delta\vec{K}_{r(k+1)} \\ \Delta\vec{K}_{s(k+1)} \end{bmatrix} = \begin{bmatrix} (c\mu_c\sigma rb/2n)\,(-p+jn\omega) & (r/R)^{n-1}\,(c\mu_g\sigma rb/2n)\,(-p+jn\omega) \\ (r/R)^{n+1}\,(c'\mu_g\sigma' Rb'/2n)\,(-p) & (c'\mu_c\sigma' Rb'/2n)\,(-p) \end{bmatrix} \begin{bmatrix} \Delta\vec{K}_{rk} \\ \Delta\vec{K}_{sk} \end{bmatrix} \quad (5)$$

Here we have used p to denote the time derivative d/dt. This motivates the variable definitions as $\tau_r = c\mu_c\sigma rb/2n$, $\tau_s = c'\mu_c\sigma' Rb'/2n$, $\delta_1 = (r/R)^{n-1}\mu_g/\mu_c$ and $\delta_2 = (r/R)^{n+1}\mu_g/\mu_c$. Since summation over repeated derivatives is very difficult to handle we will take the Laplace transform of Eq. (5) and add the terms of different orders to obtain the transfer functions between the rotor and stator currents and the applied voltage. We shall denote the transform of a function $f(t)$ by $\underline{f}(s)$, or more simply by $\underline{f}$. We get

$$\begin{bmatrix} \Delta\vec{K}_{r(k+1)} \\ \Delta\vec{K}_{s(k+1)} \end{bmatrix} = \begin{bmatrix} -\tau_r s + jn\tau_r\omega & \delta_1\,(-\tau_r s + jn\tau_r\omega) \\ \delta_2\,(-\tau_s s) & -\tau_s s \end{bmatrix} \begin{bmatrix} \Delta\vec{K}_{rk} \\ \Delta\vec{K}_{sk} \end{bmatrix}. \quad (6)$$

Since, in each round of IP, Ohm's law is used with a real conductivity, the zeroth round of rotor and stator surface currents will be proportional to the voltages applied on them through some purely geometrical factor. For the rotor of course the applied voltage is zero. Some finite voltage is applied on the stator and the corresponding zeroth order surface current will be denoted by the symbol V This notation may be a dimensional misnomer but its conceptual significance outweighs this minor inconvenience. Thus we get the expression

$$\begin{bmatrix} \Delta\underline{\vec{K}}_{rk} \\ \Delta\underline{\vec{K}}_{sk} \end{bmatrix} = \begin{bmatrix} -\tau_r s + jn\tau_r\omega & \delta_1\,(-\tau_r s + jn\tau_r\omega) \\ \delta_2\,(-\tau_s s) & -\tau_s s \end{bmatrix}^k \begin{bmatrix} 0 \\ \underline{\vec{V}} \end{bmatrix} = \begin{bmatrix} \underline{X} & \delta_1\underline{X} \\ \delta_2\underline{Y} & \underline{Y} \end{bmatrix}^k \begin{bmatrix} 0 \\ \underline{\vec{V}} \end{bmatrix}. \quad (7)$$

Here $\underline{X}$ and $\underline{Y}$, whose meaning can be obtained by a term by term comparison, represent the transforms of the rotor and stator operators X and Y. The rotor operator converts the rotor current of one order to that of the next, the stator operator does so for the stator current. In the following work, we will denote the above matrix by $\underline{\mathrm{T}}$. We first use an approximation to obtain the dynamics of the rotor and stator currents from Eq. (7); we then obtain the dynamics in full generality.

The simplification scheme applicable on Eq. (7) assumes that $\delta_1,\ \delta_2 \ll 1$. This will be a realistic model for a motor of high polarity as well as a motor where the permeability undergoes a sharp drop across the air gap, i.e., $\mu_g \ll \mu_c$. In this case it is possible to obtain the transfer functions by two methods. The first is a brute force method which proceeds by constructing linear combinations of the stator and rotor currents such that the transformation matrix for these combinations is diagonal. This calls for the eigenvalues and eigenvectors of $\underline{\mathrm{T}}^T$, i.e., the transpose of $\underline{\mathrm{T}}$. The smallness of δ (both 1 and 2 which are assumed to be of comparable order) is used to simplify the surds. The transfer functions for these current combinations are obtained and finally unscrambled to get those of the rotor and stator currents themselves.

The second method is an intuitive method which we use here. We note that the $(1,1)$th element of $\underline{\mathrm{T}}$ is an indicator of the strength of the rotor interaction with itself, the $(2,2)$th element estimates the stator interaction with itself and the off-diagonal elements represent the rotor-stator interactions. Since the self-interaction is stronger than the cross-interactions, the primary component of the resultant stator current will come from the self-interaction. This is easy to calculate. The self interaction terms are represented by the $\underline{Y}$ operator hence the successive terms in the iteration go like $\underline{V}+\underline{YV}+\underline{Y}^2\underline{V}+\ldots$ which can readily be summed to obtain the stator current transfer function

$$\underline{\vec{K}}_s = \frac{1}{1+\tau_s s}\underline{\vec{V}}. \quad (8)$$

As in the stator, the dominant terms in the rotor current come from the self-interactions. However the first term comes from the stator side as the applied rotor voltage is zero. In fact the first

term in the iterative rotor current development will be started off by the *resultant* stator current. The (Laplace transformed) vector potential at the rotor surface due to this current is $\delta_1 \frac{\mu_c r}{2n} \frac{1}{1+\tau_s s} \underline{\vec{V}}$ and the magnetic field is $\delta_1 \frac{\mu_c}{2} \frac{1}{1+\tau_s s} \underline{\vec{V}}$. The zeroth round of rotor currents is then found to be $\delta_1 \left(-\tau_r s + jn\tau_r\omega\right) \frac{1}{1+\tau_s s} \underline{\vec{V}}$. Hereafter the rotor self-interaction dominates in comparison with the further cross-interactions and we may write a series identical to the one for the stator only with $\underline{X}$ in place of $\underline{Y}$. Summing this series yields almost trivially the rotor current transfer function

$$\underline{\vec{K}}_r = \delta_1 \frac{-\tau_r s + jn\tau_r\omega}{\left(1+\tau_s s\right)\left(1+\tau_r s - jn\tau_r\omega\right)} \underline{\vec{V}}. \tag{9}$$

These transfer functions are identical to the ones obtained from the brute force method, an observation which validates the conceptual steps applied in this derivation.

Finally we note that the above reasoning can be extended to obtain the general transfer functions with no restriction on δ. Let the resultant rotor current be known. Then the zeroth round of stator currents will have a contribution from this rotor current as well as from the applied voltage. Now by including the *resultant* rotor current in the zeroth term, we have in effect taken into account *all* orders of the rotor-stator interaction. Thus, hereafter we can consider only the stator self interaction, irrespective of the relative strength of the cross-interaction. In other words, we have effectively removed the rotor by incorporating its entire contribution into the zeroth order stator current. Repeating the procedure leading to Eq. (8), we obtain the stator current transfer function

$$\underline{\vec{K}}_s = \frac{\underline{\vec{V}} - \delta_2 \tau_s s \underline{\vec{K}}_r}{1+\tau_s s}. \tag{10}$$

The identical procedure for the rotor, assuming the net stator current to be known, leads to the transfer function

$$\underline{\vec{K}}_r = \frac{\delta_1 \left(-\tau_r s + jn\tau_r\omega\right) \underline{\vec{K}}_s}{1+\tau_r s - jn\tau_r\omega}. \tag{11}$$

These transfer functions can be readily inverted to obtain the following dynamical equations for the motors:

$$\begin{bmatrix} 1+\tau_r\left(p-jn\omega\right) & \delta_1\tau_r\left(p-jn\omega\right) \\ \delta_2\tau_s p & 1+\tau_s p \end{bmatrix} \begin{bmatrix} \vec{K}_r \\ \vec{K}_s \end{bmatrix} = \begin{bmatrix} 0 \\ \vec{V} \end{bmatrix}. \tag{12}$$

Here we have used p to denote the differential operator d/dt. It is worth comparing this result with the equations in the existing literature. We cite the dynamics stated by Takahashi and Noguchi [6] in their classic work on direct torque control. Their equations for a 2-pole motor read

$$\begin{bmatrix} \vec{v}_1 \\ 0 \end{bmatrix} = \begin{bmatrix} R_1 + pL_{11} & pM \\ (p-j\dot{\theta}_m)M & R_2 + (p-j\dot{\theta}_m)L_{22} \end{bmatrix} \begin{bmatrix} \vec{i}_1 \\ \vec{i}_2 \end{bmatrix}, \tag{13}$$

where v_1 is the stator voltage vector, R_1 the stator resistance, L_{11} the stator self-inductance, M the magnetizing inductance, R_2 the rotor resistance, L_{22} the rotor self-inductance, i_1 and i_2 the stator and rotor currents and θ'_m the rotor angular velocity. On inspection, Eqs. (12) and (13) are found to be identical. For a 2-pole motor, $n = 1$. Moreover the apparent equality of the off-diagonal coefficients of the matrix in Eq. (13), which is lacking in Eq. (12), is cosmetic. The rotor voltage being zero, the first line of Eq. (12) can be multiplied by any arbitrary constant which can of course be chosen to ensure equality of the off-diagonal coefficients.

Our work has thus successfully obtained the dynamics of the induction motor starting from Maxwell's equations. The analysis has also predicted the values of the various circuital parameters which are generally determined from experiments on the motor.

REFERENCES

1. Chapman, S. J., *Electric Machinery Fundamentals*, 4th Edition, McGraw-Hill, New York, USA, 2005.
2. Krishnan, R., *Electric Motor Drives — Modeling Analysis and Control*, PHI Learning Private Limited, New Delhi, 2010.

3. Racz, I., "Dynamic behaviour of inverter controlled induction motors," *IFAC Conference Records*, 4B1–4B7, 1965.
4. Holtz, J., "The representation of ac machine dynamics by complex signal flow graphs," *IEEE Trans. on Ind. Elec.*, Vol. 42, No. 3, 263–271, 1995.
5. Roy, T., S. Ghosh, and J. K. Bhattacharjee, "Perturbation theory for Maxwell's equations with a time-dependent current source," *EPJ Plus*, Vol. 126, No. 12, 119, 2011.
6. Takahashi, I. and T. Noguchi, "A new quick response and high efficiency control strategy of an induction motor," *IEEE Trans. on Ind. Appl.*, Vol. 22, No. 5, 820–827, 1986.

The Stripline Structure with Multilayer Dielectrics by FDTD

Ellen Yoshie Sudo Lutif[1,2], **Alberto José de Faro Orlando**[1], **and Antonio Carlos da Cunha Migliano**[1,2]

[1]Aerospace Technological Institute (ITA), CTA, Brazil
[2]Advanced Study Institute (IEAv), CTA, Brazil

Abstract— The past few years have seen tremendous progress in solid state devices used for microwave applications. Many different materials are used to construct microwave components such as transmission lines, filters, capacitors, inductors, and many others. To properly design these microwave components, it is important to know the characteristics of the materials used in fabricating the circuit are very important as any anomalies result in degradation of electrical performance. Characterization of materials at microwave frequencies generally requires finding the properties, which described both conductor and dielectric materials. Conductor materials are described by their conductivity; dielectric materials may be described by their complex permittivity. Full-wave analysis of stripline planar structure with vertical interconnects in multilayer dielectric media is presented. The use of FDTD method for the description of the electromagnetic behavior of the cell discontinuities in the analysis of the S-parameters, input and output impedance and potency at the feeding ports, permits in the 0 GHz–20 GHz frequency band the achievement of a good precision for the results on materials with low electromagnetic characteristics ($\varepsilon \leq 10$). The r results show that changes in the permittivity could lead to significant changes in the overall performance of the designed circuit.

1. INTRODUCTION

The modeling of microstrip in multilayer dielectrics (or dielectric media) has been thoroughly investigated in the past, and several methods have already been introduced. The research has been based on various methods such as Finite Elements (FE), Finite Difference Time Domain (FDTD) and Method of Moments (MoM) [1, 2]. The later is the most widely employed for the modeling of planar geometries, mainly due to the fact that it does not require the meshing of the whole volume of the structure. Several methods can be found in the literature for the analysis of multilayer microstrip topologies, either for shielded [3–8] or unshielded structures [9–13]. Moreover, some methodologies have been proposed to take into account the vertical interconnects between planar structures [11, 12]. However, to the authors knowledge literature is very thin on topics regarding the modeling of planar multilayer geometries with vertical interconnects in a stripline structure. As this kind of technology profile is becoming more and more popular with the development of Radio Frequency (RF) modules implemented in materials such as Low Temperature Co-fired Ceramic (LTCC), Bismaleimide-triazine (BT) resin and other organic multilayer laminates, a robust and efficient method for the analysis of such structure becomes imperative.

2. THEORY

2.1. Stripline Design

Typical striplines are constructed to have an impedance of either 50 Ω or 90 Ω. The ratio between the width of the active conductor and the height of the active conductor above the ground plane determines the characteristic impedance. The designe given in this paper is focused on the 50 Ω stripline. Thereby, the most critical parameters that directly determine the physical design of the stripline are impedance matching at feed port (S_{11} parameter) and transmission between two ports (S_{21} parameter). All simulations presented in this paper are made with FDTD.

To compare the simulations are used Nicolson-Ross-Weir (NRW) algorithm. Nicolson and Ross [14] and Weir [15] combined the S parameters, and derived explicit formulas for the calculation of permittivity and permeability. The algorithm is usually called Nicolson-Ross-Weir (NRW) algorithm.

In the NRW algorithm, the reflection and transmission are expressed by the scattering parameters S_{11} and S_{21}. The reflection coefficient Γ is given by

$$\Gamma = K \pm \sqrt{K^2 - 1} \tag{1}$$

with

$$K = \frac{\left(S_{11}^2 - S_{21}^2\right) + 1}{2S_{11}} \tag{2}$$

The correct choice of positive or negative sign in Eq. (1) is made by requiring $|\Gamma| \leq 1$. And the output impedance is given above

$$Z = Z_0 \frac{1+\Gamma}{1-\Gamma}. \tag{3}$$

2.2. FDTD Simulations

FDTD is used to solve Maxwell's equations for arbitrary model spaces. Indeed, FDTD is a direct time-domain solution to Maxwell's curl equations [16]. The continuous-time expressions of Maxwell's equations for linear, isotropic, non-dispersive materials which will be discretized in XFDTD are:

$$\frac{\partial \bar{E}}{\partial t} = \frac{1}{\varepsilon}\nabla \times \bar{H} - \frac{1}{\varepsilon}\left(\overline{J_{source}} + \sigma \bar{E}\right) \tag{4}$$

$$\frac{\partial \bar{H}}{\partial t} = -\frac{1}{\mu}\nabla \times \bar{E} - \frac{1}{\mu}\left(\overline{m_{source}} + \sigma \bar{H}\right) \tag{5}$$

where μ represents the magnetic permeability and σ represents the magnetic conductivity.

The two curl Equations (4) and (5) can be discretized to obtain a total field FDTD technique. Alternately the fields can be expressed as:

$$E = E^{total} \equiv E^{incident} + E^{scattered} \tag{6}$$

$$H = H^{total} \equiv H^{incident} + H^{scattered} \tag{7}$$

The rationale for the separate field approach is that the incident field components can be specified analytically throughout the problem space while the scattered fields are found computationally and only the scattered fields need to be absorbed at the problem space outer boundaries. This last feature is an important one. The scattered fields, emanating from a scattering or interaction object, can be more readily absorbed than a total field by an outer radiation boundary condition applied at the problem space extremities or faces. This is especially important in situation where FDTD simulation and center conductor was excited for a source of radio frequency of 1 Volt operating in scale from 0 GHz to 20 GHz. The objective of this work is analyzing the electromagnetic sensibility, input in which the scattered fields are desired and are of much lower amplitude than the total fields.

3. RESULTS

Relative complex permittivity (permittivity) of printed circuit (PC) board and substrate material is a critical parameter that affects circuit performance. Characterizing this parameter at RF is

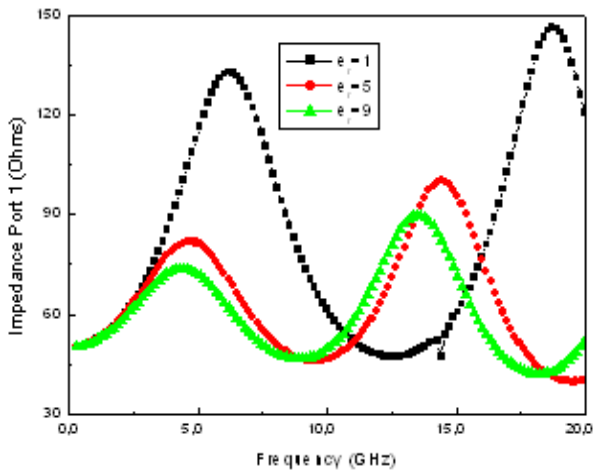

Figure 1: Impedance port 1 as a function of frequency.

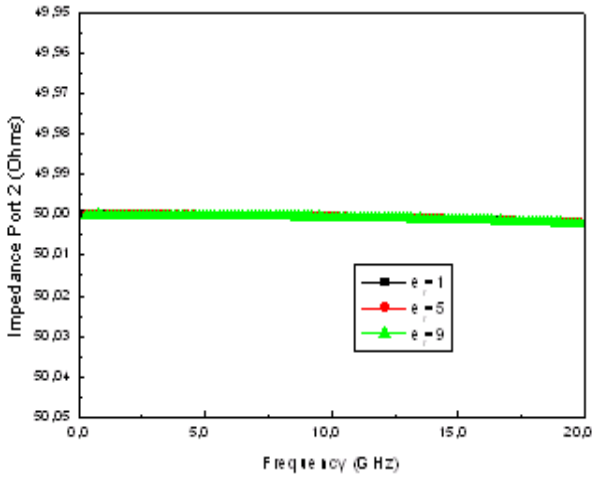

Figure 2: Impedance port 2 as a function of frequency.

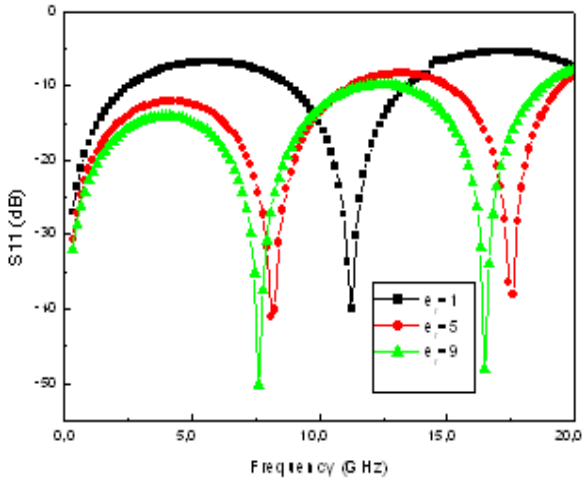

Figure 3: Transmission coefficient modulus.

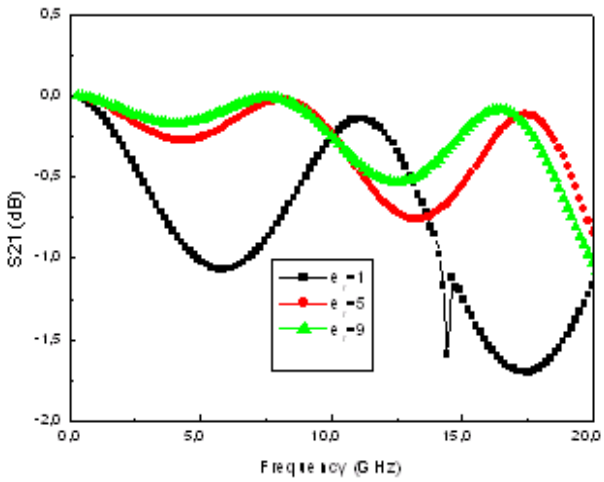

Figure 4: Reflection coefficient modulus.

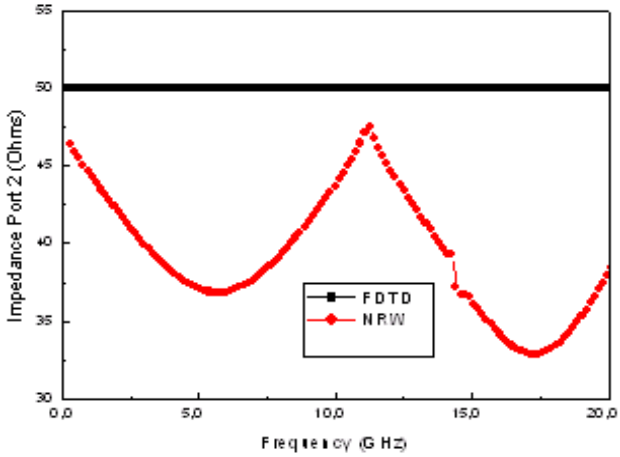

Figure 5: Comparison between NRW Algorithm and FDTD simulations for output impedance.

becoming more important because of increased clock frequencies used in today's high speed computers. In addition, performance of dielectric materials at RF is equally important for wireless communication circuits and components.

The results show the comparisons of three simulated results for the S parameters of the transmission line, input and output impedance for three different dielectric constants of the layers.

The sample port with those dimensions assures a perfect matching with 50 Ohms in the frequency of 0 GHz until 20 GHz, according Figure 2.

We can see in the Figure 3 that work area changes a lot with different magnetic materials. The electromagnetic sensibility is related with low reflection smaller than -10 dB and transmission near than 0 dB. $\varepsilon_r = 9$ showed the largest area of work of 0 GHz until 20 GHz and better electromagnetic sensibility, according Figures 3 and 4. On the other hand $\varepsilon_r = 1$ has the work area between 9 GHz and 12 GHz, and $\varepsilon_r = 5$ has two picks of transmission from 0 GHz until 10 GHz, 15 GHz until 18 GHz.

In the Figure 5 is shown that the FDTD simulations are according to the NRW algorithm.

4. CONCLUSION

Using stripline resonators for material characterization is often the most appropriate technique to use at microwave frequencies. This is the case for substrate materials used to construct microwave planar circuits. The stripline resonator configuration is favored over the others because of its simple configuration as well as it involves the fewest approximation in its analysis. This work analyzed general phenomena of the reflection and transmission as a function of frequency taken placed by a

general PCB stripline structure. The exact numerical value for the stripline and the spatial range of the electric field can be changed with any variation of the stripline frequency. The simulations show sensitivity with changes in the dielectric materials. Therefore, one must be input the specific numerical values for all variables above for FDTD simulation to obtain quantitative values for the frequency and fields of interest.

The sample holder with $\varepsilon_r = 9$ and ratio $wh = 1.1$ it showed to be a good option to do characterization of dielectric materials due to excellent electromagnetic sensibility in the scale 0 GHz to 10 GHz.

ACKNOWLEDGMENT

The authors wish to thank the laboratory of electromagnetic systems at Advanced Study Institute for infrastructure offered. And, they wish to thank Microwave Departament at Aerospace Technological Institute for the realization of this work.

REFERENCES

1. Itoh, T., *Numerical Techniques for Microwave and Millimeter Wave Passive Structures*, Wiley, New York, 1989.
2. Harrington, R. F., *Field Computations by Moment Method*, Macmilla, New York, 1968.
3. Rautio, J. C. and R. F. Harrington, "An electromagnetic time harmonic analysis of shielded microstrip circuits," *IEEE Transactions on Microwave Theory and Techniques*, Vol. 35, No. 8, 726–730, 1987.
4. Dunleavy, L. P. and P. B. Katehi, "A generalized method for analyzing shielded thin microstrip discontinuities," *IEEE Transactions on Microwave Theory and Techniques*, Vol. 36, No. 12, 1758–1766, 1988.
5. Hill, A. and V. K. Tripathi, "An efficient algorithm for the three-dimensional analysis of passive microstrip components and discontinuities for microwave and millimeter-wave integrated circuits," *IEEE Transactions on Microwave Theory and Techniques*, Vol. 39, No. 1, 83–91, 1991.
6. Eleftheriades, G. V. and R. F. Mosig, "On the network characterization of planar passive circuits using the method of moments," *IEEE Transactions on Microwave Theory and Techniques*, Vol. 44, No. 3, 438–445, 1996.
7. Khalil, A. I., A. B. Yakovlev, and M. B. Steer, "Efficient method-of-moments formulation for the modeling of planar conductive layers in a shielded guided-wave structure," *IEEE Transactions on Microwave Theory and Techniques*, Vol. 47, No. 9, 1730–1736, 1999.
8. Pereira Filho, O. M. C. and T. K. Sarkar, "Full-wave analysis of MICs in multilayer dielectric media in a rectangular waveguide," *IEEE Transactions on Microwave Theory and Techniques*, Vol. 48, No. 10, 1611–1622, 2000.
9. Mosig, J. R., "Arbitrary shaped microstrip structures and their analysis with a mixed potential integral equation," *IEEE Transactions on Microwave Theory and Techniques*, Vol. 36, No. 2, 314–323, 1988.
10. Harokopus, J. R. and P. B. Katehi, "An accurate characterization of open microstrip discontinuity including radiation losses," *IEEE MTT-S Int. Microwave Symp. Dig.*, 231–234, 1989.
11. Becks, T. and I. Wolff, "Analysis of 3-D metallization structures by a full wave spectral domain technique," *IEEE Transactions on Microwave Theory and Techniques*, Vol. 40, No. 12, 2219–2227, 1992.
12. Kinayman, N. and M. I. Aksun, "Efficient use of closed-form Green's functions for the analysis of planar geometries with vertical interconnections," *IEEE Transactions on Microwave Theory and Techniques*, Vol. 45, No. 5, 593–603, 1997.
13. Ling, F., J. Liu, and J. M. Jin, "Efficient electromagnetic modeling of three-dimensional multilayer microstrip antennas and circuits," *IEEE Transactions on Microwave Theory and Techniques*, Vol. 50, No. 6, 1628–1635, 2002.
14. Nicolson, A. M. and G. F. Ross, "Measurement of the intrinsic properties of materials by time domain techniques," *IEEE Transactions on Instrumentation and Measurement*, Vol. 19, No. 4, 377–382, 1970.
15. Weir, W. B., "Automatic measurement of complex dielectric constant and permeability at microwave frequencies," *Proceedings of the IEEE*, Vol. 62, No. 1, 33–36, 1974.
16. Jackson, J. D., *Classical Electrodynamics*, John Wiley & Sons, Inc., New York, 1999.

Simultaneous Joint Inversion of Refraction Tomography and Magnetic Data

M. De Stefano
WesternGeco GeoSolutions, Integrated EM Center of Excellence, Milan, Italy

Abstract— I describe initial results of on-going research on a magnetic inversion algorithm exploiting a novel positivity constraint and a nonlinear conjugate gradients (NLCG) algorithm for the optimization. The inversion unknown is the magnetization amplitude and not the susceptibility directly. The positivity constraint is a double-limiting quasi-linear function that allows performing a constrained optimization with an unconstrained minimization algorithm. I propose also an effective way to integrate magnetic data with refraction tomography data through simultaneous joint inversion (SJI) using a cross-gradients relation. The approach to SJI that I present minimizes, in the least-squares sense, a joint objective function that is the weighted sum of the so-called "single-domain" objective functions and the objective function of a "structural link", which relates unknowns belonging to two different model domains. The structural link is imposed through the requirement to minimize the local cross product of model gradients. This corresponds to requiring parallel gradients in the same spatial positions: because gradients are always perpendicular to shape boundaries, minimizing the cross-gradients link imposes the same shapes at the same spatial positions. Furthermore, the cross-gradients relation, and, in general, any link relation, is evaluated at specific spatial positions without requiring the velocity and the magnetization domains to be sampled on the same grid or model mesh. The benefits of using SJI with respect to separate, single-domain inversions are demonstrated through a synthetic example. As for the case of simultaneous joint inversion of seismic and gravity or seismic and magnetotelluric (MT) data, a seismic-magnetic SJI is effective for complex imaging problems, such as regions with volcanic intrusions or faults. SJI is, in general, able to compensate for poor-quality seismic illumination using another measurement. In this paper, I also discuss possible improvements to the current implementation of the algorithm: for instance, the current magnetic inversion algorithm does not yet take into account remanent magnetization. This limits at the moment its applicability to regions where remanent magnetization is very small or absent.

1. INTRODUCTION

Potential field methods were among the first techniques used for geophysical exploration. To mention an example, a 1926 oil discovery in Garza Country, Texas, was the result of the interpretation of magnetic data [6]. Strong research efforts were made in the past century to produce magnetometers, each time more precise and easy to use. Victor Vacquier developed an airborne fluxgate magnetometer that was extremely valuable in exploration and was widely used throughout World War II for submarine detection. Further developments to be mentioned are the 1955 proton-precession magnetometer and the 1960s optically pumped alkali-vapor magnetometers.

As a consequence of the Green's third identity, magnetic data inversions suffer from high non-uniqueness [3]. Geophysically interesting results can be achieved only using proper weighting and regularization [7].

In recent years, widespread interest in data measurement integration has brought new value to gravity and magnetic methods, particularly in simultaneous joint inversion (SJI) applications. For example, in [4] it is demonstrated that a seismic-gravity SJI can improve complex imaging configurations involving dyke-like structures. Another example is [13], where the technology is applied to real data sets, showing how gravity can improve thrust-belt and sub-basalt imaging. Within the scope of SJI, magnetic inversion may be used in the same way as gravity to improve seismic imaging where seismic coverage or illumination is poor.

In the following, I present the preliminary results of an ongoing research on integration of the magnetic inversion into SJI.

I propose an approach to the magnetic inversion problem, highlighting the differences with other existing methods. I also show an application of magnetics-refraction tomography SJI on synthetic data. Final results are encouraging, as they prove that a magnetics-refraction tomography SJI can produce final models where the benefits of every single-domain inversion are merged, with a resulting better characterization of the earth's subsurface.

2. METHOD

Total field magnetic acquisition records the amplitude of the magnetic vector for each measurement position. Even if anomalous magnetization patterns in the subsurface actually modify the direction of the theoretical geomagnetic field, it is reasonable to assume that the instruments detected only the amplitude along the direction of the Earth field [3]. For this reason, our forward computations model only the component along the direction of the Earth field. If we also assume the absence of any remanent magnetization [7], subsurface magnetization is completely induced by the geomagnetic field. Furthermore, neglecting anisotropy, induced magnetization is parallel to the inducing field and we can write

$$\mathbf{M} = \frac{\chi}{\mu_0 (1+\chi)} \mathbf{B}_0 \tag{1}$$

where χ is the scalar susceptibility, $\mu_0 = 4\pi \cdot 10^{-7}$ H/m is the magnetic permeability of free space, $\mathbf{B}_0$ is the inducing magnetic field and $\mathbf{M}$ is the induced magnetization.

Forward modeling is carried out dividing the subsurface into right rectangular prisms with constant magnetization. The total field anomaly is then computed exploiting the superposition principle. The Green's function of the magnetic response caused by a right rectangular prism can be conceptually expressed as

$$\xi(\mathbf{p}) = \frac{\mu_0}{4\pi} \int_V \frac{[(3\hat{\mathbf{m}} \cdot \hat{\mathbf{r}})\,\hat{\mathbf{r}} - \hat{\mathbf{m}}] \cdot \hat{\mathbf{b}}}{r^3} dv \tag{2}$$

where $\mathbf{p}$ is the vector identifying the measurement position, r is the scalar distance between the volumetric element dv and the position $\mathbf{p}$, $\hat{\mathbf{r}}$ is a versor oriented from dv towards $\mathbf{p}$, $\hat{\mathbf{m}}$ is the magnetization versor and $\hat{\mathbf{b}}$ is the geomagnetic versor at the measurement position $\mathbf{p}$. V is the volume occupied by the prism. The integral in Equation (2) has a closed-form solution ([2, 11]).

The relation between the magnetic anomaly B_i on the measurement position i and the magnetization M_j caused by cell j is linear

$$B_i = \xi_{ij}(\mathbf{p}_j) M_j \tag{3}$$

and ξ_{ij} is the (i, j) element of the Jacobian of the magnetic forward problem.

The approach for the single-domain magnetic inversion is that of [7], with three main differences on the model parametrization, the adopted positivity constraint, and the chosen solver algorithm.

The model parametrization is in terms of the 3D magnetization function m and not of the susceptibility directly. Susceptibility is recovered from the output magnetization model through the inverse of Equation (1). This choice was driven by the linearity of the relation between magnetization and magnetic anomaly (Equation (3)). For this reason, the objective function we minimize is

$$\Phi(m) = |\mathbf{W}_d (\mathbf{g}(m) - \mathbf{d})|^2 + \int_V \Gamma(m - m_{\text{pri}}) dv \tag{4}$$

where $\mathbf{g}(m)$ is the vectorial function of the 3D magnetization used to perform forward modeling, $\mathbf{W}_d$ is a diagonal matrix of data weights, $\mathbf{d}$ is the vector of observed data, m_{pri} is an a-priori model function, and Γ is the same regularization function used by [7]:

$$\begin{aligned} &\Gamma(m - m_{\text{pri}}) \\ &= \alpha_s \{w[m - m_{\text{pri}}]\}^2 + \alpha_x \left\{\frac{\partial w[m - m_{\text{pri}}]}{\partial x}\right\}^2 + \alpha_y \left\{\frac{\partial w[m - m_{\text{pri}}]}{\partial y}\right\}^2 + \alpha_z \left\{\frac{\partial w[m - m_{\text{pri}}]}{\partial z}\right\}^2 \end{aligned} \tag{5}$$

where α_s, α_x, α_y and α_z are coefficients that affect the relative importance of different components in the regularization function; w is a weighting function, dependent on forward sensitivity, that counterbalances the magnetic field decay. Its expression is [9]

$$w = \left\| \frac{d\mathbf{g}}{dm} \right\|_2 \tag{6}$$

The second difference with the approach in [7] is the chosen positivity constraint. I use a double-limiting quasi-linear function (Figure 1). The limiting function has a central, perfectly linear, region

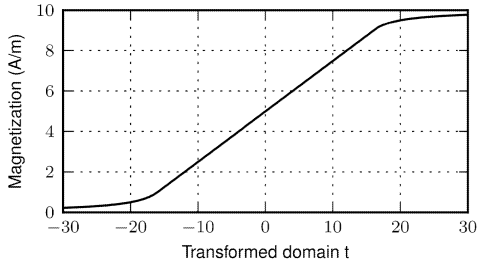

Figure 1: A double-bounded limiting function. For a transformed domain t that spans the interval $(-\infty, +\infty)$, the model domain spans the interval $(0, 10)$ A/m.

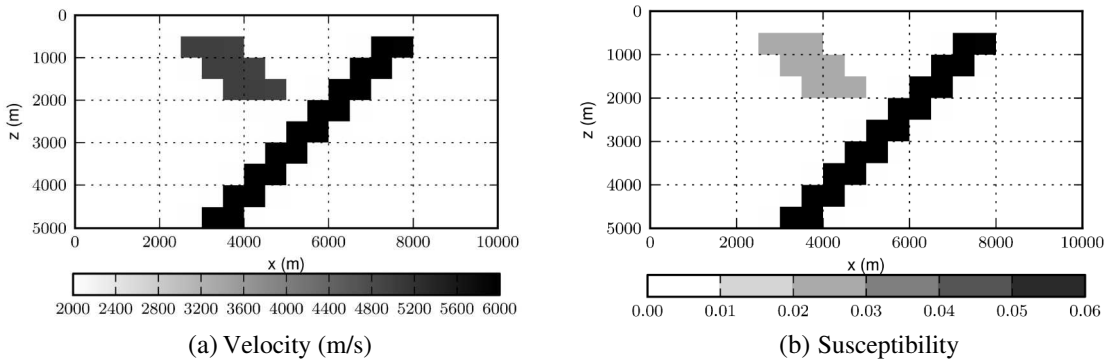

(a) Velocity (m/s) (b) Susceptibility

Figure 2: Cross section (at $y = 5000$ m) of the synthetic models. The velocities of the two dykes are 5000 m/s and 6000 m/s. The background velocity is 2000 m/s. The susceptibilities of the two dykes are 0.02 and 0.06. The background susceptibility is 0.

with hyperbolic end branches. Setting $m = f(t)$, where m is the magnetization variable, t is the unknown in the transformed domain, and f is the limiting function of Figure 1, the inverse problem is then solved into the transformed domain. The solution at convergence is finally back-converted to the magnetization domain again through the function of Figure 1.

The third difference is in the solver. For inversion of magnetic data, a linear solver is sufficient because the problem is linearizable even in presence of a limiting function. On the other hand, the magnetic inversion is integrated into existing SJI software [4] and the solver, an implementation of the nonlinear conjugate gradients (NLCG) algorithm [12], is the same as that used by SJI. The nonlinear solver gives SJI the flexibility to work both with linear and nonlinear or not easily linearizable domains [4].

A two-domain SJI can be expressed as [4]

$$\Phi_{\mathrm{SJI}}(\mathbf{m}) = \alpha_1 \Phi_1(m_1) + \alpha_2 \Phi_2(m_2) + \beta \int_U \Psi(\mathbf{m}) dv \tag{7}$$

where, $\mathbf{m}$ is a vector containing the model functions m_1 and m_2, Φ_1 is, for example, the objective function of the magnetic inversion, and Φ_2 is the objective function of another inversion domain (or vice-versa); $\alpha_{1,2}$ and β are the user-defined relative weights of the two domains and of the link; Ψ is a link function between the two domains that is active only in the user-defined spatial region U, which contains values for the two model domains.

The link between magnetics and other domains is imposed through the cross-gradients constraint [5] for Ψ

$$\Psi(m_1, m_2) = |\nabla m_1 \times \nabla m_2|^2 \tag{8}$$

This function requires parallelism between model gradients. It is well known that gradients are perpendicular to the edges of the objects [10]. The consequence is that the cross-gradients constraint forces the output models to recover the same shapes in the same spatial positions.

The implementation of magnetics and SJI is parallel, based on the message passing interface (MPI). All the underlying linear algebra is performed by the *Portable Extensible Toolkit for Scientific Computations* (PETSc) [1]. Very good scalability with large amounts of data, in a high-performance computing environment is achieved thanks to the use of this library.

3. A SYNTHETIC EXAMPLE

I present results from simulations on 3D synthetic magnetization and velocity models that are very similar to the dipping dykes example in [8]. Cross sections of these synthetic models are shown in Figure 2.

For the seismic domain, we simulate first-arrival times from 16 sources to 64 receivers whose configuration is shown in Figure 3. We add a zero-mean, random, white Gaussian noise with a 10 ms standard deviation to each data sample. Velocity and susceptibility have the same sampling, with 20 cells along x, 20 along y, and 10 along z.

For the magnetic domain, we assume that the geomagnetic field is 50000 nT and has an inclination of 44 degrees and declination of 25 degrees. Measurements are simulated on the surface at 441 evenly spaced stations, with a station interval of 500 m in both directions. We add a zero-mean, random, white Gaussian noise with a 10 nT standard deviation to each data sample.

The initial seismic model is a vertical velocity gradient spanning the interval (2500 m/s, 5500 m/s). The initial magnetic model is a uniform volume with 0 susceptibility.

Figure 4 shows the single-domain inverted models. Refraction tomography is able to properly

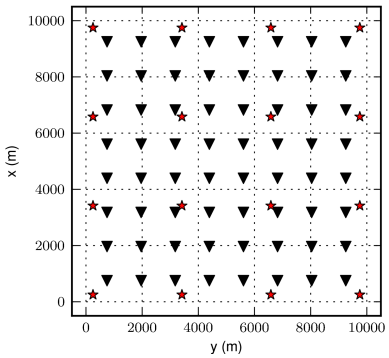

Figure 3: Configuration of sources (stars) and receivers (triangles) for the seismic simulation.

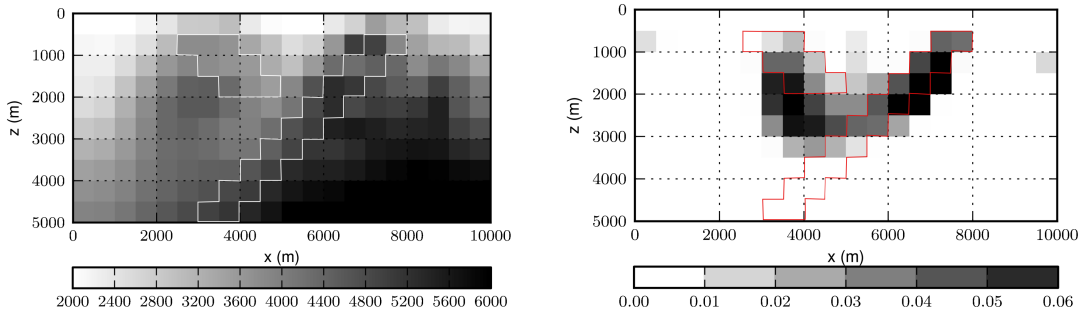

(a) Velocity (m/s) (b) Susceptibility

Figure 4: Cross section (at $y = 5000$ m) of the single-domain inverted models. The outlines show the true position of the dykes.

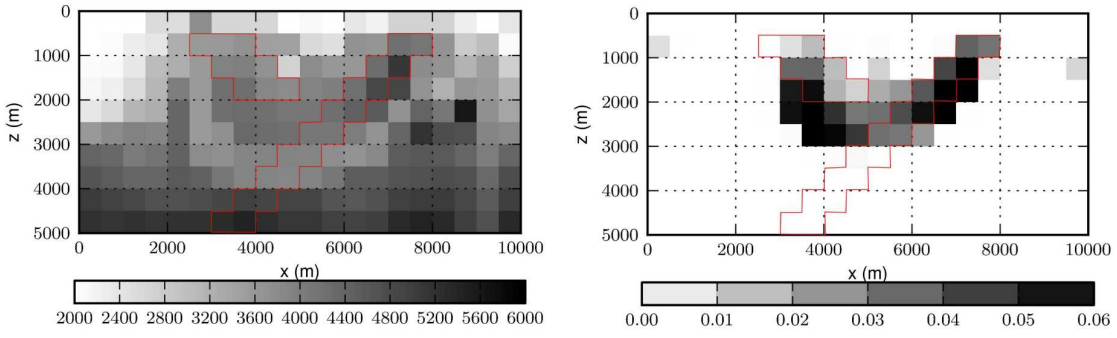

(a) Velocity (m/s) (b) Susceptibility

Figure 5: Cross section (at $y = 5000$ m) of the SJI-inverted models. The outlines show the true position of the dykes.

recover the top of the two dykes, but not their bottom. On the other hand, the magnetic output is more focused, and progressively looses resolution with increasing depth. This is a well-known problem of all potential field methods.

Figure 5 shows the SJI-inverted models with the cross-gradients link. In the velocity domain, the shapes of the dykes are more focused than in Figure 4(a). Furthermore, the high-velocity zone that was present in the lower right part of Figure 4(a) has disappeared in Figure 5(a). In the magnetic domain, the good resolution we saw in Figure 5(b) is basically maintained.

4. CONCLUSION

I described an implementation of the magnetic inversion incorporating a novel positivity constraint and a nonlinear algorithm for the optimization. Susceptibility is indirectly computed after magnetization inversion.

I showed an effective approach for integration of magnetic data with refraction tomography data: the simultaneous joint inversion with the cross-gradients constraint.

The benefits of using SJI with respect to separate, single-domain inversions were demonstrated through application to synthetic data. The synthetic results revealed an improvement in the image focusing brought by the cross-gradients link.

The research on SJI is ongoing. Other SJI combinations still must be tried. Possible examples are magnetics and gravity or full-tensor gradiometry, magnetics plus reflection tomography, magnetics plus magnetotellurics or magnetics plus surface-wave inversion.

ACKNOWLEDGMENT

I thank WesternGeco for authorization to publish this paper. Many thanks also to all my colleagues of the WesternGeco Milan Integrated EM Center of Excellence. PETSc developers Satish Balay, Matthew Knepley, Barry Smith, Hong Zhang, Jed Brown, and Lisandro Dalcin are thanked for their continuous and prompt support.

REFERENCES

1. Balay, S., W. D. Gropp, L. C. McInnes, and B. F. Smith, "Efficient management of parallelism in object oriented numerical software libraries," *Modern Software Tools in Scientific Computing*, E. Arge, A. M. Bruaset and H. P. Langtangen, Eds., 163–202, Birkhäuser Press, 1997.
2. Bhattacharyya, B. K., "Magnetic anomalies due to prism-shaped bodies with arbitrary polarization," *Geophysics*, Vol. 29, No. 4, 517–531, 1964.
3. Blakely, R. J., *Potential Theory in Gravity and Magnetic Applications*, Cambridge University Press, 1996.
4. De Stefano, M., F. Golfré Andreasi, S. Re, M. Virgilio, and F. F. Snyder, "Multiple-domain, simultaneous joint inversion of geophysical data with application to subsalt imaging," *Geophysics*, Vol. 76, No. 3, R69–R80, 2011.
5. Gallardo, L. A. and M. A. Meju, "Joint two-dimensional DC resistivity and seismic travel time inversion with cross-gradients constraints," Vol. 109, *Journal of Geophysical Research*, American Geophysical Union, 2004.
6. Gibson, R. I. and P. S. Millegan, *Geologic Applications of Gravity and Magnetics: Case Histories (SEG and AAPG)*, Vol. 8, No. 43, SEG Geophysical References, 1998.
7. Li, Y. and D. W. Oldenburg, "3-D inversion of magnetic data," *Geophysics*, Vol. 61, No. 2, 394–408, 1996.
8. Li Y. and D. W. Oldenburg, "3-D inversion of gravity data," *Geophysics*, Vol. 63, No. 1, 109–119, 1998.
9. Li, Y. and D. W. Oldenburg, "Joint inversion of surface and three-component borehole magnetic data," *Geophysics*, Vol. 65, No. 2, 540–552, 2000.
10. Pratt, W. K., *Digital Image Processing*, 2nd Edition, John Wiley & Sons, 1991.
11. Rao, D. B. and N. R. Babu, "A rapid method for three-dimensional modeling of magnetic anomalies," *Geophysics*, Vol. 56, No. 11, 1729–1737, 1991.
12. Teukolsky, S. A., W. T. Vetterling, and B. P. Flannery, *Numerical Recipes — The Art of Scientific Computing*, William H. Press, 2007.
13. Virgilio, M., S. Hallinan, and M. Mantovani, "Simultaneous joint inversion of electromagnetic, gravity and seismic data for thrust belt and sub-basalt imaging," *10th Simposio Bolivariano, Extended Abstracts*, EAGE, 2009.

Data-driving Algorithms for 3D Reconstruction from Ladar Data

Gerard Berginc[1], **Ion Berechet**[2], **and Stefan Berechet**[2]

[1]Thales Optronique S.A., 2 Avenue Gay Lussac, Elancourt Cedex 78995, France
[2]SISPIA SARL, 18 Allée Henri Dunant, Vincennes 94300, France

Abstract— There is a considerable interest in the development of new optical imaging systems that are able to give three-dimensional images. In this paper, we present some considerations concerning the field of three-dimensional laser images where significant technological advances have encouraged research over the past decade. Potential applications range across medical imaging, surveillance and robotic vision. Identifying targets or objects concealed by foliage or camouflage is a critical requirement for operations in public safety, law enforcement and defense.

1. INTRODUCTION

Laser radar (Ladar) technology has enjoyed significant advances over the past decade. Novel focal plane areas, compact laser illuminators and advanced signal processing have enabled the construction of low power 2-D and 3-D laser imagery systems. The applications of such systems range from surveillance, targeting and weapons guidance to target identification. Synthetic images of three-dimensional objects are based on extraction of laser backscattered signals [1]. The principle of 3D laser radar is based on the use of movable light sources and detectors to collect information on laser scattering, and to reconstruct the 3D object. 3D reconstruction algorithm is a major component in these optical systems for identification of camouflaged objects. But 3D reconstruction must take into account sparse collected data, i.e., concealed objects and reconstruction algorithms must solve a complex multi-parameter inverse problem. Therefore the inverse problem of recovering the surface three-dimensional shape function from intensity data is more challenging [2, 3]. The robustness of identification of three-dimensional reconstructed images is directly related to the inversion algorithms used in the process of identification. From a mathematical point of view, the technique breaks down into two steps: direct measurement, optionally processed using a model of the physical phenomena which are measured or in our case measured data, and then reconstruction by inversion on the basis of these direct measures. Artifacts from the reconstruction algorithms degrade the quality of identification and the object recognition. A notable limitation of numerous methods is that inversion algorithms produce sparse, blurred and noisy three-dimensional images. Therefore, the strategy of inversion must be optimized.

The objective of our paper is to present a new data-driving algorithmic approach for the generation of 3D surface data from sparse 3D point clouds corresponding to the reconstruction algorithm. The role of this type of algorithmic data-driving process is to complete the missing parts of the 3D image at satisfactory levels for reliable identification of concealed objects. In this paper, we present different examples of reconstruction and completion of three-dimensional images. The data used in this paper come from simulations [4–6] that are based on the calculation of the laser interactions with the different interfaces of the scene of interest. Common identification algorithms use reference databases therefore identification of unknown objects which are not included in the knowledge database of objects becomes difficult.

2. DATA-DRIVING ALGORITHMS FOR 3D RECONSTRUCTION BASED ON 3D POINT CLOUDS ENERGY

In this section, a simulated scene reconstruction is achieved to evaluate our data-driving algorithm. We simulate a complete scene containing a hidden vehicle behind a canopy. The modeling (Fig. 1) includes the physical structure of the environment, the transfer of radiation through the environment, and the interaction of the laser wave with the structure of the different elements of the scene. The results of our models have been validated against real data for a range of sensor systems [4–6]. These models incorporate a detailed understanding of the interaction of the electromagnetic wave. We may obtain the three-dimensional reconstruction by a cone-beam algorithm [2, 4–6], which is a convolution back-projection algorithm deduced from the Radon transform. This algorithm uses a set of two-dimensional projections which contain the data collected by the pixels of a focal plane area. These data are related to the intensity backscattered by the scene illuminated by a laser

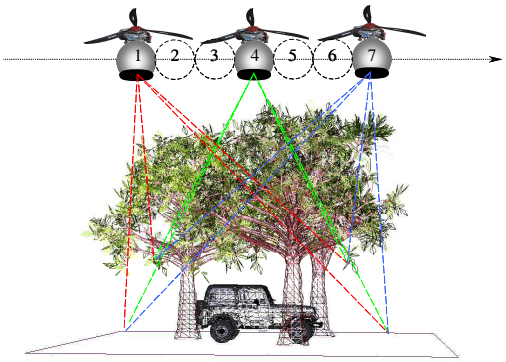

Figure 1: The vehicle is hidden under foliage and the Ladar system, mounted on a moving platform for a air-to-ground scenario collects a set of 3D laser images of the scene from several aspects.

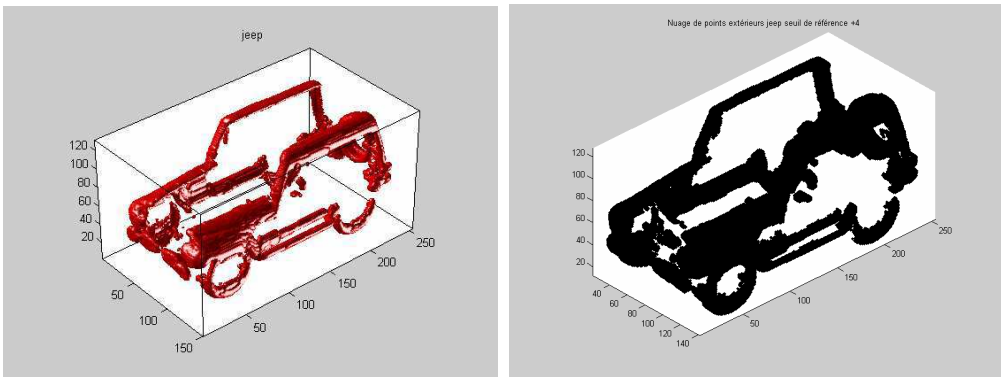

(a) (b)

Figure 2: Example of sparse 3D reconstruction: (a) isodensity and (b) 3D point clouds.

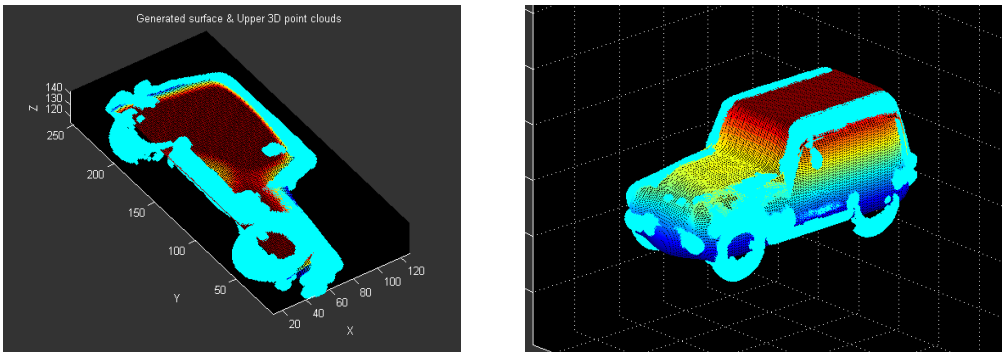

(a) (b)

Figure 3: Generated 3D surfaces in sparse 3D point clouds using 3D Data driving algorithms: (a) lateral side of vehicle, and (b) complete vehicle.

pulse. The scene is flood-illuminated with a single laser pulse (1540 nm), the eye-safe property of wavelengths around 1500 nm is perfectly suited to active laser imagery applications.

A lateral view of the scene is presented in Fig. 1. A 3D laser image is then reconstructed (Fig. 2). A vehicle of interest is viewed through a dense scattering medium, in our case a mass of foliage. Since the foliage blocks almost all the laser pulse to the target, the 3D points on the target surface are sparse. The 3D reconstruction presents some incomplete areas in the 3D point cloud. Therefore it may be difficult for observers to recognize objects from a point cloud and we must enhance visual exploitation of 3D imaging Ladar data.

The implementation of a data-driving algorithmic process [1, 2] can help to fill data in the incomplete areas and generate the object surface. This algorithmic process is based on partition

of initial incomplete point clouds in significant areas by integration of cloud minimum energy, completion of incomplete significant areas and surface generation using an MLP approach with sensibility calculation for higher capacity of generalization and fusion of partially generated surfaces. The results of this data-driving algorithmic process are not dependent on other external elements only the incomplete three-dimensional point clouds being used (Figs. 3 and 4).

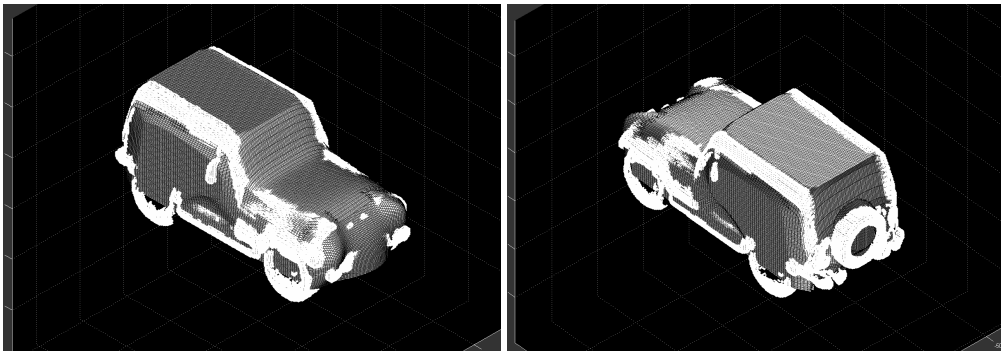

(a) (b)

Figure 4: Surfaces rendering using 3D Data driving algorithms: (a) vehicle front view, and (b) vehicle back view.

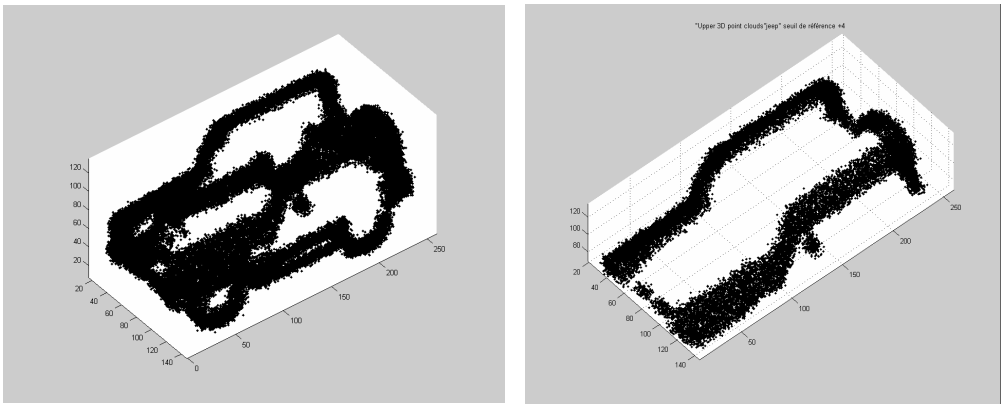

(a) (b)

Figure 5: Reconstructed 3D point clouds in turbulence: (a) complete vehicle, and (b) vehicle upper side.

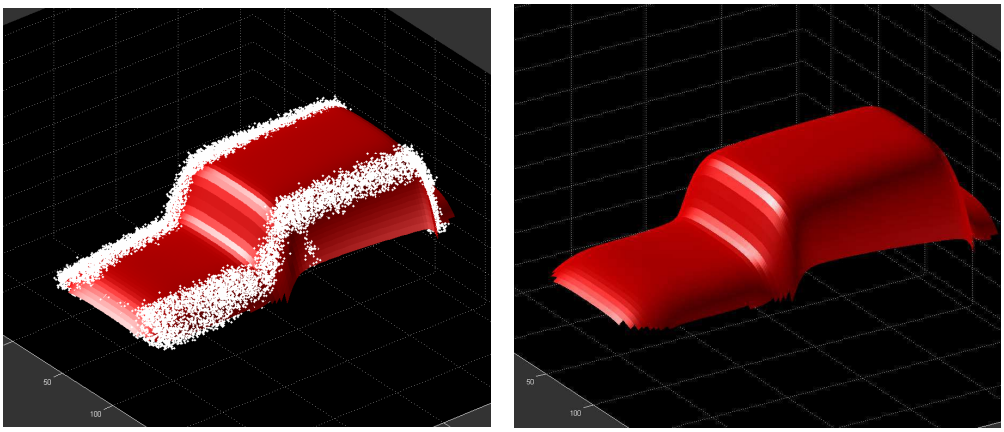

(a) (b)

Figure 6: Generated 3D surfaces with Gaussian noise for the upper side of the vehicle: (a) generated surfaces and reconstructed point clouds, (b) generated surfaces.

3. NOISE IMPACT ON 3D RECONSTRUCTION USING DATA-DRIVING ALGORITHMS

We have analyzed the 3D reconstruction with added Gaussian noise defined by its standard deviation σ. This Gaussian noise is an approximation of the different noises we can encounter in the Ladar system (speckle, detector noise). We can notice that the reconstruction algorithm is robust and gives well-defined generated surfaces (Figs. 5 and 6).

4. CONCLUSIONS

We have demonstrated new algorithmic approaches to enhance visual exploitation of 3D imaging Ladar data. We have tested the robustness of the algorithm in cases of noisy scenarios. With these reconstruction procedures, we can separate objects from foliage and reconstruct a three-dimensional image of the considered object.

ACKNOWLEDGMENT

This work is sponsored by the French Ministry of Economy, Industry and Employment (Directorate General of Competitiveness, Industry and Services). This project is part of program RAPID implemented by French Directorate General of Armament.

REFERENCES

1. Berginc, G., I. Berechet, and S. Berechet, "Method for three-dimensional synthetic reconstruction of objects exposed to an electromagnetic and/or elastic wave," US patent 2011/0019906 A1, Jan. 27, 2011.
2. Berechet, I. and G. Berginc, "Advanced algorithms for identifying targets from a three-dimensional reconstruction of sparse 3D Ladar data," *Proceedings of SPIE*, Vol. 8172, 81720Z, Optical Complex Systems, 2011.
3. Marino, M. and W. R. Davis, Jr., "Jigsaw: A foliage penetrating 3D imaging laser radar system," *Lincoln Laboratory Journal*, Vol. 15, No. 1, 23–36, 2005.
4. Berginc, G. and M. Jouffroy, "Simulation of 3D laser systems," *Proceedings of the 2009 IEEE International Geoscience & Remote Sensing Symposium*, Cape Town, South Africa, 440–444, 2009.
5. Berginc, G. and M. Jouffroy, "Simulation of 3D laser imaging," *PIERS Online*, Vol. 6, No. 5, 415–419, 2010.
6. Berginc, G. and M. Jouffroy, "3D laser imaging," *PIERS Online*, Vol. 7, No. 5, 411–415, 2011.

The Generalized n-th Order Maxwell's Equations

F. B. M. Belgacem[1] and R. Silambarasan[2]

[1]Department of Mathematics, Faculty of Basic Education, PAAET, Shaamyia, Kuwait
[2]M. S. Software Engineering, School of Information Technology
V.I.T. University, Vellore, Tamilnadu, India

Abstract— The existing Maxwell's set of equations describing TEMP waves propagating in conducting $\sigma > 0$ lossy medium is extended to the n-th order and solved using the Natural transform.

1. NATURAL TRANSFORM DEFINITON AND DUALS

The electric field vector **E** and magnetic field vector **H** of the TEMP (Transversal ElectroMagnetic Planar) waves propagating in z direction in lossy conducting medium with constant permittivity ϵ, permeability μ and conductivity σ are related to each other by the Maxwell's equations as

$$\begin{cases} \nabla \times \mathbf{E} = -\mu \frac{\partial \mathbf{H}}{\partial t} \\ \nabla \times \mathbf{H} = -\epsilon \frac{\partial \mathbf{E}}{\partial t} - \sigma \mathbf{E} \end{cases} \tag{1}$$

Being the polarization of the electric field along x direction and magnetic field along y direction, the Maxwell's Equation (1) takes the following form

$$\begin{cases} \frac{\partial \mathbf{E}_x(z,t)}{\partial z} + \mu \frac{\partial \mathbf{H}_y(z,t)}{\partial t} = 0 \\ \frac{\partial \mathbf{H}_y(z,t)}{\partial z} + \epsilon \frac{\partial \mathbf{E}_x(z,t)}{\partial t} + \sigma \mathbf{E}_x(z,t) = 0 \end{cases} \tag{2}$$

For all the functions $f(t)$ defined in the set $A = \{f(t) | \exists M, \tau_1, \tau_2 > 0, |f(t)| < Me^{\frac{|t|}{\tau_j}}$, if $t \in (-1)^j \times [0, \infty)\}$, the Natural transform is given by [1],

$$\mathbb{N}^+[f(t)] = \int_0^\infty e^{-st} f(ut) dt; \quad \mathrm{Re}(s) \in (0, \infty), \quad u \in (-\tau_1, \tau_2) \tag{3}$$

The Natural transform $R(s,u)$ is related to Laplace transform $F(s)$ and Sumudu transform $G(u)$ by the following dualities respectively [1],

$$R(s,u) = \frac{1}{u} F\left(\frac{s}{u}\right) \quad \text{and} \quad R(s,u) = \frac{1}{s} G\left(\frac{u}{s}\right) \tag{4}$$

The following lemmas will be used directly in this paper

Lemma 1.

$$\mathbb{N}^+\left[\frac{\partial^n \mathbf{E}_x(z,t)}{\partial t^n}\right] = \frac{s^n}{u^n} F(z,s,u) - \sum_{k=0}^{n-1} \frac{s^{n-(k+1)}}{u^{n-k}} \left[\lim_{t \to 0} \left| \frac{\partial^k \mathbf{E}_x(z,t)}{\partial t^k} \right| \right] \tag{5}$$

Proof. The proof is similar to Natural transform of ordinary derivative (theorem 3.3, Equation (3.4) of [1]).

Lemma 2.

$$\mathbb{N}^+\left[\frac{\partial^{2n} \mathbf{E}_x(z,t)}{\partial t^{2n}}\right] = \frac{s^{2n}}{u^{2n}} F(z,s,u) - \sum_{k=0}^{2n-1} \frac{s^{2n-(k+1)}}{u^{2n-k}} \left[\lim_{t \to 0} \left| \frac{\partial^k \mathbf{E}_x(z,t)}{\partial t^k} \right| \right] \tag{6}$$

Proof. Replacing n by $2n$ in lemma 1 Equation (5).

2. n-TH ORDER MAXWELL'S SETS AND SOLUTION ANALYSIS

In the generalized n-th order case the TEMP waves propagating in lossy conducting medium takes the following forms

$$\begin{cases} \nabla^n \times \mathbf{E} = -\mu \frac{\partial^n \mathbf{H}}{\partial t^n} \\ \nabla^n \times \mathbf{H} = -\epsilon \frac{\partial^n \mathbf{E}}{\partial t^n} - \sigma \mathbf{E} \end{cases} \tag{7}$$

$$\begin{cases} \frac{\partial^n \mathbf{E}_x(z,t)}{\partial z^n} + \mu \frac{\partial^n \mathbf{H}_y(z,t)}{\partial t^n} = 0 \\ \frac{\partial^n \mathbf{H}_y(z,t)}{\partial z^n} + \epsilon \frac{\partial^n \mathbf{E}_x(z,t)}{\partial t^n} + \sigma \mathbf{E}_x(z,t) = 0 \end{cases} \tag{8}$$

The Equation (8) can be expressed as seperate electric and magnetic fields PDE's by

$$\begin{cases} \frac{\partial^{2n} \mathbf{E}_x(z,t)}{\partial z^{2n}} = \mu\epsilon \frac{\partial^{2n} \mathbf{E}_x(z,t)}{\partial t^{2n}} + \mu\sigma \frac{\partial^n \mathbf{E}_x(z,t)}{\partial t^n} \\ \frac{\partial^{2n} \mathbf{H}_y(z,t)}{\partial z^{2n}} = \mu\epsilon \frac{\partial^{2n} \mathbf{H}_y(z,t)}{\partial t^{2n}} + \mu\sigma \frac{\partial^n \mathbf{H}_y(z,t)}{\partial t^n} \end{cases} \tag{9}$$

For the electric field, the Natural transform application of first equation of Eqnuation (9) by using the lemmas (1) and (2) and assuming the initial condition $\left\{\lim_{t\to 0} \frac{\partial^i \mathbf{E}_x(z,t)}{\partial t^i}\right\}_{i=0}^{2n-1} = f_0^i(z)$ and after mathematical derivations results in the following non-homogeneous equation (with $D^{2n} = \frac{d^{2n}}{dz^{2n}}$)

$$\left[D^{2n} - \frac{s^n \gamma^{2n}}{u^{n-1}}\right] F(z,s,u) = P_n(z,s,u) \tag{10}$$

where

$$\gamma^{2n} = \frac{s^n \mu\epsilon}{u^{n+1}} + \frac{\mu\sigma}{u} \tag{11}$$

$$P_n(z,s,u) = -\gamma^{2n}\left[\sum_{i=1}^{n}\left(\frac{s}{u}\right)^{n-i} f_0^{i-1}(z)\right] - \frac{\mu\epsilon}{u}\left[\sum_{i=1}^{n}\left(\frac{s}{u}\right)^{n-i} f_0^{i+(n-1)}(z)\right] \tag{12}$$

The homogeneous solution (by considering only the exact roots) and particular integral solution of Equation (10) are respectively given by

$$F_h(z,s,u) = \sum_{i=1}^{2n} A_i(s,u) \exp\left\{\frac{(-1)^i \gamma\sqrt{s}}{u^{\frac{n-1}{2n}}}\right\} z \tag{13}$$

$$F_p(z,s,u) = \sum_{i=1}^{2n}\left[\frac{u^{\frac{n-1}{2n}}}{2\gamma\sqrt{s}}\right] \exp\left\{\frac{(-1)^i \gamma\sqrt{s}}{u^{\frac{n-1}{2n}}}\right\} z \int \exp\left\{\frac{(-1)^{i+1} \gamma\sqrt{s}}{u^{\frac{n-1}{2n}}}\right\} z P_n(z,s,u) dz \tag{14}$$

Finiteness of $F(z,s,u)$ requires $\sum_{i=1}^{n} A_i(s,u) = 0$ and considering the boundary condition $\lim_{z\to 0} \mathbf{E}_x(z,t) = \begin{cases} \sum_{i=1}^{n} f_i(t) & \text{if} \quad t \geq 0 \\ 0 & \text{if} \quad t < 0 \end{cases}$ assuming for $z > 0$, the waves $\sum_{i=1}^{n} f_i(t)$ are travelling in lossy medium with conductivity $\sigma > 0$ so that $\mathbb{N}^+\left[\lim_{z\to 0} \mathbf{E}_x(z,t)\right] = \mathbb{N}^+\left[\sum_{i=1}^{n} f_i(t)\right] = \sum_{i=1}^{n} F_i(s,u)$ hence,

$$F(z,s,u) = \sum_{i=1}^{n} F_i(s,u) \exp\left\{\frac{-\gamma\sqrt{s}}{u^{\frac{n-1}{2n}}}\right\} z \tag{15}$$

Expanding $\left[\frac{u^{\frac{n-1}{2n}}}{2\gamma\sqrt{s}}\right] \exp\left\{\frac{-\gamma\sqrt{s}}{u^{\frac{n-1}{2n}}}\right\} z$ by using the Natural-Sumudu Duality (Equation (2.11) of [1]) to the Equation (45) through Equation (47) of [3] and after some modification we have

$$\left[\frac{u^{\frac{n-1}{2n}}}{2\gamma\sqrt{s}}\right] \exp\left\{\frac{-\gamma\sqrt{s}}{u^{\frac{n-1}{2n}}}\right\} z = \alpha \int_{z/\alpha}^{\infty} e^{-\beta t} J_{n-1}\left(\frac{\beta}{\alpha}\sqrt{z^2 - \alpha^2 t^2}\right) e^{-\frac{st}{u}} dt \tag{16}$$

where in Equation (16), $\alpha = \frac{1}{\sqrt{\mu\epsilon}}$ and $\beta = \frac{\sigma}{2\epsilon}$ and $J_{n-1}(.)$ is the first kind Bessel's function of order $n-1$. Next differentiating Equation (16) w.r.t.'z' and then substituting $v = \frac{st}{u}$ so that $t = \frac{uv}{s}$ and $dt = \frac{udv}{s}$ and noting, as $t \to \frac{z}{\alpha}$, $v = \frac{zs}{\alpha u}$ and as $t \to \infty$, $v \to \infty$, hence we end with

$$\exp\left\{\frac{-\gamma\sqrt{s}}{u^{\frac{n-1}{2n}}}\right\} z = e^{-\frac{\beta}{\alpha}z} e^{-\frac{s}{\alpha u}z} - \alpha u \mathbb{N}^+[\Phi_n(z,v)] \tag{17}$$

where

$$\Phi_n(z,v) = \begin{cases} e^{-\beta v}\frac{\partial}{\partial z} J_{n-1}\left[\frac{\beta}{\alpha}\sqrt{z^2-(\alpha v)^2}\right] & \text{for} \quad v \in \left[\frac{z}{\alpha}, \infty\right) \\ 0 & \text{for} \quad v \in \left(0, \frac{z}{\alpha}\right) \end{cases} \tag{18}$$

Therefore substituting Equation (17) in Equation (15),

$$F(z,s,u) = \sum_{i=1}^{n} F_i(s,u) e^{-\frac{\beta}{\alpha}z} e^{-\frac{s}{\alpha u}z} - \alpha u \sum_{i=1}^{n} F_i(s,u) \mathbb{N}^+[\Phi_n(z,v)] \tag{19}$$

Using the second shifting property of the Natural transform $\mathbb{N}^+[f(t-a)H_a(t)] = e^{-\frac{as}{u}} R^+(s,u)$ and the convolution theorem (theorem 4.6, Equation (4.11) of [1]), the inverse Natural transform application of Equation (19) finally results in the following theorem

Theorem 1. *The electric field solution of the n-th order Maxwell's sets describing TEMP waves travelling in lossy conducting medium is given by*

$$\mathbf{E}_x(z,t) = \sum_{i=1}^{n} e^{-\frac{\beta}{\alpha}z} f_i\left(t - \frac{z}{\alpha}\right) - \sum_{i=1}^{n} \alpha \int_{z/\alpha}^{\infty} f_i(t-\tau) e^{-\beta\tau} \frac{\partial}{\partial z} J_{n-1}\left[\frac{\beta}{\alpha}\sqrt{z^2-(\alpha\tau)^2}\right] d\tau \tag{20}$$

Proceeding in the same fashion for the second equation of Equation (9) gives the following theorem for magnetic field.

Theorem 2. *The magnetic field solution of the transverse electromagnetic planar waves propagating in lossy media with $\sigma > 0$ for the n-th order is*

$$\mathbf{H}_y(z,t) = \sum_{i=1}^{n} e^{-\frac{\beta}{\alpha}z} g_i\left(t - \frac{z}{\alpha}\right) - \sum_{i=1}^{n} \alpha \int_{z/\alpha}^{\infty} g_i(t-\zeta) e^{-\beta\zeta} \frac{\partial}{\partial z} J_{n-1}\left[\frac{\beta}{\alpha}\sqrt{z^2-(\alpha\zeta)^2}\right] d\zeta \tag{21}$$

3. PROTOTYPE 2-ND ORDER MAXWELL'S EQUATIONS

The first order (or) existing Maxwell's equations were solved by Laplace transform in [2, 5] and by Sumudu transform in [3]. Now for $n \equiv 2$ in Equation (8) gives the second order Maxwell's equations

$$\begin{cases} \frac{\partial^2 \mathbf{E}_x(z,t)}{\partial z^2} + \mu\frac{\partial^2 \mathbf{H}_y(z,t)}{\partial t^2} = 0 \\ \frac{\partial^2 \mathbf{H}_y(z,t)}{\partial z^2} + \epsilon\frac{\partial^2 \mathbf{E}_x(z,t)}{\partial t^2} + \sigma \mathbf{E}_x(z,t) = 0 \end{cases} \tag{22}$$

which resolves to give

$$\begin{cases} \frac{\partial^4 \mathbf{E}_x(z,t)}{\partial z^4} = \mu\epsilon\frac{\partial^4 \mathbf{E}_x(z,t)}{\partial t^4} + \mu\sigma\frac{\partial^2 \mathbf{E}_x(z,t)}{\partial t^2} \\ \frac{\partial^4 \mathbf{H}_y(z,t)}{\partial z^4} = \mu\epsilon\frac{\partial^4 \mathbf{H}_y(z,t)}{\partial t^4} + \mu\sigma\frac{\partial^2 \mathbf{H}_y(z,t)}{\partial t^2} \end{cases} \tag{23}$$

The Natural transformed non-homogeneous differential equation (with the initial conditions) of electric field is

$$\left[D^4 - \frac{s^2\gamma^4}{u}\right] F(z,s,u) = P_2(z,s,u) \tag{24}$$

where $\gamma^4 = \frac{s^2\mu\epsilon}{u^3} + \frac{\mu\sigma}{u}$ and $P_2(z,s,u) = -\gamma^4\left[\sum_{i=1}^{2}\left(\frac{s}{u}\right)^{2-i} f_0^{i-1}(z)\right] - \frac{\mu\epsilon}{u}\left[\sum_{i=1}^{2}\left(\frac{s}{u}\right)^{2-i} f_0^{i+(2-1)}(z)\right]$.

The homogeneous solution and particular integral solution of Equation (24) are respectively given by

$$F_h(z,s,u) = \sum_{i=1}^{4} A_i(s,u) \exp\left\{\frac{(-1)^i\gamma\sqrt{s}}{u^{\frac{1}{4}}}\right\} z \tag{25}$$

$$F_p(z,s,u) = \sum_{i=1}^{4}\left[\frac{u^{\frac{1}{4}}}{2\gamma\sqrt{s}}\right] \exp\left\{\frac{(-1)^i\gamma\sqrt{s}}{u^{\frac{1}{4}}}\right\} z \int \exp\left\{\frac{(-1)^{i+1}\gamma\sqrt{s}}{u^{\frac{1}{4}}}\right\} z P_2(z,s,u) dz \tag{26}$$

After the boundary conditions and finiteness

$$F(z,s,u) = \sum_{i=1}^{2} F_i(s,u) \exp\left\{\frac{-\gamma\sqrt{s}}{u^{\frac{1}{4}}}\right\} z \tag{27}$$

Expansion of $\left[\frac{u^{\frac{1}{4}}}{2\gamma\sqrt{s}}\right] \exp\left\{\frac{-\gamma\sqrt{s}}{u^{\frac{1}{4}}}\right\} z$ is obtained by simply substituting $n \equiv 2$ from Equation (16) through Equation (19) so that 2-nd order Maxwell's equations electric field is given by

$$\mathbf{E}_x(z,t) = \sum_{i=1}^{2} e^{-\frac{\beta}{\alpha}z} f_i\left(t - \frac{z}{\alpha}\right) - \sum_{i=1}^{2} \alpha \int_{z/\alpha}^{\infty} f_i(t-\tau) e^{-\beta\tau} \frac{\partial}{\partial z} J_1\left[\frac{\beta}{\alpha}\sqrt{z^2 - (\alpha\tau)^2}\right] d\tau \tag{28}$$

4. CONCLUSION

Hence for the non negative integer n, the n-th order Maxwell's equations describing TEMP waves requires $2n$ initial conditions and n boundary conditions, therefore the solution of the n-th order sets depends only on the n boundary conditions and $(n-1)$-th order of the Bessel's functions.

REFERENCES

1. Belgacem, F. B. M. and R. Silambarasan, "Theory of the natural transform," *Mathematics in Engg. Sci. and Aerospace (MESA) Journal*, Vol. 3, No. 1, 99–124, 2012.
2. El-Shandwily, M. E., "Solutions of Maxwell's equations for general non-periodic waves in lossy media," *IEEE Transactions Electromagn. Compact.*, Vol. 30, No. 4, 577–582, Nov. 1988.
3. Hussain, M. G. M. and F. B. M. Belgacem, "Transient solutions of Maxwell's equations based on Sumudu transform," *Progress In Electromagnetics Research*, Vol. 74, 273–289, 2007.
4. Silambarasan, R. and F. B. M. Belgacem, "Applications of the natural transform to Maxwell's equations," *PIERS Proceedings*, 899–902, Suzhou, China, Sep. 12–16, 2011.
5. Stratton, J. A., *Electromagnetic Theory*, McGraw Hill Book Company, New York, 1941.

Comparison of Microwave Path Lengths between Temperate and Tropical Region Based on Effects of Rain

U. Kesavan[1, 2], **A. R. Tharek**[1], **and Md. Rafiqul Islam**[3]

[1]Wireless Communication Centre, Electrical Engineering Faculty
Technology University of Malaysia, Malaysia
[2]Electrical Engineering Department, Sultan Haji Ahmad Shah Polytechnic, Pahang, Malaysia
[3]Faculty of Engineering, International Islamic Malaysia University, Malaysia

Abstract— Rain is a major source of attenuation for microwave propagation above 7 GHz. The problem of rain attenuation prediction has been studied along the years. In spite of the effort developed in different parts of the world, there are yet some points to be clarified. This problem is quite difficult to be solved, mainly due to the complexity of rain structure. This clearly suggests that reduction factor is the major yardstick for comparing rain attenuation prediction models. However, important parameter need to consider in the path reduction factor is the maximum effective path length for a particular link at specific operating frequency. This paper presents the summary of allowable path length for designing terrestrial microwave link at particular operating frequency at temperate and tropical region. The objective of this paper, to establish the maximum path length or hop length for terrestrial link on line of sight point to point communication at 99.99% of availability. Various frequency band such as 7 GHz, 15 GHz, 23 GHz, 26 GHz and 38 GHz been investigated using the ITU-R path reduction model. From the studies conducted, there are significant differences in path length between temperate region and tropical region. The differences are 22 km, 10 km, 5 km, 4 km and 3 km in the path length for operating frequency 7 GHz, 15 GHz, 23 GHz, 26 GHz & 38 GHz. This paper will provide useful information for microwave engineers and researchers in making valuable decision on path length for any terrestrial links point to point communication operating in a temperate and tropical region in future.

1. INTRODUCTION

The radio waves propagating through the earth atmosphere will be attenuated due to the presence of atmosphere particles, such as water vapour, water drops and the ice particles. The atmospheric gases and rain will both absorb and scatter the radio waves, and consequently degrade the performance of the link [1]. Rain is a major source of attenuation for microwave propagation above 5 GHz [2]. In tropical and equatorial regions, the rain intensity is higher and designing terrestrial and earth-to-satellite microwave links are very critical and challenging. The problem of rain attenuation prediction has been studied along the years. Many researcher's [3–5] stated path reduction factor is the major yardstick for comparing rain attenuation prediction model. However, important parameter need to consider in the path reduction factor is the maximum path length for a particular link at specific operating frequency. The path length been determine using the received signal level (RSL) or the Fris's equation, by considering the free space loss and rain attenuation in free space [6]. The rain fall rate and the regression coefficient for the drop size distribution (DSD) of rain is important factor in establishing the path length of any microwave link [7]. DSD varies from the geographical factor of a location. Various frequency band can be investigated using the most common ITU-R [2] path reduction model for terrestrial point to point communication. There a few models available besides the ITU-R model, such as Global Crane model, Revised Moupfouma model, Revised Silva Mello model, Lin Model and others but due to ITU-R model is known as Global model, this model been used as a reference in many research work conducted.

2. METHODOLOGY

Five experimental microwave links at 7, 15, 23, 26 and 38 GHz were installed at UTM Campus in Johor Bahru, Malaysia. The rain rate were measured for four years (Jan. 2003 to Dec. 2006) at the same location with one minute integration time . The maximum transmit power, antenna gain and received threshold for 10^{-6} BER with 2×2 Mbps traffic for all five experimental links are given in Table 1. The fade margins for 7, 15, 23, 26 and 38 GHz frequency bands are predicted based on one minute rain rate measurements for four years at UTM Skudai, Johor Bahru. The availabilities of terrestrial microwave links are also investigated based on rain attenuation data collected from

Table 1: Measured rainfall rate at UTM, Skudai, Johor Bahru from Jan. 2003 to Dec. 2006.

% of Time Rain Rate Exceeded	0.1	0.01	0.001
Measured Rain Rate in mm/hr	59	125	175

Table 2: Specification of the experimental links.

Frequency Band in GHz	Maximum Transmit Power in dBm	10^{-6} BER (2×2 Mbps) Rx Threshold in dBm	Tx and Rx Gains in dBi
7	25	−95	20
15	18	−84	37
23	20	−83	40
26	18	−82	41
38	15	−79	45

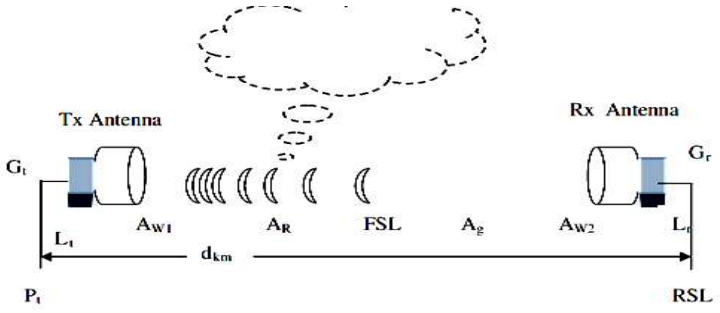

Figure 1: Link budget for a terrestrial line-of-sight radio link.

this five operational microwave links more than one year. From the measured rain fall for four years, the cumulative distribution frame at 0.01% of time, the rain rate recorded was 125 mm/hr. Table 2, summarize the specification of the experimental links. The drop size distribution (DSD) or regression coefficient on rain fall for the tropical region like Malaysia proposed by Din [6] was used.

Figure 1, shows the example of experimental test bed for each links in the studies. The rain attenuation is calculated based on the data collected thru the experiment. The rain fall rate also been recorded using Casella rain gauge using one minute time integration. These data have been used to investigate the link. The gauge is a tipping bucket type and it has sensitivity of 0.5 mm. It records the total rainfall occurring in each minute without recording non rainy events; therefore the rain rate is recorded as an integral multiple of 30 mm/h or 0.5 mm/min.

The Fris's equation been used to calculate the free space loss and other losses for the link including the rain attenuation loss which is very critical for tropical country like Malaysia. The maximum path length for a particular operating frequency is calculated base on the maximum signal can been captured by the system. The received signal level (RSL) is calculated using the equation below:

$$RSL = P_t + G_t + G_r - FSL - A_g - A_R - A_W - L_T - L_t \tag{1}$$

whereby, P_t — Transmit power, G_t & G_r — Transmit and received antenna gain, FSL — Free space loss, A_g — Losses in gaseous absorption, A_R — Losses due to rain attenuation, A_W — Losses due to wet antenna, L_T — Losses in receiving system, L_t — Losses in transmit system.

In this study, we assume at Fresnel zone, the path loss is only considering the free space loss (FSL) & rain attenuation factors, the rest is ignored. Un faded RSL can be calculated using the equation,

$$Unfaded\ RSL = P_t + G_t + G_r - 32.45 - 20\log_{10}(d_{\mathrm{km}}) - 20\log_{10}(f_{\mathrm{MHz}}) \tag{2}$$

Faded RSL due to rain,

$$Faded\ RSL = Unfaded\ RSL - kR_{\%}^{\alpha} \cdot r_{\%} d_{\mathrm{km}} \tag{3}$$

As per known, ITU-R rain attenuation model as per stated below:

$$A_{0.01} = \alpha R_{0.01}^{b} r_{0.01} d \tag{4}$$

whereby path reduction factor, r

$$r_{0.01} = 1/(1 + d/d_0) \tag{5}$$

$$d_o = 35e^{-0.015R_{0.01}}, \quad R_{0.01} \leq 100\,\text{mm/hr} \tag{5a}$$

$$d_o = 35e^{-1.5R_{0.01}}, \quad R_{0.01} \geq 100\,\text{mm/hr} \tag{5b}$$

ITU-R model was used to calculate rain attenuation due to it is used as global model for rain attenuation studies in world wide. R is the rain fall rate, a and b regression coefficient, r is the path reduction factor and d is the path length. Further analysis were done by comparing the results on the tropical region for the maximum path length achievable or allowable against the temperate region using the same set-up but regression coefficient values and the rain fall rate used are different based on the geographical factor. Temperate region, ITU-R model characteristic of precipitation for modeling [8] and specific attenuation [9] model for rain rate was used. Rain rate used for temperate region was 35 mm/hr at 0.01% of time. Based on the rain rate for the temperate region at 35 mm/hr it covers most of the country in Europe such as United Kingdom, Sweden, Finland, Norway, Republic Czech, Poland, Germany, France, Netherland and Iceland [8].

3. RESULTS AND DISCUSSION

From the analysis using the Fris's equation, Table 3, clearly summarized and shows the path length required at temperate and tropical region. There are wider differences in path length, km at lower operating frequency compare to higher operating frequency at both temperate and tropical region. As per known in the literature, when the frequency is greater the path length will be shorter. This phenomena complies in this studies. Figure 2, shows comparison of path length required between temperate and tropical region at specific operating frequency using the ITU-R model as a references for rain attenuation.

The path length differences at various operating frequency for temperate and tropical region been analysed. For 7 GHz, the path length differences at temperate region 40% (22 km) more compare to the tropical region. Thus at 15 GHz, 23 GHz, 26 GHz and 38 GHz at temperate region 62.5% (10 km), 55.5% (5 km), 57.1% (4 km) and 60% (3 km) more compare to the tropical region. Base on the observation, at lower operating frequency the differences between the path length in the regions are small compare (40%) to the higher operating frequency (> 50%) but at higher operating frequency, the path length differences for the both regions looks more stable at average of 59%.

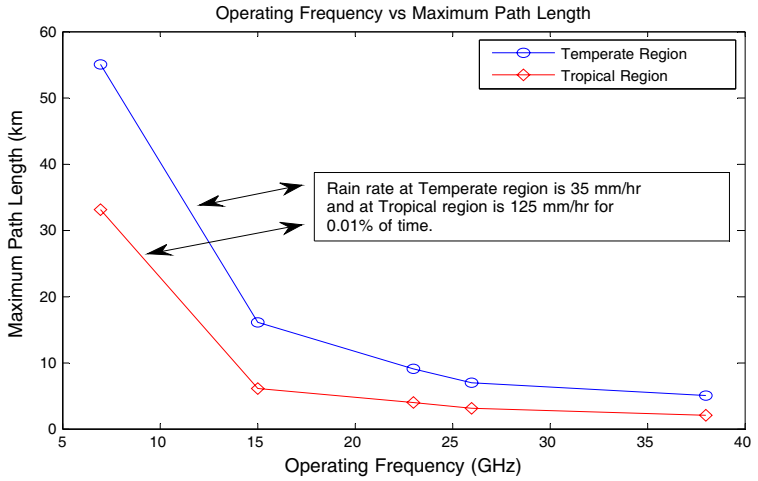

Figure 2: Comparison of path length between temperate and tropical region at specific operating frequency.

Table 3: Summary of path length required for temperate and tropical region at specific operating frequency.

Operating Frequency/GHz	Path Length for Temperate Region/km	Path Length for Tropical Region/km	Differences in Path length/km
7	55	33	22
15	16	6	10
23	9	4	5
26	7	3	4
38	5	2	3

4. CONCLUSION

Based on the results from the experiment conducted, it shows the temperate region such as European countries like United Kingdom, Sweden, Finland, Norway, Republic Czech, Poland, Germany, France, Netherland and Iceland having longer path length for all the operating frequency at 7, 15, 23, 26 and 38 GHz in the microwave communication link compare to tropical region like Malaysia, Brazil, Nigeria, Indonesia, Thailand and Singapore. This is due to the geographical location of the region, the rain fall rate and the regression coefficient for the drop size distribution (DSD) of rain which is important factor in establishing the path length of any microwave link. It's clearly indicate there are differences about 22 km ,10 km, 5 km, 4 km, 3 km differences in the length for operating frequency at 7 GHz, 15 GHz, 23 GHz, 26 GHz & 38 GHz at 0.01% of time. Further analysis will be carried out by analyzing the other frequency range for lower to higher operating frequency at temperate and tropical region at different location to validate the microwave link path length further in future.

ACKNOWLEDGMENT

The authors would like to acknowledge and express sincere appreciation to Technology University of Malaysia (UTM) and Ministry of Higher Education (MOHE) for financing the research project under the Research University Grant (RUG), title: Rain propagation studies and mitigation technique at 5.8 GHz and 26 GHz for point to point application, vote No. Q. J130000.7123.01H05.

REFERENCES

1. Crane, R. K., *Electromagnetic Wave Propagation Through Rain*, John Wiley & Son Series, 1996.
2. Recommendation ITU-R P.530-14 (02/2012), "Propagation data and prediction methods required for the design of terrestrial line of sight systems," Feb. 2012.
3. Panagopoulos, A. D., P. D. M. Arapoglou, and P. G. Cottis, "Satellite communications at Ku, Ka and V bands: Propagation impairments and mitigation techniques," *IEEE Communications Surveys and Tutorials*, 2004.
4. Kanellopoulos, J, D., et al., "Rain attenuation problems affecting the performance of microwave communication systems," *Ann. Telecommun*, Vol. 45, Nos. 7–8, 1990.
5. Mandeep, J. S. and K. Tanaka, "Effects of atmospheric parameters on satellite link," *Int. J. Infrared Milli. Waves*, Vol. 28, 789–795, 2007.
6. "Final reports on rain attenuation studies for communication systems operating in tropical regions," Wireless Communication Research Laboratory, Universiti Teknologi Malaysia, Oct. 31, 2000.
7. Crane, R. K., *Propagation Handbook for Wireless Communication System Design*, CRC Press LLC, 2003.
8. Recommendation ITU-R P.837-6 (02/2012), "Characteristics of precipitation for propagation modelling," 2012.
9. Recommendation ITU-R P.838-3 (2005), "Specific attenuation model for rain use in prediction methods," 2005.

Pulsed EM Propulsion of Unconventional Flying Objects

A. Meessen
Institute of Physics, Catholic University of Louvain, 1348, Louvain-la-Neuve, Belgium

Abstract— Specific properties of Unconventional Flying Objects of unknown origin were widely documentated in the past, but they seemed to be too mysterious for scientific studies. Indeed, the *propulsion system* of these objects is radically different from those that are familiar to us, since they have neither wings, nor propellers or jet engines. However, we can deduce from observed facts and known physical laws that they ionize the surrounding air and exert forces on the resulting charged particles by means of adequate EM fields. Lift and propulsion result then from the reaction force, but this requires *very intense magnetic fields, oscillating at low frequencies.* Having shown that they can be produced when the surface of the object is superconducting, we explain here *why these fields are needed and how they act.* This model is confirmed by observations of interactions with water. Observational evidence concerning these fields will follow.

1. INTRODUCTION

There are numerous observations of "Unconventional Flying Objects" and their effects, as shown by Richard Hall [1, 2], the astronomer Allen Hynek [3, 4] and the physicist Peter Sturrock [5]. Actually, these objects can be *identified* by their form and behavior, since they have no wings to provide aerodynamic lift, nor visible means for propulsion. Nevertheless, they are able to remain motionless and to move at low or even extremely high velocities in complete or nearly complete silence. Usually, they don't create any air motions. Their origin is unknown, but this is irrelevant when we *try to understand their propulsion system in terms of observed facts and known physical laws.* Our objective is to show that this seems to be possible. We have shown already that they could produce *low frequency EM surface waves,* if their surface were superconducting [6]. A current density **J**, oscillating around a given axis, would then be associated with an oscillating magnetic field **B** and an induced electric field **E** (Figure 1).

For disc-like or long cylindrical, but axially symmetric objects, the magnetic field lines are somewhat different, but they are situated in meridional planes and the electric field lines are still circular and parallel to the equatorial plane. The fields **E** and **B** are thus orthogonal to one another. The intensity of the magnetic field decreases rapidly below the surface of the superconductor and the magnetic field lines are there nearly parallel to the surface. However, they are refracted when they emerge, since the normal component of **B** has to be continuous, while the tangential component is not. In polar coordinates (r, θ, φ), the electric field $\mathbf{E} = (0, 0, E)$ and the magnetic field $\mathbf{B} = (B_r, B_\theta, 0)$. Outside a superconducting sphere

$$E = \frac{\omega M}{r^2} \sin\theta \sin\omega t, \quad B_r = \frac{2M}{r^3} \cos\theta \cos\omega t \quad \text{and} \quad B_\theta = \frac{M}{r^3} \sin\theta \cos\omega t \tag{1}$$

This stationary oscillation is possible for any low frequency ω and any magnetic dipole moment M, as long as superconductivity is not destroyed. Objects that are topologically similar to a sphere will behave in an analoguous way. In regard to their propulsion, our initial reasoning [7] was that

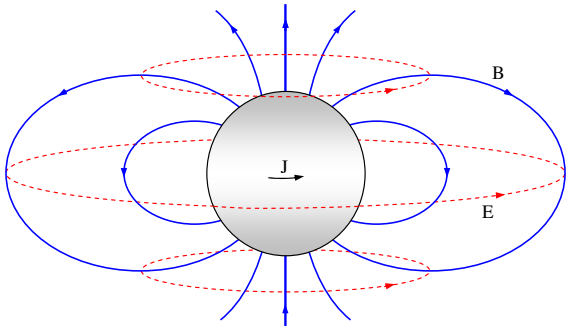

Figure 1: Configuration of the magnetic and electric field lines for a superconducting spherical shell.

any autonomous system has to apply forces on something else to be submitted itself to the reaction force. The luminosity, which was often seen to surround UFOs, sugested that they *ionize* the ambiant air. They could thus exert forces on the resulting charged particles by means of adequate *EM fields*. Actually, the intensity and color of the surrounding luminsity was sometimes seen to depend on the state of motion or to pulsate. We had thus to explore possible effects of pulsed ionization and low frequency EM fields.

2. FORCED MOTIONS OF ANY CHARGED PARTICLE

Let's consider a particle of charge q and mass m that is suddenly created by ionization at the instant $t = 0$ at a given point P. It defines the origin of a right-handed Cartesian frame, where $\mathbf{B}$ is oriented along the z-axis and $\mathbf{E}$ along the y-axis. These fields are oscillating at a sufficiently low frequency to consider their values as being *practically constant during the lifetime T of the charged particle*. Its initial velocity $\mathbf{v}$ is negligible, but it is immediately accelerated by the electric field $\mathbf{E}$ and as soon as it has aquired some velocity $\mathbf{v}$, it is pushed sideways by the magnetic field $\mathbf{B}$. Since the average effect of elastic collisions is equivalent to viscous friction, characterized by the relaxation time τ, we get the equation of motion

$$m\mathbf{a} = q(\mathbf{E} + \mathbf{v} \times \mathbf{B}) - \frac{m}{\tau}\mathbf{v} \tag{2}$$

Diffusion is negligible when ionization is homogeneous at the scale where the charged particle is moving. The velocity components v_x and v_y are thus determined by

$$\tau\dot{v}_x + v_x = \mu B v_y \quad \text{and} \quad \tau\dot{v}_y + v_y = \mu(E - Bv_x) \tag{3}$$

where $\mu = q\tau/m$ is the *mobility* of the particle. Since $\omega_c = \mathrm{qB/m}$ is the cyclotron frequency of this particle, $\mu B = \omega_c\tau$ is a numerical parameter. The general solution of (3) is

$$v_x = V_x + A\cos(\omega_c t + \phi)e^{-t/\tau} \quad \text{and} \quad v_y = V_y - A\sin(\omega_c t + \phi)e^{-t/\tau}$$

where V_x and V_y are the velocity components that subsist when the stationary state has been reached. The first terms in (3) are then negligible. Thus,

$$V_y = \frac{\mu E}{1 + (\mu B)^2} \quad \text{and} \quad V_x = \frac{\mu^2 EB}{1 + (\mu B)^2} \tag{4}$$

The constants A and ϕ are determined by the initial condition ($v_x = v_y = 0$ for $t = 0$), but the velocity vector $\mathbf{v}(t)$ varies in such a way that its tip describes a spiral (Figure 2). The particle reaches its stationary state very rapidly ($\tau \ll T$) and is then moving at the velocity $\mathbf{V}$. The transverse component V_x reaches a maximum when $\mu B = 1$ (Figure 3).

Because of (4), $(V_y - u)^2 + V_x^2 = u^2$, when $u = \mu E/2$. The components of the velocity vector $\mathbf{V}$ are such that the tip of $\mathbf{V}$ touches a half-circle of radius u (Figure 4). Θ is the Hall angle and the values of E and B are both proportional to M. Equation (2) is equivalent to $m\mathbf{a} = \mathbf{F} + \mathbf{f}$, where $\mathbf{F}$ is the EM force exerted on the charged particle. In the stationary regime $\mathbf{a} = 0$, and the applied force $\mathbf{F} = -\mathbf{f} = (m/\tau)\mathbf{V}$ is oriented like $\mathbf{V}$ and proportional to its magnitude (Figure 5). This is even valid during practically the whole lifetime of the charged particle.

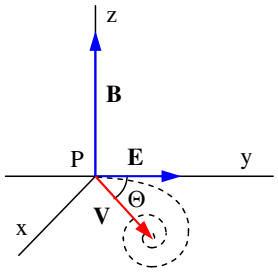

Figure 2: The fields $\mathbf{E}$ and $\mathbf{B}$ with the resulting drift velocity $\mathbf{V}$.

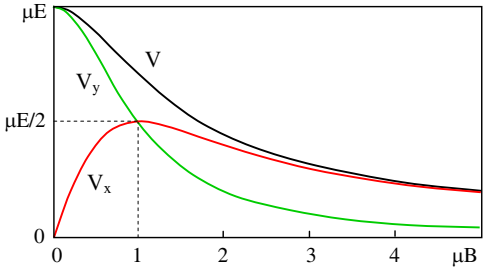

Figure 3: Variations of the magnitude of the velocity vector $\mathbf{V}$ and its components for increasing values of μB.

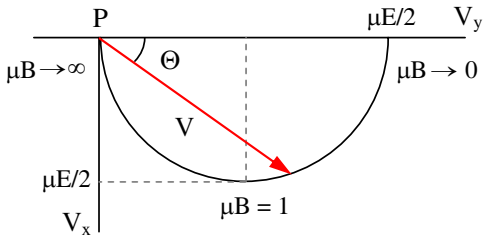

Figure 4: The magnitude and orientation of the drift velocity **V** depend on the fields **E** and **B**.

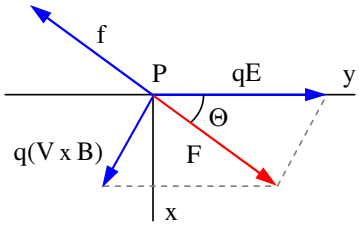

Figure 5: In the stationnary regime, the applied force **F** compensates the frictional force **f**.

An electric field alone would imply that $\mathbf{F} = q\mathbf{E}$. Since ionization produces two particles of opposite charge, the average force would be zero, while a strong magnetic field **B** deviates the force **F** with respect to the induced electric field **E**. Since the transverse force F_x is proportional to q^2, positive and negative particles will be pushed in the same direction.

3. PULSED IONIZATION IN AIR AND WATER

Atmospheric air can be ionized by microwaves. This yields *free electrons* and positive ions, while electron attachment will produce negative ions. All these particles could be set in motion, but electrons have a much higher mobility $\mu = q\tau/m$ than ions, because of their small mass and their larger relaxation time (Ramsauer effect). Usually, it is thus sufficient to consider only the momentum confered by the object to free electrons. Although they collide with ions or neutral molecules, they leave them pratically motionless. *This explains the absence of sound and air turbulence,* in contrast to what happens for helicopters. Moreover, the progressive action on the ambient air accounts for the *absence of a sonic boom* when the object passes the sound barrier. Because of (4), the magnitude of the transverse force F_x is proportional to the product EB and thus to $2\sin\omega t\cos\omega t = \sin 2\omega t = \pm 1$, when the ionization is adequately pulsed. This is very advantageous, since the driving force **F** can be reversed.

Figure 1 shows that the magnetic field **B** is horizontal at some places (when $\theta \approx 55°$ for a dipolar field). However, the orientation of **B** is opposite above and below the equatorial plane, while the perpendicular electric field **E** has there the same orientation. Since the orientation of the applied force **F** is defined by the local vector product $\mathbf{E}\times\mathbf{B}$, the resulting vertical forces would be opposite if ionization did occur there at the same instant. *By simply alternating the ionization above and below the equator*, we get equally oriented forces. The object would attract free electrons above its equatorial plane and push them downward below it, but *not* at the same instant. This doubles the average value of the reaction force acting on the object.

Ionization can even occur at instants where **E** changes sign, while **B** has a given sign, as well above as below the equator. This produces forces that are symmetrical with respect to the x-axis (Figure 5). The average transverse force **F** is then doubled and *situated in meridional planes for steady oscillations.* During sudden departures, where the intensity of the fields varies within a single period, forces oriented towards the left or right side of meridional planes will not be perfectly symmetric. Physical traces, where vegetation was laid down in clockwise or anti-clockwise spiraling patterns confirm this possibility. Lateral motions of the object can be obtained by attracting charged particles in front of the object and repelling them behind it. This requires only a modification of the distribution of the ionization density. The resulting propulsion sytem is *extremely flexible.* It allows not only for sudden changes of the direction of motion, but can even account for actually observed propulsion inside water.

Ionization produces there H^+ ions instead of free electrons. These protons have a greater mobility than other ions, because of their smaller mass and the Grotthuss mechanism. Propulsion in water is thus usually based on setting only protons in motion, but they can transfer momentum to water molecules. This should result in *visible actions on water!* Because of (1) and (4), we get as well for protons in water as for free electrons in air the same expressions for the components of the velocity vector **V** of these particles in meridional planes. When ionization occurs at optimal instants,

$$V_r = \frac{-V_0 C\rho^{-5}\sin^2\theta}{1 + C\rho^{-6}\sin^2\theta} \quad \text{and} \quad V_\theta = \frac{V_0 C\rho^{-5}\sin 2\theta}{1 + 4C\rho^{-6}\cos^2\theta} \tag{5}$$

The reduced distance $\rho = r/a$, where a is the radius of the sphere. The velocity $V_o = \omega a$ and the constant $C = \mu^2 B_o^2/2$ where $B_o = M/a^3$ is the magnetic field intensity at the surface of the sphere in its equatorial plane. The vertical and horizontal velocity components $V_v = V_r \cos\theta - V_\theta \sin\theta$ and $V_h = V_r \sin\theta + V_\theta \cos\theta$. For moderate magnetic fields ($C \ll 1$), we get

$$V_v = -V_o C \rho^{-5} 3 \sin^2\theta \cos\theta \quad \text{and} \quad V_h = V_o C \rho^{-5} \left(3\cos^2\theta - 1\right) \sin\theta \tag{6}$$

The vertical velocity and the resulting force are nearly maximal when $\theta \approx 55°$ (where $V_h \approx 0$). They vanish close to the symmetry axis (where $\sin\theta \approx 0$). The global vertical propulsive force F_p is opposed to the integral of all vertical forces $(e/\mu)V_v$, multiplied by $2\pi r^2 dr \sin\theta d\theta$ above the equator and doubled by alternate ionizations above and below the equator. We assume that the ionization density decreases like $I(a/r)^2$ outside a sphere of radius a, where I is a fraction of the normal particle density. Actually, the ionization is limited to a sphere of radius R, because of threshold effects, but $R \gg a$. We have also to take into account the relative time $\bar{t}$ (lifetime/period), where the EM field can act on the charged particles. For moderate magnetic fields and optimal ionizations, the total vertical propulsive force

$$F_p = \bar{t} I \omega a^4 e \mu B_o^2 \int_1^\infty \int_0^{\pi/2} 4\pi \rho^{-5} d\rho 3 \sin^3\theta \cos\theta d\theta = \bar{t} I \omega a^4 \frac{3\pi}{4} e \mu B_o^2$$

To estimate the *minimal* magnetic field B_o, we assume that up to 1% of neutral particles can be ionized and that $a \approx 5\,\mathrm{m}$, $\omega \approx 10\,\pi/\mathrm{s}$ at 5 Hz and $\bar{t} \approx 1\%$. *For electrons in atmospheric air at NTP,* we get then $I < 2.7 \cdot 10^{23}$ electrons/m^3 air, while their mobility $\mu \approx 1\,\mathrm{m}^2/\mathrm{Vs}$ or smaller [8] when $E > 10^4\,\mathrm{V/m}$. Simple hovering of an object of $10^3\,\mathrm{kg}$ would require a magnetic field $B_o > 0.02\,\mathrm{T}$. *For protons in water,* the same assumptions would yield $I < 3.3 \times 10^{28}/\mathrm{m}^3$, but their mobility [9] $\mu \approx 3.6 \times 10^{-7}\,\mathrm{m}^2/\mathrm{Vs}$. The same effective weight (beyond buancy) would require $B_o > 0.1\,\mathrm{T}$. Since the degree of ionization is probably weaker and since very rapid motions were also observed, possible magnetic fields have to be very great.

4. OBSERATIONAL CONFIRMATIONS

On March 29, 1974, a couple was sitting on a beach in Togo at about 50 m from the water, when a dark object approached at low altitude above the sea. It stoped at 200 to 300 m from the witnesses and hovered about 10 m over the sea. However, it generated powerful concentric waves, pushing the water up to their feet [10, 11] (Figure 6). This object had thus to exert very strong, low frequency forces on ionized water, in agreement with the model of *Pulsed EM Propulsion.* It created also a 5 to 6 m deep and 25 to 30 m large central depression. Carl Feindt, who collected numerous observations of interactions with water [12], proposed *a phenomenological model*, where a UFO surrounded by water would induce motions along flow lines that are similar to field lines of a magnetic dipole (interrupted lines in Figure 7).

It has actually been observed that before UFOs emerged from water, they produced large hemispherical swellings. After they rose above the water, there remained at first a central water column, but when they came from above the water, they created a cup-like depression (Figure 6). This confirms our theory, which has the advantage of correcting the phenomenological model by predicting *two separate circulations above and below the object.* The ionization range is limited and the

Figure 6: Water waves and central depression observed in Togo [10, 11].

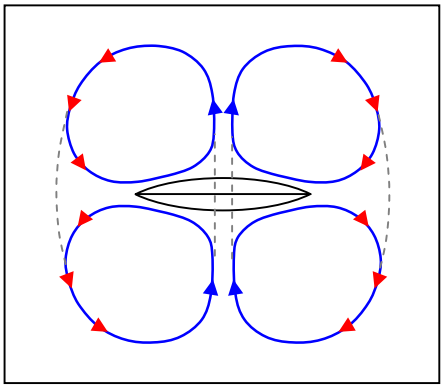

Figure 7: Predicted lines of flux.

applied forces are indicated by red arrows in Figure 7, while the flux lines are represented in blue. Agreement between observational evidence and the theoretical model is quite remarkable.

REFERENCES

1. Hall, R. H., *The UFO Evidence*, 1964.
2. Hall, R. H., *The UFO Evidence — Vol. II: A Thirty Year Report*, 2001.
3. Hynek, J. A., *The UFO Experience: A Scientific Inquiry*, 1972.
4. Hynek, J. A., *The Hyneck UFO Report*, 1977.
5. Sturrock, P. A., *The UFO Enigma: A New Review of the Physical Evidence*, 1999.
6. Meessen, A., "Production of EM surface waves by superconducting spheres: A new type of harmonic oscillators," Accepted by PIERS, 2012.
7. Meessen, A., *Inforespace*, 1973, http://www.meessen.net/AMeessen/ReflexionPropulsion.pdf.
8. Baum, C. E., 1965, http://www.ece.unm.edu/summa/notes/TheoreticalPDFs/TN006.pdf.
9. Blockris, J. O'M. and A. K. N. Reddy, *Modern Electrochemistry*, 1970.
10. Mesnard, J., *Phénomènes Spatiaux*, Vol. 47, Mar. 1976.
11. Flying Saucer Review, 23, Mar. 1977, http://www.ignaciodarnaude.com/avistamientos_ovnis/Mesnard,UFO%201974,sea%20tidal%20waves,Africa,FSR76V22N6.pdf.
12. Feindt, C. W., *Water UFOs*, Xlibris, 2010.

Quantum Blooming: The Possibility of Passing through the Classically Inaccessible Area without Attenuation

A. S. Kaklyugin
Atmospheric Plasma Instant Technology Corp., Hangenbieten 67980, France

Abstract— The problem of the quantum barrier blooming by supplementing additional barriers in the form of a local perturbation is formulated. The task is able to solve analytically for the simplest case of one-dimensional rectangular potential barrier. The antireflection perturbation in the situation represents two singular potential wells. It is proved for specific range of barrier (small barrier) the effect of blooming takes place for any values of the wave number of incident waves and obtained the limitation for barriers out of the range: in a case like that quantum blooming is available only under certain wave number restriction. The blooming possibility for the classically passable barriers considered separately and blooming providing the penetration over the potential well without scattering too. We discuss the challenges and paradoxes associated with this phenomenon.

1.

Sub-barrier tunneling (Gamow, 1928) has been described in detail in monographs and textbooks (see f.e. [1, 2]) and became a routine concept of quantum mechanics. They believe to establish the tunneling leads to an exponential decrease of the amplitude of the penetrated wave and to the appearance of the reflected wave.

The concept of tunneling initiated new ideas and found new effects: the tunnel diode, the Josephson junction, tunneling microscope. Estimates of tunneling time have proved to be a source of disturbing challenge (see below). Resonant tunneling when two barriers are separated by a well with a discrete level gets a case of (almost) complete passage of the particle. The probability of the passage has a form of resonance curve, the resonance peak corresponding to the energy level and its width corresponding its lifetime.

This phenomenon fits well within the general terms of scattering theory, it is well studied and extensively used in engineering practice [3] (resonant tunneling diodes in electronics), in physics of superconductors [4]). Note that even a normal contact with the modern point of view represents two barriers and a well between them, so the question of why the current passes between two metal samples is not so trivial.

The sub-barrier passage is incomplete in almost all cases (except for the Bloch functions or in ideal Josephson junctions). The resonance is never infinitely sharp for the level having a finite lifetime at least because of tunneling. The analogy with the electromagnetic wave propagation (for example, the light wave penetration inside the reflecting medium under internal reflection at distances about the wavelength and the blooming possibility of partially transparent films) gives the opportunity to pose the problem of complete penetration through the barrier of quantum particle or to correct any barrier to make it transparent. The propagation of electromagnetic and acoustic waves in the gradient media without reflection and attenuation [5–7] adds courage.

2.

We construct the wave function that before and after the barrier is a plane wave with the same amplitude and wave vector. We consider the symmetrical barrier for simplicity (the center of symmetry is the coordinate origin). Solution of second order linear equation (here the Schrödinger equation) with a symmetric potential with respect to x is in addition to $\psi(x)$ also $\psi(-x)$, $-\psi(x)$, $-\psi(-x)$. We construct the sub-barrier solution so that the real part of the sub-barrier wave function is an even function and the imaginary is an odd one.

The real part of the function we associate in positive half-space with $\cos(kx + \varphi)$ and the imaginary one with the sine of the same argument. Then the real part of the function changes over $\cos(kx - \varphi)$ in the negative half-space and the imaginary part changes over the appropriate sinus. Thus, the barrier provides a phase shift and the plane wave saves the amplitude, wave vector and the direction of propagation.

Let's consider a simplest barrier U_0 and a plane wave propagating along the half-axis $x > 0$. The potential energy is $U(x) = U_0$ when $a > x > 0$ and $U(x) = 0$ for $x > a$. If we measure energy

in units of $\hbar^2/2ma^2$ and the distances in units of a, the wave function of the stationary state will satisfy the Schrödinger equation that the energy, length and wave vectors will be dimensionless quantities:

$$\psi''(x) + \left(\varepsilon - q^2(x)\right)\psi(x) = 0, \tag{1}$$

where $q^2(x) = (2ma^2/\hbar^2)U(x)$. The dimensionless value $q_0^2 = (2ma^2/\hbar^2)U_0$ characterizes to what extent the barrier or well being big or small. Specify the term "big" or "small" (here the term "narrow" is the same). A deep well contains a lot of stationary states, a small one contains no more than one, the numerical criterion for the value of q_0^2 depends on the shape of the well or barrier [1, 2][1]. On the other hand, the closer the well to δ-function shape, the more likely it has only one level.

Consider a well sequence of depth C/δ and width δ (the sequence converges in a certain sense to $-C\delta(x)$), its dimensionless parameter $q_0^2 = (2ma^2/\hbar^2)U_0$ is $(m\delta^2/2\hbar^2)(C/\delta) \sim C\delta \to 0$. As soon as the well becomes more narrow, i.e., $\delta \to 0$, then kinetic energy tends to $\sim \hbar^2/2m\delta^2$ and the potential one is $-C/\delta$. The energy of discrete levels increases and the states squeezed out to the continuous spectrum until there remains only one level $-C^2/4$ (the ground state). The well becomes finally sufficiently narrow $\sim \delta \to 0$, i.e., the same result as for shallow well (the presence of only one discrete level). That's why we will believe the barrier or well big or small depending on the value of the dimensionless parameter $(2ma^2/\hbar^2)\ U_0$ (for well it corresponds to one or more discrete levels).

The solution of Equation (1) is a set of exponential functions

$$\psi(x) = \exp\{\mathbf{i}(kx + \varphi)\}, \quad x > 1 \tag{2a}$$

$$\psi(x) = c\exp(\kappa x) + b\exp(-\kappa x), \quad 1 > x > 0. \tag{2b}$$

We do not consider the exponent of $-ikx$ (the reflected wave is to be absent) because we want to find the conditions for complete passage through the potential barrier. The values of ε and q_0^2 link to the squares of the wave vectors $k^2 + \kappa^2 = q_0^2$; $q^2 = \varepsilon$. We seek a solution of Equation (1) whose real and imaginary units will be even and odd respectively. The complex coefficients a and b in (2b) override in the real A and B such a way

$$\psi(x) = A\mathrm{ch}(\kappa x) + \mathbf{i}B\mathrm{sh}(\kappa x), \quad 1 > x > 0. \tag{2c}$$

Of continuity of $\psi(x)$ at $x = 1$ (real and imaginary units separately) write down explicitly the values A and B:

$$A = \cos(k + \varphi)/\mathrm{ch}(\kappa); \quad B = \sin(k + \varphi)/\mathrm{sh}(\kappa). \tag{3}$$

The wave function derivative must be continuous at $x = 1$ too. Do the values of φ, k (respectively, κ) exist so that not only the wave functions but also the derivative coincides at $x = 1$ for certain values of q_0? I.e., does a phase shift providing the passage for the barrier without damping for certain barriers and wave vectors exist?

Let's argue the situation is impossible. For any values of $\kappa > 0$ both $\mathrm{ch}(\kappa x)$ and $\mathrm{sh}(\kappa x)$ are positive, so their derivatives are positive also. If the value of A from (3) is positive, then $\cos(kx + \varphi)$ as well as $\mathrm{ch}(\kappa x)$ must be at $x = 1$ positive, as well as its derivatives (it's true for $-\pi/2 < k + \varphi < 0$). The function $\sin(kx + \varphi)$ is negative on this interval. Hence the value of B is also negative according (3). From $B < 0$ it follows that the imaginary part of the wave function $B\mathrm{sh}(\kappa x)$ in (2c) is negative and its derivative must be negative too. However, the derivative of the function $\sin(kx + \varphi)$ is positive! Similar argue for negative A shows the derivatives cannot coincide in any way.

3.

Thus, just to pass across the barrier without attenuation is impossible. Resonant tunneling occurs in our terms as a "kink" at the origin. It corresponds to embedding scattering center in the middle of the barrier. Note the resonant-tunneling structures do not provide a dampingless penetration. The incident wave energy providing that must coincide with the resonance level, but the level himself is "inaccurate", it has a finite width (lifetime).

[1]It was erroneously stated in the book [1, p. 304] the bound states in the well depth $U_0 < \hbar^2/ma^2$ do not exist. It being not true, that the first bound state in a symmetric potential well exists always [2, p. 91].

We look for another solution by changing the shape of the barrier on its border (at $x = 1$ and -1). The optical blooming analogy evidences in favor of the solution, as well as dampingless propagation of electromagnetic waves through the gradient profile barrier [5, 6], that are like singular border barriers in a certain sense.

A possible boundary kink (at $x = 1$) can be solved by adding a potential additive $C\delta(x-1)$ to the original barrier. Can this additive provide the necessary leap of derivative values both the imaginary and real parts of (2a) and (2c) is to be resolved. We extend the wave function to the negative axis as mentioned above, so that real and imaginary parts are to be even and odd respectively (the phase shift φ changes sign on the negative half-axis). It makes just automatically plane wave moving at the same direction in the negative half-space. Moreover, the required kink (the leap of the derivative at $x = -1$) is provided by adding a symmetric singular additive $C\delta(x+1)$ with the same constant C. Indeed, the leap of the derivative at $x = -1$ for the imaginary part of the wave function must have the opposite sign, but also the imaginary part also get another sign and Equation (1) is satisfied.

A possible boundary kink can be solved by adding a potential additive $C\delta(x-1)$ to the original barrier. Can this additive provide the necessary derivative leap for both the imaginary and real parts of (2a) and (2c) is to be resolved. If we solve it, extend the wave function to the negative axis as mentioned above, so the required kink at $x = -1$ is provided by adding a symmetric singular additive $C\delta(x+1)$ with the same C.

Evaluate the wave function derivative leap $\Delta\psi'(1) = \psi'(1 + o(1)) - \psi'(1 - o(1))$ and equate it to $C\psi(1)$ as in Equation (1) (both real and imaginary units):

$$\mathrm{Re}\Delta\psi'(1) = -k\sin(k+\varphi) - \kappa\cos(k+\varphi)\mathrm{th}(\kappa) = C\cos(k+\varphi), \tag{4a}$$
$$\mathrm{Im}\Delta\psi'(1) = k\cos(k+\varphi) - \kappa\sin(k+\varphi)\mathrm{cth}(\kappa) = C\sin(k+\varphi). \tag{4b}$$

Since the equations must satisfy together, the constant C must be the same. Eliminating it, we obtain

$$k[\mathrm{tg}(k+\varphi) + \mathrm{ctg}(k+\varphi)] = \kappa[\mathrm{cth}(\kappa) - \mathrm{th}(\kappa)]. \tag{5}$$

We remind the values of k and κ are related by $k^2 + \kappa^2 = q_0^2$, so the Equation (5) except for an unknown quantity (k or κ) contains φ as a free parameter. An existence of φ parameter makes the opportunity to have a whole set of solutions, the set of values k (or κ) is a subset of the interval $(0,\ q_0)$. The solution of (5) is given in Appendix 1.

A similar analysis is valid for the over-barrier blooming, as well as in the over-well passage. So, we consider solutions on the interval $(1 > x > 0)$ in the form $\psi(x) \sim \exp(i\mathcal{K}x)$, hyperbolic functions transfer to the trigonometric ones and the relations for wave vectors are now $k^2 = q_0^2 + \mathcal{K}^2$ for the first case and $k^2 + q_0^2 = \mathcal{K}^2$ for the second.

Solutions (2) turn into the set of plane waves:

$$\psi(x) = \exp\{\mathbf{i}(kx+\varphi)\} = \cos(kx+\varphi) + \mathbf{i}\sin(kx+\varphi) \qquad \text{for } x > 1 \tag{6a}$$
$$\psi(x) = \alpha\cos\mathcal{K}x + \mathbf{i}\beta\sin\mathcal{K}x \qquad \text{for } 1 > x > 0. \tag{6b}$$

Similarly the first case we evaluate the wave function derivative leap at $x = 1$ and equate it to $C\psi(1)$:

$$\mathrm{Re}\Delta\psi'(1) = -k\sin(k+\varphi) + \mathcal{K}\cos(k+\varphi)\mathrm{tg}\mathcal{K} = C\cos(k+\varphi), \tag{7a}$$
$$\mathrm{Im}\Delta\psi'(1) = k\cos(k+\varphi) - \mathcal{K}\sin(k+\varphi)\mathrm{ctg}\mathcal{K} = C\sin(k+\varphi). \tag{7b}$$

Eliminating the constant C, as before, we obtain

$$k[\mathrm{tg}(k+\varphi) - \mathrm{ctg}(k+\varphi)] = \mathcal{K}[\mathrm{tg}\mathcal{K} - \mathrm{ctg}\mathcal{K}]. \tag{8}$$

The solution is given in Appendix 2.

4.

We have to consider the wave functions with wave vector k providing a free penetration through the classically inaccessible potential barrier U_0 (wave vector restriction q_0).

4.1.

First, there is a small barrier $q_0 \leq 1/2$ (i.e., $U_0 \leq \hbar^2/(8ma^2)$). To visualize the barrier, we rewrite the inequality as $(a/a_0)^2\,(U_0/E_H) \leq 1/4$, where $a_0 = (\hbar^2/me^2) = 0.53\,\text{Å}$, $E_H = me^4/2\hbar^2 = 13.6\,\text{eV}$. For the barrier width $2a = 1\,\text{nm}$ the barrier $U_0 \leq 0.04\,\text{eV}$ can be considered as small, a narrow barrier ($2a = 2\,\text{Å}$) is a small barrier for $U_0 \leq 1\,\text{eV}$. In this case the blooming effect takes place for all values of incident wave vectors (Appendix 1).

The value of the blooming singularities is determined by the value of sub-barrier damping $\kappa = (q_0^2 - k^2)^{1/2}$ in the expression for C. In this range of values q_0 and k the condition (11) is valid automatically, so there are two possible solutions (13). Equation (5) determines the phase shift when wave is passing through the barrier. Phase shift is determined by the barrier and incident wave properties, not by the blooming singularities.

4.2.

The situation is different for a big barrier. To penetrate the barrier should be fulfilled in this case first inequality (12), i.e., the sub-barrier damping κ should be large enough. The wave vector values are to be small, restricted as shown in Fig. 1. The higher is the barrier, the stricter is the limitation and very large barriers may be bloomed only for very slow waves. Emphasize, that for all barriers (big or small) there are two values of C, both of them are negative, i.e., the blooming additives are just well, not barriers.

4.3.

Now we shall consider a classically accessible barrier or well (Appendix 2). The algorithm looks like for inaccessible one, but now we find not damping κ but wave vector $\mathcal{K}$. The blooming (here antireflection) additives are available for certain values of $\mathcal{K}$ (the higher is the barrier, the wider is the bandwidth available for values $\mathcal{K}$ and k). There is an additional band of possible values for small $\mathcal{K}$ for small barriers. It corresponds to the situation of full range possible values of k and κ for the classically inaccessible small barrier. There are two possible values of antireflection additives for above-barrier passage, in both cases there are clarifying wells. For over-well reflectionless passage the blooming additives exist for any values of $\mathcal{K}$ and k, so there are two possible values of antireflection singularity, in some cases there are wells, in the other barriers.

4.4.

What is happened in a situation of blooming disordering? We suppose the presence of additional wells $\Delta C\delta(x+1) + \Delta C\delta(x-1)$ ($\Delta C \ll C$). If we conserve on positive half-axis the falling wave function in the form $\cos(k+\varphi) + i\sin(k+\varphi)$, the reflection wave function with the opposite wave vector has an amplitude $\sim \Delta C$. Thus, the reflection coefficient will be $\sim (\Delta C)^2$. A narrow wave packet (center ordered) passes almost complete. Passing the blooming barrier (well) the wave packet turns out more monochromatic, but it spreads out in space.

4.5.

Differences in contrast to the resonant tunneling are: (a) full passing through the barrier (well) in terms of blooming, (b) passing wave energy don't coincide with the energy of a bound state of anti-reflective additives.

5.

Let's discuss the qualitative consequences of the estimates.

5.1.

Generally accepted the phase velocity of a massive quantum particle exceeds the light speed (this value is the ratio of energy to momentum but the energy in units of the light speed is always greater than the momentum at the expense of the rest mass). The group velocity does not exceed the speed of light, of course.

However, it concerns only particles traveling in a classically accessible region. The phase shift 2φ is determined by the formula (5) and we should not confuse the ambiguity of the inverse tangent. Typically, the value of φ is of the order $\pi/4$ (such an estimate is obtained by replacing the vertical wall of a linear, a standard way to specify the WKB approximation, see, for example [1, p. 322]), and certainly no exceed $\pi/2$. Thus, the point of constant phase overcomes the barrier width for about half of the period (at least no more), the wave function depends on time as $\exp(-i\omega t)$, $\omega = \varepsilon/\hbar$. This energy is not determined by the properties of the barrier but the energy of the

incident wave only. Thereby the passing velocity may have any value depending on how wide is the barrier. Usually it is the content of the paradox Hartman [8] and the problem is discussed in detail in [9]. It was accepted to calm the researcher conscience by the argument that the wave is only partially passed through the barrier, so it does not violate the principle of causality. For the blooming barrier this explanation does not work. For a wave packet with center ordered wave vector passing a barrier almost completely (see 4.4), this circumstance is valid for the group velocity, i.e., the real speed of moving particle.

5.2.

This paradox for an electromagnetic wave propagation (the main discussion in [9] was dedicated to the subject) is not crucial. Medium with a certain refractive index arises only when on infinite medium acts an infinite (in space and time) wave. While considering on the microscopic level (in principle) we must take into account the response of each particle of the medium being by the action of the incident wave field and the field from all the particles of the medium except for this one. After smoothing procedures we can use the refraction index as a result of the averaging account of the incident wave field and its induced action on the medium. The front of the incident wave doesn't extend to the empty space, but the medium begins to behave as a refractive medium only when the front comes to it. Thus, an electromagnetic wave packet goes with the ordinary (light) speed, exciting medium by the way, losing energy, fading away and possibly slowing under the influence of dynamic screening. To represent wave packet as a sum of plane waves is incorrect: the virtual wave ahead the wave packet front does not create a modified medium!

5.3.

It was shown in 4.3 that the propagation of over-well blooming is provided by two (singular) barriers. The shape of this configuration (barrier-well-barrier) is identical to resonant tunneling.

6.

Arising problems. The inquiry is basically qualitative. It should be understood to what extent blooming is a general phenomenon. A simple task is to determine the possibility of asymmetric anti-reflection additives (inter alia, can we get blooming by just one well or barrier). The correctness of barrier and well division to big and small (concurring in a number of levels: one or lots of) needs to justification. At first glance the study can be performed using perturbation theory, but the complexity appeared notable (or the model is not too well-turned).

Visibly, there are many opportunities to create structure dampingless tunneling with a number of elements more than three as Bloch function in the crystal for example. General consistent patterns of constructing such structures are to be found (perhaps they are somehow related to the Anderson localization criteria).

Cross-over quantum mechanics → classical mechanics considered understanding well enough. Dampingless tunneling (for any barriers at least in principle) may turn out a challenge for it. It would be interesting to solve and to compare a classical passing problem and the same quantum one (in Hamilton-Jacobi form and in the form of path integrals respectively). Hartman paradox complicates the situation in the relativistic region.

Well as resonant tunneling, considered blooming may find applications in electronics. A layer of adsorbed atoms or molecules with electron affinity can perform the role of blooming additive for tunneling electrons (f.e., a molecule O_2 with an additional electron has a level of O_2^-, the energy of the level is $-0.44\,\mathrm{eV}$). Many atomic and molecular particles present similar levels, what makes possible to fit the adsorbed material selectively.

ACKNOWLEDGMENT

Author is sincerely grateful to A. B. Shvartsburg for posing the problem and discussion.

APPENDIX 1

Let's divide both sides of (4a) by $\cos(k+\varphi)$ and (4b) by $\sin(k+\varphi)$, and move terms containing hyperbolic functions on the other side of the equation by isolating the terms containing the trigonometric functions.

$$-k\mathrm{tg}(k+\varphi) = C + \kappa\mathrm{th}(\kappa), \tag{9a}$$

$$k/\mathrm{tg}\,(k+\varphi) = C + \kappa/\mathrm{th}(\kappa). \tag{9b}$$

Multiplying these equations and taking into account $k^2+\kappa^2 = q_0^2$, we obtain an equation relating C and φ:

$$C^2 + 2d(\kappa)C + q_0^2 = 0, \tag{10}$$

where $d(\kappa) = (\kappa/2)(\mathrm{th}(\kappa) + \mathrm{cth}(\kappa))$.

The condition of existence of purely real solutions of Equation (5) gives the inequality (the C value is a component of the Hamiltonian and the property of Hermitian makes it real)

$$\kappa\mathrm{cth}(2\kappa) \geq q_0 > \kappa, \tag{11}$$

that defines the existence region of solutions of Equation (5). Inversing (11), we write inequalities for κ:

$$\begin{array}{ll} q_0 > \kappa \geq D(q_0), & \text{if } q_0 > 1/2 \\ q_0 > \kappa \geq 0, & \text{if } q_0 \leq 1/2. \end{array} \tag{12}$$

where $D(q_0)$ is the inverse function of $d(\kappa)$. Here it mentioned that the value range of the function $d(\kappa)$ is an interval $[1/2,\ \infty)$, see Fig. 1 (the domain of definition $D(q_0)$). Since for any nonzero finite values a the inequality $a + 1/a > 2$ is valid, then $d(\kappa) > \kappa$, and, accordingly, $q_0 > D(q_0)$. Thus, a set of solution (12) is non-empty.

So, for $q_0 \leq 1/2$ we can choose any of the values κ satisfying $q_0 > \kappa$ and immediately determine the value of $k = (q_0^2 - \kappa^2)^{1/2}$. Now we define two values of C from Equation (10):

$$C = -\kappa\mathrm{cth}(2\kappa) \pm \left[\kappa^2\mathrm{cth}(2\kappa)^2 - q_0^2\right]^{1/2}. \tag{13}$$

Substituting C and k in (9)–(13), we can find the corresponding value of φ solving it as a trigonometric equation. A similar sequence of actions is valid for the case $q_0 > 1/2$, but at this case we choose the κ values not on the whole interval $(0, q_0)$, but taking into account the first condition (12).

APPENDIX 2

We divide Equations (7a) and (7b) by $\cos(k+\varphi)$ and $\sin(k+\varphi)$, respectively. Separating k and $\mathcal{K}$ we obtain

$$-k\mathrm{tg}(k+\varphi) = C + \mathcal{K}\mathrm{tg}\mathcal{K}, \tag{14a}$$

$$k/\mathrm{tg}(k+\varphi) = C + \mathcal{K}\mathrm{ctg}\mathcal{K}. \tag{14b}$$

We get quadratic equation for C like the previous case, taking into account that the values of k, q_0^2 and $\mathcal{K}$ are related as $k^2 = q_0^2 + \mathcal{K}^2$ for over-barrier passage and $k^2 + q_0^2 = \mathcal{K}^2$ for over-well one.

$$C^2 + 2D(\mathcal{K})C \pm q_0^2 = 0, \tag{15}$$

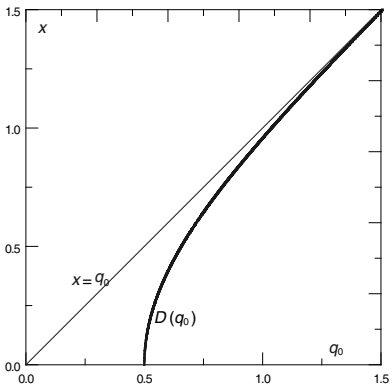

Figure 1: The solution of (13) is an area between curves $\kappa = q_0$ and $D(q_0)$. There are a small barrier case to the left of $q_0 = 0.5$ and a big one to the right.

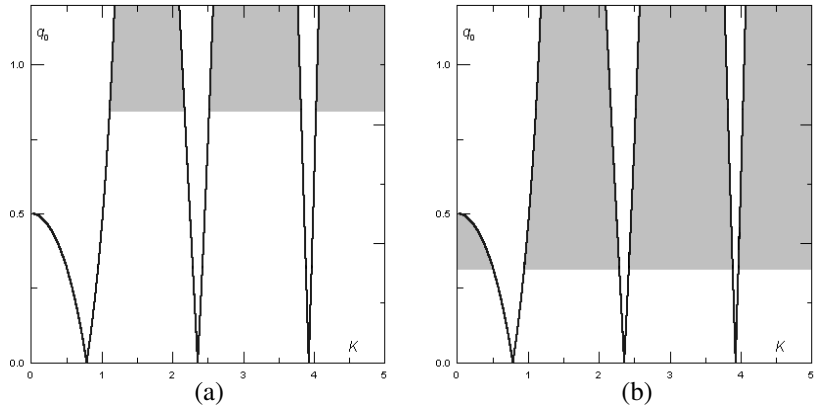

Figure 2: The solution of (16) (shaded in gray). The big barrier (Fig. 2(a)) differs from the small barrier (Fig. 2(b)), the latter has an additional band of solutions.

where $D(\mathcal{K}) = (\mathcal{K}/2)(\mathrm{ctg}\mathcal{K} - \mathrm{tg}\mathcal{K})$. The upper sign in the last term corresponds to the over-barrier passage and the lower to over-well one. The value C as a solution of (15) exists as a real number for the over-well passage for any value of $\mathcal{K}$, but for the over-barrier passage real solution of C exists only for $\mathcal{K}$ satisfying the inequality

$$|\mathcal{K}\mathrm{ctg}2\mathcal{K}| \geq q_0. \tag{16}$$

The left side is shown graphically on Fig. 2 as a bold curve. Solutions exist for all values of q_0, but there is a difference for big and small barriers. For big barriers ($q_0 > 1/2$) the set of possible solutions (and possible values of $\mathcal{K}$) is bands with an approximate center points of $\pi/2$, π, $3\pi/2$, ... (see Fig. 2(a)). The grater is $\mathcal{K}$ value, the wider bands become and the lesser room keeps for forbidden values of $\mathcal{K}$ not satisfying (16). For small barriers ($q_0 \leq 1/2$) it appears a band at small values of $\mathcal{K}$ apart from the bands indicated above (see Fig. 2(b)).

The value of C as in the previous case is determined using any of the allowed values of $\mathcal{K}$

$$C = -\mathcal{K}\mathrm{ctg}2\mathcal{K} \pm [\mathcal{K}^2\mathrm{ctg}^2 2\mathcal{K} \pm q_0^2]^{1/2}. \tag{17}$$

Here the first and second signs $\pm$ get different senses. The first sign gives two solutions of the quadratic equation, the second one denotes over-well (plus) or over-barrier (minus) passing. Using C and k, the values are uniquely determined by $\mathcal{K}$ and q_0, we obtain the value of φ solving trigonometric Equation (14).

REFERENCES

1. Bohm, D. J., *Quantum Theory*, Prentice Hall, New York, 1951; Reprint: Dover, New York, 1989.
2. Landau, L. D. and E. M. Lifshitz, *Quantum Mechanics: Non-relativistic Theory*, 3rd Edition, Pergamon Press, 1977.
3. Krayzman, V. L., E. V. Polozhentsev, and V. P. Sachenko, *The Double Potential Barriers and Resonant Tunneling*, Rostov University Press, 2001.
4. Abrikosov, A. A., "Resonant tunneling in high-Tc superconductors," *Phys. Usp.*, Vol. 41, 605–616, 1998.
5. Shvartsburg, A. B., V. Kuzmiak, and G. Petite, "Optics of subwavelength gradient nanofilms," *Phys. Rep.*, Vol. 452, 33–88, 2007.
6. Shvartsburg, A. B. and N. S. Erokhin, "Acoustic gradient barriers (exactly solvable models)," *Phys. Usp.*, Vol. 54, 605–623, 2011.
7. Shvartsburg, A. B., G. Petite, and M. Zuev, "Tunneling of femtosecond pulses through nanophotonic barriers: Superluminal precursors," *J. Opt. Soc. Am. B*, Vol. 28, No. 9, 2271–2276, 2011.
8. Hartman, T. E., "Tunneling of a wave packet," *J. Appl. Phys.*, Vol. 33, 3427–3433, 1962.
9. Shvartsburg, A. B., "Tunneling of electromagnetic waves: Paradoxes and prospects," *Phys. Usp.*, Vol. 50, 37–51, 2007.

Growth and Investigation of $LiNbO_3$ Thin Films at Nanoscale by Scanning Force Microscopy

D. A. Kiselev, **R. N. Zhukov**, **A. S. Bykov**, **M. D. Malinkovich**, **and Y. N. Parkhomenko**
National University of Science and Technology "MISiS"
Leninskiy pr. 4, Moscow 119049, Russian Federation

Abstract— In this work, an Atomic Force Microscope in the so-called Piezoresponse mode and Kelvin mode is used to image the grains, ferroelectric domains and surface potential in lithium niobate thin films. A RF magnetron sputter system was used to deposit $LiNbO_3$ thin films on (100)-oriented Si substrates with SiO_2 layer. The surface of the sample shows small grains which diameter ranges from 70 nm to 150 nm and roughness is less than 13 nm. Using the electric field from a biased conducting AFM tip, we show that possible to form and subsequently to visualize ferroelectric state. Also, we report surface charge retention on ferroelectric thin films by Kelvin probe microscope in comparison with the piezoresponse signal.

1. INTRODUCTION

Thin films of Lithium Niobate ($LiNbO_3$) posses a number of advantages over bulk material including the possibilities of producing step index profiles, selectively introducing dopants, and the fabrication of multilayer structures. In addition there are certain applications where only thin films can be used as, for example, when a large refractive index difference between the film and the substrate is necessary. The prospect of producing high quality (oriented and possessing low optical loss) thin films of $LiNbO_3$ on silicon substrates is particularly attractive because the silicon provides a rigid and flat substrate ideal for large area processing of devices by lithographic techniques and it allows for the integration of lithium niobate electro-optic and silicon integrated circuit technology.

For characterize a ferroelectric properties of the films in recent times has become relatively widely used method of piezoresponse force microscopy (PFM), which allows us to investigate the direction of polarization, as well as the local distribution of domain [1]. As was shown in previous papers [2, 3], this method can be used to obtain reliable results on ferroelectric polarization in $LiNbO_3$ films on conductive substrates, however, on isolated, containing a layer of SiO_2, the PFM method is unsuitable.

In this paper, we illustrate the first results of the scanning probe microscopy in piezoresponse mode contribution in the imaging of ferroelectric activity in $LiNbO_3$ thin films, synthesized on electrically isolated silicon substrate by RF magnetron sputtering.

2. EXPERIMENTAL DETAILS

The investigated films thickness of 150 nm obtained by RF magnetron sputtering of lithium niobate single crystal substrate dusting grown by the Czochralski method. The target was sputter in argon atmosphere ($6 * 10^{-1}$ Pa) with the power of the magnetron 150 watts. The deposition rate was 1.67 nm/min. The substrates used silicon single-layer epitaxial structure with orientation {100} and n-type conductivity ($\rho = 1\,\text{ohm} \cdot \text{cm}$) coated with a thin ($\sim 5$ nm) layer of SiO_2. The substrate was placed at a distance of 7 cm from the surface target. The heating of the substrate temperature was carried out to temperature 550°C. Thickness measurement was carried out on ellipsometer α-SETM firm J. A. Woollam Co., Inc. (USA). Scatter the thickness of the films was ± 5 nm. The measurements were performed on the phase composition X-ray diffractometer D1 System (Bede Scientific Ltd., UK) in parallel geometry parallel to the beam.

Local ferroelectric properties were investigated with piezoresponse force microscopy (PFM) using a commercial setup NTEGRA Prima (NT-MDT, Russia). Out-of-plane PFM images of the samples were obtained by applying ac voltage (10 V, peak-to-peak) with a frequency of 150 kHz. Conductive probes (stiffness $12\,\text{N} \cdot \text{m}^{-1}$, resonance frequency 240 kHz, NSG10/Pt, NT-MDT) with tip height of 15 µm and effective radius ≈ 30 nm were used for the PFM measurement. The voltage was applied on the sample base while the AFM tip was grounded. Surface potential profile (Kelvin mode — KPM) configurations are done in tapping mode. The local poling was done by applying various dc voltages to the tip followed by consequent KPM and PFM imaging.

3. DISCUSSION

The scanning probe microscopy in contact mode has become a powerful technique for both domain imaging and non-destructive evaluation of local ferroelectric properties at the nanometer scale in $LiNbO_3$ thin films [4, 5]. The following discussion is focused on the effect of both the substrate nature and the film crystallinity on the final imaging resolution. Figure 1 shows simultaneously acquired images of the topography and piezoresponse of an unpoled area of the film deposition on (100) Si.

On the topographic image a well visualized the grain, the average grain size of which ranged from 100 to 170 nm. From the statistical analysis of the topography lithium niobate thin films found that its roughness is less than 13 nm, which indicates fairly well as the sample surface.

Piezoresponse image (Figure 1(b)) on polycrystalline $LiNbO_3/SiO_2/Si$ heterostructures not showed piezocontrast from individual grains, that reflects the arrangement of domains in such non-oriented ferroelectric films, because in the case of $LiNbO_3/SiO_2/Si$ heterostructures, due to the electric insulating nature of the substrate and the lack of conductive interface, charge storage occurs at the interface during piezoresponse measurements.

However, after applied DC voltage to system "cantilever-film-substrate" we have demonstrated that it is possible to image domains (Figure 2(a)). We study the effect of poling in piezoresponse behavior, the samples were first poled with ± 20 V high dc voltage and later scanned with 5 V peak-to-peak ac voltage. The results are presented in Figure 2.

Black and white regions correspond to opposite directions of the out-of-plane spontaneous polarization. By monitoring the phase of the piezoresponse signal, it was determined that black regions correspond to domains with the polarization vector oriented toward (hereafter referred as "negative" domains) while white regions correspond to domains oriented upward the bottom electrode (hereafter referred as "positive" domains), i.e., bright and dark rectangles correspond to the regions poled with $+20$ and -20 V, respectively. We see that the domain wall is now no longer confined by grain boundaries and follows the expected path of the tip.

The cross-sections in Figure 2(b) demonstrate the evolution of the induced state in $LiNbO_3$ thin films as function time. As we expected from the PFM images, the polarization states look fluctuating. The piezoresponse of positively and negatively poled domains has been decreased with time. Average amplitude for both piezoresponse signals over the measurement time is displayed in Figure 2(c). The solid lines in Figure 2(c) show the fitting parameters in empirical relation:

$$y = y_0 + C \exp\left(-t/t_0\right). \tag{1}$$

The relaxation time (t_0) of "positive" poling area is 7.7 min and for "negative" area — 7.6 min.

Next step, we observed stability of the induced state in two regimes: PFM — contact, and KPM — non-contact, respectively. The original state of the samples did not exhibit any detectable contrast in both KPM and PFM images. The writing of the induced states was performed during the scanning of the $6 \times 6\ \mu m^2$ area in the contact regime. In the middle of the scanning the different dc bias of ± 10, ± 15 and ± 20 V was applied between the tip and the bottom electrode. As can be seen, the amplitude of the piezoresponse signal and signal of surface potential was roughly proportional to the poling voltage [6].

As shown above (Figure 2), a polarized region scanned in contact mode, quickly relax — several minutes. However, the induced state scanned in Kelvin mode is stable for several hours. The

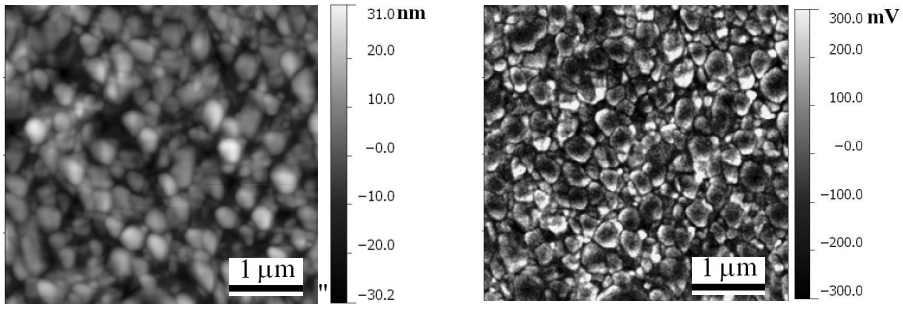

Figure 1: (a) Topography and (b) piezoresponse images of as-grown $LiNbO_3/SiO_2$ heterostructure.

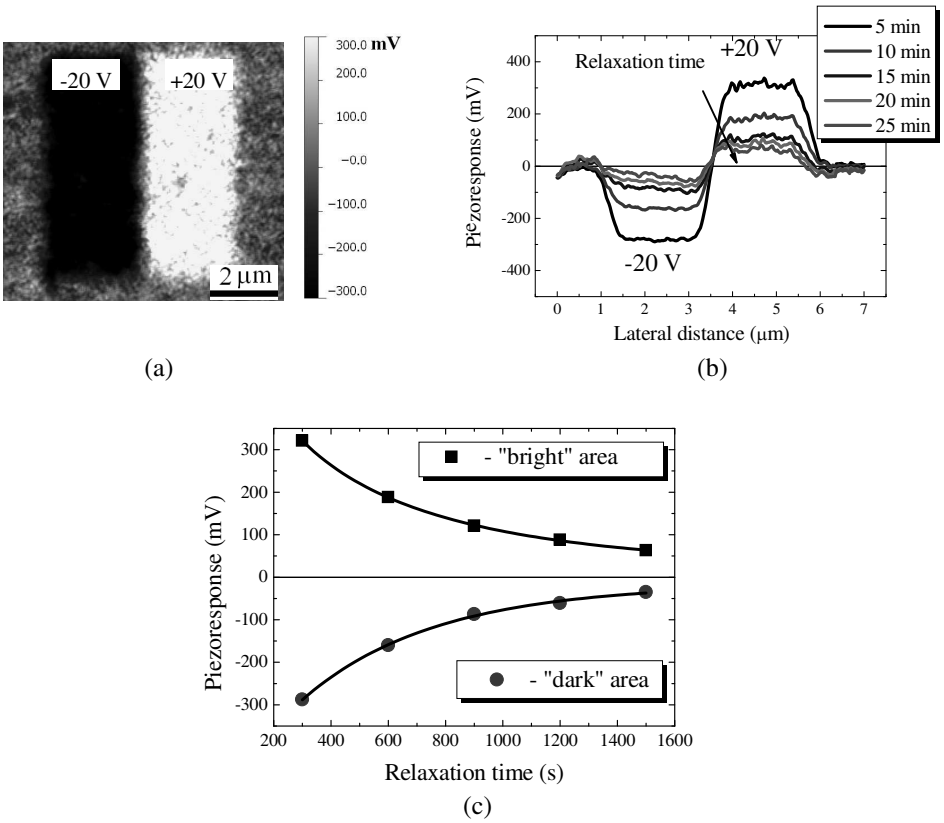

Figure 2: (a) Out-of-plane PFM images $LiNbO_3/SiO_2$ after poling with ± 20 V, (b) piezoresponse cross-sections at different times after poling process and (c) comparison of the piezoresponse cross-sections.

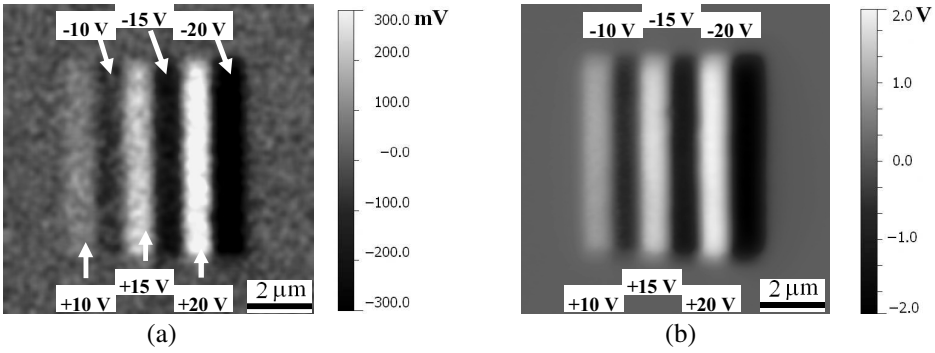

Figure 3: (a) Out-of-plane piezoresponse and (b) potential maps of area where a series of line domains have been written with different DC voltage.

piezoresponse and surface potential contrast (for locally modified area +20 V by $1 \times 6\,\mu m^2$) as a function of time (relaxation) is shown in Figure 4.

In other word, the contrast of the polarized areas increases with a poling voltage. As a result six stripes of $1 \times 6\,\mu m^2$ in size were created. The piezoresponse and surface potential images of the induced areas on the sample were obtained in the PFM and KPM modes immediately after writing (see Figures 3(a), (b)). The observed KPM image reveals a clear contrast due to the local contact potential difference and expected space charge redistribution.

In Figure 4, the surface potential contrast for poling line +20 V decreased from 2 V to 1.1 V for 144 min, but abrupt decay of surface potential contrast is observed in the first stage. Initial decrease of surface potential contrast is larger than any other one, and it is mostly attributed to the charge migration from neighbor's areas. For PFM images observed more rapid relaxation of a polarized state. Again, the solid line of Figure 4 shows the fitting parameters by formula (1). The relaxation time (t_0) of poling line is 25 min for KPM measurements and $\sim$ 8 min for PFM

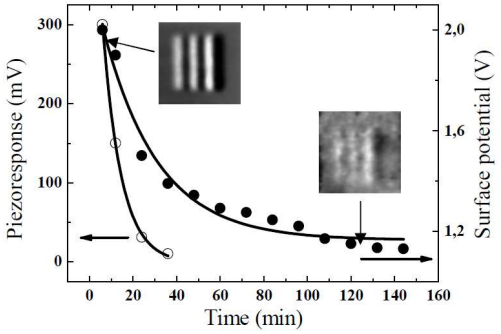

Figure 4: Comparison a relaxation of PFM (open circles) and KPM (solid circles) images in $LiNbO_3$ thin films for +20 V poling line. The inset present of KPM images ($10 \times 10\,\mu m^2$) taken immediately after poling, and after 2 h.

images. This surface potential relaxation is originated from the Coulomb repulsion and retention loss phenomena of domains. Even if there are many charges around the domain, the Coulomb repulsion force makes them unstable, and it leads them to be apart from the initial domain area. In other words, if there are many charges on the surface of domain, these charges would be unstable state by the Coulomb repulsion, and they should be go back to their initial position when the high potential is removed.

4. CONCLUSIONS

Scanning probe microscopy has been used to perform nanoscale qualitative characterizations on $LiNbO_3$ films RF sputtered on silicon-based substrates. Imaging of domain structures and domain switching combined with structural investigations provide a direct evidence of the influence of the nature of the substrate on the physical properties of as-grown heterostructures. These results suggest that it may be possible to fabricate novel structures combining the ferroelectric and optical capabilities of $LiNbO_3$ with both the electronic processing advantages of Si.

ACKNOWLEDGMENT

This study was supported by the Program for Creation and Development of the National University of Science and Technology "MISiS" and by the Federal Program "Research and Development in priority development areas of scientific and technological complex of Russia in 2007–2013." Investigations were carried out on equipment Joint Use Center "Materials Science and Metallurgy" (NUST "MISiS").

REFERENCES

1. Kiselev, D. A., A. L. Kholkin, A. A. Bogomolov, O. N. Sergeeva, E. Y. Kaptelov, and I. P. Pronin, "Piezo- and pyroelectric hysteresis in thin unipolar PZT films," *Tech. Phys. Lett.*, Vol. 34, 646–649, 2008.
2. Gautier, B. and V. Bornand, "Nanoscale observation of the distribution of the polarization orientation of ferroelectric domains in lithium niobate thin films," *Thin Solid Films*, Vol. 515, 1592–1596, 2006.
3. Bornand, V., B. Gautier, and P. Papet, "Growth and nanoscale ferroelectric investigation of radio frequency-sputtered $LiNbO_3$ thin films," *Mater. Chem. and Phys.*, Vol. 86, 340–346, 2004.
4. Bornand, V. and P. Papet, "Growth technologies and studies of ferroelectric thin films-application to $LiTaO_3$ and $LiNbO_3$ materials," *Ferroelectrics*, Vol. 288, 187–197, 2003.
5. Zhukov, R. N., D. A. Kiselev, M. D. Malinkovich, Y. N. Parkhomenko, E. A. Vigovskaya, and O. V. Toropova, "The spreading of the polarization of the ferroelectric granules in the electrically insulated lithium niobate foiles," *Materials of Electronic Technics*, No. 4, 12–16, 2011 (in Russian).
6. Hong, S., J. Woo, H. Shin, J. U. Jeon, Y. E. Pak, E. L. Colla, N. Setter, E. Kim, and K. No, "Principle of ferroelectric domain imaging using atomic force microscope," *Jour. Appl. Phys.*, Vol. 89, 1377–1386, 2001.

Evidence of Very Strong Low Frequency Magnetic Fields

A. Meessen
Institute of Physics, Catholic University of Louvain, 1348, Louvain-la-Neuve, Belgium

Abstract— We have shown *why* the propulsion of Unconventional Flying Objects of unknown origin can result from very intense low-frequency magnetic fields and an adequately pulsed ionization of the ambient medium. We also found *how* these fields could be produced, if the surface of these objects were superconducting. Now, we present *evidence of the existence of these fields.* It results from traces left on the ground by induced currents, rotating compass needles, direct magnetometer recordings and very remarkable magneto-optical effects. They provide even proof of the required pulsed ionization.

1. INTRODUCTION

Since spheres or similar objects could produce very intense low frequency magnetic fields if their surface were superconducting [1] and since this would account for Pulsed EM Propulsion of Unconventional Flying Objects [2], it is necessary to verify if observational evidence of this type of magnetic fields is really available.

2. INDUCED CURRENTS AND SPINNING COMPASS NEEDLES

On May 11, 1969, a Canadian farmer was awakened by his dog and discovered then a hemispherical object with a rim, hovering or standing slightly above the ground at about 150 m from his farm [3]. Its diameter was close to 10 m, but its luminosity was so intense that the witness had to protect his eyes. The following morning, he found there *a large ring, where the soil was depressed and dehydrated* (Figure 1). Its external diameter was 9.6 m and its width 90 cm. There were also three round 20 cm wide and 8 cm deep imprints, forming an equilateral triangle. They were attributed to the landing gear and the weight of the object, while the large ring could result from currents induced in humid soil by an oscillating magnetic field.

A vertical oscillating magnetic dipole of moment M and frequency ω produces an induced electric field $E = \omega(M/r^2)\sin\theta\sin\omega t$, whith circular horizontal field lines [1, 2]. The resulting current density $J = \sigma E$, where σ is the conductivity of the ground, increased by ionization. The soil will thus be heated. For an object that is situated at a hight h above the ground, the average dissipated power $P = \sigma E^2 = \sigma\omega^2 M^2 x^2/2(h^2 + x^2)^3$, when x is the distance from the symmetry axis. The maximum would be reached for $x = h/\sqrt{2}$ and after some time, the temperature could reach there 100°C and even more, when excess water was evaporated. Since *Pulsed EM Propulsion* (PEMP) predicts downwards oriented forces that are maximal for the same circle, the associated depression of the ground can also be explained. Even *circles of molten ice* have been observed, and ice has a higher conductivity than liquid water.

Capt. Ruppelt of the USAF investigated a related incident that happened on August 19, 1952 in Florida [4]. Since a scoutmaster thought that a plane had crashed, he searched for it and got under a large, silently hovering disk. He mentioned that the air was "oppressively moist". Capt.

Figure 1: Physical trace, due to currents.

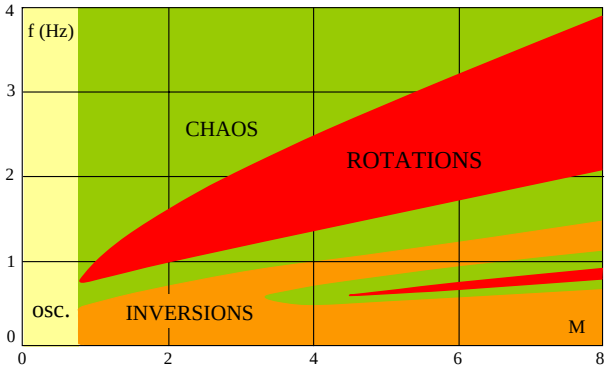

Figure 2: Possible behavior of compass needles.

Ruppelt sent lumps of earth and vegetation to a laboratory, where it was discovered that *the roots were charred,* while the grass blades were intact. The investigator suggested that this might be due to induction heating, but he didn't follow up. The electrical engineer Thomas [5] proposed an explanation that is similar to the present one, but Ruppelt didn't mention a ring and we can directly relate these observations to the propulsion system.

Another set of remarkable observations were made by pilots, who saw that *the needle of the magnetic compass was steadily rotating* when an Unconventional Flying Object accompanied their plane. This behavior was not obvious for us, since the PEMP model would only yield a magnetic field that oscillates *along a given direction* at the scale of the compass. Thus, we studied this phenomenon in detail [6]. Subjecting a compass for map reading to a magnetic field of modifiable magnitude M and modifiable frequency f, oscillating along a direction that is different from the N-S direction, we found various results (Figure 2). For low values of M, the neeedle oscillates only around the N-S direction with a resonance effect (yellow part). For very low frequencies, the needle simply follows the inversions of the magnetic field (orange part). It is possible, however, to set the needle in *steady rotation* (red parts), although the needle is subjected to viscous friction. At somewhat lower or higher frequencies, the needle turns towards the left or the right in an unpredicatble way (green parts).

This system allows thus for "order or chaos". The equation of motion is *nonlinear*, indeed, but it can be solved by numerical integration. This proves that the needle is exactly rotating at the frequency of the applied field with small superposed vibrations. Haines and Weinstein [7] provided 64 pilot reports, involving EM effets of various types. They included rotations of compass needles (cases 11, 13, 23, 34, 38, 39, 45 and even 18, because of complementary data). Gyroscopic, electric magnezyn and radio compasses were also perturbed, but reactions of a magnetic compass needle are the most useful for our purpose. The needle was said to be spinning fast, wildly or crasily, but in some cases, it was slowly rotating (even at 4 to 5 turns/min). Estimated distances of the unconventional flying objects were of the order of 50 to 200 m, but all compasses on *a ship of the Argentinian Navy* were deviated when a large, round "airship" silently stayed at a distance of about 2000 m. This event was carefully studied to exclude any conventional cause [8]. Since the compasses had to be perturbed by a stronger magnetic field than 5.8×10^{-5} T and since a magnetic dipole field varies like $1/r^3$, its strength at a distance of 20 m (possibly corresponding to the surface of the object) exceeds 58 T, although the object was not accelerating.

A complementary observation [9] was made already on July 27, 1904, when *a British steamer* was approaching Delawere (USA). Shortly after sundown, a strange gray cloud was spotted at the horizon. It was round and nearly in tangential contact with the sea, with glowing spots that became more vivid when it silently came nearer. Suddenly, it enveloped the whole ship (90 m), where the (ionized) air glowed then "like phosphorous". It contained electric charges, since head and beard hairs of the crew members "stood straight on end". There was also an oscillating magnetic field, since Captain Urquhart saw that "*the needle of the compass revolved with the speed of an electric fan.*" Moreover, the sailors were unable to move iron chains lying on the steel deck. The ship was immobilized and after about 10 minutes, the witnesses felt it difficult to move their arms and legs. They also noticed a great silence, as if the air "would not carry sound". Very strong static or ELF magnetic fields are not really harmful [10], but can act on fluids in the inner ear. The luminous cloud left only after about half an hour. The chains could then be easily moved and the compass needle was again "steadily pointing towards the north".

3. MAGNETOMETER RECORDINGS

Ray Stanford founded in 1973 and directed a team (Project Starlight International) that was dedicated to *optical and electronic detection* of Unconventional Flying Objects. With the help of donors, they acquired various instruments, including radar, magnetometer, gravimeter and cameras. In 1974, they filmed at their base station in Texas a light that pulsated at 4 Hz and another one that pulsated at 30 Hz with nearly rectangular pulses. In 1978, Stanford got a tip from a scientist at White Sands that UFOs were often "plaguing" government facilities out there. On July 19, 1978 the team went there with its mobile laboratory and had the chance to make already at *Plains in Texas* and then at the north edge of the *White Sands Proving Ground, New Mexico,* magnetometer and simultaneous gravimeter (i.e., vertical accelerometer) recordings. The horizontal magnetic field was also recorded on July 27, 1978 at *Prescott National Forest in Arizona*. UFOs were seen and filmed in all three cases. We are grateful to Ray Stanford for providing extracts of these important recordings (Figures 3 and 4).

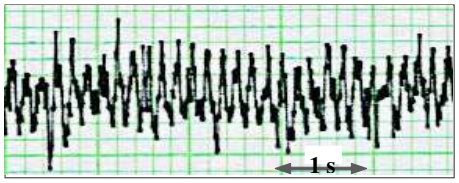

(a)

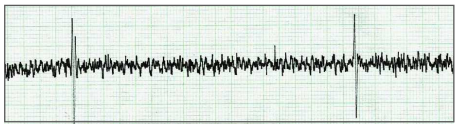

(b)

Figure 3: Extracts of magnetometer.

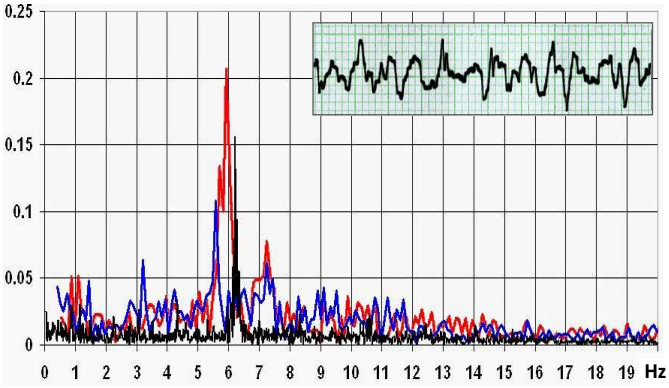

Figure 4: Spectrum of the magnetometer signal.

The oscillation of the magnetic field can be nearly harmonic (Figure 3(a)), but it usually is more irregular (insert of Figure 4). Since the witnesses saw a very great object and smaller ones, darting around, there could be some interference, but the *Fourrier spectrum* of three extracts of the recordings of July 27 (Figure 4) indicates the presence of many frequency components around 6 Hz. This is possible for the special oscillator [1] and yields steeper variations of the magnetic field. The induced electric field is then increased and also the efficiency of the propulsion system [2].

When the smaller, very red objects *suddently reversed their motions, there appeared "spikes" in the analog recording* (Figure 3(b) for two reversals of the same object, observed west of Plains, Texas). The witnesses heard loud rumbles and felt soft-tissue-shaking vibrations that were associated with these reversals and could result from plasma dynamic effects. Their delay with respect to the visually observed 180° or sometimes 90° turns indicated that this happened at about 1.6 km from the witnesses. Unfortunately, the instrument had not been calibrated to determine the magnitude of the recorded horizontal magnetic field component and to calculate the strength of the source. However, after the disappearance of all these objects it was immediately verified that the signal had been far above any background noise.

4. FARADAY EFFECT AND MAGNETO-REFRACTION OF EM WAVES

Anomalous Aerial Objects can also modify the propagation of EM waves, because of very intense magnetic fields and ionization of atmospheric air. Let's review and generalize the theory, by considering a *linearly polarized EM wave* of frequency ϖ that is propagating along a given z-axis. At $z = 0$, its electric field $\mathbf{E}$ is oriented along the x-axis, but this wave can be decomposed into two circularly polarized waves that propagate at different velocities. The x and y components of the corresponding electric fields $\mathbf{E}^{\pm}$ are $E_x = E^+ \cos\phi^+ + E^- \cos\phi^-$ and $E_y = E^+ \sin\phi^+ - E^- \sin\phi^-$, where the phase factors $\phi^{\pm} = k^{\pm} z - \varpi t$ and $E^{\pm} = E_o$. Thus, $E_x = E_o \cos\phi \cos\theta$ and $E_y = E_o \cos\phi \sin\theta$, where $\phi = kz - \varpi t$ with $k = (k^+ + k^-)/2$, while $\theta = \varphi z$ with $\varphi = (k^+ - k^-)/2$. This defines the velocity $v = \varpi/k$ of the linearly polarized light wave, while the plane of polarization is rotating at the rate $d\theta/dz = \varphi$. This requires that the circularly polarized waves are propagating at different velocities: $v^{\pm} = \varpi/k^{\pm} = c/n^{\pm}$, which happens when there is a magnetic field $\mathbf{B}$ along the z-axis. Indeed, the dielectric constant $\varepsilon^{\pm} = 1 + \mathbf{P}^{\pm}/\varepsilon_o \mathbf{E}^{\pm} = (n^{\pm})^2$, where the polarization densities $\mathbf{P}^{\pm}$ are respectively due to the $\mathbf{E}^{\pm}$ fields. $\mathbf{P}^{\pm} = Nq\mathbf{u}^{\pm}$ for a density N of particles of charge q and mass m, but the displacements $\mathbf{u}^{\pm}$ result from the equations of motion. Taking into account the magnetic field, we get $\ddot{u}_x = (q/m)\, E_x + \omega_c \dot{u}_y$ and $\ddot{u}_y = (q/m)\, E_y + \omega_c \dot{u}_x$, where $\omega_c = \mathrm{qB/m}$. It follows that $u_x = A^+ \cos\phi^+ + A^- \cos\phi^-$ and $u_y = A^+ \sin\phi^+ - A^- \sin\phi^-$. For low frequency magnetic fields and pulsed ionization, the values of B and N are practically constant during the lifetime of these particles. Thus,

$$A^{\pm} = \frac{\pm(q/m)E^{\pm}}{\varpi(\omega_c \mp \varpi)} \quad \text{and} \quad \varepsilon^{\pm} = 1 - \frac{\omega_o^2}{\varpi(\varpi \mp \omega_c)} \quad \text{where} \quad \omega_o^2 = \frac{Nq^2}{\varepsilon_o m}$$

Usually, we can assume that $\varpi \gg \omega_o$ and ω_c, so that

$$n^{\pm} = 1 - \frac{\omega_o^2}{2\varpi^2}\left[1 \pm \left(\frac{\omega_c}{\varpi}\right) + \left(\frac{\omega_c}{\varpi}\right)^2\right] \quad \text{and} \quad \varphi = \frac{-\omega_o^2 \omega_c}{2c} = \frac{e^2 N B}{2c\varepsilon_o m^2} \tag{1}$$

The rate φ of the Faraday rotation along the z-axis is *proportional to the local value of B and the local density N of free electrons.* There are no second order effects and the action on ions is negligible. However, the velocity of the wave is $v = c/n$, where

$$n^2 = \varepsilon = \frac{(\varepsilon^+ + \varepsilon^-)}{2} = 1 - \frac{\omega_o^2}{(\varpi^2 - \omega_c^2)} \to 1 - \frac{\omega_o^2}{\varpi^2}\left(1 + \frac{\omega_c^2}{\varpi^2}\right). \tag{2}$$

The index of refraction n *decreases* for high ionization densities and even more for extremely intense magnetic fields. This effect is proportional to B^2 and could account for the fact that *optically visible UFOs* are *not always detectable by radar.* Microwave beams could simply be deflected by progressive refraction, without requiring any other cloaking system.

The result (2) can also account for the *perturbation of the autopilot system of airplanes, guided by VOR* (very-high frequency omnidirectional radio contact). Dr. Haines reported that this happened on March 12, 1977 for a DC-10 of United Airlines during a non stop flight from San Francisco to Boston (case 41 of Reference [7]). When the aircraft was just south of Syracuse NY and flying by radio navigation through VOR contact with Albany, *the airplane suddenly and unexpectedly began to turn left, making a 15° bank.* The captain, first officer and flight engineer saw then "an extremely white light source" at their left side and at about their own altitude (37,000 feet). This perfectly round light had an estimated diameter of about 30 m and kept a distance of about 1000 m. Its angular size was thus larger than three times the apparent diameter of the moon. Three cockpit compasses, using sensors in different parts of the plane, gave different readings, but the essential point is that the VOR system combines two signals emitted by a given ground station. One of them is omnidirectional, while the other corresponds to a narrow rotating beam, where the phase of the EM wave changes from 0 to 360° in proportion to the azimuth. When this beam is deflected by an intermediate magnetic field and the presence of free electrons, the calculated azimuth is not the correct one.

There are also cases where very strange optical effects [11] were photographed below and above UFOs. Local luminosities result from ionization and extremely intense magnetic fields can prohibit transmission of background light when n^2 defined by (2), becomes negative.

The *Faraday Effect* was observed on May 5, 1953 by the chemist *Wells Allen Webb* near Yuma, Arizona, between 9:45 and 10:00 AM local time. He saw an elongated white object on an otherwise blue sky at about 90° with respect to the Sun. Scattered sky light was thus vertically polarized, while his Polaroid sunglasses blocked horizontally polarized light. Putting them on and off, no difference appeared when the object was steadily advancing sideways, but after about 5 minutes, it became a white circle. It had changed its direction of motion and was moving away, since it slowly vanished like that. However, when the witness was looking along its axis, there appeared *several dark rings* around the central light, every time he used the sunglasses [12]. These rings were nearly equidistant and their ensemble had the size of the full moon. This fits the theory of the Faraday Effect, since the plane of polarization of the scattered light could be rotated by 90° for the external circle and by additional 180° turns closer to the object, where the magnetic field and ionization were more intense. When the line of sight was orthogonal to the axis of the magnetic dipole, the plane of polarization was rotated at first towards one side and then towards the other. The total effect was zero, by symmetry.

Ray Stanford documentated this phenomenon in a very impressive way. On December 4, 1980, while flying fom Mexico City to San Antonio, Texas, he spotted anomalous objects in the sky, grabed his Super 8 Canon camera and filmed for about 25 s at 70 mm focal length. This happened after sunset, but the Sun was still illuminating the sky in the direction he was filming. Vertical sunrays were scattered in the west at about 90°, yielding horizontally polarized light that passed near the objects. The beam-splitter of the camera acted like an analyser, by reflecting mainly horizontally polarized light toward the film. Viewing the resulting pictures one by one, Ray Stanford discovered *in one frame an extraordinary set of at least 12 white concentric rings* (Figure 5).

They were centered on one of the small objects dashing in various directions. By chance, this picture was taken exactly at the instant where one these objects encountered a long unidentified structure (dark edge in Figure 5). To reverse its motion, the smaller object produced a very intense magnetic field and a short ionization pulse, the pictures being taken at 54 frames per second. The white rings resulted from horizontally polarized light and many 180° rotations near the object. Its symmetry axis was oblique with respect to the plane of the film, yielding ellipses instead of circles. It is possible to account for the progressive change of the distances between successive rings by considering the velocity $\mathbf{V}$ of free electrons in very strong magnetic fields and auto-ionization,

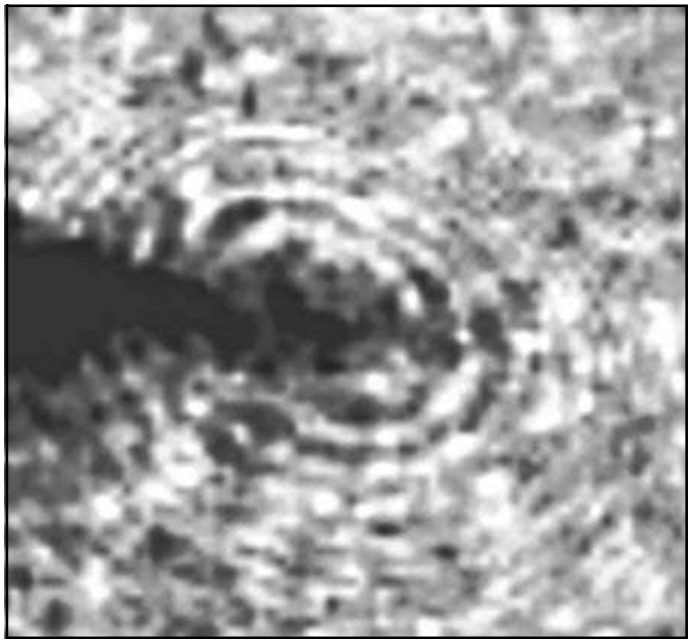

Figure 5: Ray Stanford's set of Faraday rings.

proportional to the average kinetic energy of free electrons. Ray Stanford discovered also some other Faraday rings on other occasions.

5. CONCLUSION

The general conclusion is that *the phenomenon of Unidentified Flying Objects merits scientific interest* and that its study raises questions that could foster progress in various fields. This includes the search of new types of superconductors, which could eventually be graded metamaterials.

REFERENCES

1. Meessen, A., "Production of EM surface waves by superconducting spheres: A new type of harmonic oscillators," Accepted by PIERS, 2012.
2. Meessen, A., "Pulsed EM propulsion of unconventional flying objects," Accepted by PIERS, 2012.
3. Bondarchuk, Y., Ovnis, 1979, http://www.geocities.ws/hbccufo/ontario1960.html.
4. Ruppelt, E. J., *The Report of Unidentified Flying Objects*, Ace Books, 232–245, 1956.
5. Thomas, J. K., "Ruppelt rings," *MUFON UFO Journal*, 197, Sep. 1984.
6. Meessen, A., VOB2, SOBEPS, 1994 and 2001, http://www.meessen.net/AMeessen/Boussole/.
7. Haines, R. F. and D. F. Weinstein, http://www.narcap.org/reports/emcarm.htm.
8. http://www.nicap.org/madar/arg.htm.
9. http://www.waterufo.net/item.php?id=1308; http://www.flickr.com/photos/robert_a_goerman/5410100905/.
10. Kangarlu, A. and P. M. Robitaille, 2000, http://www.imrser.org/PDF/Kangarlu.Concepts.Mag%20Res.pdf.
11. Ballester Olmos, V. G., UFOCAT Report #6, http://www.ikaros.org.es/fotocat/approach.pdf.
12. Harder, J. A., *Hearing Committee on Science and Astronautics*, US House of Representatives, Jul. 29, 1968, http://project1947.com/shg/symposium/harder.html.

Production of EM Surface Waves by Superconducting Spheres: A New Type of Harmonic Oscillators

A. Meessen
Institute of Physics, Catholic University of Louvain, Louvain-la-Neuve 1348, Belgium

Abstract— It is shown that a superconducting sphere or spherical shell can produce EM surface waves that are stationary at *any* low frequency. This applies in particular to *magnetic dipole oscillations*, generated by a current density **J** that oscilllates around a given axis on the surface of the sphere. In the quasistatic approximation, it creates a synchronously oscillating magnetic field **B**, while the resulting electric field **E** provides feedback to sustain the current. This yields a new type of oscillators, where the magnetic energy is not completely transformed into electric energy as in classical LC circuits. EM energy is conserved, however, by means of energy fluxes. The purpose of this theory is to account for *evidence of very intense magnetic dipole fields*, produced by unconventional flying objects of unknown origin. These observations would make sense and suggest that superconductivity is possible at normal atmospheric temperatures. We also examine the propagation of plasma waves along superconducting surfaces and consider possible pairing mechanisms.

1. INTRODUCTION

This research was motivated by the fact that the propulsion system of "Unconventional Flying Objects" (UFOs) can be explained when we assume that they are able to produce very intense dipolar magnetic fields, oscillating at low frequencies [1]. We want thus to find out how these fields could be produced and if they have a finite range as well as other special properties. There is also an intrinsic, physical reason. Indeed, EM waves were initially produced as "surface waves", since Heinrich Hertz tried to verify the validity of Maxwell's theory by coupling *a long metal wire* to an LC circuit [2, 3]. The HF oscillating current, surrounded by oscillating electric and magnetic fields, was reflected at the end of the wire. This should produce a standing wave pattern and allow for an indirect measurement of the velocity c, but the EM surface wave was also reflected by laboratory walls. This perturbed the experiment so much, that Hertz prefered to use an oscillating electric dipole, emitting freely propagated EM waves. Since Lecher found that *two parallel wires* produce much more concentrated EM surface waves, he could realize the initially projected measurement [4]. Considerable effort was then devoted to the theoretical understanding of wave guides, formed by a single wire [5] and two parallel wires of finite conductivity [6].

Zenneck [7] considered the propagation of EM surface waves along *an infinite plane surface*, separating air from a material of given conductivity σ and dielectric constant ε. This problem was also treated by other authors [8–10]. EM surface waves were then considered for thin metal films, to account for characteristic electron energy losses [11] and optical resonance absorption [12]. These effects result from the creation of surface plasmons. Here, we consider stationary EM surface waves for a superconducting sphere and EM waves that propagate along a superconducting plane. Since UFOs are topologically equivalent to a sphere, we will adopt this model to concentrate on essential features. The nature of the surface material is unknown, but it is sufficient that it contains a high density of electron pairs to be a superconductor, obeying known physical laws. To evaluate the intrinsic properties of this system, we assume here that the outside medium contains no free charges.

2. BASIC EQUATIONS

The *quasistatic approximation* is valid for electric fields **E** and magnetic fields **B** that oscillate at extra-low frequencies (ELF) in a portion of space that is small compared to the corresponding wavelength. Retardation effects can then be neglected, as if c were infinite. For nonmagnetic and electrically neutral media, Maxwell's equations are thus reduced to

$$\boldsymbol{\nabla} \times \mathbf{B} = \mu_o \mathbf{J} \quad \text{and} \quad \boldsymbol{\nabla} \cdot \mathbf{B} = 0 \tag{1}$$

$$\boldsymbol{\nabla} \times \mathbf{E} = -\partial_t \mathbf{B} \quad \text{and} \quad \boldsymbol{\nabla} \cdot \mathbf{E} = 0 \tag{2}$$

J is the current density, acting as a source. We can also use the vector potential **A**, since

$$\mathbf{B} = \boldsymbol{\nabla} \times \mathbf{A} \quad \text{and} \quad \mathbf{E} = -\partial_t \mathbf{A} \tag{3}$$

$$\Delta \mathbf{A} = -\mu_o \mathbf{J} \quad \text{and} \quad \boldsymbol{\nabla} \cdot \mathbf{A} = 0 \tag{4}$$

We will solve these equations *inside and outside a superconducting sphere* or spherical shell of radius R. The outside medium is unionized air, where the current density $\mathbf{J} = 0$, but the superconducting material contains *free electron pairs* (of mass $2\,m$ and charge $-2e$). Being bosons, they remain in their ground state of momentum $\mathbf{p} = 2(m\mathbf{v} - e\mathbf{A}) = 0$. When n is the density of electrons in the superconducting state, the current density $\mathbf{J} = -en\mathbf{v}$, since there are $n/2$ electron pairs of charge $2e$. Thus,

$$\mu_o \mathbf{J} = -\alpha^2 \mathbf{A} \quad \text{where} \quad \alpha^2 = \mu_o n e^2/m = \mu_o s \tag{5}$$

Combining (5) with (4), we get two equations for **A** alone:

$$\Delta \mathbf{A} = \alpha^2 \mathbf{A} \quad \text{with} \quad \boldsymbol{\nabla} \cdot \mathbf{A} = 0 \tag{6}$$

They are valid outside and inside the sphere, where α is either zero or very great. This parameter is essential for the current density **J**, which is not only the source of **E** and **B**, but depends also itself on these fields. However, Ohm's law is not valid anymore inside a superconductor. It has to be replaced by *the London equations*

$$\partial_t \mathbf{J} = s\mathbf{E} \quad \text{and} \quad \nabla \times \mathbf{J} = -s\mathbf{B} \tag{7}$$

Since electron pairs cannot leave the state $\mathbf{p} = 0$, their equation of motion would be $2m\partial_t \mathbf{v} = -2e\mathbf{E}$ when $\mathbf{B} = 0$. The second Equation (7) accounts for the Meissner effect and the finite penetration depth of magnetic fields inside superconductors. We are actually considering *a macroscopic quantum state* with a rather stable wavefunction.

3. MAGNETIC DIPOLE OSCILLATION

Now, we solve Equation (6) to determine the vector potential **A** and the resulting fields **E** and **B** when the current density **J** is oscillating at frequency ω on the surface of the superconducting sphere around a given z-axis. Using spherical coordinates (r, θ, φ), we set

$$\mathbf{J} = (0, 0, J)\cos\omega t \quad \text{and} \quad \mathbf{A} = (0, 0, A)\cos\omega t \tag{8}$$

Because of (5), $\mu_o J = -\alpha^2 A$. The second Equation (6) requires that $A = A(r, \theta)$ and (3) yields

$$\mathbf{E} = \omega(0, 0, A)\sin\omega t \quad \text{and} \quad \mathbf{B} = (B_r, B_\theta, 0)\cos\omega t \tag{9}$$

with

$$rB_r = \frac{1}{\sin\theta}\partial_\theta(\sin\theta A) \quad \text{and} \quad rB_\theta = -\partial_r(rA) \tag{10}$$

At the poles, $J = A = 0$. The simplest solution of the first Equation (6) corresponds thus to

$$A = \frac{u(r)}{r}\sin\theta \quad \text{where} \quad u'' - \frac{2}{r^2}u = \alpha^2 u$$

Outside the sphere, $\alpha = 0$, so that $u(r)$ decreases like $1/r$ for increasing distances from the center of the sphere. Inside the sphere, we could use Bessel functions for $u(r)$, but it is sufficient to consider an exponential decrease towards the inside of the sphere (for $r \approx R$ and $\alpha R \gg 1$). Distinguishing solutions outside and inside the sphere by subscripts + (when $r > R$) and − (when $r < R$), we get

$$A^+ = \frac{M}{r^2}\sin\theta \quad \text{and} \quad A^- = \frac{M}{Rr}e^{\alpha(r-R)}\sin\theta \tag{11}$$

This accounts for the continuity of the tangential component of **E**, defined by (9). Because of (10), the components of the magnetic field **B** are

$$B_r = \frac{2u(r)}{r^2}\cos\theta \quad \text{and} \quad B_\theta = \frac{-u'(r)}{r}\sin\theta$$

Thus,

$$B_r^+ = \frac{2M}{r^3}\cos\theta \quad \text{while} \quad B_r^- = \frac{2M}{Rr^2}e^{\alpha(r-R)}\cos\theta \tag{12}$$

$$B_\theta^+ = \frac{M}{r^3}\sin\theta \quad \text{while} \quad B_\theta^- = \frac{-\alpha M}{Rr}e^{\alpha(r-R)}\sin\theta \tag{13}$$

Outside the sphere, we get *a perfect magnetic dipole field*, but inside the superconducting sphere, the fields **E** and **B** decrease very rapidly, since the penetration depth $1/\alpha$ is small compared to R. The radial component of **B** is continuous at the surface, but the tangential component is not. This requires *a surface current density* $\mathbf{J}_s = (0, 0, J_s)\cos\omega t$, where

$$\mu_o J_s = B_\theta^+ - B_\theta^- = \alpha\frac{M}{R^2}\sin\theta \qquad (\text{for } \alpha R \gg 1) \tag{14}$$

Inside the sphere, the volume current density (8) is also parallel to the surface, but has the opposite sign and for $r = R$, its magnitude is α times greater than (14). The quasi-infinite surface current density J_s accounts for the Meissner effect or perfect diamagnetism. We could also consider other multipole oscillations, but magnetic dipole oscillations are sufficient to become aware of remakable facts.

4. ENERGY CONSERVATION AT ANY LOW FREQUENCY

LC circuits are based on a complete conversion of magnetic energy into electric energy and vice-versa. These energies are respectively associated with the magnetic field **B** near the current carrying coil and the electric field **E** inside the charged condensor. However, there are no condensors that could prevent breakdown for extremely intense electric fields, while EM surface waves around a spherical superconductor yield *non segregated* electric and magnetic fields. Moreover, there is *no eigenfrequency* as for LC circuits. Any low frequency ω is possible and *it is not necessary to convert the whole magnetic energy into electric energy*, although we have to consider work done by the electric field **E**. Since it acts on electron pairs inside the superconductor, the dissipated power per unit volume is

$$P = \mathbf{J}\cdot\mathbf{E} = JE\sin\omega t\cos\omega t$$

It varies like $\sin 2\omega t$, but (1) and (2) lead to *a special form of Poynting's theorem* in the quasistatic approximation:

$$P = -\boldsymbol{\nabla}\cdot\mathbf{S} - \partial_t U \quad \text{where} \quad \mathbf{S} = (\mathbf{E}\times\mathbf{B})/\mu_o \quad \text{and} \quad U = B^2/2\mu_o$$

S defines the energy flux, which varies also like $\sin 2\omega t$. The magnetic energy density U varies like $\cos^2\omega t$, but its time derivative is proportional to $\sin 2\omega t$. For radiation in free space, we would have to consider also the electric energy $\varepsilon_o E^2/2$, where $\varepsilon_o = 1/\mu_0 c^2$, which is negligible when c is quasi-infinite and there are no static charges. With the previous notations, energy conservation would thus require that

$$\mu_o JE = -\frac{1}{r^2}\partial_r(r^2 EB_\theta) + \frac{1}{r\sin\theta}\partial_\theta(\sin\theta EB_\theta) - \omega(B_r^2 + B_\theta^2)$$

Setting $J = j(r)\sin\theta$, $B_r = F(r)\cos\theta$, $B_r = G(r)\sin\theta$ and $E = H(r)\cos\theta$, where j, F, G and H are defined by (8), (9), (11), (12), (13) and (14), the energy conservation would be insured if

$$\mu_o jH = -\frac{1}{r^2}\partial_r(r^2 HG) + \frac{3}{r}HF + \omega(F^2 - G^2) \quad \text{and} \quad \frac{2}{r}HF = \omega F^2$$

This is easily verified outside the superconductor, where $j = 0$, but is also true inside the superconductor, where all these functions are exponentially decreasing towards the center of the sphere, with $\alpha R \gg 1$. To account for the surface current density $\mathbf{J}_s$ we enclose an element of unit surface at the interface between two infinitely close parallel surfaces. Inside this layer, the dissipated power is $P_s = J_s E$, while the magnetic energy is zero. However, the energy flux **S** has a discontinuous radial component:

$$S_r^\pm = -\frac{1}{\mu_o}EB_\theta^\pm \quad \text{so that} \quad J_s E = -(S_r^+ - S_r^-)$$

This is equivalent to the definition (14) of J_s. The total energy is *always and everywhere* perfectly conserved, but not only because of the absence of resistive and radiative energy losses. It is also due to the quasistatic approximation, allowing for energy fluxes.

5. PROPAGATION OF SURFACE PLASMA WAVES

For a more complete exploration of this matter, we consider also EM waves that are propagating along the surface of a superconductor. Even a small portion of a large spherical surface can be treated like a plane, when the wavelength is small compared to the radius of this sphere. Using Cartesian coordinates, where the x-axis is normal to this surface, situated at $x = 0$, we consider an EM wave that propagates along the y-axis:

$$\mathbf{A} = (A_x, A_x, 0)e^{i(ky-\omega t)} \quad \text{and} \quad \mathbf{B} = (0, 0, B)e^{i(ky-\omega t)}$$

while $\mathbf{J} = -s\mathbf{A}$ and $\mathbf{E} = i\omega\mathbf{A}$. The divergence and the curl of $\mathbf{A}$ yield

$$\partial_x A_x + ikA_y = 0 \quad \text{and} \quad B = \partial_x A_y - ikA_x$$

We set $A_x = a^{\pm}u^{\pm}(x)$, $A_y = au^{\pm}(x)$ and $B = b^{\pm}u^{\pm}(x)$, where the + and − signs do correspond to $x > 0$ and to $x < 0$ (outside and inside the superconductor). This accounts for the fact that the tangential component of $\mathbf{E}$ has to be continuous, while the amplitude of the oscillations decreases exponentially towards the inside and the outside of the superconducting material: $u^-(x) = e^{\beta x}$ and $u^+(x) = e^{-\gamma x}$, where

$$\gamma a^+ = -\beta a^- = ika, \quad \gamma b^+ = (k^2 - \gamma^2)a \quad \text{and} \quad -\beta b^- = (k^2 - \beta^2)a$$

The purely tangential magnetic field is continuous, when $k^2 = \beta\gamma$ and $b^{\pm} = (\beta - \gamma)a$. No surface current density is required, but the first Equation (6) becomes $\Delta\mathbf{A} - \partial_{ct}^2\mathbf{A} = \alpha^2\mathbf{A}$. This yields the dispersion relation $(\omega/c)^2 = k^2 - \gamma^2$ and $\beta^2 = \alpha^2 - \gamma^2$. We can set $\gamma \approx 0$, $\beta \approx \alpha$ and $\omega \approx ck$. The surface wave is thus nearly propagating at the velocity c and extending far outside the superconductor ($a^- \approx 0$), but the normal component of the electric field is discontinuous at the interface. This yields oscillating surface charge densities, characteristic of surface plasma waves.

6. THE PAIRING MECHANISM

Production of low frequency *stationary* EM surface waves should be verifiable by means of low temperature superconductors. However, this theory applies also to *Unconventional Flying Objects* of unknown origin, since there is evidence that they produce very intense magnetic fields, oscillating at extra-low frequencies [13]. These facts seem to imply that *superconductivity is possible at atmospheric temperature and even higher ones.* That would be of tremendous theoretical and practical importance, but requires the existence of a yet unknown mechanism, gluing two electrons together with a pairing energy $\Delta \approx kT_c$, where T_c is the higher transition temperature.

Any electron repels other electrons and attracts positive ion cores inside a solid. We know that this leads to Debye-Hückel screening, but other processes are also possible. Since ionic motions are slow, they create a wake of positive charge that can attract another electron. This was the basic idea of the BCS theory, where electron pairing was attributed to an exchange of virtual phonons. That accounts for conventional low-temperature superconductivity, but not for *high-T_c superconductivity* (HTS), where the transition temperature T_c is of the order of 100 K. Even 20 years after its discovery, one could say that "the physics behind this strange state of matter remains a mystery" [14]. Many ideas were proposed and experiments yielded so many surprizing results that "we can expect the unexpected" [15]. This justifies even the search for normal temperature superconductivity.

To elucidate the pairing mechanism for HTS, Dal Conte et al. measured the relaxation times in one type of cuprate superconductors for very short pulses of optical excitation [16]. They concluded that electron-phonon interactions contribute much less to the "glue" than *collective electronic excitations,* such as spin fluctuations for instance. Gademaier et al. [17] performed similar measurements for pnictides, cuprates and bismuthates, but they concluded that their T_c depends mainly on the strength of electron-phonon interactions. They added even that the experimental results are only consistent with *bipolaronic pairing.* A polaron is an electron that is accompanied by mobile lattice distorsions, corresponding to a cloud of virtual phonons. Optical phonons have higher energies than acoustic phonons and allow for the formation of small "bipolarons" [18], where two electrons are bound to one another by means of local polarization waves. Today, the theory of superconducting bipolarons is well developed [19, 20]. Although it is quite complex, the basic ideas can be explained in terms a simple model [21]. These ideas were also illustrated by the impotance of the large polarizability of As anions in Fe-based superconductors [22], involving bound electrons.

Normal temperature superconductvity (NTS) seems to require another pairing mechanism. There are already propositions for room-temperature superconductivity [23, 24]. Since layered structures are essential for known high-T_c superconductors and since the present model for the production of very strong low frequency magnetic fields requires only superconductivity for the outer surface of UFOs, it is quite probable that it involves the Electrodynamics of Inhomogeneous Media and Gradient Metamaterials. Moreover, the dielectric constant of free electrons and electron pairs tends toward $-\infty$, when the frequency becomes very small, which has also an effect on image forces. Anyway, the theoretical results presented here, combined with empirical data [1, 13], seem to justify further research of materials that allow for superconductivity at normal atmospheric temperatures and even higher ones.

7. CONCLUSIONS

We found that it is *possible* to generate very intense, low frequency EM surface waves by means of superconducting spheres and that such a system has *remarkable properties.* It is thus important to examine evidence that Unconventional Flying Objects of unknown origin do produce magnetic dipole oscillations of this type. It suggests that *superconductivity is possible at normal temperature and even higher ones,* which justifies the search of a new pairing mechanism of electrons.

It could involve *virtual plasmons* instead of virtual phonons, but we don't know the material that constitutes the external surface of UFOs. Since the type of superconductivity we are considering has only to exist near their outer surface, it may involve surface effects. Anyway, it appears that an objective study of the UFO phenomenon without preconceptions or beliefs is necessary and useful. It raises questions of a new type, which is always important for basic and applied science. It could stimulate the search of normal temperature superconductivity and motivate the conception of new Graded Metamaterials or some other physical process.

REFERENCES

1. Meessen, A., "Pulsed EM propulsion of unconventional flying objects," Accepted by PIERS, 2012.
2. Hertz, H., *Ann. Physik*, Vol. 270, 155, 1888.
3. Hertz, H., *Electrical Waves*, 1893, Dover, 1962.
4. Lecher, E., *Phil. Mag.*, Vol. 30, 128, 1890.
5. Sommerfeld, A., *Ann. Phys.*, Vol. 67, 233, 1899.
6. Mie, G., *Ann. Phys.*, Vol. 6, 201, 1900.
7. Zenneck, J., *Ann. Phys.*, Vol. 23, 846, 1907.
8. Frank, P. and R. V. Mises, *Die Differential- und Integralgleichungen der Mechanik und Physik*, Vol. 2, 876–895, 919–940, Vieweg, 1935.
9. Epstein, P. S., *Proc. Nat. Ac. Sc.*, Vol. 40, 1158, 1954.
10. Sturm, K., *Z. Physik*, Vol. 209, 329, 1968.
11. Ritchie, R. H., *Phys. Rev.*, Vol. 106, 874, 1957.
12. Steinmann, W., *Phys. Stat. Sol.*, Vol. 28, 437, 1068.
13. Meessen, A., "Evidence of very strong low frequency magnetic fields," Accepted by PIERS, 2012.
14. Timusk, T., *Physics World*, 31–35, July 2005.
15. Cover Story, *Nature Physics*, Vol. 2, March 2006.
16. Dal Conte, S., et al., *Science*, 335, 1600–1603, 2012.
17. Gademaier, C., et al., ArXive: 1205.4978.
18. Alexandrov, A. S., *Phys. Rev. B*, Vol. 38, 925–927, 1988.
19. Alexandrov, A. S., ArXive: 0803.3666.
20. Devreese, J. and A. S. Alexandrov, ArXive: 0904.3682.
21. Komyushin, Y., ArXive: 0702259.
22. Berciu, M., et al., ArXive: 0811.02, *Phys. Rev. B*, Vol. 78, 214507, 2009.
23. Mourachkine, A., *Room-temperature Superconductivity*, Cambridge Intl. Sc. Publication, 2004.
24. Pickett, W. E., ArXive: 0603482.

An Ultra-wideband Dielectric Resonator Antenna with Reconfigurable Band Rejection

M. Y. Abou Shahine, **M. Al-Husseini**, **K. Y. Kabalan**, **and A. El-Hajj**
ECE Department, American University of Beirut, Beirut 1107 2020, Lebanon

Abstract— The design of an ultra-wideband (UWB) dielectric resonator antenna with reconfigurable band rejection is presented in this paper. The induced band notch helps to limit interference to a narrowband service operated inside the UWB frequency range. The proposed antenna is based on a cylindrical dielectric resonator (DR) with a relative permittivity of 12, which is excited by a bevel-shaped patch printed on a Rogers RO3203 substrate over a partial ground plane. A rectangular split-ring slot is etched on the microstrip-line-fed patch, and is responsible for the creation of a band notch. A DC stepper motor, placed below the substrate, is used to rotate the DR and change its position with respect to the patch and the slot. As a result of the DR rotation, notch reconfigurability is achieved over the lower part of the UWB range, where most narrowband systems operate.

1. INTRODUCTION

Dielectric Resonator Antennas (DRAs) have undergone important development and received attention due to their attractive features and advantages. Compared to typical antennas where radiation occurs from conducting edges only, DRAs have the vital feature of radiating in the entire sphere, which leads to higher radiation efficiency. DRAs have a compact size, light weight, low cost, and high versatility regarding their shapes. Moreover, they have several feeding mechanisms (probes, slots, microstrip lines, ...) and have the characteristic of being excited in various modes producing different radiation patterns. A larger bandwidth is also an advantage offered by DRAs [1].

Due to these appealing features, there has been extensive work by antenna engineers and researchers to create new and effective DRA designs, including ones with enhanced wideband operation, and other designs with notched bands. The trapezoidal DRA reported in [2] exhibits a larger bandwidth than the common rectangular DRA by treating the dielectric trapezoid as a geometrical extension of the dielectric rectangle. In [3], a simple cylindrical DRA is designed to enhance the bandwidth by simply exciting two radiating modes with similar radiation characteristics. The wideband circularly polarized DRA in [4] is designed with a quadruple strip feed utilizing a pair of 90° hybrid couplers. In [5], a wideband rectangular DRA design offers a wider bandwidth with the use of high dielectric constant material. A dual-mode bridge-shaped DRA of high permittivity materials is designed and reported in [6]. It is used in multiband operation by coupling with a rectangular dielectric slab. In [7], a DRA combined with a quarter-wave monopole is designed so that the antenna can simultaneously act as a radiator and a loading element to produce an ultra wide bandwidth. The UWB DRA in [8] is designed to match several wireless and microwave applications. Band notched DRAs are also designed to minimize the interference between the UWB system and some narrowband systems such as WiMAX and WLAN. In [9], a dual-band DRA is designed to create notches in the WiMAX and WLAN bands by splitting a rectilinear DR and removing some of the dielectric material.

Whereas the notches induced by the design in [9] are fixed, reconfigurable notches are often required when the narrowband services to which interference should be avoided are changing. Several microstrip antennas with reconfigurable band rejection are reported in [10–12]. In [10], a reconfigurable bandstop filter is embedded in the feed line of a microstrip-fed patch antenna to obtain dual reconfigurable band stops. Cascaded complementary split-ring resonators (CSRRs) are embedded on the patch of the antenna in [11]. These CSRRs, which are controlled using electronic switches, induce a band stop that occurs at one of three frequencies. In [12], a single CSRR is etched on the patch, but several switches are mounted over it and are used to configure the band rejection. Three CSRRs are operated independently in [13], and hence three separate band notches are generated and can be controlled.

In this paper, we introduce a UWB DRA with a reconfigurable band rejection to help limit interference to different narrowband services operating inside the 3.1–10.6 GHz UWB frequency range. The reconfigurability of the notch is achieved by rotation of the dielectric resonator part of the antenna. The geometry and the design guidelines of the proposed antenna structures are

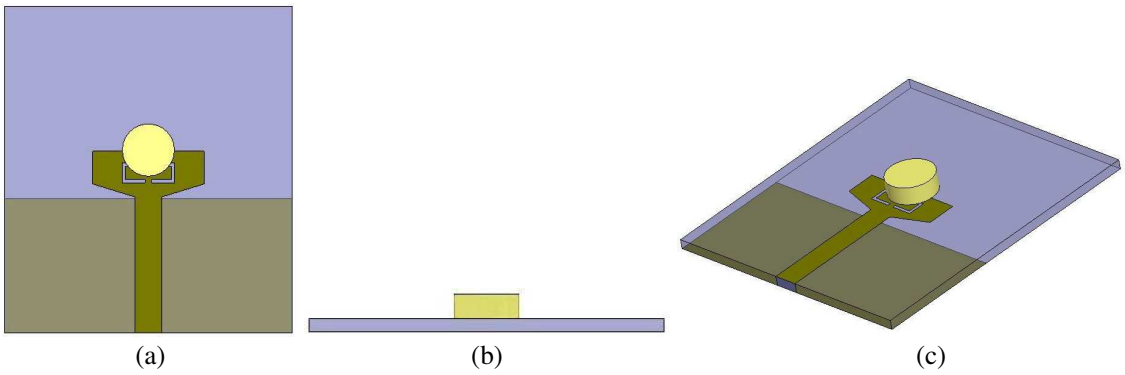

Figure 1: Geometry of the proposed antenna. (a) Front view, (b) side view, (c) panoramic view.

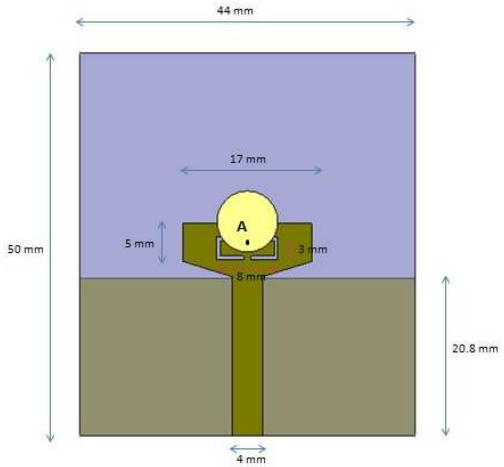

Figure 2: Configuration and dimensions of the proposed antenna.

presented in Section 2. Simulation and experimental results are presented in Section 3. Finally, a conclusion is given in Section 4.

2. ANTENNA STRUCTURE AND DESIGN

The geometry of the proposed antenna is shown in Figure 1. The antenna is designed a on Rogers RO3203 substrate with a thickness $h = 1.6$ mm and a dielectric loss tangent of 0.016. It is based on a cylindrical dielectric resonator (DR) with a radius of 4 mm and a height of 3 mm. The DR is made of the TCI Ceramic-K12 material, which has a with a relative permittivity of 12, and is excited by a bevel-shaped patch fed by a microstrip line over a partial ground plane. A rectangular split-ring slot of a width of 0.5 mm is etched on the patch. The detailed dimensions of the antenna are shown in Figure 2.

The bevel-shape of the patch and the partial ground lead to the UWB operation, whereas the rectangular split-ring slot in the patch is responsible for creating a band notch in the UWB range. The notch frequency depends on the dimensions of the split-ring slot as well as on the DR dielectric constant and its relative position.

Notch reconfigurability is attained by rotating the DR to change its position with respect to the patch and the slot. This is achieved by connecting the DR, at point A shown in Figure 2, to a DC stepper motor placed below the substrate. The stepper motor can be controlled using an FPGA. The idea of rotating parts of an antenna was used in [14], where the authors had to care about keeping metal contact between feed and radiator. In the design proposed here, only the DR is rotated, so keeping metal-to-metal contact is not an issue. Figure 2 shows the DR in position 0. Figures 3(a) and 3(b) show the DR rotated clockwise by 60° and 180°, respectively. The antenna is designed and simulated using Ansoft HFSS.

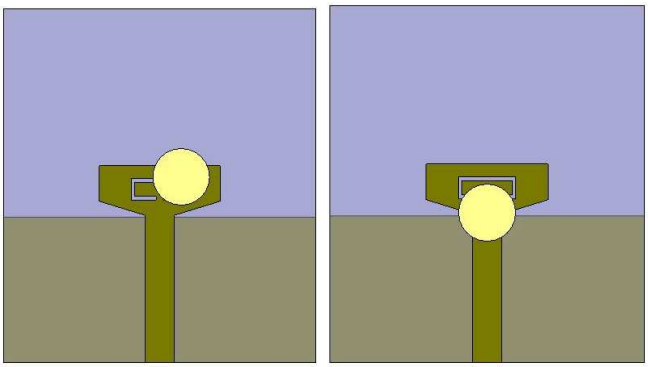

Figure 3: DR rotated by (a) 60°, and (b) 180°.

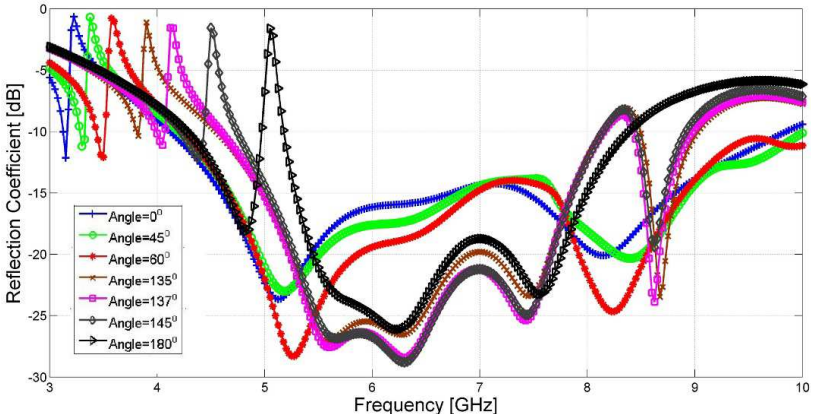

Figure 4: Reflection coefficient of the antenna for different rotation angles of the DR.

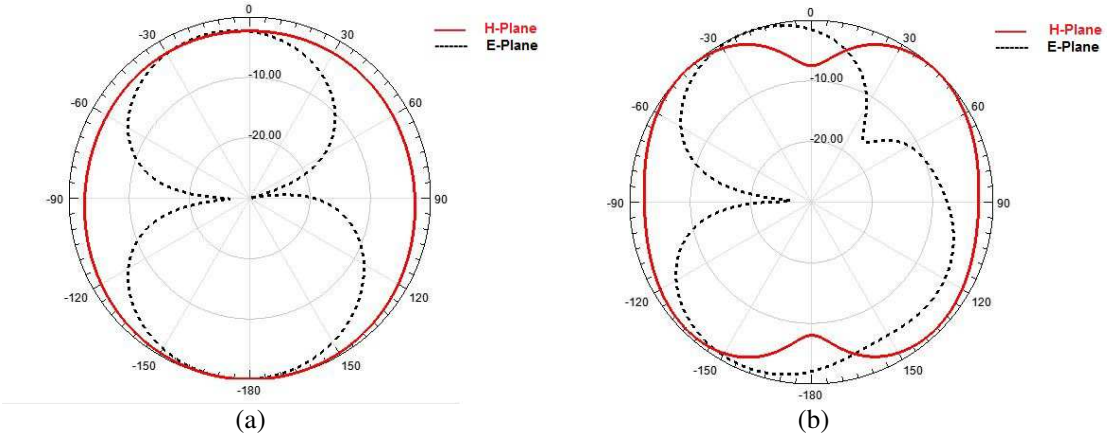

Figure 5: Simulated radiation patterns of the proposed antenna at (a) 4 GHz and (b) 6 GHz.

3. RESULTS AND DISCUSSION

The simulated reflection coefficient plots of the reconfigurable DRA are given in Figure 4 for the indicated rotation angles. It is clear that band notch reconfigurability has been attained. For example, narrow band rejections at 3.2, 3.4, 3.6, 3.9, 4.2, 4.5 and 5.1 GHz correspond to rotation angles of 0°, 45°, 60°, 135°, 137°, 145° and 180°, respectively. Due to design symmetry, and for the given design parameters, the notch band is limited within the 3.2–5.1 GHz range. A rejection at any frequency inside this range is possible, by one corresponding rotation angle. This range is where most narrowband systems operating inside the 3.1–10.6 GHz band are concentrated. The induced band notches help to limit interference to many services such as WiMAX, WLAN and

other wireless applications.

Figure 5 shows the simulated radiation patterns at 4 GHz and 6 GHz. It is observed that the radiation patterns are omni-directional, with almost equal radiation in the H-plane, and radiation with the shape of digit 8 in the E-plane.

4. CONCLUSION

A UWB DRA with reconfigurable band rejection was proposed. The antenna is based on a cylindrical DR excited using a bevel-shaped patch. A rectangular split-ring slot etched on the patch induces a band notch. A DC stepper motor is attached to the DR from below the antenna's substrate. By rotating the DR, the notch frequency is changed, thus leading to notch reconfigurability. For the presented design, a narrowband rejection at any frequency inside the 3.2–5.1 GHz range is possible with a specific corresponding DR rotation angle. An induced notch helps to limit interference to a narrowband system that transmits in its band. The simplicity, compact size, low cost, and the band rejection reconfigurability make this antenna suitable for UWB applications and UWB Cognitive Radio systems, where interference avoidance is a key issue.

REFERENCES

1. Petosa, A. and A. Ittipiboon, "Dielectric resonator antennas: A historical review and the current state of the art," *IEEE Antennas and Propagation Magazine*, Vol. 52, No. 5, 91–116, Oct. 2010.
2. Almpanis, G., C. Fumeaux, and R. Vahldieck, "The trapezoidal dielectric resonator antenna," *IEEE Trans. Antennas Propag.*, Vol. 56, No. 9, 2810–2816, Sep. 2008.
3. Chair, R., A. A. Kishk, and K. F. Lee, "Wideband simple cylindrical dielectric resonator antennas," *IEEE Microw. Wireless Compone. Lett.*, Vol. 15, No. 4, 241–243, Apr. 2005.
4. Khoo, K.-W., Y.-X. Guo, and L.-C. Ong, "Wideband circularly polarized dielectric resonator antenna," *IEEE Trans. Antennas Propag.*, Vol. 55, No. 7, 1929–1932, Jul. 2007.
5. Khalily, M., M.-K. A. Rahim, M.-R. Kamarudin, and M.-F. Ismail, "Wide-band rectangular dielectric resonator antenna design," *Proceedings of 2010 IEEE Asia-Pacific Conference on Applied Electromagnetics, APACE 2010*, Negeri Sembilan, Malaysia, Nov. 9–11, 2010.
6. Almpanis, G., C. Fumeaux, and R. Vahldieck, "Dual-mode bridge-shaped dielectric resonator antennas," *IEEE Trans. Antennas Propag.*, Vol. 9, 103–106, 2010.
7. Lapierre, M., Y. M. M. Antar, A. Ittipiboon, and A. Petosa, "Ultra wideband monopole/dielectric resonator antenna," *IEEE Microw. Wireless Compone. Lett.*, Vol. 15, No. 1, 7–9, Jan. 2005.
8. Denidni, T. A. and Z. Weng, "Hybrid ultrawideband dielectric resonator antenna and band-notched designs," *IET Microwaves, Antennas and Propagation*, Oct. 2010.
9. Chang, T.-H. and J.-F. Kiang, "Dualband split dielectric resonator antenna," *IEEE Trans. Antennas Propag.*, Vol. 55, No. 11, 3155–3162, Nov. 2007.
10. Al-Husseini, M., L. Safatly, A. Ramadan, A. El-Hajj, K. Y. Kabalan, and C. G. Christodoulou, "Reconfigurable filter antennas for pulse adaptation in UWB cognitive radio systems," *Progress In Electromagnetics Research B*, Vol. 37, 327–342, 2012.
11. Al-Husseini, M., J. Costantine, C. G. Christodoulou, S. E. Barbin, A. El-Hajj, and K. Y. Kabalan, "A reconfigurable frequency-notched uwb antenna with split-ring resonators," *Proceedings of the 2010 Asia-Pacific Microwave Conference, APMC 2010*, Yokohama, Japan, Dec. 7–10, 2010.
12. Al-Husseini, M., Y. Tawk, C. G. Christodoulou, K. Y. Kabalan, and A. El-Hajj, "Design of an antenna with reconfigurable band rejection for UWB cognitive radio," *PIERS Proceedings*, 830–833, Marrakesh, Morocco, Mar. 20–23, 2011.
13. Al-Husseini, M., A. Ramadan, Y. Tawk, C. G. Christodoulou, A. El-Hajj, and K. Y. Kabalan, "Design based on complementary split-ring resonators of an antenna with controllable band notches for UWB cognitive radio applications," *Proceedings of the 2011 IEEE AP-S International Symposium on Antennas and Propagation, IEEE AP-S 2011*, Spokane, Washington, USA, Jul. 3–8, 2011.
14. Tawk, Y. and C. G. Christodoulou, "A new reconfigurable antenna design for cognitive radio," *IEEE Antennas and Wireless Propagation Letters*, Vol. 8, 1378–1381, Dec. 2009.

Symmetrical Slot Loaded Dual Band Elliptical Microstrip Patch Antenna

Abdullah Al Noman Ovi[1], **Nandita Saha**[2], **Shuvashis Dey**[2], **and Nuzat Naury Alam**[2]

[1]Department of Electrical and Electronic Engineering
Bangladesh University of Engineering and Technology, Dhaka, Bangladesh
[2]Department of Electrical and Electronic Engineering
American International University of Bangladesh, Dhaka, Bangladesh

Abstract— In this paper, a concept of mode modification to obtain dual band performance in elliptical microstrip patch antenna has been proposed. Previously, mode modification in rectangular microstrip patch antenna was performed by using symmetrical rectangular slots closed to radiating edges. Symmetrical slots were introduced in rectangular microstrip patch antenna to lower the resonant frequency of TM_{030} mode to act like TM_{010} mode and thus dual band antennas were successfully modeled. But implementing this concept in elliptical microstrip patch antenna to obtain dual band performance is a novel idea. The original TM_{010} mode and the modified TM_{030} mode constitute the dual band and two modes show almost similar radiating properties, with high directivity and gain. The potential application of symmetrical slots in elliptical microstrip patch may help the researchers to obtain dual band antennas for elliptical patches. It also leads the way to design multiband antennas using appropriate metamaterials (ENG or MNG) and using the idea of additional modified modes in elliptical patches also.

1. INTRODUCTION

Dual or multi-frequency operations are quite common in Radar and Satellite communications and a unique radiating structure is desirable to accomplish these operations. An ideal dual frequency antenna should have a similar performance in both operating modes in terms of radiating properties and simultaneous matching [1]. Dual frequency patch antennas provide an alternative to large bandwidth planner antennas. When the two operating frequencies are far apart, a dual frequency patch structure can be conceived to avoid the use of separate antennas [2]. Compact microstrip antennas with dual-frequency operation have attracted much attention. The recent growth of wireless communication systems has produced a great demand for compact antennas which may fit inside the handset without protruding out. The most admired structure among the miniature antennas is the microstrip patch antenna. Microstrip patch antennas provide significant advantages such as low profile, low weight, relatively low manufacturing cost and polarization diversity & also planner & can be made conformal to shaped surface [3]. However the limitations like narrow bandwidth, poor gain, low power handling capacity & low radiation efficiency associated with conventional patch antennas cannot be ignored [4]. Compact microstrip antennas can be designed by embedding suitable slots on the radiating patch. The loading can be varied by varying the length and width of the slot. Slots can be of different shapes and some slots or combination of two slots on the patch can produce dual frequencies [5, 6]. Among the conventional patch geometries microstrip patch antennas with rectangular, circular, triangular shapes extensively analyzed. Other regular shapes of patch geometries are rarely touched upon perhaps due to involvement of difficult mathematical modeling. For example elliptical patch geometry could not become popular perhaps due to involvement of elliptical coordinate system & application of Mathieu function in theoretical analysis [7, 8]. However owing to the advantage of smaller patch size at a given frequency as compared to rectangular & circular patch antennas, several papers on elliptical patch antenna have been published [9, 10]. In this paper a microstrip elliptical patch antenna has designed in free space & its performance has been observed. By loading a pair of narrow slots, an elliptical patch with dual-frequency operation with original TM_{010} mode and the modified TM_{030} mode have been reported. Commercial electromagnetic simulation package CST Microwave Studio was used for design & simulation purposes.

2. SLOT LOADING IN ELLIPTICAL MICROSTRIP PATCH ANTENNA

Prior to our work, applying symmetrical slots in a 40 mm × 30 mm rectangular microstrip patch antenna TM_{030} mode was modified to act like TM_{010} mode [1]. Slot loaded condition has been devised to operate the antenna in dual band. The geometry of the slot-loaded elliptical patch

Table 1: Elliptical microstrip patch antenna measurements for designing.

Ground plane	Elliptical patch & substrate	Substrate height	Substrate's relative permittivity, ε_R	Substrate's relative permeability, μ_R	Feed position	Probe radius
60 mm × 60 mm	Major axis = 15 mm Minor axis = 11.25 mm	5 mm	9.8	1	$x = 7.5$, $y = 0$	0.3 mm

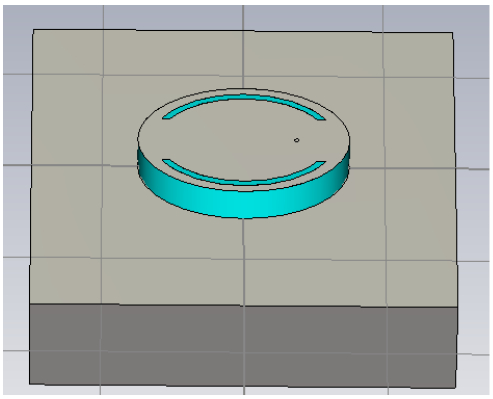

Figure 1: Geometry of the elliptical microstrip patch antenna.

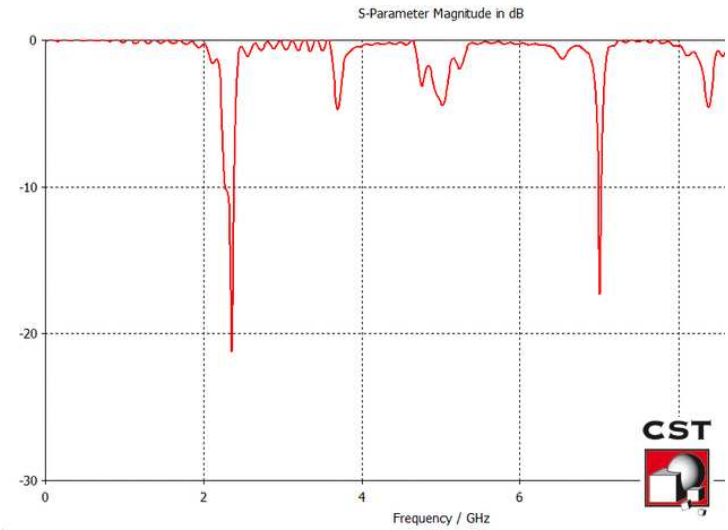

Figure 2: S-parameter performance of proposed elliptical dual band microstrip patch antenna.

antenna is given below in the table — Two narrow slots of 1 mm are etched on the elliptical patch.

3. PERFORMANCE ANALYSIS OF SLOT LOADED ELLIPTICAL MICROSTRIP PATCH ANTENNA

This paper presents performance of a dual-band elliptical microstrip patch antenna with symmetrical slots. From S-parameter analysis it has been observed that microstrip antenna with elliptical patch giving dual band resonance frequency at 2.256 GHz and 7.01 GHz with reflection coefficient of −22 dB and −18 dB respectively.

The radiation patterns found from the simulation (Figures 3 and 4) tells that at broadside it gets maximum radiation. The directivity and gain of TM_{010} mode are 5.827 dB and 5.618 dB respectively. For TM_{030} mode the directivity and gain are 6.626 dB and 6.161 dB respectively.

From Figure 5, we see that the surface current of TM_{030} mode is modified to act like TM_{010}

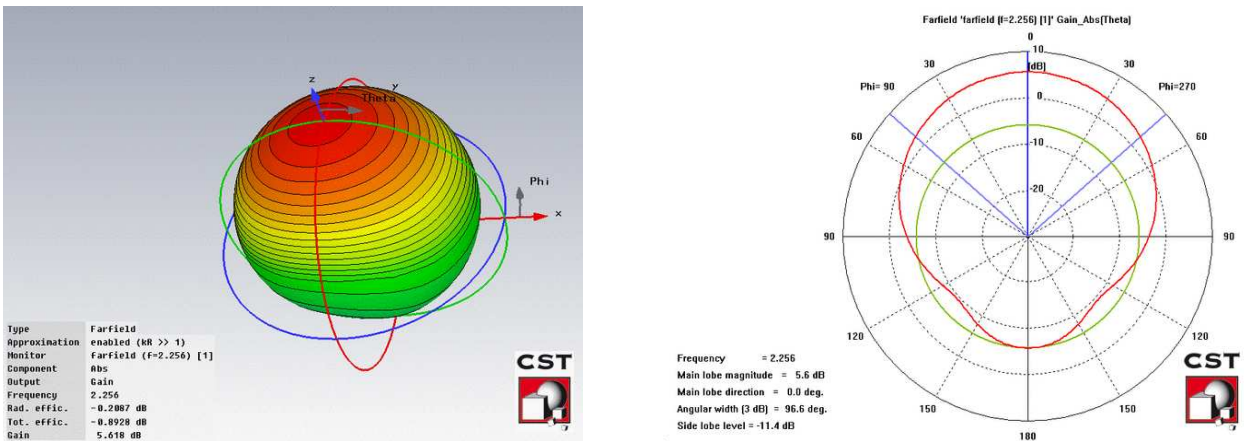

(a) (b)

Figure 3: (a) 3-D radiation pattern. (b) Polar plot of radiation pattern of TM_{010} mode (at 2.256 GHz).

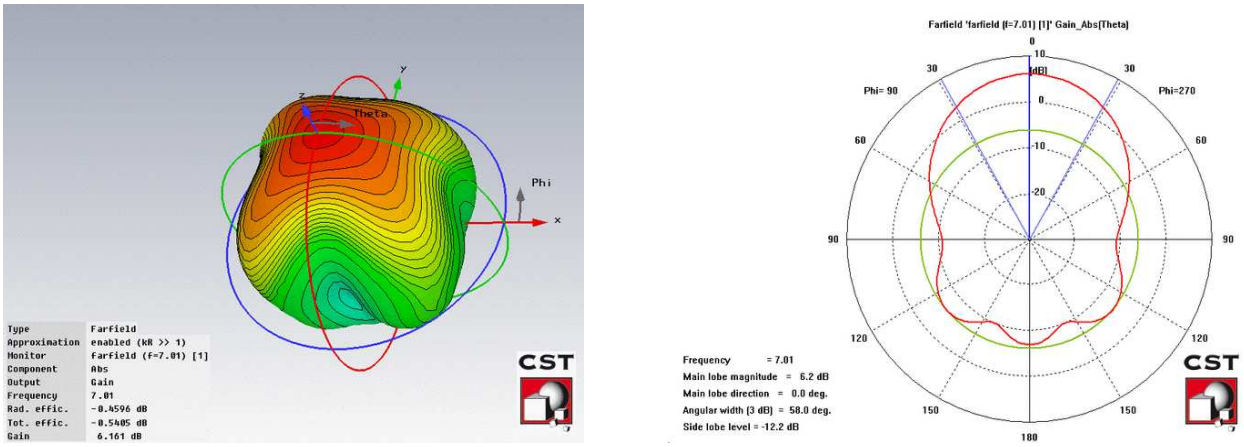

(a) (b)

Figure 4: (a) 3-D radiation pattern. (b) Polar plot of radiation pattern of TM_{030} mode (at 7.01 GHz).

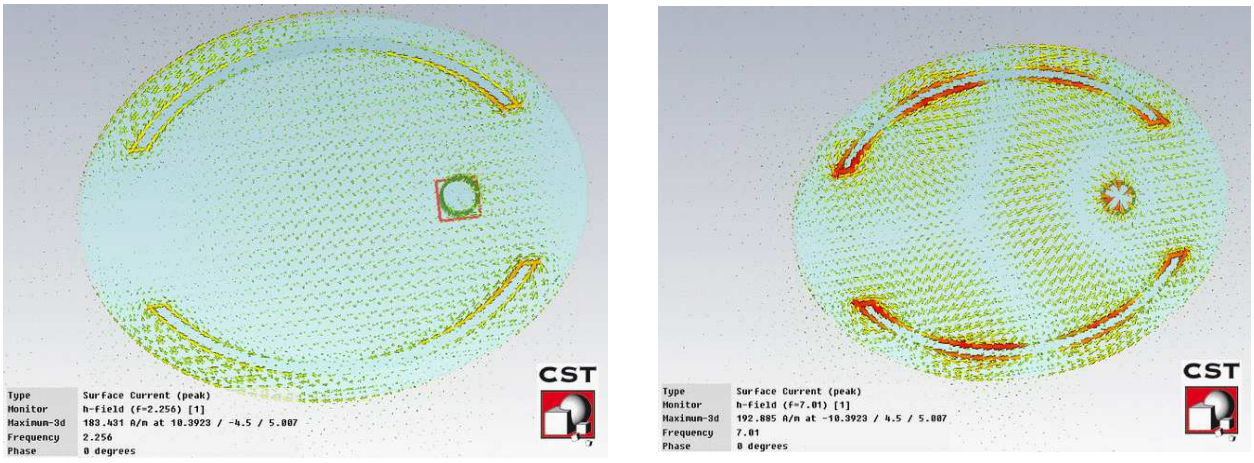

(a) (b)

Figure 5: Surface current densities of (a) TM_{010} mode and (b) TM_{030} mode.

mode. The effect of slots on TM_{030} mode is verified by the high value of surface current density around slots at 7.01 GHz.

4. CONCLUSIONS

In this contribution, we have found that using symmetrical slots in elliptical microstrip patch antenna dual band performance can be obtained. It is realized that with the introduction of elliptical patch with symmetrical slots, the effective patch size is marginally reduced but the performance of antenna is significantly improved in both impedance bandwidth and gain. Since the functionality of microstrip antenna can be maintained with elliptical patch, it could be inferred that the novel idea of using symmetrical slots in elliptical microstrip patch antenna could be a potential for dual band and multi-band applications.

REFERENCES

1. Maci, S., G. B. Gentili, P. Piazzesi, and C. Salvador, "Dual-band slot-loaded patch antenna," *IEE Proc. Microw. Antennas Propag.*, Vol. 142, No. 3, Jun. 1995.
2. Maci, S., G. B. Gentili, and G. Avitabile, "Single-layer dual-frequency patch antenna," *Electronics Letters*, Vol. 29, No. 16, Aug. 1993.
3. James, J. R., *Handbook of Microstrip Antenna*, Peter Peregrinus Ltd., London, 1989.
4. Pozar, D. M. and D. H. Schaubert, *Microstrip Antennas: The Analysis and Design of Microstrip Antennas and Arrays*, IEEE Press, Piscataway, NJ, 1995.
5. Wong, K. L., *Compact and Broadband Microstrip Antennas*, Wiley, 2002.
6. Kumar, G. and K. P. Ray, *Broadband Microstrip Antennas*, Artech House, Boston, 2003.
7. Kretzschmar, J. G., "Wave propagation in hollow conduction elliptical waveguides," *IEEE Trans. Microw. Theory Techn.*, 547–554, Vol. 18, No. 7, USA, 1970.
8. Kumpiasert, N. and W. Kiranon, "Simple and accurate formula for the resonant frequency of the circular microstrip disc antenna," *IEEE Trans. Antennas Propag.*, 1332–1333, Vol. 43, No. 11, USA, 1995.
9. Rengaranjan, S. R., "Resonance frequency of elliptical microstrip antennas," *Electronics Letters*, 1066–1067, Vol. 29, No. 12, UK, 1993.
10. Long, S. A., L. C. Shen, D. H. Schaubert, and F. G. Ferrar, "An experimental study of the circularly polarized elliptical printed circuit antenna," *IEEE Trans. Antennas Propag.*, Vol. 29, No. 1, 95–99, USA, 1991.

Symmetrical Slot Loading in Elliptical Microstrip Patch Antennas Partially Filled with Mue Negative Metamaterials

Abdullah Al Noman Ovi[1], **Nandita Saha**[2], **Shuvashis Dey**[2], **and Nuzat Naury Alam**[2]

[1]Department of Electrical and Electronic Engineering
Bangladesh University of Engineering and Technology, Dhaka, Bangladesh
[2]Department of Electrical and Electronic Engineering
American International University of Bangladesh, Dhaka, Bangladesh

Abstract— In this paper, an idea of radiation pattern modification using symmetrical slots in an elliptical microstrip patch antenna partially loaded with mue-negative (MNG) metamaterial has been proposed. Previously, size reduction of conventional elliptical microstrip patch antenna has been possible by using MNG metamaterial. But the idea of using symmetrical slots to modify higher modes in such metamaterial loaded elliptical patch antenna is different and a novel concept. Using this idea novel design of slot loaded elliptical microstrip patch antenna partially loaded with MNG metamaterial has been introduced successfully. In this paper, slot loaded elliptical patch antenna partially loaded with MNG metamaterial is theoretically and numerically analyzed. Actually, this mode modification has been done by MNG metamaterial & newly introduced symmetrical arc shaped slots with the help of proposed better radiation conditions, relevant theory of dispersive metamaterial and realistic simulated results. The potential application of this novel idea is the way to design multiband antennas using appropriate metamaterials (ENG or MNG) and using the idea of additional modified modes in elliptical patches also.

1. INTRODUCTION

Dual or multi-frequency operations are quite common in Radar and Satellite communications and they provide an alternative to large bandwidth planar antennas. A unique radiating structure is desirable to accomplish these operations. Compact microstrip antennas with dual-frequency operation have attracted much attention. The recent growth of wireless communication systems has produced a great demand for compact antennas which may fit inside the handset without protruding out. The most admired structure among the miniature antennas is the microstrip patch antenna. Microstrip patch antennas provide significant advantages such as low profile, low weight, relatively low manufacturing cost and polarization diversity [1–4]. However the limitations like narrow bandwidth, poor gain, low power handling capacity & low radiation efficiency associated with conventional patch antennas cannot be ignored [2, 3]. Metamaterial based patch antennas may be the good solutions to meet all these requirements.

Alu et al. [5] has proposed design method to obtain sub-wavelength rectangular patch antennas using DPS-ENG bi-layer. But it has been shown that such rectangular patches give broadside null radiation pattern [5, 6]. This has been referred as 'zero radiation problem' [7]. Before and even after the work of Alu et al., several works have been proposed in case of partially loaded rectangular microstrip patch antenna, but they were without considering the radiation efficiency of such cavities [6, 8, 9]. It has been predicted that: These rectangular antennas partially loaded with metamaterial can only be good resonators but may not be good radiators [10]. Later, Jiang Xiong et al. [11] showed that using MNG metamaterials, modification of conventional TM_{020} mode radiation pattern is possible for very large patch antennas. In [12], an algorithm for radiation pattern modification using metamaterial (for any patch size) has been proposed. Applying that algorithm of mode modification and the idea of symmetrical slots, a novel design of small elliptical microstrip patch antenna partially loaded with MNG metamaterial has been proposed here. By loading a pair of narrow symmetrical slots, an elliptical patch with multi-frequency operation with original TM_{010} mode, modified ${TM_{0\delta0}}^1$ mode due to metamaterial and the modified ${TM_{0\delta0}}^2$ due to the symmetircal slots mode have been reported. Commercial electromagnetic simulation package 'CST Microwave Studio' [13] was used for design & simulation purposes.

2. NOVEL DESIGN OF SLOT LOADED ELLIPTICAL MICROSTRIP PATCH ANTENNA LOADED WITH MNG METAMATERIAL

Prior to our work, using MNG metamaterial dual band performance has been obtained [14] by producing the unconventional plasmonic ${TM_{0\delta0}}^1$ mode ($0 < \delta < 1$) following the algorithm described in [12]. In this contribution, we are using the same algorithm to produce an unconventional

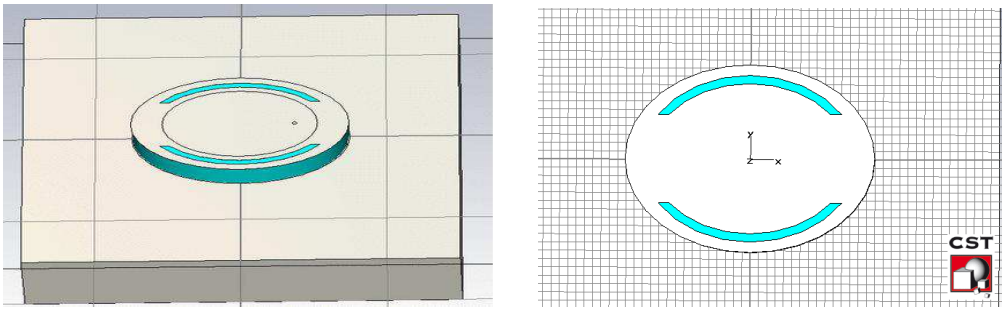

(a) side view (b) top view

Figure 1: Geometry of the elliptical microstrip patch antenna partially filled with mue negative metamaterial (MNG).

Table 1: Elliptical microstrip patch antenna measurements for designing.

Ground plane	Elliptical patch & substrate	DPS Substrate height	DPS Substrate's relative permittivity, ε_R	DPS Substrate's relative permeability, μ_R	Feed position	Feed radius
60 mm × 60 mm	Major axis, $a_1 = 15$ mm Minor axis, $b_1 = 11.25$ mm	5 mm	9.8	1	$x = 7.5$, $y = 0$	0.3 mm

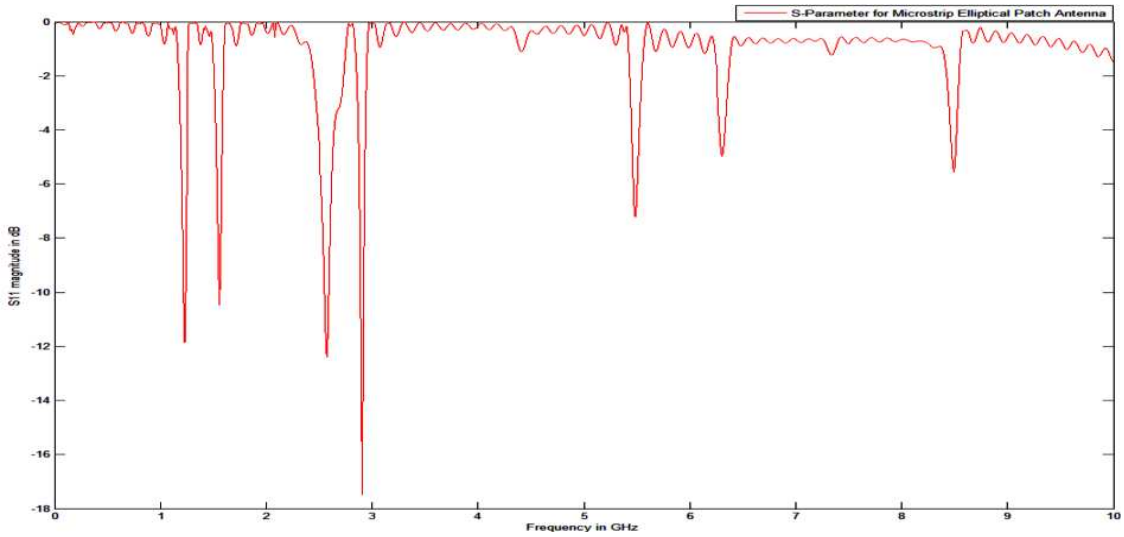

Figure 2: S-parameter performance of proposed elliptical microstrip patch antenna.

plasmonic $TM_{0\delta 0}{}^1$ mode ($0 < \delta < 1$) along with the modified higher mode $TM_{0\delta 0}{}^2$ mode due to the symmetrical slot loading. Thus it becomes a triple band antenna with good radiation performance and S-parameter performance. The geometrical measurements of the slot-loaded elliptical patch antenna are given in Table 1.

The geometry of the slot-loaded elliptical patch antenna is given in Fig. 1.

The elliptical substrate is composed of two concentric ellipses. The MNG ellipse completely lies within the substrate, around which the DPS region exists. The major and minor axis radius for the substrate is 15 mm and 11.25 mm respectively. The major and minor axis radius for MNG ellipse is 10.67 mm and 8 mm respectively. The filling ratio (ratio of MNG area to the total substrate area), $\Gamma = 0.505837$ in this case. The relative permeability and permittivity of DPS material (μ_1 and ε_1) is 1 and 9.8 respectively. In case of MNG metamaterial, we have used Lorentz model. The reason is that metamaterials are inherently dispersive and lossy. So, without using dispersive lossy model (i.e., Lorentz model), the simulated results cannot give proper realistic results.

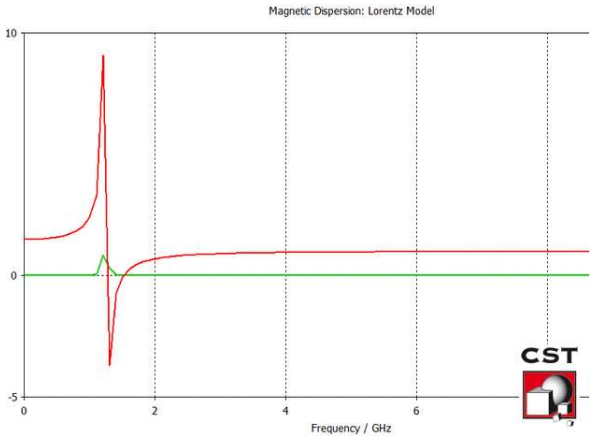

Figure 3: Magnetic dispersion: Lorentz model.

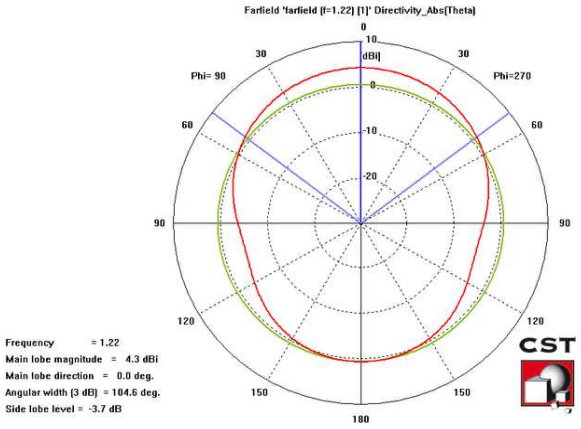

Figure 4: Polar plot of radiation pattern of $TM_{0\delta0}{}^{1}$ mode (at 1.22 GHz).

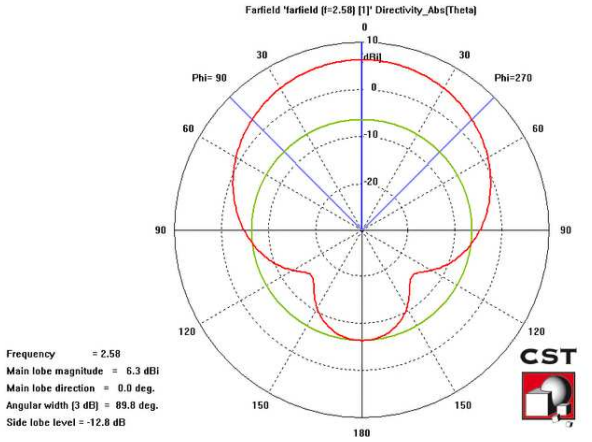

Figure 5: Polar plot of radiation pattern of TM_{010} mode (at 2.58 GHz).

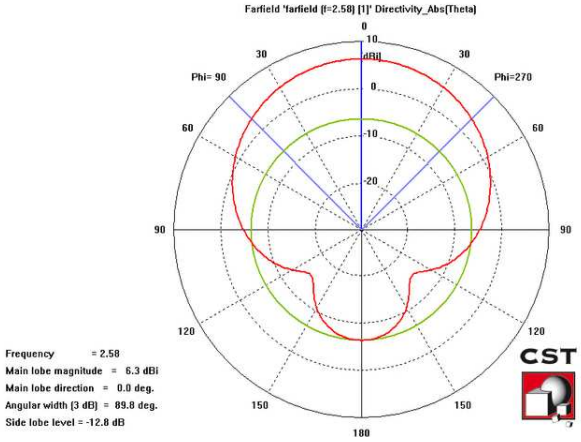

Figure 6: Polar plot of radiation pattern of $TM_{0\delta0}{}^{2}$ mode (at 2.91 GHz).

The Lorentz model for MNG metamaterial:

$$\mu_{2r}(\omega) = \mu_\infty + \frac{(\mu_s - \mu_\infty)\omega_0^2}{\omega_0^2 - \omega^2 + j\omega\delta}$$

where, $\mu_\infty = 10$, $\mu_s = 1488$, $f_r = 7853981634\,\text{rad/s}$, $\delta = 50\,\text{MHz}$. The Lorentz model is shown in Fig. 3.

3. PERFORMANCE ANALYSIS OF SLOT LOADED ELLIPTICAL MICROSTRIP PATCH ANTENNA LOADED WITH MNG METAMATERIAL

This paper presents performance of a multi-band elliptical microstrip patch antenna loaded with MNG metamaterial with symmetrical slots. From S-parameter analysis it has been observed that microstrip antenna with elliptical patch giving resonance frequencies at 1.22 GHz, 2.58 GHz & 2.91 GHz with reflection coefficient of $-11.85\,\text{dB}$, $-12.39\,\text{dB}$ & $-17.487\,\text{dB}$ respectively. Original TM_{010} is located at 2.58 GHz, and two modified modes $TM_{0\delta0}{}^{1}$ and $TM_{0\delta0}{}^{2}$ are at 1.22 GHz and 2.91 GHz respectively.

The radiation patterns found from the simulation (Fig. 4, Fig. 5 and Fig. 6) tells that at broadside it gets maximum radiation. The directivity is 4.383 dB at 1.22 GHz, 6.344 dB at 2.58 GHz and 6.729 dB at 2.91 GHz respectively. So the antenna gives us a satisfactory radiation performance.

4. CONCLUSION

In this contribution, we have found that using symmetrical slots in elliptical microstrip patch antenna loaded with MNG metamaterial, multi band performance can be obtained. It is realized

that by properly choosing the constitute parameters, following the general idea of better radiation, proper optimization of feed position and with careful introduction of elliptical patch with symmetrical slots, the effective patch size is marginally reduced but the performance of antenna is significantly improved in both impedance bandwidth and gain. Since the functionality of microstrip antenna can be maintained with elliptical patch, it could be inferred that the novel idea of using symmetrical slots in elliptical microstrip patch antenna could be a potential for multi-band applications.

REFERENCES

1. James, J. R., *Handbook of Microstrip Antenna*, Peter Peregrinus Ltd., London, 1989.
2. Pozar, D. M. and D. H. Schaubert, *Microstrip Antennas: The Analysis and Design of Microstrip Antennas and Arrays*, IEEE Press, Piscataway, NJ, 1995.
3. Wong, K. L., *Compact and Broadband Microstrip Antennas*, Wiley, 2002.
4. Kumar, G. and K. P. Ray, *Broadband Microstrip Antennas*, Artech House, Boston, 2003.
5. Alù, A, A., F. Bilotti, N. Engheta, and L. Vegni, "Sub wavelength, compact, resonant patch antennas loaded with metamaterials," *IEEE Transactions on Antennas and Propagation*, Vol. 55, No. 1, Jan. 2007.
6. Zheng, K. S., W. Y. Tam, and D. B. Ge, "Impedance matching of rectangular microstrip antennas partially loaded with DNG metamaterials," *38th European Microwave Conference, EuMC*, Oct. 2008.
7. Zheng, K. S., W. Y. Tam, and D. B. Ge, "Broadside subwavelength microstrip antennas partially loaded with metamaterials," *International Workshop on Metamaterials*, Nov. 2008.
8. Xu, W., L.-W. Li, H.-Y. Yao, and T.-S. Yeo, "Left-handed material effects on waves modes and resonant frequencies: Filled waveguide structures and substrate-loaded patch antennas," *Journal of Electromagnetic Waves and Applications*, Vol. 19, No. 15, 2005.
9. Yang, R., Y. Xie, D. Li, J. Zheng, and J. Jiang, "Bandwidth enhancement of microstrip antennas with metamaterial bilayered substrate," *Journal of Electromagnetic Waves and Applications*, Vol. 21, No. 15, 2321–2330, 2007.
10. Capolino, F., *Handbook of Artificial Materials: Applications of Metamaterials*, Vol. 2, 18.1–18.14, Taylor and Francis, CRC Press, Oct. 2009.
11. Xiong, J., H. Li, Y. Jin, and S. He, "Modified TM_{020} mode of a rectangular patch antenna partially loaded with metamaterial for dual-band applications," *IEEE Antennas and Wireless Propagation Letters*, Vol. 8, 2009.
12. Mahdy, M. R. C., M. R. A. Zuboraj, A. A. N. Ovi, and M. A. Matin, "A novel design algorithm and practical realization of rectangular patch antenna loaded with SNG metamaterial," *Progress In Electromagnetics Research M*, Vol. 17, 13–27, 2011.
13. CST Microwave Studio, CST of America [Online], 2009, Available: http://www.cst.com.
14. Chowdhury Mahdy, M. R., M. R. Alam Zuboraj, A. Al Noman Ovi, and M. Abdul Matin, "Novel application of MNG metamaterial in rectangular microstrip patch antenna (partially loaded case) for dual band application," *PIERS Proceedings*, 935–938, Marrakesh, Morocco, Mar. 20–23, 2011.

Research on Capacity Performance of TD-LTE System with Different Antenna Schemes

Jiangbo Dong, Yuan Fang, Nan Li, Wei Liu, Hao Sun, Yunbo Han, and YanLei Chen
China Mobile Design Institute, Beijing, China

Abstract— Network capacity performance, especially cell edge user average throughput is compared between 2-path antenna and 8-path antenna schemes in TD-LTE system. Simulation results show that the 8-antenna has about 30% gain. And when the real construction condition is unlimited, 8-antenna scheme is a better choice.

1. INTRODUCTION

There are several different transmission modes in TD-LTE system [1]. For transmission mode 7/8, 8-path smart antenna is necessary to implement beamforming, and for transmission mode 2/3, 2-path antenna can also work well. Considering the engineering factors, such as antenna size, antenna weight, the 8-path antenna is more difficult to build than 2-path antenna during the real network deployment; while the cell edge user data rate performance maybe better than the latter. Therefore, performance comparison between 2-path and 8-path antenna is an important problem and the comparison results will be an important technical basis for choosing the proper antenna scheme during the network deployment.

This paper addresses the planning of TD-LTE cellular radio networks for data services, enabling the evaluation of the network capacity performance, such as cell edge user data rate with different antenna scenarios. The modeling schemes of TD-LTE key techniques are proposed and developed to finish the research. Such schemes are also embedded in ANPOP® radio network planning tool.

The simulation results show that, when the ICIC (Inter Cell Interference Cancellation) function is off, cell edge user data rate with 8-path antenna is 32.4% higher than that with 2-path antenna; and this is also met with the field test results. When the ICIC function is on, the gain is down to 28.8%. It shows that ICIC can also enhance the ability of cell edge interference cancellation in the 2-path case. So we can draw an conclusion from the simulation results that 8-path antenna is a better choice for TD-LTE system, when the real construction condition is unlimited. This research is very important for construction of the large scale TD-LTE network.

The rest of the paper is organized as follows: In Section 2, the modeling schemes of TD-LTE key technique are introduced. Section 3 gives a brief presentation of the structure of the simulator. Evaluation assumption and simulation results are presented and analyzed in Section 4. Finally, some conclusions about choosing the proper antenna scheme are drawn in the Section 5.

2. SYTEM MODEL

The starting point of the model is a given TD-LTE radio network deployment. The goal is to determine the cell edge user average throughput and cell average throughput with different antenna schemes. So first of all, a reasonable simulation model of TD-LTE should be proposed. AMC, OFDM, MIMO, Packet Scheduling, ICIC, Downlink Power Assignment and Uplink Power Control are the key techniques of TD-LTE system. In TD-LTE system, radio resource block, time slot, power and antenna are all radio resources which can be allocated according to the instantaneous channel conditions. A static simulation method is basically used as the TD-LTE system simulation algorithm.

Similar with HSDPA system [2], AMC is modeled through the process diagram which shows in the Figure 1. The SINR can be calculated or measured for any point in the network, and also at which the most efficient transport block can be achieved by lots of link level simulations; and then the transmission throughput can be calculated accordingly. So, the following mapping Table 1 can be pre-configured in the simulation tool to evaluate the AMC performance.

For packet scheduling, the multi-user gain of the network throughput can be achieved because the TD-LTE system can always schedule the special UE which has the proper channel quality condition to transmit. But for the static simulation, its time independent feature is incompatible with the time related character of packet scheduling. And dynamic simulation is time-assuming for

Table 1: Transport block mapping table.

Transport Block Size for one RB at different MCS	Channel Model	SINR (dB)
TBS1	PA,VA .etc	a
TBF...	...	...

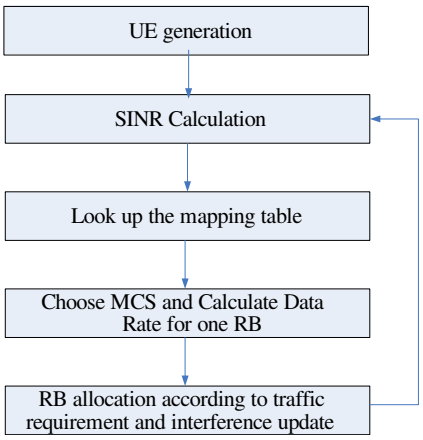

Figure 1: The working procedure of AMC.

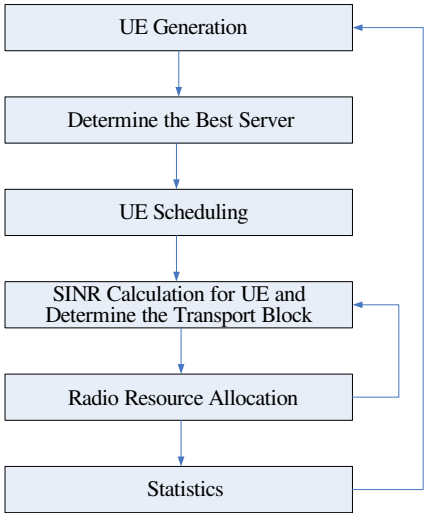

Figure 2: Simulator diagram of TD-LTE.

the planning work of a real network which has thousands of E-NodeBs. Considering the complexity of the implementation, the method in paper [2] is used in this research.

Static ICIC is also studied in this paper, the user at the cell edge can only use part of the radio resources. In ideal cell structure, the interference among the neighbor cells can be reduced efficiently when the radio resources are divided into three groups. But in real environment, the number of the groups may be larger than three to cancel the inter-cell interference, and it should be investigated to find an optimal value. And how to determine that the user is at cell edge should also be studied. In this research, the difference between the received power of the best server and that of the second best cell is used as the index to justify whether the user is at cell edge or not.

In 3GPP Release 8, there are seven kinds of transmission mode, but the transmission method of one dedicated user can only be chosen from diversity, multiplexing and beamforming at one time. And for the cell edge user, it only can be chosen from diversity and beamforming. Thus the performance comparison between 2-path and 8-path antenna is essentially the cell edge performance comparison between diversity and beamforming, and then diversity is used in the 2-path antenna scenario while beamforming is used in the 8-path antenna scenario.

From the description above, the TD-LTE is modeled in the static simulation successfully. The simulation procedure is introduced in the next section.

3. SIMULAITON DIAGRAM

All the algorithms above are implemented in the simulation tool ANPOP®. The basic blocks of the simulator are Geographical Information System (GIS), Coverage prediction, user generation and Monte Carlo simulation.

The simulation diagram is shown in Figure 2. In the UE generation block, the TD-LTE UE is distributed according to some real traffic distribution map. The best server is determined through RS received power level of the UEs' position. For one SNAPSHOT, the UE is scheduled according to the selected scheduling method. And then, the number of allocated Radio Blocks and the selected MCS of the UE is determined iteratively according to the interference level of the network and the UE position. The transport block is chosen through the look-up table when the SINR is calculated, and then the throughput of the user can be decided. The cell edge throughput can be statistically achieved by a lot of snapshots.

Detailed simulation parameters are shown in the next section.

4. SIMULAITON PARAMETERS AND RESULTS

Performance comparison between different antenna schemes is the major task of this paper. Considering the practical application scenarios, the 2-path and 8-path antennas are both dual-polarized, and the antenna gain and antenna pattern used in the simulation are the same with which used in the real networks. The performance comparison between 2-path and 8-path antenna schemes is respectively evaluated with and without the static ICIC function in the dense urban area, which has 340 base stations shown in Figure 3.

And the diversity is applied in 2-path case, while beamforming is applied in 8-path case. The antenna gain pattern for 2-path antenna is shown in Figure 4, and the broadcast beam and traffic beams of different angles for 8-path antenna are shown in Figure 5.

The other simulation parameters are shown in Table 2.

The simulation results are listed in Table 3.

The simulation results show that, when the ICIC function is off, cell edge user data rate with 8-path antenna is 32.4% higher than that with 2-path antenna. When the ICIC function is on, the gain is down to 28.8%. It shows that ICIC can also enhance the ability of cell edge interference cancellation in the 2-path case.

So we can draw an conclusion from the simulation results that 8-path antenna is a better choice for TD-LTE system, when the real construction condition is unlimited. This research is very important for construction of the large scale TD-LTE network.

Table 2: Detailed key simulation parameters.

Parameter	Value
Subframe Congifuration (UL : DL)	2 : 2
Special Subframe Configuration	10 : 2 : 2
ICIC threshold (dB)	6
Radio Resource Sub-Groups at cell edge	4
Scheduling Algorithm	Proportional Fair
Number of Scheduled User in a TTI	5

Table 3: Simulation results.

Cell edge user average throughput (kbps)	8-path	2-path	gain
Without ICIC	764.5	577.1	32.4%
With ICIC	820.3	636.8	28.8%

Figure 3: E-NodeB distribution.

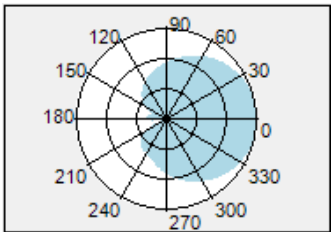

Figure 4: Antenna gain pattern for 2-path antenna.

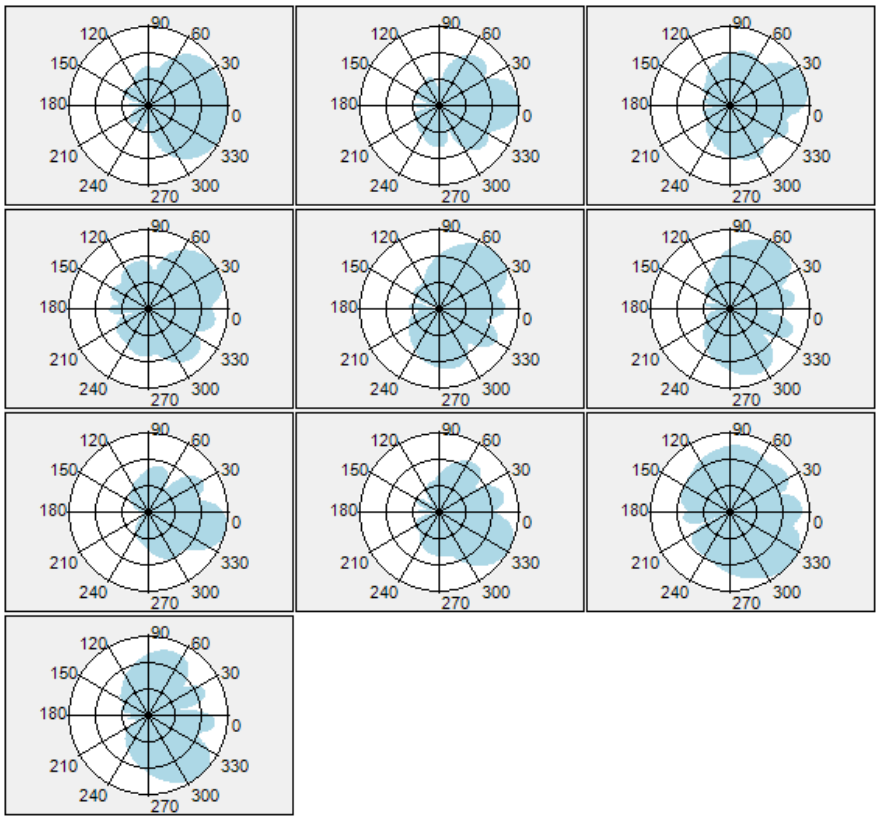

Figure 5: Antenna gain patterns for 8-path antenna.

5. CONCLUSIONS

The transmission method of the cell edge user is the mainly difference between 2-path and 8-path antenna scheme for TD-LTE system. So this research focused on the cell-edge user throughput with and without ICIC. Using the radio network plan tool ANPOP, the performance is evaluated. Simulation results show that the 8-path antenna has obvious throughput gain, and when the real construction condition is permitted, the 8-path antenna should be preferred to choose.

ACKNOWLEDGMENT

This work is supported by National Major Science & Technology Specific Projects-Next Generation Broadband Wireless & Mobile Communications (2012ZX03001028).

REFERENCES

1. Jia, S., *3GPP Long Term Evolution: Principle and System Design*, 158–169, Posts & Telecom Press, 2008.
2. Dong, J. and X. Wu, "Research on TD-SCDMA network planning for data services based on HSDPA," *IEEE International Conference on Communication Technology and Application (IEEE ICCTA2009)*, 251–254, 2009.

A Reconfigurable Antenna Based on an Ultrawideband to Narrowband Transformation

M. Al-Husseini, **A. Ramadan**, **A. El-Hajj**, **and K. Y. Kabalan**
ECE Department, American University of Beirut, Beirut 1107 2020, Lebanon

Abstract— This paper presents a frequency reconfigurable printed antenna obtained from the modification of a simple ultrawideband (UWB) design. The initial UWB version is based on a patch with round corners, for smoother current flow, and a microstrip-line feed. The ground plane is partial and rectangular in shape. The used substrate is a Rogers RO3203 board with $\varepsilon_r = 3.02$ and a height of 1.52 mm. A narrowband (NB) antenna is obtained by incorporating a rectangular split-ring slot in the ground plane of the UWB design, below the feed line, and by introducing a narrow gap into its feed line. The ground slot acts as a complementary split-ring resonator (CSRR), which resonates and creates a band notch around its resonance frequency. The feed gap acts as a capacitor, which transforms the CSRR's band rejection behavior to a band pass one. The position of the CSRR split affects its notch frequency, and consequently the resonance frequency of the NB antenna. Frequency reconfigurability is thus obtained by mounting electronic switches at several locations over the CSRR, and activating one switch at a time, to represent the split.

A prototype with two switches is fabricated. The measured reflection coefficient is in accordance with the simulations, which show frequency reconfigurability over two bands. More bands can be made operable by using more switches at optimized locations.

1. INTRODUCTION

Historically, antennas have been static devices with constant operational characteristics that remain unchanged once the antenna design is finalized. This started to change with the advent of microelectromechanical system (MEMS) components, which have made it easier to create dynamic radiators that can be reconfigured during operation. These reconfigurable antennas have the ability to dynamically adjust their frequency of operation, radiation patterns, polarization, and other parameters. They are robust in their support for multi-standard wireless communications systems with a single antenna, their compactness, and their resistance to jamming and co-site interference [1]. Frequency reconfigurable antennas, which are the most widely researched type, have out of band rejection. Compared to multiband or wideband antennas, they do not require highly efficient noise filters to be used, and thus the cost of the overall system is reduced [2].

Reconfigurability is obtained when the current path on the radiator surface is dynamically changed. This is usually done using MEMS or other switching components such as PIN diodes. In [3], the authors propose a pattern and frequency reconfigurable microstrip antenna based on a single-turn square spiral shape. Several fractal-shaped reconfigurable antennas are surveyed in [4]. Recently, a cedar-shaped frequency reconfigurable antenna has been proposed in [5].

In this paper, a modification to a simple UWB antenna is used to produce a frequency reconfigurable antenna. The next section describes the antenna geometry. Section 3 presents the obtained results, and a conclusion is given in Section 4.

2. ANTENNA CONFIGURATION

The configuration of the proposed antenna is shown in Fig. 1. It has a rounded patch, which allows for a smooth current flow leading to better matching, and a partial rectangular ground plane. These two techniques, the round corners and the partial ground, are employed to obtain a UWB operation. The Rogers RO3203 material, with $\varepsilon_r = 3.02$, is used for the 1.52 mm-thick substrate. The detailed dimensions are shown on the figure.

Modifications are made to the basic UWB configuration to obtain a reconfigurable relatively-narrowband design: 1) a narrow gap is introduced in the feed line, 2) a rectangular split-ring slot is incorporated in the ground plane below the feed line, and 3) electronic switches are mounted at several locations over the ground slot. The prototype presented in this paper has two switches only. The ground slot acts as a single-ring complementary split-ring resonator (CSRR). CSRRs are used for the synthesis of negative-permittivity media. They are known to create band notches around their resonance frequency. In [6–8], they have been used in the design of antennas with

reconfigurable band rejection for possible application in UWB cognitive radio. The feed gap acts as a capacitor, which transforms the band stop behavior into a band pass one. The idea of using such gaps to make the band-stop to band-pass transformation is used in [9], where the authors surround their band-notching element, a T-shape feed slit for instance, with two gaps. In the design we present here, the band rejection mechanism is due to a CSRR implemented in the ground plane instead. In this case, one gap, placed centered above the CSRR in the feed line, is proven to offer the same transformation effect. The location of the CSRR split is crucial to determining its band of rejection. Changing the position of the split moves the notch to a different band, and with the feed gap present, the obtained relatively-narrowband resonance is also changed to a different frequency. Using switches across a ring slot to act as splits, and controlling these switches to choose which is active and which is not, lead to frequency reconfigurability of the design in Fig. 1.

3. RESULTS AND DISCUSSION

Without the feed gap and the ground CSRR, the antenna offers UWB operation. A prototype of the UWB version is fabricated, and its reflection coefficient S_{11} is measured. The measured and simulated reflection coefficient plots are shown in Fig. 2. A UWB response covering the 2.5–9 GHz range, and adequate similarity between measured and simulated results are shown. The simulations are done using Ansoft HFSS [10].

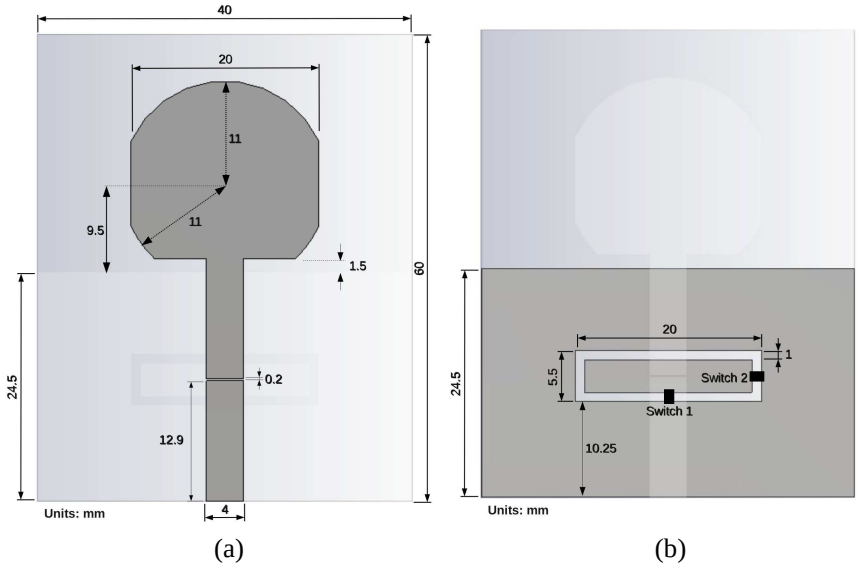

Figure 1: Reconfigurable narrowband antenna configuration: (a) top view and (b) bottom view.

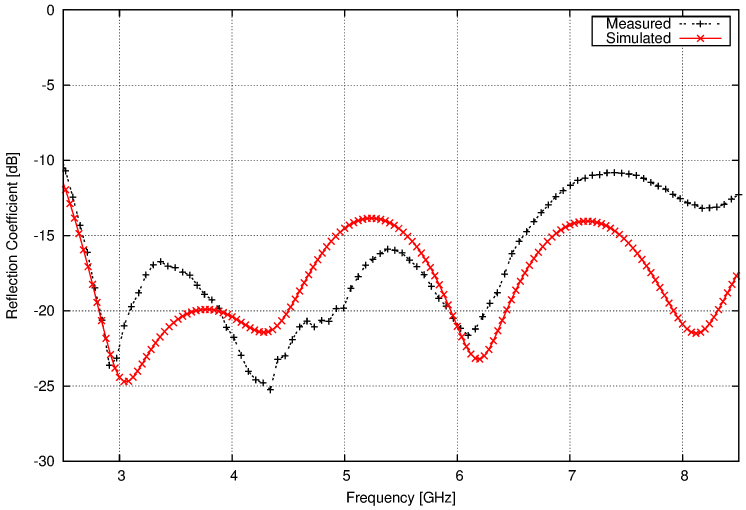

Figure 2: Measured and simulated S_{11} of the UWB antenna.

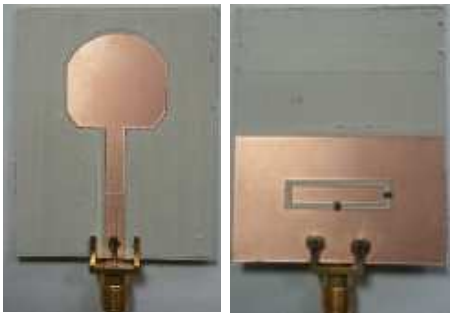

(a) (b)

Figure 3: Photo of the reconfigurable antenna prototype: (a) top view and (b) bottom view.

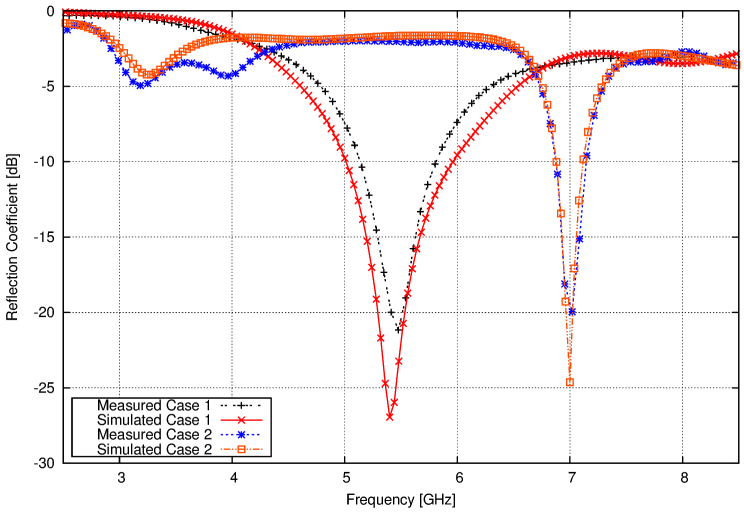

Figure 4: Measured and simulated S_{11} of the reconfigurable antenna.

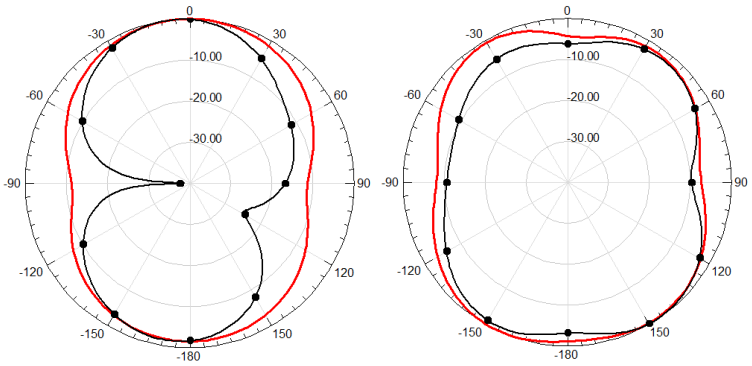

(a) 5.7 GHz (b) 7 GHz

Figure 5: Normalized radiation patterns in the H-plane (red line) and the E-plane (black line with symbol).

A prototype of the reconfigurable design is also fabricated and tested. Its photo is shown in Fig. 3. With two switches used in this prototype, two switching cases are of interest: Case 1, where Switch 1 is ON and Switch 2 is OFF, and Case 2 where opposite switching is used. A hardwired connection is used when a switch is ON, and removed when it is OFF. The carried simulations indicate that for a certain switching state, the resulting resonant frequency depends on the dimensions of the CSRR, which dictate its notch frequency, and on the width of the feed gap, which relates to the capacitance value. For the dimensions shown on Fig. 1, the obtained measured and simulated S_{11} plots are given in Fig. 4. For Case 1, the antenna is operable in the 5.2–5.8 GHz range. For Case 2, the antenna resonates at 7 GHz.

The normalized H-plane and E-plane radiation patterns are plotted in Fig. 5, for 5.7 GHz and 7 GHz. Since the antenna is the printed-monopole type with a partial ground plane, omnidirectional patterns, with equal gain in the H-plane, are expected. The ground slot has little effect on the radiation patterns, comparing them to the patterns of the original UWB design. At 5.7 GHz, the obtained peak gain is 5.5 dB. At 7 GHz, the peak gain is 4.75 dB.

The positions of the two switches can be altered to have the resonances at two different frequencies, and more switches can be embedded over the CSRR, at optimized locations, to obtain reconfigurability over additional bands of interest. Having the switches in the ground plane makes it easier to bias them with little effect on the antenna characteristics.

4. CONCLUSION

A simple frequency reconfigurable antenna was presented in this paper. Starting with a UWB antenna, a CSRR was added to the ground plane below the antenna's microstrip line. Incorporating a gap in this line transforms the band stop characteristic of the CSRR into a band pass one. The obtained band pass frequency depends on the location of the CSRR's split. Using switches to represent several possible split positions, frequency reconfigurability was made possible by controlling these switches.

A prototype with two switches was fabricated and tested. In addition to operation over one of two selective bands, the design showed good radiation patterns and gain figures. There was clear agreement between the measured and simulated results. The inclusion of additional switches is possible to obtain more bands of operation.

REFERENCES

1. Peroulis, D., K. Sarabandi, and L. P. B. Katehi, "Design of reconfigurable slot antennas," *IEEE Transactions on Antennas and Propagation*, Vol. 53, No. 2, 645–654, February 2005.
2. Yang, S., Z. Chunna, P. Helen, A. Fathy, and V. Nair, "Frequency-reconfigurable antennas for multiradio wireless platforms," *IEEE Microwave Magazine*, Vol. 10, No. 1, 66–83, February 2009.
3. Huff, G. H., J. Feng, S. Zhang, and J. T. Bernhard, "A novel radiation pattern and frequency reconfigurable single turn square spiral microstrip antenna," *IEEE Microwave and Wireless Components Letters*, Vol. 13, No. 2, 57–59, February 2003.
4. Ramadan, A., M. Al-Husseini, K. Y. Kabalan, and A. El-Hajj, "Fractal-shaped reconfigurable antennas," *Microstrip Antennas*, InTech, April 2011, ISBN 978-953-307-247-0.
5. Madi, M., M. Al-Husseini, A. Ramadan, K. Y. Kabalan, and A. El-Hajj, "A reconfigurable cedar-shaped microstrip antenna for wireless applications," *Progress In Electromagnetics Research C*, Vol. 25, 209–221, 2012.
6. Al-Husseini, M., L. Safatly, A. Ramadan, A. El-Hajj, K. Y. Kabalan, and C. G. Christodoulou, "Reconfigurable filter antennas for pulse adaptation in UWB cognitive radio systems," *Progress In Electromagnetics Research B*, Vol. 37, 327–342, 2012.
7. Al-Husseini, M., A. Ramadan, A. El-Hajj, K. Y. Kabalan, Y. Tawk, and C. G. Christodoulou, "Design based on complementary split-ring resonators of an antenna with controllable band notches for UWB cognitive radio applications," *Proceedings of the 2011 IEEE International Symposium on Antennas and Propagation (IEEE AP-S 2011)*, 1120–1122, Spokane, USA, July 2011.
8. Al-Husseini, M., J. Constantine, C. G. Christodoulou, S. E. Barbin, A. El-Hajj, and K. Y. Kabalan, "A reconfigurable frequency-notched UWB antenna with split-ring resonators," *Proceedings of the 2010 Asia-Pacific Microwave Conference (APMC 2010)*, 618–621, Yokohama, Japan, December 2011.
9. Kazerooni, M., A. Cheldavi, and M. Kamarei, "A novel bandpass defected microstrip structure (DMS) filter for planar circuits," *PIERS Proceedings,* 1214–1217, Moscow, Russia, August 18–21, 2009.
10. HFSS, ANSYS, Canonsburg, PA 15317, USA.

Multi-band Dual Polarized Indoor Antenna for Diversity and MIMO Applications

Feng Gao[1], **Peng Gao**[1], **Tong Wu**[2], **and Runhong Shan**[3]

[1]China Mobile Group Design Institute, Beijing 100080, China
[2]China National Institute of Metrology, China
[3]Copyright Protection Center of China, China

Abstract— This paper proposes a novel dual polarized omni-directional indoor antenna, which can be used as multi-input multi-output (MIMO) antenna in LTE system. The vertical dipole covers from $0.8 \sim 3$ GHz and the horizontal dipole covers GSM1800, TD-SCDMA, wireless local area network (WLAN) and long term evolution (LTE) systems. This indoor antenna has been experimented in MIMO systems for the WLAN system and LTE-TDD scale testing network separately. Based on the experiment, the cumulative distribution function (CDF) curve of Timing offset between uplink and downlink radio frames, reference signal received power (RSRP), signal to noise ratio (SNR) and throughput of downlink and uplink are studied, compared with single-input single-output (SISO) system.

1. INTRODUCTION

In radio, multiple-input and multiple-output is the use of multiple antennas at both the transmitter and receiver to improve communication performance. The 3rd generation partnership project (3GPP) has launched the study item of the long term evolution (LTE) system. MIMO technology has attracted attention in wireless communications, because it offers significant increases in data throughput and link range without additional bandwidth or increased transmit power. Because of these properties, MIMO is an important part of modern wireless communication standards such as IEEE 802.11n (Wifi), 4G, 3GPP LTE, WiMAX and HSPA [1, 2].

China Mobile Communications Corporation (CMCC) have made progress for the TD-LTE system through LTE scale experimental network. This paper proposes a novel dual polarized omni-directional indoor antenna, which can be used as multi-input multi-output (MIMO) antenna in LTE system. The vertical dipole covers from $0.8 \sim 3$ GHz and the horizontal dipole covers GSM1800, TD-SCDMA, wireless local area network (WLAN) and LTE systems.

2. CONFIGURATION OF INDOOR MIMO ANTENNA MODEL

In MIMO systems, a transmitter sends multiple streams by multiple transmit antennas. The transmit streams go through a matrix channel which consists of all $N_t N_r$ paths between the N_t transmit antennas at the transmitter and N_r receive antennas at the receiver. Then, the receiver gets the received signal vectors by the multiple receive antennas and decodes the received signal vectors into the original information. A narrowband flat fading MIMO system is modelled as [3]

$$\mathbf{Y} = \mathbf{H}\mathbf{x} + \mathbf{n} \tag{1}$$

where $\mathbf{Y}$ and $\mathbf{x}$ are the receive and transmit vectors, respectively, and $\mathbf{H}$ and $\mathbf{n}$ are the channel matrix and the noise vector, respectively. The system is shown in Figure 1.

The MIMO antenna is regarded as a multi-port microwave network. The incident wave and reflected wave relationship is given below [4]

$$\begin{bmatrix} \bar{a}_{(N\times 1)} \\ \bar{b}_{(\infty\times 1)} \end{bmatrix} = S \cdot \begin{bmatrix} a^+_{(N\times 1)} \\ b^+_{(\infty\times N)} \end{bmatrix} = \begin{bmatrix} S_{aa(N\times N)} & S_{ab(N\times\infty)} \\ S_{ba(\infty\times N)} & S_{bb(\infty\times\infty)} \end{bmatrix} \cdot \begin{bmatrix} a^+_{(N\times 1)} \\ b^+_{(\infty\times N)}) \end{bmatrix} \tag{2}$$

Referring to information theory, the ergodic channel capacity of MIMO systems where both the transmitter and the receiver have perfect instantaneous channel state information is [5]

$$C_{p-CSI} = E\left[\max_{Q;tr(Q)\leq 1} \log_2 \det\left(1 + \rho \mathbf{H}\mathbf{Q}\mathbf{H}^{\mathbf{H}}\right)\right] = E[\log_2 \det(1 + \rho \mathbf{D}\mathbf{S}\mathbf{D})] \tag{3}$$

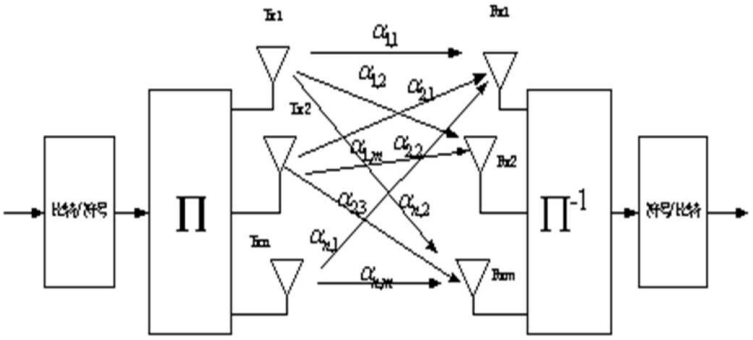

Figure 1: MIMO antenna channel model.

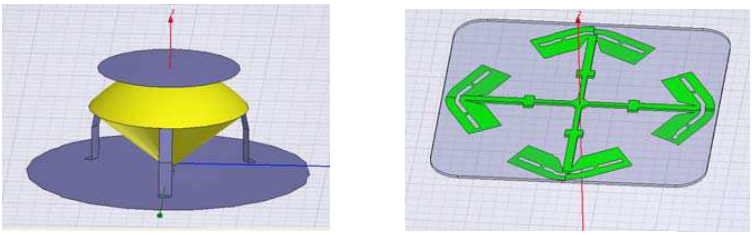

(a) vertical element (b) horizontal element

Figure 2: Structure of the dual-polarized antenna.

where $()^H$ denotes Hermitian transpose and ρ is the ratio between transmit power and noise power (i.e., transmit SNR). The upper bound of SINR of the mobile receiver for a cell with K users is obtained as follows [6]

$$SINR^k = \frac{\det[H_k^{-1} H_k]}{\sigma^2_{v_1^k} + \sigma^2_{v_2^k}} \tag{4}$$

Under the Gaussian approximation [7], the bit error rate (BER) can be written with the SINR as

$$\overline{BER}^k = Q\left(\sqrt{SINR^k}\right) \tag{5}$$

where $Q(\cdot)$ is Gaussian approximation function.

3. SIMULATION AND ANALYSIS OF DUAL-POLARIZED INDOOR ANTENNA

The Figure 2 shows the vertical polarized and the horizontal element of the antenna. The horizontal polarized element is formed with four folded dipoles which are rotating feed, and the vertical polarized element is formed with the inverted-cone monopole and the bottom board. Because the horizontal polarized element and vertical polarized element are coaxial, which can decrease the interplay, reduce the interference, and increase the isolation each other.

The frequency range of the dual-polarized antenna as shown in Figure 2 covered 824 $\sim$ 960 MHz, 1710 $\sim$ 3000 MHz by vertical polarized element and covered 1710 $\sim$ 2700 MHz by horizontal polarized element. The simulations of the antenna pattern are shown in Figure 3.

From the simulation and analysis, the non-circularity of the dual-polarized antenna is lower than ± 1.5 dB.

4. PERFORMANCE EVOLUTION OF INDOOR MIMO TESTED

4.1. Indoor LTE MIMO System Tested

In order to clarify the basic characteristics of our indoor MIMO tested, we have conducted measurements and indoor environment. Figure 4 shows the single and dual channel indoor distribution systems.

For the indoor LTE system tested, there are two environments respectively shown in Figure 4. The Figure 4(a) shows the single channel indoor distribution system and the Figure 4(b) shows the dual channel indoor distribution system.

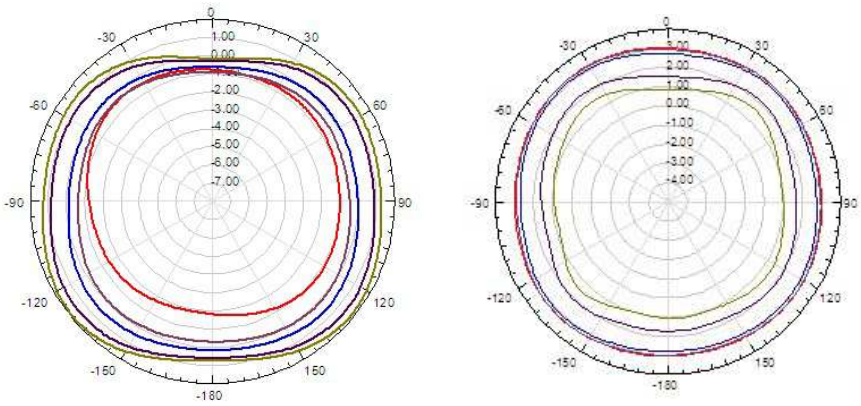

(a) vertical polarization (b) horizontal polarization

Figure 3: Pattern of the dual-polarized antenna.

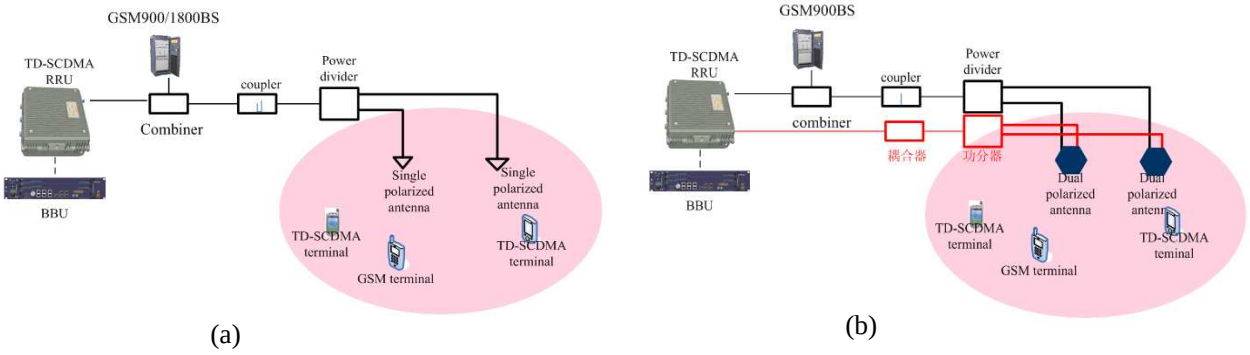

Figure 4: (a) Single channel indoor distribution system. (b) Dual channel indoor distribution system.

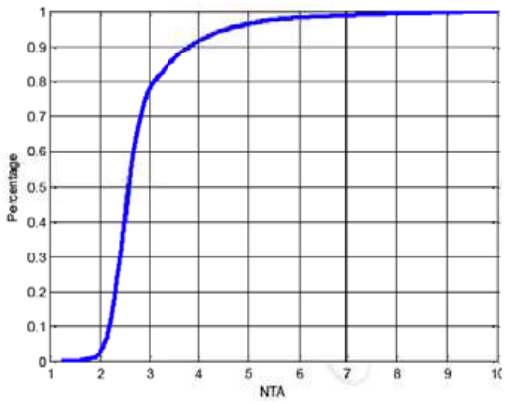

Figure 5: Dual polarized antenna CDF curve in middle section.

Antenna signal correlation can be used to solve pattern relationship. Figure 5 shows the dual polarized MIMO antenna NTA CDF distribution curve in midpoint region.

Figure 6 shows downlink throughput of six equipment manufacturers (EM) in LTE scale experimental network test. Several RRU should be integrated for same distribution system to save the network construction cost. Different frequency network could be recommended if several cells exist in same distribution system carrier bandwidth of 20 MHz.

4.2. Indoor WLAN MIMO System Tested

In order to verify the 802.11n WLAN performance based on MIMO systemthe wireless signal strength test, signal to noise ratio test, ping test, AP configuration check and interference test and FTP test are implemented. Figure 7 and Figure 8 respectively show the dual polarization 2×2 MIMO 40 M mode uplink and downlink throughput.

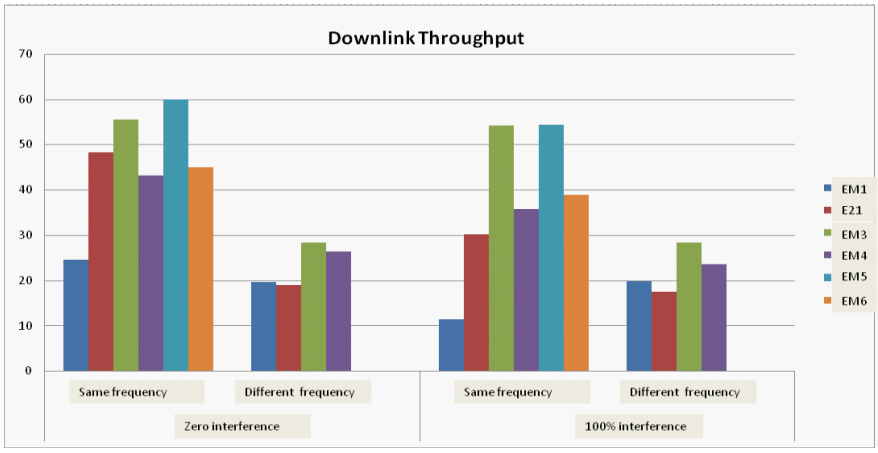

Figure 6: Downlink throughput for same or different frequency network.

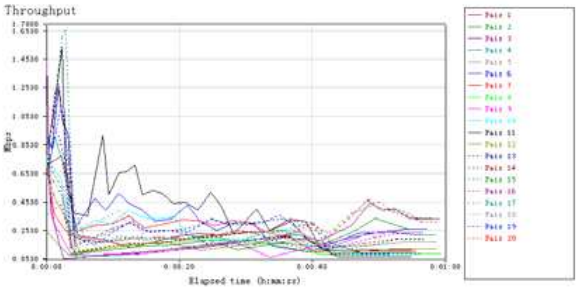

Figure 7: Uplink throughput in 40 M model 2×2 MIMO system in middle section.

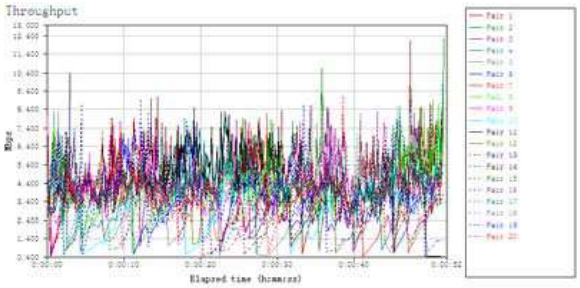

Figure 8: Downlink throughput in 40 M model 2×2 MIMO system in middle section.

5. CONCLUSION

The system capacity and correlation of indoor WLAN system and LTE system are analyzed in this paper, comparation of SISO and MIMO system is tested. The test shows that transmitting power of terminal of dual channel MIMO antenna system can be reduced t using multipath effect, improve the downlink throughput, and SNR and anti-interference ability are improved obviously.

REFERENCES

1. Dong, L., H. Choo, R. W. Heath, Jr., and H. Ling, "Simulation of MIMO channel capacity with antenna polarization diversity," *IEEE Transactions on Wireless Communication*, Vol. 4, No. 4, 2005.
2. Jamlos, M. F., T. B. A. Rahman, M. R. B. Kamarudin, P. Saad, O. Abdul Aziz, and M. A. Shamsudin, "Adaptive beam steering of RLSA antenna with RFID technology," *Progress In Electromagnetics Research*, Vol. 108, 65–80, 2010.
3. Telatar, E., "Capacity of multi-antenna gaussian channels," Technical Report, AT & T Bell Labs, Jun. 1995.
4. Collin, R. E. and F. J. Zucker, *Antena Theory*, Part I, McGraw-Hill Book Co., NewYork, 1969.
5. Love, D., R. Heath, V. Lau, D. Gesbert, B. Rao, and M. Andrews, "An overview of limited feedback in wireless communication systems," *IEEE Journal on Selected Areas Communications*, Vol. 26, 1341–1365, 2008.
6. Xiao, Y., Y. Zhao, and M. H. Lee, "Canceling co-channel interference for MIMO CDMA systems," *Signal Processing 8th International Conference*, Beijing, 2006.
7. Xiao, Y., L.-Y. Lu, and Y.-C. Wang, "Space-time spreading in downlink of TD-SCDMA systems," *Proceedings of the IEEE 6th Circuits and Systems Symposium on Emerging Technologies: Frontiers of Mobile and Wireless Communication*, Vol. 2, 635–638, 2004.

Applicability of DCA in HAPS-based Systems in 5850–7075 MHz Band

Mastaneh Mokayef[1], **Walid A. Hassan**[1], **Yassir A. Ahmad**[2], **and Tharek Abd. Rahman**[1]

[1]Wireless Communication Center, University of Technology Malaysia (UTM), Malaysia
[2]Department of Communications Engineering, University of Diyala, Iraq

Abstract— The High Altitude Platform System (HAPS) which will provide a worldwide connectivity in wireless networks operates in 5850–7075 MHz spectrum endorsing the safety of primary services such as terrestrial systems (TS). The suppleness and innate characteristics of HAPS made it a trustable system that can adapt itself to operate as a secondary system in this allotment. To efficiently develop the restricted resources of the radio spectrum, the spectrum has to be divided into sub-channels to be reused. This paper offers the status of a feasibility study on the Dynamic Channel Assignment (DCA) in the mentioned band. In contrast to other mitigation techniques, the DCA technique is likely to evade either causing or accepting interference from/to TS by seeking for a part of a spectrum that is vacant so far; hence, sensing carriers transmitted from TS is the most critical issue in this technique. In this paper, a computer simulation is dispensed to assess the effect of deploying the HAPS as a secondary activated system that shares the band with TS. The paper utilizes the DCA scheme to mitigate the interference caused by HAPS into TS in order to share the spectrum between the two services. Additionally, the possibility of assigning DCA and the ability of sensing signal a victim time by the HAPS gateway (HAPSGS) with separation distance of up. 6 km is proven In order to enhance the DCA performance, the sensing threshold level is diminished from 1dB to 0.3 dB. Accordingly, the feasibility of DCA improved from 6 km to 7 km far from the urban edge of coverage (EOC) area of HAPS.

1. INTRODUCTION

A novel broadband telecommunication system has been anticipated for stipulation of fixed and mobile services known as the High Altitude Platform System (HAPS) [1]. The HAPS is located in the stratospheric layer at altitudes between 17 and 50 km from the ground. The International Telecommunication Union (ITU) has allocated a pair of 80 MHz of spectrum for HAPS in 5850–7075 MHz band to be shared on a non-destructive basis with terrestrial service (TS) for this service [1, 2]. As a complementary network to TS, HAPS has a brilliant role in telecommunication infrastructure [3]. It should be mentioned that rain attenuation is sensibly insignificant for frequencies trifling than 10 GHz [4]. Hence the TS face less amount of propagation attenuation in 5850–7075 MHz band. Since the TS operate in the spectrum range between the spectrum from 5850 MHz to 7075 MHz, the compatibility between the HAPS and TS services is improbable. Hence, the tolerable interference level from HAPS has to respect the essential sharing allowances of previously allocated systems. Thus the interference mitigation is one of the most essential issues to enhance the HAPS-based networks [5]. Applying the dynamic channel assignment (DCA) technique in HAPS service, scrutinizes the status of frequency use of TS and assigns the non-use frequency channel for HAPSGS communication link. Earlier works [6, 7] proposed some channel assignment algorithms for the DCA technique. Among them, [6] combined the frequency division multiple access (FDMA) and the time division multiple access (TDMA) and to utilize them in DCA algorithm, while the novelty of [7] was in forming grid-loops. Study [8] has scrutinized the feasibility of sensing the carriers at HAPSGS from fixed services (FS) in the frequency band 31 GHz and 28 GHz. Interference from the fixed satellite service (FSS) in uplink (UL) and from the HAPS downlink (DL) communication to the Earth Exploration Satellite Service (EESS) has been also evaluated. Our work differs from previous work as we utilized the 5.8 GHz band in which the rain attenuation can be ignored. Hence our study investigates the sharing scenario for tropical areas and regions with heavy rain.

2. SYSTEM MODEL AND PARAMETERS

We assumed a single HAPS airship (HAPSAS) situated in stratosphere utilizing multi-beam array antenna operating with HAPS gateway (HAPSGS). The Urban Area of HAPS coverage (UAC) contains the sub-platform point known as Nadir Point (NP). The NP is located at the center of the HAPS coverage area. In our study, the NP is considered as a starting point in the sharing scenario. The HAPSGS is fixed 36 km away from NP (i.e., located at EOC) causing interference

Table 1: System simulation parameters [8].

Parameters	HAPS	TS
Transmit power (dBm)	−22	−4
Antenna pattern	Resolution 221 (Rev.WRC07)	ITU-R.F.699
Transmit feeder loss (dB)	4.1	3
Frequency (GHz)	5.7	5.7

to TS. To achieve the most sympathetic compatibility results, the highest value mentioned in the Table 1 for transmit power has been considered here in conjunction with the highest value of the gain of HAPS. Assumed characteristics for the UL transmission are given in Table 1.

Tolerable interference to noise ratio level of −10 dB with respect to the interference threshold level of −147 dB is assumed. The interference to noise ratio (INR) amount depends on the azimuth of the main beam axis.

3. METHODOLOGY

Our study methodology considers the *INR* of the TS that moves in diminutive steps of 1 km along the shortest path between EOC and NP. We assume the interference threshold value of −147 dB in order to find the results of the safe separation distance away from HAPSGS. Since the HAPS and TS sharing the same frequency band, the DCA technique could be an effective mitigation method to search the non-utilized frequency channel not to give nor receive interference from/to TS/HAPS. In applying the DCA technique, the HAPSGS uses its frequency monitoring function to scrutinize the availability of TS with which frequency sharing is done and finally dispenses the relevant channel for communication link. To enlighten, the methodology is divided and described in three steps. In the first step, the HAPSGS must sense the carrier from TS. Second step is to find the raised noise level from HAPSGS at TS. Finally the DCA technique will be applied and the HAPS will operate in the non-used channel.

The interference I (dBm) signal power at the TS is obtained from the following equation:

$$I = P_H + G_H + G_T - PL_H \tag{1}$$

where P_H (dBm) is transmitted power G_T (dBi) is the gain of TS from HAPSGS, G_H (dBi) is the gain of HAPSAS and the PL_H (dB) is the free space path loss calculated as:

$$PL_H = 92.4 + 20\log(f) + 20\log(d) \tag{2}$$

where f (GHz) represents the frequency and d (km) stands for the propagation path's length between interferer and the sufferer.

In order to assess the interference, the *INR* level at the TS is found as:

$$INR = I - N \tag{3}$$

where N (dBm) is the noise floor of the TS.

The following formula (3) inspects the sensing level of transmitted signal of victim based on the separation distance between TS and HAPSGS.

$$P_{GS} = P_{TS} + A_{TS} - PL_H + A_{GS} - 10\log(B) \tag{4}$$

where P_{GS} (dBm) represents the transmit power from HAPSGS, P_{TS} (dBm) stands for the transmit power from TS, A_{TS} (dBi) is the antenna gain of TS and A_{GS} (dBi) antenna gain of HAPSGS.

4. RESULTS AND DISCUSSION

The simulation re results shows that the TS faces a sever interference from HAPSAS when located at the NP. Moreover, the minimum horizontal separation distance of 14 km from NP is necessary to mitigate the interference as depicts in Figure 1. Figure 2 shows the ability of HAPSGS in sensing the transmitted signal of TS in order to detect the channel in use by TS. As result illustrates, the HAPSGS can only sense TS signals when TS is located up to 6 km away from HAPSG (i.e., 30 km away from NP).

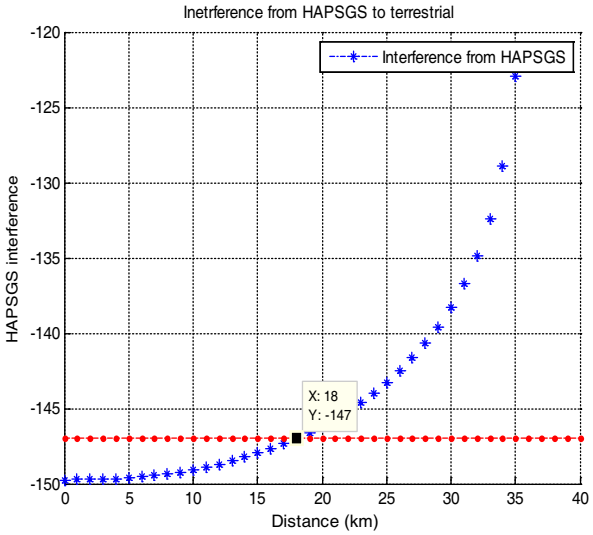

Figure 1: Interference level from HAPSGS.

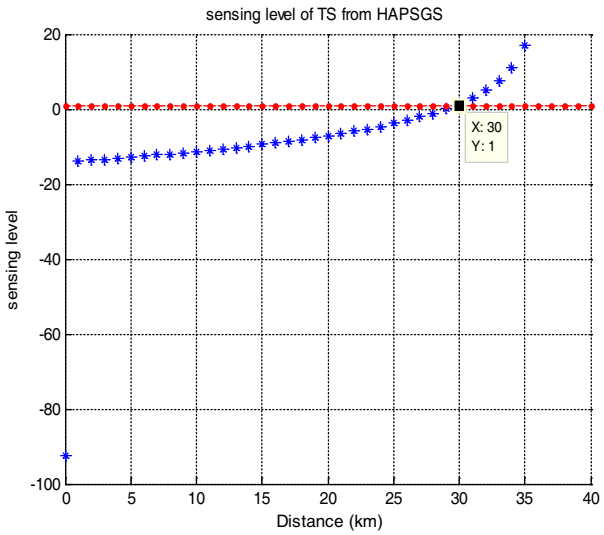

Figure 2: Sensing signal level of TS by HAPSGS.

5. CONCLUSION

The feasibility of DCA in HAPS-based system operating in 5850–7075 MHz band is investigated. The results obtained from the initial performed simulations, shows that in spite of possibility of existing interference from HAPSGS in a distance between 18 km to 30 km away from NP. Moreover, the HAPSGS is capable of sensing signal of TS up to 6 km away from its own location. The comparison with the coordination distances previously proposed for TS illustrates that DCA is feasible up to 6 km away from EOC of HAPS. In our analysis, the sensing threshold level of 1 dB was employed. However this amount can be reduced in order to enhance the obtained result. Out suggested methodology can be a basis to improve the sharing and coexisting of HAPS and TS in UAC of HAPS.

REFERENCES

1. Milas, V. F. and P. Constantinou, "Interference environment between high altitude platform networks (HAPN), geostationary (GEO) satellite and wireless terrestrial systems," *Wireless Personal Communications*, Vol. 32, No. 3, 257–274, 2005.
2. Likitthanasate, P., D. Grace, P. D. Mitchell, "Dynamic spectrum sharing for High Altitude Platform and terrestrial WiMAX systems sharing a common downlink frequency band," *1st Workshop on High Altitude Platforms (WHAPS)*, 2005.
3. "Interference analysis modelling for sharing between HAPS gateway links," ITU, 2009.
4. Nia, M. M. and T. A. Rahman, "High altitude platform system (HAPS) and co-existence with fixed satellite service (FSS) in frequency range 5850–7075 MHz," *IEEE*, 1–6, 2011.
5. Nia, M. M. and T. A. Rahman, "Fixed satellite service (FSS) and high altitude platform (HAP) interference evaluation for adjacent channels outside platform area coverage," *2011 4th International Conference on. Modeling, Simulation and Applied Optimization (ICMSAO)*, 1–4, April 19–21, 2011.
6. Chuang, J. C. I. and N. R. Sollenberger, "Performance of autonomous dynamic channel assignment and power control for TDMA/FDMA wireless access," *IEEE Journal on Selected Areas in Communications*, Vol. 12, No. 8, 1314–1323, 1994.
7. Xia, Y., et al., "Loop-based dynamic channel assignment for multi-radio multi-channel wireless mesh networks," *IEEE*, 265–268, 2010.
8. Su, L. and D. Chen, "Dynamic channel allocation schemes based on SINR analysis for cellular relaying networks," *IEEE*, V13-104–V13-108, 2010.

Utilizing ATPC Scheme to Facilitate Sharing between HAPS and Terrestrial in 5.7 GHz Band

Mastaneh Mokayef[1], **Walid A. Hassan**[1], **Yassir A. Ahmad**[2], **and Tharek Abd. Rahman**[1]

[1]Wireless Communication Center, University of Technology Malaysia (UTM), Malaysia
[2]Department of Communications Engineering, University of Diyala, Iraq

Abstract— The development of sharing spectrum between High Altitude Platform System (HAPS) and Terrestrial System (TS) in the 5.8 GHz band is the paper main aim. This paper focuses on Automatic Transmitting Power Control (ATPC) as an interference mitigation scheme capable of utilizing the spectrum sharing between the HAPS and TS operating in the 5.8 GHz band. We employ the ATPC as a fundamental mitigation technique that can reduce the transmission power from a HAPS airship (HAPSAS) or HAPS gate station (HAPSGS). Although customarily, the ATPC techniques have been utilized to conflict rain attenuation by increasing or decreasing the transmission power, we utilized it to mitigate the co-channel interference (CCI) from HAPS into the TS, since both systems operate in the spectrum below the 11 GHz band with negligible rain attenuation. Hence, deep discussion on the interference analysis procedure and interference mitigation possessions from both HAPSAS and HAPSGS is done. Our paper presents the performance of an ATPC in a sharing scenario containing HAPS and TS operating in the same frequency band. The performance of the TS system is evaluated based on the Interference-to-Noise Ratio (INR) level. Accordingly, results show that the adjusted power between −46.1 and −13.67 dBW/MHz is required for HAPS to achieve the coexistence with TS at 5.8 GHz band. Our results can enhance the spectrum sharing between the two services, and thus the spectrum can be utilized more efficiently.

1. INTRODUCTION

The High Altitude Platform System (HAPS) is an innovative delivery platform or airship (manned or unmanned) [1] with emphasized position in telecommunication infrastructures [2]. Since HAPS operate in the stratosphere, its brilliant spatial position enables it to offer a much more ample coverage area than the terrestrial system (TS). The complementary way of communications between HAPS and TS leads to interference increment between the two systems in the same frequency band.

In order to enhance the coexistence of HAPS based communication systems and decrease the interference level between them, it is necessary to deploy a proper mitigation technique. In case of HAPS and TS spectrum sharing, the Automatic Transmitting Power (ATPC) is one of the interference mitigation candidates. The ATPC is an essential way of avoiding redundant transmission power of the signal to the victim. Recently several types of power control techniques have been premeditated based on the estimation of the received power [3].

Since the spectrum frequency of the 5850–7075 MHz band is first allocated for TS and other FS systems, the operation of HAPS in this band should not cause additional interference with these systems. Hence, the primary services must be protected from the harm of interference of the prospective secondary services [4]. Conventionally, the ATPC techniques have been utilized in microwave radio links to struggle with the rain attenuation. In the beginning, the link is deliberated such that the transmission power is adequately bulky to accomplish a given quality of service. Then the transmit power will be increased gradually due to the attenuation experienced [3]. The ATPC is defined as a process of diverging the transmit power in a microwave link to preserve the desired restricted service license [5]. The IEEE 802.16 mulls over ATPC applications in fixed wireless networks [6]. The Federal Communications Commission (FCC) synchronized the convention and restrictions of ATPC techniques point to point wireless systems over higher frequency bands [7].

2. SHARING SCENARIO

The sharing scenario of this study is based on a single HAP positioned at the altitude of 21 km above its sub platform point known as Nadir Point (NP). Single TS located within the urban area of coverage (UAC) of the HAPS. The HAPSGS is located at the edge of coverage (EOC) of HAPS. An assumption in our study is extracted from [8] in which range of acceptable Equivalent Isotropic Radiated Power (E.I.R.P) is determined based on different elevation angles. Figure 1 shows the sharing scenario between the HAPS and TS in urban areas.

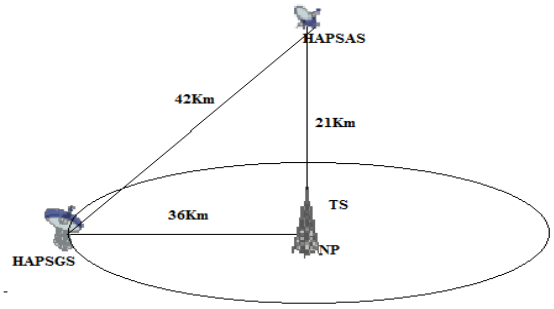

Figure 1: Sharing scenario between HAPS and TS in UAC.

Table 1: The HAPS and TS parameters.

Parameters	HAPS	TS
Transmitter power (dBm)	−22	−4
Antenna gain (dBi)	30	15
Coverage (km)	0.5	36
Simulation environment	Urban	
Frequency band (GHz)	5.7	
Bandwidth (MHz)	11	
INR (dB)	−10 (ITU-R F.1094)	
Noise figure (dB)	-	4 [10]
Noise power (dBm)	-	−139.98 [10]

Since the spectrum sharing is proscribed in a noise restricted manner, the *INR* threshold level of −10 dB [9] is presupposed in this study. The adroitness expanses between operations areas of systems are delineated by *INR* level. Sharing spectrum absorbed lots of attentions and still researches are under consideration to find a more liberal way of sharing. In order to cover the whole UAC, the off-axis angle of HAPS varies between 0 and 60 degrees from NP. The first district contains the off-axis angle range of zero to twenty degrees; the second group incorporates off-axis angles of twenty to forty three degrees, and the last district contains the off-axis angles from forty three to sixty degrees. Accordingly, a specific level of E.I.R.P dedicated to each group defined as follows:

- the E.I.R.P range between −0.5 dBW/10 MHz and 0 dBW/10 MHz considered for the first district;
- the E.I.R.P. should be fulfilled with the range between 0 dBW/10 MHz and 2.1 dBW/10 MHz in the second category and;
- the E.I.R.P. should be abided by range between 2.1 dBW/10 MHz and 0.5 dBW/10 MHz [8].

The imperative system parameters for both HAPS and TS are summarized in Table 1.

3. METHODOLOGY

The acceptable level of *INR* is the main parameter utilized in this paper to evaluate the performance of the system. Accordingly, it is the reference to apply the proper adjusted power to reduce the interference level from HAPS to TS. HAPS transmit power must be adjusted in accordance with principles in which the interference is acceptable between the HAPS and the TS. In the methodology, an assumption has been considered to make the results base on practical situation; since the 5850–7075 MHz band is primarily allocated for TS, the HAPS is the new technology that will occupy a frequency that is adjacent to the TS, and will cause interference.

The first step in the compatibility calculation is to activate the TS and assume there are no HAPS services to cause interfere. After a while, the HAPS is activated and starts to transmit with

its highest transmit power. The HAPS activation will cause degradation of performance to the TS; hence the *INR* is calculated based on three steps [11]; First to calculate the interference from HAPS into TS, second to compute the noise level of the TS receiver, and third we find the INR level of the receiver in order to extract the required adapted to transmit power from HAPS. In the following sub-section, each of the above steps is described in details.

3.1. Calculation of the Interference from HAPS to TS

The following equation evaluates the interference level I (dBm) from the HAPSGS or HAPSAS into the TS:

$$I = P_H + G_H + G_T - PL_H \tag{1}$$

where P_H (dBm) is the transmitted power from HAPS. G_T (dBi) is the gain of TS, G_H (dBi) is the gain of HAPS and the PL_H (dBm) is the free space path loss calculated as follows [14]:

$$PL_H = 92.4 + 20\log(f) + 20\log(d) \tag{2}$$

in which f (GHz) is the operating frequency, d (km) is the distance between HAPS and TS.

3.2. Calculation the Noise Power (dBm)

The Noise level N (dBm) is expressed as:

$$N = -114 + 10\log(B_W) + N_F \tag{3}$$

where N_F (dB) and B_W (MHz) represent noise power and bandwidth respectively.

3.3. Evaluates the INR Level at the TS

Since the *INR* level determines whether the transmitted power of HAPS needs to be adjusted or not, the *INR* level at the TS receiver antenna is calculated as:

$$I/N = I - N \tag{4}$$

After comparing the results with the interference threshold, the adjusting of the interference level is applied; at this stage, if the *INR* level is less than -10 dB, the transmitted power from HAPS needs no adjustment. Contrary if the *INR* is above -10 dB, then first interference level must be adjusted based on the following equation:

$$I_{adj} = INR_{desired} \times N_F \tag{5}$$

where I_{adj} is the acceptable interference level and $INR_{desired}$.

The HAPS has to transmit with newly adjusted power by the following equation:

$$P_{adj} = I_{adj}/G_H(O)G_T(Q)PL_H \tag{6}$$

in which $G_H(O)$ (dBi) is the gain of HAPS at an angle of O degree away from bore sight and $G_T(Q)$ (dBi) is the gain of TS at angle Q degree away from its bore-sight.

4. RESULTS AND OBSERVATIONS

Figure 2 shows the obtained epitomized results when applying the ATPC with respect to E.I.R.P restrictions and finding the adjusted required power. Additionally, Figure 2 depicts the required adjusted power for HAPSGS. It is shown that at least a power of -46.1 dBW/MHz is necessary for HAPSGS to mitigate its harmful interference effect. Moreover, the HAPSGS can operate at the maximum transmit power of -19.26 dBW/MHz when TS is located at the NP. Accordingly, when TS is located closer to the EOC, the transmit power from HAPS must be reduced. This reduction process continues till TS locates at the EOC, and the transmit power is reduced to -46.1 dBW/MHz.

As illustrated in Figure 3, the increment of about 10 dBW/MHz is observed in power adjustment procedure in one cycle. A separation distance of 36 km away from the NP proves to be adequate for the maximum power of -13.67 dBW/MHz.

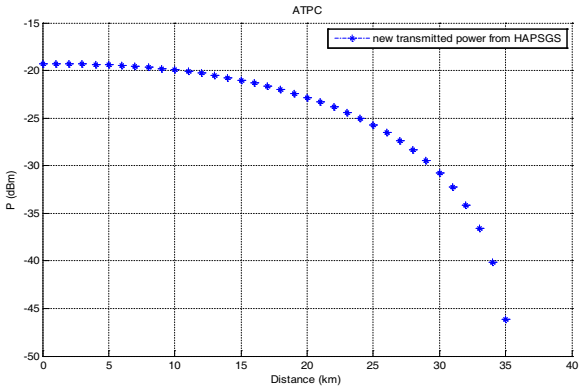

Figure 2: Adjusted power for HAPSGS.

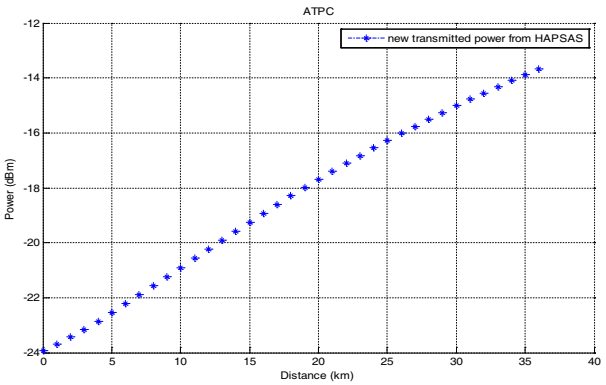

Figure 3: Adjusted power for HAPSAS.

5. CONCLUSION

The possibility of spectrum sharing enhancement between the HAPS and the TS services operating in the UAC is investigated. The study also described a methodology for adjusting the transmit power from both HAPSAS and HAPSHGS into the TS in order to reduce the CCI. Evaluation of the CCI level created by HAPS in uplink and downlink communications is illustrated by a mathematical modeling to compute the amount of interference received by TS from HAPSAS in the 5850–7075 MHz band. Our results gain reduction in the required separation distance by utilizing the ATPC technique. Our results also show that the transmitted power from HAPSAS and HAPSGS is reduced from −22 dBW/MHz two −46.1 dBW/MHz and −24 dBW/MHz respectively, which lead to significant decrease with the separation distance to about 9 km.

REFERENCES

1. Widiawan, A. K. and R. Tafazolli, "High altitude platform station (HAPS): A review of new infrastructure development for future wireless communications," *Wireless Personal Communications*, Vol. 42, No. 3, 387–404, 2007.
2. Likitthanasate, P., D. Grace, and P. Mitchell, "Spectrum etiquettes for terrestrial and high-altitude platform-based cognitive radio systems," *IET Communications*, Vol. 2, No. 6, 846–855, 2008.
3. Rahman, T. A. and T. C. Leng, "Design and performance analysis of adaptive transmit power control in point-to-point microwave link for rain attenuation problem," *IEEE*, Vol. 2, 1159–1164, 2003.
4. Yoon, Y. K., "Effective method of interference mitigation for UWB cooperation with WiMAX," *IEEE*, 329–332, 2010.
5. Kim, J., S. Chang, and Y. Kwon, "ODTPC: On-demand transmission power control for wireless sensor networks," *IEEE*, 1–5, 2008.
6. Callaghan, S., I. Inglis, and P. Hansell, "Impact of introducing automatic transmit power control in PP fixed service systems operating in bands above 13 GHz extension: Soft boundary frequency assignment techniques and adaptive coding," 2007.
7. Marin, S., *Interference Relationships Between Point-to-Multipoint Stations at about 28 GHz Authorized by Area License*, SpectraPoint Wireless LLC, 2000.
8. ECC Report 156, "Conditions for possible co-existence between HAPS gateway links and other services/systems in the 5850–7075 MHz band," *Electronic Communications Committee (ECC) within the European Conference of Postal and Telecommunications Administrations (CEPT)*, CEPT, 2011, http://www.ecodocdb.dk/doks/doccategoryECC.aspx?doccatid=4.
9. ITU-R F.758-4, "Considerations in the development of criteria for sharing between the fixed service and other services," ITU, 2005, http://www.itu.int/rec/R-REC-F.758/enm, Acess Date: May 29, 2012.
10. Callaghan, S., "Rain field modelling for fixed radio systems using fade mitigation techniques," 2008.
11. Abdulrazak, L., et al., "Study HAPS interference power to noise level ratio of fixed services and related separation distance," *IEEE*, 690–693, 2010.

Enhancement of Coexistence between HAPS and Terrestrial System in 5.8 GHz Band

Mastaneh Mokayef[1], **Walid A. Hassan**[1], **Yassir A. Ahmad**[2], **and Tharek Abd. Rahman**[1]

[1]Wireless Communication Center, University of Technology Malaysia (UTM), Malaysia
[2]Department of Communications Engineering, University of Diyala, Iraq

Abstract— The 5.850–7.075 GHz frequency band is allocated utterly for terrestrial radio communications. The High Altitude Platform System (HAPS) operates in this allotment certifying the protection of existing services. The expected sharing scenario in the mentioned band is between the HAPS system and the Terrestrial System (TS). Both systems operate in the adjacent channel frequency band; and thus, interference between these systems is a critical issue, which requires comprehensive spectrum sharing study. This paper investigates the performance of uplink (UL) and downlink (DL) communications of both systems. The study analyzes the interference caused by HAPS into the TS as a function of distance from the Nadir Point (NP) to the HAPS Gateway Station (HAPSGS). It is assumed that the HAPS system operates at an adjacent channel to the TS system. The coexistence performance is evaluated based on the interference-to-noise ratio (INR) of the victim link. In order to avoid adjacent channel interference, the simulation results shows that the separation distances should be 10 km from the HAPS airship (HAPSAS), and 22 km from HAPSGS. Therefore, in order to mitigate the interference, the required isolations for TS to coexist with the HAPSAS and HAPSGS should be 5.6 dB and 45.14 dB respectively.

1. INTRODUCTION

The High Altitude Platform System (HAPS) is an aircraft or an airship flying in the low density, non tumultuous air stream at the stratospheric altitude of 21 km from the surface of the earth [1, 2]. The vacillation of HAPS at this altitude is not devastating [3, 4]; and it is capable of delivering a large number of broadband services [1]. Since HAPS and TS operate in the 5.850–7.075 GHz band, the adjacent channel interference (ACI) between HAPS and TS is a critical issue. Therefore, the compatibility study between the two systems is imperative in order to achieve spectrum optimization. Earlier work [5] investigates the compatibility between the Fixed Satellite Service (FSS) and HAPS systems by considering the ACI sharing scenario. The ACI in urban and suburban area deployments is evaluated. The separation distance of 38.5 km is required to protect both systems. Moreover, the study concluded that the second adjacent channel commences more reliable outcome than first adjacent channel. As illustrated in study [6], it is assumed that the location of TS is considered to be out of the HAPS coverage area. The enhancement of coexistence between FSS and HAPS was also provided in terms of interference-to-noise ratio (INR). The interference issue between TS and HAPS gateway links was also analyzed in [7]. Three different regions of the HAPS coverage area have been investigated. The study depicts that higher elevation angles have established shorter distances; whereas, the higher elevation angle activates the harsh interference in the HAPS coverage area. The effect of rain on the interference level was illustrated in [8], it was concluded that rain rate can cause degradation in carrier-to-interference ratio (CIR). Clearly, it could be observed that the performances of the TS and HAPS were not evaluated in the previous studies. Another gap is that the mentioned researches did not focus on possible mitigation techniques to reduce the separation distance. These two identified issues are properly addressed in this paper.

2. INTERFERENCE MODEL AND SHARING SCENARIOS

The key element of sharing model for HAPS and TS is the interference level. It is generally assumed that the accepted interference level is -147 dBW/10 MHz [9]. In order to calculate the interference from HAPS to TS, the parameters and interference criteria are required for both systems. These requirements are summarized in Table 1. It is also assumed that the path loss can be represented by the free space propagation model in all cases.

The sharing scenario is illustrated in Figure 1. A single HAPS airship (HAPSAS) and HAPSGS are located 21 km and 36 km away from the sub platform point know as Nadir Point (NP) respectively. An elevation angle of 60 degrees is assumed for HAPS to cover the whole Urban Area of Coverage (UAC) of HAPS. The separation distance will vary from 0 to 36 km as of NP. The free space propagation model is assumed in this scenario.

Table 1: System simulation parameters [9].

Parameters	HAPS	TS
Transmit power (dBm)	−22	−4
Antenna gain (dBi)	30	15
INR (dB)	−10 (ITU-R.F.1094)	-
ACS (dB)	56	-
ACLR (dB)	50	-

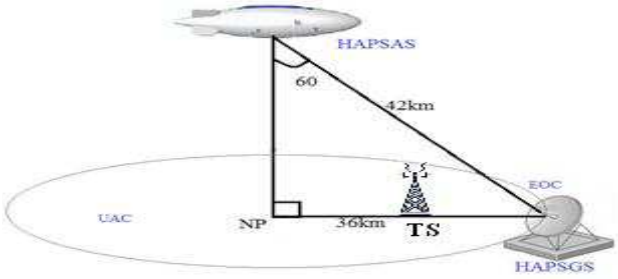

Figure 1: Sharing scenario between HAPS and TS system.

3. METHODOLOGY

One classical approach of calculating the minimum separation distance between HAPSGS and TS is to deploy TS on the straight path from NP to the HAPSGS inside an UAC of HAPS. The minimum separation distance is calculated based on the compliant with the maximum long-term interference of −147 dBW/10 MHz and INR of −10 dB [9]. Two sharing scenarios are defined in this paper based on the interferer object and discussed in the next Subsections 4.1 and 4.2. The offset angle from NP diverges between 0° and 60°. This angle fluctuation allows the HAPSAS to cover all 36 km radius of the urban area. The maximum separation distance between HAPSAS and TS is 42 km.

A model is needed to quantify the ACI. The ratio of the wanted power to the unwanted power coming from adjacent channel is known as Adjacent Channel Interference Ratio (ACIR). The ACI can be quantified by the ACIR as:

$$ACIR = \frac{1}{\left(\frac{1}{ACS} + \frac{1}{ACLR}\right)} \tag{1}$$

where ACS (dB) is Adjacent Channel Selectivity of TS and ACLR (dB) is an Adjacent Channel Leakage Ratio of the HAPS.

4. RESULTS AND DISCUSSION

To facilitate inspection of coexistence and sharing concerns, it is necessary to illuminate the ACI caused by HAPSAS and HAPSGS to TS. The compatibility results are in the next subsection.

4.1. Interference from HAPSAS to TS

The sharing scenario is based on a single HAPSAS located in the altitude of 21 km above the NP communicating with its gateway located at the right edge of UAC i.e., 36 km away from NP. The performance evaluation is based on the INR values as a function of separation distance between the TS location and HAPSAS. Figure 2 shows the required minimum separation distance from TS to NP.

As mentioned earlier, increasing separation distance leads to reduction in interference level. The results show that a separation distance of 10 km in vertical access is required to avoid harmful interference from HAPSAS with respect to the interference threshold level (i.e., −147 dBW/10 MHz).

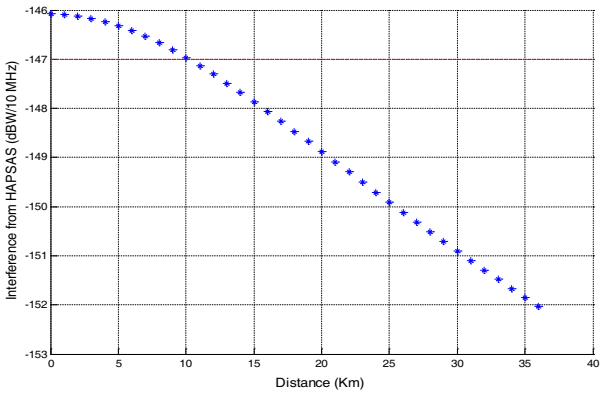

Figure 2: Interference from HAPSAS to TS.

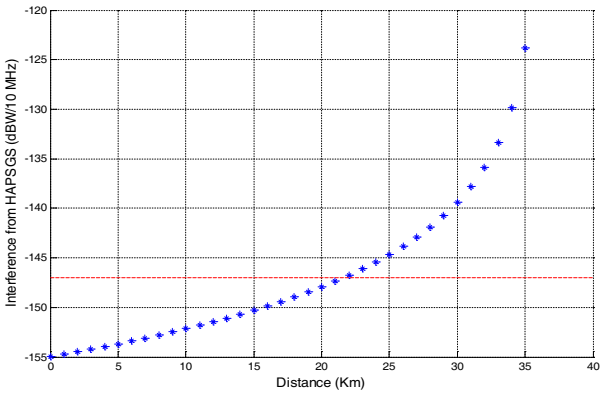

Figure 3: Interference from HAPSGS to TS.

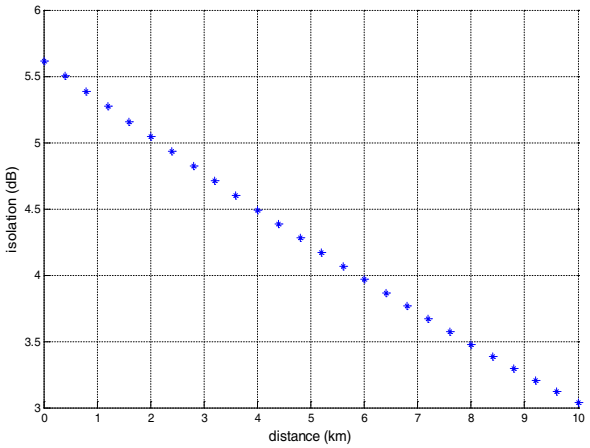

Figure 4: Essential shielding to protect TS from HAPSAS' interference.

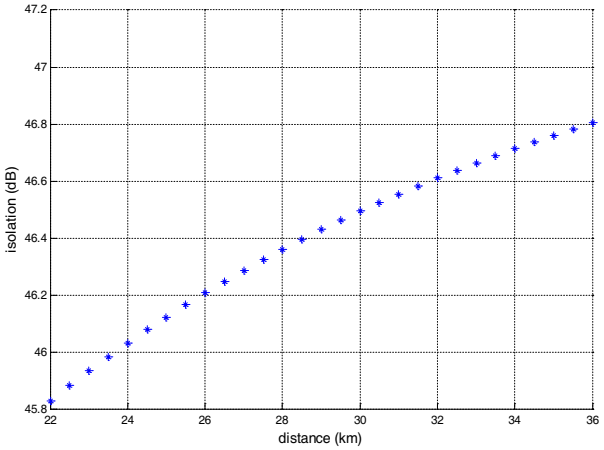

Figure 5: Essential shielding to protect TS from HAPSGS' interference.

4.2. Interference from HAPSGS to TS

Figure 3 shows the interference in terms of separation distance in the path from NP toward the HAPSGS.

Unlike in the first scenario, the TS is located in the same place as HAPSGS and the movement starts from this point towards NP. The figure also shows the ratio between the interference from HAPSGS to TS and the separation distance. As demonstrated in Figure 3, the minimum separation distance of 22 km in vertical access is needed for TS in order not to exceed the interference threshold level of -147 dBW/10 MHz.

As a summery, the distance between NP and HAPS Edge of Coverage (EOC), is divided into three regions. The acceptable interference range of 12 km which is between 10 and 22 km away from the NP is considered as the accepted region for both systems to coexist. In order to make use of the remaining two regions (i.e., 0 to 10 km and 22 to 36 km), a mitigation technique is required to have an acceptable interference level. We propose the isolation technique to get the Palpable mitigation results.

The isolation is applied to the two interference regions. Figures 4 and 5 illustrate the required isolation in each case. In Figure 4, the maximum isolation of 5.6 dB is required for the 0 km separation distance (i.e., located at the NP) when HAPSAS is considered as an interferer to the TS operation. Whereas, in Figure 5, the isolation of 45.14 dB is necessary to avoid interference from HAPSGS to TS for the separation distance of 36 km which shows that TS is in EOC of HAPS.

5. CONCLUSION

The possibility of coexistence between HAPS and TS operating in the UAC is investigated. The results show that it is possible to use the HAPS system in the adjacent channel to TS in certain distances. Two sharing scenarios were considered, first, from HAPSAS to TS and, secondly from

HAPSGS to TS. It has been shown that in both cases the isolation technique is a suitable mitigation method. The simulation results show that the interference from HAPSGS into TS is more severe than the one from HAPSAS to TS. Therefore, a more reliable and feasible isolation is needed at the edge of UAC to avoid interference from HAPSGS to TS in the NP, since the HAPSGS requires higher separation distance compared to HAPSAS. The results of this study can enhance the compatibility between the two systems, and thus increase the utilization of the spectrum.

REFERENCES

1. Mohammed, A., et al., *Advanced Communication Techniques and Applications for High-altitude Platforms*, Hindawi Pubishing Corporation, 2008.
2. "Preferred characteristics of systems in the fixed service using high altitude platforms operating in the bands 47.2–47.5 GHz and 47.9–48.2 GHz, R.I.-R. F.1500, 2005, Available from http://www.itu.int/rec/R-REC-F/en, Acess Date: Feb. 2, 2012.
3. Yang, A. M. Z., "Broadband communications and applications from high altitude platforms, 2009.
4. RECOMMENDATION ITU-R V.573-5, "Radiocommunication vocabulary," 2007, Available from http://www.itu.int/rec/R-REC-V/en, Acess Date: Feb. 2, 2012.
5. Ahmed, M. Y., A. R. B. Tharek, S. K. B. A. Rahim, and Z. A. Shamsan, "Interference coupling loss between high altitude platform gateway and fixed satellite service earth station at 5850–7075 MHz," *Journal of Electromagnetic Waves and Applications*, Vol. 25, No. 2–3, 339–350, 2011.
6. Nia, M. M. and T. A. Rahman, "Fixed satellite service (FSS) and high altitude platform (HAP) interference evaluation for adjacent channels outside platform area coverage," *2011 4th International Conference on Modeling, Simulation and Applied Optimization (ICMSAO),* 1–4, Apr. 19–21, 2011.
7. Nia, M. M. and T. A. Rahman, "High altitude platform system (HAPS) and co-existence with fixed satellite service (FSS) in frequency range 5850–7075 MHz," *IEEE*, 1–6, 2011.
8. Abdulrazak, L., et al., "Study HAPS interference power to noise level ratio of fixed services and related separation distance," *IEEE*, 690–693, 2010.
9. ECC REPORT 165, "Compatibility study between MSS complementary ground component operating in the bands 1 610.0–1 626.5 MHz and 2 483.5–2 500.0 MHz and other systems in the same bands or in adjacent bands," Montegrotto Terme, CEPT, 2011, Available from www.cept.org, Acess Date: Feb. 2, 2012.
10. "Example of a possible mathematical implementation of the methodology for statistically calculating the interference received by the fixed service from space-to-Earth emissions for frequency bands above about 17 GHz," ITU, 2010, Available from: www.itu.int, Acess Date: Feb. 2, 2012.

Proficiency Testing of Radiated Emission Testing Laboratory in China

Tong Wu[1], **Qingfei Shen**[1], **Bin Lin**[2], **and Hongyan Yin**[3]

[1]China National Institute of Metrology, China
[2]Shenzhen Academy of Metrology and Quality Inspection, China
[3]Beijing Entry-Exit Inspection and Quarantine Bureau, China

Abstract— This paper reports the results of a radiated emission proficiency testing round with the major electromagnetic compatibility (EMC) laboratories in China. Nineteen Radiated emission sites are compared using a comb generator in the frequency range of 30 to 1000 MHz. The guidelines of international standards such as ISO/IEC Guide 43-1 was followed, while the scope of the tests focused on EMC compliance of information technology devices, based on CISPR 22. Statistical metrics such as Z-score and normalized error have been adopted to assess global and individual performances of the participant laboratories. As the result of this program, to find the laboratory which had an isolated data from the group and analysis influence factors of difference of the test results.

Radiated emission testing is one of the most important electromagnetic compatibility (EMC) testing items. The test result of Radiated emission is influenced by various factors. Using the comparison between laboratory, we can examine the difference among different labs. So we can design a proficiency testing (PT) of radiated emission testing to improve the consistency of the test results. Proficiency testing is an important method to confirm the testing ability of lab and is commonly used assessment performance by means of interlaboratory comparisons. China National Accreditation Service for Conformity Assessment (CNAS) ask EMC lab attending at least one proficiency testing every 2 years. China National Institute of Metrology (NIM) organized a proficiency testing of radiated emission testing according ISO/IEC17043. All the participant labs of this PT are accredited by CNAS according ISO/IEC 17025.

Two factors are important for a proficiency testing (PT) of radiated emission testing. The first factor is reference sample and the second factor is statistical method.

1. THE STABILITY OF REFERENCE SAMPLE

The stability of reference sample influences the judging satisfaction or not to lab. The stable reference sample can reduce nondeterminacy of testing result, and it can reflect the real ability of lab. The reference sample shall meet the following requirements:

- The most important for reference sample is stability in testing process. The stability is not the performance of sample, but the emission signal of sample is stable. The stability of sample can ensure the consistency of the measurement results in difference time. The stability of the reference sample should be reflected in many times in the measurement results.

- The consistency of the test setup is another factor for testing result. The little change for the sample setup may bring about the large change of testing results. We should select the simplified sample setup. This can reduce inconsistency results because the difference of the sample setup.

There are two general type of the sample transfer schemes by interlaboratory comparison: sequential or simultaneous participation schemes. In sequential participation schemes, the proficiency test item to be measured circulates successively form one participating laboratory to the other, occasionally going back to the PT provider for checking. There are usually standard deviations of measured value to evaluate the stability of sample.

There are repetitive measure n times (n as far as possible big), so can get n measure values y_i, $i = 1, 2, \ldots, n$. The mean is $\bar{y}$, so The stability is:

$$s(y) = \sqrt{\frac{\sum_{i=1}^{n}(y_i - \bar{y})^2}{n-1}} \tag{1}$$

The stability of reference sample should be less than the uncertainty of participant labs. The uncertainty of participant labs are about 5 dB, so the reference sample is comply with the requirements if the stability is less than 2 dB.

The PT plan select VSQ 1000 as reference sample. The VSQ 1000 is radiation source for the frequency range form 30 to 1000 MHz. It consists of a battery operated comb generator and biconical broadband. The comb generator is supplied by a high stable temperature compensated crystal oscillator (TCXO) and generates a frequency spectrum with a line spacing of 1 MHz, 5 MHz or 10 MHz. Combined with an antenna the generator represents a precise radiation source. The frequency stability (TCXO, 10 MHz) is less than 1 ppm (0°C to 50°C). The signal stability is less than ±0.2 dB (20°C const.), less than ±0.5 dB (+10°C to +30°C) and less than ±0.8 dB (0°C to +50°C). For three months of stability test, the result of the sample is 1.1 dB.

2. STATISTICAL METHODS FOR PT

Scoring is the method of converting a participant's raw result into a standard form that adds judgemental information about performance.

Laboratory performance is assessed by comparing reported results to the assigned value using both Z-scores and E_n-scores.

Z-scores are indication of how much the reported result differs form assigned value. The assigned value (X) and the target standard deviation (σ) have a critical influence on the calculation of Z-scores and must be selected with care if they are to provide a realistic assessment of laboratory performance.

$$Z = \frac{x - X}{\sigma} \tag{2}$$

where:

$Z = Z$-score.
$x =$ individual laboratory result.
$X =$ assigned value.
$\sigma =$ target standard deviation.

Z-scores are interpreted as follows:

$|Z| \leq 2$ satisfactory
$2 < OZ < 3$ questionable
$|Z| \geq 3$ unsatisfactory

E_n-scores are an alternative to Z-scores. They provide a measure of how closely a reported laboratory result agrees with the assigned value, taking account of uncertainties in both the result and assigned value. The E_n-scores is an objective measure of whether or not an individual result is consistent with the assigned value. Unlike Z-scores, E_n-scores do not require the setting of a target standard deviation.

$$E_n = \frac{x - X}{\sqrt{U_{\mathrm{LAB}}^2 + U_{\mathrm{REF}}^2}} \tag{3}$$

where:

$E_n = E_n$-scores.
$x =$ individual laboratory result.
$X =$ assigned value.
$U_{\mathrm{LAB}} =$ expanded uncertainty of the individual laboratory result.
$U_{\mathrm{REF}} =$ expanded uncertainty of the assigned value.

E_n-scores are interpreted as follows:

$|E_n| \leq 1$ satisfactory
$|E_n| > 1$ unsatisfactory

The PT have nineteen participant labs. The number of laboratory not enough and the results of Radiated emission is more decentralized. So it is not suitable for using Z-scores to statistical analysis.

There are similar test equipments which comply with CISPR16.1 and similar test site which comply with CISPR 22. The uncertainty of this labs are about 5.0 dB.

According CISPR16-4-2, if U_{lab} is less than or equal U_{cispr} then

Table 1: Statistical features of the data — horizontal polarization.

Frequency (MHz)	Range	Minimum	Maximum	Mean	Std. Deviation	Variance	Skewness	Kurtosis
50	16.0	43.0	59.0	45.1	3.5	12.2	3.879	16.024
100	6.5	62.8	69.3	65.4	1.6	2.7	0.354	0.347
230	4.9	71.2	76.1	73.2	1.2	1.5	0.328	0.244
400	4.9	69.7	74.6	73.0	1.1	1.3	−1.034	2.645
800	9.6	60.0	69.6	64.9	1.9	3.7	−0.315	2.937
950	10.3	55.3	65.6	60.2	2.2	4.8	0.196	1.795

Table 2: Statistical features of the data — vertical polarization.

Frequency (MHz)	Range	Minimum	Maximum	Mean	Std. Deviation	Variance	Skewness	Kurtosis
50	6.7	48.2	54.9	51.2	1.9	3.5	0.527	−0.224
100	6.8	61.5	68.3	64.8	1.8	3.1	0.718	0.279
230	7.5	65.3	72.8	68.6	1.9	3.5	1.104	1.491
400	3.8	70.9	74.7	72.5	0.9	0.8	0.686	0.738
800	9.3	58.9	68.2	62.9	2.0	4.2	0.668	1.616
950	5.2	56.6	61.8	59.4	1.7	2.7	−0.390	−1.029

- compliance is deemed to occur if no measured disturbance level exceeds the disturbance limits;
- non-compliance is deemed to occur if any measured disturbance level exceeds the disturbance limit.

If U_{lab} is greater than or equal U_{cispr} then

- compliance is deemed to occur if no measured disturbance level, increase by $(U_{\text{lab}} - U_{\text{cispr}})$, exceeds the disturbance limits;
- non-compliance is deemed to occur if any measured disturbance level, increase by $(U_{\text{lab}} - U_{\text{cispr}})$, exceeds the disturbance limit.

All participant labs are accredited by CNAS and accredited to do testing of China compulsory certification. These labs declare that the uncertainty is less than U_{cispr}. The U_{cispr} of frequency range form 30 to 1000 MHz is 5.2 dB.

So Equation (3) change into:

$$E_n = \frac{x - X}{\sqrt{\frac{n-1}{n}} U_{\text{cispr}}} \tag{4}$$

X is assigned value which is arithmetic mean value of all the participant labs. If one test result is less or greater 5.1 dB than assigned value, the test result is unsatisfactory.

3. STATISTICAL PROCESSING RESULTS

All 19 participant labs submitted data according process of measurement. There are statistical features of the data and some basic data analysis.

The range is too big on 50 MHz horizontal polarization. After examination, a laboratory data is obvious errors. The instrument of the laboratory have fault. In order to avoid the influence of statistical data, go out some obvious errors data.

One test result is unsatisfactory on 950 MHz horizontal polarization. 17 participant labs' performance is satisfactory.

Form the range of all test data, the uncertainty of labs is suitable, and it is comply with CISPR 16.4 requirement.

4. TECHNICAL ANALYSIS FOR PT

There are need technical analysis to look for the reasons of unsatisfactory. Though most of participant labs are satisfactory, the test results are much discordance on some frequencies.

Table 3: Statistical features of the data — horizontal polarization (go out obvious errors).

Frequency (MHz)	Range	Minimum	Maximum	Mean	Std. Deviation	Variance	Skewness	Kurtosis
50	3.3	43	46.3	44.3	0.9	0.9	0.788	−0.163

The test site is anechoic chamber or open area test site for radiated emission testing. In fact, all participant labs are testing in anechoic chamber. The error analysis of the measuring results show that the performance of anechoic chamber obvious influence emission testing result. The anechoic chamber need NSA (the normalized site attenuation) measurement, and NSA comply with CISPR22. The performance of absorbing material obvious influence the NSA of anechoic chamber. The lab should periodically measure NSA. There are many other factors such as grounded system, shielding effectiveness and filter system will affect measuring results, so a higher measuring accuracy can be obtained only when multiple systems have been employed in anechoic chamber.

The electromagnetic compatibility test for instrument has a strong dependence. In the test process, often appear to the deviation of the instrument that is difficult to discover. There are need use antenna factors form calibration report. Need to pay attention to instrument traceability. In order to maintain the credibility of checking and calibration of the measurement equipment, period checking should be carried out.

The radiated emission testing system include coaxial cable, coaxial cable, attenuator and all kinds of testing instruments. The impedance of this testing instruments is 50 Ω. The impedance mismatch of test system can cause the testing results error. If the impedance mismatch is too much, the measurement results would can not be accept. Special attention to the influence of connector, RF cables and antenna connection, RF cables and amplifier connection, etc..

The testing instruments of radiated emission testing system are EMI receiver and preamplifier. If the level of disturbance single is too big, the preamplifier will saturate. One of participant labs is satisfactory because the preamplifier is saturate.

5. CONCLUSION

The PT plan based on interlaboratory measurement comparison was adopted, with focus on the performance of the participant labs for radiated emission measurements. Though the PT plan, there are realize the condition of the major EMC testing labs in China. There are insure accurate and reliable of the testing results though comparing the testing data. The conclusion of this PT Plan is a strong evidence to the performance of the labs. The accreditation service can evaluate the ability of labs depend on this PT plan.

REFERENCES

1. "Confotmity assessment — General requirements for proficiency testing," International Organization for Standardization (ISO)/International Electrotechnical Commission (IEC), 17043, 2010.
2. "Specification for radio disturbance and immunity measuring apparatus and methods — Part 4-3: Uncartainties,statistics and limit modeling — Statistical considerations in the determination of EMC compliance of mass-produced products," International Electrotechnical Commission (IEC), International Special Committee on Radio Interference (CISPR), 16-4-3.
3. Guimaraes, J. V., M. H. C. Dias, J. Carlos, and A. D. Santos, "Proficiency testing of electromagnetic compatibility (EMC) labs in Brazil by measurement comparisons," *Meas. Sci. Technol.*, Vol. 20, 107–115, 2009.
4. Osabe, K., R. Watanabe, A. Maeda, and M. Yamaguchi, "Inter-laboratory comparison result as the proficiency testing program of EMI test sites in Japan," *IEEE International Symposium on Proceeding of Electromagnetic Compatibility, EMC 2007*, 2007.
5. Feng, Y.-Q., W. Wang, and W.-Y. Ma, "Reference radiator application in EMC comparison," *Journal of Astronautic Metrology and Measurement*, Vol. 26, No. 2, 2006.

On Performance Analysis of SLNR-based Multistream Transceiver in Multiuser MIMO Downlink Channels

R. K. Mai, F. Y. Qian, Y. S. Zhu, and H. Li
Peking University, China

Abstract— Directed transmission offered by smart antennas has made it possible to implement spatial multiplexing (SM) in multiple-input-multiple-output (MIMO) wireless communications. On the level of digital signal processing, appropriate design of transceivers becomes an enabling technology to harness such a capability to dramatically increase data rates while still achieving decent error performance. In the case of multiuser MIMO downlink channels, special attention should be paid to handle system performance degradation caused by interchannel interference (ICI) among users. Traditionally, the focus of a wide variety of designs is on optimization of received signal-to-interference-noise ratio (SINR) per user, which is directly relevant to the channel capacity and bit error rate (BER). Recently, the so-called signal-to-leakage-plus-noise ratio (SLNR) has been proposed as the ratio of one user's received signal power to the interference posed by its transmission to the other users. This can be interpreted as SINR from the perspective of the transmitter. Although SLNR is not exactly the same as SINR, a remarkable benefit of such a definition lies in its decoupling of all users' precoders which would otherwise depend on each other in the conventional SINR. In this paper, a closed-form optimal precoder is derived based on the generalized Rayleigh quotient theorem to the optimization of SLNR. In light of the disparity, the capacity of multiple receive antennas to cooperate is utilized for compensation. Geometric mean decomposition (GMD) is employed to decompose the effective channels, followed by successive interference cancellation to create equivalently parallel subchannels. Each subchannel is endowed with an equal channel gain, which translates to improvement in one user's overall BER since the BER is dominated by the weakest subchannel at moderate to high signal-to-noise ratios (SNR). Numerical results verify the superiority of the proposed scheme to the original one with matched filters in terms of error performance under different system configurations.

1. INTRODUCTION

Multiple-Input Multiple-Output (MIMO) is the key enabling technology for next-generation wireless communication systems. For example, the recently finalized WLAN standard IEEE 802.11n has adopted MIMO as its essential PHY component which guarantees a data rate up to 600 Mbits/s. The reason for the high spectral efficiency and link reliability lies in the additional space dimension thanks to the presence of multiple antennas. In the course of extensive research on this topic over a decade, the focus has gradually shifted from the point-to-point case to the multiuser case. A remarkable difference between the two is that in the latter case, users are incapable of cooperating with each other, which gives rise to interchannel interference (ICI). Especially, the overall quality-of-service (QoS) is dominated by such ICI at moderate to high signal-to-noise ratios (SNR).

When it comes to the handling of ICI in the downlink channels, the literature roughly falls into two categories. One is based on complete cancellation of interference. As proven in [1], dirty-paper coding (DPC) is able to achieve the capacity region of broadcast channels at the cost of extremely high complexity. To alleviate that problem, an alternative scheme, known as linear zero-forcing in [2, 3], eliminates ICI by block-diagonalizing the aggregate channel. Built upon such block-diagonal structure, various transmission techniques from the single-user case can be employed to further optimize different design criteria such as minimum mean square error (MMSE) or throughput [4, 5] Block-diagonalization (BD), though simple and effective, is subject to a dimensional constraint on transmit and receive antennas. An technique to generalize the BD scheme while relaxing the dimensional constraint was considered in [6]. The other aims at suppression, not necessary elimination of mutual interference while a power allocation can be possibly adopted for optimization of QoS. For example, in [7], under the assumption of multiple-input single-output (MISO), uplink-downlink duality is utilized to optimize precoder and equalizer design by progressive power allocation with a constraint on signal-to-interference-plus-noise ratio (SINR), which was extended to the case of MIMO in [8]. Inspired by the definition of SINR, signal-to-leakage ratio (SLR) was defined in [9] and optimized in transceiver design. An extension was made in [10] by considering the impact of noise, leading to the definition of signal-to-leakage-plus-noise ratio (SLNR) as a vehicle for a mitigation of ICI.

In this paper, the restriction to matched filters in [10] is lifted by a two-step design. The first step aims at suppressing ICI to the greatest extent while handling of intra-stream interference is left to the second step. In doing this, we derive several benefits immediately: a closed-form solution which facilitates theoretical analysis, flexibility in equalizer design, and most importantly, an dramatic increase in error performance by fully employing the cooperating ability of multiple receive antennas.

Notations: $(\cdot)^{-1}$ and $(\cdot)^H$ denote matrix inverse and conjugate transpose respectively. $\mathbf{I}_N$ is the $N \times N$ identity matrix. diag($\mathbf{x}$) is the diagonal matrix whose diagonal is $\mathbf{x}$. Besides, $\mathbf{X}(:, 1 : M_s)$ represents the first M_s columns of $\mathbf{X}$.

2. SYSTEM MODEL

We consider a typical flat fading MIMO downlink channel, where the base station is equipped with M_t antennas and serve a total of K users, each with M_{r_i} antennas (without loss of generality, we assume $M_{r_i} = M_r$ for $i \in \{1, \ldots, K\}$), as illustrated in Figure 1. For each user i, M_s data streams are spatially multiplexed and the estimated signal vector can be expressed as

$$\hat{\mathbf{s}}_i = \underbrace{\mathbf{W}_i\mathbf{H}_i\mathbf{P}_i\mathbf{s}_i}_{\text{desired signal}} + \underbrace{\mathbf{W}_i \sum_{k=1,k\neq i}^{K} \mathbf{H}_k\mathbf{P}_k\mathbf{s}_k}_{\text{interference}} + \mathbf{W}_i\mathbf{n}_i \tag{1}$$

where each data stream of $\mathbf{s}_i$ is assumed to be independent and normalized, i.e., $\mathbb{E}\{\mathbf{s}_i\mathbf{s}_i^H\} = \mathbf{I}_{M_s}$, $\mathbf{H}_i$ is supposed to be block Rayleigh-fading which indicates that its entry is identically and independently distributed (*i.i.d.*) according to $\mathcal{CN}(0, 1)$, $\mathbf{n}_i \sim \mathcal{CN}(0, \sigma_n^2\mathbf{I}_{M_r})$. The problem is to design the precoder $\mathbf{P}_i \in \mathbb{C}^{M_t \times M_s}$, and equalizer $\mathbf{W}_i \in \mathbb{C}^{M_s \times M_r}$ so as to minimize the symbol error rate (SER) or bit error rate (BER).

3. MULTIUSER PRECODER AND EQUALIZER DESIGN

Suppose that full channel state information (CSI) is available at the base station. According to [10], the SLNR for user i is defined as:

$$\begin{aligned} \text{SLNR}_i &= \frac{||\mathbf{H}_i\mathbf{P}_i||_F^2}{\sum_{j\neq i} ||\mathbf{H}_j\mathbf{P}_i||_F^2 + ||M\sigma_n^2\mathbf{I}_N||_F^2} \\ &= \frac{\text{tr}\left\{\mathbf{P}_i^H\mathbf{H}_i^H\mathbf{H}_i\mathbf{P}_i\right\}}{\text{tr}\left\{\mathbf{P}_i^H\left(\tilde{\mathbf{H}}_i^H\tilde{\mathbf{H}}_i + M\mathbf{I}\sigma_n^2\right)\mathbf{P}_i\right\}} \end{aligned} \tag{2}$$

where $\tilde{\mathbf{H}}_i = [\mathbf{H}_1^T, \ldots, \mathbf{H}_{i-1}^T, \mathbf{H}_{i+1}^T, \ldots, \mathbf{H}_K^T]^T$. In the first step of our design, a precoder $\tilde{\mathbf{P}}_i$ is derived for ICI-suppression by optimizing (2), i.e.,

$$\begin{aligned} &\max_{\tilde{\mathbf{P}}_i} \ \text{SLNR}_i, \quad i = 1, \ldots, K \\ &\text{s.t. } ||\tilde{\mathbf{P}}_i||_F = 1 \end{aligned} \tag{3}$$

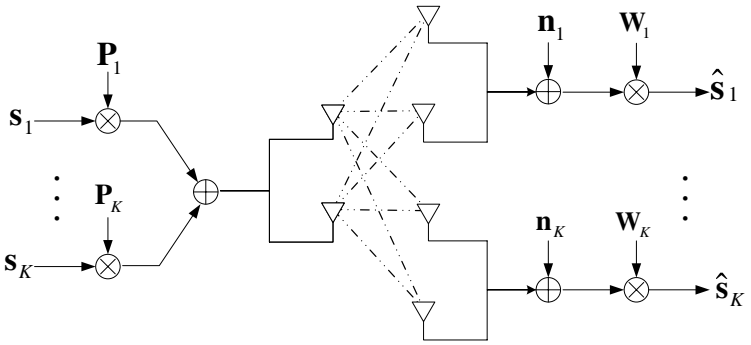

Figure 1: Block diagram of the multi-user precoder and equalizing system.

According to [11], there exists a non-singular matrix $\mathbf{X}_i \in \mathbb{C}^{M_t \times M_t}$ such that

$$\begin{aligned} &\mathbf{X}_i^H \mathbf{H}_i^H \mathbf{H}_i \mathbf{X}_i = \mathrm{diag}\left(\lambda_{i,1}, \lambda_{i,2}, \ldots, \lambda_{i,M_t}\right) \\ &\mathbf{X}_i^H \left(\tilde{\mathbf{H}}_i^H \tilde{\mathbf{H}}_i + M\mathbf{I}\sigma_n^2\right) \mathbf{X}_i = \mathbf{I}_{M_t} \end{aligned} \tag{4}$$

where $\lambda_{i,k}(1 \le k \le M_t)$ are the generalized eigenvalues of $\left(\mathbf{H}_i^H \mathbf{H}_i, \tilde{\mathbf{H}_i^H} \tilde{\mathbf{H}}_i + M\mathbf{I}\sigma_n^2\right)$, and the column vectors of $\mathbf{X}_i$ are correspondingly called the generalized eigenvectors. Without loss of generality, suppose $\lambda_{i,k} \ge \lambda_{i,k+1}$. Then, the optimal solution to (3) is

$$\tilde{\mathbf{P}}_i = \mathbf{X}_i\left(:, 1 : M_s\right) \tag{5}$$

The computation procedures are detailed in Algorithm 3. Thus, user i's effective channel becomes: $\bar{\mathbf{H}}_i = \mathbf{H}_i \tilde{\mathbf{P}}_i$. Next, we introduce the geometric mean decomposition (GMD) [12]:

$$\bar{\mathbf{H}}_i = \mathbf{H}_i \tilde{\mathbf{P}}_i = \mathbf{U}_i \mathbf{R}_i \mathbf{Q}_i^H \tag{6}$$

where $\mathbf{U} \in \mathbb{C}^{M_r \times M_s}$, $\mathbf{Q} \in \mathbb{C}^{M_s \times M_s}$ are semiunitary, i.e., $\mathbf{U}\mathbf{U}^H = \mathbf{I}_{M_r}$, $\mathbf{Q}\mathbf{Q}^H = \mathbf{I}_{M_s}$, $\mathbf{R} \in \mathbb{C}^{M_s \times M_s}$ is upper triangular with equal diagonal elements, the geometric mean of the eigenvalues of $\bar{\mathbf{H}}_i$, i.e., $r_i = \left(\prod_{k=1}^{M_s} \sigma_k^i\right)^{1/M_s}$. Given the semiunitariness of $\mathbf{U}$ and $\mathbf{Q}$, we arrive at

$$\mathbf{R}_i = \mathbf{U}_i^H \mathbf{H}_i \tilde{\mathbf{P}}_i \mathbf{Q}_i \tag{7}$$

Thus, for user i, if $\mathbf{P}_i = \tilde{\mathbf{P}}_i \mathbf{Q}_i$ and $\mathbf{W}_i = \mathbf{U}_i^H$, becomes:

$$\begin{aligned} \tilde{\mathbf{s}}_i &= \mathbf{U}_i^H \mathbf{H}_i \mathbf{P}_i + \mathbf{U}_i^H \mathbf{n}_i \\ &= \mathbf{U}_i^H \mathbf{U}_i \mathbf{R}_i \mathbf{Q}_i \mathbf{Q}_i^H \mathbf{s}_i + \tilde{\mathbf{n}}_i \\ &= \mathbf{R}_i \mathbf{s}_i + \tilde{\mathbf{n}}_i \end{aligned} \tag{8}$$

where $\tilde{\mathbf{n}}_i = \mathbf{U}_i^H \mathbf{n}_i$. Next, in light of the upper triangularity of $\mathbf{R}_i$, we employ successive interference cancellation (SIC) to decouple M_s data streams. The expansion of (8) is:

$$\begin{bmatrix} \tilde{s}_{i,1} \\ \tilde{s}_{i,2} \\ \vdots \\ \tilde{s}_{i,M_s} \end{bmatrix} = \begin{bmatrix} r_i & r_{12} & \cdots & r_{1,M_s} \\ & r_i & \cdots & r_{2,M_s} \\ & & \ddots & \vdots \\ & & & r_i \end{bmatrix} \begin{bmatrix} s_{i,1} \\ s_{i,2} \\ \vdots \\ s_{i,M_s} \end{bmatrix} + \begin{bmatrix} \tilde{n}_{i,1} \\ \tilde{n}_{i,2} \\ \vdots \\ \tilde{n}_{i,M_s} \end{bmatrix} \tag{9}$$

With the application of SIC to $[\tilde{s}_{i,1}, \ldots, \tilde{s}_{i,M_s}]$:

$$\begin{aligned} \tilde{\tilde{s}}_{i,M_s-t} &= \tilde{s}_{i,M_s-t} - \sum_{k=M_s}^{M_s-t+1} r_{M_s-t,k} \tilde{\tilde{s}}_{i,k} \\ &\approx r_i s_{i,M_s-t} + n_{i,M_s-t} \quad t = 1, \ldots, M_s - 1 \\ \tilde{\tilde{s}}_{i,M_s} &= r_i s_{i,M_s} + n_{i,M_s} \quad t = 0 \end{aligned} \tag{10}$$

we obtain M_s parallel subchannels with an equal gain r_i.

Algorithm 1 Computation of Precoder $\tilde{\mathbf{P}}_i$ for user i.

Input: $\mathbf{A}_i = \mathbf{H}_i^H \mathbf{H}_i$, $\mathbf{B}_i = \left(\tilde{\mathbf{H}}_i^H \tilde{\mathbf{H}}_i + M\mathbf{I}\sigma_n^2\right)$

1. Cholesky factorization: $\mathbf{B}_i = \mathbf{G}_i \mathbf{G}_i^H$; $\mathbf{C}_i = \mathbf{G}_i^{-1} \mathbf{A}_i \mathbf{G}_i^{-H}$
2. Schur decomposition: $\mathbf{S}_i^H \mathbf{C}_i \mathbf{S}_i = \mathrm{diag}\left(\lambda_{i,1}, \lambda_{i,2}, \ldots, \lambda_{i,M_t}\right)$; $\mathbf{X}_i = \mathbf{G}_i^{-H} \mathbf{S}_i$

Output: $\tilde{\mathbf{P}}_i = \mathbf{X}_i(:, 1 : M_s)$.

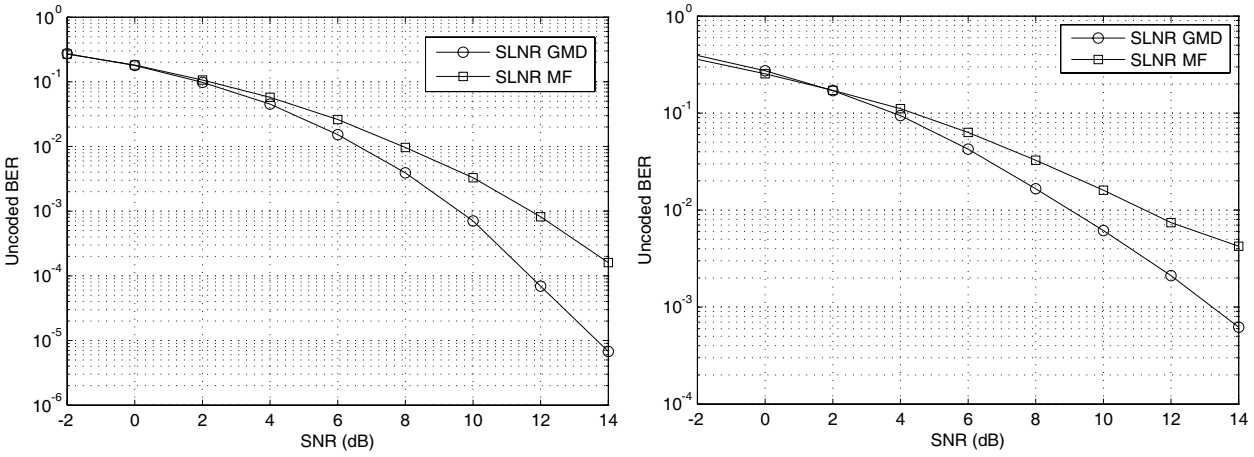

Figure 2: BER against SNR curves under two different system configurations. (a) $M_t = 8$, $M_r = 3$, $K = 2$, $M_s = 2$. (b) $M_t = 12$, $M_r = 3$, $K = 3$, $M_s = 2$.

4. NUMERICAL RESULTS

In this section, compared with [10] (SLNR-MF), we carry out Monte-Carlo simulations to verify the effectiveness of the proposed algorithm (SLNR-GMD) in terms of error performance. A total of 1000 channel realizations is simulated, on each of which 3×10^4 bits, mapped into QPSK symbols, are transmitted. The signal-to-noise ratio (SNR) is defined as: $\mathrm{SNR} = 10 \lg M_s/\sigma_n^2$ dB.

In Figure 2(a), we plot the BER curves with the system parameters $M_t = 8$, $M_r = 3$, $K = 3$, and $M_s = 2$. In the noise-limited region (low SNR's), SLNR-GMD exhibits hardly any performance advantage. As the SNR increases, the system gradually enters the interference-limited region. It should be noted that at BER = 14 dB, the proposed SLNR-GMD offers a power gain of approximately 2 dB. This advantage arises from our treatment of ICI and inter-stream interference separately. First, SLNR-GMD effectively controls the interference among users by optimizing SLNR, and then the overall BER is further alleviated by balancing the gains among subchannels. A similar trend can be observed in Figure 2(b) where the system setting is $M_t = 12$, $M_r = 3$, $K = 3$, and $M_s = 3$.

5. CONCLUSION

In multiuser MIMO spatial multiplexing downlink channels, a step-by-step strategy for transceiver design is proposed. A closed-form precoder, aiming at suppressing interchannel interference (ICI), is first derived based on optimization of signal-to-leakage-plus-noise ratio (SLNR). Next, a pair of precoder and equalizer is obtained to transform the effective channel into an upper triangular one. In light of the capability of multiple receive antennas to cooperate, successive interference cancellation (SIC) is employed to create parallel equal-gain subchannels. Numerical results show that our scheme can better manage ICI and offer more flexibility in equalizer design. It is observed that our design offers a noticeable power gain in comparison with the original SLNR one.

ACKNOWLEDGMENT

The work described in this paper was supported by 973 Program 2012CB315904, China, and the Research Program of Shenzhen, China.

REFERENCES

1. Weingarten, H., Y. Steinberg, and S. Shamai, "The capacity region of the Gaussian MIMO broadcast channel," *Proceedings of IEEE International Symposium on Information Theory*, 174, Chicago, USA, 2004.
2. Choi, L. U. and R. D. Murch, "A transmit preprocessing technique for multiuser MIMO systems using a decomposition approach," *IEEE Trans. Wireless Commun.*, Vol. 3, No. 1, 20–24, 2004.
3. Spencer Q. H., A. L. Swindlehurst, and M. Haardt, "Zero-forcing methods for downlink spatial multiplexing in multi-user MIMO channels," *IEEE Trans. Signal Process.*, Vol. 52, No. 2, 461–471, 2004.

4. Bourdoux, A. and N. Khaled, "Joint TX-RX optimisation for MIMO SDMA based on a null-space constraint," *Proceedings of IEEE Vehicular Technology Conference*, 171–174, Vancouver, Canada, 2002.
5. Lin, S., W. W. L. Ho, and Y. C. Liang, "Block diagonal geometric mean decomposition (BD-GMD) for MIMO broadcast channels," *IEEE Trans. Wireless Commun.*, Vol. 7, No. 7, 2778–2789, 2008.
6. Stankovic, V. and M. Haardt, "Generalized design of multi-user MIMO precoding matrices," *IEEE Trans. Wireless Commun.*, Vol. 7, No. 3, 953–961, 2008.
7. Schubert, M. and H. Boche, "Solution of the multiuser downlink beamforming problem with individual SINR constraints," *IEEE Trans. Veh. Technol.*, Vol. 53, No. 1, 18–28, 2004.
8. Khachan, A. M., A. J. Tenenbaum, and R. S. Adve, "Linear processing for the downlink in multiuser MIMO systems with multiple data streams," *Proceedings of IEEE International Conference on Communications*, 4113–4118, Istanbul, Turkey, 2006.
9. Tarighat, A., M. Sadek, and A. H. Sayed, "A multiuser beamforming scheme for downlink MIMO channels based on maximizing signal-to-leakage ratios," *Proceedings of IEEE International Conference on Acoustics, Speech, and Signal Processing*, 1129–1132, Philadelphia, USA, 2005.
10. Sadek, M., A. Tarighat, and A. H. Sayed, "A leakage-based precoding scheme for downlink multiuser MIMO channels," *IEEE Trans. Wireless Commun.*, Vol. 6, No. 5, 1711–1721, 2007.
11. Golub, G. H. and C. F. Van Loan, *Matrix Computations*, 3rd Edition, The Johns Hopkins University Press, Baltimore, 1996.
12. Jiang, Y., W. W. Hager, and J. Li, "The geometric mean decomposition," *Linear Algebra and Its Applications*, No. 396, 373–384, 2005.

Design of Novel Monopole Antenna Using Dual Rectangular Ring Patches and L-slots

Y. J. Shin, S. W. Lee, and N. Kim
Chungbuk National University, South Korea

Abstract— In this paper, a dual rectangular ring-shaped monopole antenna is presented for multi-band service. The antenna is composed of two rectangular ring-shaped antenna and two different sizes of slots on the ground plane. By using coupling between the inner and outer rectangular patches, the optimized matching characteristic is obtained. Using the rectangular patches only, two impedance bandwidths, which occur at 1.44–2.72 GHz and 3.19–3.84 GHz, are obtained. By adding the two L-slots on the ground plane we also get two more impedance bandwidths at 5.14–5.35 GHz and 5.56–5.89 GHz. We take a final measurement and find that the rectangular ring-shaped monopole antenna can realize quad impedance bandwidths at 1200 MHz (1.6–2.8 GHz), 800 MHz (3.2–4.0 GHz), 300 MHz (5.14–5.44 GHz), and 690 MHz (5.56–6.25 GHz), which are applicable to DCS1800, PCS1900, WCDMA, WLAN, and Mobile WiMAX band services.

1. INTRODUCTION

With the rapid growth wireless communications, new wireless communication devices and portable electronic devices have been developed and used. Recently it has become clear that mobile phones are tools for more than just voice and text services. So, the antenna employed in wireless communication devices must have more functionality while being smaller. Because of the advantages of low cost, light weight, and easy fabrication, the printed monopole antennas have been drawing much attention for dual or multi-band operations.

In this paper, we designed a dual rectangular ring-shaped monopole antenna for quad bandwidth operations from 1.6 to 2.6 GHz, 3.2 to 4.0 GHz, 5.14 to 5.35 GHz, and 5.56 to 6.25 GHz. The proposed antenna is composed of two rectangular ring-shaped antennas and two L-slots on the ground plane. Each of the frequency bands can be determined by some main parameters such as the length of two rectangular ring-shaped patches and L-slots, gaps between the two rectangular ring-shaped patches and the off-set distance of the slots. We designed the antenna to use the effect of coupling between the two rectangular ring-shaped patches and adding the L-slots to the ground.

2. ANTENNA STRUCTURE AND DESIGN

Figure 1 shows the structure of the proposed antenna. The overall size of the antenna is designed to be $45 \times 85 \times 0.8\,\text{mm}^3$. We used the FR-4 substrate having a permittivity of 4.4. A ground plane patch of $45 \times 41.5\,\text{mm}^2$ is printed on one plane with two L-slots and two rectangular ring-shaped antenna patches of $28 \times 25\,\text{mm}^2$ are printed on the other plane. A $50\,\Omega$ microstrip having a width of 1.55 mm is formed at the center of the substrate by calculating the width of a fitting line after preferentially considering the thickness and permittivity of the substrate.

Table 1: Optimized parameters for the proposed antenna.

Parameter	Value [mm]	Parameter	Value [mm]
W	45	gap_1	0.1
L	85	gap_2	0.5
L_f	43.5	sl_1	20
L_g	41.5	sl_2	22
W_1	28	D_1	24
L_1	25	D_2	33.3
W_2	22	r_1	0.775
L_2	13.5	r_2	0.775

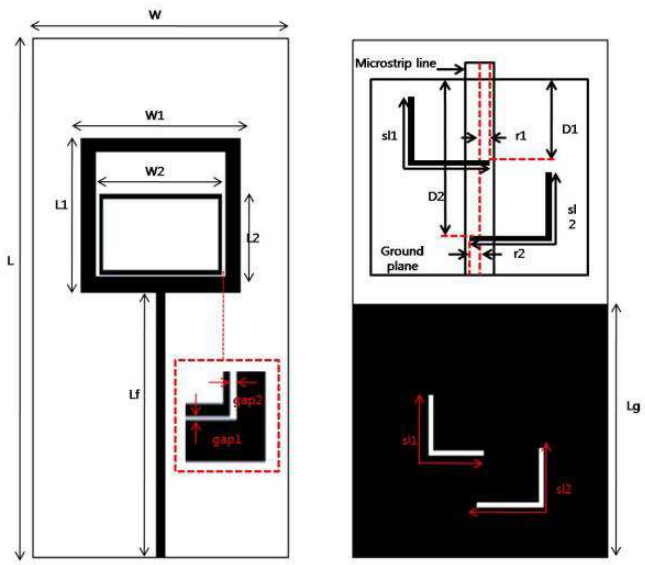

Figure 1: Structure of the proposed antenna.

The inner rectangular ring-shaped patch is placed inside the outer rectangular ring-shaped patch with two gaps. The coupling effect occurring in the two gaps increases capacitance, which reduces the reactance in the antenna impedance, thereby improving matching characteristics.

So the two gaps between the outer and inner rectangular ring-shaped patches are used as the main parameters. By properly tuning the parameters of the gaps, matching characteristics and good antenna performance is achieved. The outer rectangular ring-shaped patch is responsible for the 1.6–2.8 GHz band, whereas the inner rectangular ring-shaped patch is responsible for the 3.2–4.0 GHz band. In addition, by adding two L-slots on the ground plane for WLAN 802.11a, we also obtained two impedance bandwidths operating at 5.14–5.44 GHz and 5.56–6.25 GHz. The parameter sl_1 and sl_2 are the lengths of the slots and the lengths D_1, D_2 of the ground terminates beyond the edge of the slots. The parameters r_1 and r_2 are the off-set distances from the center axis of the microstrip line. The parameters sl_1 and sl_2 are adjusted to satisfy the operating frequency, and the parameters D_1, D_2, r_1, and r_2 are adjusted to satisfy the desired impedance matching. The parameter slot 1 is responsible for the 5.56–6.25 GHz band, whereas the parameter slot 2 is responsible for the 5.14–5.44 GHz band.

Finally, the proposed dual rectangular ring-shaped monopole antenna is successfully designed to operate quad-bandwidths and the optimized antenna parameters for the proposed antenna are shown in Table 1.

3. ANTENNA FBRICATION AND MEASUREMENT

Figure 2 shows the photographs of the fabricated antenna. Its performance is measured by the Agilent E5071C network analyzer. Figure 3 is a graph in which the simulation result and the measurement result of the optimized antenna are compared. Both tests meet the bandwidth requirements for DCS1800, PCS1900, WCDMA, WLAN, and Mobile WiMAX applications. The resonance frequency of the measurement result is slightly different from that of the simulation result, but it was confirmed that the measurement result is similar to the simulation result as a whole. Figure 4 shows the radiation patterns of the dual rectangular ring-shaped antenna in DCS1800 bands of 1.795 GHz, PCS1900 bands of 1.920 GHz, WCDMA bands of 2.045 GHz, tri-band WLAN bands of 2.45 GHz, 5.25 GHz, and 5.775 GHz, and tri-band Mobile WiMAX bands of 2.35 GHz, 2.6 GHz, and 3.6 GHz. In a general monopole antenna, an H-plane (azimuth plane) characteristic should be isotropic, but in an antenna proposed in this paper, a pattern similar to the isotropic pattern of the monopole antenna can be obtained. However, the radiation patterns at the 5.25 GHz and 5.775 GHz bands appear more directional.

This is because the radiation pattern at the 5.25 and 5.775 GHz radiates from the asymmetric slots. The measured peak gains are shown in Table 2. The gain values at the wireless application frequency band are low. However, the gain values are sufficient for most wireless applications.

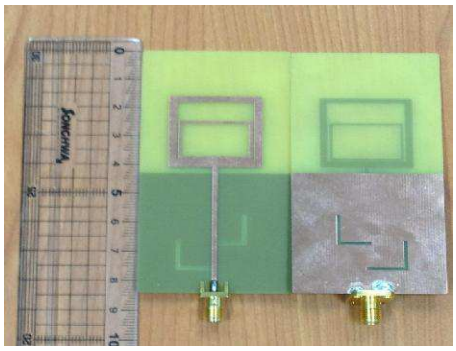

Figure 2: Photograph of the fabricated antenna.

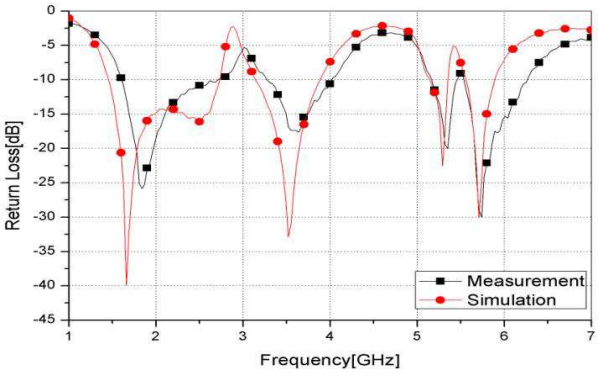

Figure 3: Comparison of the simulated and measured return loss on the optimized antenna.

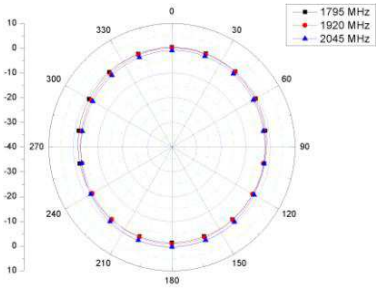

(a) DCS/PCS/WCDMA *H*-plane

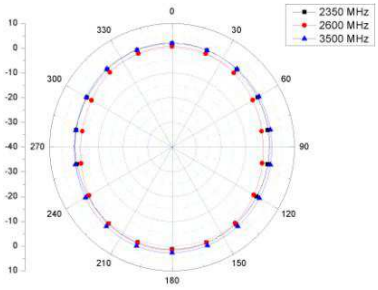

(b) Mobile WiMAX *H*-plane

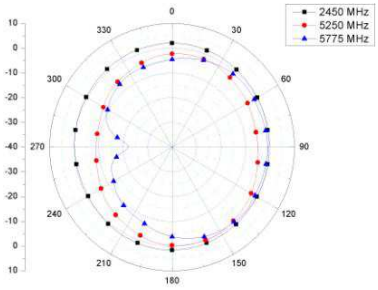

(c) WLAN *H*-plane

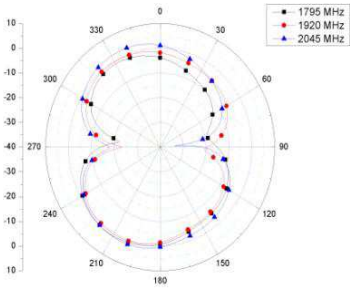

(d) DCS/PCS/WCDMA *E*-plane

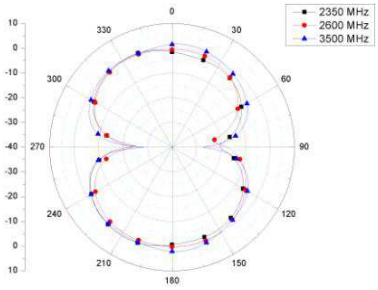

(e) Mobile WiMAX *E*-plane

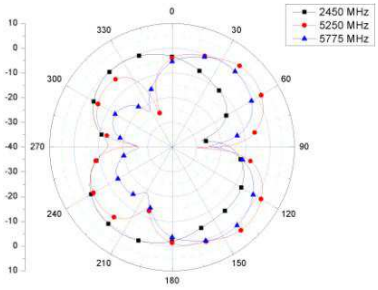

(f) WLAN *E*-plane

Figure 4: Radiation patterns of the fabricated antenna.

Table 2: Measured peak gains for proposed antennas.

Frequency [MHz]	1795 MHz	1920 MHz	2045 MHz	2350 MHz	2450 MHz	2600 MHz	3500 MHz	5250 MHz	5775 MHz
Gain [dBi]	0.79	0.44	0.49	2.26	2.28	2.01	2.9	2.33	4.07

4. CONCLUSIONS

This paper presented the design of a dual rectangular ring-shaped monopole antenna for quad-band operations. By using the coupling effect between the inner and outer rectangular patches, the optimized matching characteristic is obtained and antenna performance is improved. It is realized that coupling occurred between two rectangular patches that affected the matching characteristics. Also, by adding the two L-slots in the ground plane, two bandwidths are additionally obtained. The distinct frequency band can be controlled by adjusting some main parameters. The proposed antenna satisfied the frequency bands of 1.6–2.8 GHz, 3.2–4.0 GHz, 5.14–5.44 GHz, and 5.56–6.25 GHz as a result of measurement. Thus, this antenna is suitable for DCS1800, PCS1900, WCDMA, WLAN, and Mobile WiMAX applications.

REFERENCES

1. Shin, C. S., H. S. Shin, N. Kim, J. I. Choi, and J. D. Park, "Internal monopole antenna design for multiband operation and sar analysis," *The Journal of Korea Electromagnetic Engineering Society*, Vol. 15, No. 12, 1190–1198, 2004.
2. Choi, D. G., H. S. Shin, N. Kim, and Y. K. Kim, "Design of the broadband PIFA with multiband for SAR reduction," *The Journal of Korea Electromagnetic Engineering Society*, Vol. 16, No. 1, 66–77, 2005.
3. Lee, H. M., S. W. Lee, and N. Kim, "The design and SAR analysis of the broadband printed monopole antenna with Z-patch," *The Journal of Korea Electromagnetic Engineering Society*, Vol. 18, No. 12, 1391–1401, 2007.
4. Lee, S. H., S. W. Lee, and N. Kim, "The design and fabrication of the triple-band planar monopole antenna for coupled U patch line and rectangular patch," *The Journal of Korea Electromagnetic Engineering Society*, Vol. 22, No. 8, 745–753, 2011.
5. Park, J. W., T. J. Cho, B. I. Moon, and H. M. Lee, "Monopole antenna with a triangular patch structure for penta-band service," *The Journal of Korea Electromagnetic Engineering Society*, Vol. 21, No. 2, 136–142, 2010.
6. Yoon, C. M., K. K. Kim, and S. S. Jo, "Tri-band antenna design and fabrication using ground slots," *The Journal of Korea Institute of Information Technology*, Vol. 8, No. 12, 131–139, 2010.
7. Koo, T. W., D. Kim, J. I. Ryu, J. I. Kim, and J. G. Yook, "A coupled dual-U-shaped monopole antenna for WiMAX triple-band operation," *Microwave and Optical Technology Letters*, Vol. 53, No. 4, 745–748, 2011.
8. Paitoon, R., A. Noppin, J. Kanok, and W. Toshio, "Multiband microstrip-fed right angle slot antenna design for wireless communication systems," *ETRI Journal*, Vol. 31, No. 3, 271–281, 2009.
9. Ren, X., Y. Yin, S. Zheng, S. Zuo, and B. Liu, "Triple-band rectangular ring monopole antenna for WLAN/WiMAX applications," *Micro. and Tech. Lett.*, Vol. 53, No. 5, 974–978, 2011.
10. Deng, H., X. He, B. Yao, and Y. Zhou, "A compact square-ring printed monopole ultra wide-band antenna," *International Conference on Microwave and Millimeter Wave Technology*, Vol. 4, 1644–1646, 2008.
11. Park, S. M., N. Kim, and J. M. Kim, "The design and SAR analysis of the spiral planar monopole antenna for dual-band," *The Journal of Korea Electromagnetic Engineering Society*, Vol. 18, No. 12, 1370–1382, 2007.
12. Zhang, L. N., S. S. Zhong, X. L. Liang, and C. H. Li, "Compact meander monopole antenna for tri-band WLAN application," *Microwave and Optical Technology Letters*, Vol. 49, No. 4, 986–988, 2007.

A Multiband Antenna Based on Mushroom Composite Right/Left-handed Transmission Line Structure

X. Li, Q.-Y. Feng, and Q.-Y. Xiang
School of Information Science and Technology
Southwest Jiaotong University, Chengdu, Sichuan 610031, China

Abstract— In this paper, a novel multiband planar antenna based on 2-D mushroom-like composite right/left-handed transmission line (CRLH-TL) structure is proposed. The metal patch of the mushroom cell is connected to the ground plane through via and planar inductor. It shows that the proposed structure gives an efficient approach to achieve multiband response and miniaturization. The operation frequency of the multiband antenna is dependent on the mushroom structure size and the equivalent parameters of the CRLH-TL, including capacitance and inductance. The proposed antenna is built with a total volume of 21 mm × 26 mm × 1 mm, and four resonant bands have been got. The radiation patterns are similar with the omnidirectional characteristics and the gains are 1.27 dBi, 2.23 dBi, 2.86 dBi, and 5.2 dBi at 2.62 GHz, 3.91 GHz, 6.52 GHz, and 8.05 GHz, respectively. The results show that the presented structure has reasonable radiation characteristics of efficiency, bandwidth, and size that it will be suitable for multiband wireless application.

1. INTRODUCTION

Small size and multiband antennas with well radiation characteristics are hot research topics recently due to the rapid development of the wireless communications. One attractive solution to realize the compact multiband antenna is using the metamaterials. Metamaterials are artificial composite materials, exhibiting unusual properties compared with conventional nature materials, such as the negative refraction, anti-parallel phase and group velocities [1, 2]. The CRLH-TL metamaterial structure, which is a transmission line type metamaterial, can be represented by the series inductor (L_R), series capacitor (C_L), shunt inductor (L_L), and shunt capacitor (C_R). C_L and L_L determine the left-handed mode, while L_R and C_R determine the right-handed mode [3]. The left-handed and right-handed modes can be indicated by the dispersion curve shown in Fig. 1. The $\beta > 0$ side is the right-handed region, and the $\beta < 0$ side is the left-handed region [4]. When $\beta = 0$, an infinite wavelength can be obtained and the more compact size of the antenna can be realized. The CRLH-TLs have been widely applied for multi-band antenna design [5]. A compact coplanar waveguide (CPW)-fed zeroth-order resonant antennas with extended bandwidth and high efficiency was proposed in [1]. A resonant antenna using DGS dual composite right/left handed transmission line (D-CRLH TL) is presented in [6], exhibiting multiband property. The CRLH-TL could be realized in many ways. One of the typical CRLH-TL structures is the mushroom-like structure that was first proposed by D. Sievenpiper for the high-impedance surface. Later the negative refraction property has been investigated widely. Zeroth-order resonant antennas using mushroom-type structures are shown in [7]. The miniaturized low-profile patch antenna with the mushroom-like CRLH structures and a reactive impedance surface (RIS) has been developed in [8]. In this paper, a multiband antenna based on mushroom CRLH-TL configuration was proposed. The gains are 1.27 dBi, 2.23 dBi, 2.86 dBi, and 5.2 dBi at 2.62 GHz, 3.91 GHz, 6.52 GHz, and 8.05 GHz, respectively. The antenna was fabricated in Fr-4 substrate, and both the measured and simulated results are presented.

2. ANTENNA STRUCTURE

It is well known that one approach to describe and implement the metamaterials is the composite right/left-handed transmission-line theory. As mentioned in [9], due to the unavoidable parasitic effects which come from the RH mode, the purely LH-TL cannot be realized. So the CRLH-TL has both LH and RH metamaterial properties. One of the representative implementations of CRLH metamaterials is the mushroom-like structure which is the two-dimensional structure. In this paper, the mushroom-like CRLH-TL structure is composed of the metal patch and via connected to the ground plane. The top surface and the bottom surface of this antenna are shown in Fig. 2(a) and Fig. 2(b), respectively.

As shown in Fig. 2, the mushroom-like structure and the meander line are adopted by the antenna for multi-resonances and size reduction. The antenna is a planar structure where the

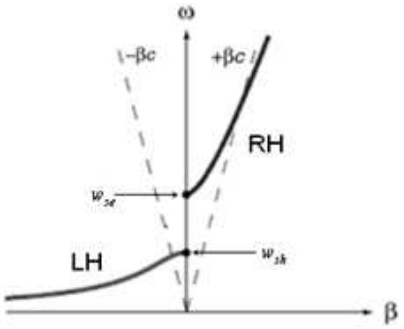

Figure 1: The dispersion diagram.

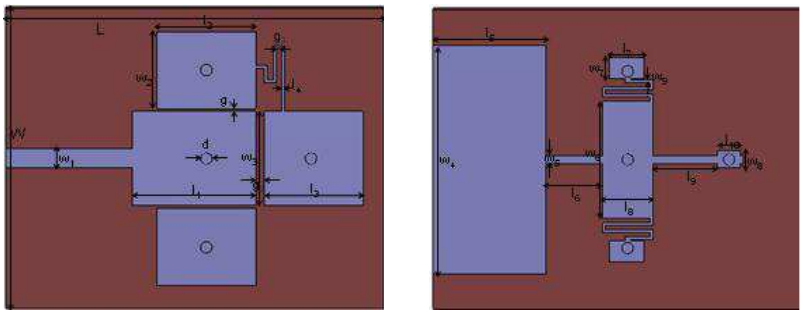

(a) top view (b) bottom view

Figure 2: Geometry of the proposed antenna.

Table 1: The optimized parameters (Unit: mm).

Parameters	L	l_1	l_2	l_3	l_4	l_5	l_6	l_7	l_8
Optimized Size	26	8.5	6.8	6.8	0.2	8	4	2.5	3.6
Parameters	l_9	l_1	W	w_1	w_2	w_3	w_4	w_5	w_6
Optimized Size	4.6	1.6	21	1.34	5.4	6.6	16	0.6	8.2
Parameters	w_7	w_8	w_9	g_1	g_2	g_3	d		
Optimized Size	1.5	1.2	0.2	0.2	0.6	0.4	0.8		

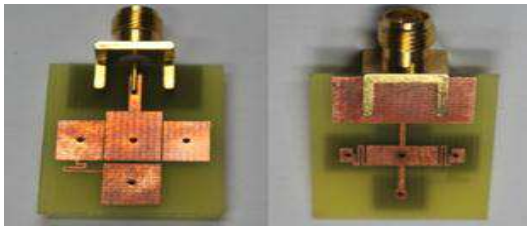

(a) top view (b) bottom view

Figure 3: Photograph of the fabricated antenna.

dielectric substrate is "FR-4 Epoxy" with a relative permittivity of 4.4, a thickness of 1 mm, and the planar size of 21 mm × 26 mm. The top patches comprise four sections which are coupled with each other and the first section is connected to a traditional 50-Ohm microstrip feed line. These mushroom-shape sections have different side lengths, the radius of the via is 0.4 mm and the width of the meander line connected to the two patches is 0.2 mm. The two sectional patches on both sides of the first section is coupled to the first section through a 0.2 mm coupling gap and another coupling gap between the first section and the last section is 0.6 mm in width. The ground plane is not the full ground, but the truncated ground with the meander line underneath the mushroom-shape sections.

The coupling of adjacent top patches is equivalent to the left-handed (LH) capacitance (C_L), whereas the LH inductance (L_L) is provided by the metallic via connected between the top patch and the ground plane on the back of the substrate, as well as the parasitic (right-handed) RH series inductance and RH shunt capacitance existed [8]. The C_L can be adjusted by changing the width of the coupling gap between patches, and the diameter of the via gives the influence on L_L. Using the full wave electromagnetic (EM) software to model and simulate the proposed antenna, the optimized parameters are shown in Table 1.

3. SIMULATION AND MEASUREMENT RESULTS

Figure 3 shows the photograph of the fabricated antenna sample. Figs. 4(a) ∼ (d) show the simulated electric field distribution in the x-y plane of the proposed antenna at each resonance. In this figure, the E-field magnitude mainly generated at the edge of gaps, via-holes, and the meander lines. It means that the E-field distributions are influenced by the left handed parameters.

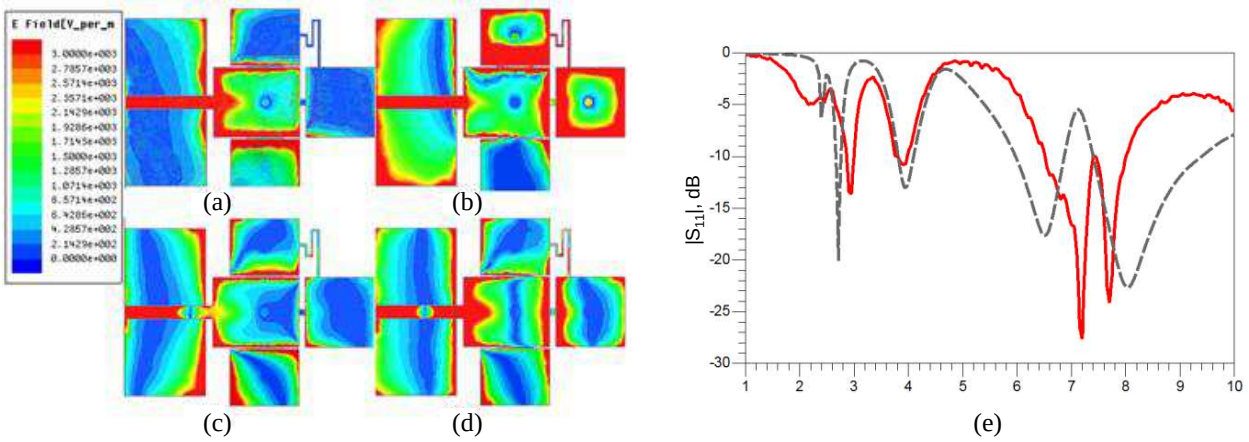

Figure 4: E-field distributions of the proposed antenna: (a) 2.62 GHz, (b) 3.91 GHz, (c) 6.52 GHz, (d) 8.05 GHz, and (e) the simulated and measured S_{11}.

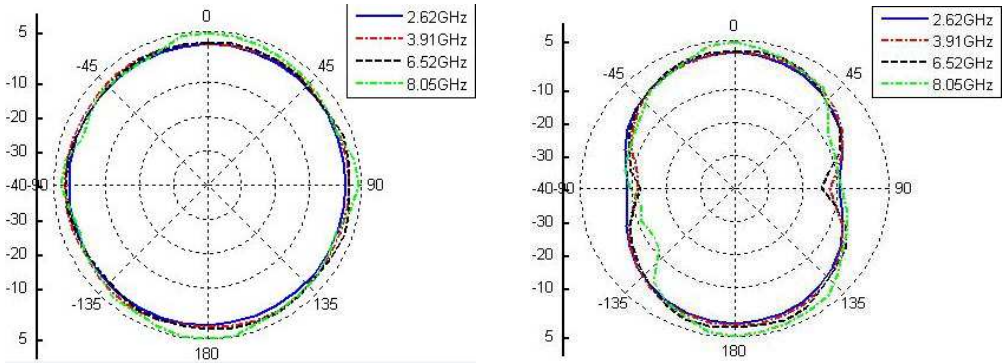

Figure 5: Simulated radiation patterns at the center frequencies in the H-plane and the E-plane.

It is obvious that for the lower frequency (3.91 GHz), the E-field distribution is relatively well-distributed.

The antenna was tested using Agilent network analyzer. The simulated and measured reflection coefficients are presented in Fig. 4(e), and it shows that four resonances are excited between 2 GHz and 10 GHz. The simulated -10 dB bands are located at the ranges of 2.59 $\sim$ 2.68 GHz, 3.76 $\sim$ 4.09 GHz, 5.98 $\sim$ 6.88 GHz and 7.39 $\sim$ 9.4 GHz, namely, 3.4%, 8.4%, 13.8%, 24.9% impedance bandwidth, respectively. These multi-frequencies can be controlled by the mushroom CRLH-TL structures and the meander line between the two patches. The measured results are in good agreement with the simulation, though a small frequency shift is detected. The discrepancy is mainly due to the fabrication tolerances and the influence of the input feeding.

The simulated radiation patterns of the proposed antenna at each resonant frequency in both H-plane and E-plane are displayed and compared in Fig. 5. Apparently, the radiation patterns in the H-plane are fairly good omnidirectional characteristics. In addition, the maximum gains are simulated as 1.27 dBi, 2.23 dBi, 2.86 dBi, and 5.2 dBi at 2.62 GHz, 3.91 GHz, 6.52 GHz, and 8.05 GHz, respectively. Therefore, the proposed antenna shows good radiation characteristics, which could satisfy the requirement of the wireless communication.

4. CONCLUSIONS

A compact multiband antenna based on mushroom-like CRLH resonator has been described in this paper. It has been revealed that using the CRLH-TLs structure can provide an opportunity to realize multi-frequency. According to the simulation results, the impedance bandwidths (return loss $\geqslant$ 10 dB) are 3.4%, 8.4%, 13.8%, 24.9%, respectively. The simulated radiation patterns show the omnidirectional characteristics and the simulated gains at the center frequencies are reasonable. The antenna prototype with the compact size of 21 mm $\times$ 26 mm $\times$ 1 mm is fabricated. The measured

and simulated results show good agreement.

ACKNOWLEDGMENT

This work is supported by a grant from the National 863 Project of China (No. 2012AA012305) and Major Program of the National Natural Science Foundation of China (No. 60990320; 60990323).

REFERENCES

1. Jang, T., J. Choi, and S. Lim, "Compact coplanar waveguide (CPW)-fed zeroth-order resonant antennas with extended bandwidth and high efficiency on vialess single layer," *IEEE Transactions on Antennas and Propagation*, Vol. 59, 363–372, 2011.
2. Caloz, C., T. Itoh, and A. Rennings, "CRLH metamaterial leaky-wave and resonant antennas," *IEEE Antennas and Propagation Magazine*, Vol. 50, 25–39, 2008.
3. Lee, C., W. Huang, A. Gummalla, and M. Achour, "Small antennas based on CRLH structures: Concept, design, and applications," *IEEE Antennas and Propagation Magazine*, Vol. 53, 10–25, 2011.
4. Caloz, C. and T. Itoh, *Electromagnetic Metamaterials: Transmission Line Theory and Microwave Applications, The Engineering Approach*, John Wiley & Sons, New York, 2005.
5. Yu, A., F. Yang, and A. Elsherbeni, "A dual band circularly polarized ring and antenna based on composite right and left handed metamaterials," *Progress In Electromagnetics Research*, Vol. 78, 73–81, 2008.
6. Ryu, Y., J. Park, J. Lee, and H. Tae, "Multiband antenna using +1, −1, and 0 resonant mode of DGS dual composite right/left handed transmission line," *Microwave and Optical Technology Letters*, Vol. 51, 2485–2488, 2009.
7. Park, J. H., Y. H. Ryu, J. G. Lee, and J. H. Lee, "Epsilon negative zeroth-order resonator antenna," *IEEE Transactions on Antennas and Propagation*, Vol. 55, 3710–3712, 2007.
8. Dong, Y., H. Toyao, and T. Itoh, "Compact circularly-polarized patch antenna loaded with metamaterial structures," *IEEE Transactions on Antennas and Propagation*, Vol. 59, 4329–4333, 2011.
9. Lai, A., C. Caloz, and T. Itoh, "Composite right/left handed transmission line metamaterials," *IEEE Microwave Magzine*, Vol. 5, 34–50, 2004.

New Multiple Loop Antenna Design for 13.56 MHz RFID Reader

Cheol Yong Yang, **Seong Ha Lee**, **and Woon Geun Yang**
Department of Electronics, University of Incheon, Incheon 406-772, South Korea

Abstract— In this paper, a new multiple loop antenna structure for 13.56 MHz RFID (Radio Frequency Identification) reader is proposed. As the size of the loop antenna for 13.56 MHz RFID reader is enlarged, the magnetic field at the central area of the loop antenna is weakened. To compensate this, serial feed multiple loop antenna, parallel feed multiple loop antenna and serial-parallel feed multiple loop antenna were proposed.

From previous our design, the simulation results on the magnetic field strength averaged for transponder size in the central area showed about 0.15 A/m, 0.32 A/m, 0.84 A/m and 0.95 A/m in the cases of the single loop antenna and serial feed multiple loop antenna and parallel feed multiple loop antenna and serial-parallel feed multiple loop antenna. In addition, as to the induced voltage for the central area of the antenna, the single loop antenna showed 0.84 V and serial feed multiple loop antenna was 2.84 V and parallel feed multiple loop antenna was 4.24 V and serial-parallel feed multiple loop antenna was 7.01 V. That is, we obtained a better magnetic field strength performance and induced voltage performance which will result longer interrogation distance.

In this paper, we propose a new antenna structure. It consists of outer loop and inner parallel loops. Outer loop looks like primary coil of the transformer and one inner loop operates just like secondary coil of the transformer. In fact, inner loops operate accepter and donor antennas of the repeater. HFSS (High Frequency Structure Simulation) based on the FEM (Finite Element Method) from Ansys was used for the simulations of the proposed antenna. The outer most loop diameter of the proposed example design was 150 mm and number of turns was 2.

The performance of the proposed antenna was compared with the those of single loop antenna, serial feed multiple loop antenna, parallel feed multiple loop antenna, and serial-parallel feed multiple loop antenna in the view points of magnetic field intensity especially at the central point of each antennas.

1. INTRODUCTION

RFID (Radio Frequency IDentification) system has many applications in the various fields including communication, security, finance, traffic and electronic commerce. Particularly, in case of South Korea, it is remarkably used in the public transportation fare collection system. And RFID applications are proceed to physical distribution entrance control, automated collecting fee and parking management, animal identification [1].

ISO (International Standardization Organization)/IEC (International Electrotechnical Commission) 14443 standard is used for many applications in South Korea which adopts 13.56 MHz. The operating power for transponder is delivered from reader antenna as alternating field. Inductive coupling make wireless power transfer possible with the transmission frequency of 13.56 MHz [2]. In ISO/IEC 14443 standard, the RFID reader antenna forms the electromagnetic field which supports transponder operation [3]. In many cases, the most important interests lie on interrogation distance.

In this paper, a new antenna structure is proposed for longer interrogation distance. By using HFSS (High Frequency Structure Simulation) from Ansys Corporation, the characteristics of the previous loop antennas and the proposed antenna are analyzed and compared.

2. ANTENNA DESIGN

RFID reader and transponder usually adopt loop antenna. Generally, in case of loop small loop antenna the strong radiation is observed in the direction of the loop plane [4]. Typically, loop antenna has a single winding group. As the diameter is extended, the field intensity at the central area of the loop is weakened. To compensate this, applying several winding groups with serial connection, parallel connection or serial-parallel connection are proposed previously [5, 6].

Figure 1 shows (a) conventional single loop antenna, (b) series fed multiple loop antenna, (c) parallel fed multiple loop antenna, (d) series-parallel fed multiple loop antenna and (e) proposed antenna. The structure of the proposed antenna is like this. The proposed antenna has three winding groups. The outer loop is same as conventional single loop. And middle winding group

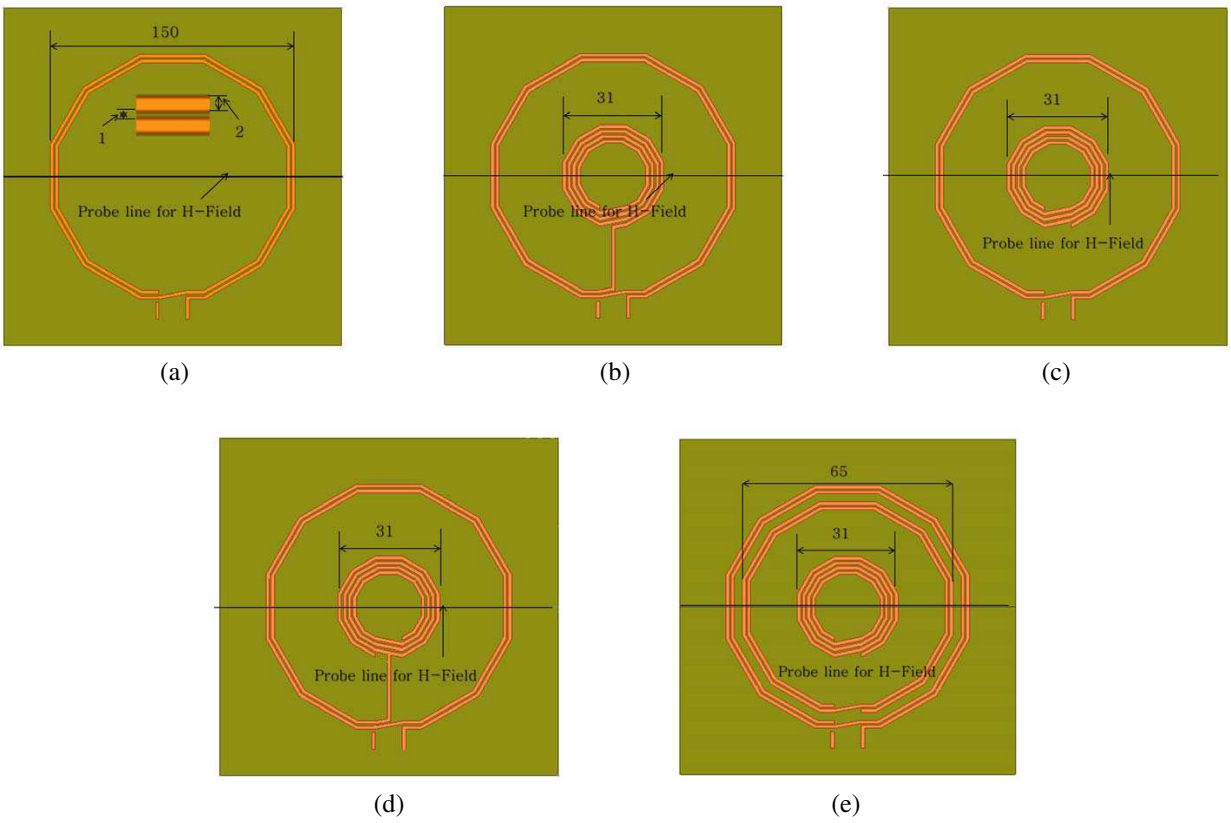

Figure 1: RFID reader antennas studied. (a) Single loop antenna. (b) Series fed multiple loop antenna. (c) Parallel fed multiple loop antenna. (d) Series-parallel fed multiple loop antenna. (e) Proposed antenna.

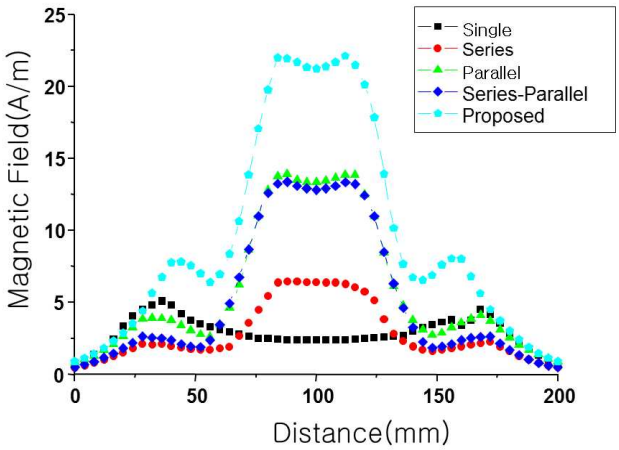

Figure 2: Simulation results on magnetic field for various antennas.

and inner winding group is connected in parallel. Middle winding group and outer winding group are inductively coupled. So inner parallel winding groups seems like donor and acceptor antenna. The diameter of the outer loop is 150 mm and 2 turns, middle winding has 2 turns and inner winding has 4 turns. The diameter of the middle winding is 65 mm and inner loop diameter is 31 mm.

3. SIMULATION RESULTS

Figure 2 shows simulation results on magnetic field for various antennas. In order to compare the intensity of the magnetic field at the central part of the suggested antenna structure, we designed 5 antennas with different structures. Table 1 shows simulated magnetic fields for various antennas

Table 1: Simulated magnetic fields for various antennas at the central point of each antennas (Unit: A/m).

	Single	Series	Parallel	Series-Parallel	Proposed
Magnetic Field	2.38	6.4	13.34	12.85	21.24

at the central point of each antennas with same driving source. From Table 1, and Fig. 2, we can see the proposed antenna has better performances compared with previously studied structures.

4. CONCLUSIONS

Multiple loop antenna for RFID reader was proposed. The proposed antenna showed a strong magnetic field strength at the central point of the antenna. Strong field can result a long interrogation range. Compared with previous structure, the proposed antenna showed a better field performance with same size. We expect that the proposed antenna can have proper application chances for touch and go system with improved interrogation ranges.

ACKNOWLEDGMENT

This work was supported by S I T KOREA Co., Ltd.

REFERENCES

1. Lee, G. H. and G. Y. Kim, "RFID Technology Tendency," *The Proc. of the Korea Electromagnetic Engineering Society*, Vol. 12, No. 4, 43–49, 2001.
2. Finkenzeller, K., *RFID Handbook*, 2nd Edition, 41–65, John Wiley & Sons, 2003.
3. ISO/IEC 14443-2, "Identification cards — Contactless integrated circuit(s) cards — Proximity cards — Part 2: Radio frequency power and signal interface," 2001.
4. Stutzman, W. L. and G. A. Thiele, *Antenna Theory and Design*, 68–76, John Wiley & Sons, 1998.
5. Yang, W. G., Y. J. Park, H. J. Kim, J. M. Cho, and J. H. Kim, "Parallel-fed multi loop antenna for 13.56 MHz RFID reader," *Proc of ICEIC*, 334–338, 2004.
6. Kim, H. J., W. G. Yang, and H. J. Yoo, "A study on the magnetic field improvement for 13.56 MHz RFID reader antenna," *Journal of IEEK*, Vol. 43-TC, No. 1, 1–8, 2006.

High Isolation MIMO Antenna Design by Using Ground Slits for Mobile Handset

Seong Ha Lee, Cheol Yong Yang, and Woon Geun Yang
Department of Electronics, University of Incheon, Incheon 406-772, South Korea

Abstract— In this paper, we designed and implemented the MIMO (Multiple-Input Multiple-Output) antenna with high isolation by using ground slits for the mobile handset that could be used for multiple services. The proposed system incorporates multiple slits between the two antennas in the ground plane, which operate like a band-stop filter, suppressing mutual coupling between antennas and resulting in improved isolation.

The characteristics of the proposed antenna were simulated by using HFSS (High Frequency Structure Simulator) of Ansoft which is based on the FEM (Finite Element Method). Results showed S_{11} values less than -6 dB (VSWR < 3) for LTE (Long Term Evolution) 700/2300/2500, WCDMA (1920 $\sim$ 2170 MHz), Wibro (2,300 $\sim$ 2,390 MHz), Bluetooth (2,400 $\sim$ 2,483 MHz), and US-WiMAX (US-World interoperability for Microwave Access: 2,400 $\sim$ 2,590 MHz) frequency bands.

The proposed MIMO antenna was designed as folded monopole antenna in order to reduce the size of the antenna. On the right side, the longest branch is the major radiation element for the proposed antenna at low band. On the left side, a short branch plays a major role for high band. The proposed antenna is composed of two branches. And one branch has a rectangular slit. The rectangular slit has influences on whole impedance matching.

The antenna size of example design is 50 mm (W) $\times$ 20 mm (L) $\times$ 5 mm (H). For the design studied here, the antenna is fabricated on an inexpensive FR4 substrate with the dielectric constant of 4.4 and the substrate thickness of 1.60 mm. Ground size is 60 mm (W) $\times$ 100 mm (L). Measured results of the fabricated antenna are validated by the LTE 700/2300/2500, WCDMA, Wibro, Bluetooth, US-WiMAX.

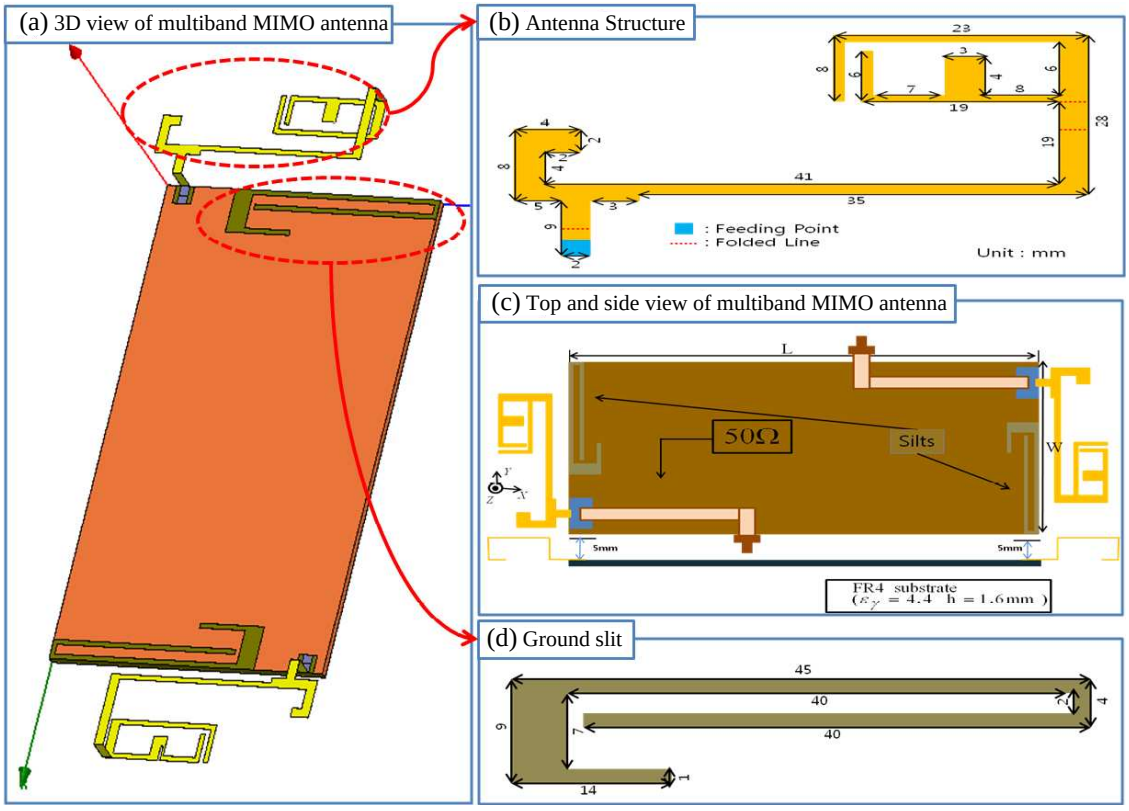

Figure 1: Geometry of the proposed multiband MIMO antenna for 4G systems.

1. INTRODUCTION

The use of multiple antennas for diversity, including MIMO (Multiple Input Multiple Output), is one of the most promising wireless technologies for broadband communication applications [1]. A MIMO antenna system is a well-known technique to enhance the performance of wireless communication systems. Channel capacity of a MIMO antenna system is much larger than that provided by a conventional wireless system [2–4]. However, it is very challenging to place multiple antennas closely into a small and slim mobile handset while maintaining good isolation between antenna elements since the antennas are strongly coupled with each other and even with the ground plane by sharing the surface currents distributed on it. So far, many researchers have been trying to find new techniques for isolation improvement between antenna elements inside mobile handsets [5–7].

In this paper, we propose the method to improve the isolation performance of two-antenna systems for LTE terminals. The proposed multiband MIMO antenna consists of two monopole antennas which provide wideband characteristics. In order to improve the isolation characteristic at the LTE700 band, ground slits are introduced. Ground slits are used to disperse the surface currents at the specific frequency band. The designed multiband MIMO antenna has been successfully implemented and experimental results are presented and discussed.

2. ANTENNA DESIGN AND EXPERIMENTAL RESULTS

The geometry of the proposed multiband MIMO antenna for 4G system is shown in Fig. 1. Top end part of the monopole has branches which widen the bandwidth in low frequency band near 750 MHz. The overall size of the radiating element is $50\times20\times5\,\mathrm{mm}^3$. Two same elements are placed at the top and bottom sides of a FR4 ($\varepsilon_r = 4.4$) substrate having volume of $60 \times 100 \times 1.6\,\mathrm{mm}^3$, which simulates the ground plane of a practical bar type mobile handset. In order to improve the isolation characteristic at the LTE 700 band, ground slits are used at the top and bottom of ground plane.

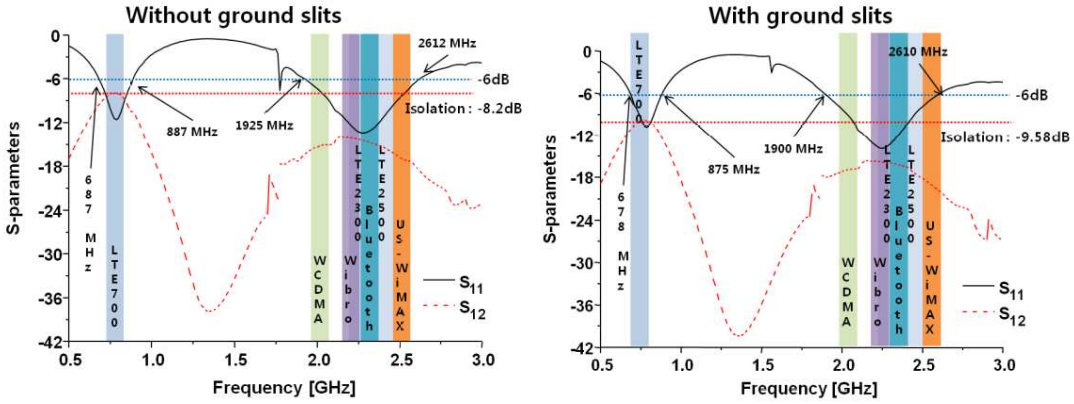

(a) Simulated *S*-parameter characteristics

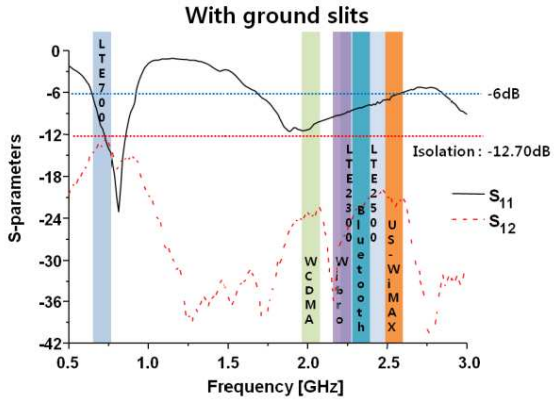

(b) Measured *S*-parameter characteristics

Figure 2: *S*-parameter characteristics without and with ground slits.

The S-parameter characteristics with and without ground slits are given in Fig. 2. It is shown that simulated S-parameter characteristics are similar to those of measurement. Without ground slits, the MIMO antenna has the isolation characteristic of −8.2 dB at LTE 700 band. When ground slits are added, the simulated isolation characteristic at LTE 700 band is increased by 1.38 dB as shown in Fig. 2.

Figure 3 shows the excited surface current distributions, obtained from the HFSS simulation on the radiation element of the proposed antenna and ground plane at 750 MHz.

Table 1 shows the results of maximum peak gain and average gain measurement of the implemented the antenna. On each band, the peak gain is the maximum measured gain of the antenna. And average gain is the averaged value of the measured gain for each frequency band measurement. Through this table we can see that the maximum peak gain and average gain of LTE 700 band are −4.1 dBi, −7.1 dBi, respectively. 2.9 dBi and −6.5 dBi at the WCDMA, 3.5 dBi and −2.9 dBi at the LTE 2300, 4.2 dBi and −1.7 dBi at the Bluetooth, 3.5 dBi and −2.4 dBi at the LTE 2500, 2.83 dBi and −3.65 dBi at the US-WiMAX , respectively.

The measured radiation patterns of the implemented multiband MIMO antenna are shown in Fig. 4. Radiation patterns are normalized.

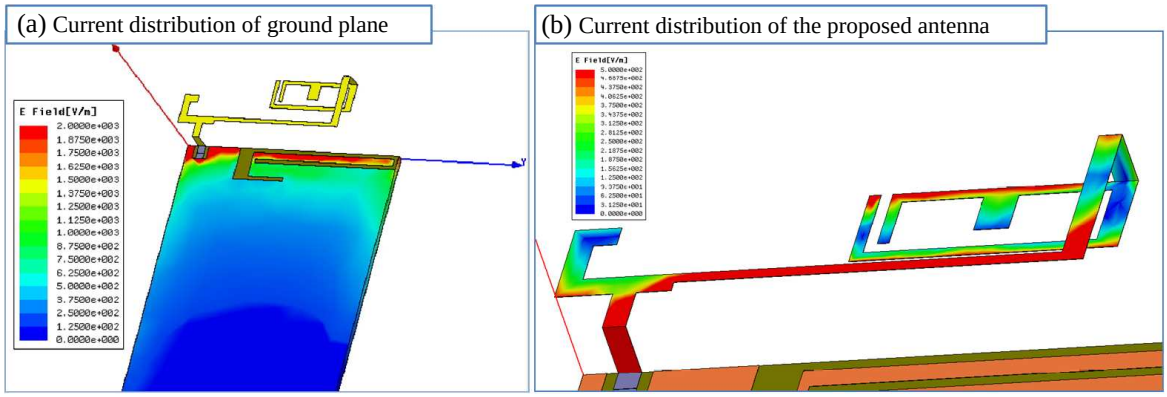

Figure 3: Current distribution at 750 MHz.

Table 1: Measured antenna gains.

Frequency (GHz)	0.750	2.045	2.350	2.442	2.495	2.595
Antenna Peak Gains (dBi)	−4.1	2.9	3.5	4.2	3.5	2.83
Antenna Average Gains (dBi)	−7.1	−6.5	−2.9	−1.7	−2.4	−3.65

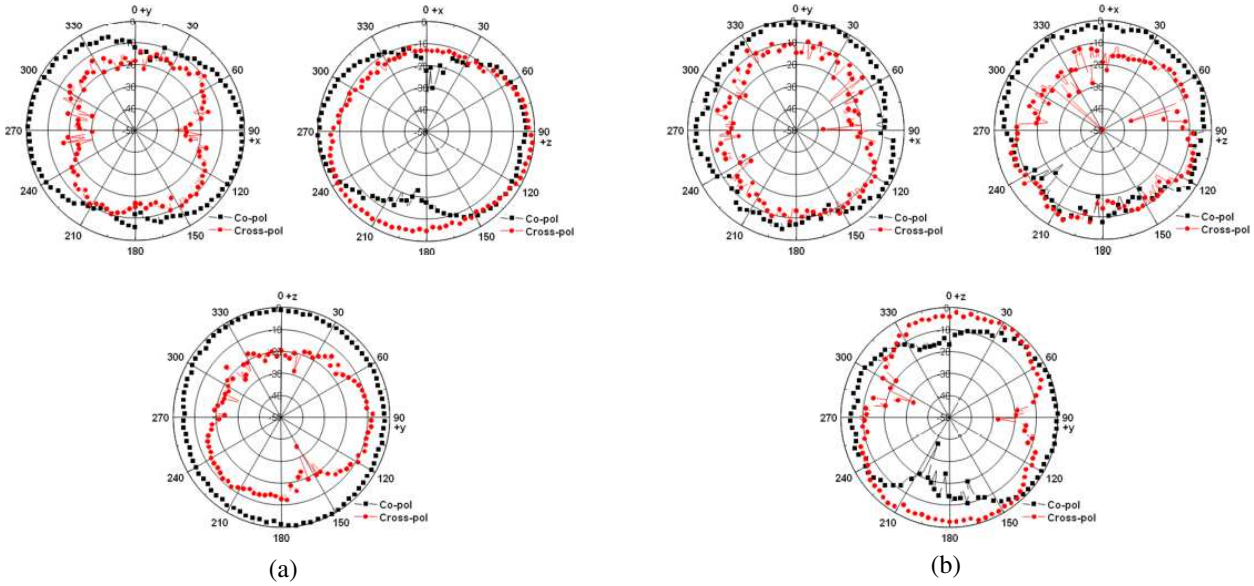

(a) (b)

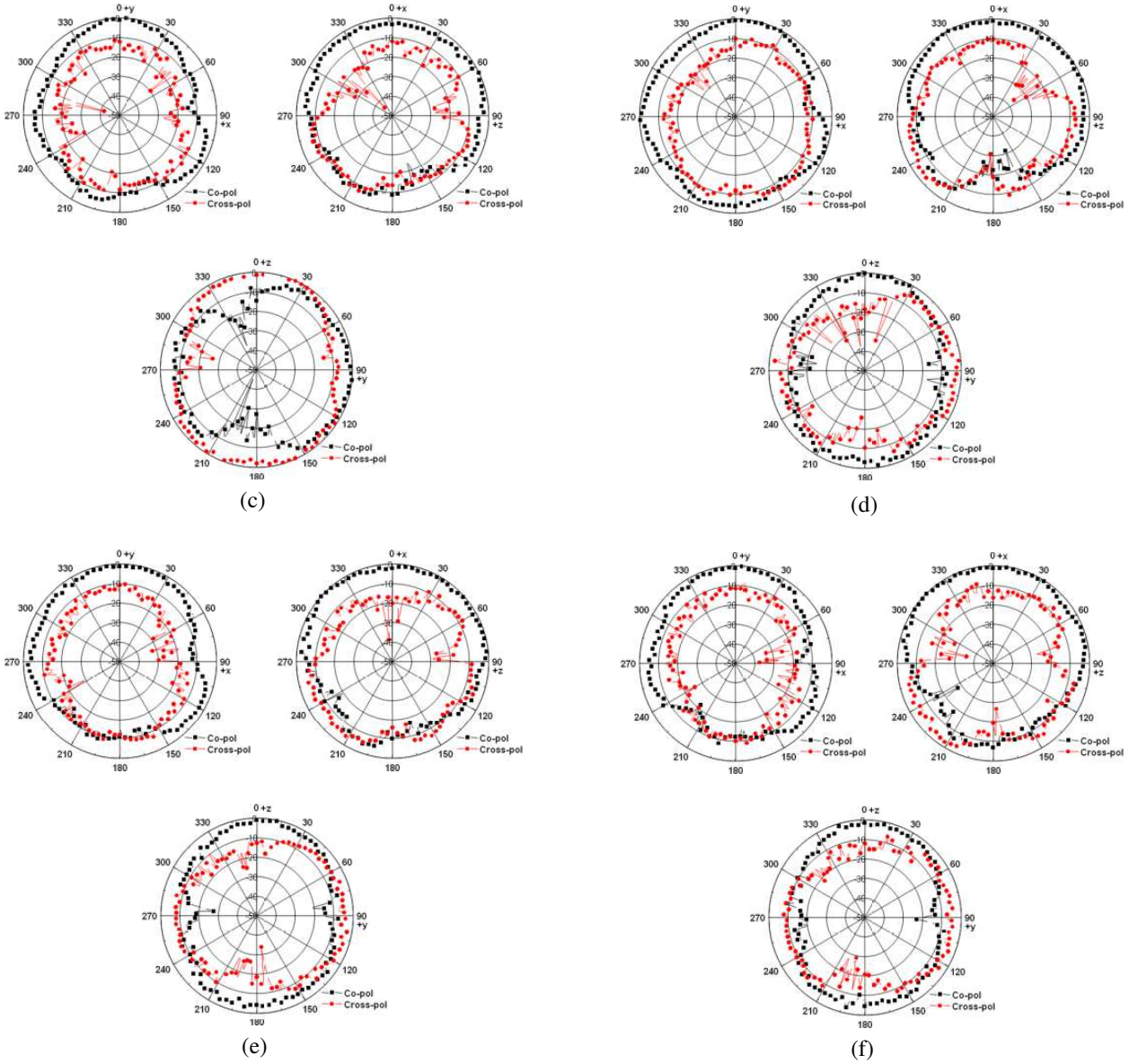

Figure 4: Measured co-polarization and cross-polarization radiation patterns: (a) at 750 MHz; (b) at 2045 MHz; (c) at 2350 MHz; (d) at 2442 MHz; (e) at 2495 MHz; (f) at 2595 MHz.

3. CONCLUSIONS

Internal multiband MIMO antenna with high isolation characteristic for LTE applications was proposed. In order to enhance the isolation characteristic at LTE700 band ground slits are added. The fabricated antenna has the isolation of −12.70 dB at the low band. The measured peak gains and average gains of antenna elements are −4.1 dBi and −7.1 dBi at the LTE700 band, 2.9 dBi and −6.5 dBi at the WCDMA band, 3.5 dBi and −2.9 dBi at the LTE 2300 band, 4.2 dBi and −1.7 dBi at the Bluetooth band, 3.5 dBi and −2.4 dBi at the LTE 2500 band and 2.83 dBi and −3.65 dBi at the US-WiMAX band, respectively. The simulated and measured results show that the proposed multiband MIMO antenna could be a good candidate for 4G mobile systems.

REFERENCES

1. IEEE 802.11n, Joint Proposal: High throughput extension to the 802.11 Standard: PHY, doc.: IEEE 802.11-05/1102r4.
2. Shiu, D. S., G. J. Foschini, M. J. Gans, and J. M. Kahn, "Fading correlation and its effect on the capacity of multi element antenna systems," *IEEE Trans. on Comm.*, Vol. 48, No. 3, 502–513, Mar. 2000.

3. Heidari, T., A. Motevasselian, M. Salehi, and A. Tavakoli, "Mutual coupling reduction of microstrip antennas using defected ground structure," *IEEE Int. Communication Systems Conference*, 1–5, Oct. 2006.
4. Wong, K.-L., C.-A. Lyu, and L.-C. Chou, "Small-size multiband planar antenna for LTE700/2300/2500 operation in the tablet computer," *Microwave and Optical Technology Letter*, Vol. 54, No. 1, 81–86, Jan. 2012.
5. Kang, T.-W. and K.-L. Wong, "Isolation improvement of 2.4/5.2/5.8 GHz WLAN internal laptop computer antennas using dual-band strip resonator as a wavetrap," *Microwave and Optical Technology Letter*, Vol. 52, 58–64, 2010.
6. Park, G., M. Kim, T. Yang, J. Byun, and A. S. Kim, "The compact quadband mobile handset antenna for the LTE700 MIMO application," *Proc. IEEE Antennas Propag. Soc. Int. Symp.*, 1–4, 2009.
7. Hsieh, C. P., T. Chiu, and H. B. Wu, "Band-stop filter design of coplanar stripline," *IEEE Proc. of Asia-Pacific Microwave Conference*, 2007.

Design and Simulation of Different Types of Meander Line Antennas with Improved Efficiency

A. Jahanbakhshi[1], **Gh. Moradi**[2], **and R. Sarraf Shirazi**[2]

[1]Amirkabir University of Technology, Iran
[2]Electrical Department, Amirkabir University of Technology, Iran

Abstract— The advent of new technology in communication systems and widespread use of this technology, leads engineers to design cheaper and simpler communication equipments. One of the most usage aspect of communication field is WLAN and RFID systems. Antenna is an inseparable part of these systems. Meander line antenna is the most usage of antenna that use in design of these applications. Classic meander line antenna has low efficiency in some aspects, such as antenna bandwidth and operation in only one resonance frequency (single band). In this present various kind of these antennas have been proposed, to get better characteristics and efficiency such as log periodic meander line antenna, meander line antenna with different length of vertical segment and symmetrical meander line antenna.

1. INTRODUCTION

In recent years, the wireless communication business has expanded greatly. Wireless systems such as WLAN has been popular [1, 2]. With development of communication equipment, control and security devices are commonly use such as RFID. As we know, in these system the antenna is an important part of devices that determining system size and performance.

Recently, meander line antenna has extremely used in design of these systems such as RFID tags and WLAN systems [1–7].

Meander line antenna has significant advantages, it is electrically small, low profile antenna and has simple structure [8]. But these antennas have some disadvantages, low radiation efficiency. When the size of antenna is reduced, the radiation resistance is reduced. This results in the problem of decreased radiation efficiency because the ratio of the Ohmic loss of the antenna conductor to the radiated power is increased [9].

The other problem with classic meander line antennas, is their low bandwidth. As the meander line antenna is one of the microstrip antenna, so it has low bandwidth (less than 5%) [10]. Having a Dual band response is the other key factor for meander line antennas. As wireless communication systems are becoming more and more flexible and even a less expensive than today cable based systems, equipment working in these systems requires a low profile, dual band and wide band antennas [11].

Meander line antennas, which has small size, wideband and ability to operate in dual band frequency is suitable choice for these applications.

In this paper, for obtaining better characteristics different kinds of meander line antenna have been proposed. For each one, the antenna design procedure, simulation for return loss, current distribution, 3D pattern and Co and Cross Pol component are presented.

2. DESIGN DIFFERENT TYPE OF MLA

2.1. MLA with Different Thickness of Vertical Segment

An important application of meander line antenna is in wireless communication systems such as WLAN. In these applications, bandwidth is an important factor. As it mentioned before meander line antenna has low efficiency [10]. So if this kind of antenna want to use in WLAN systems, it must to improve it bandwidth.

If we analysis current distribution of classic meander line antennas it could be observed that vertical segment of meander line antenna has more role in constructing electrical field of this antenna. Fig. 1 shows the current distribution of classic meander line antenna.

Therefore, with applying some changes in this segment, such as different thickness, it might get better results. Fig. 2 shows MLA with different thickness of vertical segment.

In this structure, thickness of vertical segment and feed line are 2 mm and thickness of horizontal segment is 1 mm. Fig. 3 shows the return loss of this antenna, as it seen, bandwidth has improved significantly.

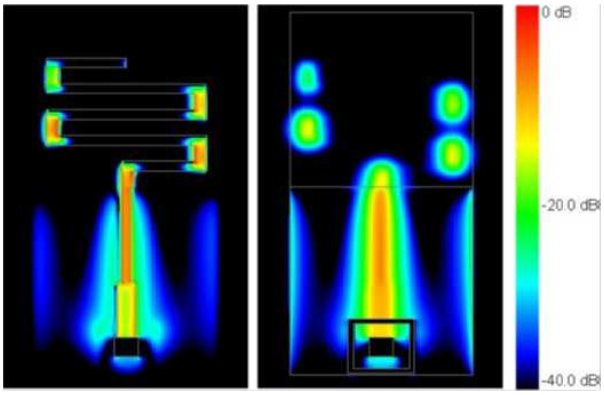

Figure 1: Current magnitude distribution of classic meander line antenna [12].

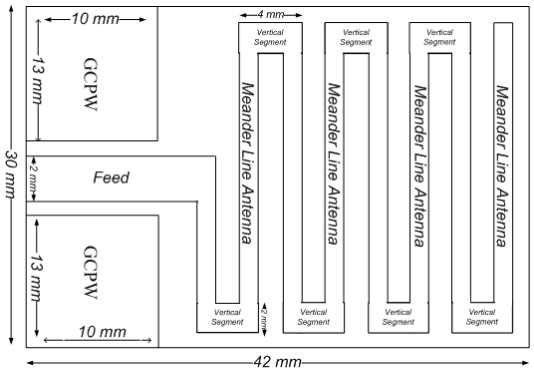

Figure 2: Illustration of MLA with different length of vertical segment.

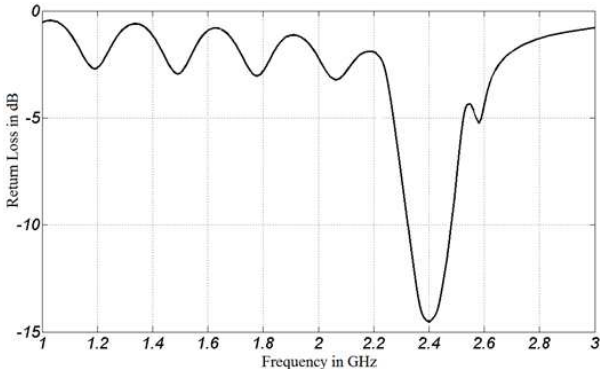

Figure 3: Return loss of MLA with different length of vertical segment.

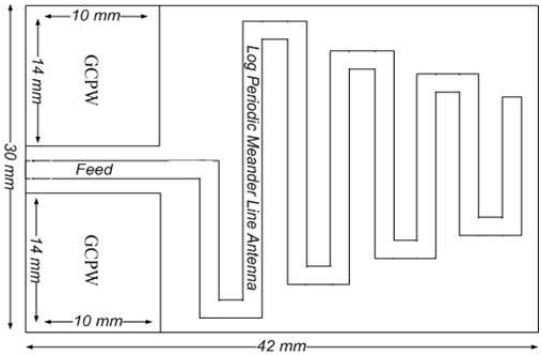

Figure 4: Illustration of Log periodic Meander line antenna.

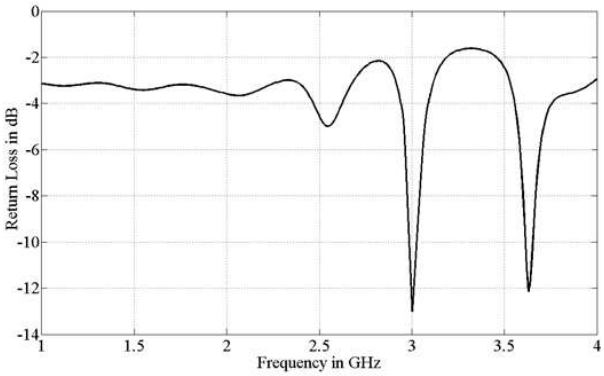

Figure 5: Return loss of log periodic MLA.

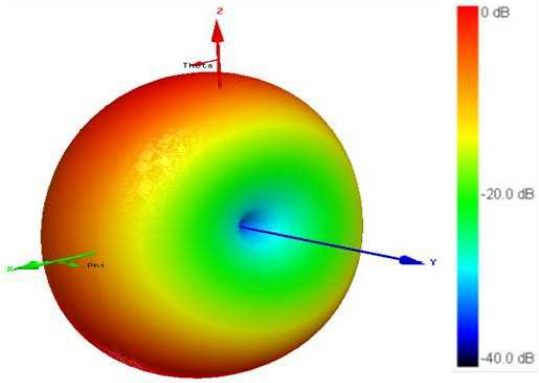

Figure 6: 3D electrical pattern of log periodic MLA.

2.2. Log Periodic Meander Line Antenna

The increasing use of wireless communication systems, demands the antennas for different systems and standards with properties like compact, broadband and multiple resonant frequencies. Classic meander line antenna is able to perform in single band. Log periodic antenna is a kind of frequency independent antenna and is able to achieve multi-band performance [13]. Therefore, log periodic technique has been combined with classic meander line antenna to get dual band antenna. Fig. 4 shows illustration of this antenna.

Log periodic MLA with dimension of $30 \times 42 \times 0.55\,\text{mm}$ has been designed. Fig. 5 shows the return loss of this antenna. Of course, with nearing two resonance frequencies it can be used to increase bandwidth of this antenna. Radiation pattern is another important factor of antenna. For RFID and WLAN applications Omni-directional is a key property. Fig. 6 shows 3D pattern of this antenna.

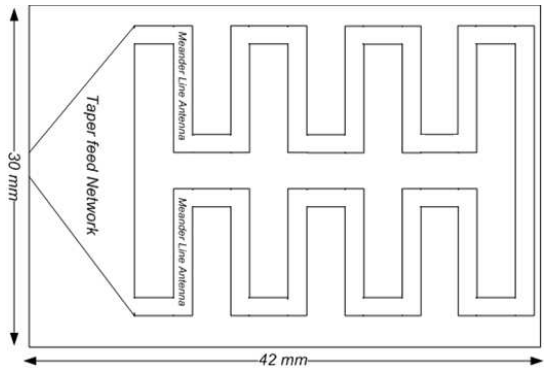

Figure 7: Illustration of symmetrical MLA.

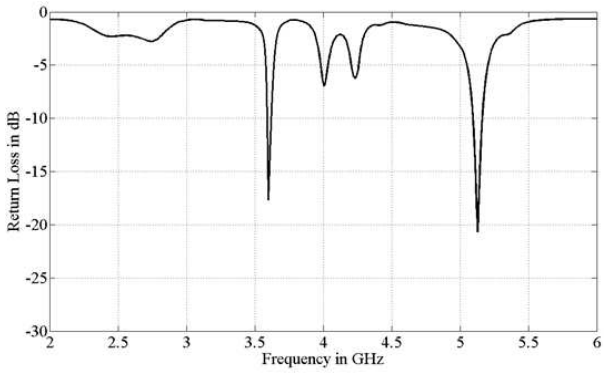

Figure 8: Return loss of symmetrical MLA.

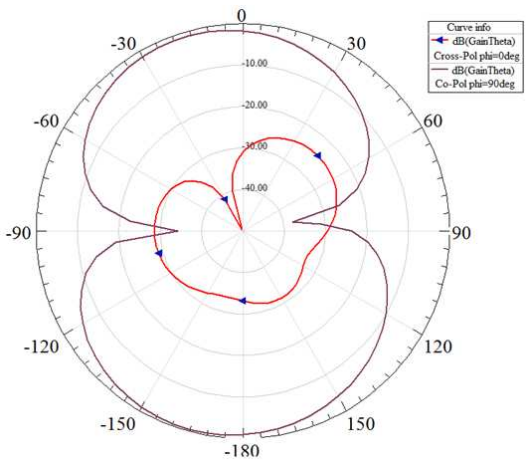

(a)

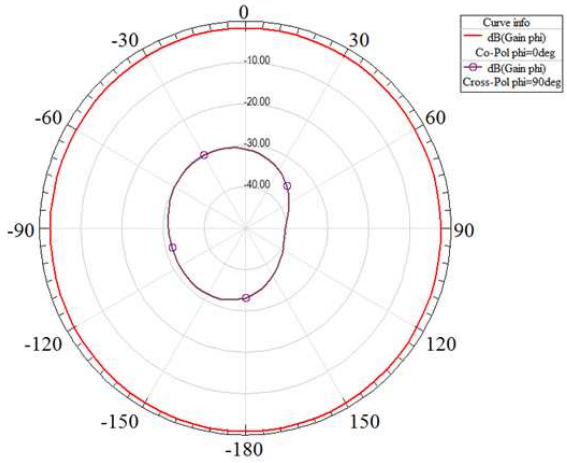

(b)

Figure 9: (a) Co-Pol and Cross-Pol component of H-plane pattern. (b) Co-Pol and Cross-Pol component of E-plane pattern.

2.3. Symmetrical Meander Line Antenna

Nowadays, communication devices which have more properties are more usable than other devices. One of its properties is devices that able to operate in dual band frequencies [14]. As it mentioned before, log periodic MLA approach is one of them. Another technique to get dual-band resonance is two segment MLA. In this mode main antenna, composes in two sub MLA. Each one can be designed to operate in one resonance frequency. These segments can be symmetrical or asymmetrical [15]. In this paper symmetrical meander line antenna has been presented. Fig. 7 shows the illustration of this antenna. In this structure taper plane has been designed to get better matching network.

This symmetrical MLA has been proposed to operate in dual band frequencies, which are 3.6 GHz and 5.2 GHz for WMAX and WLAN application. Fig. 8 shows the return loss of this antenna.

Figures 9(a) and 9(b) show Co-Pol and Cross-Pol of this antenna in H-plane and E-plane respectively. As seen, the designed antenna has a very linear-polarized characteristics.

3. CONCLUSIONS

Classic meander line antenna has good properties such as, small, low profile, simple and cheap. These nice features make meander line antenna very popular and usable in many aspect of communication systems such as RFID and WLAN.

Classic meander line antenna has some disadvantages. They have low efficiency, low bandwidth and can not operate in multi band frequencies.

In this paper, with applying some changes in classic meander line antenna, different shape of meander line antennas have been proposed to improve these issues. Meander line antenna with different length of vertical segment has been presented to get better bandwidth.

Furthermore, log periodic and symmetrical meander line antennas have been designed to operate

in dual-band frequencies.

REFERENCES

1. Lin, C.-C., S.-W. Kuo, and H.-R. Chuang, "A 2.4-GHz printed meander-line antenna for USB WLAN with notebook-PC housing," *IEEE Microwave and Wireless Components*, Vol. 15, No. 9, September 2005.
2. Galehdar, A., D. V. Thiel, S. G. O'Keefe, and S. P. Kingsley, "Efficiency variations in electrically small, meander line RFID antennas," *IEEE Antennas and Propagation Society International Symposium*, 2007.
3. Braatenll, B. D., M. Reich, and J. Glower, "A compact meander-line UHF RFID tag antenna loaded with elements found in right/left-handed coplanar waveguide structures," *IEEE Antenna and Wireless Propagation Letters*, Vol. 8, 2009.
4. Ide, K., S. Ijiguchi, and T. Fukusako, "Gain enhancement of low-profile, electrically small capacitive feed antennas using stacked meander lines," *International Journal of Antennas and Propagation*, Volume 2010, Hindawi Publishing Corporation, 2010.
5. Bentaher, K., F. Choubani, T.-H. Vuong, and J. David, "Design of non uniform meander line antennas for passive RFID tags in the UHF band," *PIERS Proceedings*, 400–403, Marrakesh, Morocco, March 20–23, 2011.
6. Marrocco, G. "Gain-optimized self-resonant meander line antennas for RFID applications," *IEEE Antennas and Wireless Propagation Letters*, Vol. 2, 2003.
7. Ma, M. J. and K. Deng "The study and implementation of meander line antenna for an integrated transceiver design," Master Thesis in Electronics/Telecommunications, February 2010.
8. Ide, K., S. Ijiguchi, and T. Fukusako, "Gain enhancement of low-profile, electrically small capacitive feed antennas using stacked meander lines," *International Journal of Antennas and Propagation*, Vol. 2010, Article ID 606717, 8 Pages, 2010.
9. Endo, T., Y. Sunahara, S. Satoh, and T. Katagi, "Resonant frequency and radiation efficiency of meander line antennas," *Electronics and Communications in Japan*, Part 2, Vol. 83, No. 1, 2000.
10. Balanis, C. A., *Antenna Theory Analysis and Design*, 3rd Edition, Copyright 2005 by John Wiley & Sons, Inc., 2005.
11. Khaleghi, A., "Dual band meander line antenna for wireless LAN communication," *IEEE Trans. Antennas Propagat.*, Vol. 55, 1004–1009, March 2007.
12. Bancroft, R., "Fundamental Dimension Limits of Antennas," Unknown published.
13. Mruk, J., M. Uhm, and D. Filipovic, "Dual-wideband log-periodic antennas," *IEEE Antennas and Propagation Society International Symposium*, 2008.
14. Roy, J. S., N. Chattoraj, and N. Swain, "New dual-frequency microstrip antennas for wireless communication," *Romanian Journal of Information Science*, Vol. 10, No. 1, 113–119, 2007.
15. Rabinovich, V., B. Al-Khateeb, B. Oakley, and N. Alexandrov, "Small printed meander symmetrical and asymmetrical antenna performances, including the RF cable effect, in the 315 MHz frequency band," *Microwave and Optical Technology Letters*, Vol. 48, No. 9, September 2006.

Design of Dual Frequency Notched Semicircular Slot Antenna with Semicircular Tuning Stub

Anwer S. Abd El-Hameed[1], **Haythem H. Abdullah**[2], **Deena A. Salem**[1], **and Esmat A. F. Abdallah**[1]

[1]Microstrip Department, Electronic Research Institute, Egypt
[2]Microwave Department, Electronic Research Institute, Egypt

Abstract— In this paper, a novel antenna design constituting a semicircular slot excited by an extended semicircular patch is presented. The operational bandwidth of this antenna extends from 2.3 GHz to 12.7 GHz, to cover the UWB range of frequencies and Bluetooth, covering almost all indoor communication system applications. Two frequency notches were implemented to ensure coexistence with the narrow band applications sharing some of these frequency bands namely, WLAN and WiMAX (3.3–3.6 GHz and 5–6 GHz). These notches were obtained by using L-slit in the ground plane and C-slot in the tuning patch, the dimensions of which were optimized using parametric analysis. The proposed antenna was fabricated using photolithographic technique. Measured and simulated results were compared and very good agreement was observed. The bandwidth of the proposed antenna increased by almost 2.5 GHz (30%) than previously presented UWB antennas with dual frequency notches, especially at the lower end of the spectrum which enables inclusion of Bluetooth applications.

1. INTRODUCTION

The release of the unlicensed UWB technology for commercial communications by the Federal Communication Commission (FCC) unleashed the interest in UWB communication systems [1], in which the antennas received the greatest portion of that interest. Literature is congested with different designs in various topologies [2–5]. The planar structures attracted most of this attention for its intrinsic advantages over other types, such as the simple structure, small size, low profile, low cost, easiness of fabrication and conformity and most important of which is that they lend themselves to miniaturization. Among the popular planar structures is the CPW fed planar slot antenna, which have attractive increased attention mainly for the ease of integration of monolithic microwave integrated circuits (MMIC). Beside various challenges of designing narrowband antennas, UWB antennas have more challenges to meet, namely, stable radiation pattern, gain, and group delay, all over the band. Covering this ultra wide bandwidth arouses a coexistence problem with narrowband technologies sharing with UWB some of the frequency bands such as WLAN and WIMAX operating in the bands 3.3–3.6 GHz and 5–6 GHz. To overcome this problem and avoiding interference, UWB antennas uses filters to suppress dispensable bands. An alternative approach to notch-out specific frequencies is to design UWB antennae with band-notch characteristic [6]. An alternative approach to overcome this issue is to implement techniques in the design that notches out certain frequencies of narrow band applications. Ref. [7] achieved two notches by etching two nested C-shaped slots in the patch.

In this paper, a CPW UWB semicircular slot antenna with dual band-notched characteristics for WIMAX and WLAN bands and provides omnidirectional radiation pattern, and stable gain over the entire band is presented with dimensions $30 \times 28 \times 1.5\,\text{mm}^3$. By embedding L-shaped slit in the ground plane and a C shaped slot in the tuning stub, dual frequency band-notches are obtained.

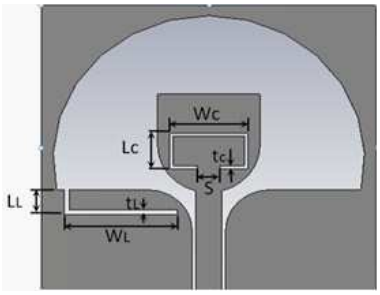

Figure 1: The geometric description of the L-slit and C-slot added to the proposed antenna.

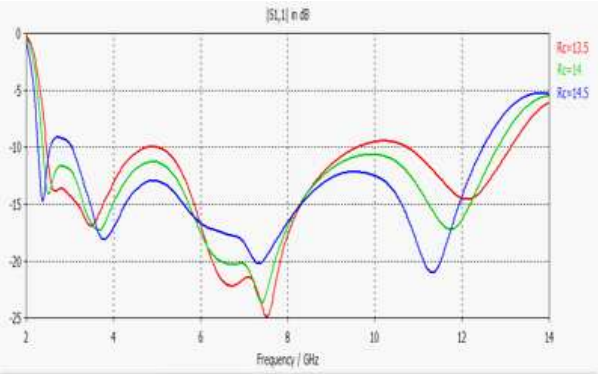

Figure 2: Simulated return loss for different values of R_c.

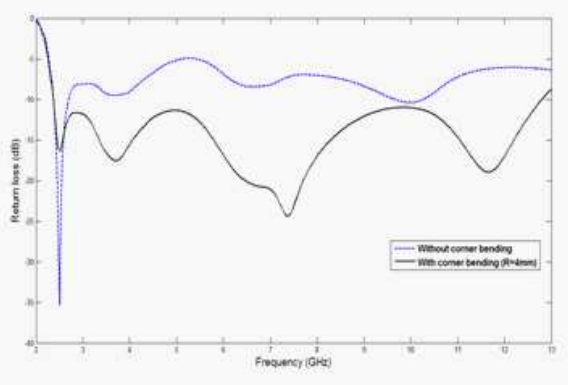

Figure 3: The effect of curving the corners of the ground plane.

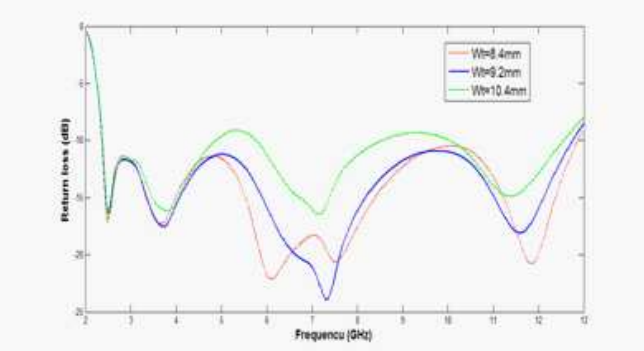

(a)

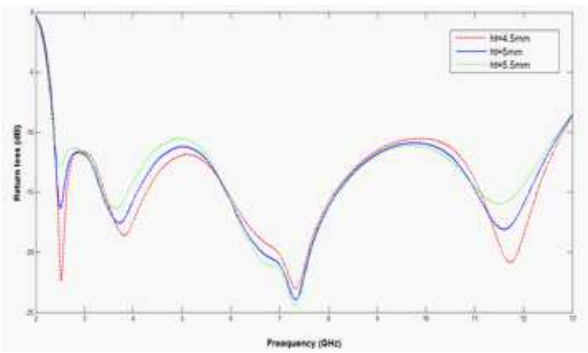

(b)

Figure 4: Parametric study of (a) W_t and (b) h_t.

2. ANTENNA DESIGN

In Fig. 1, the proposed UWB slot antenna with dual band frequency notches, by etching an L-shaped slit and an inverted C-shaped slot in the ground plane and tuning stub, respectively, is shown. The antenna is printed on FR4 substrate with dimensions $W_s \times L_S \times h$ equal $30 \times 28 \times 1.5\,\text{mm}^3$ and relative permittivity of 4.65. The antenna is composed of semicircular slot tuned by an extended semicircular (semicircle and a rectangle) feed by a 50 ohm CPW of center line of width W_f and separation g. The corners of the ground plane of the CPW structure are curved to enhance the matching of the antenna. By embedding an L-slit in the ground plane and an inverted C-slot in the tuning stub, dual band-notches are achieved.

The simulations were carried out using Computer Simulation Technology CST, version 12. To adjust the center frequencies of the notches and the notches bandwidths to achieve an efficient dual band-notched UWB antenna was the challenge at this point. The total lengths of the etched slots control the position of the rejected bands. Optimized dimensions of the slit and the slot are introduced in Table 2.

Design of the proposed antenna started by two alternative approaches; the first considers the half disk slot is similar to that of circular slot. The resonance frequency of half circular disk shape is defined as $f_r = 1.8412c/2\pi R_c\sqrt{\varepsilon}_r$ [8]. Considering the dominant mode TM_{110} for a circular patch, c is the velocity of light, and ε_r is the substrate dielectric constant. The second approach is considering the area equivalence with a rectangular patch where $W = 2a$ and $L = \pi a/4$, (W and L are the width and length of the equivalent rectangular patch) where $f_r = c/2W\sqrt{2/\varepsilon_r + 1}$. The two approaches are compared the results of which are $a = 13\,\text{mm}$ and $14.4\,\text{mm}$, respectively. f_r considered in both approaches is 3.1 GHz, which is the lower limit of the UWB range.

Parametric analysis was applied to extend the required UWB range of frequencies at the lower end to 2.3 GHz, to include Bluetooth applications. This parametric analysis included R_c, W_t, L_t and R. The simulated results of which are shown in Figs. 2–4. The optimized parameters are listed in Table 1.

The data shown in Table 1, is that of the UWB antenna without frequency notches. To achieve the required band notches at the two frequency band 3.5 GHz and 5.2 GHz. An L-shaped slit and a

Table 1: Optimized parameters of the proposed antenna (mm).

L_s	W_s	L_g	L_f	W_f	W_{mt}	h_t	h	R	R_c	g
28	30	10	9.5	2.3	9.2	5	1.5	4	14	0.35

Table 2: Parameters of the slit and slot in Fig. 7 (in mm).

W_c	L_c	t_c	S	t_L	L_L	W_L
7	3.5	0.3	2	0.4	2.4	10.2

Figure 5: Prototype fabricated antenna.

C-slot were etched in the ground plane and tuning stub of the proposed antenna, with parameters shown in Table 1. The L-shaped slit acts as a quarter-wavelength resonator and its electrical length is about $0.25\lambda_g$ (λ_g is the guide wavelength at $f = 3.5$ GHz), whereas, the electrical length of the C-shaped slot is about $0.5\lambda_g$. To adjust the center frequencies of the notches and their bandwidths to achieve an efficient dual band-notched UWB antenna was the challenge at this point. The total lengths of the etched slots control the position of the rejected bands. Optimized dimensions of the slit and the slot are introduced in Table 2.

3. RESULTS AND DISCUSSION

The proposed antenna with the optimized parameters was simulated, and fabricated using photolithographic technique, Fig. 5. In this section, both simulated and measured results are presented. Fig. 6 shows the two results for VSWR of the proposed antenna with one notch at 3.5 GHz, which results from the L-shape slit; Fig. 6(b) displays the results of the two notches. From Fig. 6(b), it is clear that both measured and simulated frequency bands of the notches, showed good agreement. Gain of the proposed antenna over the operational frequency band is shown in Fig. 7, from which it is observed that the gain ranges between 2.5 and 4.5 over the bandwidth that extends from 2.3 to 12.5 GHz, except for the frequency bands 3.3–3.6 and 5–6 GHz. Simulated and measured radiation patterns of the proposed antenna are shown in Fig. 8, for three different frequencies, namely 2.6 GHz, 3.5 GHz, and 4.5 GHz. The radiation patterns of the fabricated antenna were measured using compact multi probe antenna test station model STARLAB-18, STAR-007-A-0019, equipped with VNA model Agilent PNA E8363B.

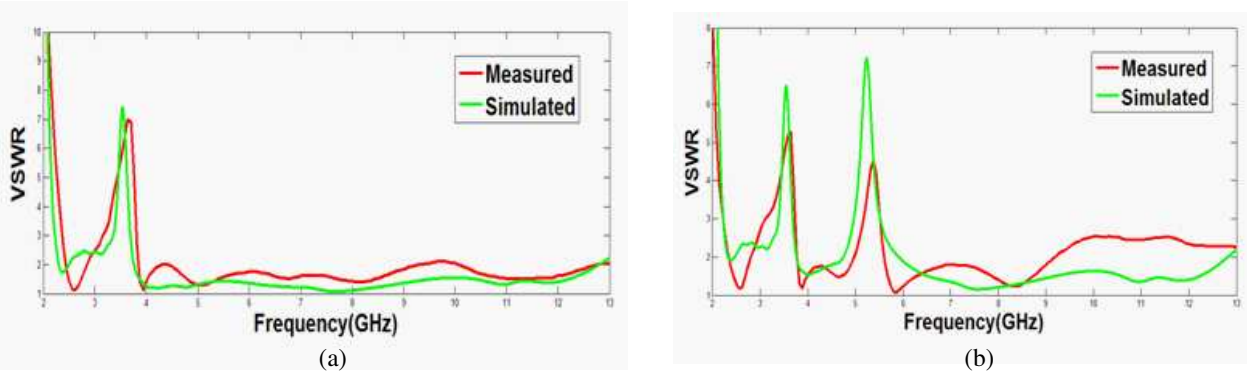

Figure 6: Simulated and measured results for (a) single notch, (b) double notch.

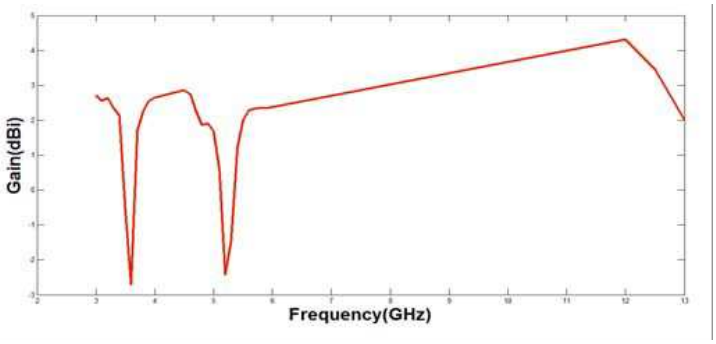

Figure 7: Gain of the proposed antenna.

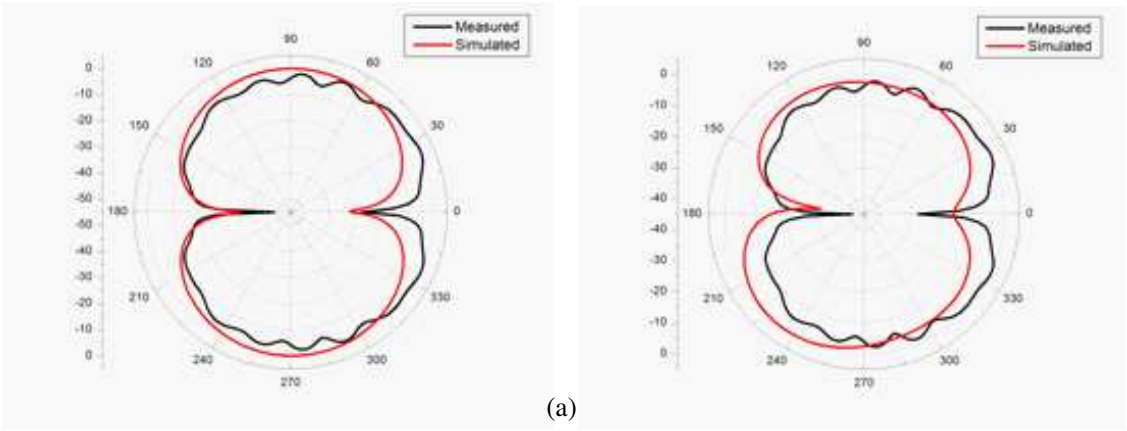

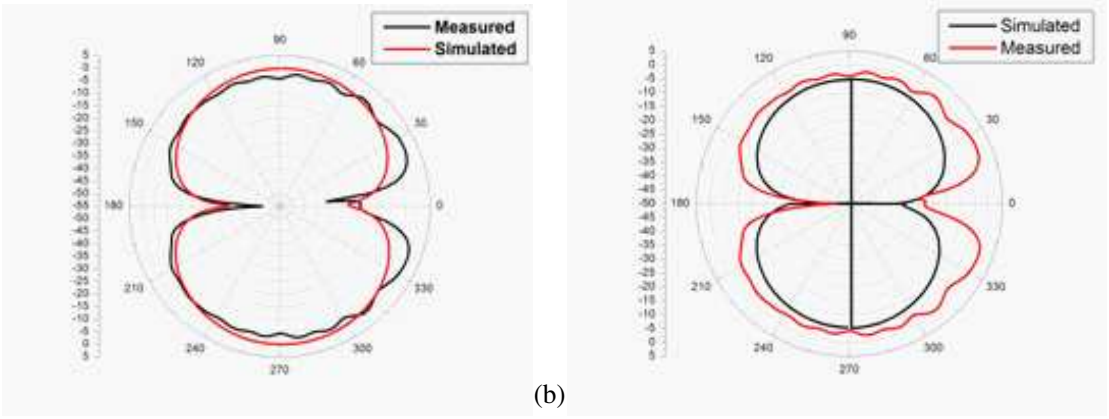

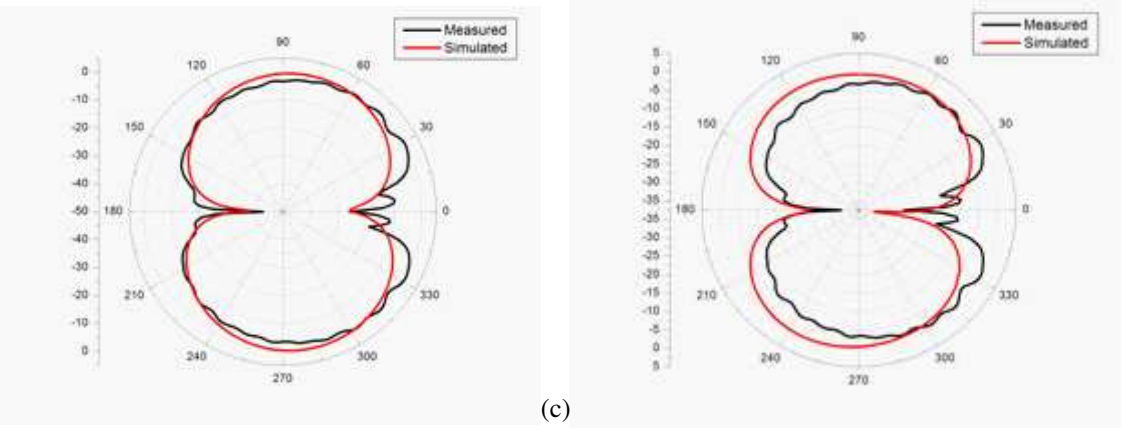

(c)

Figure 8: Radiation patterns for frequencies (a) 2.6 GHz, (b) 3.5 GHz, and (c) 4.5 GHz.

4. CONCLUSION

In this paper, a novel UWB slot antenna with dual band-notched frequency characteristics was presented. The bandwidth of the proposed antenna extends from 2.3 to 12.5 GHz, providing coverage to Bluetooth service with UWB. To enable coexistence of these applications and narrow band applications that share some of these bands with the proposed antenna, frequency notching is introduced. These band notches were obtained using an L-shaped and a C-slot. These band notches maintain coexistence with WIMAX and WLAN bands in the frequency ranges 3.3–3.6 GHz and 5–6 GHz. The antenna shows stable gain and near omnidirectional patterns. The proposed antenna was fabricated using photolithographic technique. Measured and simulated results were compared and very good agreement was observed. The bandwidth of the proposed antenna increased by almost 2.5 GHz (30%) than previously presented UWB antennas with dual frequency notches, especially at the lower end of the spectrum which enables inclusion of Bluetooth applications.

REFERENCES

1. Federal Communications Commission, "First report and order," Revision of Part 15 of the Commission's Rules Regarding Ultra-Wideband Transmission Systems, Feb. 2002.
2. Zhang, R., G. Fu, Z.-Y. Zhang, and Q.-X. Wang, "A wideband planar dipole antenna with parasitic patches," *Progress In Electromagnetics Research Letters*, Vol. 20, 137–145, 2011.
3. Yang, J. and A. Kishk, "The self-grounded bow-tie antenna," *IEEE International Symposium on Antennas and Propagation (APSURSI)*, 1452–1455, Aug. 2011.
4. Sharma, S. K. and S. K. Rajgopal, "Investigations on ultra-wide bandwidth pentagon shape microstrip slot antenna backed by reflecting sheet for directional radiation patterns," *IEEE Transactions on Antennas and Propagation*, Vol. 57, 1353–1359, May 2009.
5. Pitra, K., Z. Raida, and J. Bartyzal, "Antenna structures for emerging frequency bands," *18th Telecommunications forum TELFOR 2010 Serbia*, Belgrade, Nov. 2010.
6. Lee, J. N. and J. K. Park, "Impedance characteristics of trapezoidal ultra-wideband antennas with a notch function," *Micow. Opt. Technol. Lett.*, Vol. 46, No. 5, 503–506, 2005.
7. Chu, Q.-X., "A compact ultra wide band antenna with 3.4/5.5 GHz dual band-notched characteristics," *IEEE Transactions on Antennas and Propagation*, Vol. 56, No. 12, 3637–3644, Dec. 2008.
8. Booker, H., "Slot aerials and their relation to complementary wire aerials (Babinet's principle)," *J. IEE.*, Vol. 93, 620, 1946.

Gradient of Radio Refractivity in Troposphere

M. Zilinskas[1, 2], **M. Tamosiunaite**[2], **M. Tamosiuniene**[3], **E. Valma**[2], **and S. Tamosiunas**[2, 4]

[1]Department of Radio Communication
Communications Regulatory Authority of the Republic of Lithuania, Lithuania
[2]Faculty of Physics, Vilnius University, Lithuania
[3]Semiconductor Physics Institute, Center for Physical Sciences and Technology, Lithuania
[4]Institute of Applied Research, Vilnius University, Lithuania

Abstract— The dependence of radio refractivity on height above the Earth's surface has been examined. The method proposed by International Telecommunication Union has been used. The gradient of radio refractivity has been analyzed over Kaunas, the city of Lithuania. This location was chosen considering our previous studies, which showed that the yearly variation of N is highest in Kaunas, in comparison with other localities of Lithuania. The local meteorological data, which was measured near the ground and also at the different heights above the Earth's surface, have been used in calculation of radio refractivity. It was concluded, that the super-refraction of radio waves and ducting phenomenon could occur at the end of April in Kaunas.

1. INTRODUCTION

The lower atmosphere is not homogeneous. This circumstance affects the electromagnetic (EM) wave propagation in the lower atmospheric layers. Worse propagation conditions lead to decreased power levels at transmitter/receiver and to increased fading on communication links [1].

Therefore, the radio link systems must be planned and designed in such way, that its optimal performance would be achieved. One of primary steps in radio link system design is estimation of the atmospheric refractive index, n. It is a ratio of radio wave's propagation velocity in free space and its velocity in a specified medium [2]. Refractive index is always required when measurements are made in air [3]. It was noted in [4] and [5] that even small changes of temperature, humidity and partial water vapor pressure lead to changes of the atmospheric refractive index. Therefore, n variations are observed in the path of radio wave. The refractive effect is associated with the bending of EM waves and is related to the vertical pressure, temperature and humidity distributions in the atmosphere [6]. The anomalous electromagnetic wave propagation could cause problems for radars, because variation of the refractive index can induce loss of radar coverage [7]. In practice, for most cases the actual propagation conditions are more complicated in comparison with the conditions that are predicted in radio system's design. The meteorological conditions have a significant impact on radio wave propagation through atmosphere. Moreover, the climatic conditions are very unstable in Lithuania [8]. The territory of Lithuania (the Baltic Sea region) belongs to the area where there is the excess of moisture. The relative humidity is about 70% in spring and in summer and 85–90% in winter [9]. Lithuanian climate is also characterized by large temperature fluctuations. Difference between the temperatures of the warmest and the coldest months is 21.8°C [8].

Short time variation of the refractive index over line-of-sight paths of approximately 3 km in mountainous coastal waters using X-band was presented in [7]. In [10], the measurements of these meteorological parameters were made in the different time of year and also different time of day. The values of the refractive index have been determined using measured meteorological data. In [11], it was mentioned that seasonal variation of refractivity gradient could cause the unavailability of the microwave systems.

Having in mind the variable character of Lithuanian climatic conditions, in [12] the variations of radio refractivity for different localities, seasons and times of the day have been determined. It was concluded in [13], that the atmospheric refractive index, n, varies mostly in July. The variations of n in diurnal time are similar in all localities that are situated in the Continental part of Lithuania and are slightly different in Seacoast [13].

The first attempt to determine variation of radio refractivity with 1.2 km height above ground on 4 and 28 November 2010 in localities of Lithuania has been analyzed in [14]. There was concluded, that the vertical gradient of the radio refractivity was lower than the value, which was recommended by ITU in [15].

In this work, our activities will be concentrated on the analysis of variation of the atmospheric radio refractivity with height above ground surface in the mid-spring in Kaunas, the city of Lithuania.

2. CALCULATION OF RADIO REFRACTIVITY GRADIENT

The value of the radio refractive index, n, is very close to the unit and changes of this value are very small in the time and space.

With aim to make those changes more notable, the term of radio refractivity N is used [2, 15]:

$$N = (n-1) \times 10^6. \tag{1}$$

According to the Recommendation of ITU [12]:

$$N = \frac{77.6}{T}\left(p + 4810\frac{e}{T}\right), \tag{2}$$

where T (K) is the temperature; p (hPa) is the atmospheric pressure; e (hPa) is the partial water vapor pressure. The refractivity is expressed in N-units.

It was mentioned in [2] and [15], that (2) expression may be used for all radio frequencies. For frequencies up to 100 GHz, the error is less than 0.5%. There are two terms (the "dry term" and the "wet term") in relationship (2). The relationship between the partial water vapor pressure e and the relative humidity H is presented in [2].

Radio refractivity gradient, G, can be expressed as:

$$G = \frac{N_1 - N_2}{h_1 - h_2}, \tag{3}$$

where N_1 and N_2 are the values of radio refractivity at heights above ground surface h_1 and h_2 respectively.

The G-value determines the type of refraction. The vertical gradient of refractivity at the lower layer of the atmosphere is an important parameter for estimation of path clearance and propagation effects, such as sub-refraction, super-refraction, or ducting [16]. More detail classification of the refraction in the Earth's atmosphere is presented in [17]. If N is constant in some height above the ground surface intervals, the non-refraction of EM wave is observed. At standard atmosphere's temperature, air pressure and relative humidity are decreasing with height above the ground surface, and N decreases with altitude. The condition in which the temperature of the atmosphere increases with altitude in contrast to the normal decrease with altitude is called temperature inversion. The air condition with temperature inversion can cause channels, or ducts, of cool air to be sandwiched between the surface of the ground and a layer of warm air, or between two layers of warm air [16] and [17].

In [18], the refraction of radio waves is classified into normal refraction (whenever $G = -40$ N-units/km), super-refraction (whenever $-41 > G > -156.9$ N-units/km), and ducting (whenever $G = -157$ N-units/km). The following criteria for sub-refraction are presented in [16]: $G > -40$ N-units/km. Despite certain differences in the classification of refraction, the basic principles are the same in all cases. The G-value is compared with G-value of positive normal refraction ($G = -40$ N-units/km). Super-refraction occurs when the bending of the trajectory of propagating radio wave bends towards the ground surface is greater than its bending in case of normal positive refraction. Ducting is named as exceptional super-refraction [20]. In the case of positive critical refraction, the trajectory of radio wave is parallel to the ground surface. The ray path is important for identifying storm characteristics and for proper use of the radar data in initialization of numerical weather prediction models [20].

3. RESULTS AND DISCUSSION

Kaunas is the second-largest city in Lithuania (Coordinates: 54°53′ N; 23°50′E; Altitude: 77 m: Climatic region: Middle Lithuania Lowland). Although Kaunas is located far enough from Baltic Sea, it is sufficiently close to large bodies of water: River Neman and Kaunas Lagoon. The yearly variation of N is the highest in Kaunas in comparison with the other localities of Lithuania [12].

The meteorological data used in determination of radio refractivity have been taken from the Lithuanian Hydro-meteorological Service under the Ministry of Environment. The atmospheric radio sensing was carried out on uneven days, starting probe on 02 : 30 (local time) for the winter and summer times. Sometimes due to certain mechanical and technical reasons, the probe is released at different time (up to one-sixth of an hour from the standard time). The probe RS92-SGP (made by Finnish Company VAISALA) has been used to measure the temperature, pressure, and the relative

humidity of the year. Probe is equipped with GPS wind direction, air pressure, temperature and humidity sensors, that are based on the principle of bimetallic plate. The antenna sends signals of 400 MHz radio frequency and complies with European ETSI standards. The balloon, attached to the probe is filled with helium gas.

In standard atmosphere, the temperature, pressure, and relative humidity decrease with altitude above the ground surface. And the radio refractivity decreases as well. However, the temperature inversions are observed in some cases in the localities of Lithuania. The conditions for super-refraction and ducting can occur. As it was mentioned above, our previous investigation showed, that in Vilnius, the vertical gradient of the radio refractivity in autumn was lower than the value, which was recommended by ITU. The conditions for radio waves low positive refraction have been observed in most cases, investigated in [14]. However, analysis of meteorological data, which was measured at the different altitudes above the ground in spring, shows that the conditions for super-refraction could occur in the mid-spring. The data presented in Figs. 1–4 confirm this fact. The data of the air pressure, temperature, and relative humidity was measured on 21 April 2009, 21 April 2010, and 21 April 2011.

The temperature inversion has been observed in the lowest layers of troposphere on nights of 21 April 2009, 21 April 2010, and 21 April 2011 (see Fig. 1). Fig. 2 shows variation of relative humidity H. It varied each year. Variations of air pressure p with height above (see Fig. 3) ground in the years 2009 and 2011 (as can be seen in Fig. 3, those variations almost coincide) were similar to one in the year 2010.

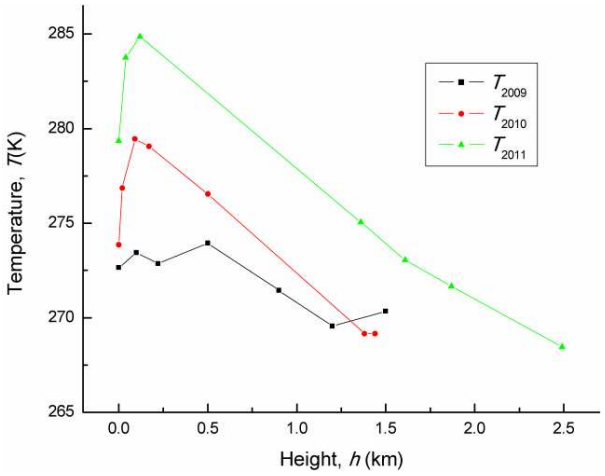

Figure 1: Dependence of the air temperature T on the height above ground h.

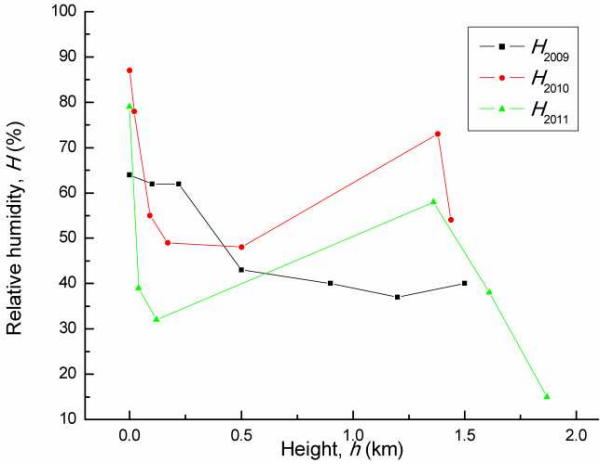

Figure 2: Dependence of relative humidity H on height above ground h.

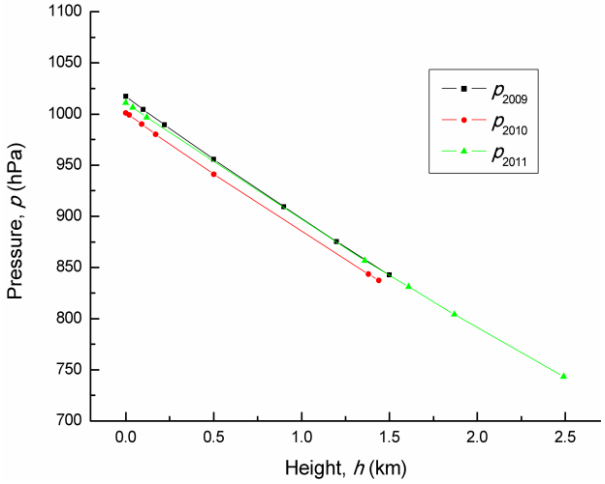

Figure 3: Dependence of the atmospheric pressure p on height above ground h.

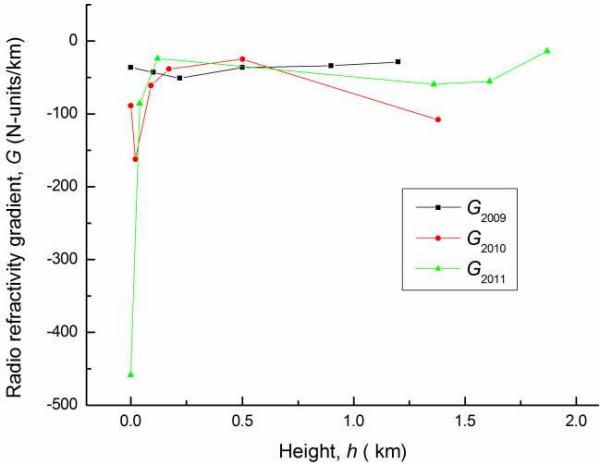

Figure 4: Dependence of radio refractivity gradient G on the height h.

The conditions for positive increased refraction (super-refraction) have been observed on 21 April 2009 in the layer starting from 100 m up to 500 m above ground surface (see Fig. 4). In the year 2010, the conditions for positive increased refraction emerged in the layer from the ground surface up to 170 m above ground. The conditions for radio wave ducting have been sufficient in the layer starting from 20 m up to 90 m. In the year 2011, the conditions for radio wave ducting have been sufficient in the lowest layer of troposphere up to 40 m above ground surface. It is obvious in Fig. 4. Though we presented the data measured on 21 April, it is worth to mention, that the conditions for electromagnetic waves super-refraction or ducting have been observed also in the several nights at the end of April. The conditions for temperature inversion could occur when the warm air mass goes over the still, not yet melted snow on the ground surface or it is moving over cold ground or over the water surface.

4. CONCLUSIONS

The temperature inversions have been observed at the end of April of the years 2009, 2010, and 2011 in Kaunas. The super-refraction and ducting conditions for electromagnetic waves propagation have been observed. Though the conditions for positive low refraction are observed in most cases, the conditions for super-refraction can occur in spring in the countries with four seasons of the year.

ACKNOWLEDGMENT

The authors thank the Lithuanian Hydrometeorological Service under the Ministry of Environment for the possibility to use the data measured at the Kaunas Hydrometeorological Station.

REFERENCES

1. Ali, S., S. A. Malik, K. S. Alimgeer, S. A. Khan, and R. L. Ali, "Statistical estimation of tropospheric radio refractivity derived from 10 years meteorological data," *Journal of Atmospheric and Solar-Terrestrial Physics*, Vol. 77, 96–103, 2012.
2. Freeman, R. L., *Radio System Design for Telecommunications*, 3rd Edition, Wiley-Interscience, John Wiley&Sons, INC., New York, 2007.
3. Guo, G. and S. Li, "Study on the vertical profile of refractive index in the troposphere," *Int. Journal of Infrared and Millimeter Waves*, Vol. 21, No. 7, 1103–1111, 2000.
4. Priestley, J. T. and R. J. Hill, "Measuring high-frequency refractive index in the surface layer," *Journal of Atmospheric Surface Layer*, Vol. 2, No. 2, 233–251, 1985.
5. Kablak, N. I., "Refractive index and atmospheric correction to the distance to the Earth's artificial satellites," *Kinematics and Physics of Celestial Bodies*, Vol. 23, No. 2, 84–88, 2007.
6. Ayantunji, B. G., P. N. Okeke, J. O. Urama, and Y. Najib, "A semi-empirical model for vertical extrapolation of surface refractivity, over nigeria," *The African Review of Physics*, Vol. 6, No. 0014, 121–128, 2011.
7. Norland, R., "Temporal variation of the refractive index in coastal waters," *Proceedings of International Radar Symposium IRS 2006*, 221–224, Poland, Krakow, May 24–26, 2006.
8. Pankauskas, M. and A. Bukantis, "The dynamics of the baltic sea region climate humidity in 1950–2004," *Annales Geographicae*, Vol. 39, No. 1, 5–14, January 2006 (in Lithuanian).
9. Bagdonas, A. and R. Karalevičienė, *The Reference Book of Agrometeorologist*, Vilnius, Mokslas, 1987 (in Lithuanian).
10. Falodun, S. E. and M. O. Ajewole, "Radio refractive index in the lowest 100-m layer of the troposphere in Akure, South Western Nigeria," *Journal of Atmospheric and Solar-Terrestrial Physics*, Vol. 68, No. 2, 236–243, 2006.
11. Serdega, D. and G. Ivanovs, "Refraction seasonal variation and that influence on to GHz range microwaves availability," *Electronics and Electrical Engineering*, No. 6(78), 39–42, 2007.
12. Valma, E., M. Tamošiūnaitė, S. Tamošiūnas, M. Tamošiūnienė, and M. Žilinskas, "Determination of radio refractive index using meteorological data, *Electronics and Electrical Engineering*, No. 10(106), 125–128, 2010.
13. Tamošiūnaitė, M., M. Žilinskas, M. Tamošiūnienė, and S. Tamošiūnas, "Atmospheric attenuation due to humidity," *Electromagnetic Waves*, Chapter 8, 157–172, V. Zhurbenko, Ed., InTech, 2011.

14. Valma, E., M. Tamosiunaite, S. Tamosiunas, M. Tamosiuniene, and M. Zilinskas, "Variation of radio refractivity with height above ground," *Electronics and Electrical Engineering*, No. 5(111), 23–26, 2011.
15. "The radio refractive index: its formula and refractivity data," Recommmendation ITU–R, 453–9, 1970-1986-1990-1992-1994-1995-1997-1999-2001-2003.
16. Adediji, A. T. and M. O. Ajewole, "Vertical profile of radio refractivity gradient in Akure South-West Nigeria," *Progress In Electromagnetics Research C*, Vol. 4, 157–168, 2008.
17. Radartutorial.eu., "Propagation of electromagnetic waves," http:www.radartutorial.eu/07.waves/wa17.en.html, viewed March 03, 2012.
18. Falodun, E. S. and L. B. Kolawole, "Studies of super-refractivity and ducting of radiowaves in Nigeria," *Nigeria Journal of Pure and Applied Physics*, Vol. 1, 5–10, 2000.
19. Haby, J., "What happens during ducting?" http://www.theweatherprediction.com/habyhints/234/, viewed March 03, 2012.
20. Gao, J., K. Brewster, and M. Xue, "Variation of radio refractivity with respect to moisture and temperature and influence on radar ray path," *Advances in Atmospheric Sciences*, Vol. 25, No. 6, 1098–1106, 2008.

A Simple Miniaturized Triple-band Antenna for WLAN/WiMAX Applications

H. M. El Misilmani, M. Al-Husseini, K. Y. Kabalan, and A. El-Hajj
ECE Department, American University of Beirut, Beirut 1107 2020, Lebanon

Abstract— The design of a simple small-size multi-band antenna for wireless local area network (WLAN) and worldwide interoperability for microwave access (WiMAX) application is presented in this paper. The antenna covers the 2.4/5.2/5.8-GHz WLAN operating bands and the 2.5/3.5/5.5-GHz WiMAX bands. The proposed printed-type antenna is based on a 1.6 mm-thick FR4 epoxy substrate with dimensions 25 mm × 38 mm. It has a rectangular split-ring slot enclosed inside a rectangular patch. The inclusion of the split-ring slot and the U-shaped slot in the partial ground plane gives resonance at two additional frequencies. The dimensions of the patch, the ground, and the two slots are optimized to obtain these desired functional frequency ranges.

1. INTRODUCTION

Due to the rapid and wide development of wireless communications, the design goal is heading towards the desired features of compact, lightweight, multi-band and low cost antennas. UWB antennas have the advantage of covering a very wide frequency range. In [1], a UWB antenna operational over the 2–11 GHz range is presented. However, UWB antennas are prone to noise from unwanted frequencies, which could degrade the original message. On the other hand, reconfigurable antennas are designed to be able to control the resonance of the antenna and limit the disadvantage of UWB antennas. A frequency reconfigurable antenna is proposed in [2]. Though very robust, reconfigurable antennas are complex as they require the use of switching elements and their biasing lines, or other complicated reconfiguration mechanisms. Multi-band antennas can be thought of as an intermediate solution combining simplicity and multi-frequency operation.

The advantage of the multi-band antennas is to be able to integrate several frequency bands on one single antenna, making it useful for several frequency ranges. These multi-band antennas could contain frequency ranges from several wireless applications. [3, 4] represent two antennas working on multi-frequency bands. In this paper, the antenna presented is capable of working on triple-frequency bands, for the two different applications, WLAN and WiMAX.

In [5–18] several printed antenna designs for both WLAN and WiMAX applications have been presented. In [5–7], the triple-band characteristic is designed by etching two narrow slots with different lengths on a wideband monopole antenna. In [8], the design uses a trapezoidal ground to achieve the triple-band frequencies of WLAN/WiMAX applications. In [9], a triple-band unidirectional coplanar antenna is presented, but with a large size of $100 \times 60\,\text{mm}^2$. Usually, to meet the requirements of mutli-band frequency range, a various types of configurations could be used. In [10], a meander T-shape with a long and a short arm are used to achieve multi-band frequency. A multifractal structure is used in [11]. In [12, 13], a flared shape with V-sleeve or Y-shape is implemented to realize the multi-band operation. However these antennas have a large size comparing to the limited space of mobile wireless terminals. Through the development of antenna design, slot structures have been proposed to reduce the size of the multi-band antennas. In [14], the use of U-slots with a combination with an L-probe feed is used to produce dual and multi-band characteristics. A triangular-slot loaded multi-band antenna excited by the strip monopole is presented in [15]. In [16], the adjustment of the size of the slots on the radiating patch improves the performance of the coplanar waveguide-fed monopole antenna, but with a low antenna gain. Meandering slot antennas, in [17, 18], could also be used as well with different slots to generate two resonant modes. However, the complex structures of these antennas make them unsuitable for the practical applications. In [19] a miniaturized multi-frequency antenna is proposed using circular ring, a Y-shape-like strip, and a defected ground plane.

In this paper, using a split-ring slot enclosed inside a rectangular patch and etching a U-shaped slot in the partial ground plane are the two techniques used to achieve not only triple-band operation performance, but also smaller size and simpler structure. By using the three different resonant frequencies, the proposed antenna can generate three resonant modes to cover three desired bands for WLAN and WiMAX applications. The geometry and the design guidelines of the proposed

antenna structures are presented in Section 2. Experimental results are presented in Section 3. In Section 4 a brief conclusion is given.

2. ANTENNA STRUCTURE AND DESIGN

The configuration of the proposed triple-band antenna is shown in Figures 1(a)–(b). The rectangular patch is the main radiating element of the antenna combined with split-ring slot enclosed inside of it. The proposed printed-type antenna is based on a 1.6 mm-thick FR4 epoxy substrate with dimensions 25 mm × 38 mm, fed by a 50 Ω microstrip feed line with a width of 3 mm and a length of 12.06 mm. The partial ground plane is located on the backside of the dielectric substrate, shown in Figure 1(b), where a U-shaped slot is illustrated.

Figures 2(a)–(d) and Figure 3 represent the design evolution of the proposed antenna and its corresponding simulated reflection coefficient. Initially, the antenna in Figure 2(a) consists of a rectangular patch in addition to a partial rectangular ground. As shown in Figure 3(a), there is one operating band from 3 to 5 GHz. The inclusion of the split-ring slot, Figure 2(b), leads to the excitation of an additional coverage of the 2.4–2.5 GHz band, shown in Figure 3(b), without increasing the size, where the current will be divided between the rectangular patch and the split-

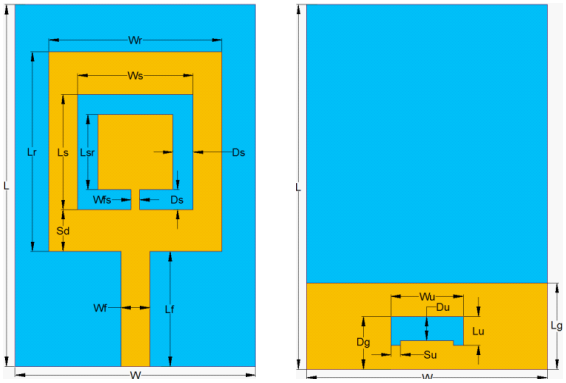

Figure 1: Geometry of the proposed antenna. (a) Front view, (b) back view.

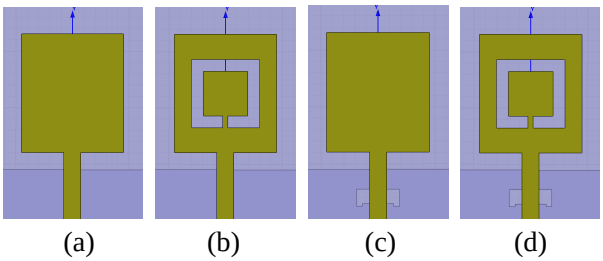

Figure 2: (a)–(d) The evolution of the antenna design.

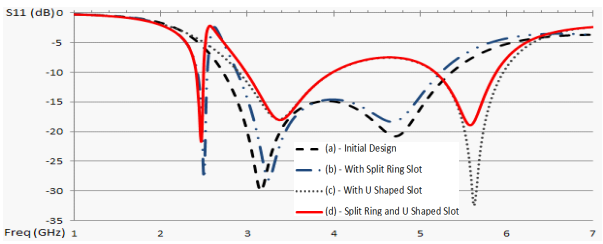

Figure 3: Simulated reflection coefficient of each design.

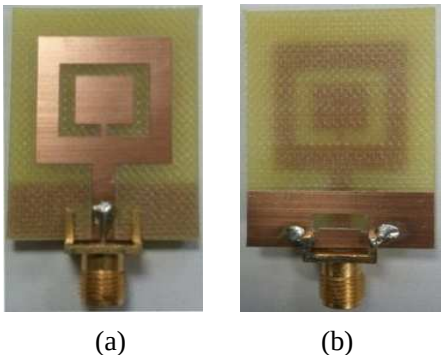

Figure 4: The fabricated antenna. (a) Font view, (b) back view.

ring slot giving two resonance frequencies. In Figure 2(c) and under the 50 Ω microstrip feed line, the ground plane is defected by etching a U-shaped slot without adding a split-ring slot in the rectangular patch. The U-shaped slot, as shown in Figure 3(c), gives resonance in the 3–4 and 5.2–5.9 GHz bands. Finally, in Figure 2(d), the two slots were added to the design to achieve resonance in the three frequency bands, 2.4–2.5, 3–4, 5.2–5.9 GHz, as shown in Figure 3(d). The dimensions of the patch, the ground, and the two slots are optimized to obtain these desired functional frequency ranges using Ansoft HFSS.

Figures 4(a)–(b) show the fabricated antenna, with the dimensions shown in Table 1 for both upper and lower part.

3. RESULTS AND DISCUSSION

The computed and measured reflection coefficient plots are given in Figure 5, where good analogy is revealed.

From the measured results it is seen that the antenna covers three frequency bands, 2.4–2.5, 3–4, and 5.4–5.9 GHz bands, making it suitable for WLAN operating in the 2.4, 5.2 and 5.8 GHz bands, and WiMAX networks operating in the 2.5, 3.5 and 5.5 GHz bands.

Due to its geometry as a printed monopole, and the use of the partial ground plane, the antenna has omnidirectional radiation patterns, as shown in Figure 6 for the 2.4, 3.5, and 5.8 GHz frequen-

Table 1: The antenna dimensions (in mm).

Parameter	Size (mm)	Parameter	Size (mm)	Parameter	Size (mm)
W	25	Ws	12	Lg	9
L	38	Ls	12.10	Wu	7.5
Wf	3	Ds	2.10	Lu	3
Lf	12.06	Lsr	7.9	Du	2.5
Wr	18	Wfs	0.9	Dg	5.5
Lr	21	Sd	4.4	Su	1

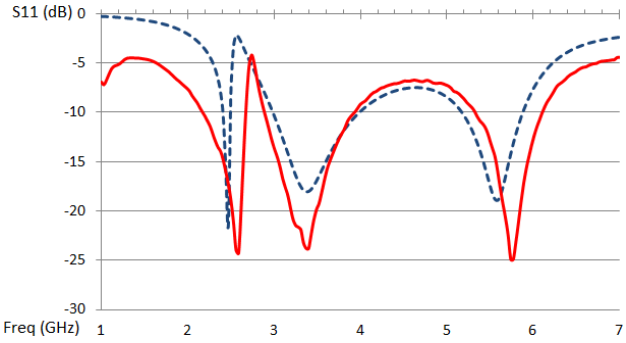

Figure 5: Simulated (dashed line) and measured (solid line) reflection coefficient.

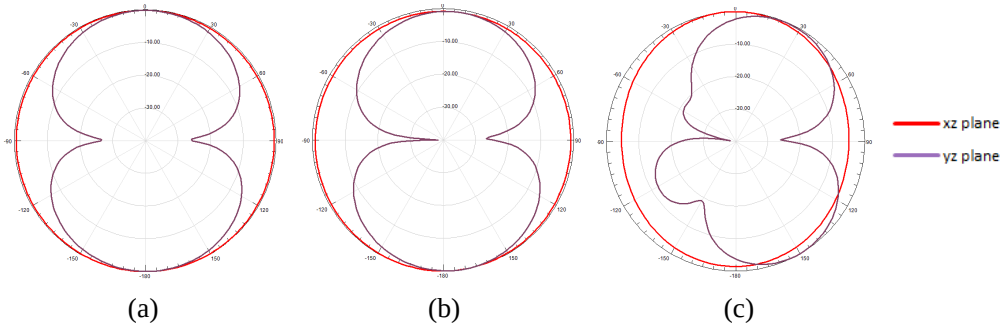

Figure 6: The antenna gain computed at (a) 2.4, (b) 3.5 and (c) 5.5 GHz in the XZ plane (H-plane) and YZ plane (E-plane).

Table 2: Simulated antenna gain at the frequencies of operation.

Frequency (GHz)	Gain (dB)	Frequency (GHz)	Gain (dB)
2.40	1.8811	4.00	2.0398
2.45	1.7991	5.20	2.0568
2.50	1.6529	5.50	1.8904
3.00	1.7120	5.80	1.3232
3.50	1.8529	5.90	1.4112

cies. These simulated patterns reveal an equal gain in the XZ plane (H-plane), and a pattern with the shape of digit 8 in the YZ plane (E-plane).

The antenna gain computed at 2.4–2.5, 3–4, 5.2–5.9 GHz is given in Table 2. As shown, the gain of the proposed antenna within the operating bands satisfies the requirement of several wireless communication terminals.

4. CONCLUSION

A novel triple-band antenna suitable for WLAN/WiMAX applications is proposed in this paper. Using a split-ring slot implanted in the rectangular patch and a U-shaped slot etched partial ground plane, three resonant modes with excellent impedance performance are achieved.

The compact size, triple-band frequency, excellent radiation patterns, good gain and a simple structure makes this antenna suitable for practical wireless communication systems, working on WLAN and WiMAX networks, in three different frequency bands, 2.4–2.5, 3–4, 5.2–5.9 GHz.

REFERENCES

1. Al-Husseini, M., Y. Tawk, A. El-Hajj, and K. Y. Kabalan, "A low-cost microstrip antenna for 3G/WLAN/WiMAX and UWB applications," *Proceedings of International Conference on Advances in Computational Tools for Engineering Applications*, 68–70, Zouk Mosbeh, Lebanon, July 2009.
2. Al-Husseini, M., A. Ramadan, A. El-Hajj, and K. Y. Kabalan, "A reconfigurable antenna based on an ultrawideband to narrowband transformation," *PIERS Proceedings*, Moscow, Russia, August 2012.
3. Du, Y. and A. Zhao, "An internal quad-band antenna for oval-shaped mobile phones," *IEEE Antennas Wireless Propag. Lett.*, Vol. 9, 830–833, 2010.
4. Liu, C.-L., Y.-F. Lin, C.-M. Liang, S.-C. Pan, and H.-M. Chen, "Miniature internal penta-band monopole antenna for mobile phones," *IEEE Antennas Propag. Mag.*, Vol. 58, No. 3, 1008–1011, 2010.
5. Cai, L. Y., G. Zeng, and H. C. Yang, "Compact triple band antenna for Bluetooth/WiMAX/WLAN applications," *Proceedings of International Symposium on Signals, Systems and Electronics.*, 1–4, Nanjing, China, September 17–20, 2010.
6. Krishna, D. D., M. Gopikrishna, and C. K. Aanandan, "A CPW-fed triple band monopole antenna for WiMAX/WLAN applications," *Proceedings of the 38th Eur. Microwave Conf.*, 897–900, Amsterdam, Netherlands, October 2008.
7. Liu, H.-W., C.-H. Ku, and C.-F. Yang, "Novel CPW-fed planar monopole antenna for WiMAX/WLAN applications," *IEEE Antennas Wireless Propag. Lett.*, Vol. 9, 240–243, 2010.
8. Thomas, K. G. and M. Sreenivasan, "Compact triple band antenna for WLAN/WiMAX applications," *Electron. Lett.*, Vol. 45, No. 16, 811–813, 2009.
9. Li, R. L., T. Wu, and M. M. Tentzeris, "A triple-band unidirectional coplanar antenna for 2.4/3.5/5-GHz WLAN/WiMax applications," *Proceedings of IEEE Antennas Propag. Soc. Int. Symp.*, 1–4, Charleston, SC, June 1–5, 2009.
10. Chang, T. N. and J.-H. Jiang, "Meandered T-shaped monopole antenna," *IEEE Trans. Antennas Propag.*, Vol. 57, No. 12, 3976–3978, 2009.
11. Manimegalai, B., S. Raju, and V. Abhaikumar, "A multifractal cantor antenna for multiband wireless applications," *IEEE Antennas Wireless Propag. Lett.*, Vol. 8, 359–362, 2009.
12. Augustin, G., P. C. Bybi, V. P. Sarin, P. Mohanan, C. K. Aanandan, and K. Vasudevan, "A compact dual-band planar antenna for DCS-1900/ PCS/PHS, WCDMA/IMT-2000, and WLAN applications," *IEEE Antennas Wireless Propag. Lett.*, Vol. 7, 108–111, 2008.

13. Liu, W.-C. and C.-F. Hsu, "Dual-band CPW-fed Y-shaped monopole antenna for PCS/WLAN application," *Electron. Lett.*, Vol. 41, 390–391, 2005.
14. Lee, K. F., S. L. S. Yang, and A. A. Kishk, "Dual- and multiband U-slot patch antennas," *IEEE Antennas Wireless Propag. Lett.*, Vol. 7, 645–647, 2008.
15. Augustin, G., S. V. Shynu, P. Mohanan, C. K. Aanandan, and K. Vasudevan, "Compact dual-band antenna for wireless access point," *Electron. Lett.*, Vol. 42, 502–503, 2006.
16. Parkash, D. and R. Khanna, "Design of a dual band monopole antenna for WLAN/WiMAX applications," *Proceedings of 7th Wireless And Optical Communications Networks*, 1–4, Colombo, Sri Lanka, September 6–8, 2010,
17. Hsieh, C. P., T. C. Chiu, and C. H. Lai, "Compact dual-band slot antenna at the corner of the ground plane," *IEEE Trans. Antennas Propag.*, Vol. 57, No. 10, 3423–3426, 2009.
18. Liu, W.-C., C.-M. Wu, and N.-C. Chu, "A compact CPW-fed slotted patch antenna for dual-band operation," *IEEE Antennas Wireless Propag. Lett.*, Vol. 9, 110–113, 2010.
19. Pei, J., A.-G. Wang, S. Gao, and W. Leng, "Miniaturized Triple-Band Antenna With a Defected Ground Plane for WLAN/WiMAX Applications," *IEEE Antennas Wireless Propag. Lett.,* Vol. 10, 298–301, 2011.

An Ultra-wideband Printed Monopole Antenna with a Fractal Based Reduced Ground Plane

Jawad K. Ali, **Ali J. Salim**, **Ali I. Hammoodi**, **and Hussam Alsaedi**
Microwave Research Group, Department of Electrical Engineering
University of Technology, Baghdad, Iraq

Abstract— Recently, the ultra-wideband (UWB) systems have attracted much attention because of its advantages including high speed data, small size, low cost, and low complexity. Consequently, the UWB antenna has received an increased attention due to its impedance bandwidth, simple structure and omni-directional radiation pattern. In this paper, the effects of the ground plane of a printed monopole UWB antenna, fed with a 50 Ω microstrip line, have been investigated. A Koch fractal based ground plane structure has been proposed as a means to enhance the UWB antenna performance. Different ground plane structures and feeding methods have been applied to a notched band monopole antenna structure that is a nearly square with embedded E-shaped slot. The proposed antenna has been supposed to be etched using a substrate with relative permittivity of 4.6 and thickness of 1.6 mm. Modeling and performance evaluation of the presented antenna designs have been carried out using a method of moments based EM simulator, IE3D. Simulation results have shown that the antenna with Koch based ground plane and asymmetrical feed offers larger fractional bandwidth of about 124%. By this increment in the antenna bandwidth, it is expected that by suitable dimension scaling of the enhanced bandwidth UWB antenna, many communication services below 3.1 GHz could be integrated with the UWB systems.

1. INTRODUCTION

Ultra-wideband (UWB) communication system is attracting more and more attention because of its advantages such as low power consumption, high data rate transmissions as in the multimedia communications, robustness against jamming, high degree of reliability etc. [1]. Consequently, an increased interest has been reported to the UWB antenna design. For portable devices, an additional challenge is encountered; the antenna has to be miniaturized. The printed UWB antenna has been found to be a good option because it can be easily embedded into wireless devices or integrated with other RF circuits [2]. In 2002, the Federal Communication Commission (FCC) officially released the regulations for UWB technology with allocated spectrum from 3.1 to 10.6 GHz for unlicensed UWB indoor medical, measurement and communication applications [3]. Since then, intensive research work has been devoted to the UWB antenna design.

Regarding the purpose of reducing the potential interference between the UWB system and others operating at 5/6 GHz, the antennas reported in the literature can be classified into three categories. The first one includes antenna that are not characterized with a band notch in their return loss, or VSWR, responses [2–5]. In this context, microstrip fed printed monopole antennas having radiators with E-shape [2], swan-like shape patch with reduced ground plane [3], circular shape monopole with trapezoid shape ground [4], and octagon shape [5], are presented for UWB applications. In the other hand, the CPW feed line has been also used for UWB antennas with various possible slotted patch structures [6, 7]. The UWB antennas of the second category are characterized with a single 5/6 GHz band notch in their return loss responses [8–12]. Again, almost similar techniques have been adopted to achieve the UWB impedance bandwidth. Slotted elements of various shapes have been added to create the required notch in the antenna response. In addition, the use of the electromagnetic-bandgap (EBG) structure is proven to be effective create the required band notched response [13]. Elliptical monopoles with CPW feeds were fabricated on liquid crystal polymer (LCP) with reconfigurable 5/6 GHz band-notch characteristics has been presented in [14]. In the third category, antennas are characterized with two band notches in their return loss, or VSWR, responses [15–20].

In this paper, the effects of the ground plane of a printed monopole UWB antenna have been investigated. In an attempt to enhance the UWB antenna performance a new fractal based ground plane structure has been proposed. Many ground plane structures and feeding methods have been applied to a notched band monopole antenna structure that is a nearly square with E-shaped slot embedded in it. It is expected that by suitable dimension scaling of the enhanced bandwidth UWB antenna, many communication services below 3.1 GHz could be integrated with the UWB systems, as recently reported in [21–23].

2. THE ANTENNA DESIGN

The proposed UWB antenna is a printed monopole with a nearly square shaped radiator. An E-shaped slot has been cut in the radiator to produce the notched band. On the other side of the substrate, a reduced ground plane has been printed. The geometry of the proposed UWB printed monopole antenna is shown in Figure 1.

The antenna is to be modeled using an FR4 substrate with thickness of 1.6 mm and relative permittivity of 4.6. For design convenience, the proposed antenna is fed by a 50 Ohm microstrip line printed on the radiator side of the substrate. The feed line width is of about 3 mm, and is symmetrically located with respect to both the radiating element and the ground plane. On the front surface of the substrate, a nearly square radiating patch with initial dimensions of $13.45 \times 14.55\,\text{mm}^2$, has been etched; while on the other side of the substrate, a conducting ground plane of $19.90 \times 9.20\,\text{mm}^2$ is placed. An E-slot is etched on the rectangular radiating element with slot width, $W_{MS} = 6.25$ mm, slot length, $L_{MS} = 9.05$ mm, and slot trace width, $L_{TS} = 1.5$ mm. The slot is symmetrically cut in the X-axis, while it is away from the upper edge of the radiating element by a distance, $W_T = 1.70$ mm.

A printed monopole antenna with E-slot has been designed to resonate with the lower frequency is located at 3.1 GHz, as a starting step. After suitable dimension scaling, the resulting antenna radiating element length, L_E, has to be determined. Observing the influence of the various parameters on the antenna performance, it has been found that the dominant factor in the antenna is the monopole element perimeter, $2(L_E + W_E)$, in terms of the guided wavelength λ_g.

$$\lambda_g = \frac{\lambda_0}{\sqrt{\varepsilon_{eff}}} \tag{1}$$

where ε_{eff} is the effective dielectric constant.

Then the lower resonant frequency, f_L, relative to the radiating element length is formulated by

$$f_L \approx \frac{C_o}{2(L_E + W_E)\sqrt{\varepsilon_{eff}}} \tag{2}$$

where C_o is the speed of light in free space.

In this paper, the effects of the ground plane of the printed monopole UWB antenna have to be investigated. The previously designed antenna has been considered as reference for the sake of comparison with other antennas with different feeding and ground planes. This antenna will be referred to as Ref. Ant. In an attempt to enhance impedance bandwidth, for $S_{11} \leq -10$ dB, of this antenna, a modified reduced ground plane is proposed. The proposed ground plane has been modified by making its top edge in the form of the 2nd Koch fractal geometry. Three other antennas have been presented and referred to as Ant. I, Ant. II, and Ant. III, as shown in Figure 2, where the proposed Koch fractal based ground plane structure has been depicted. The top edge of the reduced ground plane has been modified to be in the form o the 2nd iteration Koch fractal geometry for Ant. II and Ant. III.

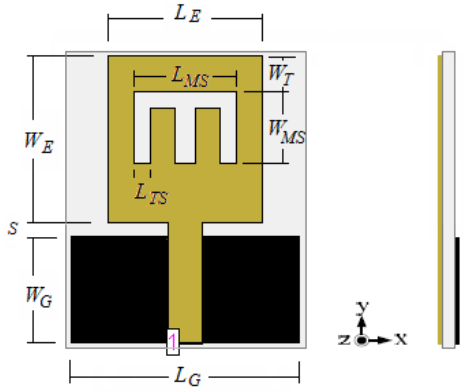

Figure 1: The geometry of the modeled reference antenna.

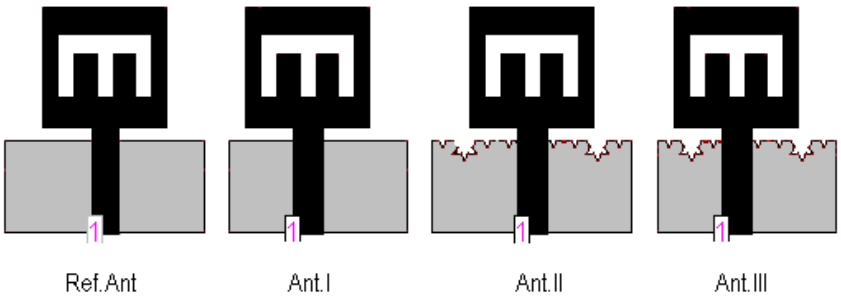

Figure 2: The four modeled UWB antennas with different feed positions and ground planes as depicted in Table 1.

Table 1: Summary of the modeled antennas and the corresponding ground planes, feeding method and the realized fractional bandwidths.

Antenna Type	Ground Plane	Feed Method	Resulting Bandwidth %
Ref. Ant	Reduced GP	Symmetrical	105
Ant. I	Reduced GP	Asymmetrical	113
Ant. II	Koch Based Reduced	Symmetrical	124
Ant. III	Koch Based Reduced	Asymmetrical	118

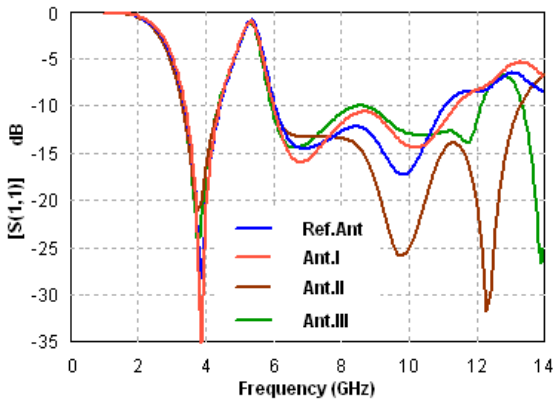

Figure 3: Return loss responses of the four UWB antennas with the different ground plane structures.

3. PERFORMANCE ASSESMENT AND SIMULATION RESULTS

The four UWB printed monopole antennas, depicted in Figure 2, have been modeled and their performances have been evaluated using the commercially available software IE3D, from Zeland Software Inc. [24]. These antennas have the same parameters as previously stated; the only change is the ground planes and the feeding methods. Table 1 summarizes the related differences among these antennas.

Figure 3 presents the simulated return loss responses of the four antennas. It is implied that at low frequencies, below 6.0 GHz, the four antennas perform equally, since the lowest resonant frequency, according to (2), is primarily determined by the monopole radiating element parameters. Furthermore, the position of the notched band, from 4.41 to 5.98 GHz, has not changed, because it is attributed to E-slot parameters as prescribed. The effects of the ground planes of the modeled antennas started beyond this frequency. In this context, the four antennas offer different fractional bandwidths, as it is clearly shown in Figure 3.

The realized fractional bandwidths corresponding to each of these antennas are summarized in Table 1. It is clear that antennas with the modified ground planes, Ant. II and Ant. III, possess the largest fractional bandwidths. However, Ant. II, with Koch based ground plane and symmetrical feed, offers larger fractional bandwidth of about 124%. By this increment in the antenna bandwidth,

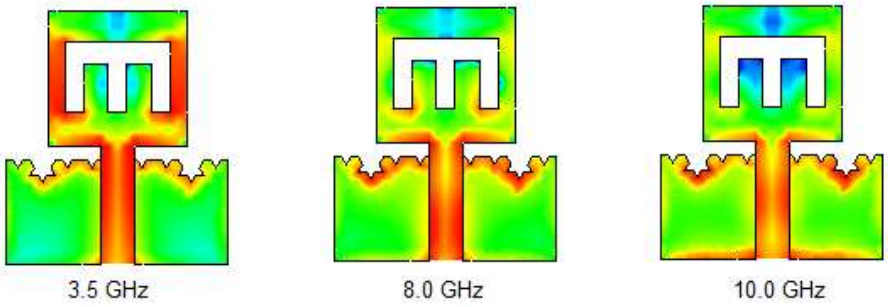

Figure 4: Simulated current distributions on the surface of the Ant. II at different frequencies.

it is expected that by suitable dimension scaling of the enhanced bandwidth UWB antenna, many communication services below 3.1 GHz could be integrated with the UWB systems.

4. CONCLUSIONS

The use of a new fractal based modified ground plane of the printed UWB antenna has been investigated in this paper as a means to enhance its fractional bandwidth. The 2nd iteration Koch fractal geometry has been applied to shape the ground plane of a printed UWB monopole antenna with symmetrical and asymmetrical feeding positions. It is found that at low frequencies, below 6.0 GHz, the modeled antenna perform equally independent on the type of the ground plane and the feeding method. The use of the Koch fractal based ground plane has proved it impact in the resulting fractional bandwidth. Simulation results show that the resulting bandwidth extends to 13.29 GHz, beyond the extent required by the FCC standards. By this increment in the antenna bandwidth, it is expected that by suitable dimension scaling of the enhanced bandwidth UWB antenna, many communication services below 3.1 GHz could be integrated with the UWB systems. Additional work could be carried out to explore the use of other fractal geometries on the UWB antenna performance.

REFERENCES

1. Ali, J. K. and A. S. Hussain, "A new miniaturized E-shaped printed monopole antenna for UWB applications," *PIERS Proceedings*, 1273–1276, Suzhou, China, Sep. 12–16, 2011.
2. Chen, Z. N., T. S. P. See, and X. M. Qing, "Small printed ultrawideband antenna with reduced ground plane effect," *IEEE Trans. Ant. and Propag.*, Vol. 55, No. 2, 383–388, 2007.
3. Federal Communication Commission, First Report and Order, "Revision of part 15 of the commission's rules regarding ultra-wideband transmission systems," FCC 02-48, 2002, available: http://transition.fcc.gov/Bureaus/Engineering_Technology/Orders/2002/fcc02048.pdf.
4. Zhang, Y., Y. Sakurai, and T. Miyashita, "Small planar UWB antenna with a trapezoid shape ground," *Proceedings of China-Japan Microwave Joint Conf., CJMW*, Hangzhou, China, Apr. 2011.
5. Ren, W., "Compact microstrip-fed monopole antenna for UWB applications," *Advances in Information Sciences and Service Sciences, AISS*, Vol. 3, No. 8, 146–153, 2011.
6. William, J. and R. Nakkeeran, "CPW-fed UWB slot antenna with triangular tuning stub," *International Journal of Computer and Electrical Engineering*, Vol. 2, No. 4, 1793–8163, 2010.
7. Morales-Silva, C. and J. Wang, "CPW-fed arrow-shaped slot antenna design for ultra wideband (UWB) applications," *Proceedings of 10th Annual Wireless and Microwave Technology Conf., WAMICON*, Clearwater, USA, Apr. 2009.
8. Zamel, H. M., A. M. Attiya, and E. A. Hashish, "Design of a compact UWB planar antenna with band-notch characterization," *Proceedings of National Radio Science Conf., NRSC 2007*, Cairo, Egypt, Mar. 2007.
9. Amini, F., M. N. Azarmanesh, and M. Ojaroudi, "Small Semi-circle-like slot antenna for ultra-wideband applications," *Progress In Electromagnetics Research C*, Vol. 13, 149–158, 2010.
10. Lizzi, L., G. Oliveri, P. Rocca, and A. Massa, "Planar monopole UWB antenna with UNII1/UNII2 WLAN band characteristics," *Progress In Electromagnetics Research B*, Vol. 25, 277–292, 2010.

11. Naghshvarian-Jahromi, M., "Compact UWB band notch antenna with transmission-line-fed," *Progress In Electromagnetics Research B*, Vol. 3, 283–293, 2008.
12. Bao, X. L. and M. J. Ammann, "Printed UWB antennas with coupled slotted element for notch-frequency function," *International Journal of Antennas and Propagation*, Vol. 2008, 1–7, 2008.
13. Peng, L. and C.-L. Ruan, "UWB band-notched monopole antenna design using electromagnetic-bandgap structures," *IEEE Trans. Microwave Theo. and Tech.*, Vol. 59, No. 4, 1074–1081, 2011.
14. Nikolaou, S., N. D. Kingsley, G. E. Ponchak, J. Papapolymerou, and M. M. Tentzeris, "UWB elliptical monopoles with a reconfigurable band notch using MEMS switches actuated without bias lines," *IEEE Trans. Ant. and Propag.*, Vol. 57, No. 8, 2242–2251, 2009.
15. Zhou, Z. L., L. Li, and J. S. Hong, "Compact UWB printed monopole antenna with dual narrow band notches for WiMAX/WLAN bands," *Electronic Lett.*, Vol. 47, No. 20, 1111–1112, 2011.
16. Tilanthe, P., P. C. Sharma, and T. K. Bandopadhyay, "A compact UWB antenna with dual band rejection," *Progress In Electromagnetics Research B*, Vol. 35, 389–405, 2011.
17. Hong, Z., Y.-C. Jiao, B. Yang, and W. Zhang, "A dual band-notched antenna for ultra-wideband applications," *Proceedings of 2011 IEEE Int. Conf. on Microwave Technology and Comput. Electromag., ICMTCE*, Beijing, China, May 2011.
18. Zhang, W., Y.-C. Jiao, B. Yang, and Z. Hong, "CPW-fed ultrawideband antenna with 3.5/5.5 GHz dual band-notched characteristics," *Proceedings of 2011 IEEE Int. Conf. on Microwave Technology and Comput. Electromag., ICMTCE*, Beijing, China, May 2011.
19. Li, L., Z.-L. Zhou, J.-S. Hong, and B.-Z. Wang, "Compact dual-band-notched UWB planar monopole antenna with modified SRR," *Electronic Lett.*, Vol. 47, No. 17, 950–951, 2011.
20. Liu, C.-Y., T. Jiang, and Y.-S. Li, "A compact wide slot antenna with dual bandnotch characteristic for ultra wideband applications," *Journal of Microwaves, Optoelectronics and Electromagnetic Applications*, Vol. 10, No. 1, 55–64, Jun. 2011.
21. Gao, P., Z. Li, and Y. Zheng, "An integrated UWB and bluetooth antenna with dual WLAN band-notched," *Proceedings of 2011 IEEE Int. Conf. on Ultra-Wideband, ICUWB*, Bologna, Sep. 2011.
22. Mishra, S. K., R. K. Gupta, A. Vaidya, and J. Mukherjee, "A compact dual-band fork-shaped monopole antenna for bluetooth and UWB applications," *IEEE Ant. and Wireless Propag. Letts.*, Vol. 10, 627–630, 2011.
23. Law, K. C., S. W. Cheung, and T. I. Yuk, "An integrated UWB and bluetooth antenna with dual band-notched characteristic," *PIERS Online*, Vol. 7, No. 7, 621–624, 2011.
24. IE3D User's Manual, Release 12.3, Zeland Software, Inc., Fremont, CA, 2007.

A Printed Fractal Based Slot Antenna for Multi-band Wireless Communication Applications

Jawad K. Ali, Mahmood T. Yassen, Mohammed R. Hussan, and Ali J. Salim
Microwave Research Group, Department of Electrical Engineering
University of Technology, Baghdad, Iraq

Abstract— Different slot structures have been widely used in numerous designs to produce antennas with enhanced bandwidths. In this paper, a printed slot antenna has been introduced as a candidate for use in the multi-band wireless communication applications. The antenna slot structure has a rectangular shape with its width, from the side of feed, has been modified in the form of Koch fractal curve of the second iteration. The antenna has been fed with 50 Ohm microstrip transmission line etched on the reverse side of the substrate. Modeling and performance evaluation of the proposed antenna design have been carried out using a method of moments based EM simulator, IE3D. Simulation results show that the resulting antenna exhibits a multi-resonant behavior making it suitable for a wide variety of multi-band wireless communication applications. The first resonant band, centered at 2.58 GHz, extends from 2.40 to 2.89 GHz. This band covers the 2.4 GHz WLAN band (frequency range 2.4–2.483 GHz) and the 2.5 GHz mobile WiMAX operating band (frequency range 2.5–2.7 GHz). The second resonant band, centered at 4.03 GHz, extends from 3.40 to 4.50 GHz. This band covers the 3.5 GHz mobile WiMAX operating band (frequency range 3.4–3.6 GHz). While the third resonant band centered at 5.74 GHz, extends from 5.42 to 6.18 GHz. This band covers the U-NII mid-band (frequency range 5.47–5.725 GHz) and U-NII high-band (frequency range 5.725–5.875 GHz). Parametric study has been carried out to explore the effect of varying the antenna feed line length on its performance.

1. INTRODUCTION

The term fractal, which means broken or irregular fragments, was originally coined by Mandelbrot [1] to describe a family of complex shapes that possess an inherent self-similarity in their geometrical structures. A wide variety of applications for fractal has been found in many areas of science and engineering. One such area is the fractal electrodynamics [2, 3] in which fractal geometry is combined with electromagnetic theory for the purpose of investigating a new class of radiation, propagation, and scattering problems. One of the most promising areas of fractal electrodynamics research is its application to the antenna theory and design. Another prominent benefit that has been derived from using fractal geometries has been to design antenna with multiple resonances [3, 4]. Fractals are complex geometric shapes that repeat themselves, and are thus self similar. Because of the self-similarity of the geometry due to the iterative generating process, the multiple scales of the recurring geometry resonate at different frequency bands.

Hilbert, Peano, and Gosper space-filling curves have attracted the researchers to achieve antenna miniaturization with multiple resonances [5–14]. Many Hilbert fractal-based structures have been proposed to produce printed and microstrip dipole and monopole antennas with compact size and multiband performance for different applications [5–11]. Peano space-filling curves have also drawn the interest of many research groups, where different aspects of many Peano fractal antennas have been reported [11–14]. Gosper space-filling curve has been used to model reduced size multiband antenna [15]. Moreover, structures based on these space-filling geometries have been successfully used in different ways to form parts (or the whole) of the ground plane of miniature and multiband antennas [16]. It is worth to note that, in the majority of the published works, the different types of space-filling curves have been used to model dipole and monopole antennas. Slot antennas based on space-filling curves have drawn less attention from antenna designers; to name a few [10, 17–20].

In this paper, a printed slot antenna structure has been introduced as a candidate for use in the modern compact and multi-function communication systems. The proposed structure has a rectangular slot shape with one of its sides has been modified to be in the form of the second iteration Koch fractal curve. The proposed antenna is expected to possess a considerable compact size owing to the space filling property of the Koch fractal curve.

2. THE PROPOSED ANTENNA STRUCTURE

The starting pattern for the proposed antenna as a fractal is the straight line segment, Figure 1(a). From this starting pattern, this straight line segment is replaced by the generator shown in Figure 1(b). To demonstrate the process, the first three iteration steps are shown in Figure 1.

The resulting pre-fractal structure has the characteristic that the length increases to infinity while maintaining the space occupied [21]. This increase in length decreases the required space occupied for the pre-fractal antenna at resonance. It is found that:

$$L_n = \left(\frac{4}{3}\right)^n L_\circ \tag{1}$$

where, L_n is the length of the nth iteration pre-fractal structure. The ability of the resulting structures to increase its length in the successive iterations was found very triggering for examining its size reduction capability as a microstrip antenna. It has been concluded that the number of generating iterations required to reap the benefits of miniaturization is only few before the additional complexities become indistinguishable [4].

The presence of the irregular radiating edges in the pre-fractal based slot antenna structures is a way to increase the surface current path length compared with that of the conventional rectangular slot antenna, Figure 2; resulting in a reduced resonant frequency or a reduced size antenna if the design frequency is to be maintained. The geometry of the proposed fractal shaped slot antenna is shown in Figure 2. The rectangular slot has been constructed with one its sides takes the form of the 2nd iteration Koch curve, on the ground plane side of a dielectric substrate. The dielectric substrate is supposed to be the FR4 with a relative dielectric constant of 4.4 and thickness of 1.6 mm. The slot antenna is fed by a 50 Ω microstrip line printed on the reverse side of the substrate. The microstrip line, with a width of 3.0 mm, is placed on the centreline of the slot structure (x-axis).

3. THE ANTENNA DESIGN

A rectangular slot antenna, with one of its side lengths based on the 2nd iteration Koch pre-fractal curve, has been designed for the ISM band applications at 2.4 GHz. Observing the influence of the various parameters on the antenna performance, it has been found that the dominant factor in the proposed antenna is the slot external perimeter, L_{ext}. At first, the external perimeter of the slot structure, that matches the resonant frequency, has to be calculated in terms of the guided

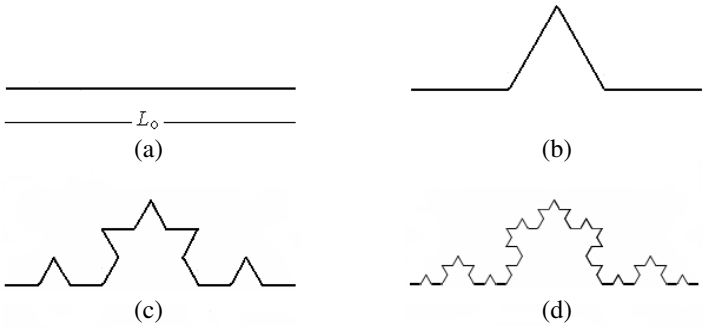

Figure 1: The generation process of the Koch fractal curve up to the 3rd iteration.

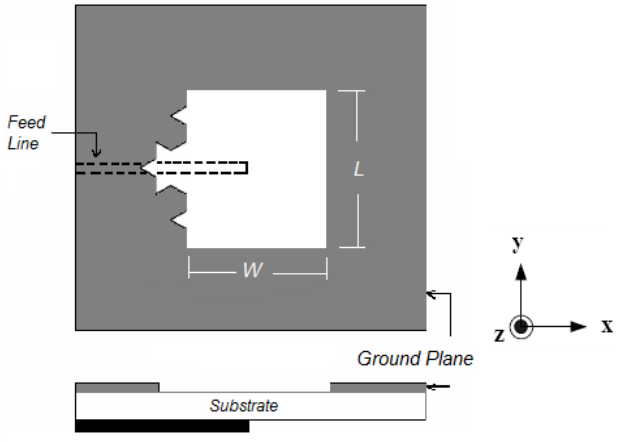

Figure 2: The geometry of the proposed fractal shaped slot antenna.

wavelength λ_g which is given by:

$$\lambda_g = \frac{\lambda_0}{\sqrt{\varepsilon_{eff}}} \tag{2}$$

where ε_{eff} is the effective dielectric constant.

For nth iteration Koch fractal curve, the external perimeter L_{ext} of the antenna slot structure, shown in Figure 2, can be formulated as:

$$L_{ext} = 2W + L\left(1 + \left(\frac{4}{3}\right)^n\right) \tag{3}$$

Then the lowest resonant frequency, f_{01}, relative to twice the slot external side length is formulated by:

$$f_{01} = \frac{C_o}{2L_{ext}\sqrt{\varepsilon_{eff}}} \tag{4}$$

where C_o is the speed of light in free space. Higher order resonances are attributed to the smaller self-similar structures constituting the slot.

4. ANTENNA PERFORMANCE EVALUATION

The fractal based slot antenna with the layout, depicted in Figure 2, has been modeled and analyzed using a method of moments based EM simulator IE3D, from Zeland Software Inc. [24].

Simulation results show that the slot dimensions matching the specified first resonant frequency, f_{01}, are: $L = 23.4$ mm, and $W = 32.78$ mm. According to (3), the slot external length has been found to be of about 137.85 mm. This is in good agreement with the resulting resonant frequency as calculated using (4). The microstrip line feed length has an affective role in different degrees to establish the matching levels at the rest resonances. However, the variation of the feed line length, measured away from the slot center, has been demonstrated in Figure 3, for feed line length varies in steps of 2 mm with respect to the antenna slot center. Different values of the feed line length result in different responses as a result of coupling satisfied at each length. This makes the antenna suitable for single or multi-band applications.

Figure 4 shows the resulting antenna return loss response for a feed line length of 3 mm away from antenna center. The antenna exhibits an impedance bandwidth, for $S_{11} \leq -10$ dB, which constitutes three resonances in the swept frequency range 0–7 GHz. The first resonant band, centered at 2.58 GHz, extends from 2.40 to 2.89 GHz. This band covers the 2.4 GHz WLAN band (frequency range 2.4–2.483 GHz) and the 2.5 GHz mobile WiMAX operating band (frequency range 2.5–2.7 GHz). The second resonant band, centered at 4.03 GHz, extends from about 3.40 to 4.50 GHz. This band covers the 3.5 GHz mobile WiMAX operating band (frequency range 3.4–3.6 GHz). While the third resonant, band centered at 5.74 GHz, extends from 5.42 to 6.18 GHz. This band covers the U-NII mid-band (frequency range 5.47–5.725 GHz) and U-NII high-band (frequency range 5.725–5.875 GHz).

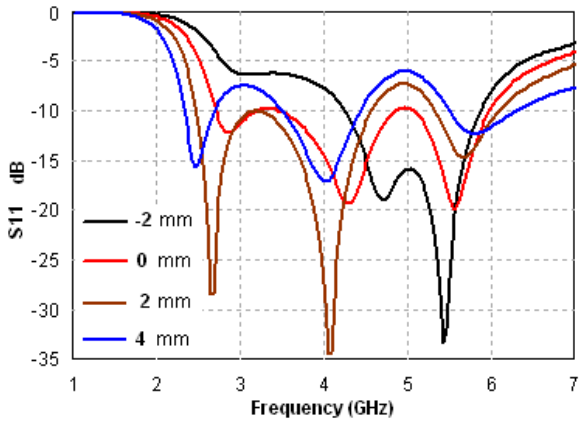

Figure 3: Return loss responses of the modeled antenna with the feed line length as the parameter.

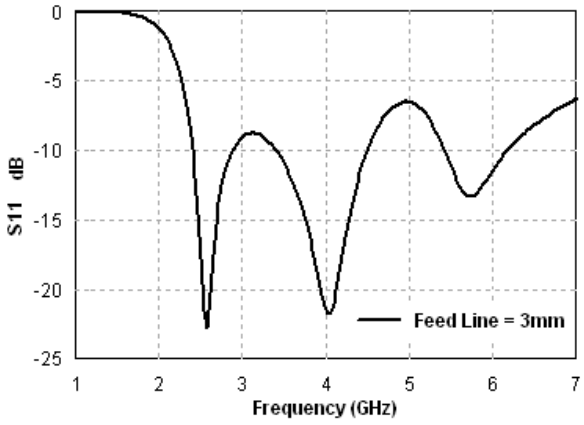

Figure 4: Return loss response of the modeled antenna with a feed line length of 3 mm away from the center.

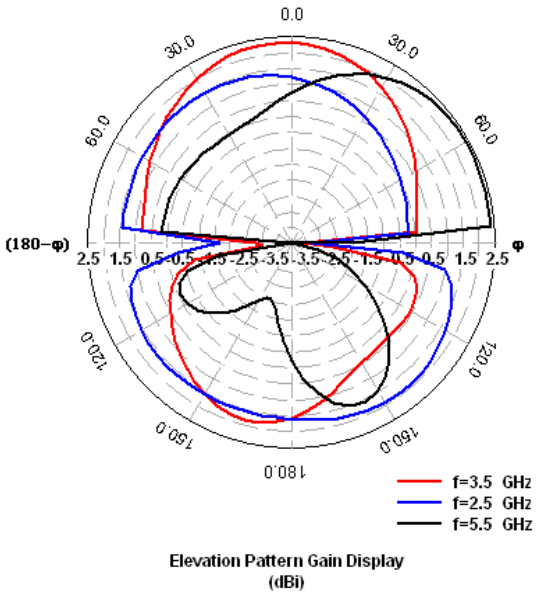

Figure 5: The 2D E-field radiation patterns of the modeled fractal slot antenna with a feed line length equals to 3 mm away from the center, at 2.5, 3.5, and 5.5 GHz.

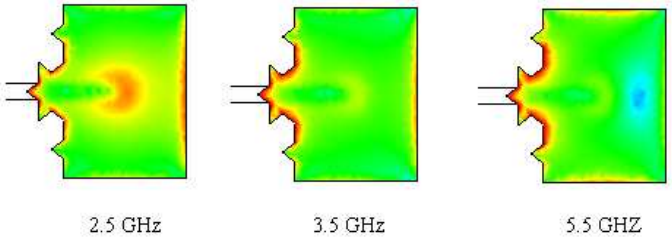

Figure 6: The surface current distributions on the slot structure of the modeled antenna with a feed line length equals to 3 mm away from the center, at 2.5, 3.5, and 5.5 GHz.

The 2D radiation patterns at specified frequencies through the three bands have been shown in Figure 5, where an average gain of about 2.5 dB has been satisfied. The antenna almost offers omnidirectional radiation patterns. The surface current distribution on the slot structure at 2.5, 3.5, and 5.5 GHz are shown in Figure 6, where it has been clearly depicted the parts of the slot structure that contribute in the radiation at each assigned frequency. Additional work has to be carried out to explore the effects of Koch fractal curve indentation angle on the antenna performance. It is expected to gain interesting features with antenna performance that supports the operating band of many other communication services.

5. CONCLUSIONS

A fractal shaped slot antenna design based on the second iteration Koch fractal curve has been presented in this paper, for use in the modern multiband compact wireless applications. It is expected that the antenna presented in this paper will have a variety of applications in wireless applications. Simulation results show that the modeled fractal antennas have a multi-resonance behavior with fractional bandwidths sufficient for most of the wireless applications. Careful tuning of the feed has been found helpful in getting best matching conditions in a considerably reliable manner. Additional work has to be carried out to explore the performance of the proposed antenna when varying the indentation angle of the Koch fractal curve. This will, absolutely, result in different multi-resonant frequency allocations which might be suitable for many wireless communication applications.

REFERENCES

1. Mandelbrot, B. B., *The Fractal Geometry of Nature*, W. H. Freeman, New York, 1983.

2. Jaggard, D. L., "Fractal electrodynamics: From super antennas to superlattices," *Fractals in Engineering*, J. L. Vehel, E. Lutton, and C. Tricot, Eds., Springer-Verlag, 1990.
3. Jaggard, D. L., "On fractal electrodynamics," *Recent Advances in Electromagnetic Theory*, H. N. Kritikos and D. L. Jaggard, Eds., Springer-Verlag, 1990.
4. Gianvittorio, J. P. and Y. Rahmat-Samii, "Fractal antennas: A novel antenna miniaturization technique, and applications," *IEEE Antennas and Propagation Magazine*, Vol. 44, 20–36, 2002.
5. Vinoy, K. J., K. A. Jose, V. K. Varadan, and V. V. Varadan, "Hilbert curve fractal antenna: A small resonant antenna for VHF/UHF applications," *Microwave Opt. Technol. Lett.*, Vol. 29, 215–219, May 2001.
6. Best, S. R., "A comparison of the performance properties of the Hilbert curve fractal and meander line monopole antennas," *Microwave Opt. Technol. Lett.*, Vol. 35, 258–262, Nov. 2002.
7. Anguera, J., C. Puente, E. Martinez, and E. Rozan, "The fractal Hilbert monopole: A two-dimensional wire," *Microwave Opt. Technol. Lett.*, Vol. 36, 102–104, Jan. 2003.
8. Zhu, J., A. Hoorfar, and N. Engheta, "Bandwidth, cross-polarization, and feed-point characteristics of matched Hilbert antennas," *IEEE Antenna Wireless Propag. Lett.*, Vol. 2, 2–5, 2003.
9. Azad, M. Z. and M. Ali, "A miniaturized Hilbert PIFA for dual-band mobile wireless applications," *IEEE Antennas Wireless Propag. Lett.*, Vol. 4, 59–62, 2005.
10. Azad, M. Z. and M. Ali, "Characteristics of a microstrip-fed miniature printed Hilbert slot antenna," *Progress In Electromagnetics Research*, Vol. 56, 1–18, 2006.
11. McVay, J. A. and A. Hoorfar, "An overview of space-filling curves in novel antenna designs: Theory, simulations, and experiments," *Proc. EMTS 2007 Int. URSI Commission B — Electromag. Theory Symp.*, Ottawa, ON, Canada, Jul. 26–28, 2007.
12. Zhu, J., A. Hoorfar, and N. Engheta, "Peano antennas," *IEEE Antenna Wireless Propag. Lett.*, Vol. 3, 71–74, 2004.
13. Huang, H. and A. Hoorfar, "Miniaturization of dual-band planar inverted-F antennas using Peano-curve elements," *Proc. Int. Symp. Antenna and Propag., ISAP'06*, Singapore, Nov. 2006.
14. McVay, J. A. and A. Hoorfar, "Miniaturization of top-loaded monopole antennas using Peano curves," *Proc. IEEE Radio and Wireless Symp.*, Long Beach, California, USA, Jan. 9–11, 2007.
15. Haji-Hashemi, M. R., M. Moradian, and H. M. Sadeghi, "Space-filling patch antennas with CPW feed," *PIERS Online*, Vol. 2, No. 1, 69–73, 2006.
16. Quintero, R. and C. Puente, "Multilevel and space-filling ground-planes for miniature and multiband antennas," US Patent 7 362 283 B2, Apr. 22, 2008.
17. Sayem, A. T. M., M. Ali, and H. S. Huang, "Miniaturized dual-band Hilbert slot antenna for wireless application," *Proc. IEEE Antenna and Propaga. Soc. Int. Symp.*, Monterey, CA, Jun. 2004.
18. Ghali, H. A. and T. A. Moselhy, "Broadband and circularly polarized space-filling-based slot antennas," *IEEE Trans. Microwave Theory and Techniques*, Vol. 53, 1946–1950, Jun. 2005.
19. Ali, J. K., "A new microstrip-fed printed slot antenna based on Moore space-filling geometry," *Loughborough Antenna and Propag. Conf., LAPC 2009*, Loughborough, UK, Nov. 2009.
20. Ali, J. K. and E. S. Ahmed, "A new fractal based printed slot antenna for dual band wireless communication applications," *PIERS Proceedings*, 1518–1521, Kuala Lumpur, Malaysia, Mar. 27–30, 2012.
21. Falconer, K., *Fractal Geometry; Mathematical Foundations and Applications*, 2nd Edition, John Wiley and Sons Ltd., 2003.
22. Bahl, I. J. and P. Bhartia, *Microstrip Antennas*, Artech House, Dedham, MA, 1980.
23. James, J. R. and P. S. Hall, *Handbook of Microstrip Antennas*, Vol. 1, Peter Peregrines Ltd., London, 1989.
24. IE3D User's Manual, Release 14.1, Zeland Software Inc., Fremont, CA, May 2008.

Wide Band Switched Beam Circular Patch Antenna

W. M. A. Abdulkawi, A. F. A. Sheta, and M. A. S. Alkanhal
Department of Electrical Engineering, King Saud University
P. O. Box 800, Riyadh 11421, Kingdom of Saudi Arabia

Abstract—The paper presents a new wideband switched beam patch antenna for the recent wireless applications. The proposed antenna is designed to cover the band from 1.22 GHz to 1.945 GHz with $S_{11} < -10$ dB. The presented antenna has the ability to switch the beam into two different directions at the same resonant frequency. Two artificial switches (PIN diodes) are used in this antenna to make reconfigurability. The design has been achieved on Duroid substrate with a dielectric constant 2.2, thickness 1.57 mm, and loss tangent 0.0009. The two PIN diodes (S_1 and S_2) are used to connect or disconnect the two circular patches. In ON-OFF state the antenna has a maximum beam direction of $\theta_{\max} = 215°$ at $\phi = 80°$. In OFF-ON state the maximum beam direction switched to $\theta_{\max} = 145°$ at $\phi = 80°$. The peak gains of the proposed antenna are 2.91 dBi for two cases. The characteristics of the proposed antenna have been investigated using IE3D simulator.

1. INTRODUCTION

Microstrip antennas have a several advantages, such as low manufacturing cost, low profile, less weight, conformable to surfaces, ease of fabrication, and good electrical performance [1]. The beam steering antennas are widely used in satellite, recent wireless communications, radar, and telemedicine [2]. A reconfigurable beam steering antenna using double loops has been reported in [3]. The operating frequency of this antenna is 14.5 GHz. The antenna uses two artificial switches to steer the beam into three directions. In [4] a wideband frequency reconfigurable printed log periodic dipole array (LPDA) operating in the 0.8–2.4 GHz range was presented. A narrow band circular patch antenna on metamaterial substrate for C-band applications is proposed in [5]. In [6] enhanced gain was presented of a compact circular antenna for personal communication systems (PCS). This antenna operates at 1.8 GHz with 100 MHz bandwidth. A beam steering radial line slot array (RLSA) antenna with reconfigurable operating frequency has been proposed in [7]. The structure uses PIN diodes switches that are integrated with the feed line. It is found that the beam steering ability was greatly affected by spiral; whoever the reconfigurable operating frequency was greatly affected by the radius of feed line.

In this paper, we presented a wideband switched beam circular patch antenna with more than 47% bandwidth. The proposed antenna is capable to cover the frequencies from 1.22 GHz until 1.945 GHz and able to steer the maximum beam direction into two directions in the elevation plane.

2. DESCRIPTION OF THE ANTENNA

As shown in Fig. 1, the proposed antenna consists of ground plane of dimension $60 \times 170\,\text{mm}^2$ and two circular patches with radius $R = 35$ mm. The two radiating circular patches are placed on the top layer and fed with a microstrip lines. The two PIN diodes (S_1 and S_2) are used to connect or disconnect the two circular patches. The switches are located 6 mm from the center of the microstrip feed line. The beam direction can be switch into two different directions depending on the states of the two switches, explained as ON-OFF state and OFF-ON state.

The radius of the circular patch can be calculated as a function of the resonance frequency f_r by [1]:

$$a = \frac{F}{\left\{1 + \frac{2h}{\pi\varepsilon_r F}\left[\ln(\frac{\pi F}{2h}) + 1.7726\right]\right\}^{0.5}} \tag{1}$$

where

$$F = \frac{8.791 \times 10^9}{f_r\sqrt{\varepsilon_r}} \tag{2}$$

For circular patch antenna a correction is introduced by using effective radius a_e as:

$$a_e = a\left\{1 + \frac{2h}{\pi\varepsilon_r F}\left[\ln(\frac{\pi a}{2h}) + 1.7726\right]\right\}^{0.5} \tag{3}$$

Table 1: The actual and effective radiuses of the circular patch.

Parameter	Calculated (mm)	Optimized (mm)
a	37.31	35
a_e	38.47	35

Table 2: Proposed antenna parameters.

Optimized R (mm)	L_g (mm)	W_g (mm)	W_f (mm)
35	60	170	3

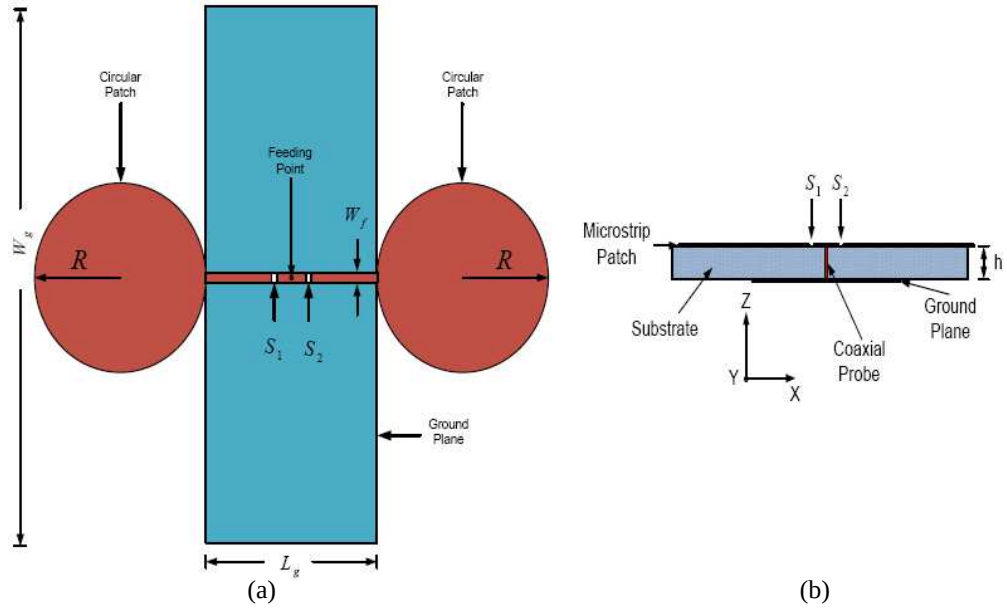

Figure 1: The proposed circular patch antenna geometry, (a) top view and (b) side view.

where, a is the circular patch radius in centimeters when h is in centimeters and f_r is given in hertz. These equations give good accuracy for small dielectric constant materials. RT Duroid dielectric material 5880 with 2.2 relative permittivity and 1.57 mm thickness is used for this analysis. The loss tangent is ($\tan\delta = 0.0009$). This antenna is fed by a coaxial probe posted on the center of the microstrip feed line. The antenna is designed to operate at 1.54 GHz with fractional bandwidth of about 50%. So when the resonant frequency (f_r) is 1.54 GHz the actual and effective radiuses of this antenna can be calculated by using the above equations as shown on Table 1. The antenna physical parameters are summarized on Table 2.

3. SIMULATION RESULTS

The proposed antenna covers the band from 1.22 GHz to 1.945 GHz with $S_{11} < -10$ dB. The characteristics of the proposed antenna have been investigated using IE3D simulator. Fig. 2 illustrates the simulated return loss of the wideband circular patch antenna for ON-OFF and OFF-ON states. These results show that the return loss is almost unaffected by the switches states. The presented antenna has the ability to switch the beam into two different directions at the same resonant frequency. Two artificial switches (PIN diodes) are used in this antenna to make reconfigurability. In ON-OFF state the antenna has a maximum beam direction of $\theta_{\max} = 215°$ at $\phi = 80°$. In OFF-ON state the maximum beam direction switched to $\theta_{\max} = 145°$ at $\phi = 80°$. The peak gain of the proposed antenna is 2.91 dBi for both cases ON-OFF and OFF-ON. The simulated 3D radiation pattern of the wideband circular patch antenna is shown on Fig. 3.

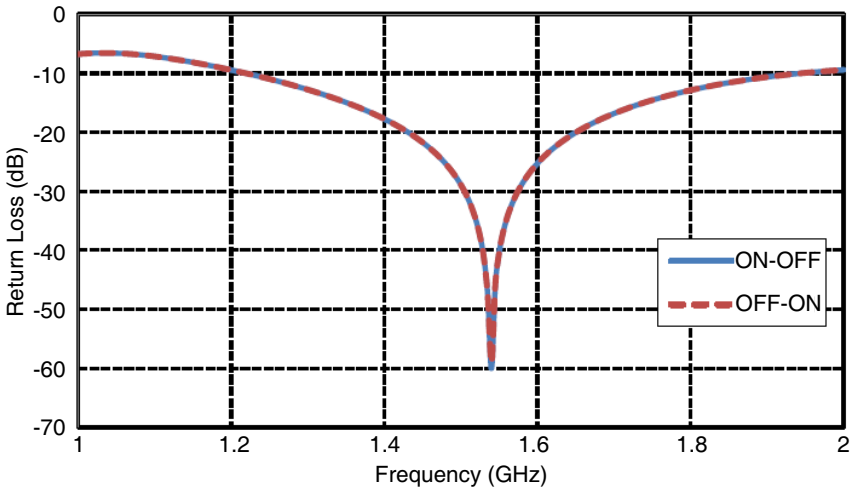

Figure 2: Simulated return loss of the proposed antenna at ON-OFF and OFF-ON states. ON state.

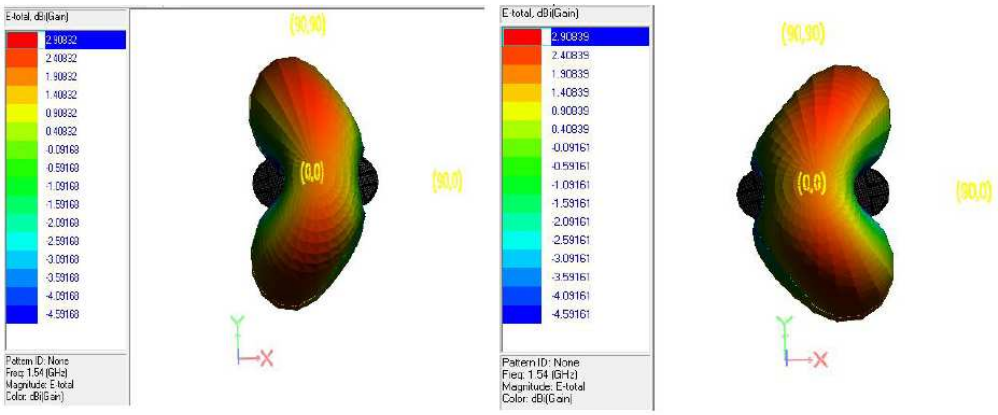

Figure 3: Simulated 3D radiation pattern for ON-OFF and OFF-ON states respectively.

4. CONCLUSIONS

This paper proposed a wideband microstrip circular patch antenna operating at the band 1.22–1.945 GHz. The results obtained shows that there is a very good agreement in simulated return loss for both ON-OFF and OFF-ON states. This antenna has been ability to steer the beam into two directions with a 2.91 dBi maximum peak gain for both states ON-OFF and OFF-ON. In ON-OFF state the antenna has a maximum beam direction of $\theta_{\max} = 215°$ at $\phi = 80°$, however in OFF-ON state the maximum beam direction switched to $\theta_{\max} = 145°$ at $\phi = 80°$.

ACKNOWLEDGMENT

This work is supported by the National Plan for Science and Technology Program, Kingdom of Saudi Arabia, Research Grant: 08-ADV210-2.

REFERENCES

1. Balanis, C. A., *Antenna Theory Analysis and Design*, John Wiley & Sons, USA, 2005.
2. James, J. R. and P. S. Hall, *Handbook of Microstrip Antennas*, Peter Peregrinus Ltd, London, 1989.
3. Kim, J. Y., B. Lee, and C. W. Jung, "Reconfigurable beam-steering antenna using double loops," *Electronics Letters*, Vol. 47, No. 7, March 2011.
4. Mirkamali, A. and P. S. Hall, "Wideband frequency reconfiguration of a printed log periodic dipole array," *Microwave and Optical Technology Leters*, Vol. 52, No. 4, 861–864, April 2010.

5. Sulaiman, A. A., M. Z. M. Zani, M. H. Jusoh, N. H. Baba, R. A. Awang, and M. F. Ain, "Circular patch antenna on metamaterial," *European Journal of Scientific Research*, Vol. 45, No. 3, 391–399, 2010.
6. Tilanthe, P., P. C. Sharma, and T. K. Bandop, "Gain enhancement of circular microstrip antenna for personal communication systems," *IACSIT International Journal of Engineering and Technology*, Vol. 3, No. 2, 175–178, April 2011.
7. Jamlos, M. F., O. A. Aziz, A. R. B. Tharek, M. R. B. Kamarudin, P. Saad, M. T. Ali, M. N. Md Tan, "A beam steering radial line slot array (RLSA) antenna with reconfigurable operating frequency," *Journal of Electromagnetic Waves and Applications*, Vol. 24, No. 8–9, 1079–1088, 2010.

An Overview of Microwave Imaging towards for Breast Cancer Diagnosis

S. Raghavan and M. Ramaraj
Department of Electronics and Communication Engineering
National Institute of Technology (NIT), Tiruchirappalli-620015, India

Abstract— Breast cancer is the most common type of cancer found in women worldwide. Digital Mammography is considered as the "gold standard" in the evaluation of the breast cancer in the form of an imaging perspective. Apart from mammography, ultrasound examination, magnetic resonance imaging and microwave imaging techniques are being offered as adjuncts to the preoperative workup. However, there is still controversy over the most appropriate use of these new modalities. This review paper concentrates mainly on the evaluation of microwave techniques in the screening and diagnosis of breast cancer and in the medical field. It reviews the current applications and future potential of microwave imaging methods. This report gives an overview of the old and new modalities used in the field of breast imaging based on relevant literatures. It shows clearly that though various new techniques and methods have emerged, none have substituted mammography. Last two decades, medical imaging applications on microwaves has been developed. The emerging ultra wide band microwave (UWB) imaging gives better result with the advantages of non-ionizing, comfortable, sensitive to tumors and specific to malignancies. In microwave imaging techniques recently hybrid microwave induced acoustic imaging is developed, ultra wide band radar based imaging and microwave tomography are also being offered.

1. INTRODUCTION

Microwave imaging is the technique used to sense a given object by means of examining microwave pulses. It has been recently proved that it is much useful by providing excellent diagnostic capabilities in several areas which includes civil and industrial engineering and biomedical engineering. Microwave Imaging is the most important technique which offers comprehensive descriptions so far for the proposed short-range microwave imaging including reconstruction procedures & imaging systems and apparatus enabling. It creates a path to the researcher to use microwaves for diagnostic purposes in a wide range of applications.

The research in the area of application for microwaves in biomedical imaging and diagnostics still exists due to the field remains with many uncharted areas. Even though in the field of medical imaging the microwave community has so far limited contributions, with the exception of magnetic resonance imaging (MRI) systems. In the last two decades, to detect breast cancer mammography has emerged as the golden standard methodology. But still it has some demerits like invasive detection, compression of the breast tissues, radiation and discomfort to the patient which should be rectified and can be rectified in the proposed microwave imaging methodologies.

The microwave imaging in the medical field is an acquisition of human body parts by using electromagnetic waves for cancer detection especially in the microwave region. Experimental studies made on the human tissues show significant contrast in dielectric properties between the malignant tumors and normal fatty tissue at microwave frequencies. Main aim in the microwave imaging is to achieve non-ionizing detection, increased the sensitivity of tumors specific to malignancies and gives comfort to the patient. In digital mammogram, images are composed by applying the concentration of X-rays over a breast using illumination process. The concentration of X-ray will gives white region for fibroglandular tissues and black region for breast tissues. Maximum part of the fatty breast consists of fibroglandular regions. So the discovered tumor part using X-ray illumination is also gives white regions. It not shows much difference between the breast tumor and breast fatty tissues. This is the one main disadvantage of the mammogram methodology.

2. METHODS & METHODOLOGIES

Initially microwave radiation is used to scan the kidney images by Larsen and Jacobi in 1970's with scattering parameters [1]. Then the chirp signals are used in time domain measurement techniques [2]. The imaging applications point of view, in eighties hybrid microwave induced acoustic imaging technique was introduced. Hybrid methods use microwave to selectively heat tumors and

ultrasound transducers to detect pressure waves generated by the expansion of heated tissues. In hybrid method, heat is applied to the high conductivity malignant tissues than surrounding normal tissues. The induced acoustic signals are sensed by ultra sensors which produce the images.

In microwave tomography, the breast is illuminated by using transmitting antennas in the microwave region and on particular domain the scattering fields is collected by using receiving antennas. Then reconstruction approaches (proposed by different researchers) are used to reconstruct the dielectric and/or conductivity profile of the breast. Microwave imaging is used to determine the permittivity and conductivity distribution which is the function of position [4, 5]. It precedes the measured data in the form of scatters, i.e., the properties of the observed objects which differ from those in the normal or healthy state of the imaged volume. Thus, the tumor which is more electrically similar surrounded around the healthy tissue becomes more difficult to detect. The difference in the electrical properties of a scatter and the medium is embedded and referred as "contrast". The contrast is often defined as ratio, most probably in terms of percentage of the permittivities and/or the conductivities of the scatter to the host medium. Initially it was explained that there is a large contrast between malignant tissue and healthy breast tissue with higher permittivity and conductivity of the malignant tissues.

The emerging ultra wide band microwave (UWB) imaging gives better result with the advantages in detecting malignancies than existing one. Breast tissue phantoms (artificial objects of human tissues or organs) are often used to illustrate the typical electrical parameters of breast tissues which are of the major type's lies in the frequency range of 3–10.6 GHz [6–8]. There is an electrical similarity between tumors and fibroglandular tissues, but it varies in low-water-content fatty tissue. However, the low contrast between malignant and healthy fibroglandular tissue does not deter the research towards microwave breast-cancer diagnostic systems. Even though X-ray mammography, considered as the golden standard for breast-cancer diagnostics, which has the contrasts as low as 4–10%. Note that the above technique won't give the solution in case of a low-contrast inverse problem. These techniques such as diffraction tomography and holography are much faster to exploit the low contrast which in turn simplifies the reconstruction procedure unlike the optimization based procedures. The contrast agents are used to improve the imaging quality for microwave tissue imaging applications.

3. CHALLENGES

Electromagnetic simulations of biological structures require complex algorithm and huge computational techniques. This consumes much more time to do optimization-based reconstruction. Moreover during simulations fidelity (measuring parameter) plays an important role which often fails to reproduce the measurements of known objects. Typically increasing the frequency in higher range makes the fidelity much lower and lower. The fidelity also depends on the complexity of the modeled structure, which ideally should include the sensors where it plays an important role in imaging techniques.

This is the major reason for the microwaves to quickly become the subject of intense research worldwide. It creates a path for the new modality of early-stage towards breast-cancer detection. The research articles show that both permittivity and conductivity is large as 10% in contrasts between malignant and fatty breast tissue, which in turn as low as 10% between malignant and healthy fibroglandular tissues [4, 5, 9]. This gives much importance since most of the breast tumors appear in the fibroglandular tissues. More attention should be needed in this regard as the variability of the existing results is much larger. The contrast parameters are unsatisfactory because they were acquiring from the measurement of ex vivo samples. Another problem with ex vivo measurements is that the electrical parameters of living tissue change significantly during certain period initially after excision. In case of in vivo samples the indirect estimation of the electrical parameters using microwave tomography is also unnoticeable one. The free water content is the major reason for choosing microwave frequencies. In the form of samples at microwave frequencies will affects the permittivity and conductivity due to drain in fluids. This shows clearly that the estimated contrasts for the abnormal (benign and malignant) and normal breast tissues are getting affected using microwave-tomography measurements. In terms of conductivity "no more than about 10%" for ex vivo samples are reported [9]. Results from the direct in vivo measurements of cancerous breast tissues have been reported and have been compared to the results of the ex vivo measurements of the same sample after excision. In the frequency range 1–8.5 GHz, the observed decrease in conductivity and permittivity after excision is anywhere between 20% and 40%. The direct in vivo measurements of both healthy and abnormal breast tissues won't provide sufficient

information.

4. SUMMARY

Now a day's either in microwave or in other methods imaging modalities plays a significant role. Each method is actively pursued as an alternative to the existing techniques. One of the most particularly promising areas is breast-cancer diagnostics due to the relatively short required penetration depth, possibility to compress the soft tissue, further reduction in signal propagation path and increased accessibility from different angles. The non-ionizing property of microwaves makes it a promising approach, thus permitting frequent examinations. Microwave electronics and test instrumentation is mature, compact, and relatively cheap compared to X-ray or MRI equipment. More importantly, breast cancer continues to be an important and unsolved health and societal problem. According to the statistics of the American Cancer Society, 1 in 8 women at North America suffer from breast cancer during her lifetime. Such high statistical concern makes early detection even more crucial. The chances of survival are better than 90%, if malignant growth is seized before it reaches a size of about 1.5 cm in any given direction. Regular mass screening of all women is necessary for better early-stage breast cancer diagnostics but it is risk.

All women above the age of 45–50 years must ensure scheduled yearly check-ups. However for mass screening purpose the existing breast imaging methods such as X-ray mammography and MRI are not suitable. Due to the use of ionizing radiations in X-ray mammography, it is not advisable for frequent check-ups. Besides, it requires significant breast compression, which is often painful. MRI on the other hand is too expensive and time-consuming. Ultrasound is considered to be too operator-dependent and of low specificity. Microwave Imaging for Breast Cancer detection is by far the best approach — A boon to woman and the society as a whole.

5. CONCLUSIONS

From the literature it is clear that modern radiology's impact on diagnosis, endorsement and patient's record shows that mammography is the only screening test proven for breast imaging. Microwave holography is proved as a near field imaging method with its transmitting and receiving antennas. This is experimentally determined with phantom tissues only but not yet used at clinical trials. Microwave tomography also plays an important role in diagnosing breast cancer and in monitoring treatment response too. As imaging techniques improves, the role of imaging will continue to evolve with the goal remaining a decrease in breast cancer mortality. Progress in the design and development of UWB breast imaging system will definitely help to promote other systems and applications based on the radar imaging methods. The design of ultra wide band antenna and image reconstruction algorithm is the important challenges in microwave imaging modalities. But, Microwave based imaging modalities will be the best in tomorrow's clinical practice and these techniques enhance the radiologist's ability to detect cancer and assess disease extent, which is crucial in treatment development and performance.

ACKNOWLEDGMENT

The authors thankfully acknowledge all the authors of the reference papers given.

REFERENCES

1. Larsen, L. E. and J. H. Jacobi, *Medical Applications of Microwave Imaging*, IEEE Press, New York, 1986.
2. Pedersen, P. C., C. C. Johnson, C. H. Durney, and D. G. Bragg, "Microwave reflection and transmission measurements for pulmonary diagnosis and monitoring," *IEEE Trans. Biomed. Eng.*, Vol. 25, No. 1, 40–48, Jan. 1978.
3. Lin, J. C., "Frequency optimization for microwave imaging of biological tissues," *Proc. IEEE*, Vol. 73, No. 2, 374–375, Feb. 1985.
4. Sha, L., E. R. Ward, and B. Story, "A review of dielectric properties of normal and malignant breast tissue," *Proc. IEEE Southeast Conf.*, 457–462, 2002.
5. Chaudhary, S. S., R. K. Mishra, A. Swarup, and J. M. Thomas, "Dielectric properties of normal and malignant human breast tissues at radiowave and microwave frequencies," *Indian J. Biochem. Biophys.*, Vol. 21, No. 1, 76–79, Feb. 1984.
6. Abbosh, A. M., H. K. Kan, and M. E. Bialkowski, "Compact ultra-wideband planar tapered slot antenna for use in a microwave imaging system," *Microwave Opt. Technol. Lett.*, Vol. 48, No. 11, 2212–2216, Nov. 2006.

7. Nilavalan, R., I. J. Craddock, A. Preece, J. Leendertz, and R. Benjam, "Wideband microstrip patch antenna design for breast cancer tumour detection," *IET Microwaves, Antennas Propagat.*, Vol. 1, No. 2, 277–281, Apr. 2007.
8. Klemm, G. M., I. J. Craddock, J. A. Leendertz, A. Preece, and R. Benjamin, "A comparison of a wide-slot and a stacked patch antenna for the purpose of breast cancer detection," *IEEE Trans. Antennas Propagat.*, Vol. 58, No. 3, 665–674, Mar. 2010.
9. Lazebnik, M., L. McCartney, D. Popovic, C. B. Watkins, M. J. Lindstorm, J. Harter, S. Sewall, A. Magliocco, J. H. Brooske, M. Okoniewski, and S. C. Hagness, "A large-scale study of the ultrawideband microwave dielectric properties of normal, benign and malignant breast tissues obtained from cancer surgeries," *Phys. Med. Biol.*, Vol. 52, No. 20, 6093–6115, Oct. 2007.

Elliptical Split Ring Resonator: Mathematical Analysis, HFSS Modeling and Genetic Algorithm Optimization

M. Ramaraj, S. Raghavan, Sumanta Bose, and Swadhyaya Kumar
National Institute of Technology, Trichirappalli 620 015, India

Abstract— In this paper, a novel equivalent circuit model and mathematical analysis is proposed to estimate the resonant frequency of an Elliptical Split Ring Resonator (ESRR) for a range of major to minor axis ratios. Performance enhancement is achieved by employing MATLAB based Genetic Algorithm (GA) to optimize the physical parameters of the ESRR by iterative convergence to the desired resonant frequency. HFSS EM CAD Tool is used to model the optimized ESRR & plot its S-parameters for a range of frequency sweep to validate its Negative Refractive Index Material (NRIM) property.

1. INTRODUCTION

Split Ring Resonators (SRR) are common in the metamaterial design as they exhibit negative permittivity and permeability for frequencies close to their resonant frequency. It is a major engineering concern to estimate the resonant frequency due to the existence of negative value of permeability over a very narrow band of frequency. Analysis of Circular and Square SRR are commonplace, with relevant literature available [1]. However, the analysis of Elliptical SRR is only on a simulation level yet [2]; and no substantial mathematical analysis exists, to the best of the author's knowledge. ESRRs are of special interest as they can be easily incorporated with microstrip antennas to get highly directional beam patterns because of their enhanced NRIM properties. This work covers a 3-fold analysis: Mathematical formulation, Performance Optimization & EM CAD Simulation.

2. RESONANT FREQUENCY: MATHEMATICAL FORMULATIONS

2.1. ESRR Geometry & Mathematical Modeling

Figure 1(a) shows the schematic geometry of a ESRR with dimensions indicated. Fig. 1(b) shows the equivalent circuit model of the ESRR, forming a L-C network. The inductance is due to the gap between the rings and the capacitance is due to the rings and the gaps in the rings itself.

When a magnetic field is applied along the z-axis, an electromotive force appears around the ESRR which induces a current passing from one ring to the other through the gaps and the structure behaves like an L-C network having resonant frequency f_o expressed as:

$$f_o = \frac{1}{2\pi\sqrt{L_{net}C_{net}}} \tag{1}$$

where L_{net} and C_{net} are the net-effective inductance and capacitance of the equivalent L-C network.

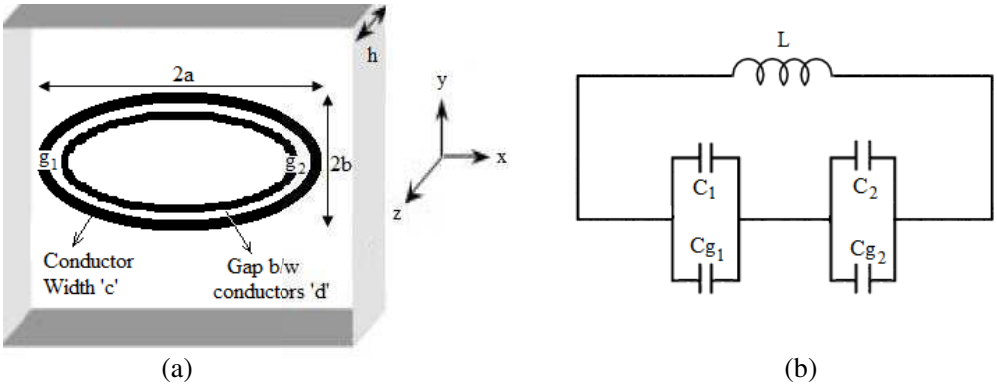

Figure 1: (a) Schematic diagram of a ESRR; (b) Equivalent L-C circuit network.

2.2. Net Capacitance Calculation

Considering an axis through the vertically opposite gaps g_1 and g_2 of the ESRR, we denote the capacitance of its upper and lower half rings with C_u and C_l. Due to zero skew rotation, C_u must equal C_l and is given by:

$$C_{ring} = C_u = C_l = \left(\frac{l-g}{2}\right) \cdot C_{pul} \tag{2}$$

where l is the effective perimeter (Appendix A); $g = g_1 = g_2$ (assumption) is the gap width; and C_{pul} is the per-unit-length capacitance (Appendix B) of the ESRR. For an accurate estimation of the resonant frequency, the effect of the gap capacitance is also computed using parallel plate capacitance approximation. For $g = g_1 = g_2$, the gap capacitance C_{g1} must equal C_{g2} and is given by :

$$C_{gap} = C_{g1} = C_{g2} = \frac{\varepsilon_o \cdot c \cdot h}{g} \tag{3}$$

where c is the width of the conductor and h is the depth of the substrate, as shown in Fig. 1(a). It is evident that each of the half ring capacitor is in parallel with the gap capacitor and the two such systems are in series. Hence, the net-equivalent capacitance of the ESRR, C_{net}, after some algebraic manipulations can be expressed as :

$$C_{net} = \frac{C_{ring} + C_{gap}}{2} \tag{4}$$

2.3. Net Inductance Calculation

Maxwell showed that the self-inductance of a conducting loop is equal to the mutual inductance between a pair of filaments spaced orthogonally apart at a distance termed as the *geometric mean distance (g.m.d.)* of the area of the Section [3]. It can be computed using the general Neumann expression [4],

$$M = \int_s \int_{s'} \frac{ds \cdot ds' \cos\psi}{r} \tag{5}$$

where s and s' are the pair of filament loops; r is the distance from the center of any element on one loop to the center of any other element on the other loop; and ψ is the angle between s and s' filament loops. Cooke showed that the Neumann double integral can be simplified into two sets of infinite series [5], and that the self-inductance of an elliptical loop can be expressed as the infinite series:

$$L = 8 \cdot E(\Omega) \cdot a \left[\log_e \frac{16 \cdot E(\Omega) \cdot a}{\pi \cdot h} - 2 - 0.4375\Omega^2 - 0.1445\Omega^4 - \ldots\right] \tag{6}$$

where a is the semi-major axis; h is the *g.m.d.* of the cross-section; $E(\Omega)$ is the complete elliptical integral of the second kind (Appendix B); and $\Omega = \left(a^2 - b^2\right)/\left(a^2 + b^2\right)$ where b is the semi-minor axis of the ESRR. This formula holds good with an error $\leq 0.175\%$ for $0 < \Omega < 1/3$, which is the case for most practical designs. For $\Omega > 1/3$, other closed form expressions [5] must be considered.

For computational convenience, Bashenoff deduced a simpler expression to compute the self-inductance of any closed loop conductor using semi-empirical methods [6]. The self-inductance of any closed loop conductor is :

$$L_{net} = 0.002l \left[\log_e \frac{2l}{\rho} - \left(2\log_e \frac{l}{\sqrt{S}} + \phi\right) + \frac{\mu}{4}\right] \tag{7}$$

where l is the perimeter of the ESRR (Appendix A); and $S = \pi ab$ is the area of the ESRR; ρ is half of the thickness of the cross-section of the conductor ($= c/2$ for ESRR); and μ is the permeability of the conductor, taken to incorporate the internal linkage of the flux in the cross section of the conductor. The parameter ϕ is a constant which depends on the geometry of the closed loop. In case of ESRR, $\phi \cong -0.034$, when eccentricity $e = 1/\sqrt{2}$. For other values of e, the corresponding ϕ is tabulated in [7].

2.4. Resonant Frequency Computation

The resonant frequency f_o of the ESRR can be computed using $eq^n_{\ldots}$ (1) by substituting C_{net} and L_{net} from $eq^n_{\ldots}$ (4) and $eq^n_{\ldots}$ (7) respectively. Clearly, f_o is a strong function of the geometrical and electrical parameters.

3. GENETIC ALGORITHM OPTIMIZATION

3.1. Genetic Algorithms Steps

Step 1: Create an initial population of all the parameter forming a binary sequence known as chromosomes.

Step 2: Rank the chromosomes according to their fitness using fitness function and select the best few.

Step 3: Perform *Cross-Breeding* and *Mutation* to get the next generation offspring with new characteristics.

Step 4: Repeat *Step 2* and *Step 3* for a number of generations to get the overall best candidate chromosomes.

Step 5: Extract the optimal valued chromosomes and plot them to get the least error and best candidates.

It should be noted that the initial population must be large enough so that there is no domination of gene. This ensures satisfactory convergence to obtain the optimal values.

3.2. Implementation of Genetic Algorithm for ESRR Optimization

The Genetic Algorithm optimization of the physical parameters of the ESRR is carried out in MATLAB, with the numerical data tabulated in Table 1.

3.3. Genetic Algorithm Optimized Results

Genetic Algorithm optimization of ESRR in MATLAB yields the optimized parameter values, that are tabulated in Table 2. They are best suited to match the desired frequency and minimize the error.

The optimized population swarm of the 4 parameters viz. 'a', 'b', 'c' & 'd' for minimum relative error between the desired and the calculated frequency are plotted in Figure 2.

Table 1: Numerical range and value of parameters for MATLAB simulation.

Parameter	Range/Value	Parameter	Range/Value
Major Axis	$5\,\text{mm} < 2a < 11\,\text{mm}$	μ	1 (FR4 Substrate)
Minor Axis	$2\,\text{mm} < 2b < 8\,\text{mm}$	ε_r	4 (FR4 Substrate)
Conductor Width	$0.01\,\text{mm} < c < 0.2\,\text{mm}$	Desired Frequency	22 GHz
Conductor Spacing	$0.01\,\text{mm} < d < 0.3\,\text{mm}$	% Crossover	45%
Split Gap	$g = 0.3\,\text{mm}$	% Mutation	4%
Substrate Depth	$h = 0.5\,\text{mm}$	Total Population	800

Table 2: GA optimized parameter values for best performance of ESRR.

Parameter	Best Value	Parameter	Best Value
Major Axis	$2a = 5\,\text{mm}$	Conductor Width	$c = 0.2\,\text{mm}$
Minor Axis	$2b = 2\,\text{mm}$	Conductor Spacing	$d = 0.3\,\text{mm}$

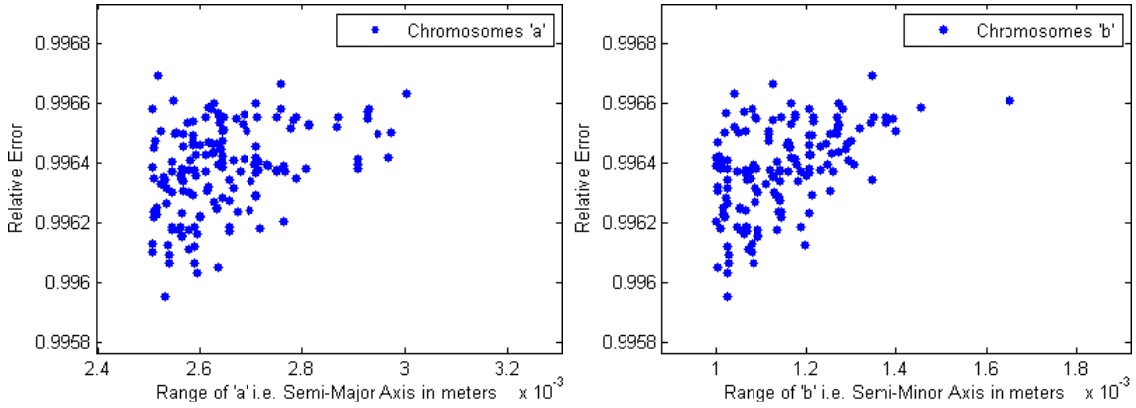

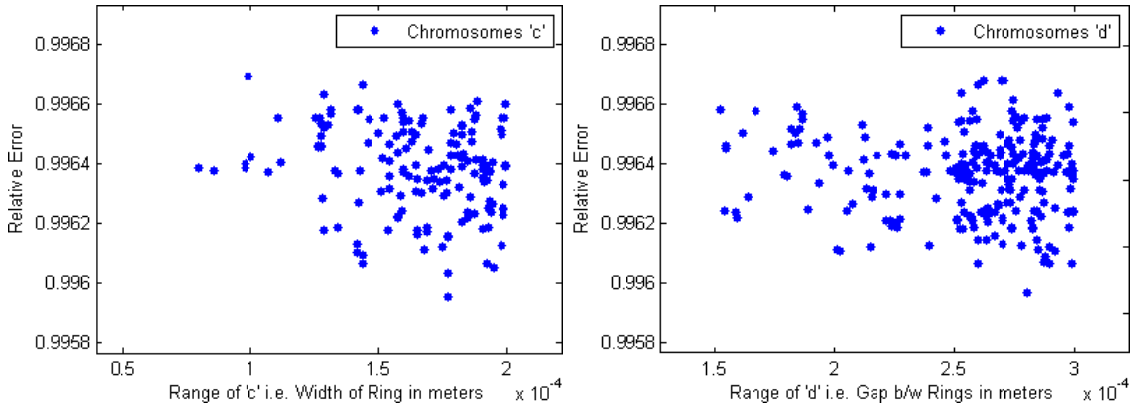

Figure 2: Plot of relative error in frequency vs. range of 'a', 'b', 'c' & 'd'.

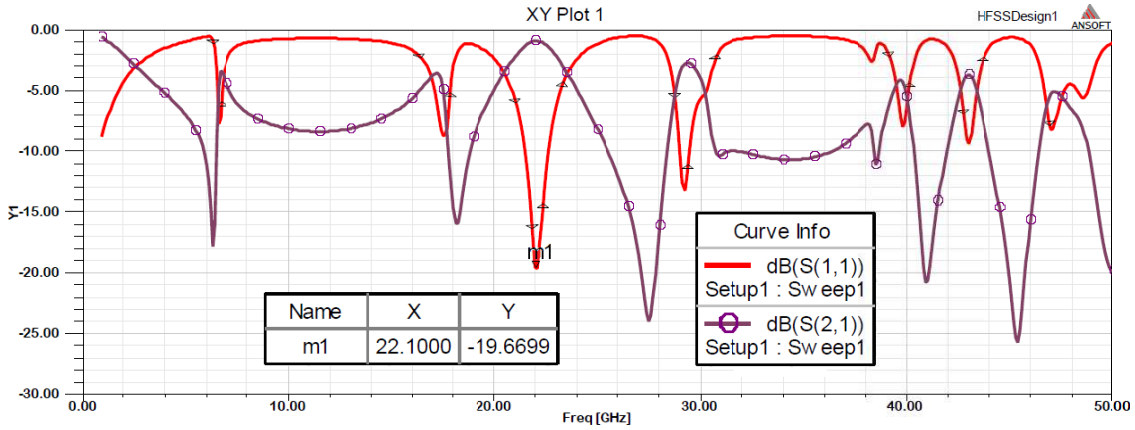

Figure 3: Scattering parameters (S_{11} & S_{21}) of ESRR modelled in HFSS over a frequency sweep of 0–50 GHz.

4. HFSS MODELING OF ESRR: NRIM PROPERTY VALIDATION

The ESRR has been modeled in Finite Element Method (FEM) based Electromagnetic (EM) CAD Tool HFSS (High Frequency Structure Simulator) using the optimized physical parameter values of Table 2. The Scattering Parameter plot of the ESRR generated using HFSS is shown in Figure 3. The crossovers of S_{11} & S_{21} at multiple frequency bands clearly indicate the enhanced NRIM property of the ESRR [2].

5. RESULTS & CONCLUSION

The Elliptical Split Ring Resonator (ESSR) geometry was discussed, followed by a detailed mathematical analysis by considering its geometrical dimensions and electrical specifications such as the μ and ε_r of the substrate in itself. A novel closed form expression for the resonant frequency was derived considering all the associated and affecting parameters. It is noteworthy that a designer can start with the Circular SRR and then deviate the semi-major axis, 'a' and the semi-minor axis, 'b' away from the radius value of the CSRR. This gives the designer 2 tweaking parameters, viz. 'a' & 'b', to accurately design an ESRR resonating at certain desired resonant frequency. Varying the 'a' & 'b' essentially varies the C_{net} (due to varying 'l' in C_{ring} — Equation (2)), and also L_{net} (due to varying 'l' & 'S' in L_{net} — Equation (7)); but there are no changes in C_{gap} and C_{pul} as these do not depend on 'a' & 'b'. However these may be varied by changing 'c', 'd', 'g' & 'h'.

The optimum geometrical dimensions of the ESRR were estimated for a desired resonant frequency. MATLAB based Genetic Algorithm (GA) Optimization was used to successfully converge the values of geometrical dimensions of the ESRR for a particular desired resonant frequency value by minimizing the frequency estimation error. The optimum geometrical dimensions value has been tabulated with remarks.

The CAD model of the ESRR was simulated on a commercially available electromagnetic simulator, High Frequency Structure Simulator (HFSS) based on the Finite Element Method elec-

tromagnetic mode solver. The S-parameters (S_{11} & S_{21}) of the ESRR were plotted for a range of frequency sweep. The cross-cuttings in the S_{11} & S_{21} plot give the indication of the NRIM property of the ESRR. An ESRR loaded microstrip antenna can be used efficiently for wireless communication in the microwave regime due to its NRIM property.

APPENDIX A

The perimeter l of an ellipse with semi-major axis 'a' and semi-minor axis 'b' can be expressed as an infinite series, called the *Gauss-Kummer Formula*, utilizing the hypergeometric function $F(\cdot)$ where:

$$l = \pi(a+b) \cdot F\left(-\frac{1}{2}, -\frac{1}{2}; 1; \left\{\frac{a-b}{a+b}\right\}\right) = \pi(a+b) \cdot \int_{n=0}^{\infty} \begin{pmatrix} 1/2 \\ n \end{pmatrix} \cdot \left\{\frac{a-b}{a+b}\right\}^{2n}$$

APPENDIX B

The per-unit-length capacitance $C_{pul} = \varepsilon_o \cdot \left(\frac{\varepsilon_r+1}{2}\right) \cdot \frac{E\left(\sqrt{1-\sigma^2}\right)}{E(\sigma)}$, where $\sigma = \frac{d}{d+2c}$ and $E(\cdot)$ is the complete elliptical integral of the second kind, defined as $E(k) = \int_0^{\pi/2} \sqrt{1-(k\sin\theta)^2}\, d\theta$.

REFERENCES

1. Noginov, M. A. and V. A. Podolskiy, *Tutorials in Metamaterials*, CRC Press, May 2010.
2. Sharma, V., "A microstrip metamaterial split ring resonator," *Int. J. of Physical Sciences*, Vol. 6, 2011.
3. Maxwell, J. C., *A Treatise on Electricity and Magnetism*, Clarendon Press, Oxford, 1881.
4. Jeans, S. J. H., *The Mathematical Theory of Electricity and Magnetism*, Cambridge University Press, 1925.
5. Cooke, N., "Self-inductance of the elliptical loop," *Proc. of the Inst. of Elec. Engrs.*, Vol. 110, No. 7, 1963.
6. Bashenoff, V. J., "Abbreviated methods for calculating the inductance of irregular plane polygons of round wire," *Proc. Inst. Radio Engrs.*, 1927.
7. Grover, F., *Inductance Calculations: Working Formulas and Tables*, Dover Publications, New York, 1946.

Novel Microstrip-fed UWB Antenna with CSRR Slot for Signal Rejection in 5–6 GHz Band

S. Raghavan, **A. Subbarao**, **and M. Ramaraj**
National Institute of Technology, Tiruchirappalli 620015, India

Abstract— A compact microstrip-fed antenna is proposed for Ultra-wide band applications. The antenna has compact size of $25 \times 30\,\text{mm}^2$. The antenna has $-10\,\text{dB}$ impedance bandwidth from 2.7 GHz to 12 GHz. Details of antenna are presented with parametric study. The antenna has consistent gain and stable radiation pattern. Later, the design was modified with complementary split ring resonator (CSRR) slot to avoid interference from 5–6 GHz WLAN band. The antenna is analyzed with method of moment based Ie3D electromagnetic solver. The results meet standard specifications.

1. INTRODUCTION

Ultra-wide band (UWB) technology has become more popular due to various applications such as ground penetrating radar, medical imaging and sensor networks [1–3]. Antenna is key component in UWB systems and its design has become challenging task for antenna designers. The antenna should also be compact and easily be integrated with RF and microwave circuitry. The antenna should be designed with stable radiation pattern and broad impedance bandwidth. Federal Communication commission (FCC) has assigned a frequency bandwidth of 3.1–10.6 GHz for commercial UWB applications. Several wideband antennas like log periodic, bow-tie and vivaldi antennas [4, 5] were designed for UWB communications. But, they are unable to be integrated with low profile RF circuitry. Several broad band antennas such as pentagonal, stacked patch and plate antennas [6–8] have been designed for UWB communications. They have large bandwidth, simple structure and stable radiation pattern. But, there is a disadvantage in these antennas that the radiator is perpendicular to ground layer, which increases the size of antenna.

Printed planar structures have become popular for design of UWB antenna due to wide bandwidth and ease of fabrication and low cost. Recently, printed monopole antenna has been designed [9]. But, it has large size of $100 \times 85\,\text{mm}^2$. The antenna design is specified and parametric study is performed to observe the effects of various geometrical parameters of antenna. The radiation pattern and gain are discussed. The antenna design is modified with CSRR slot to reject WLAN band to avoid interference signals.

2. ANTENNA DEDIGN

The antenna is printed on FR4 substrate with dielectric permittivity of 4.4, thickness of 1 mm as shown in Figure 1. The antenna is fed by microstrip feed. The feed has width of 2 mm and height of 10.5 mm to obtain $50\,\Omega$ impedance characteristic. The microstip feed has SMA connector at its end. The antenna has compact size of $25 \times 30\,\text{mm}^2$. The antenna has half circular shaped slot at the top of ground plane to provide wide impedance bandwidth. The parameters of antenna are optimized to obtain wide impedance matching over UWB. The various optimized parameters are $W = 25\,\text{mm}$, $W_1 = 11.5\,\text{mm}$, $W_2 = 2\,\text{mm}$, $W_3 = 4.62\,\text{mm}$, $W_4 = 2\,\text{mm}$, $W_5 = 5.8\,\text{mm}$, $L = 30\,\text{mm}$, $L_1 = 10.5\,\text{mm}$, $L_2 = 0.7\,\text{mm}$, $L_3 = 4.9\,\text{mm}$, $L_4 = 4.45\,\text{mm}$, $L_5 = 2.4\,\text{mm}$, $r = 11\,\text{mm}$, $M = 2\,\text{mm}$, $N = 3.5\,\text{mm}$. A rectangular slot is etched at lower middle of ground to provide better impedance matching between 4 GHz and 7 GHz.

3. RESULTS AND DISCUSSION

The proposed antenna is simulated and optimized with method of moment based Ie3D electromagnetic solver. The return loss response of the antenna is shown in Figure 2(a). The curve indicates that the antenna has operating bandwidth from 2.7 GHz to 12 GHz which covers entire UWB.

The antenna has three resonant frequencies 3.75 GHz, 6.86 GHz and 8.4 GHz. The Ultra-wide bandwidth is achieved due to overlapping between these three resonant frequencies. Parametric study is performed on antenna to observe the effect of sensitive parameters of antenna. Figure 2(b) shows the effect of different lengths L_2 on return loss. When L_2 decreases from 1.3 mm to 0.1 mm, first and second resonant frequencies increase. The impedance matching becomes poor at higher frequencies, which result in the reduction of bandwidth.

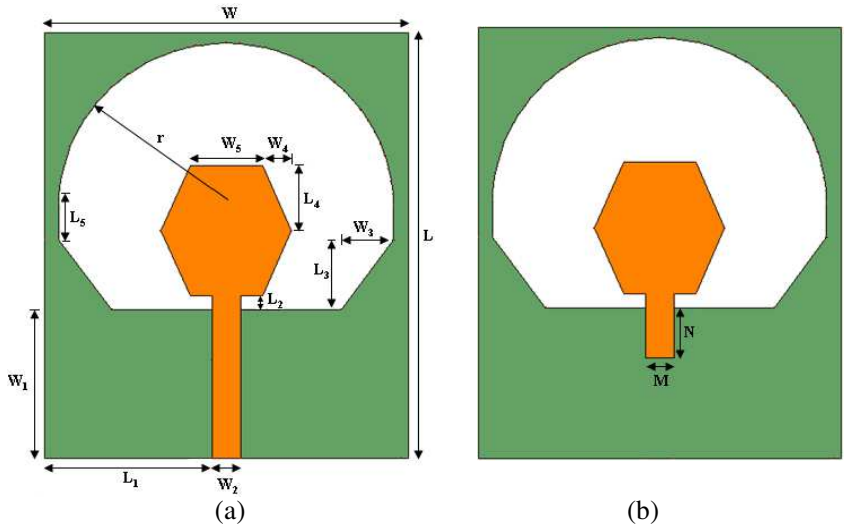

Figure 1: Structure of proposed antenna. (a) Front view. (b) Back view.

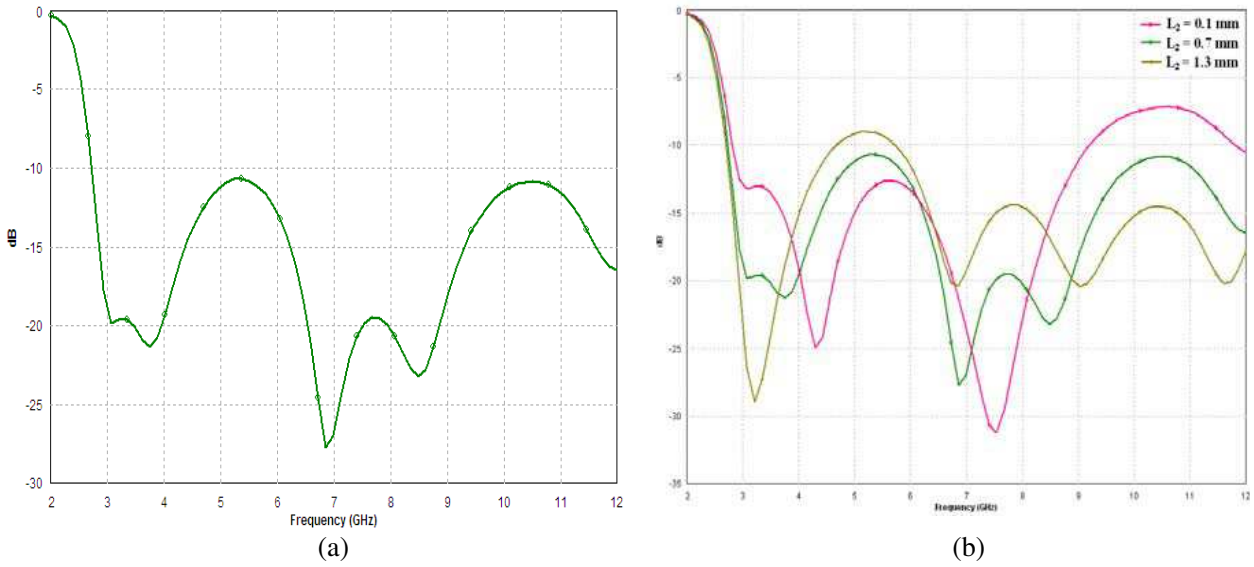

Figure 2: (a) Return loss of proposed antenna against frequency. (b) Effect of height L_2 on return loss.

Figure 3 presents the change in return loss for various radii 'r' of half circular slot in ground plane. When r increases from 10 mm to 12 mm, impedance becomes poor at higher frequencies and resonant frequencies also change. Hence, the antenna has better impedance matching with UWB at $r = 11$ mm. It is concluded from Figure 3 that the antenna has good impedance matching at $r = 11$ mm. The gain of antenna is shown in Figure 4. The antenna has reasonably good constant gain in the operating band.

Figures 5(a) and 5(b) present radiation patterns of proposed antenna at 3.75 GHz, 6.86 GHz and 8.48 GHz in both E-plane and H-planes respectively. The antenna has monopole-like radiation pattern in E-plane and the pattern is not distorted even at higher frequencies. The antenna has omni-directional radiation pattern in H-plane. The antenna has almost 80% efficiency in the operating bandwidth. The compact size, stable radiation pattern make the antenna suitable for UWB applications.

4. BAND NOTCHED DESIGN

The band-notched UWB antenna is important to avoid interference from in 5–6 GHz WLAN band. The proposed antenna shown in Figure 1 is modified to include circular CSRR slot in hexagonal patch to reject the WLAN band and is presented in Figure 6. The optimized dimensions of CSRR

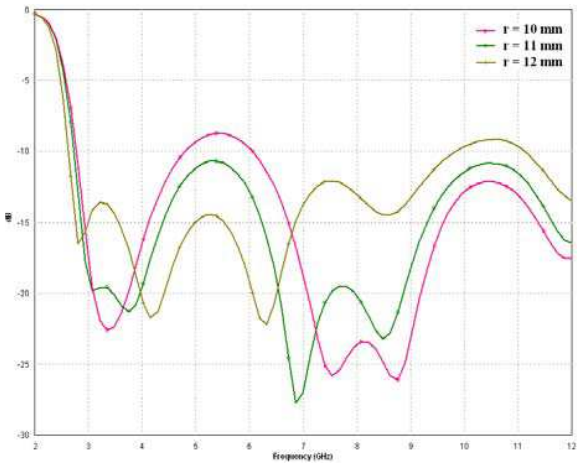

Figure 3: Effect on return loss for different slot radii r.

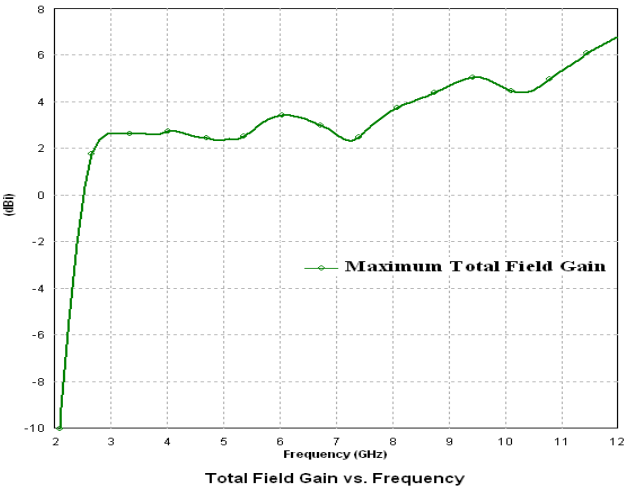

Figure 4: Gain of antenna against frequency.

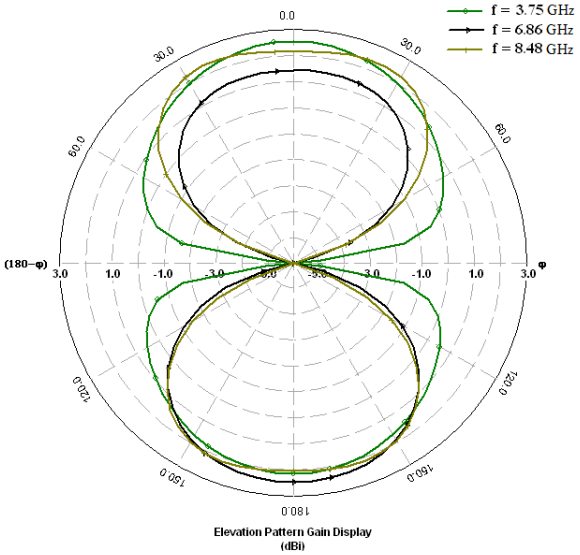

(a)

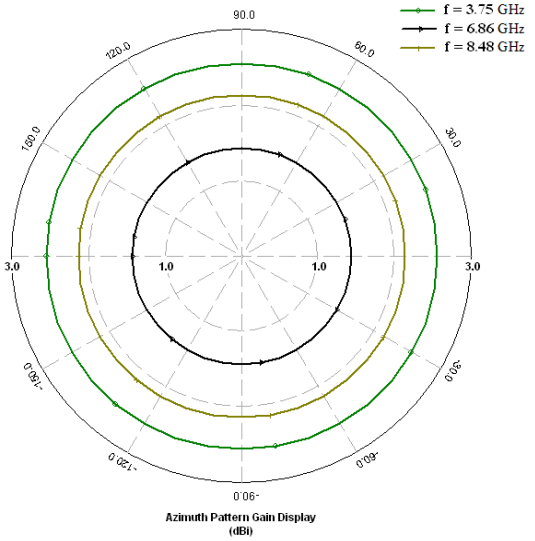

(b)

Figure 5: Radiation pattern at 3.75 GHz, 6.86 GHz, 8.48 GHz in (a) E-plane. (b) H-plane.

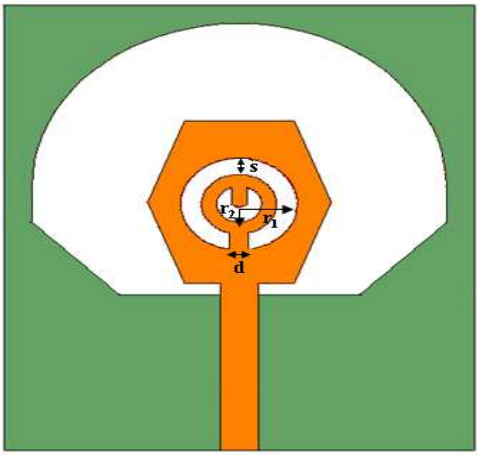

Figure 6: Band notched antenna design.

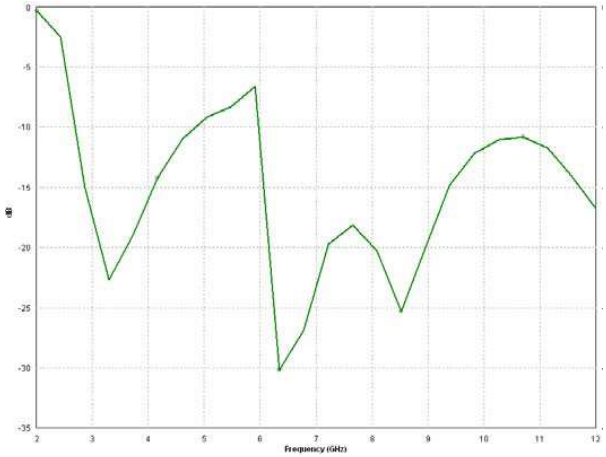

Figure 7: Return loss of band-notched antenna.

slot are $r_1 = 3\,\text{mm}$, $r_2 = 1.3\,\text{mm}$, $s = 1\,\text{mm}$, $d = 0.8\,\text{mm}$. The Figure 7 shows that the $-10\,\text{dB}$ impedance bandwidth of band-notched UWB antenna is from 3.1 GHz to 12 GHz with rejected WLAN band of 5–6 GHz. It confirms rejection of interference signals from WLAN band.

5. CONCLUSIONS

A hexagonal monopole antenna with a half circular slot in ground plane is presented for UWB applications. The antenna has compact size of $25 \times 30\,\text{mm}^2$ and it can be easily integrated with microwave circuitry with low cost. The antenna has operating bandwidth from 2.7 GHz to 12 GHz, which fully covers bandwidth specified by FCC. The antenna has consistent gain and stable radiation pattern. The antenna is modified with CSRR slot to avoid interference from 5–6 GHz WLAN band.

REFERENCES

1. Viani, F., L. Lizzi, R. Azaro, and A. Massa, "A miniaturized UWB antenna for wireless dongle devices," *IEEE Antennas and Wireless Propagation Letters*, Vol. 7, 714–717, 2008.
2. Turk, S. and H. Nazli, "Hyper-wide band TEM horn array design for multi band impulse ground penetrating radar," *Microwave and Optical Technology Letters*, Vol. 5, No. 1, 76–81, 2008.
3. Bialkowski, M., W. Khor, and S. Crozier, "A planar microwave imaging system with step-frequency synthesized pulse using different calibration methods," *Microwave and Optical Technology Letters*, Vol. 48, No. 3, 511–516, 2006.
4. Mehdipour, A., K. M. Aghdam, R. F. Dana, and A. R. Sebak, "Modified slot bow-tie antenna for UWB application," *Microwave and Optical Technology Letters*, Vol. 50, No. 2, 429–432, 2008.
5. Cerny, P., J. Nevrly, and M. Mazane, "Optimization of tapered slot Vivaldi antenna for UWB application," *International Conference on Applied Electromagnetics and Communications,* 1–4, 2007.
6. Toh, W. K., Z. N. Chen, and X. Qing, "A planar UWB antenna with a broadband feeding structure," *IEEE Transactions on Antennas and Propagation*, Vol. 57, No. 7, 2172–2175, 2009.
7. Shakib, M. N., M. T. Islam, and N. Misran, "Stacked patch antenna with folded patch feed for ultra-wideband application," *IET Microwaves, Antennas & Propagation*, Vol. 4, No. 1, 1456–1461, 2010.
8. Antonino-Daviu, E., M. Cabedo-Fabre's, M. Ferrando-Bataller, and A. Valero-Nogueira, "Wideband double-fed planar monopole antennas," *Electronics Letters*, Vol. 39, No. 23, 1635–1636, 2003.
9. Nazli, H., E. Bicak, B. Turetken, and M. Sezgin, "An improved design of planar elliptical dipole antenna for UWB applications," *IEEE Antennas and Wireless Propagation Letters*, Vol. 9, 264–267, 2010.

Performance Enhancement of Patch Antenna by Fishnet Metamaterial

Anand Kumar and Dinesh Kumar Vishwakarma
PDPM Indian Institute of Information Technology, Design and Manufacturing, Jabalpur, India

Abstract— In this paper, a novel fishnet metamaterial structure operating around 93 GHz was investigated and this structure is used as a cover to a patch antenna having same resonant frequency to enhance its performance. Metamaterials are artificial materials engineered to have properties that may not be found in nature and recently they are widely being used to improve the performance of antenna. This paper describes a novel way to improve the gain and directionality of Patch antenna. The gain of antenna is improved very near to its theoretical maximum value. Effective medium theory and standard parameter retrieval methods were used to show that the fishnet structure have the value of effective permittivity and effective permeability negative simultaneously over a frequency range 85 to 98 GHz. We retrieved real part of permittivity $\mathrm{Re}(\varepsilon_{\mathrm{eff}}) = -2.2$ and real part of permeability $\mathrm{Re}(\mu_{\mathrm{eff}}) = -2$, this tends to the negative value of refractive index. These parameters value of the metamaterial verifies its left-handed behavior. The radiation pattern of final structure is investigated which shows that the metamaterial cover has increased the gain of the patch antenna by a value of 10.96 dB at an operating frequency of combined structure 88.56 GHz. The reason of this improvement is given and the variation of gain as a function of separation between patch and metamaterial cover is given.

1. INTRODUCTION

Metamaterials is a term consists of Meta + Material, which means a material having property beyond the property of naturally occurring materials. These materials are also called the Double Negative Material (DNG) because they have the value of permeability and permittivity both negative. These materials are first introduced by V. G. Veselago [1] in 1964. In the recent years, this field attracts the attention of many researchers who investigated the interesting properties of these materials. Pendry first investigated the propagation of light through this material and proposed the possibility that a DNG material have a negative index of refraction that may overcome the limitation of the conventional lenses and perfect lenses can be realized which could focus both the propagating as well as evanescent spectra [2].

In recent years metamaterial has attracted the attention of many antenna engineers and it is widely used for the improvement of the characteristics of patch antenna [3–7]. Metamaterial have periodic structures like photonic band gap structures. In this paper, it is used as a cover of an antenna, which is illuminated by the radiation of the antenna and all the dielectric elements of the cover, is exited which acts as aperture antenna and hence improve the directivity of the antenna.

2. DESIGN AND RESULT

2.1. Metamaterial Design

It has already been shown that a structure consists of metal rods arranged in a fishnet type structure can exhibit the DNG behavior at optical frequency range [8]. We investigated the fishnet structure at microwave frequency. To obtain this we used PEC rods in periodic manner both sides of a substrate in a fishnet like shape. The unit cell of this structure is given in Fig. 1. This structure is quite different from the fishnet structure described in [8]. It contains two electric conductors in a single unit cell. For the polarization configuration shown in Fig. 1 the structure can be thought of as consisting of double-plate as "magnetic atoms" and long wires as "electric conductor" [9, 10]. When the period of square lattice is less than the operating wavelength, this structure can be viewed as a metal thin wire array. This Metamaterial structure has characteristic response to electromagnetic wave due to plasma resonance of the electron gas. Many researchers have shown experimentally and theoretically that such a structure of continuous wire can be characterized by a resonance frequency. Approximate analytical theory and homogenization theory shows that the effective permittivity has a behavior governed by the plasma frequency given as

$$\varepsilon_{\mathrm{eff}} = 1 - \omega_p^2/\omega^2 \tag{1}$$

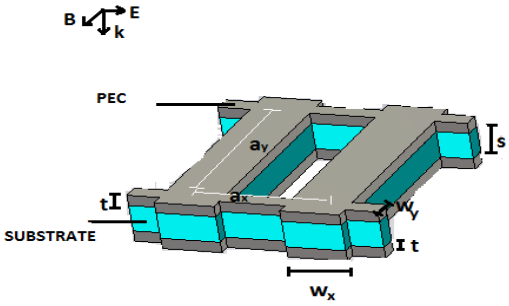

Figure 1: Fishnet unit cell. The metamaterial unit cell given has a length and width of $-2.61\,\text{mm}$, a substrate with dielectric constant 2.3 with $S = 0.22\,\text{mm}$, width of electric conductor $W_y = 0.14\,\text{mm}$ and magnetic conductor $W_x = 0.6214\,\text{mm}$ wide the thickness of these metal plates $t = 0.02\,\text{mm}$. The periodicity of electric field rods $a_x = 2.175\,\text{mm}$ and the periodicity of magnetic rods $a_y = 1.205\,\text{mm}$. Our metamaterial cover is composed of $7 * 7$ unit of these unit cells.

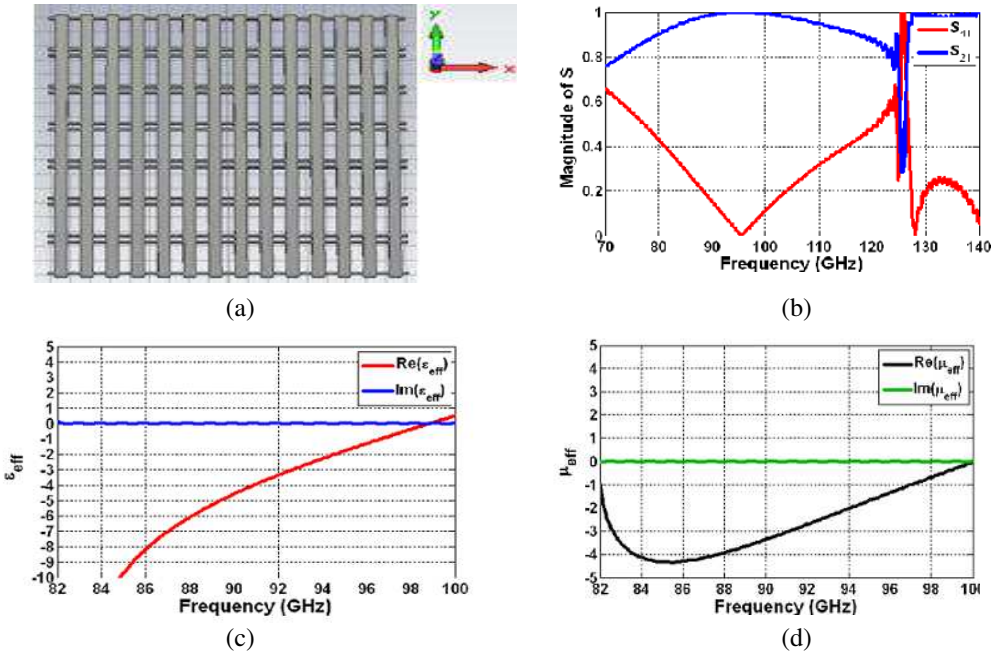

Figure 2: Various parameters of fishnet structure alone. (a) Metamaterial structure. (b) S-parameters results from the simulation of metamaterial structure. (c) Effective permittivity (ε_{eff}). (d) Effective permeability (μ_{eff}).

Here ω_p is the plasma frequency and ω is the frequency of electromagnetic wave. Now depending upon the frequency the permittivity can be positive or negative.

By considering effective medium theory and using standard parameter retrieval technique to retrieve the parameters from these S-parameters [11]. We found that over a range of microwave frequency the value of effective permittivity $\text{Re}(\varepsilon_{\text{eff}})$ and effective permeability $\text{Re}(\mu_{\text{eff}})$ is simultaneously less than zero. The negative permittivity in this structure is due to the periodic arrangement of thin wire which acts like a continuous plasma [12], and the negative permeability is due to the Plasmon resonance between the two layers of metallic plates [13]. Richard Ziolkiowski and Heyman have recently investigated the propagation of wave through the medium having negative permittivity and negative permeability and shows that such medium shows Left Handed behavior and have negative index of refraction $\text{Re}(n_{\text{eff}})$ [14].

When this metamaterial structure is simulated under open boundary condition and with a plane wave source, we obtained the transmission parameters as shown in Fig. 2(a). The transmission and reflection coefficient of the metamaterial shows that this structure has maximum transmission at a frequency about 94 GHz. Retrieved permittivity and permeability is shown in Figs. 2(b) and 2(c) respectively. Result shows that the real part of effective permittivity and permeability has

negative value over a range of frequency and it shows that this structure is having negative index of refraction and possesses left-handed behavior around the frequency of operation. At this frequency the value of $\mathrm{Re}(\varepsilon_{\mathrm{eff}})$ and $\mathrm{Re}(\mu_{\mathrm{eff}})$ is about -2.2 and -2 respectively.

2.2. Antenna Design

A patch antenna having an operating frequency around 95 GHz is designed. The antenna and its transmission parameters are shown in Fig. 3. A co-axial feed Patch antenna with a 0.22 mm thick substrate having dielectric constant of 1.5 is shown in Fig. 3(a). Length and Width of substrate are 9 mm each. The length and width of patch are 1.5714 mm and 1.1 mm respectively. Fig. 3(b) shows the return loss of the antenna which have a resonance around 93 GHz. The radiation pattern of this antenna shows a gain of 8.52 dB and a HPBW is around 76.3 degree at this frequency.

2.3. Metamaterial Antenna

The combined structure of Metamaterial Antenna and its radiation characteristics are shown in Fig. 4. When we placed the metamaterial cover over the patch every element of cover got illuminated by the radiation of patch antenna and since the cover is a left-handed material it shows the congregation effect for the radiation and focus field in a single direction this effect is similar to the congregation effect of convex lenses for the light rays [15]. It is clear from the transmission parameters shown in Fig. 4(b) that the metamaterial structure has increased the return loss of the antenna and hence gain. Obviously, the frequency of operation has been shifted to 88.66 GHz but it does not affect the scope of impedance [3]. The radiation from patch antenna alone and with the metamaterial cover is shown. The radiation from a patch antenna alone has a spherical wave front but metamaterial convert this spherical wave front into a flat and it verifies the.

In this design the gain and the directionality of the antenna depends on the separation 'd' of the patch antenna and the metamaterial cover. The variation of the gain with different value of 'd' is shown in Fig. 6.

For a optimum distance $d = 18.21$ the gain is maximum and at this distance the HPBW of the antenna is around 5.2 degree.

Theoretically the maximum directivity of an aperture antenna is $D_{\max} = 4\pi A/\lambda^2$, where $A = 9\,\mathrm{mm} * 9\,\mathrm{mm}$, $\lambda = c_0/f_0 = 3.2258\,\mathrm{mm}$ and the gain $G_{\max} = k * D_{\max}$, k is the efficiency assuming $k = 1$ the maximum gain of the aperture antenna is around 19.91 dB. Our result shows that the gain of the metamaterial antenna is already very close to the maximum possible gain of the antenna with the same size.

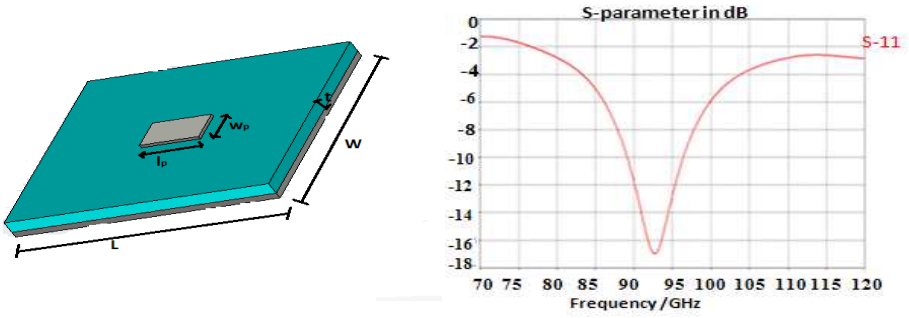

(a) (b)

Figure 3: Patch Antenna. (a) Antenna design. (b) Transmission parameter of antenna.

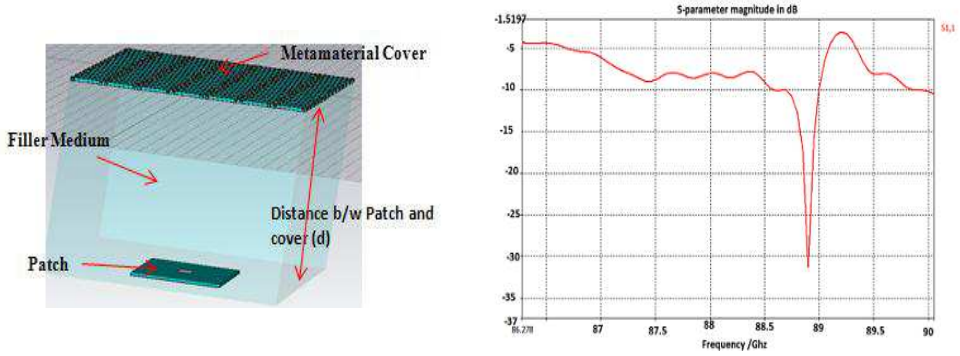

(a) (b)

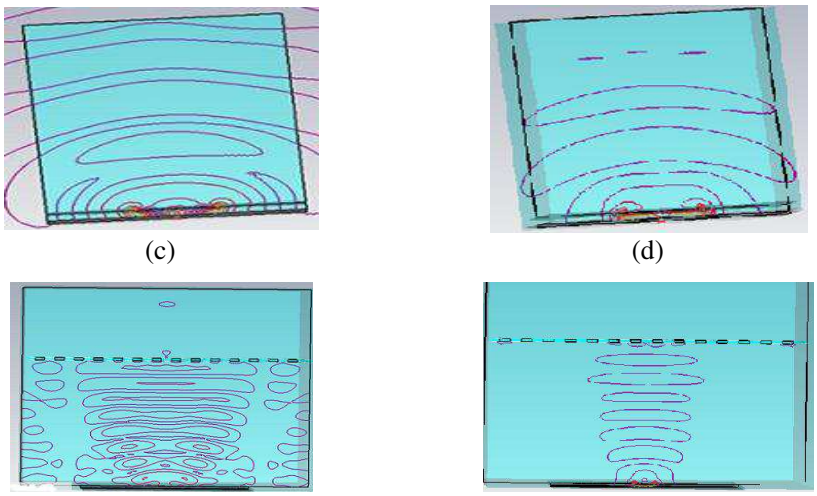

(c) (d)

(e) (f)

Figure 4: Patch with metamaterial as a cover and the field distribution inside the structure. (a) Combined structure of antenna where metamaterial structure is placed on a material of dielectric constant 1.24 separating it from the patch. (b) Return loss of combined structure. (c) Electric field distribution of patch alone. (d) Magnetic field distribution of patch alone. (e) Electric field distribution of patch with cover. (f) Magnetic field distribution of patch with cover.

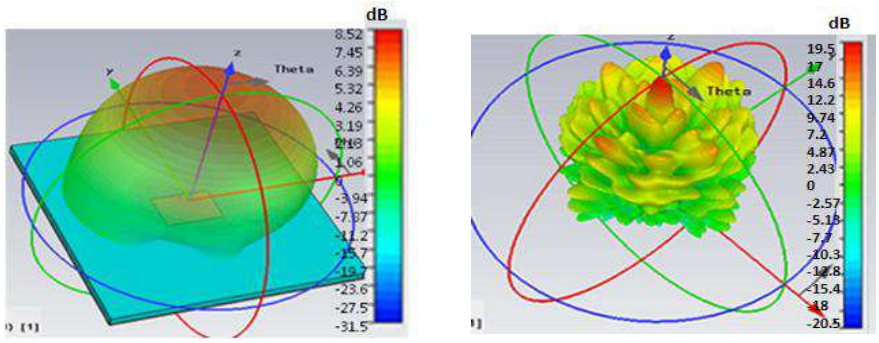

(a) (b)

Figure 5: Radiation pattern of the antenna. (a) Conventional antenna. (b) Antenna with metamaterial cover.

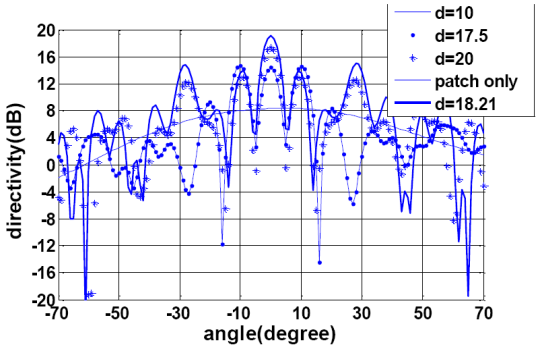

Figure 6: Variation of gain for different distances between patch and metamaterial.

Table 1: The electrical characteristics of antenna with and without metamaterial cover.

	Gain (dB)	**HPBW (x-z plane)**	**HPBW (y-z plane)**
Conventional antenna	8.52	72.2°	72.1°
Metamaterial antenna	19.5	5.2°	6.5°

3. CONCLUSION

In this paper, a new fishnet type metamaterial structure operating at microwave range is designed and its radiation characteristic and parameters are verified. By selecting working frequency its effective index is around -2. This structure is used as a cover for the conventional type patch antenna and its near and far field patters were investigated. The combined structure shows 10.96 dB improvement in the gain and a great improvement in the directionality. These improvements are better than given in [3] and [4], where a similar patch antenna operating under the metamaterial cover was discussed. Here only one layer of metamaterial was used and this structure is quite small and lighter in weight.

REFERENCES

1. Veselago, V. G. and P. N. Lebedev, "The electrodynamics of substances with simultaneously negative value of ε and μ," *Usp. Fiz. Nauk*, Vol. 92, 517–526, Physics Institute, Academy of Sciences, U.S.S.R., July 1964.
2. Pendry, J. B., "Negative refraction makes a perfect lens," *Physical Review Letters*, Vol. 85, No. 21, 3966–3969, 2000.
3. Hu, J., C.-S. Yan, and Q.-C. Lin, "A new patch antenna with metmaterial cover," *Journal of Zhejiang University SCIENCE A*, Vol. 7, No. 1, 89–94, 2006.
4. Weng, Z.-B., N.-B. Wang, and Y.-C. Jiao, "Study on high gain patch antenna with metamaterial cover," *Antennas, Propagation & EM Theory*, 2006.
5. Zhou, H., Z. Pei, S. Qu, S. Zhang, and J. Wang, "A novel high directivity microstrip patch antenna based on zero-index metamaterial," *IEEE Antennas and Wireless Propagation Letters*, Vol. 8, 2009.
6. Burokur, S. N., M. Latrach, and S. Toutain, "Theoretical investigation of a circular patch antenna in the presence of a left-handed medium," *IEEE Antennas and Wireless Propagation Letters*, Vol. 4, 2005.
7. Li, L.-W., Y.-N. Li, T. S. Yeo, J. R. Mosig, and O. J. F. Martin, "A broadband and high gain metamaterial microstrip antenn," *Applied Physics Letters*, Vol. 96, 164101, 2010.
8. Dolling, G., C. Enkrich, and M. Wegener, "Low-loss negative-index metamaterial at telecommunication wavelengths," *Optics Letters*, Vol. 31, No. 12, June 15, 2006.
9. Dolling, G., C. Enkrich, M. Wegener, J. Zhou, C. M. Soukoulis, and S. Linden, *Optics Letters*, Vol. 30, 3198, 2005.
10. Grigorenko, N., A. K. Geim, H. F. Gleeson, Y. Zhang, A. A. Firsov, I. Y. Khrushchev, and J. Petrovic, *Nature*, Vol. 438, 335, 2005.
11. Szabó, Z., G.-H. Park, R. Hedge, and E.-P. Li, "A unique extraction of metamaterial parameters based on Kramers-Kronig relationship," *IEEE Transactions on Microwave Theory and Techniques*, Vol. 58, No. 10, October 2010.
12. Sigalas, M. M., C. T. Chan, K. M. Ho, and C. M. Soukoulis, "Metallic photonic band-gap materials," *Physical Review B*, Vol. 52, 11744–11751, 1995.
13. Pendry, J. B., A. J. Holden, D. J. Robbins, and W. J. Stewart, "Magnetism from conductors and enhanced nonlinear phenomena," *IEEE Transactions on Microwave Theory and Techniques*, Vol. 47, No. 11, November 1999.
14. Ziolkowski, R. W. and E. Heyman, "Wave propagation in media having negative permittivity and permeability," *Physical Review E*, Vol. 64, No. 5, 056625:1–15, 2001.
15. Enoch, S., G. R. Tayeb, P. Sabouroux, N. G. Guérin, and P. Vincent, "A metamaterial for directive emission," *Physical Review Letters*, Vol. 89, 213902, 2002.

A Improved Structure for Substrate Integrated Waveguide Composite Right/Left-handed Cell

Qingshan Yang, Xiangkun Zhang, and Yunhua Zhang
Key Laboratory of Microwave Remote Sensing
Chinese Academy of Sciences, Beijing 100190, China

Abstract— The composite right/left-handed (CRLH) transmission line (TL) based leaky-wave antennas (LWAs) are usually constrained by wide frequency scanning bandwidths to achieve certain beam scanning range. This is mainly due to that the fast wave region of the CRLH cell dispersion is insensitive to the frequency. In this work, we propose a substrate integrated waveguide (SIW) CRLH cell structure with dispersion sensitivity improved. This advantage makes the structure have a narrower fast wave region and thus have a potential application to the LWA with a large beam scanning range (BSR)/bandwidth ratio. The simulated and experimental results of this CRLH unit cell are both given to confirm the validity of the dispersion sensitivity promotion.

1. INTRODUCTION

The CRLH TL metamaterials are known as artificial electromagnetic structures that have been studied extensively due to its unique properties, especially its application in LWAs to achieve broadside radiation that is hard to achieve for traditional LWAs [1, 2]. Many CRLH TL cell structures using microstrip, planar waveguide, SIW etc. were proposed and applied to the LWAs to achieve continuous beam steering from the backward to forward [2–4]. However, the CRLH LWAs reported before are usually constrained by wide frequency scanning bandwidths to achieve certain scanning range [2–4]. The main reason is that the proposed CRLH cell dispersions are insensitive to the frequency in the fast wave region, especially in the right-handed radiating region, thus cause a wide frequency bandwidth for the propagation constant β changing from $-k_0$ to $+k_0$, where k_0 is the wave number in the air. Till now, little work has been done with the sensitivity of propagation constant for the CRLH cell. In this paper, we will study this problem and propose a SIW CRLH cell structure with improved dispersion sensitivity so as to achieve large beam scanning range (BSR)/bandwidth ratio for LWAs.

Three parts are mainly contained in this paper. In Section 2, the CRLH dispersion is discussed to analyze the potential possibility of sensitivity promotion. In Section 3, the CRLH cell structure is proposed based on the analysis in Section 2. In Section 4, the proposed structure is simulated, fabricated and measured, and the sensitivity of the CRLH structure is demonstrated. Finally, a conclusion is drawn in Section 5.

2. PRINCIPLE

A CRLH TL cell is composed of left-handedness and right-handedness, where the left-handed (LH) components contain series capacitance C_L and shunt inductance L_L, while the right-handed (RH) components are series inductance L_R and shunt capacitance C_R, respectively. Two types of CRLH TL called balanced and unbalanced CRLH TLs are distinguished by whether or not the series and shunt resonant frequencies are equal with each other [1]. In practical application, the prior type of CRLH TL is usually preferred because no gap (stop band) is occurred in the operating frequency range. This balanced condition can be expressed as

$$\omega_{se} = \omega_{sh} = \omega_0 \tag{1}$$

or equivalently

$$L_R C_L = L_L C_R \tag{2}$$

where ω_{se} and ω_{sh} are the series and shunt resonant frequencies, respectively, ω_0 is the transition frequency where gap-less transition occurs between the LH and RH ranges.

In a balanced CRLH TL, the propagation constant can be simply expressed as the sum of the propagation constants of a purely RH TL and of a purely LH TL [1]

$$\beta = \beta^{RH} + \beta^{LH} = \frac{\omega}{p}\sqrt{L_R C_R} - \frac{1}{\omega p \sqrt{L_L C_L}} \tag{3}$$

where p is the length of the unit cell.

In order to achieve a much more sensitive propagation constant β, the expression of $d\beta/d\omega$ in (4) must be as large as possible:

$$\frac{d\beta}{d\omega} = \frac{1}{p}\sqrt{L_R C_R} + \frac{1}{\omega^2 p\sqrt{L_L C_L}} \tag{4}$$

We can see from (4) that the sensitivity of the propagation can be improved by enlarging L_R (C_R). Besides, C_L (L_L) should be decreased simultaneously to keep the same transition frequency according to (2), and this would also be helpful to get a better sensitive propagation constant β. Thus achieving a sensitive β does not conflict to the balanced condition of CRLH TL.

3. CRLH CELL STRUCTURE

In the realization of CRLH TLs using microstrip or other planar TLs, the right-handed components are usually provided by the parasitic reactance of the TL, which is usually difficult to change after the balanced condition is satisfied.

In this paper, we propose a improved SIW CRLH cell structure with a transverse slot included, as shown in Figure 1. This CRLH cell is realized on the substrate of Rogers RT/duroid 5880 with a dielectric constant $\varepsilon_r = 2.2$ and thickness $h = 0.508$ mm. Two symmetrical interdigital capacitors are etched on the surface of the cell, which provide the necessary series capacitor for left-handed application. The metallized via-holes in the two sides are working as shunt inductors below the cutoff frequency, which provides the other necessary component for left-handedness. All the via-holes have the same dimension with a radius of 0.5 mm and a distance of 1.7 mm between neighboring via-holes. When the operating frequency is above the cutoff frequency, the right-handedness of the SIW is in the dominant position. The transverse slot is introduced in the design procedure to enlarge the right-handed component, L_R. It is similar to a transverse slot on the broad face of traditional rectangular waveguide, where the slot is equivalent to a series impedance of $R + jX$ [5]. When the slot length is smaller than the resonant length, $X > 0$ can be achieved, thus the slot will work as an extra series inductor. The cell can be called the series-inductively enhanced CRLH structure. In a certain range, the equivalent inductance of the transverse slot is related to its length. According to (4), the larger X we get, the more sensitive β can be achieved.

The slot equivalent impedance can be calculated using the formula expressed in [5]. Another method of microwave network using $ABCD$ matrix can be employed to extract the slot impedance. Let's consider a SIW of length l_{SIW} has a transverse slot in the middle, as shown in Figure 2. The $ABCD$ matrix of the slot is A_{slot}, which is defined as

$$A_{slot} = \begin{bmatrix} a_0 & b_0 \\ c_0 & d_0 \end{bmatrix} \tag{5}$$

A_1 and A_2 are both symmetric networks of $l/2$ length SIW and equal to each other, thus the cascaded ABCD matrix the entire model can be written as

$$A_M = A_1 \times A_{slot} \times A_2 \tag{6}$$

with $A_1 = A_2$.

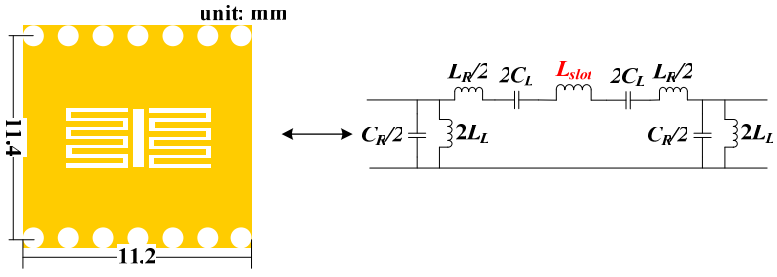

Figure 1: Prototype of the proposed CRLH cell and its equivalent circuit.

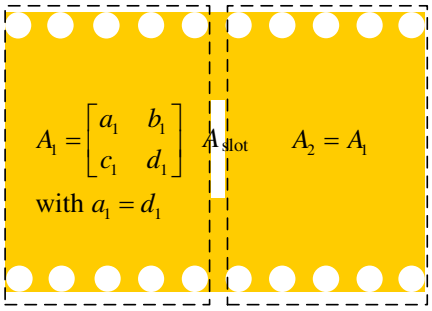

Figure 2: Cascaded network of a SIW with a transverse slot etched in the middle.

Removing the slot, the cascaded $ABCD$ matrix becomes as

$$A_N = A_1 \times A_2 \tag{7}$$

A_M and A_N can be obtained by full wave simulation, thereby A_1 and A_2 are calculated according to (7). Finally, A_{slot} is written by

$$A_{slot} = A_1^{-1} \times A_M \times A_2^{-1} \tag{8}$$

where its element b_0 is the slot impedance.

4. RESULTS

Figure 3(a) shows the equivalent reactance normalized to 50 Ohm of different transverse slots calculated by the microwave network technique presented in Section 3, in the frequency range of interest (8 GHz–12 GHz), the slot length is smaller than the resonant length and the normalized reactance $X > 0$ are clearly shown. Figure 3(b) also confirms that in a certain range, the longer slots correspond to the larger reactance. Figure 3(b) shows the simulated dispersion curves of this novel CRLH cell with different slot lengths. All the CRLH cell structures are designed to fulfill the balanced condition at the frequency of 9 GHz approximately. From Figure 3(b), one can obviously see that the fast wave region of this CRLH structure for β to achieve $[-k_0, +k_0]$ becomes narrower as the equivalent inductance of the transverse slot becomes larger, i.e., the dispersion becomes more sensitive with frequencies.

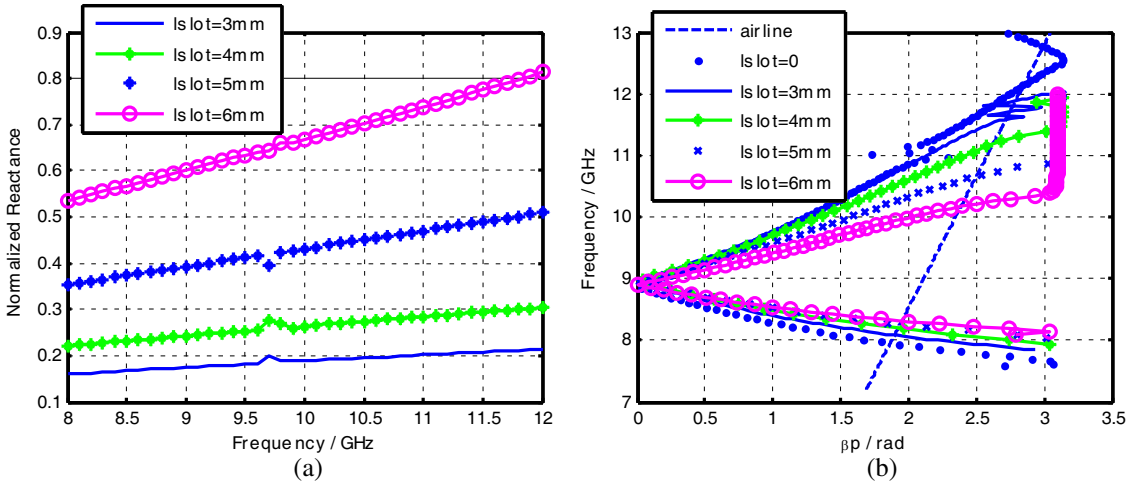

Figure 3: (a) Normalized reactance of slots, (b) simulated dispersion curves of proposed CRLH cells.

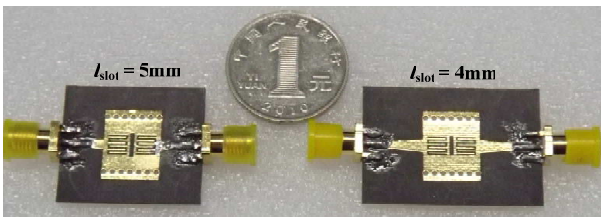

Figure 4: Photography of the fabricated CRLH cells.

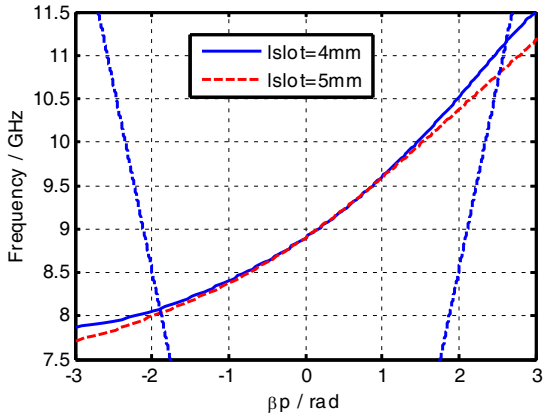

Figure 5: Measured dispersion of the proposed CRLH, blue real line: cell with 4 mm slot length; red dashed line: cell with 5 mm slot length; blue dashed lines: airlines.

Two CRLH cells with 4 mm slot length and 5 mm slot length are fabricated, as shown in Figure 4. Two taper lines are used on the two sides of the cell for the impedance matching to the SMA connectors of 50 Ω. Because the most important property of CRLH dispersion is related to the phase, it is essentially to de-embed the taper lines in the experimental procedure. The measured dispersion curves of the two CRLH cells are given in Figure 5. The measured results are in accordance to the simulated results as shown in Figure 3(b). We can further see that the dispersion improvement is obvious in the high frequency range of RH while not in the low frequency range of LH. This is due to the difference of equivalent inductance between the two slots are become larger as the frequency rises.

5. CONCLUSIONS

A improved structure for SIW CRLH cell is proposed in this paper as well as the dispersion sensitivity of the CRLH cell is analyzed. Both the simulated and measured results are given to confirm the improvement of the dispersion sensitivity to frequencies. The CRLH cell can be applied to the LWA for achieving large BSR/bandwidth ratio.

REFERENCES

1. Caloz, C. and T. Itoh, *Electromagnetic Metamaterials: Transmission Line Theory and Microwave Applications: The Engineering Approach*, Wiley-IEEE Press, 2006.
2. Lei, L., C. Caloz, and T. Itoh, "Dominant mode leaky-wave antenna with backfire-to-endfire scanning capability," *Electronics Letters*, Vol. 38, 1414–1416, 2002.
3. Weitsch, Y. and T. F. Eibert, "A left-handed/right-handed leaky-wave antenna derived from slotted rectangular hollow waveguide," *European Microwave Conference*, 917–920, 2007.
4. Yuandan, D. and T. Itoh, "Composite right/left-handed substrate integrated waveguide and half mode substrate integrated waveguide leaky-wave structures," *IEEE Transactions on Antennas and Propagation*, Vol. 59, 767–775, 2011.
5. Oliner, A., "The impedance properties of narrow radiating slots in the broad face of rectangular waveguide: Part I — Theory, Part II — Comparison with measurement," *IRE Transactions on Antennas and Propagation*, Vol. 5, 12–20, 1957.

A Shunt-capacitance-aided Composite Right/Left-handed Leaky Wave Antenna with Large Scanning-range/Bandwidth Ratio

Qingshan Yang, Xiangkun Zhang, and Yunhua Zhang
Key Laboratory of Microwave Remote Sensing
Chinese Academy of Sciences, Beijing 100190, China

Abstract— In this paper, we propose an improved shunt-capacitance-aided composite right/left-handed (CRLH) leaky wave antenna (LWA) with large beam-scanning-range (BSR)/bandwidth ratio based on substrate integrated waveguide (SIW) structure. The CRLH LWA is constructed by etching interdigital capacitor on the waveguide surface, which behaves as the series capacitor for left-handedness as well as radiating cell. Two longitudinal slots locate at upside and downside of the interdigital capacitor, respectively, which are working as the aided shunt capacitance to achieve large BSR/bandwidth ratio. An X-band LWA composed of 15 CRLH cells is fabricated. The simulated results of S-parameters and radiation patterns are presented. Compared with other frequency scanning CRLH LWAs reported before, this LWA has the advantage of large BSR from $-57°$ to $+65°$ within a fractional bandwidth of 28% (from 9.2 GHz to 12.2 GHz).

1. INTRODUCTION

Metamaterial LWAs based on CRLH transmission lines (TLs) have been studied intensively for its outstanding advantage of continuous BSR from backfire to endfire [1], which can be used in modern radar system for frequency scanning application. Many researches on SIW structure CRLH TLs with the application in LWA have been reported [2, 3]. However, the required frequency scanning bandwidths of the before proposed CRLH SIW LWAs are usually as large as 40% fractional bandwidth or even larger in order to achieve certain BSR of $[-60°, +60°]$ [2, 3]. A large BSR/bandwidth ratio is usually preferred for radar systems with high performance beam scanning characteristic required. In this paper, we propose a shunt-capacitance-aided CRLH LWA using SIW structure so as to achieve wide continuous scanning range within a narrow fractional bandwidth.

Three sections are contained in the main body of this paper. In Section 2, we show the LWA configuration and discuss the leaky wave principle. The dispersion of this CRLH cell is analyzed in Section 3. In Section 4, the S-parameters and radiation patterns of the LWA are presented.

2. CONFIGURATION & LEAKY WAVE PRINCIPLE

A LWA is basically a uniform or periodic waveguiding structure that possesses a mechanism that permits it to leak power all along its length. Our design is based on the substrate of Rogers 5880 with a permittivity of 2.2, loss tangent of 0.0009 and thickness of 0.508 mm. The unit cell and the LWA configurations are shown in Figure 1. Interdigital slots are etched on the surface of the SIW CRLH cell, which behave as series capacitors as well as leaky wave unit. The via-holes adopted in our SIW structure acting as the shunt inductors have the same dimension with a radius of 0.35 mm and a center-to-center distance of 1.35 mm between neighboring via-holes. Two longitudinal slots locate at upside and downside of the interdigital capacitor, respectively, which are working as the aided shunt capacitances which help to achieve large BSR/bandwidth ratio. The bottom of the substrate is covered by copper so as to act as ground plane.

In a LWA, the free space wave number k_0 corresponds to radiation direction of the main beam, and can be decomposed into longitudinal (x) and transversal (z) components, as indicated in Figure 1(b). The longitudinal component is

$$k_x = \beta(\omega) - j\alpha(\omega) \tag{1}$$

where $\beta(\omega)$ and $\alpha(\omega)$ are the phase factor and the leaky factor, respectively. The transversal component k_z depends on both $\beta(\omega)$ and frequency (via k_0)

$$k_z = \sqrt{k_0^2 - \beta^2} \tag{2}$$

If $|\beta| > k_0$ (phase velocity $v_p < c$, slow wave), k_z is imaginary, and the field will be exponentially decaying along z, which means the wave is completely guided. If $|\beta| < k_0$ ($v_p > c$, fast wave), k_z is real, therefore leakage radiation occurs.

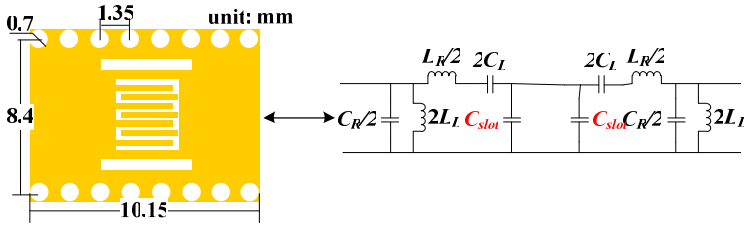

(a)

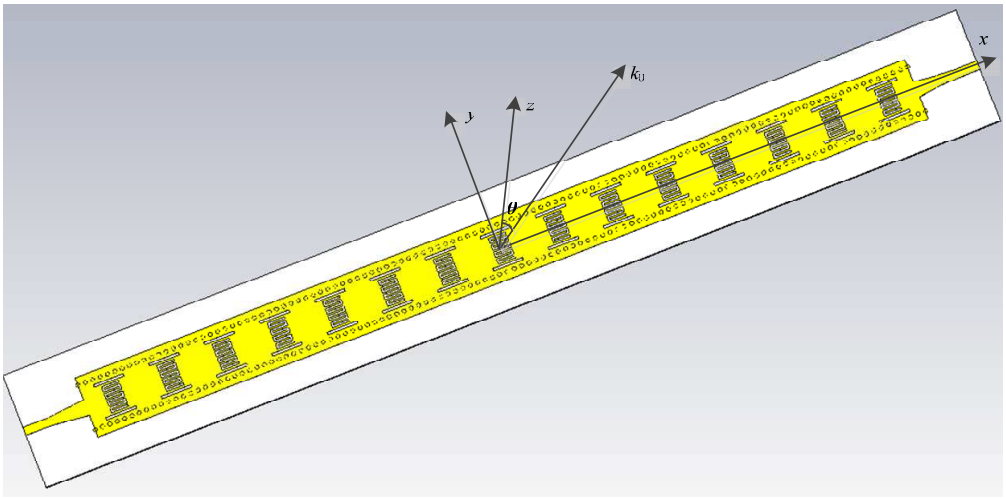

(b)

Figure 1: Figuration of the proposed (a) SIW CRLH cell & its equivalent circuit, (b) LWA.

The radiation angle of the main beam is straightforwardly determined by Figure 1(b) as [4]

$$\theta(\omega) = \sin^{-1}\left[\beta(\omega)/k_0\right] \tag{3}$$

which shows a beam steering can be achieved by frequency scanning.

3. DISPERSION ANALYSIS

A CRLH TL is commonly constructed by embedding repetition of series capacitance and shunt inductance into a traditional right-handed (RH) TL which exhibits left-handed (LH) property at low frequency band and RH property at high frequency band. Because of the effect of parasitic series inductance and shunt capacitance, a pure LH TL cannot exist physically, even if we intentionally provide only series capacitance and shunt inductance, thus the CRLH model represents the most general structure.

In original SIW cell, the top and the ground metal surfaces behave effectively as a two-wire TL with distributed series inductance and shunt capacitance. The short-circuit via-holes can be regarded as shunt inductance, so for the CRLH model, just series capacitance is needed, which can be realized by the interdigital slots. The equivalent circuit of the proposed CRLH cell is shown in Figure 1(a), where C_R and L_R represent the distributed series inductance and shunt capacitance, while C_L and L_L represent the interdigital slots and via-holes, respectively. The two longitudinal slots are equivalent to the shunt admittance of $G + jB$ [5]. This is similar to the longitudinal slot on the broad wall of a rectangular waveguide. When the slot length is smaller than the resonant length, $B > 0$ can be achieved, thus the longitudinal slot will work as an extra shunt capacitor C_{slot}.

In the CRLH model of Figure 1(a), a balanced condition can be achieved if the series and shunt resonant frequencies are equal with each other or equivalently

$$L_R C_L = L_L C_R \tag{4}$$

Under this balanced condition, the propagation constant β can be simply expressed as the sum of

a (linear and positive) RH TL and a (negative and hyperbolic) LH TL [1]

$$\beta = \beta^{RH} + \beta^{LH} = \frac{\omega}{p}\sqrt{L_R C_R} - \frac{1}{\omega p \sqrt{L_L C_L}} \tag{5}$$

The propagation constant β exhibit zero at the frequency called the transition frequency:

$$\omega_0 = 1/\sqrt[4]{L_R C_R L_L C_L} \tag{6}$$

According to (5), the sensitivity of propagation constant with frequency can be obtained by

$$\frac{d\beta}{d\omega} = \frac{1}{p}\left(\sqrt{L_R C_R} + \frac{1}{\omega^2\sqrt{L_L C_L}}\right) \tag{7}$$

From (7), we can see the aided shunt capacitor C_{slot} will enlarge the RH capacitor C_R, thus the sensitivity of propagation constant $d\beta/d\omega$, which means this CRLH cell has a narrower fast wave region compared to that does not has the aided longitudinal slots. In our CRLH cell design, the interdigital capacitor parameters are chosen as: finger length $lc = 2.8\,\text{mm}$, finger width $wc = 0.3\,\text{mm}$, space between neighboring fingers $ws = 0.35\,\text{mm}$. The length and width of the longitudinal slot are chosen to be 5.5 mm and 0.45 mm, respectively. Now, let's compare the dispersion curves of the novel cell and that proposed in [2], as depicted in Figure 2. It is shown that both of them are balanced at 10 GHz approximately, and the fast wave region of the new cell is much narrower than that of the cell in [2]. The difference between the airlines of the two CRLH cells is due to the different lengths of unit cells. It is to say the proposed CRLH cell can be a good candidate to LWA for achieving large BSR/bandwidth ratio. Based on this CRLH cell, a LWA composed of 15 cells is designed and simulated in Section 4.

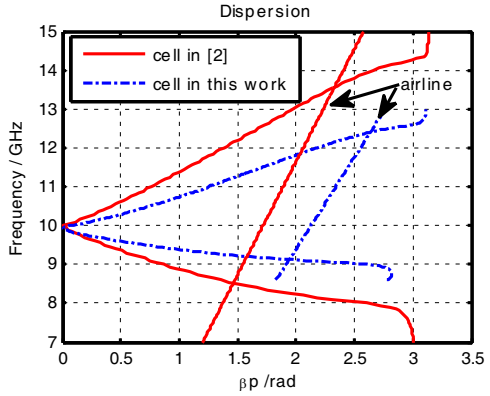

Figure 2: Dispersion of CRLH, red real line: cell in [2]; blue dashed line: cell in this paper.

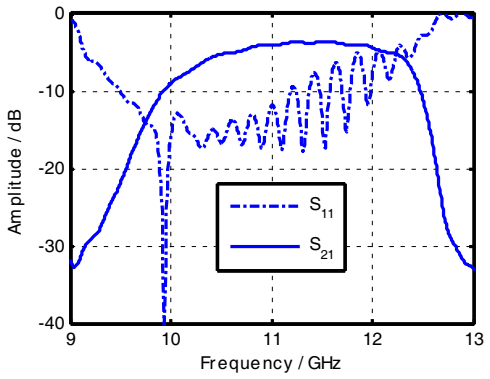

Figure 3: Simulated S-parameters of the shunt-capacitor-aided LWA.

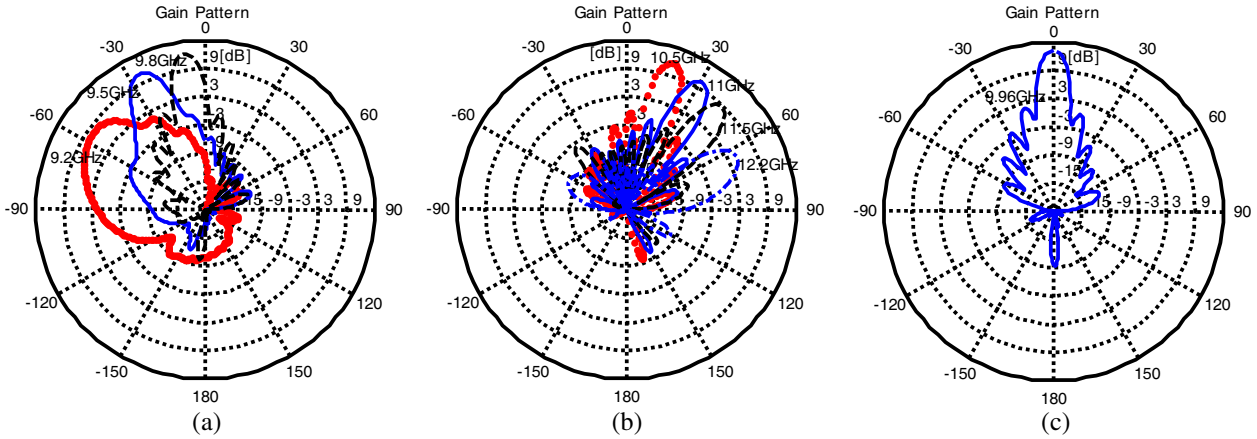

Figure 4: E-plane radiation patterns of (a) LH region, (b) RH region, (c) transition frequency.

4. SIMULATION RESULTS OF THE LWA

The designed LWA is realized by cascading 15 identical CRLH cells. Two taper lines are adopted in the two ends of the LWA for impedance matching to 50 Ω, as shown in Figure 1(b). The simulated S-parameters of the LWA using CST Microwave Studio are shown in Figure 3. A bandwidth of $S_{11} < -10$ dB is achieved from 9.5 GHz to 11.2 GHz. The E-plane radiation patterns at different frequencies are simulated, as shown in Figure 4. A BSR of $[-57°, +65°]$ is achieved within a bandwidth from 9.2 GHz to 12.2 GHz and the maximum gain of 13 dBi is obtained in the broadside radiation.

5. CONCLUSIONS

A shunt-capacitor-aided CRLH LWA with large BSR/bandwidth ratio is proposed in this paper. Simulation results of S-parameters and radiation patterns are presented. The BSR can be from $-57°$ to $+65°$ within a fractional bandwidth of 28% (from 9.2 GHz to 12.2 GHz). The performance of BSR/bandwidth ratio is better than that of the LWA reported in [2], which has a fractional bandwidth of 40% (from 8.6 GHz to 12.8 GHz) for achieving a BSR of $[-70°, +56°]$.

REFERENCES

1. Caloz, C. and T. Itoh, *Electromagnetic Metamaterials: Transmission Line Theory and Microwave Applications: The Engineering Approach*, Wiley-IEEE Press, 2006.
2. Yuandan, D. and T. Itoh, "Composite right/left-handed substrate integrated waveguide and half mode substrate integrated waveguide leaky-wave structures," *IEEE Transactions on Antennas and Propagation*, Vol. 59, 767–775, 2011.
3. Jin, C., A. Alphones, and L. C. Ong, "Broadband leaky-wave antenna based on composite right/left handed substrate integrated waveguide," *Electronics Letters*, Vol. 46, 1584–1585, 2010.
4. Oliner, A., "Leaky-wave antennas," *Antenna Engineering Handbook*, R. C. Johnson, Ed., McGraw Hill, 1993.
5. Oliner, A., "The impedance properties of narrow radiating slots in the broad face of rectangular waveguide: Part I — Theory, Part II — Comparison with measurement," *IRE Transactions on Antennas and Propagation*, Vol. 5, 12–20, 1957.

Electrical Characteristics Dependence of Monstera Leaf on Moisture Content

O. Kurnaz, Y. E. Yoruk, and S. Helhel
Department of Electrical and Electronics Engineering, Akdeniz University, Turkey

Abstract— Transmittance and reflection dependence of monstera leaf on moisture content has been investigated at X-band. In measurement campaign, forward transmission and forward reflection coefficients S_{21} and S_{11} have been observed with respect to the change of moisture content within the leaf. It is found that transmittance is strongly dependent on the moisture content; however, reflection is almost independent of the moisture content, which implies that most of the electrical power is absorbed within the water content of the leaf.

1. INTRODUCTION

Leaves are one of the most important parts of any vegetation canopy. Some existing microwave models superpose the electromagnetic scatter from discrete leaves and branches to determine the total reflectivity of the vegetation canopy. There are lots of empirical relationships proposed in the literature [1–3].

In 1987, Senior et al. [1] measured backscattering cross section of coleus leaf in varying stage of dryness and they showed that a uniform resistive sheet constitutes an effective model for a planar leaf. In 1995, Chuah et al. [2] reported the measured dielectric constants of rubber and oil palm leaves as a function of moisture content at X-band. They compared the model of Ulaby and El-Rayes and the simple dielectric theory of Fung and Fung with the experimental data. Their findings confirmed that the model of Ulaby and El-Rayes has better estimation.

In 2011, Seker and Kunter [3] described a theoretical propagation model and simulation for horizontal and vertical polarization for different types, size and shape of trees. They found that the loss from the vegetation is substantially higher for higher frequencies.

Although the approaches developed so far present rather good models, new models, approaches and further research are required to understand microwave interaction with plant leaves so that efficient calculations can be developed for purposes such as military and governmental applications, agricultural planning, and radio-link development. For this reason, a correct understanding and investigation of electrical characteristics of vegetation canopies is important. In this study, a piece of a monstera leaf has been investigated by measuring the forward transmittance and reflection coefficients.

2. THEORY

In a linear electrical system, the relationship between the input/output terminals is expressed in terms of S parameters. In an n-port network system, there are totally n^2 S-parameters, which are S_{11}, S_{12}, S_{21} and S_{22}. A sample two-port network is shown in Figure 1.

For a 2-port network, the relationship between the ports [4] can be expressed as in the following:

$$\begin{aligned} b_1 &= S_{11}a_1 + S_{12}a_2 \\ b_2 &= S_{21}a_1 + S_{22}a_2 \end{aligned} \tag{1}$$

where S_{11} is forward reflection coefficient and expressed as

$$S_{11} = \frac{b_1}{a_1}|_{a_2=0} \tag{2}$$

and S_{21} is the forward transmission coefficient and expressed as

$$S_{21} = \frac{b_2}{a_1}|_{a_2=0} \tag{3}$$

It should be noted that all S values are complex.

3. MEASUREMENT SETUP

Measurements have been conducted in Near Field Antenna Measurement Laboratory, inside Industrial and Medical Application Based Microwave Research Center (EMUMAM) at Akdeniz University. The laboratory contains a vector network analyzer operating in 10 MHz–9 GHz frequency range (Anritsu MS4624B). Vector network analyzer is associated with measurement setup mechanism which consists of receiving antenna probe, monstera leaf, leaf holder and transmitting antenna waveguide, respectively. Leaf holder is simply an aluminum metal box, one side of which has been connected to a WR90 open-ended rectangular waveguide, which is the measuring probe and capable of measuring at X-band, and the other side has been connected to source signal. The system can be controlled and logged via computer graphical interface. The experimental setup is shown in Figure 2.

A piece of a monstera leaf having 6 cm length, 4 cm width and 770 µm thickness has been put

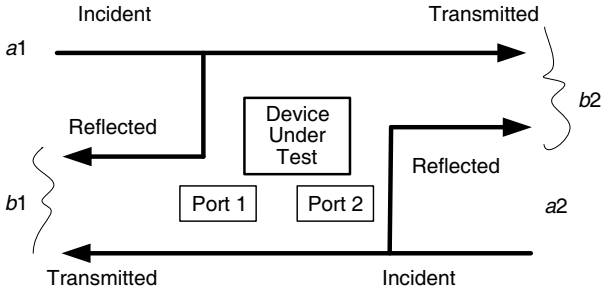

Figure 1: Two-port network representation.

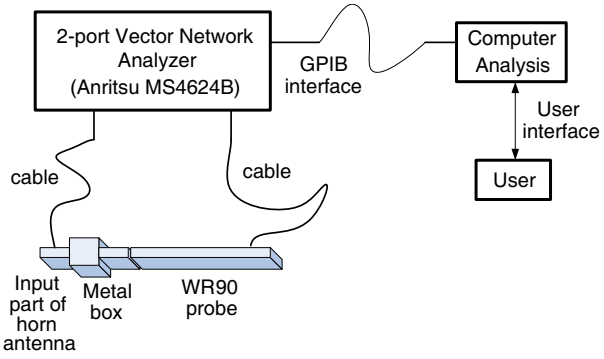

Figure 2: Graphical representation of experimental setup.

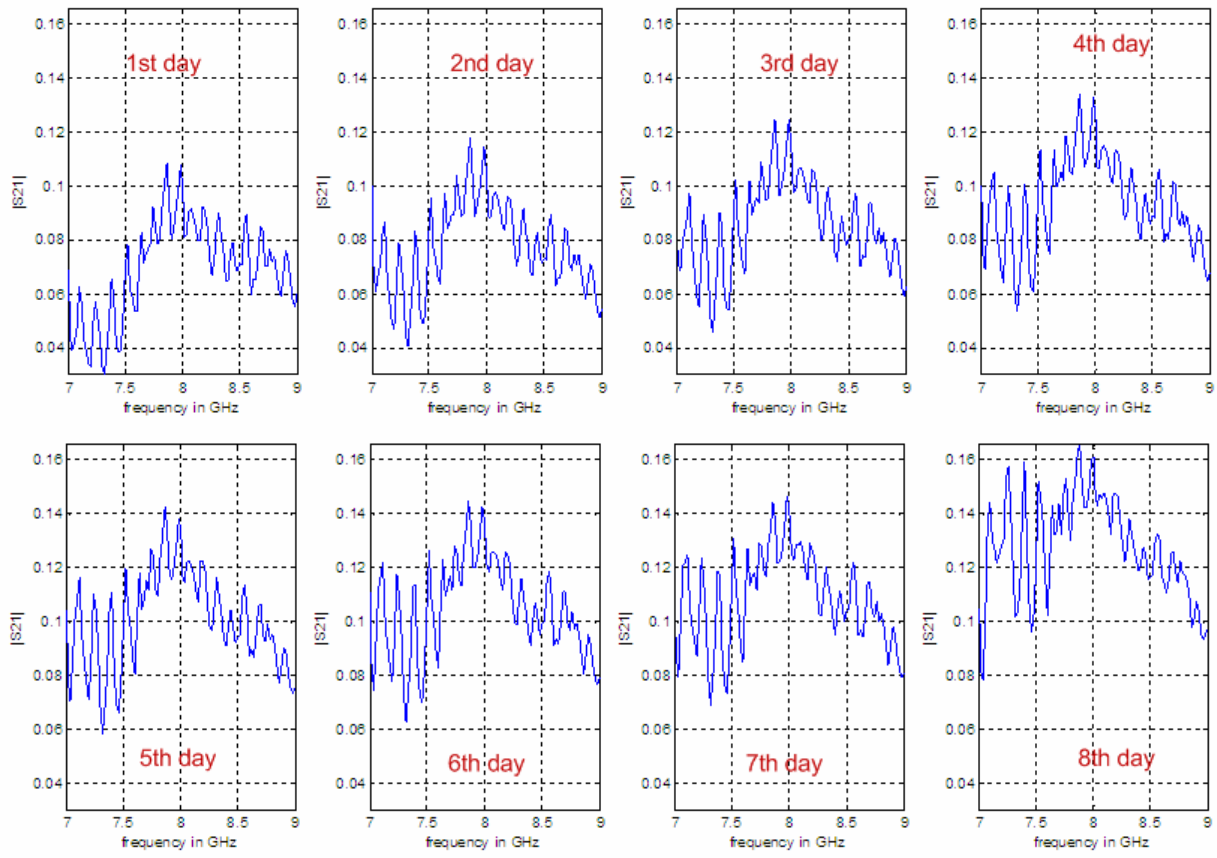

Figure 3: The change of transmittance with respect to day number. All plots are against frequency.

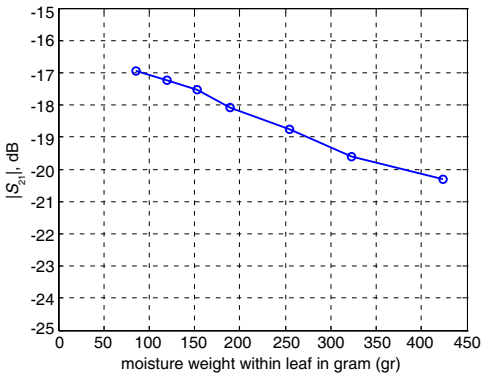

Figure 4: Transmittance with respect to moisture content.

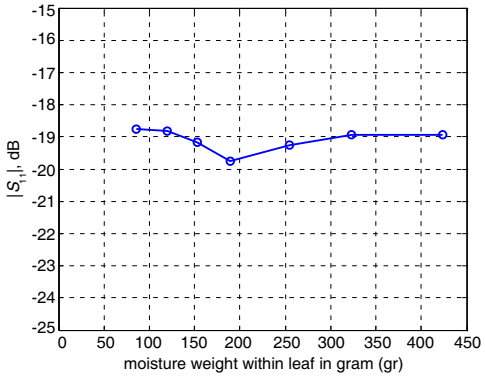

Figure 5: Reflection with respect to moisture content.

within a thin metal box. One side of the box has been connected to an open-ended rectangular waveguide (WR90 probe) which is used as measuring probe and other side has been connected to the source signal via the rectangular waveguide part of a horn antenna, which is compatible and has the same dimension profile with the measuring probe.

Transmittance is measured by using S_{21} parameter and reflection is measured by using S_{11} parameter. Measurements have been carried out between 7 GHz and 9 GHz with 20 MHz intervals through eight days.

4. RESULTS AND CONCLUSION

Transmittance change with respect to days is shown in Figure 3. The transmittance coefficient is plotted against frequency and it is observed that transmittance increases from beginning to the end at all frequencies.

At the end of eight-day period, the leaf has lost 65.93% of its total weight. Meanwhile, it has been observed that transmittance increases as moisture content decreases and the transmittance at the end is almost two times that at the beginning. Also, the change of transmittance at 8 GHz, which is the center frequency, with respect to moisture weight within the leaf is shown in Figure 4. Similar results are observed when values at different frequencies other than 8 GHz are plotted. It is deducted from Figure 4 that the measured $|S_{21}|$ value at first day is -17 dB and it is less than -20 dB at 8th day, which shows that more than 3 dB difference has occurred between the beginning and end of the period.

On the other hand, magnitude of forward reflection coefficient $|S_{11}|$, which is plotted in Figure 5, shows very little change through the eight-day period. The difference is below 5% from beginning to the end. Therefore, it can be concluded that most of the electrical power is absorbed within the moisture content of the leaf when the moisture content of the leaf is high. At the same time, it is found that maximum transmittance has occurred at 8 GHz and maximum reflection has occurred at 7.6 GHz where both coefficients show a fluctuating behavior between 7 GHz and 9 GHz, which is a result seen in Figure 3.

REFERENCES

1. Senior, T. B. A., K. Sarabandi, and F. T. Ulaby, "Measuring and modeling the backscattering cross section of a leaf," *Radio Science*, Vol. 22, No. 6, 1109–1116, Nov. 1987.
2. Chuah, H. T., K. Y. Lee, and T. W. Lau, "Dielectric constants of rubber and oil palm leaf samples at X-band," *IEEE Trans. Geosci. and Rem. Sens.*, Vol. 33, No. 1, 221–223, Jan. 1995.
3. Seker, S. and F. C. Kunter, "Multi-components mobile propagation model of park environment," *IEEE Trans. Magnetics*, Vol. 47, 1494–1497, May 2011.
4. Riad, T. and Q. Jing, "A Nonlinear *S*-parameters behavioral model for RF LNAs", *2010 2nd Asia Symposium on Quality Electronic Design*, Aug. 3–4, 2010, Paper DOI: 10.1109/ASQED.2010.5548227.

Microwave Vegetation Index from SMOS

Jiancheng Shi
State Key Laboratory of Remote Sensing Science
Institute of Remote Sensing Applications and Beijing Normal University, Beijing, China

Abstract—Monitoring global vegetation can be of importance in understanding land surface processes and their interactions with the atmosphere, biogeochemical cycle, and primary productivity. The commonly used vegetation indices derived from the visible-near infrared sensors are mainly dependent on the green leaf material of the vegetation cover and often limited by the effects of atmosphere, background soil conditions, and saturation at high levels of vegetation. In our previous study [1], we developed the microwave vegetation indices (MVIs) with the dual-frequency technique under the Advanced Microwave Scanning Radiometer (AMSR-E) sensor configuration on the Aqua satellite. The MVIs derived in this study are less affected by soil surface emission signals, and depend mainly on vegetation properties such as vegetation fractional coverage, biomass, water content, temperature, the characteristics of the scatterer size, and the geometry of the vegetation canopy. It demonstrated that the microwave derived vegetation indices can provide complementary vegetation information (both the leafy and woody parts of the vegetation) by optical sensors. This method provides a new opportunity to establish a long-term global dataset for monitoring vegetation cover using all-weather passive microwave instruments. In this study, we will explore and demonstrate a new technique for deriving Microwave Vegetation Indices (MVIs) using the passive microwave radiometer SMOS data. It provides the global microwave brightness temperature observations at L-band (1.4 GHz) with dual polarizations (V, H) and a range of viewing angles [2].

1. INTRODUCTION

In deriving vegetation indices from satellite measurements using either optical or microwave observations we face two problems: the effects of the atmosphere and the background (surface underlying the vegetation) signals. Microwave observations are less affected by atmospheric conditions than traditional optical methods. On the other hand, the variability in the background emission signals resulting from the soil state can have a greater effect on the microwave observations than when using optical sensors that only sense the canopy. The effect of the background emission signal must be incorporated in order to derive a reliable and useful vegetation index. Furthermore, we expect that the AMSR-E sensor will have specific penetration limitations over different land cover vegetation types and properties. The MVIs derived by AMSR-E sensor have only an unique relationship vegetation bare soil and short vegetation when both frequencies can "see" through the vegetation covers. However, the MVIs derived by AMSR-E sensor will have a non-unique relationship in regions where the sensor can "see" the ground surface at both frequencies and the regions where the sensor can not "see" ground surface at one or both frequencies. For instance, the B parameters derived from the bare surfaces could have a similar magnitude as that derived from a dense forest with the fraction cover $Fv < 1$. It is a limitation of the AMSR-E sensor due to its vegetation penetration capability. Therefore, AMSR-E sensor derived MVIs may only be reliable for the short vegetation covers [1]. Unlike microwave vegetation indexes derived in previous study [1], SMOS observations have much higher vegetation penetration capability than that of AMSR-E and can provide a new tool for monitoring global vegetation cover, especially for forested regions.

2. EVALUATION OF RELATIONSHIPS BETWEEN THE MULTI-INCIDENCE BARE SURFACE EMISSION SIGNALS

As shown in [1], the key to derive the microwave vegetation indices is to minimize the background surface emission signals. For AMSR-E observations, this can be done since the bare soil surface emissivities at different frequencies can be characterized by a linear function with parameters that are dependent on the pair of frequencies used. For SMOS observations, we need first to evaluate the characteristics of bare surface emission signals at the different SMOS observation angles. This was done by generating a simulated surface emission database for the sensor parameters of SMOS with frequency: 1.41 GHz, polarizations: v and h, and a range of incidence angles, using the Advanced Integral Equation Model (AIEM) [3]. This database included a wide range of volumetric soil moistures (2% to 44% at a 2% interval). Surface roughness parameters included rms height

from 0.25 cm to 3 cm at a 0.25 cm interval and correlation length from 2.5 cm to 30 cm at a 2.5 cm interval. In total there were 2,904 simulated emissivities for each frequency and polarization. The commonly used Gaussian and Exponential correlation functions were used in the simulations since they are the most commonly used two extreme cases and the most of the natural random surfaces are between them [4].

Through the analysis of numerical simulations at the different incidences at L-band by AIEM [3] simulated surface emissivity data, we found that soil surface emissivities at different incidences can be characterized by a linear function with parameters that are dependent on the pair of observation angles used, as long as the difference in the pair of observation angles less than or around 10 degree. This makes it possible to minimize the surface emission signal and maximize the vegetation signal when using multi-angle radiometer measurements. Figure 1 shows the entire set of AIEM model simulated L-band surface emissivities including both Gaussian and Exponential correlation functions. They are the polarizations of V, H and the polarization difference V-H from left to right columns. The y-axes of top and bottom rows are the simulated data at 20° and 40°, respectively. Their x-axes are the corresponding emissivities for the same surface properties (soil moisture and roughness properties) at the observation angle of 30°.

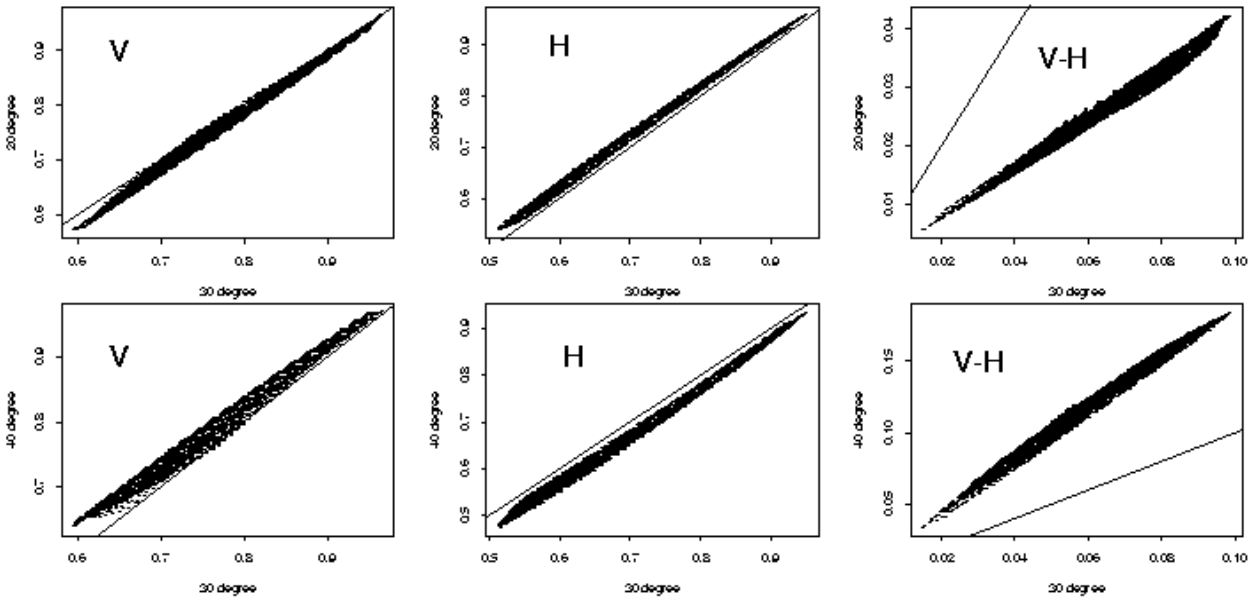

Figure 1: AIEM model simulated L-band surface emissivities.

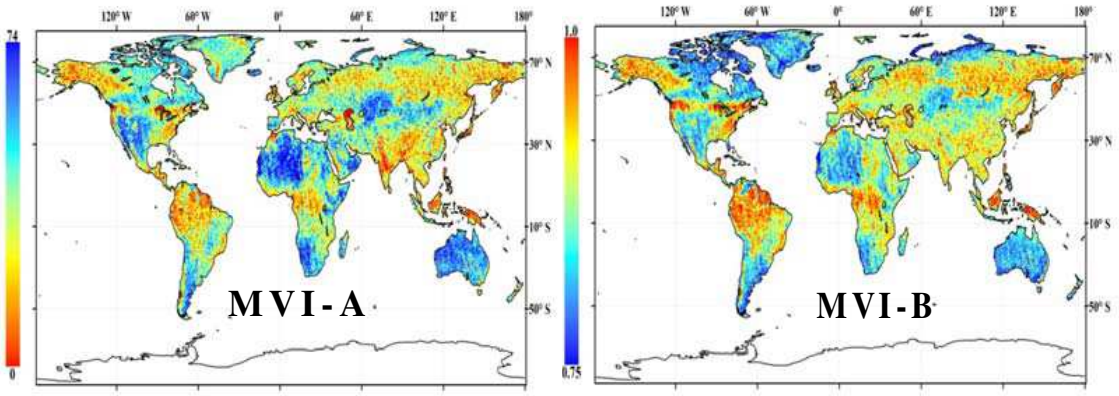

Figure 2: The mean monthly values of the MVIs in July, 2010 with the two observation angles of 40° and 50°.

3. DERIVING MICROWAVE VEGETATION INDICES WITH SMOS MEASUREMENTS

Following the techniques developed in [1], by replacing two frequencies measurements with the two incidence angle measurements, we can derive the microwave vegetation indices:

$$MVI\_B(\theta_1, \theta_2) = \frac{T_{Bv}(\theta_2) - T_{Bh}(\theta_2)}{T_{Bv}(\theta_1) - T_{Bh}(\theta_1)} \tag{1}$$

$$MVI\_A(\theta_1, \theta_2) = \frac{1}{2}[T_{Bv}(\theta_2) + T_{Bh}(\theta_2) - B(\theta_1, \theta_2) \cdot (T_{Bv}(\theta_1) + T_{Bh}(\theta_1))] \tag{2}$$

Figure 2 shows the mean values of the microwave vegetation indices for its A and B parameters in July, 2010 with the SMOS's two observation angles measurements at 40° and 50°.

We will show the details on analyses of comparisons of the MVIs and NDVI (MODIS) in assessing the global vegetation pattern during different seasons and on examining its response in global pattern and to seasonal vegetation phenology.

REFERENCES

1. Shi, J., T. Jackson, J. Tao, J. Du, R. Bindlish, L. Lu, and K. S. Chen, "Global microwave vegetation indices from satellite passive microwave sensors," *Remote Sensing Environment*, Vol. 112, No. 12, 4285–4300, Dec. 2008.
2. Kerr, Y. H., P. Waldteufel, J.-P. Wigneron, S. Delwart, F. Cabot, J. Boutin, M.-J. Escorihuela, J. Font, N. Reul, C. Gruhier, S. E. Juglea, M. R. Drinkwater, A. Hahne, M. Martín-Neira, and S. Mecklenburg, "The SMOS mission: New tool for monitoring key elements of the global water cycle," *Proceedings of the IEEE*, Vol. 98, No. 5, May 2010.
3. Chen, K. S., T. D. Wu, L. Tsang, Q. Li, J. Shi, and A. K. Fung, "The emission of rough surfaces calculated by the integral equation method with a comparison to a three-dimensional moment method simulations," *IEEE Transactions on Geoscience and Remote Sensing*, Vol. 41, No. 1, 90–101, 2003.
4. Shi, J., J. Wang, A. Hsu, P. O'Neill, and E. T. Engman, "Estimation of bare surface soil moisture and surface roughness parameters using L-band SAR image data," *IEEE Transactions on Geoscience and Remote Sensing*, Vol. 35, No. 5, 1254–1266, 1997.

A Simple Parameterization for Sensible and Latent Heat Fluxes during Unstable Daytime

Jing Lu[1, 2, 3], **Zhao-Liang Li**[1, 3], **Hua Wu**[1], **Bohui Tang**[1], **and Jelila Labed**[3]

[1]State Key Laboratory of Resources and Environmental Information System
Institute of Geographic Sciences and Natural Resources Research, Chinese Academy of Sciences
Beijing 100101, China
[2]Graduate University of Chinese Academy of Sciences, Beijing 100049, China
[3]LSIIT, UdS, CNRS, Bld Sebastien Brant, BP10413, Illkirch 67412, France

Abstract— This study firstly develops a simple parameterization for sensible and latent heat fluxes under unstable conditions. The parameterization consists of some unknown variables considered as constants during the daytime and some known functions related to surface temperature and air temperature. The sensible heat flux (H) is expressed as a quadratic function of the difference between surface temperature and air temperature, and the latent heat flux (LE) is parameterized as a function of the saturated water vapor pressure at surface temperature as well as the difference between surface temperature and air temperature. The accuracy of the parameterization for H and LE is evaluated by the measurements from Yucheng station, north of China. For H, the coefficient of determination (R^2) is 0.925, the root mean square error (RMSE) is 27.8 W/m^2, and the bias (BIAS) is -14.2 W/m^2, and for LE, the R^2, RMSE, and BIAS are 0.946, 24.7 W/m^2, and 0.5 W/m^2, respectively. With the assumption that surface available energy is known, the minimization technique is used to inverse heat fluxes. The H is underestimated by 30.7 W/m^2, and the corresponding LE is overestimated by 30.4 W/m^2. The RMSEs of H and LE are 54.1 and 56.6 W/m^2, and R^2 are 0.775 and 0.806, respectively. The method can estimate H and LE at any time during unstable daytime without the need to calculate the resistance. The remotely sensed data from the geostationary meteorological satellite can be utilized adequately by the method in the future.

1. INTRODUCTION

Sensible and latent heat fluxes (H and LE) are the important components in energy balance equation. Especially for the evapotranspiration (ET, namely, latent heat flux), more attention has been paid in the fields of hydrology, agriculture, ecology, climate, and so on. The development of remote sensing provides an opportunity to estimate ET on the regional scale. The current ET models based on remotely sensed data mainly include SEBS (surface energy balance system), SEBAL (surface energy balance algorithm for land), Ts-VI (surface temperature vs. vegetation indices), and two-source model [1]. From the process of parameterization, apart from the Ts-VI method, all other models need to estimate the resistance by complex equations. Although these methods are based on clear physical principles, the more complicated these equations are, the larger uncertainties are brought for the estimation of ET. Ts-VI method based on the spatial information of remotely sensed data has been widely used without the need of calculating resistance and the meteorological data. Especially in arid and semi-arid areas, higher accuracy can be obtained [2]. However, the method is based on the hypothesis that atmospheric condition is similar in the research region and the dry and wet points exist for all the fraction of vegetation cover. Actually, it is difficult to satisfy these hypotheses. Compared with the spatial information from remote sensing, time information from remote sensing is less applied. Although in ALEXI model, the change rate of surface temperature between the 1.5 h to 5.5 h after sunrise was used to estimate surface fluxes by combining the atmospheric boundary model, the utility of time information is finite [3].

Raffy and Becker proposed a minimization technique to solve the inverse problems of remote sensing [4], which can simultaneously estimate the surface fluxes without the calculation of resistance by using the continuous information from remote sensor observation over one day. Based on this method, this study develops a simple parameterization for H and LE under unstable conditions. The details about the parameterization are shown in Section 2. The evaluation of the parameterization as well as the preliminary application is given in Section 3. The conclusion and discussion are presented in Section 4.

2. METHOD

2.1. Raffy and Becker's Method

According to the surface energy balance and the study of Hechinger [5], the soil heat flux Φ at the surface can be expressed by

$$\Phi(T_s, t, D) = \varphi_0(T_s, t) + \sum_{k=1} d_k \varphi_k(T_s, t) \tag{1}$$

where T_s is the surface temperature; t is the time; φ_k are functions assumed to be known and related to the known T_s; and d_k are the soil parameters and can be considered as constants along one day period, which contribute to the set D.

The key process in the Raffy and Becker's method is to parameterize the energy balance components as some unknown constants and some known functions [4]. Given these constants, the components in energy balance equation can be obtained simultaneously. The set D changes with the different known conditions. The unknown parameters in set D can be obtained by minimization technique. Two methods are used to solve the inverse problem, i.e., flux method and temperature method. The flux method minimizes the root mean square difference between calculated and measured flux, while temperature method minimizes the difference between calculated and measured surface temperatures. More details can be found in [4, 6, 7].

2.2. The Parameterization for Sensible and Latent Heat Fluxes

Based on the parameterization for H from Blümel and the method of Raffy and Becker [4, 8], a parameterization for H is proposed by the following equation

$$H(t) = A[\rho_a c_p \times (Ts(t) - Ta(t))] + B[\rho_a c_p g \times (Ts(t) - Ta(t))^2] \tag{2}$$

where A and B are the unknown variables related to the surface and atmosphere characteristics, and are positive from the point of view of physics; ρ_a is the density of air; c_p is the heat capacity of air; g is the acceleration due to gravity; and T_a is the air temperature.

Taking into account the relationship between H and the LE in the parameterization of Raffy and Becker, LE can be expressed as

$$\begin{aligned} \mathrm{LE}(t) = {} & C[\rho_a c_p \times P_s(T_s(t))] + D[\rho_a c_p g \times P_s(T_s(t)) \times (T_s(t) - T_a(t))] \\ & + E\left[\rho_a c_p \times \frac{\partial P_s(T)}{\partial T}\Big|_{T_s(t)} \times (T_s(t) - T_a(t))\right] + F\left[\rho_a c_p g \times \frac{\partial P_s(T)}{\partial T}\Big|_{T_s(t)} \times (T_s(t) - T_a(t))^2\right] \end{aligned} \tag{3}$$

where C, D, E, and F are the unknown variables related to the surface and atmosphere characteristics; and $P_s(T)$ is the saturation vapor pressure at temperature T. E and F are positive, while C and D depend on the underlying condition and are positive in most situations.

3. THE EVALUATION AND APPLICATION OF PARAMETERIZATION

3.1. The Evaluation of Parameterization

In order to evaluate the accuracy of parameterization for H and LE, the data from the EC measurement at Yucheng station are used in this study. The Yuchaeng station is located in the southwest of Yucheng County, Shandong province with winter wheat and summer corn crop rotation in North China. It is part of the Chinese terrestrial ecosystem flux network, and aims at measuring the exchange of carbon dioxide, water vapor and heat between land and atmosphere. The climate at this station is subhumid and monsoon climate with mean annual temperature and precipitation of 13.1°C and 528 mm, respectively. Because the parameterization for H is developed under unstable condition, the data with most temperature gradient larger than 0 during the daytime will be used, and finally 24 days in the years 2009 and 2010 are selected. The unknown variables (A, B, C, D, E, and F) in the parameterization are obtained by fitting with the least square method.

The H and LE from parameterization are in good agreement with those from the measurements (see Figure 1). For H, the coefficient of determination (R^2) is 0.925, the root mean square error (RMSE) is 27.8 W/m^2, and the bias (BIAS) is -14.2 W/m^2. For LE, the R^2, RMSE, and BIAS are 0.946, 24.7 W/m^2, and 0.5 W/m^2, respectively. The accuracy of parameterization for LE is slightly better than that for H, which may be related to the more unknown variables in the parameterization for LE. For most of the selected days, the RMSEs of H and LE can be less than 50 W/m^2, the

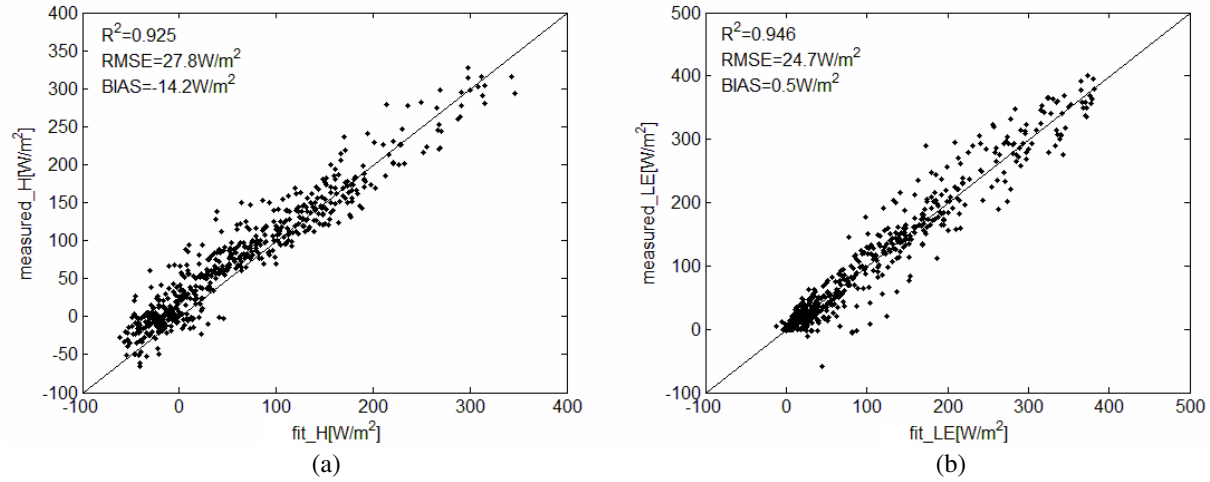

Figure 1: The comparison of (a) the sensible heat flux and (b) the latent heat flux from the parameterization with the EC measurements.

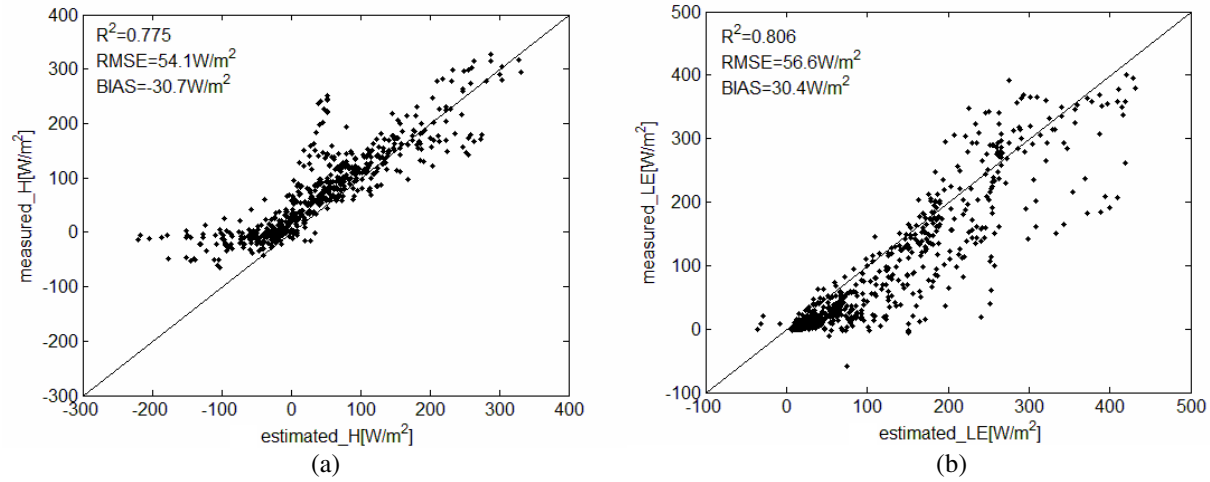

Figure 2: The inverse (a) sensible heat flux and (b) latent heat flux for 24 selected days compared with the measurements.

absolute BIAS can be less than 30 W/m^2, and the R^2 can be larger than 0.9. The parameterization for H is more sensitive to the difference between surface temperature and air temperature. The larger the difference during the daytime, the higher the parameterization accuracy is. The parameterization for LE is not only related to the difference between surface and air temperatures, but also to the saturation vapor pressure at surface temperature.

3.2. The Application of Parameterization

When the parameterization is determined, the main problem for the estimation of H and LE is to obtain the unknown variables A, B, C, D, E, and F. The minimization technique is used to help the solution. Given the complexity to solve the heat conduction equation, this study assumes that the surface available energy is known, and the unknown variables are solved by flux method. The input variables are only the surface temperature and the air temperature. Without the aid of any *a priori* knowledge, the RMSEs of H and LE are 54.1 and 56.6 W/m^2, and R^2 are 0.775 and 0.806, respectively (see Figure 2). The H is underestimated by 30.7 W/m^2, which is consistent with the accuracy of parameterization shown in the Figure 1. Because the energy balance is implied in the minimization technique, the corresponding LE is overestimated by 30.4 W/m^2. Due to the lack of the stabilized procedure, some discrete points can be observed in Figure 2. The inverse results on the day 105 of the year 2010 are displayed in the Figure 3. The R^2 of H and LE are 0.979 and 0.989, respectively, almost close to 1. The H is only underestimated by 7.5 W/m^2. The RMSEs are

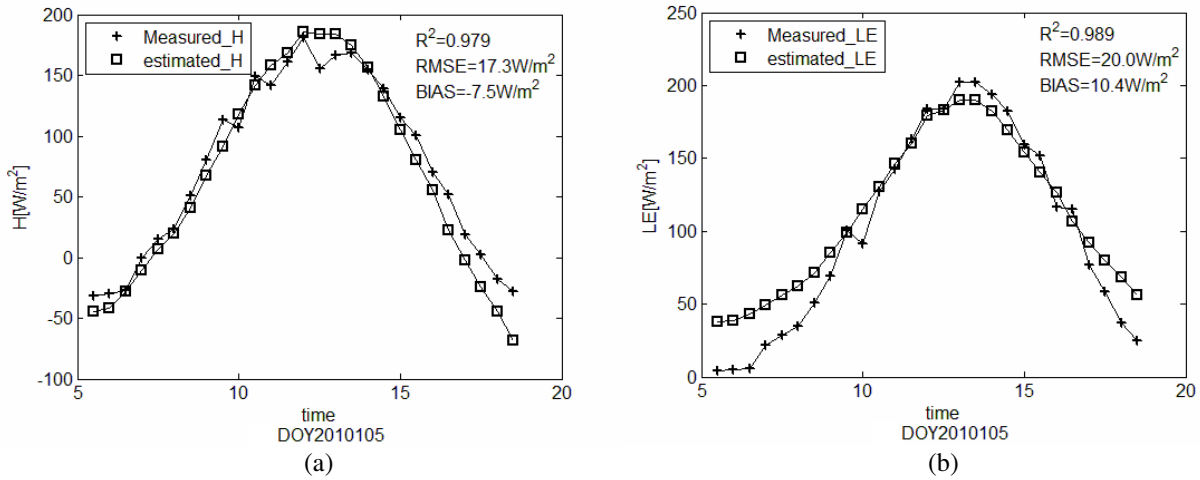

Figure 3: The inverse (a) sensible heat flux and (b) latent heat flux on the day 105 of the year 2010 compared with the measurements.

17.3 W/m^2 and 20.0 W/m^2, respectively. In addition, the inverse accuracy at the sunrise and the sunset is slightly worse than that during the noon on this day, because the stable condition as well as the negative temperature gradient is common at that time.

4. CONCLUSION AND DISCUSSION

According to the study of Raffy and Becker, the H and LE can be parameterized by some unknown constants and some known functions. This work proposed a simple parameterization for H under unstable condition during the daytime, and subsequently the parameterization for LE is also proposed. The accuracy of parameterization is acceptable. If these unknown variables can be obtained accurately, the H and LE at any time during the daytime can be estimated, and consequently the daily ET can be calculated. The main problem for this method is how to obtain those unknown constants. Some *a priori* knowledge and stabilized procedure can be used to optimize the results. However, because the work is only a preliminary approach, *a priori* knowledge is not considered in this study so that some inverse results are unsatisfied. Therefore, more work need to be done in the future:

1) To minimize surface temperature by solving the heat conductivity equation so that those unknown variables can be estimated with a better accuracy.
2) To find the relationship between these unknown variables and those parameters that can be obtained from remotely sensed data so that the initial value for minimization technique can be determined.
3) To add some *a priori* information and some constrain conditions to stabilize the iterative procedure.

The main advantage of the method is that it is not necessary to calculate the resistance, and the heat flux at any time during the daytime can be estimated. It is then more convenient to obtain the daily ET. This method can adequately utilize the time information from geostationary meteorological satellite data in the future. However, it may be improper for this method to use the data from polar orbital satellite. Another problem for this method is how to obtain the air temperature at the pixel scale when satellite data are used.

ACKNOWLEDGMENT

This work was supported by the independent innovation project of the Institute of Geographic Sciences and Natural Resources Research, Grant No. 201003007. Ms. J. Lu is financially supported by China Scholarship Council for her stay in LSIIT, Strasbourg, France.

REFERENCES

1. Li, Z. L., et al., "A review of current methodologies for regional evapotranspiration estimation from remotely sensed data," *Sensors*, Vol. 9, No. 5, 3801–3853, 2009.

2. Tang, R., Z. L. Li, and B. Tang, "An application of the Ts-VI triangle method with enhanced edges determination for evapotranspiration estimation from MODIS data in arid and semi-arid regions: Implementation and validation," *Remote Sensing of Environment*, Vol. 114, No. 3, 540–551, 2010.
3. Anderson, M., et al., "A two-source time-integrated model for estimating surface fluxes using thermal infrared remote sensing," *Remote Sensing of Environment*, Vol. 60, No. 2, 195–216, 1997.
4. Raffy, M. and F. Becker, "An inverse problem occurring in remote sensing in the thermal infrared bands and its solutions," *Journal of Geophysical Research*, Vol. 90, No. D3, 5809–5819, 1985.
5. Hechinger, E., M. Raffy, and F. Becker, "Comparison between the accuracies of a new discretization method and an improved Fourier method to evaluate heat transfers between soil and atmosphere," *Journal of Geophysical Research*, Vol. 87, No. C9, 7325–7339, 1982.
6. Abdellaoui, A., F. Becker, and E. Olory-Hechinger, "Use of meteosat for mapping thermal inertia and evapotranspiration over a limited region of mali," *Journal of Applied Meteorology*, Vol. 25, 1489–1506, 1986.
7. Raffy, M. and F. Becker, "A stable iterative procedure to obtain soil surface parameters and fluxes from satellite data," *IEEE Transactions on Geoscience and Remote Sensing*, Vol. 3, 327–333, 1986.
8. Blümel, K., "Estimation of sensible heat flux from surface temperature wave and one-time-of-day air temperature observation," *Boundary-Layer Meteorology*, Vol. 86, No. 2, 193–232, 1998.

Wireless Power Transmission by Scalar Waves

Konstantin Meyl
Faculty of Computer and Electrical Engineering, Furtwangen University, Germany

Abstract— Current RFID technology explains how the transfer of energy takes place on a chip card by means of longitudinal wave components in close range of the transmitting antenna. It is scalar waves which spread towards the electrical or the magnetic field pointer. That provides the better explanation. Using the wave equation proposed by Maxwell's field equations these wave components were set to zero. Why were only the postulated model computations provided after which the range is limited to the sixth part of the wavelength.

This text proposes instead the rationale for scalar wave components in the wave equation of Laplace. Physical conditions for the development of scalar wave transponders become operable well beyond the close range. Scalar wave information and energy is transferred with the same carrier wave and not carried over two separated ways as with RFID systems. Bi-directional signal transmission with energy transfer in both directions is achieved when there is a resonant coupling between transmitter and receiver.

The first far range transponders developed on the basis of the extended field equations are already functional as prototypes, according to the US-Patent No. 787,412 of Nikola Tesla: Art of transmitting electrical energy through the natural medium [11], New York 1905.

1. INTRODUCTION

Transponders serve the transmission of energy, e.g., on a chip card in combination with a transmission of information. The range is with the presently marketable devices (RFID technology) less than one meter [2]. The energy receiver must be in close range of the transmitter. The far range transponders developed by the first transfer centre for scalar wave technology are able to transfer energy beyond close range (10 to 100 m) with fewer losses and/or a higher efficiency. The energy using the same carrier wave is transferred as well as information vs. the RFID technology which uses two separate systems [2].

A condition for new technologies is a technical-physical understanding, as well as a mathematically correct and comprehensive field description, which include all well known effects of the close range of an antenna. We encounter here a central problem of the field theory, which forms the emphasis of this paper and the basis for advancements in transponder technology.

In today's times of bluetooth and Wireless LAN one quickly becomes accustomed to the amenities of wireless communication. For example garage gates, the barrier of the parking lot, or the car trunk are opened by radio.

However, the limited life span and often polluting batteries used in numerous radio transmitters and remote maintenances create a great disadvantage.

Ever more frequently the developers see themselves confronted with the demand for a wireless transfer of energy. Accumulators are to be reloaded or replaced completely. In entrance control systems (ski elevator, stages, department stores...) these systems are already successfully used. But new areas of application with increased requirements are constantly added apart from the desire for a larger range:

- In telemetry plants rotary sensors are to be supplied with energy (in the car, e.g., to control tire-pressure).
- Also with heat meters the energy should come from a central unit and be spreadly wireless in the whole house to the heating cost meters without the use of batteries.
- In airports contents of freight containers are to be seized, without having been opened (security checks).
- The forwarding trade wants to examine closed truck charges by transponder technology.
- In the robot and handling technique the wirings are to be replaced by a wireless technology due to wear-out problem.
- Portable radio devices, mobile phones, Notebooks and remote controls working without batteries and Accumulators will reduce the environmental impact.

A technical solution, which is based on pure experimenting and trying, is to be optimised unsatisfactorily and hardly. It should stand rather on a field-theoretically secured foundation, whereby everyone thinks first of Maxwell's field equations. Here however a new hurdle develops itself engaged closely.

2. FIELD THEORETICAL PROBLEM

In the close range of an antenna, the current level of knowledge is longitudinal based — towards a field pointer portions of the radiated waves present. These are usable in the transponder technology for the wireless transmission of energy. The range amounts to only $\lambda/2\pi$ and that is approximately the sixth part of the wavelength [6]. The problem consists now of the fact that the valid field theory from Maxwell, is only able to describe transversal and not longitudinal wave components. All computations of longitudinal waves or wave components, which run toward the electrical or the magnetic pointer of the field, are based without exception on postulates [12].

The near field is not considered in vain as an unresolved problem of the field theory. The experimental proof may succeed, but not the field-theoretical proof. The wave equation derived from the field equations according to Maxwell on one hand is a transverse electro-magnetic wave [10]:

$$\underbrace{-\text{curl curl}\,\mathbf{E}\cdot c^2}_{\text{transverse}} = \underbrace{\delta^2\mathbf{E}/\delta t^2}_{-\text{ wave}} \underbrace{+(1/\tau_1)\cdot\delta\mathbf{E}/\delta t}_{+\text{ vortex damping}} \tag{1}$$

On the other hand there is a damping term in the equation which is responsible for the losses of an antenna. It indicates the wave component, which is converted into standing waves, can also be called field vortices, which produce vortex losses for their part with the time constant τ_1 in the form of heat.

Where, at close range of an antenna proven and with transponders technically used longitudinal wave components hide themselves in the field Equation (1)?

3. WAVE EQUATION

The wave equation found in most textbooks has the form of an inhomogeneous Laplace equation. The famous French mathematician Laplace considerably earlier than Maxwell did find a comprehensive formulation of waves and formulated it mathematically:

$$\underbrace{\Delta\mathbf{E}\cdot c^2}_{\text{Laplace operator}} = \underbrace{-\text{curl curl}\,\mathbf{E}\cdot c^2}_{\text{transverse-(radio wave)}} + \underbrace{\text{grad div}\,\mathbf{E}\cdot c^2 = \delta^2}_{\text{longitudinal-(scalar wave)}}\ \underbrace{\mathbf{E}/\delta t^2}_{\text{wave}} \tag{2}$$

On the one side of the wave equation the Laplace operator stands, which describes the spatial field distribution and, according to the rules of vector analysis, can be decomposed into two parts. On the other side the description of the time dependency of the wave can be found as an inhomogeneous term.

If the wave equation according to Laplace (2) is compared to Equation (1) derived from the Maxwell equations, then two differences clearly come forward:

1. In the Laplace equation the damping term is missing.
2. With divergence E a scalar factor appears in the wave equation and a scalar wave as a consequence.

A Practical example of a scalar wave is the plasma wave. This case forms according to the Maxwell Equation (3):

$$\text{div}\,\mathbf{D} = \varepsilon\cdot\text{div}\,\mathbf{E} = \rho_{el} \tag{3}$$

the space charge density consisting of charge carrier's ρ_{el} the scalar portion. These move in form of a shock wave longitudinal forward and present in its whole an electric current.

Since both descriptions of wave's posses equal validity, we are entitled in the sense of a coefficient comparison to equate the damping term due to eddy currents according to Maxwell (1) with the scalar wave term according to Laplace (2).

Physically seen the generated field vortices form and establish a scalar wave.

The presence of div $\mathbf{E}$ proves a necessary condition for the occurrence of eddy currents. Because of the well-known skin effect [3] expanding and damping acting eddy currents, which appear as a consequence of a current density $\mathbf{j}$, set ahead an electrical conductivity σ.

4. VIEW OF DUALITY

Within the near field range of an antenna opposite conditions are present. With bad conductivity in a general manner a vortex with dual characteristics would be demanded for the formation of longitudinal wave components. I want to call this contracting antivortex a potential vortex contrasting the expanding vortex by eddy currents.

If we examine the potential vortex with the Maxwell equations for validity and compatibility, then the potential vortex would be Zero. The derivation of the damped wave Equation (1), [7] can take place in stead of the electrical also for the magnetic field strength. Both wave Equations (1) and (2) do not change their shape. In the inhomogeneous Laplace equation in this dual case however, the longitudinal scalar wave component through div $\mathbf{H}$ is described and this is according to Maxwell zero!

Maxwell's Equation (4):

$$\operatorname{div} \mathbf{B} = \mu \cdot \operatorname{div} \mathbf{H} = 0 \tag{4}$$

If this is correct, then there may not be a near field, no wireless transfer of energy, and finally also no transponder technology. Therefore, the correctness (of Equation (4)) is to be examined, what would be the result if potential vortices exist forming scalar waves in the air around an antenna, as the field vortices form among themselves a shock wave.

Besides still another boundary problem will be solved: since in div D electrical monopoles can be seen (3) there should result from duality magnetic monopoles to div $\mathbf{B}$ (4). In October 2009 the search has been successful the first time [9]. Vortex physics will give the answer and the derivation in mathematic is still published [8]. What is the result?

5. TESLA'S DREAM, WIRELESS ENERGY SUPPLY

It is apparent from Tesla's patents that instead of using a connection line he grounded his pancake coils on one side. At the high voltages and frequencies he used the earth behave as part capacitive and part electrical conductor [11]. However with this technique any grounded consumer load in resonance can deduct energy. That might include a disagreeable competitor. That's why the project to wirelessly supply ships on the ocean with energy wasn't put into practice. However the feasibility of this principle was proven in 2001 by the "First Transfer Centre for Scalar Wave Technology" using a miniature boat.

"The boat is working without a battery", proclaims the narrator in a ZDF documentary. "*Also, it isn't dragging a cable along"*. The power output of its motor is approximately 5 Watts and the installation's efficiency is about 100%. As the electrical circuit closure is much easier to realize in practice than the magnetic one, at an unattainably high efficiency, especially the Tesla principle is considered economically viable.

In addition, metal parts are oftentimes present, functioning as potential equalization panel or return conductor, in a car for example the body, or the iron parts in a machine tool, the conduction system of heating pipes in consumption counters or the guiding rails in elevators or other rail-bound vehicles.

No one can ignore the fact that only in the case of resonance; energy will reach the receiver, i.e., at the same frequency and opposite sign. For the layman, that can be illustrated by the image of power "flowing out" of a power plant then "flowing in" to its consumer. Both leads in the cable thereby induce resonance as the two-poled plug is put into the socket.

In principle, this is also possible with only one cable, only then, the resonance is no longer forced, which is why the receiver can drop (i.e., energy does not reach it any longer). By optimising range and conservation of resonance, for example by variation of the coil and antennae geometry, these problems are manageable.

In wireless energy supplies as utilized in remote controls or mobile phones no "return conductor" is available. It is in these circumstances that magnetic coupling with all its disadvantages comes into play. The disadvantages culminate at the point where the receiver, entirely without guidance wires or other means of connection to the emitter, doesn't know which signal to resonate with. The limiting factor in practical use is not the distance over which resonance can still be maintained, but the tuning distance over which the wireless transmission system is capable of starting up without foreign assistance.

The tasks of a transponder include not only wireless energy, but also information transfer. Now both systems benefit from the fact that intertwined with the magnetic radiation field, magnetic scalar waves always appear, analogous to the electric ones accompanying electrical energy radiation.

To keep down transmission losses a minimization of scalar waves is the aim. In any case, the wave remainder is modulateable and usually sufficient for information conduction in both ways (i.e., from emitter to receiver and vice versa). That would be a ***point-to-point****-connection of energy and information.*

A ***multi-point****-connection* is set up so a power emitter supplies many stations with radiation energy, eliminated the need for a battery or external power supply. If a receiving station is being modulated (i.e., fed with information), this is noticeable at all other stations. Equipped with a code (i.e., with a pattern match comparable to a telephone number), individual communications within a vast network are also conceivable. That's the basis of a cell phone network relying on scalar waves, without radio masts, without harmful e-smog and with less that a thousandth of the emitting power common today.

6. SUMMARY, RFID TECHNOLOGY OR SCALAR WAVE TRANSPONDER?

In comparison, RFID technology (radio frequency identification) comes off badly, especially when both energy and bidirectional information transmission each rely on a separate system. While a scalar wave transponder can unify all three systems. The verdict on using RFID becomes even more devastating when examining the occurring scatter fields.

Today's RFID technology is a compromise, making clear the limitations of Hertz'ian wave technology. Energy transmission occurs at around 120 kHz, so that the useful near-field area is maximized, while information is sent back in the microwave spectrum, so that its emitter is small enough for storage in a credit card. People in the vicinity are exposed to the sum of both scatter fields. That is a fact, regardless of the biological effects of VLF- or microwave radiation. For precautionary measure, but also for reasons of efficiency, in the future all signal routes such as wireless LAN or Bluetooth are to be combined with a wireless energy transmission on the basis of scalar waves as the only way to eliminate scatter fields and to prevent biological effects.

7. FROM PRACTICAL EXPERIENCE

If the antenna efficiency is very low (i.e., in case of misadjusted antennae), the useful amplitude decreases while simultaneously antenna noise increases. According to the wave equation, the explanation could be different: From all the emitted waves the transversal waves decrease in favour of longitudinal waves. But the latter are being utilized in transponder technology, which is why unconventional antennae structures oftentimes allow for better results than common or time tested ones. Spherical antennae have proven especially useful in electrical transmission lines. The larger the sphere, the more the reception area for energy can be extended past the near field. This effect can be demonstrated experimentally quite convincingly. So far, high frequency technicians have only concerned themselves with maximizing the transversal wave so that it wouldn't be overwhelmed by noise. The construction of far range transponders calls for misadjusted antennae, the very opposite of what is being taught today in the field of HF technology, for inverted technical solutions.

And thus, the introduction and development of a new transponder technology first demands an extended view and secondly novel ways of high frequency technology education.

8. THE EXTENDED FIELD THEORY

It could be demonstrated that Maxwell's field equations contain an approximation and therefore only constitute a special case of a new, dually formulated and more universal approach. The mathematical derivations of the Maxwell field and the wave equation uncover what the Maxwell approximation is. The dual counter vortex, with its skin effect expanding and contracting towards the vortex current, also referred to as potential vortex, is being omitted. Is it capable of forming structures and propagates as longitudinal scalar wave in badly conductive materials such as air or vacuum. At relativistic velocities, the potential vortices are affected by Lorentz contraction. As scalar waves propagate longitudinally in the direction of an oscillating field pointer, the potential vortices experience a steady oscillation in size, consequently to their oscillating propagation. Imagining the field vortex as planar but coiled transversal wave, it follows from the oscillations in size and thus wavelength at a constant vortex velocity ($= c$) a permanent change in frequency, which is being measured as noise.

This noise turns out to be the potential vortex term omitted from the Maxwell equations. If, for example, a noise signal is being measured at an antenna this proves the existence of potential vortices. If, however, the Maxwell equations' scope of validity is left behind, misinterpretations and

ignorance of accordant phenomena from the field theory are the consequence and the noise or near field can not be further calculated or conclusively explained.

For example this leads to mobile phone industry claims that a mobile phone is less harmful to the human organism when the antenna efficiency is reduced by artificially shortening the antenna, thereby fewer Hertz'ian waves are being emitted.

In fact, the antenna noise (i.e., the biological relevant scalar wave proportion), is being increased, only it is not measured in a laboratory for electromagnetic environmental compatibility (EMC).

Already in principle, it is impossible to reproduce measure vortices since they will vortex at the probe, or else they wouldn't be vortices!

It's being said that there are faithful apostles of science who only think of the measurable as real. What they can not measure can not exist, and therefore they have trouble accepting the existence of scalar waves. It's that easy to deny the existence of scalar waves, although only until it comes to an industrial practical usage of this physical phenomenon, for example for scalar wave transponders.

REFERENCES

1. Jackson, J. D., *Classical Electrodynamics*, 2nd Edition, Wiley & Sons, NY, 1975.
2. Kolnsberg, S., "Drahtlose signal- und energieübertragung mit hilfe von hochfrequenztechnik in CMOS-sensorsystemen," *RFID-Technologie*, Dissertation Uni Duisburg, 2001.
3. Küpfmüller, K., *Einführung in Die Theoretische Elektrotechnik*, 12th Edition, Springer Verlag, 1988.
4. Lehner, G., *Elektromagnetische Feldtheorie*, 1st Edition, 239, Springer Verlag, 1990.
5. Maxwell, J. C., *A Treatise on Electricity and Magnetism*, Dover Publications, New York, 1873.
6. Meinke, H. H. and F. W. Gundlach, *Taschenbuch der Hochfrequenztechnik*, 4th Edition, No. 2, Springer Verlag, 1986.
7. Meyl, K., *Scalar Wave Transponder*, Indel-Verlag, www.etzs.de, 2006; 3rd Edition, 2012.
8. Meyl, K., "Field-physical basis for electrically coupled bi-directional far range transponders," *Proc. of the RFID Eurasia Conference 2007, IEEE Catalogue*, No. 07EX1725, 78–89, 2007, http://www.k-meyl.de/go/Primaerliteratur/Proc_RFID_Eurasia.pdf.
9. Morris, D. J. P., D. A. Tennant, S. A. Grigera, B. Klemke, C. Castelnovo, R. Moessner, C. Czternasty, M. Meissner, K. C. Rule, J.-U. Hoffmann, K. Kiefer, S. Gerischer, D. Slobinsky, and R. S. Perry, "Dirac strings and magnetic monopoles in the spin ice $Dy_2Ti_2O_7$," *Science*, Vol. 326, No. 5951, 411–414, Oct. 16, 2009.
10. Simonyi, K., *Theoretische Elektrotechnik*, 7th Edition, Vol. 20, 654, VEB Verlag, Berlin, 1979.
11. Tesla, N., "Art of transmitting electrical energy through the natural medium," United States Patent, No. 787, 412, Apr. 1905.
12. Zinke, O. and H. Brunswig, *Lehrbuch der Hochfrequenztechnik, 1. Band*, 3rd Edition, 335, Springer-Verlag, by Prof. Dr. Konstantin Meyl, Furtwangen University, Germany, 1986.

Study of Transmission Performance on Strong Coupling Wireless Power Transfer System in Free Position

X. L. Huang, W. Wang, L. L. Tan, J. M. Zhao, and Y. L. Zhou
School of Electrical Engineering, Southeast University, Nanjing 210096, China

Abstract— Based on transformer theory and the SP model, this paper have an in-depth discussion of changing relationships between output power or transmission efficiency of the system and the receiving coil in different free position. Simulation by Matlab, we find that when two coil axis distance are in close proximity and the radial offset distance or deflection of receiving coils are smaller, the transmission efficiency is maximum, but the output power is not the biggest. Appropriate adding axial distance, radial offset distance between coils or deflection angle of receiving coils, greater output power are available. Finally, the correctness of the theory can be verified through a series of experiments. We can also obtain that surrounding environment of the wireless transmission system has a effect on output power and transmission efficiency of the system. It laid the foundation for further applied research of the wireless transmission system.

1. INTRODUCTION

In recent years, as research of the wireless power transmission technology continue to heat up and its related applications continue to broadenmore and more scientists give sufficient recognition of this technology. Many research areas are racing to chase, such as wireless charging of portable small household appliances, wireless power supply of implanted human medical devices, wireless charging for electric vehicles, etc., and technology in application has made a definite breakthrough [1]. In contrast, the traditional cable transmission system shows a growing number of drawbacks. In the special area of deep sea, coal, chemicals and so on, a large series of security and constructive problems such as spark, the laying and maintenance difficulties of transmission lines have made the wireless power transmission technology an urgent need to these fields [2].

At present, the receiver coil of magnetic coupling wireless power transmission system in a free position is becoming a hot spot. In this paper, according to the change status of output power and transmission efficiency of the receiving coil in different free position, the optimal location of receiver coil for output power and transmission efficiency in the system is explored by the method of simulation analysis and experimental validation. Based on the above, in the case of the same compensation capacitor of the system, the method of the maximum output power or transmission efficiency has been obtained in different axial distance, radial offset distance or offset angle of coils.

2. THE ESTABLISHMENT OF THE TRANSMISSION SYSTEM MODE

At present, according to take capacitors in series resonant compensation or parallel resonant compensation of the transmitter and the receiver coils, the wireless power transmission system model can be divided into four categories: Series-Series (SS), Series-Parallel (SP), Parallel-Series (PS) and Parallel-Parallel (PP) [3]. In this paper, the model of SP has been chosen as the analytical model of wireless power transmission system.

Take the same parameter of coils as the receiver and the transmitter in Figure 1, U_s is high frequency power, R is the equivalent resistance of transmitter and receiver coil, L is equivalent inductance, C_e is parasitic capacitance in high-frequency, C_t is external tunable capacitors. In the

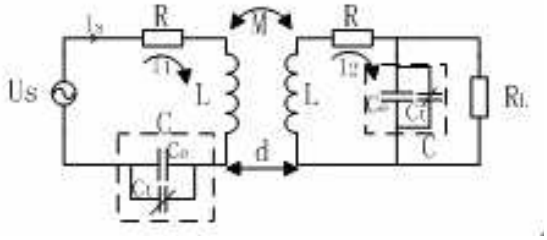

Figure 1: SP model.

condition of parallel compensation, and for the convenience of theoretical analysis, the terminal adjustable capacitors of the transmitter and the receiver are adjusted to the same value considered to take the ideal load (Infinite resistance). It does not affect the transmission power and its corresponding efficiency. R_L takes purely resistive load.

For these two models, the KVL equation can be listed based on equivalent circuit [4]:

$$\begin{cases} \dot{I}_1 Z_1 - j\omega M \dot{I}_2 = \dot{U}_s \\ \dot{I}_2 Z_2 - j\omega M \dot{I}_1 = 0 \end{cases} \tag{1}$$

Loop current can be obtained: $\dot{I}_1 = \frac{Z_2 \dot{U}_s}{Z_1 Z_2 + (\omega M)^2}$, $\dot{I}_2 = \frac{j\omega M \dot{U}_s}{Z_1 Z_2 + (\omega M)^2}$. In which $Z_1 = R + j\omega L + \frac{1}{j\omega C}$; $Z_2 = R + j\omega L + \frac{\frac{R_L}{j\omega C}}{R_L + \frac{1}{j\omega C}}$, when two coils in resonance, we can draw simplified expression of efficiency as follows:

$$\eta = \frac{(\omega M)^2 R_L}{\left[(1 + \omega^2 C^2 R_L^2)R + R_L\right]\left[R(R + \frac{R_L}{1+\omega^2 C^2 R_L^2}) + (\omega M)^2\right]} \tag{2}$$

3. THEORETICAL ANALYSIS

For a more comprehensive analysis of general laws of energy transferring between coils in free position in the transmission process, the power and efficiency formulas use more general forms of expression under the model of parallel resonance. That is: $P_{in} = \mathrm{Re}[\dot{U}_s \dot{I}_1^*]$, $P_{out} = |\dot{I}_2|^2 R_L$. Therefore, the efficiency of system is $\eta = \frac{P_{in}}{P_{out}}$. By further calculation, the analytical solution of output power P_{out} and efficiency η are:

$$P_{out} = U_s^2 \frac{\left(k_3 R_L \omega^2 MC - k_4 \omega M\right)^2 + \left(\omega M k_3 + k_4 \omega^2 MC R_L\right)^2}{\left(1 + \omega^2 C^2 R_L^2\right)^2 \left(k_3^2 + k_4^2\right)^2} \cdot R_L; \tag{3}$$

$$\eta = \frac{\left(k_3 R_L \omega^2 MC - \omega M k_4\right)^2 + \left(\omega M k_3 + k_4 \omega^2 MC R_L\right)^2}{(k_1 k_3 + k_2 k_4)\left(1 + \omega^2 C^2 R_L^2\right)^2 \left(k_3^2 + k_4^2\right)} \tag{4}$$

in which: $k_1 = \frac{R + R\omega^2 C^2 R_L^2 + R_L}{1 + \omega^2 C^2 R_L^2}$, $k_2 = \omega L - \frac{\omega C R_L^2}{1 + \omega^2 C^2 R_L^2}$, $k_3 = k_1 R + k_2 \frac{1 - \omega^2 LC}{\omega C} + (\omega M)^2$, $k_4 = k_2 R + k_1(\omega L - \frac{1}{\omega C})$.

However, the essence of the achievement of performance indicators in the magnetic coupling wireless power transmission system, such as power or efficiency, has relationship with the change of mutual inductance of coupled coils in free position. The following paper focuses on the relationship of mutual inductance between coils in the space free position.

3.1. The Mutual Inductance of Two Parallel Coils in Space

Figure 2 shows the space location of two parallel coils, as follows.

According to the Neumann formula, $M = \frac{\mu_0}{4\pi} \oint_{C1} \oint_{C2} \frac{d\ell_1 d\ell_2}{|X_2 - X_1|}$; μ_0 is the magnetic constant. Taking two same conductive rings in axis of Figure 2, ignoring the effect of a small amount of factors, such

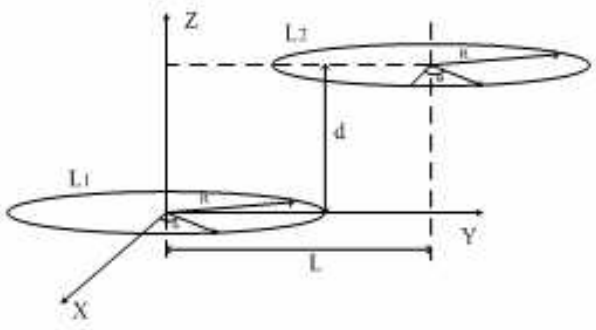

Figure 2: Axial, radial offset positions of coils.

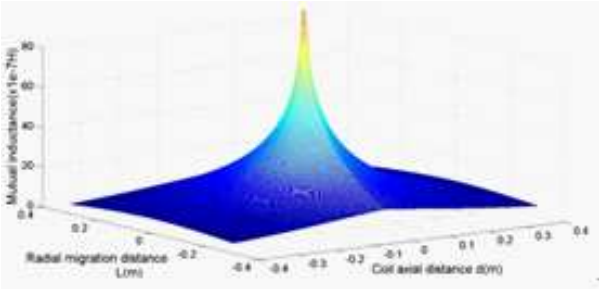

Figure 3: M_{12} varies with L, d.

as the uneven shape of coils, the mutual inductance can be expressed as [5]:

$$M_{12}=\frac{\mu_0}{4\pi}\oint_{C1}\oint_{C2}\frac{d\ell_1 d\ell_2}{|X_2-X_1|}=\frac{\mu_0}{4\pi}\int_0^{2\pi}d\phi\int_0^{2\pi}\frac{R^2\cos(\theta-\phi)d\theta}{\sqrt{R^2(\cos\theta-\cos\phi)^2+(L+R\sin\theta-R\sin\phi)^2+d^2}} \quad (5)$$

in which, μ_0 is the vacuum magnetic permeability, Value: $4\pi\times10^{-7}$ (A/m), R is radius of coils. In order to verify the accuracy of experiment, R takes the value 0.1 m that is radius of coils in experiment. L is radial offset distance of two coils, d stands for axial offset distance.

As is shown in Figure 3, when the radial offset distance and axial offset distance of two coils are relatively small, the mutual inductance value is larger and coils are more closely coupled. The mutual inductance value continues to decay with the axial and radial distance gradual widening. It can be concluded that when coils are in close proximity, they are in a strongly coupled state.

3.2. The Mutual Inductance between Two Coaxial but Not Parallel Coils in Space

Figure 4 is for two coaxial non-parallel coils, in which exists a certain deflection α in coil 1, 2, ignoring the effect of a small amount of factors, such as the uneven shape of coils.

We can get the relationship between mutual inductance of L_1, L_2 and axial distance d, radial distance L_2, angle of rotation α:

$$M_{12}=\frac{\mu_0}{4\pi}\int_0^{2\pi}d\phi\int_0^{2\pi}\frac{R^2(\cos\theta\cos\phi+\sin\theta\sin\phi\cos\alpha)d\theta}{\sqrt{(R^2\cos\theta\cos\phi)^2+(R\sin\theta\cos\alpha-R\sin\phi)^2+(-R\sin\theta\sin\alpha+d)^2}} \quad (6)$$

The mutual inductance is simulated in Figure 5. It is shown that When the two coils fit closely, the maximum mutual inductance appears in $\alpha=0$, and this time two coils stay in a strongly coupled state. There is a maximum mutual inductance value in a deflection angle when the axial distance between two coils is gradual widening.

4. RESEARCH WITH SIMULATION AND EXPERIMENTAL

4.1. Analysis with Simulation

In order to study the link between power, efficiency of system and the receiver in free position, this paper starts from mutual inductance of coils in free position, drawn the relationship between

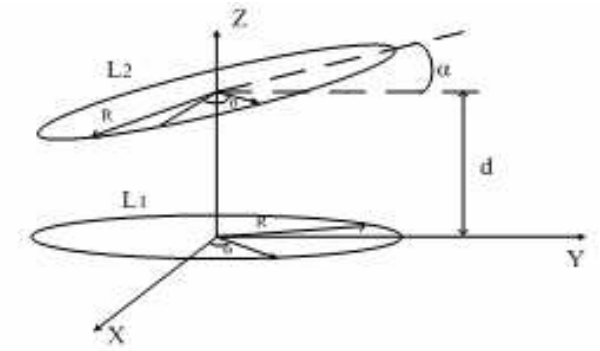

Figure 4: Rotational position of receiving coil.

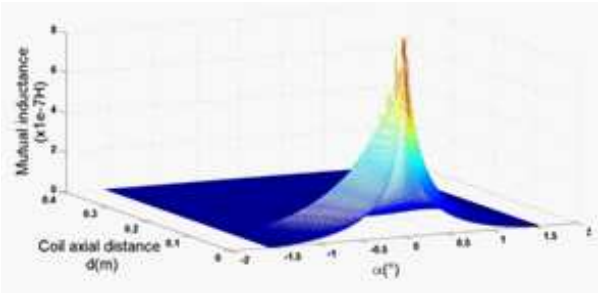

Figure 5: M_{12} varies with d, α.

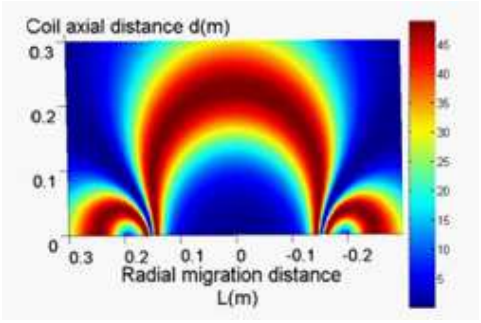

Figure 6: P varies with d, L.

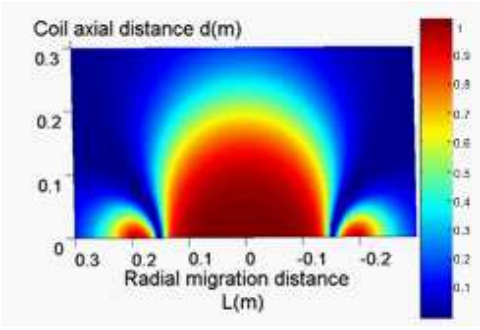

Figure 7: η varies with d, L.

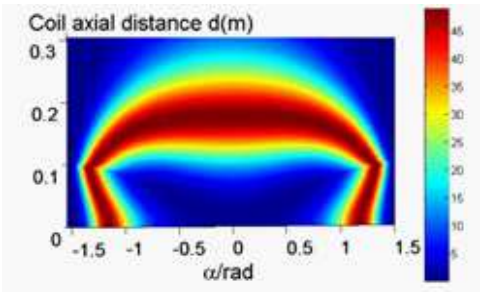

Figure 8: P varies with d, α.

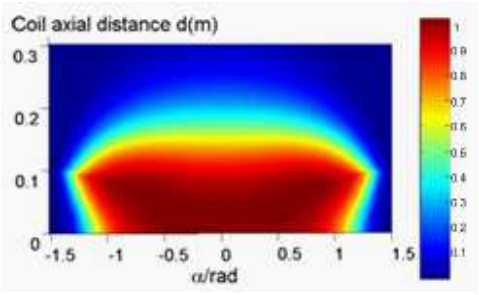

Figure 9: η varies with d, α.

power, efficiency of system and the location parameter of coils through the simulation, and make the conclusion.

The parameters of system come from the actual measurement: turns of two coils are $N = 31$, considering the skin effect in high frequency, equivalent resistance of coils are $R = 0.73\,\Omega$, inductance $L = 300\,\mu\text{H}$, compensation capacitor $C = 2200\,\text{pF}$, output frequency of power $\omega = 1/\sqrt{LC} = 1.23 \times 10^6$, take constant resistive load $R_L = 484\,\Omega$.

(1) Simulation results of transferring efficiency, power with axial, radial offset of receiving coils.

In this paper, figures about P, η with d, L have been drawn by MATLAB simulationas shown in Figures 6, 7.

It can be seen from Figure 6 that when radial offset and axial distances are small, two coils are in a strongly coupled state. The output power of system is too small, but the efficiency is very high. To maintain the axial distance constant, appropriate pulling the radial offset distance or to keep radial offset distance unchanged, increasing the axial offset distance, output power of system will increase and the efficiency decrease. In a certain position, the output power can be achieved maximum under the same condition. Through Figures 6, 7 we can clearly see that there is a clear frequency splitting phenomenon when the axial distance $d \leq 5\,\text{cm}$. The maximum points of output power and transmission efficiency do not appear at the same point in a free position.

(2) Simulation results of transferring efficiency, power with axial, angle offset of receiving coils.

In different axial distances, the relationship between transmission efficiency, output power and the deflection angle of receiver coils has been studied of. Figures about P, η with d, α have been drawn by MATLAB simulationas shown in Figures 8, 9.

As is shown in Figures 8, 9, when axial offset distance is small, two coils are in a strongly coupled state. The output power is very small, but the transmission efficiency high. Maintaining the same axial distance, proper turning the deflection of receiving coils, the output power gradually increases, and the maximum output power appears at a certain angle in the same axial distance. However, the transmission efficiency η decreases with the deflection α increasing. When the coil deflection angle is small and fixed, there is a power transferring optimization region in a given axial distance. In this region, the maximum output power is reached under the same deflection. But with axial distance widening, the transmission efficiency decreases in the same deflection. It also can be seen from Figures 8, 9, when $\alpha \sim [57°, 85°]$, there is a clear frequency splitting phenomenon.

4.2. Experimental Verification

In order to verify the theory, the experimental system similar to simulation has been designed in this paper. Fixed frequency of power, the relationship between output power, transmission efficiency and radial offset distance L, deflection α has been drawn when $d = 5\,\text{cm}$ and $d = 20\,\text{cm}$. At the same time, a set of obstacles experiments have also been designed for the specific application environment, such as wireless charging for electric vehicles. That is, at $D = 10\,\text{cm}$, symmetric adding two iron panels on both sides of the system. The following figures are plotted by experiment in several different situations, in which the blue line represents the experimental system with iron panels.

It can be seen from Figure 10(a), when the axial distance is 5 cm and the radial distance is 0, the output power is not the largest. Appropriate Increasing the radial distance, the output power is gradually increased to the maximum. When $L = \pm 21\,\text{cm}$, frequency splitting point appears, and there is an extreme value in a small range. From Figure 10(b) we can find that when $L \sim [-10, 10]\,\text{cm}$, Transmission efficiency is above 80%. As $L \approx \pm 23\,\text{cm}$, there is an extreme value. The above two points further validate the correctness of theory. As adding iron panel, both output power and transmission efficiency decrease.

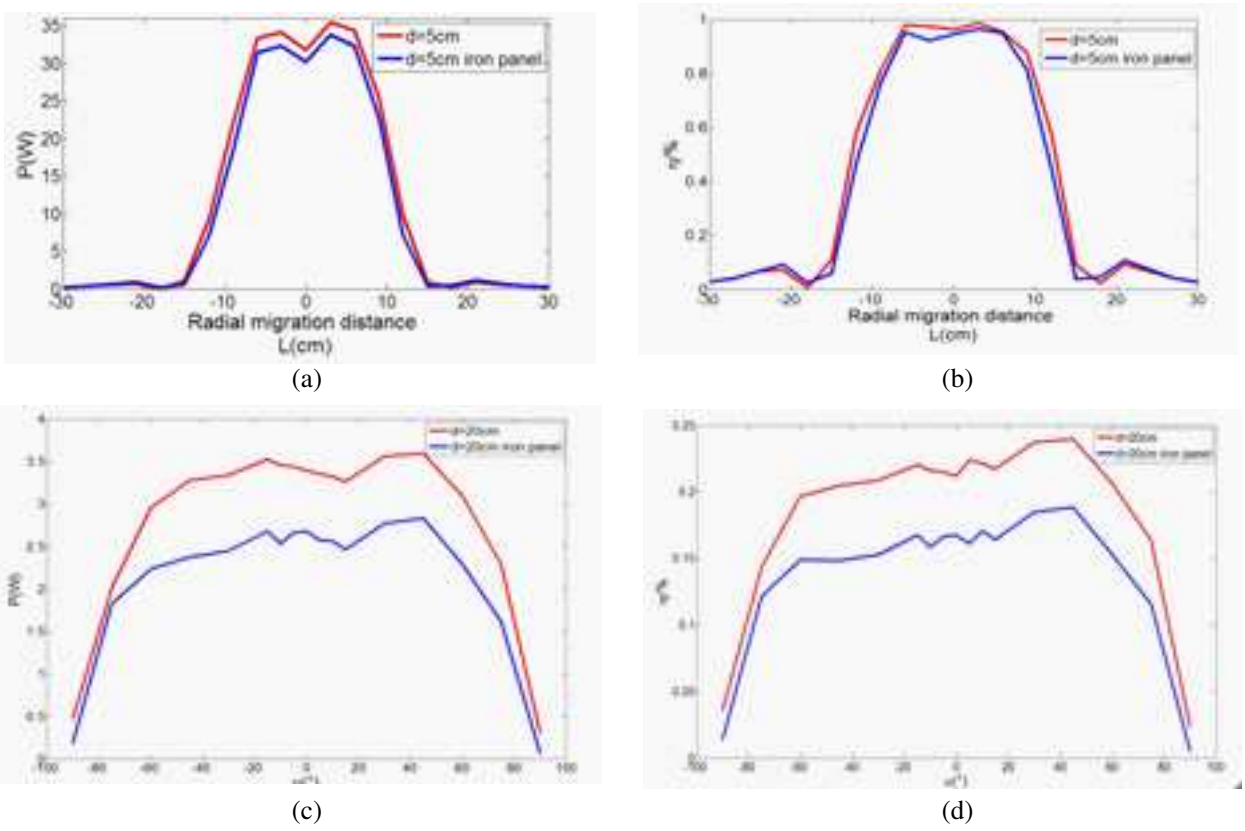

Figure 10: (a) $d = 5\,\text{cm}$, P varies with L. (b) $d = 5\,\text{cm}$, η varies with L. (c) $d = 20\,\text{cm}$, P varies with α. (d) $d = 20\,\text{cm}$, η varies with α.

It can be seen clearly from Figures 10(c), 10(d) that when the axial distance $d = 20\,\text{cm}$, the output power and transmission efficiency decreases gradually with the deflection increasing. Ignoring the error of the experiment system, the above figures have verified the correctness of theory.

5. CONCLUSIONS

When two coils are close proximity, the mutual inductance is large, so two coils are in the state of strong coupling. Although the efficiency of system is high, the energy is not easy to be transmitting. Therefore, the radial offset or rotation angle can reduce the coupling coefficient between coils, resulting in more attuned to load matching and increasing the output power. At the same time, the frequency splitting point will appear. When the axial distance increases to a certain extent, coils are in the state of weak coupling and the frequency splitting phenomenon disappears. Therefore, in magnetic coupling wireless power transmission system with fixed power frequency, points of maximum output power and transmission efficiency do not match. We need to find out the best free position of receiving coils to improve the performance of system such as output power and transmitting efficiency. In addition, to specific applications such as wireless charging for electric vehicle with fixed power frequency, we need to avoid the influence of the magnetic material to charging performance. The relationship concluded from the analysis of theory and experiment has a good guiding significance for actual applications.

ACKNOWLEDGMENT

This work was supported by the Research Innovation Program for College Graduates of Jiangsu Province Nos. CXZZ11_0150 and the National Natural Science Foundation of China Nos. 51177011, National High Technology Research and Development of China Nos. 2012AA050210.

REFERENCES

1. Tan, L., X. Huang, W. Wang, et al., "Application of magnetic coupled resonance wireless power transfer technology in electric vehicle," *Lectute Notes in Information Technology*, Vol. 9, 70–75, 2011.

2. Qiang, H., X. Huang, et al., "Study on topology design of wireless power transfer for electric vehicle based on magnetic resonance coupling," *Advanced Materials Research*, No. 303, 1000–1003, 2011.
3. Tan, L., X. Huang, et al., "Efficiency analysis and optimization on magnetic resonance coupled wireless transfer system," *Advanced Materials Research*, Vol. 5, No. 308, 1345–1348, 2011.
4. Wu, Y., "Study on new conatctless power supply system," Institute of Electrical Engineering, Chinese Academy of Science, 2004.
5. Kim, K.-B., E. Levi, Z. Zabar, et al., "Mutual inductance of noncoaxial circular coils with constant current density," *IEEE Transactions on Magnetics*, Vol. 33, No. 5, 4303–4309, 1997.

Investigation of Characteristics of the Current for the Maximum Power Transfer in Wireless Power Transmission

X. L. Huang, Q. J. Ji, L. L. Tan, W. Wang, and H. Qiang
School of Electrical Engineering, Southeast University, Nanjing 210096, China

Abstract— At present, most problems related to wireless power transfer are explained by the coupled mode theory and equivalent electric circuit. However, as a kind of electromagnetic phenomena, electromagnetic energy transfer can always be described by the Poynting vector. In this paper, we use the way of numerical simulation with Comsol to get the distribution of magnetic field and the Poynting vector. The relationship of power transferred and the currents' phase angle difference was researched under the condition of the other parameters were fixed. The result shows that maximum energy transfer is achieved when the current phase in transmitting coil is $\pi/2$ ahead of current in receiving coil.

1. INTRODUCTION

Nowadays, with the development of mobile appliances and the electric vehicles, the need for a technique to wirelessly charge these applications has increased. The research of wireless power transfer (WPT) has also increased. In WPT equipment, when two or more coils are placed closely, they are coupled to each other, and the energy of each coil can be transferred. Presently, the main wireless power transfer technologies are the electromagnetic induction, the microwave power transfer, and the wireless power transfer via strongly coupled magnetic resonances. It has been recently demonstrated that power can be transferred with high efficiency between two strongly coupled self-resonant coils. Until now, this phenomenon was explained using the coupling mode theory [1] and the equivalent circuits [2]. The two theories respectively give explanations on the WPT transmission mechanism from different point of view. However, as a kind of electromagnetic phenomena, it can be always analyzed from the electromagnetic field. Electric and magnetic fields are utilized to evaluate the Poynting vector, which defines the direction and power density carried by the electromagnetic field.

The Poynting's theorem is described as:

$$-\nabla \cdot (\mathbf{E} \times \mathbf{H}) = \frac{\partial}{\partial t}\left(\frac{1}{2}\mathbf{H} \cdot \mathbf{B} + \frac{1}{2}\mathbf{E} \cdot \mathbf{D}\right) + \mathbf{E} \cdot \mathbf{J}$$

or

$$-\oint_S (\mathbf{E} \times \mathbf{H}) \cdot \mathrm{d}\mathbf{S} = \frac{\mathrm{d}}{\mathrm{d}t}\int_V \left(\frac{1}{2}\mathbf{H} \cdot \mathbf{B} + \frac{1}{2}\mathbf{E} \cdot \mathbf{D}\right)\mathrm{d}V + \int_V \mathbf{E} \cdot \mathbf{J}\mathrm{d}V$$

It means the electromagnetic energy is conservative in any volume of space. Define vector $\mathbf{S} = \mathbf{E} \times \mathbf{H}$ as Poynting vector. The law shows that the power crossing the closed surface S bounding the volume V equals the power supplied to the charged particles by the field plus the rate of changes of stored electromagnetic energy. The Poynting theorem is a complete description of how energy be transferred. Calculate the Poynting vector on closed surface surrounded the coil, the transmission power can be accurately calculated.

In this paper, with the method of numerical simulation, we obtain the magnetic field and the Poynting vector distribution. Keep the geometric parameters and the amplitudes of two coils' currents fixed, the relation of power transferred and the phase-angle difference is researched. The aim of this work is to provide a fresh look on wireless power transfer in the context of an electromagnetics framework.

2. NUMERICAL SIMULATIONS

Strictly speaking, the current and the electromagnetic are interactive. The current stimulates the electromagnetic field, meanwhile the electromagnetic field reacts to the current, changing the current distribution in the coil. However, the working frequencies of most WPT systems are between 10 kHz to 10 MHz. In this case, the size of the system and the distance of coils are far less than the wavelength, so the electromagnetic induction is in the near field. Therefore we think the current is uniform in the coil.

We pay close attention to the two coils and do not focus on the periphery of the specific circuit. When the geometry parameters and distance of the coils are fixed, main variables at two coils are the amplitude and their phase difference of currents, the voltage of the coils will be determined if the currents are given. In the receiving coil, we also load a current to simulate the induced current of receiving coil in the actual situation. Because the coils' geometric parameters are given, the inductance is fixed, so we can get any given value of the current in load circuit through a combination of any capacitance and resistance. The current in transmitting coil is expressed as I_T, the current in receiving coil is expressed as I_R. Take the I_T as reference, assume $I_T = A\sqrt{2}\cos(\omega t)$, $I_R = B\sqrt{2}\cos(\omega t + \varphi)$, the complex vector is $\dot{I}_T = A\angle 0$, $\dot{I}_R = B\angle\varphi$, φ is the phase angle difference of two currents. The power transferred between the coils is related with the variation of A, B and the φ, the characteristics of the current when the maximum power transferred in wireless power transmission is our research point.

The coils' parameters are shown as in Figure 1. We use the AC/DC model of Comsol to simulate the electromagnetic field. Our concern is the electromagnetic field of the space distribution and energy flow density, the field in the wire is not our consideration. In the software, the coils will be regarded as helixes with no volume the currents are loaded in them. Give a certain frequency and start to simulate, the space of the electromagnetic field distribution will be obtained. The simulate parameters are as follows: $A = 5$, $B = 2$, $\omega = 2 \times 10^6 \times 2\pi$. When φ equals $\pi/2$ the magnetic field of the coils and the Poynting vector distribution between two coils are respectively shown in Figure 2 and Figure 3.

It can be seen from the Figure 2 that the average magnetic field is strong near the coils. This is a certain result. In the Figure 3, the Poynting vector is from the current $B\angle\varphi$ to $A\angle 0$. Because the $\varphi > 0$, that means the coil that has a lead current phase angle is the transmitting coil. Integrate the Poynting vector in the closed surface S surround the receiving coil, the power transferred is obtained. By the function of parametric sweep in the Comsol, make φ as parameter and the keep the other parameters fixed, watch the relation of the power and φ.

The Figure 4 shows that the power has the maximum when the φ equals $\pi/2$. We can explain this result with the help of mutual inductance. The current in transmitting coil excite the magnetic flux $\mathbf{B}$, the $\mathbf{B}$ is synchronized with the current. The $\mathbf{B}$ induce the voltage ξ in the receiving coil. Because the $\xi = -\frac{\partial B}{\partial t}$, the phase of ξ is behind $\pi/2$ compare to $\mathbf{B}$, also behind the current in transmitting coil. So if the current in receiving coil has the same phase with the ξ, that is the transmitting coil's current phase is $\pi/2$ ahead of the receiving coil's, the maximum power will be got. That is the explanation of the result.

3. MODEL VALIDATION AND EXPERIMENTAL RESULTS

We make a 5 turns system to confirm the simulation results, the distance is 10 cm, the capacitance in series is 500 pF. In experiment the maximum power transmission of system can be achieved when operating frequency is 2.56 MHz. The measurement is that: the RMS value of source coil's current is 0.7 A and the RMS value of receiving coil is 1.1 A, the power that the load received is 7 W. Take the same geometric parameters to simulation the result is 6.86 W, in good agreement with experimental result. Meanwhile, in the experiment, we found that by changing the system's

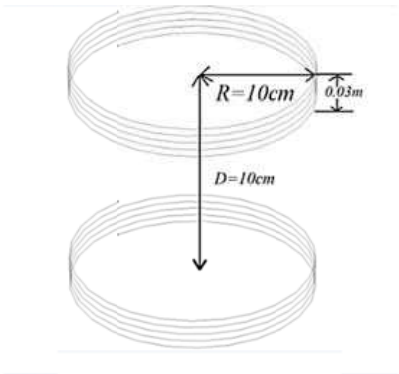

Figure 1: The geometrical parameters of coils.

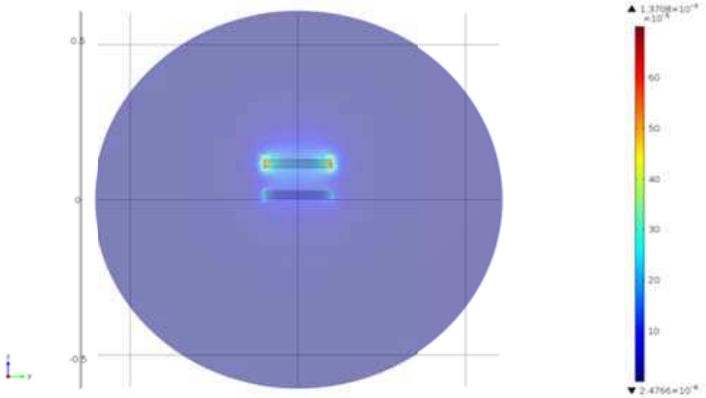

Figure 2: The average magnetic field intensity ($\varphi = \pi/2$).

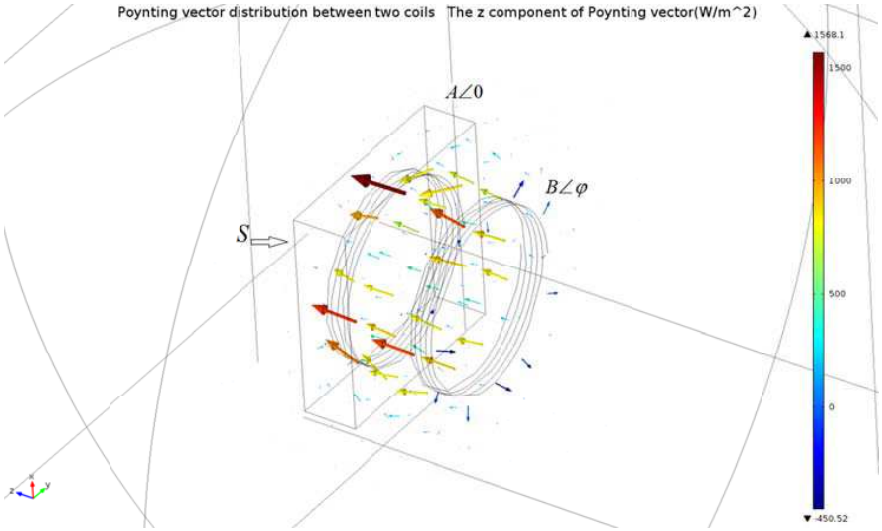

Figure 3: The Poynting vector distribution between two coils, the color stands for the value of z direction of the vector ($\varphi = \pi/2$).

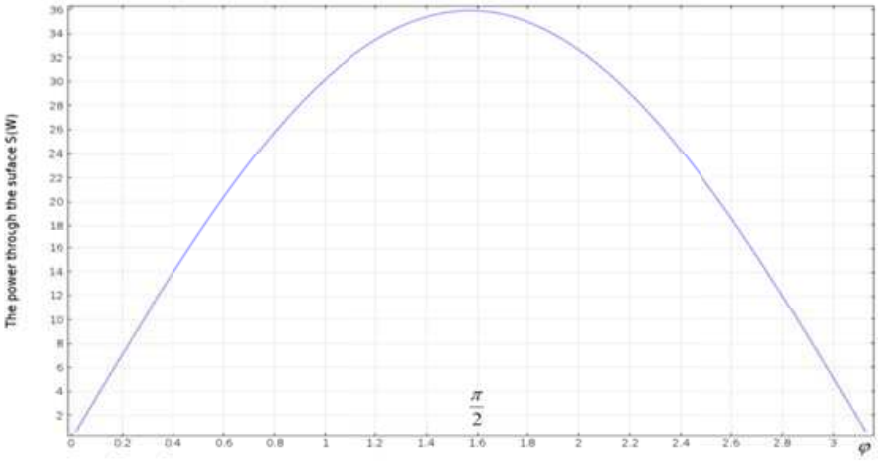

Figure 4: The power crossed the closed surface S with the change of φ

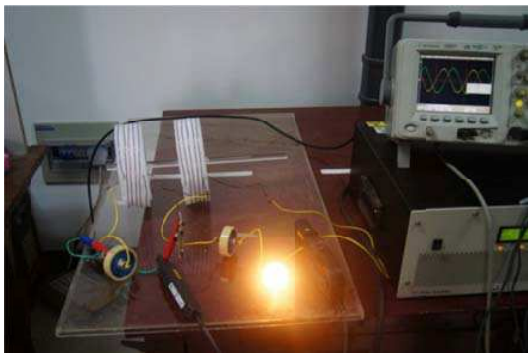

Figure 5: The experiment figure, the current phase of transmitting coil is ahead of receiving coil $\pi/2$.

working frequency to change the phase difference, when the current phase of transmitting coil is ahead of receiving coil $\pi/2$, the power transferred is maximum. Figure 5 is the experiment photo, in the oscilloscope the current phase of transmitting coil (the yellow line) is ahead of receiving coil's current (the green line) $\pi/2$.

4. CONCLUSIONS

In this paper, by using the numerical simulation of Comsol, we get the magnetic field and the Poynting vector distribution. Only change the phase angle difference, the power cross the surface bounding the coil changes. When the transmitting coil's current phase is ahead of $\pi/2$ than the receiving coil's current, the maximum power transfer is achieved.

ACKNOWLEDGMENT

This work was supported by the Research Innovation Program for College Graduates of Jiangsu Province No. CXZZ11_0150 and the National Natural Science Foundation of China No. 51177011, National High Technology Research and Development of China No. 2012AA050210.

REFERENCES

1. Kurs, A., A. Karalis, M. Rober, et al., "Wireless power transfer via strongly coupled magnetic resonances," *Science Express*, Vol. 317, No. 5834, 83–86, 2007.
2. Imura, T. and Y. Hori, "Maximizing air gap and efficiency of magneticresonant coupling for wireless power transfer using equivalent circuit and neumann formula," *IEEE Transactions on Industrial Electronics*, Vol. 58, No. 10, 4746–4752, 2011.
3. Brandão Faria, J. A., "Poynting vector flow analysis for contacteless energytransfer in magnetic systems," *IEEE Transactions on Power Electronics*, Vol. 27, No. 10, 4292–4300, 2012.
4. Guru, B. S., *Electromagnetic Field Theory Fundamentals*, Cambridge University Press, Cambirdge, 2004.
5. Qiang, H., X. L. Huang, L. L. Tan, et al., "Study on topology design of wireless power transfer for electric vehiclebased on magnetic resonance coupling," *Advanced Materials Research*, Vol. 308–310, 1000–1003, 2011.

The Coil Misalignment Model of Inductively Coupled Wireless Power Transfer System: Mutual Inductance Analysis and Transfer Efficiency Optimization

X. L. Huang[1], **H. Qiang**[1,2], **and L. L. Tan**[1]

[1]School of Electrical Engineering, Southeast University, Nanjing 210096, China
[2]School of Information Science and Engineering, Changzhou University, Changzhou 213164, China

Abstract— A novel means of optimizing transfer efficiency of Inductively Coupled wireless power transfer (WPT) system is presented for the first time. In the applications envisaged, such as electric vehicles and biomedical implants, generally the receiving coil is laterally and angularly misaligned from the transmitting coil. The numerical solution of mutual inductance between the two coils is derived and simulation result shows there is a partial optimal solution in the ranges of lateral and angular misalignments. The bigger is mutual inductance, the higher transfer efficiency is. The novel means presented in this study allows the coil to be removable and rotatable for achieving bigger mutual inductance and optimizing transfer efficiency. Finally the experimental results show the means is efficient and greatly improves the transfer efficiency. If the transfer distance is 15 cm and there is no lateral misalignment, the transfer efficiency can be improved about from 38.6% to 60.5% by turning the transmitting coil to make the tilt angle varied from 0 to $\pi/4$. This introduced technique can be widely applied to WPT system to optimize the transfer efficiency.

1. INTRODUCTION

As the development of mobile devices such as electric vehicles and portable devices [1–3], the requirement of wireless charging made WPT technology become increasing important. Inductive coupling and resonant coupling are two major means, and in inductive or magnetic coupled systems, power is transferred from a primary transmitter (Tx) coil to a secondary receiver (Rx) coil with the aid of an alternating magnetic field as shown in Fig. 1. In the applications envisaged, such as electric vehicle and biomedical implants [4], the misalignment between the two coils including lateral displacement and angular tilt generally took place. And the impact of coil misalignment on the transfer efficiency has received little attention by researchers.

The aim of this work is to optimize the transfer efficiency of inductive coupled WPT system. A novel means is presented based on the mutual inductance analysis of coil misalignment. In experiments, the primary Tx coil is designed to be removable and rotatable for obtaining the partial optimal solution of mutual inductance so that optimizing the transfer efficiency. The experimental results show that if the transfer distance is 15 cm and there is no lateral misalignment, the transfer efficiency can be improved about from 38.6% to 60.5% by turning the transmitting coil to make angular misalignment varied from 0 to $\pi/4$. And if the lateral misalignment occurs, changing the tilt angle can also change the transfer efficiency and the optimal efficiency is according to the partial maximum mutual inductance.

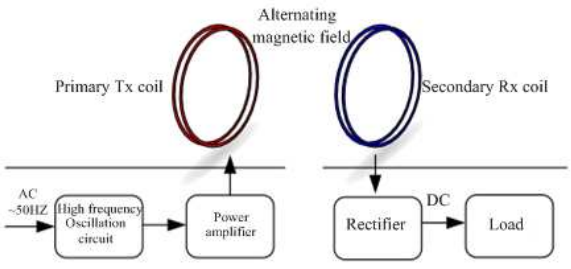

Figure 1: Structure of the wireless power transfer system.

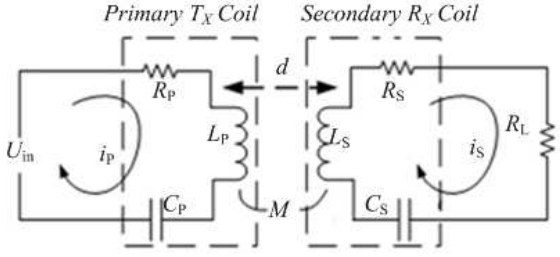

Figure 2: Model of the wireless power transfer system.

2. INDUCTIVE COUPLED WPT SYSTEM MODEL

In the inductive coupled WPT operation represented by the equivalent circuit of Fig. 2 [5, 6], d is the coil separation distance, M is the mutual induction of two coils, U_{in} is the induced potential source; R_P, R_S, C_P and C_S are the parasitic parameters in HF and L_P, L_S are the self-inductances of the two coils (the subscripts "P" and "S" stand for the primary and secondary respectively); R_L stands for the load resistance. The Rx coil is situated within the near-field of the Tx coil and the interaction between two coils is considered as magnetoquasistatic [7].

Suppose the system operating angular frequency equals to ω, the KVL equations of primary and secondary circuits are easily deduced from Fig. 2.

$$\begin{bmatrix} R_P + jX_P & j\omega M \\ j\omega M & R_S + R_L + jX_S \end{bmatrix} \begin{bmatrix} I_P \\ I_S \end{bmatrix} = \begin{bmatrix} U_{in} \\ 0 \end{bmatrix}, \quad \begin{cases} X_P = \omega L_P - 1/(\omega C_P) \\ X_S = \omega L_S - 1/(\omega C_S) \end{cases} \tag{1}$$

The physical meaning of the power transfer efficiency studied in this paper is defined as the ratio of the output power P_{out} in the load R_L to the input power P_{in} generated by the Tx coil, denoted η.

$$P_{in} = \frac{u_{in}^2 Z_S}{Z_P Z_S + (\omega M)^2}, \quad P_{out} = \frac{u_{in}^2 (\omega M)^2 R_L}{[Z_P Z_S + (\omega M)^2]^2}, \quad \eta = \frac{P_{out}}{P_{in}} = \frac{(\omega M)^2 R_L}{Z_S [Z_P Z_S + (\omega M)^2]} \times 100\% \tag{2}$$

When resonance occurs in Tx and Rx circuits, the maximum power is delivered to the resistive component of the load and the losses of the reactive components are canceled [8, 9]. Then η can be rewrite as

$$\eta = \frac{(\omega M)^2 R_L}{(R_S + R_L)[R_P(R_S + R_L) + (\omega M)^2]} \times 100\%. \tag{3}$$

From (3), the impact of mutual inductance on transfer efficiency is obvious and big mutual inductance implies high efficiency. The mutual inductance M can be derived by solving the double integral in Neumann's formula.

$$M = \frac{N_{Tx} N_{Rx} \mu_0}{4\pi} \oint_{l_{Tx}} \oint_{l_{Rx}} \frac{dl_{Tx} \cdot dl_{Rx}}{R} \tag{4}$$

where N_{Tx}, N_{Rx}, l_{Tx}, l_{Rx}, dl_{Tx} and dl_{Rx} define the coil turns, the length of each turn and infinitesimal of l of the resonant Tx and Rx coils, respectively. R is the distance between dl_{Tx} and dl_{Rx}, and μ_0 is the magnetic permeability of free-space.

It is evident that the mutual inductance M of (4) depends on the shapes and the orientations of the two coils. In this paper, the impact of coil orientation on the mutual inductance is studied in Section 3 that follows.

3. MISALIGNMENT AND MUTUAL INDUCTANCE ANALYSIS

Clearly, coil orientation is a key parameter in the design of the inductively coupled systems. In practical application, coil misalignment is normal. And there are three following forms of misalignment:

1) Lateral misalignment: In this case the pair of Tx and Rx coils are situated in parallel planes, which are separated by a vertical distance d and their centers are displaced by a lateral distance l, as shown in Fig. 3(a).

2) Angular misalignment: In this case the plane of the Tx coil is tilted to form an angle θ and the axis of one coil passes through the center of the other coil, as shown in Fig. 3(b).

3) Incorporated misalignment: This case incorporates both lateral displacement and angular tilt of the coils, as shown in Fig. 3(c).

A general misalignment case is the third case presented above. Suppose that the projection of O_2 in the Tx plane is O_2', using the vector O_1O_2' to indicate the direction of the x axis we can establish the Cartesian coordinate system, shown in Fig. 3(c). Then for mutual inductance analysis and efficiency optimization, we assume the angle θ is formed around the x axis. In paper [10], Soma had demonstrated that there is no strong interaction between the lateral misalignment effect

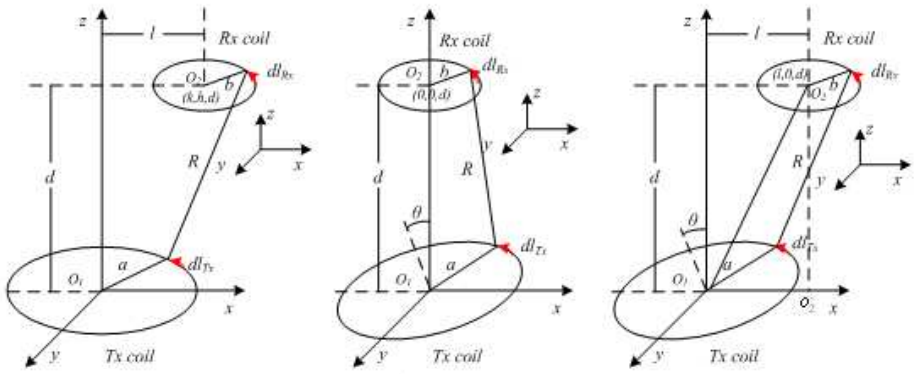

(a) (b) (c)

Figure 3: Misalignment configurations of the Tx and Rx coils.

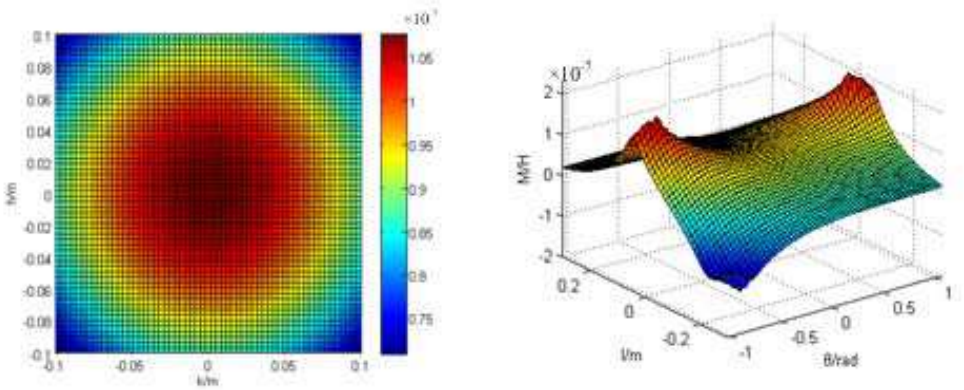

(a) (b)

Figure 4: Mutual inductance of coil misalignment: (a) lateral misalignment, (b) incorporated misalignment.

and the angular misalignment effect. And paper [11] had studied the two displacement configurations independently for the maximum permissible angular and lateral displacements for different applications.

Any theoretical investigation of the mutual inductance in the misalignment cases is extremely complex due to the heavy work required to solve the double integral as (4) and the analytical solution is almost impossible to be derived. Hence, in this study, Matlab is used to obtain the numerical solution of the mutual inductance in varied misalignment cases with the separate distance of 15 cm as shown in Fig. 4.

In Fig. 4, the positive and negative of l and θ just stand for the position in the special coordinate system and the direction of rotation (anticlockwise or clockwise), respectively. It is evident that in lateral misalignment, the mutual inductance is become smaller with the increase of the lateral distance l. And in incorporated misalignment, the mutual inductance is varied with the lateral distance and tilt angle, and there are partial optimal solutions in their ranges shown in Fig. 4(b). It is also worth noting that with a specific separate distance, the peaks of the mutual inductance in Fig. 4(b) do not occur in perfect alignment. This implies that in inductively coupled WPT system, there are some constraints to guarantee the maximum power transfer occurs in perfect alignment.

4. EXPERIMENTAL RESULTS

In order to verify the above theory results and the proposed means of optimizing the transfer efficiency, an inductively coupled WPT system shown in Fig. 5 is set up according to the parameters listed in Table 1.

In Fig. 5, we adjust the power supply AG1017L to output the high-frequency signal of 0.58 MHz and read the RF output power as the system input power P_{in}. Using the oscilloscope DSO5014A to detect the voltage signal of the load and reading the U_{RMS}, we can calculate the output power P_{out} in the load by $P_{out} = \frac{U_{RMS}^2}{R_L}$.

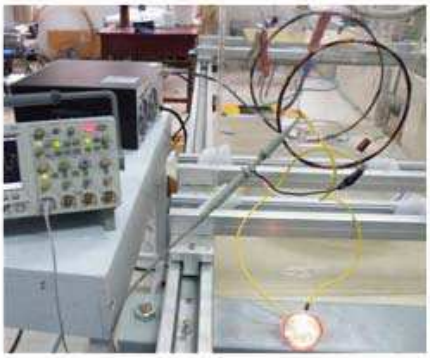

Figure 5: Photograph of the experiment setup.

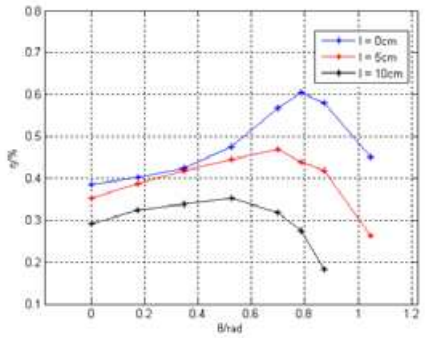

Figure 6: The measured transmission efficiency.

Table 1: Experiment device parameters.

FACTORS		
Radius	Tx Coil	$R_{Tx} = 0.20\,\mathrm{m}$
	Rx Coil	$R_{Rx} = 0.16\,\mathrm{m}$
Turns	Tx Coil	$N_{Tx} = 13$
	Rx Coil	$N_{Rx} = 16$
Resonant Frequency		$f = 0.58\,\mathrm{MHz}$
Load Resistance		$R_L = 7.2\,\Omega$

Setting the separate distance of 15 cm, the measured transfer efficiencies are shown in Fig. 6 with the removable and rotatable Tx coil and the fixed Rx coil.

It can be seen in Fig. 6 that in perfect alignment the system can only achieve about 38.6% efficiency, whereas turning the Tx coil to make a tilt angle of $\pi/4$ can improve the efficiency up to 60.5%. If the separate distance is constant, the smaller is the lateral distance, the higher transfer efficiency is. And if the lateral distance is constant, the efficiency is varied with the tilt angle and there is a partial optimal solution. It is also evident in Fig. 6 that the tilt angle corresponding to the partial solution becomes smaller with increasing lateral distance.

5. CONCLUSION

Coil misalignment is an inhere problem of inductively coupled links and its impact on transfer efficiency is complex. In this paper, we use Neumann's formula to solve the numerical solutions of the mutual inductance in varied coil misalignment cases. Simulation results show that only meeting certain constraints, the mutual inductance and the transfer efficiency can achieve maximum and optimal in perfect alignment. If not, there are partial optimal solutions in coil misalignment. Then for some practical applications, such as electric vehicles, a novel method proposed in this study allows the coil to be removable and rotatable for achieving bigger mutual inductance and optimizing transfer efficiency. Finally, the experimental results verify the theoretical results and show the proposed method is feasible. With the distance of 15 cm, if there is no lateral distance, the transfer efficiency can reach up to about 60.5% by rotating the Tx coil to make a tilt angle $\pi/4$ from 38.6% in perfect alignment.

ACKNOWLEDGMENT

This work was supported in part by the National High-tech R&D Program of China (863 Program), the National Natural Science Foundation of China (No. 51177011), the Research Innovation Program for College Graduates of Jiangsu Province (No. CXZZ11_0150) and Scholarship Award for Excellent Doctoral Student granted by Ministry of Education.

REFERENCES

1. Hirai, J., T. W. Kim, and A. Kawamura, "Wireless transmission of power and information for cableless linear motor drive," *IEEE Trans. Power Electro.*, Vol. 15, No. 1, 21–27, 2000.

2. Jang, Y. and M. M. Jovanovic, "A contactless electrical energy transmission system for portable-telephone battery chargers," *IEEE Trans. Industrial Electro.*, Vol. 50, No. 3, 520–527, 2003.
3. Imura, T., H. Okabe, and Y. Hori, "Basic experimental study on helical antennas of wireless power transfer for electric vehicles by using magnetic resonant couplings," *Proceedings of VPPC*, 936–940, Dearborn, MI, Sep. 2009.
4. Jung, K. H., Y. H. Kim, J. Kim, and Y. J. Kim, "Wireless power transmission for implantable devices using inductive component of closed magnetic circuit," *Electro. Letters*, Vol. 45, No. 1, 21–22, 2009.
5. Selvakumaran, R., W. Liu, B. H. Soong, M. Luo, and S. Y. Loon, "Design of inductive coil for wireless power transfer," *IEEE/ASME International Conference on Advanced Intelligent Mechatronics*, 584–589, Singapore, Jul. 2009.
6. Yu, C. L., R. G. Lu, Y. H. Mao, L. T. Ren, and C. B. Zhu, "Research on the model of magnetic-resonance based wireless energy transfer system," *IEEE Vehicle Power and Propulsion Conference*, 414–418, Dearborn, MI, Sep. 2009.
7. Yates, D. C., A. S. Holmes, and A. J. Beudett, "Optimal transmission frequency for ultralow-power short range radio links," *IEEE Trans. Circuits Syst. I*, Vol. 51, No. 7, 1405–1413, 2004.
8. Tan, L. L., X. L. Huang, H. Huang, Y. W. Zou, and H. Li, "Transfer efficiency optimal control of magnetic resonance coupled system of wireless power transfer based on frequency control," *Sci. China Tech. Sci.*, Vol. 54, No. 6, 1428–1434, 2011.
9. Fu, W. Z., B. Zhang, D. Y. Qiu, and W. Wang, "Maximum efficiency analysis and design of self-resonance coupling coils for wireless power transmission system," *Proceedings of the CSEE*, Vol. 19, No. 18, 21–26, 2009.
10. Soma, M., C. D. Galbraith, and R. White, "Radio-frequency coils in implantable devices: Misalignment analysis and design procedure," *IEEE Trans. Biomed. Eng.*, Vol. 34, No. 4, 276–282, 1987.
11. Fotopoulou, K. and B. W. Flynn, "Wireless power transfer in loosely coupled links: Coil misalignment model," *IEEE Trans. Magn.*, Vol. 47, No. 2, 416–430, 2011.

Resonant Frequency Splitting Analysis and Optimation of Wireless Power Transfer System

X. L. Huang, L. L. Tan, W. Wang, Y. L. Zhou, and H. Qiang
School of Electrical Engineering, Southeast University, Nanjing 210096, China

Abstract— Frequency optimal control for magnetic resonance coupled wireless power transfer system to improve the system transfer efficiency, which requires the system should have one unique stable resonant frequency. Actually, transmitted at close distance the system will appear multiple resonant frequencies (frequency splitting) phenomenon which results in unstable and increase control complexity. In order to study the frequency splitting mechanism, the system equivalent load model is established on the base of bilateral capacitor parallel-compensated topology in this paper. And then the transfer distance and load resistance threshold conditions are presented when the resonant frequency splitting occurred. On this basis, frequency optimal control method and solutions for system frequency splitting is proposed. Finally, simulations and experiments verify the feasibility of the analysis.

1. INTRODUCTION

With the rapid social development and people's pursuit of amenities, the traditional wired power supply cannot meet the requirements. In order to get rid of the power wired problems to achieve wireless power transmission, mountains of work have been done on this topic and lots of methods have been proposed by scientists [1–4]. The most noteworthy is MIT's use of magnetic resonance coupled theory to achieve power wireless transfer in 2007 [5], which successfully avoids obstacles to transfer power in meter-scale range, and indicates a new research direction for medium-range (meter level) wireless power transmission. This technology quickly becomes a hot pursuit for research institutions [6–10].

Currently, studies reveal that while at long-distance transmission, the wireless power transfer system has only one stable resonant frequency and that the transmitting and receiving coils circuits should be in their self-resonance respectively under this frequency to achieve efficient performance. But, at close transfer distance, the system resonant frequency will give rise to two or three resonant frequencies which increase the power transfer instability and difficult to determine the ideal frequency controlling points. It can be seen that the uniqueness and variation characteristics of the system resonant frequency are core of system optimal control, and also one of the main research contents in this paper. In order to achieve system resonance, varieties of capacitor compensated modes can be used in transmitting and receiving circuits. In this paper, the bilateral capacitor parallel-compensated topology is studied, and the system load equivalent model is established to analyze the variation characteristics of the system input impedance. In conclusion, an optimization control method is proposed to ensure the system a single stable resonant frequency and effective work in resonant status.

2. TRANSMISSION MODEL AND PP TOPOLOGY

Theory suggests that the wireless power transfer system is composed of high-frequency power U_s, receiving and transmitting coils L_1 and L_2, capacitor C_1, and C_2, and the load R_L. Only in terms of transfer system, the specific circuit of the system is shown in Fig. 1. R_1, R_2 are coils equivalent resistance [5] respectively, M, d for mutual inductance and the distance (transfer distance) between two coils, respectively. And the high frequency influence is ignored for simplification.

3. EQUIVALENT LOAD MODEL

Suppose that ω_0 is the self-resonant frequency of receiving coil circuit, Q_2 is quality factor, $L_1 = L_2$, $C_1 = \alpha C_2$, $\omega = \beta\omega_0$, where α for capacitance ratio, β for operating frequency ratio. Then the relations are as follows:

$$\begin{cases} \omega_0 = 1/\sqrt{L_2C_2} \\ Q_2 = R_L/(\omega_0 L_2) \\ \kappa = M/\sqrt{L_2L_1} = M/L_2 \end{cases} \tag{1}$$

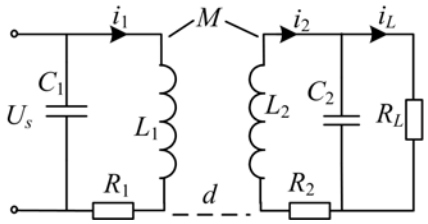

Figure 1: System PP compensated mode.

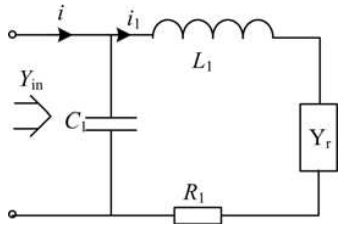

Figure 2: The normalized equivalent circuit.

Here k is coupling coefficient between two coils, and the receiving coil circuit self-impedance is converted to the transmitting circuit (as shown in Fig. 2), the normalized receiving equivalent impedance Z_r in transmitting circuit is

$$\begin{aligned} Z_r \;=\; & \frac{\beta^2 k^2 R_L^2 Q_2 (1+\beta^2 Q_2^2)\left[R_2(1+\beta^2 Q_2^2)+R_L\right]}{Q_2\left[(R_2 Q_2(1+\beta^2 Q_2^2)+R_L Q_2)^2+(\beta R_L(1+\beta^2 Q_2^2)-\beta Q_2^2 R_L)^2\right]} \\ & -j\frac{\beta^3 k^2 R_L^3 (1+\beta^2 Q_2^2)(1+\beta^2 Q_2^2-Q_2^2)}{Q_2\left[(R_2 Q_2(1+\beta^2 Q_2^2)+R_L Q_2)^2+(\beta R_L(1+\beta^2 Q_2^2)-\beta Q_2^2 R_L)^2\right]} \end{aligned} \tag{2}$$

If Z_r is defined as a form of $Z_r = R_r - jX_r$, then the system input admittance Y_{in} watched from the transmitting side is

$$Y_{\text{in}} = \frac{Q_2^2(R_1+R_r)}{Q_2^2(R_1+R_r)^2+(\beta R_L - X_r Q_2)^2} + j\left(\frac{\alpha\beta Q_2}{R_L} - \frac{Q_2(\beta R_L - X_r Q_2)}{Q_2^2(R_1+R_r)^2+(\beta R_L - X_r Q_2)^2}\right) \tag{3}$$

The imaginary part of Y_{in} should be zero while the system is working efficiently in resonant state, and under U_s, the system input power P and transfer efficiency η can be obtained by Equation (4)

$$P = (\text{Re}Y_{\text{in}})U_s^2 \tag{4}$$

4. FREQUENCY ANALYSIS AND SPLITTING PHENOMENON

For the above analysis it can be concluded that the system input impedance imaginary part $\text{Im}Y_{in}$ is zero when the system works in resonant, so the study of resonant frequency points can be converted to the study of the frequency solutions of the equation $\text{Im}Y_{in} = 0$. Since mutual inductance's calculation is quite complex, we have $M \approx \pi\mu_0 r_4 N_2/(d_2+r_2)^{1.5}$ [11], in which μ_0 is the permeability, N is turns of coils, r is the radius.

4.1. Resonant Frequency Splitting

The stability of the system is one of the key performances, which requires a single stable resonance frequency. The resonant frequency is the frequency solutions which ensure zero of the system's input impedance imaginary part $\text{Im}Y_{in}$. With a fixed R_L, there exists a minimum threshold distance when frequency splitting occurs, denoted as d_c. When the transfer distance is greater than d_c, the system will only have one stable resonant point. In order to solve the d_c, the threshold value of coupling coefficient k_c should be given when system frequency splitting occurs. Regardless of R_1, R_2, we propose the constraint relationship between coupling coefficient k, load resistance R_L, capacitance ratio α and the operating frequency ratio β as $\text{Im}Y_{in} = F(k, R_L, \alpha, \beta) = 0$ while frequency splitting occurs. Substituting the relevant parameters, which can be further organized into a fourth-order equation on k, that $F(k, R_L, \alpha, \beta) = ak_4 + bk_2 + c$. Here, a, b, c, are the function on the load R_L, capacitance ratio α, operating frequency ratio β, which be expressed as

$$\begin{cases} a = \left(1+\beta^2 Q_2^2\right)^2\left[\alpha\beta^5 Q_2^3 R_L^2 + \alpha\beta^7 Q_2 R_L^2\left(1+\beta^2 Q_2^2-Q_2^2\right)^2\right] \\ b = \left|\begin{array}{l} \left(\beta^3 Q_2 R_L^2 - 2\alpha\beta^5 Q_2 R_L^2\right)\left(1+\beta^2 Q_2^2\right)\left(1+\beta^2 Q_2^2-Q_2^2\right) \\ \left[Q_2^2+\beta^2\left(1+\beta^2 Q_2^2-Q_2^2\right)^2\right] \end{array}\right| \\ c = \left[Q_2^2+\beta^2\left(1+\beta^2 Q_2^2-Q_2^2\right)^2\right]^2\left(\alpha\beta^3 Q_2 R_L^2 - \beta Q_2 R_L^2\right) \end{cases} \tag{5}$$

Then, the boundary condition of equation $F(k, R_L, \alpha, \beta) = 0$ has only one positive solution besides zero is $\beta = (1/\alpha)^{0.5}$, and the threshold value k_c is

$$\kappa_c = \sqrt{\frac{-b - \sqrt{b^2 - 4ac}}{2a}} \tag{6}$$

Especially when $\alpha = \beta = 1$, k_c is $(-b/a)0.5 = [1/(1 + Q_2^2)]^{0.5}$. By Equation (3), we can see that if $k \ll 1$, $\mathrm{Im}Y_{in}$ is approximately proportional to β, and the frequency splitting disappears. Then $\mathrm{Im}Y_{in}$ can be simplified as $Q_2(\beta^2\alpha - 1)/R_{L\beta}$. If α is not equal to 1, according to $\mathrm{Im}Y_{in} = 0$ we can obtain the similar relationship between β and α: $\beta = (1/\alpha)^{0.5}$, which suggests that the system resonant frequency is determined uniquely by α.

4.2. The Impact of Load Changes on Resonance Frequency

If we investigate on $\mathrm{Im}Y_{in}$ changed with β under different quality factor while $\alpha = 1$, the results are shown as Fig. 3. With R_L changed from large to small at close distance, the system resonant frequencies change from multiple into single. Evidently, if d is fixed, there exists a threshold load which makes the system produce only one resonant frequency, denoted as R_{Lc}. As the distance increases, the coupling relation between two coils will be reduced, which leads to the decreased impact of load on system resonant frequency, as is shown in Fig. 3(b) and Fig. 3(c). By comparing research we find that no matter how the load changes, the system has a common resonant frequency if distance d and capacitance ratio α are fixed, which gradually approaches ω_0 with the coupling between two coils weaken. At short distance, the system resonant frequency will deviate from ω_0 and the frequency splitting phenomenon may occur.

5. DESIGN AND FREQUENCY OPTIMIZATION

Based on the above analysis it can be found that at close distance, a single stable resonant frequency of the transfer system for an easy control can be achieved as following: fixing α, and adjusting R_L to achieve only one resonant frequency at the whole distance under the context of $d < d_c$. For the actual system parameters simulation studying, $L_p = L_s = 8.02\,\mu\mathrm{H}$, $N = 3$, $r = 0.3\,\mathrm{m}$, $C_2 = 265\,\mathrm{pF}$. Simulation and experimental studies are carried out to verify the above theoretical analysis.

When $\alpha = 1$, the curve of β varied with d is shown as Fig. 4. It can be easily seen if d is greater than d_c (threshold distance), the resonant frequency is almost close to ω_0, otherwise deviates from ω_0 obviously. If the power source frequency output ω can change around ω_0, this requires the system working resonant be near ω_0 with d changing, and has only one stable resonance frequency. If $R_L = 1500\,\Omega$ in long-distance transmission is given, we measured d_c is 0.45 m when resonance

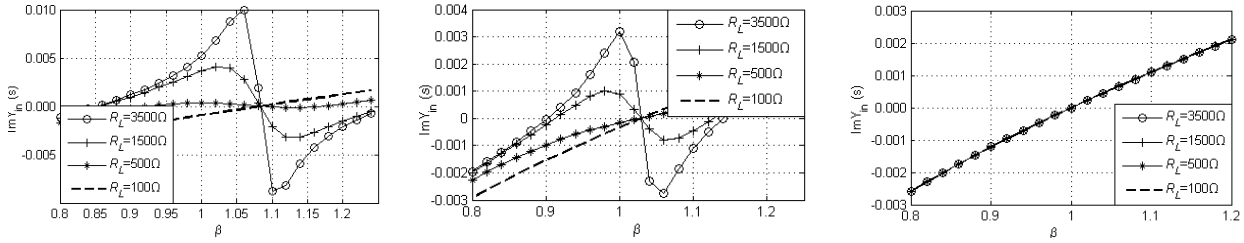

(a) α=1, *d*=0.2 m (b) α=1, *d*=0.3 m (c) α=1, *d*=1.0 m

Figure 3: $\mathrm{Im}Y_{in}(\beta)$ at different transfer distance and load.

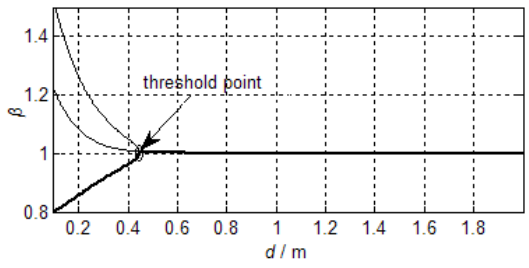

Figure 4: The curve of β varied with d.

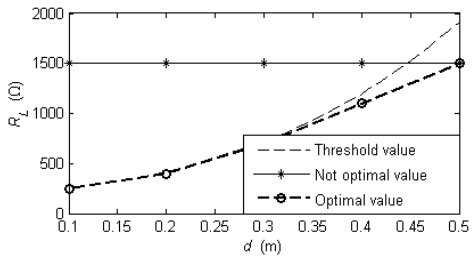

Figure 5: The curve of R_L varied with d.

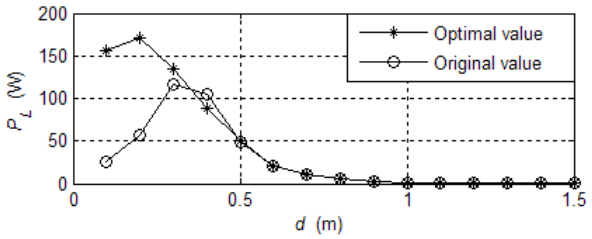

Figure 6: Load received power varied with d.

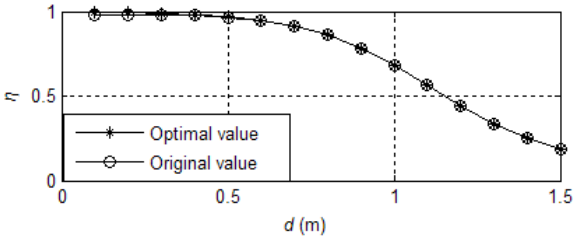

Figure 7: Transfer efficiency varied with d.

frequency splitting occurred. If the transfer distance is less than d_c, we can adjust R_L to make the system have a unique resonant frequency, and the actual resistance value is shown in Fig. 5.

Figures 6 and 7 indicate the curves of load received power and transfer efficiency by adjusting R_L to make the system work in a single stable resonance frequency near ω_0. By comparison we can see that through controlling the system has only one resonant frequency, which increase the stability of the system. Due to without frequency splitting at the long-distance the system transfer power and transfer efficiency has not been improved significantly before and after the optimization, But at close distance, the load received power and transfer efficiency are larger.

6. CONCLUSIONS

This paper has an in-depth study of the load model of magnetic resonant coupled wireless transfer system with PP topology. By exploring the relations between the system's resonant frequencies, coupling coefficient and the capacitance ratio, the variation of system resonant frequency are analyzed in detail. And then the threshold value of load and distance are investigated when system resonant frequency splitting occurs. On this basis, an optimization method is proposed to make the system work in a single stable resonant frequency by changing the load resistance and capacitance ratio at different transfer distance, thus improving the system stability and controllability. Both the simulations and experiments manifest that the system enjoys a higher transfer efficiency and power output under this optimal control method. The research of this paper will also prove a significant theoretical guidance and reference for the system stability control and optimized operation.

ACKNOWLEDGMENT

This work was supported by Scholarship Award for Excellent Doctoral Student granted by Ministry of Education, the Research Innovation Program for College Graduates of Jiangsu Province (No. CXZZ11_0150) and the National Natural Science Foundation of China (No. 51177011).

REFERENCES

1. Nikola, T., "The transmission of electrical energy without wires as a means for furthering peace," *Electrical World and Engineer*, Vol. 7, 21–24, Jan. 1905.
2. Hideyuki, K., K. Tamotsu, and S. Hideo, "Power and information transmission to implanted medical device using ultrasonic," *Japanese Journal of Applied Physics*, Vol. 40, No. 5B, 3865–3866, Feb. 2001.
3. Junji, H., K. Tae-Woong, and K. Atsuo, "Integral motor with driver and wireless transmission of power and information for autonomous subspindle drive," *IEEE Transactions on Power Electronics*, Vol. 15, No. 1, 13–20, Jan. 2000.
4. Wang, G. X., W. T. Liu, and M. Sivaprakasam, "High efficiency wireless power transmission with digitally configurable stimulation voltage for retimal prosthesis," *Proceedings of the 2th International IEEE EMBS Conference on Neural Engineering*, Arlington, Virginia, Mar. 16–19, 2005.
5. Kurs, A., A. Karalis, R. Moffatt, and J. D. Joannopoulos, "Wireless power transfer via strongly coupled magnetic resonances," *Science Express*, Vol. 317, No. 5834, 83–86, Jul. 2007.
6. Zhen, N. L., A. C. Raul, and T. Ryan, "Design and test of a high-power high-efficiency loosely coupled planar wireless power transfer system, "*IEEE Trans. on Industrial Electronics*, Vol. 56, No. 5, 1801–1812, May 2009.
7. Villa, J. L., A. Liombart, and J. F. Sanz, "Design of a high frequency inductively coupled power transfer system for electric vehicle battery charge," *Applied Energy*, Vol. 86, No. 3, 355–363, Mar. 2009.

8. Segura-Quijiano, F., J. Garcia_Canton, and J. Sacristan, "Wireless powering of single-chip systems with integrated coil and external wire-loop resonator," *Applied Physics Letters*, Vol. 92, No. 7, 074102-1–074102-3, Feb. 2008.
9. Tan, L. L., X. L. Huang, and H. Huang, "Transfer efficiency optimal control of magnetic resonance coupled system of wireless power transfer based on frequency control," *Science China Technological Sciences*, Vol. 54, No. 6, 1428–1434, Jun. 2011.
10. Sedwick, R. J., "Long rang inductive power transfer with superconducting oscillators," *Annals of Physics*, Vol. 325, No. 2, 287–299, Feb. 2010.
11. Huang, H., X. L. Huang, and L. L. Tan, "Research on the transmitter and receiver of wireless power transmission based on magnetic resonance," *Advanced Technology of Electrical Engineering and Energy*, Vol. 30, No. 1, 32–35, Jan. 2011.

A Comparison of Analytical Models for Resonant Inductive Coupling Wireless Power Transfer

E. Bou[1], **E. Alarcon**[1], **and J. Gutierrez**[2]

[1]Electronic Engineering Department, Technical University of Catalonia UPC BarcelonaTech, Spain
[2]Applied Physics Department, Technical University of Catalonia UPC BarcelonaTech, Spain

Abstract— Recent research in wireless power transfer (WPT) using resonant inductive coupling has demonstrated very high efficiencies (above 40%) at large distances compared to the antenna dimensions, which has exponentially increased the number of potential applications of WPT. Since resonant inductive coupling is a very multidisciplinary field, different approaches have been proposed to predict the behaviour of these systems from physical theory of resonators, reflected load theory and the circuit point of view. However, the relation between these methods is still obscure. In this article, we compare the results of these models to find the efficiency of a Resonant Inductive Coupling WPT system under Steady-State sonditions and to analyze the relation between the optimal load values obtained from this perspectives and the ones obtained using impedance matching techniques.

1. INTRODUCTION

In this paper, three different Resonant Inductive Coupling Theories are revisited in terms of Power Transfer Efficiency, namely: Coupled Mode Theory, Reflected Load Theory and Lumped Circuit Theory (Sections 2, 3 and 4 respectively). The results are then described and compared in Section 5. In Section 6, the optimal load values have been derived from the efficiency formulas previously obtained and compared to optimal load values resulting from the application of Impedance Matching Techniques.

2. COUPLED MODE THEORY

Resonant Inductive Coupling (hereafter referred to as RIC) was presented using Coupled Mode Theory Form [1, 2]. This model, which is based on the physical theory behind resonators, provides a framework to analyze a wireless power transfer system in strong coupling regime as a first order differential equation. Although it is an approximate method, it does predict very accurately the steady-state response of a Resonant Inductive Coupling link.

In this case, the two coils forming a WPT system with low losses are approximated by two resonators where their time-domain field amplitudes can be described as [3]:

$$\begin{aligned} \dot{a}_1 &= -(j\omega_1 + \Gamma_1)a_1(t) + jK_{12}a_2(t) + F_S(t) \\ \dot{a}_2 &= -(j\omega_2 + \Gamma_2 + \Gamma_L)a_2(t) + jK_{12}a_1(t) \end{aligned} \tag{1}$$

where $a_\pm$ is the mode amplitude:

$$a(t)_\pm = \sqrt{\frac{C}{2}}v(t) \pm j\sqrt{\frac{L}{2}}i(t) \tag{2}$$

$\omega_{1,2}$ are the eigenfrequencies (frequencies at which the coils resonate), $\Gamma_{1,2}$ are the rates of intrinsic decay due to the coils losses (absorption and radiative), $F_S(t)$ is the excitation applied to the first coil and K_{12} is the coupling rate between both resonant objects:

$$\Gamma_{1,2} = \frac{R_{1,2}}{2L_{1,2}}; \quad K_{12} = \frac{\sqrt{\omega_1\omega_2}k_{12}}{2} = \frac{j\sqrt{\omega_1\omega_2}M_{12}}{2\sqrt{L_1L_2}} \tag{3}$$

where ω is the resonant frequency of the system ($\omega_1 = \omega_2 = \omega$), and k_{12} is the mutual coupling between the coils.

In steady state, being $F_S(t)$ a sinusoidal function described as $F_S(t) = A_s e^{-j\omega t}$, the field amplitudes in first and secondary coils are $a_1(t) = A_1 e^{-j\omega t}$ and $a_2(t) = A_2 e^{-j\omega t}$. It can be shown that the amplitudes A_1 and A_2 verify:

$$\frac{A_2}{A_1} = \frac{jK_{12}}{\Gamma_2 + \Gamma_L} \tag{4}$$

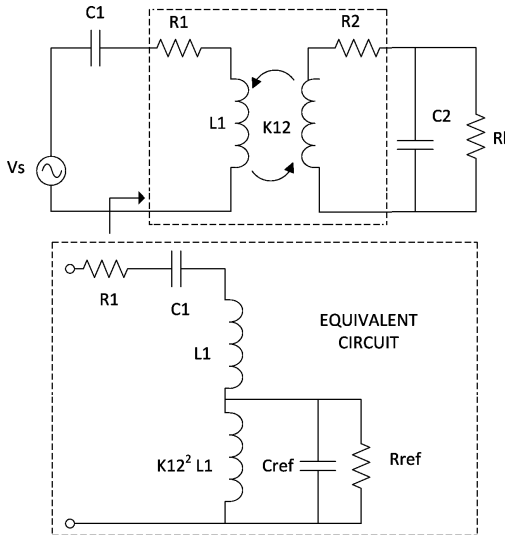

Figure 1: Reflected load theory schematic [3].

and therefore the power at the first coil, second coil and load is, respectively:

$$P_1 = 2\Gamma_1|A_1|^2; \quad P_2 = 2\Gamma_2|A_2|^2; \quad P_L = 2\Gamma_L|A_2|^2 \tag{5}$$

Finally, the efficiency can be described as the ratio between the power delivered to the load P_L and the total power delivered to the system:

$$\eta_{CMT} = \frac{P_L}{P_T} = \frac{\Gamma_L|A_2|^2}{|A_1|^2\Gamma_1 + |A_2|^2(\Gamma_2+\Gamma_L)} = \frac{\Gamma_L K_{12}^2}{\Gamma_1(\Gamma_2+\Gamma_L)^2 + (\Gamma_2+\Gamma_L)K_{12}^2} \tag{6}$$

3. REFLECTED LOAD THEORY

Reflected Load Theory has been widely used by electrical engineers to analyze transformers and it is now also used to predict RIC behaviour in the near-field [3, 4]. Reflected Load Theory states that the amount of current that flows through the primary coil is affected by the load present in the secondary coil. This load does not appear to the primary coil with the same actual value of the load, but instead as a function of the load value and the mutual impedance between primary and secondary coils.

In reflected load theory, the inductive link is described using the mutual coupling between coils $k_{12} = \frac{M_{12}}{L_1 L_2}$ and their quality factors (Q_1, Q_2):

$$Q_{s,x} = \frac{\omega L_x}{R_x}; \qquad Q_{p,x} = \frac{R_x}{\omega L_x} \tag{7}$$

where $Q_{s,x}$ and $Q_{p,x}$ represent the quality factors of an element placed in series and in parallel respectively.

At resonance frequency, the secondary coil is reflected onto the primary and the value that this coil sees is represented by R_{ref} [3]:

$$R_{ref} = k_{12}^2 \frac{L_1}{L_2} = k_{12}^2 \omega L_1 Q_{2L} \tag{8}$$

where k_{12} is the coupling between the coils and Q_{2L} is the loaded quality factor of the load $Q_{2L} = Q_2 Q_L/(Q_2+Q_L)$.

Because at resonance the impedance of the two coils is purely resistive, the power provided by the source V_s is divided between R_1 and R_{ref} (which also divides between R_2 and R_L). This leads to the definition of the WPT RIC efficiency in Reflected Load Theory:

$$\eta_{RLT} = \frac{R_{ref}}{R_2+R_{ref}} \frac{Q_2^2 R_2}{Q_2^2 R_2 + R_L} = \frac{k_{12}^2 Q_1 Q_{2L}}{1+k_{12}^2 Q_1 Q_{2L}} \frac{Q_{2L}}{Q_L} \tag{9}$$

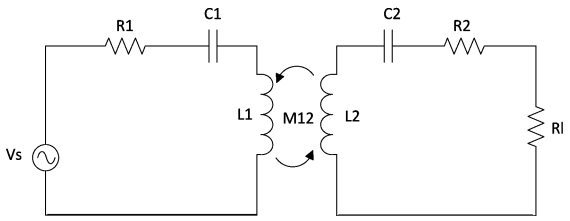

Figure 2: Lumped circuit theory schematic.

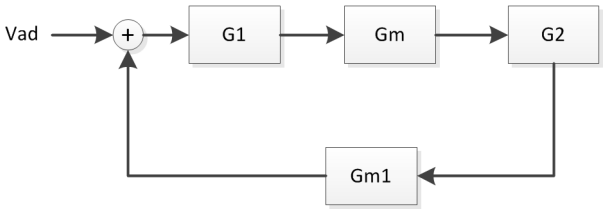

Figure 3: Lumped circuit theory — block diagram.

4. LUMPED CIRCUIT THEORY

The resonant inductive coupling between two electromagnetic resonators can also be described by Lumped circuit theory using a coupled RLC representation system. In this circuit, the capacitances and inductances model the resonant nature of the loops while the resistors model the radiative and ohmic losses.

In Resonant Inductive Coupling, the effect of the first coil to the second (mutual inductance) can be represented by a compensation source Z_{2M} on the coil. Similarly, the effect of the second coil to the first one (back EMF) can be represented also by a compensation source Z_{1M}.

$$Z_{2M} = \frac{\omega M_{12} V_{ad}}{Z_1} = \frac{\omega M_{12} V_{ad}}{R_1 + j\omega L_1 + \frac{1}{j\omega C_1}} \tag{10}$$

The power at the first coil, second coil and load is:

$$\begin{aligned} P_1 &= \frac{V_{ad}^2}{Z_1} \\ P_2 &= I_2^2 Z_2 = \left(\frac{Z_{2M}}{Z_2 + Z_L}\right)^2 Z_2 = \left(\frac{\omega M_{12} V_{ad}}{Z_1(Z_2 + Z_L)}\right)^2 Z_2 \\ P_L &= I_2^2 Z_L = \left(\frac{Z_{2M}}{Z_2 + Z_L}\right)^2 Z_L = \left(\frac{\omega M_{12} V_{ad}}{Z_1(Z_2 + Z_L)}\right)^2 Z_L \end{aligned} \tag{11}$$

where M_{12} is the mutual inductance between coils.

Defining the efficiency as the ratio between the power dissipated in the load (P_L) and the total power ($P_1 + P_2 + P_L$):

$$\eta_{RLC} = \frac{(\omega M_{12})^2 Z_L}{Z_1(Z_2 + Z_L)^2 + (\omega M_{12})^2 (Z_2 + Z_L)} \tag{12}$$

The Lumped Circuit system can also be analyzed expressing each subsystem's power transfer functions as gains. Figure 3 shows the interrelations between them.

Using this model, the current that flows at first and second coils can be written as:

$$I_1 = (V_{ad} + I_2 G_m) G_1; \quad I_2 = (I_1 G_m G_2) \tag{13}$$

where G_m is the transfer function from intensity in coil 1 to voltage in coil 2 ($G_m = \omega M_{12}$), G_1 is the transfer function from Voltage to current in first coil and G_2 is the equivalent at second coil:

$$G_1 = \frac{s}{s^2 L_1 + s R_1 + 1/C_1}; \quad G_2 = \frac{s}{s^2 L_2 + s(R_2 + R_L) + 1/C_2} \tag{14}$$

where s is the complex frequency $s = j\omega$.

The efficiency of the system can be found by dividing the power transferred to the load by the total power available (power on the source coil plus power dissipated on R_2 and R_L).

$$\eta_{RLC,2} = \frac{I_2^2 R_L}{I_1^2 R_1 + I_2^2 (R_2 + R_L)} = \frac{R_L G_m^2}{R_1 (R_2 + R_L)^2 + G_m^2 (R_2 + R_L)} \tag{15}$$

Finally, knowing that the gain functions G_1, G_2 are the inverse of the impedances in coils 1 and 2: $G_1 = 1/Z_1$, $G_2 = 1/Z_2$, the efficiency can be found equivalent to the one obtained in Equation (12):

$$\eta_{RLC} = \frac{(\omega M_{12})^2 Z_L}{Z_1(Z_2 + Z_L)^2 + (\omega M_{12})^2 (Z_2 + Z_L)} = \frac{G_m^2 Z_L}{\frac{1}{G_1 G_2^2} + G_m^2 \frac{1}{G2}} = \eta_{RLC,2} \tag{16}$$

5. COMPARISON

The Power Transfer Efficiency of Coupled Mode Theory (6) can be found equivalent to the efficiency of Reflected Load Theory (9) using the relationships:

$$K_{12} = \frac{\omega k_{12}}{2}; \quad Q_{s,x} = \frac{\omega L_x}{R_x} = \frac{\omega}{2\Gamma_{s,x}}; \quad Q_{p,x} = \frac{R_x}{\omega L_x} = \frac{\omega}{2\Gamma_{p,x}} \tag{17}$$

$$\eta_{CMT} = \frac{\Gamma_L K_{12}^2}{\Gamma_1(\Gamma_2+\Gamma_L)^2 + (\Gamma_2+\Gamma_L)K_{12}^2} = \frac{k_{12}^2}{\frac{Q_L}{Q_1}\left(\frac{Q_2+Q_L}{Q_2Q_L}\right)^2 + k_{12}^2\frac{Q_2+Q_L}{Q_2}} = \eta_{RLT} \tag{18}$$

Similarly, it can be demonstrated that the efficiencies obtained using Lumped Circuit Theory are also equivalent to the ones obtained by CMT and RLT:

$$\eta_{RLC} = \frac{(\omega M_{12})^2 Z_L}{Z_1(Z_2+Z_L)^2 + (\omega M_{12})^2(Z_2+Z_L)} = \frac{k_{12}^2 Z_L}{\frac{\omega L_2}{Q_1}\left(\frac{Q_2+Q_L}{Q_2Q_L}\right)^2 + \omega k_{12}^2 L_2\frac{Q_2+Q_L}{Q_2Q_L}} = \eta_{RLT} \tag{19}$$

6. OPTIMAL LOAD

Once the efficiencies of the different theoretical models have been found, it is interesting to analyze the optimal values of load that maximize them.

To find the optimal load in Coupled Mode Theory, we can differentiate the efficiency expression (6) with respect to Γ_L, obtaining:

$$\Gamma_{\mathrm{L},\eta_{\max}} = \sqrt{\Gamma_2^2 + \frac{\Gamma_2}{\Gamma_1}K_{12}^2} \tag{20}$$

Similarly, we can set the derivative of (9) with respect to Q_L to 0:

$$Q_{\mathrm{L},\eta_{\max}} = \frac{Q_2}{\sqrt{1+k_{12}^2 Q_1 Q_2}} \tag{21}$$

Using the relationships defined in (7), it can be demonstrated that resistor needed to match the optimal load Q factor to maximize the efficiency is the same as the one obtained using CMT theory [3].

$$\Gamma_{L,RLT} = \Gamma_2\sqrt{1+\frac{4K_{12}^2}{\omega^2}\frac{\omega}{2\Gamma_1}\frac{\omega}{2\Gamma_2}} = \sqrt{\Gamma_2^2 + \frac{K_{12}^2\Gamma_2}{\Gamma_1}} = \Gamma_{L,CMT} \tag{22}$$

We could also differentiate the efficiency obtained using Lumped Circuit Theory (16)

$$R_{L,RLC} = \sqrt{R_2^2 + Gm^2\frac{R_2}{R_1}} \tag{23}$$

and using the Equation (17) it can be demonstrated that the equivalent optimal load found in CMT and RLT is equal to the load found in (23):

$$R_{L,CMT} = R_{L,RLT} = 2L_2\sqrt{\left(\frac{R_2}{2L_2}\right)^2 + \frac{\omega^2 k_{12}^2}{4}\frac{R_2 L_1}{R_1 L_2}} = \sqrt{R_2^2 + \omega^2 k_{12}^2 L_1 L_2\frac{R_2}{R_1}} = R_{L,RLC} \tag{24}$$

To compare the load values obtained from optimizing the efficiency function to the ones from applying impedance matching techniques, we must first find the output impedance seen by the load. From the circuit model:

$$Z_{out} = j\omega L_2 - \frac{j}{\omega C_2} + R_2 + \frac{(\omega M_{12})^2}{j\omega L_1 - \frac{j}{\omega C_1} + R_1} \tag{25}$$

To maximize the efficiency using impedance matching techniques, it can be seen that the system must be totally matched, this is, the load should be conjugately matched to the output resistance: $Z_{out} = Z_L^*$.

$$Z_{L,RLC} = \left(\frac{j}{\omega C_2} - j\omega L_2\right) + \sqrt{R_2^2 + (\omega M_{12})^2\frac{R_2}{R_1}} \tag{26}$$

In resonance, $Z_L = Z_{out}*$ becomes purely real:

$$R_L = \sqrt{R_2^2 + (\omega M_{12})^2 \frac{R_2}{R_1}} = R_{L,CMT} = R_{L,RLT} = R_{L,RLC} \tag{27}$$

Therefore, we have demonstrated that using impedance matching techniques (conjugately matching the load to the output resistance) leads to the same optimal values than the ones obtained by setting the derivative of the efficiencies obtained using Coupled Mode Theory, Reflected Load Theory and Lumped Circuit Theory with respect to the load equal to zero.

7. CONCLUSIONS

We have successfully demonstrated that Coupled Mode Theory, Reflected Load Theory and Lumped Circuit theory are equivalent when calculating the Power Transfer Efficiency of a Resonant Inductive Coupled link in Steady-State. Also, the optimal values of load have been found for each theory, showing complete accordance. Finally, it has been demonstrated that applying impedance matching techniques (this is, conjugately matching the load to the output resistance of the system) is equivalent to optimizing the PTE efficiency by setting its derivative with respect to the load equal to zero.

ACKNOWLEDGMENT

Partial funding by projects TEC2010-15765 and RUE CSD2009-00046 (Consolider-Ingenio 2010), from the Spanish ministry of Science and Innovation is acknowledged. Partial funding by Thales Alenia Spain is acknowledged.

REFERENCES

1. Kurs, A., A. Karalis, and R. Moffat, "Wireless power transfer via strongly coupled magnetic resonances," *Science*, Vol. 6, 83–86, June 2007.
2. Kurs, A., J. Joannopoulos, and M. Soljacic, "Efficient wireless non-radiative mid-range energy transfer," *Annals of Physics*, Vol. 323, 34–48, 2008.
3. Kiani, M. and M. Ghovanloo, "The circuit theory behind coupled-mode magnetic resonance-based wireless power transmission," *IEEE Transactions on Circuits and Systems I: Regular Papers*, Vol. PP, No. 99, 1, 2012.
4. Kiani, M., U.-M. Jow, and M. Ghovanloo, "Design and optimization of a 3-coil inductive link for efficient wireless power transmission," *IEEE Transactions on Biomedical Circuits and Systems*, Vol. 5, No. 6, 579–591, Dec. 2011.

Adaptive Impedance Matching for Magnetically Coupled Resonators

Benjamin H. Waters[1], **Alanson P. Sample**[1, 2], **and Joshua R. Smith**[1, 2]

[1]Department of Electrical Engineering, University of Washington, USA
[2]Departments of Computer Science Engineering, University of Washington, USA

Abstract— For high quality factor magnetically coupled resonator wireless power systems, constant wireless power transfer efficiency can be achieved over a greater range and higher efficiency than an inductively coupled system. However, as the distance varies between two near-field resonators, the input and output impedances to the resonators change. Therefore, in order to achieve constant efficiency, the resonator input impedance must be adaptively matched to the source impedance of the transmit resonator and the load impedance of the output device. Previous techniques have demonstrated adaptive frequency tuning control algorithms to track the resonant peaks. However, government regulations strictly limit the radiating electric field strength of wireless applications outside specific bandwidths which will be exceeded by these frequency tuning algorithms. Adaptive impedance matching (AIM) networks automatically change the input and output impedances in order to maintain maximum wireless power transfer efficiency. In this paper, the input impedance is characterized for a four-element resonant wireless power system. Two algorithms are presented to determine the component values for any adaptive impedance matching network topology to achieve constant wireless power transfer efficiency at a single frequency. These techniques are demonstrated and verified with a π-match network.

1. INTRODUCTION

Wireless power technology using magnetically coupled resonators (MCRs) is becoming more prevalent in common applications that demand efficient wireless power delivery for an entire volume of space, such as consumer electronics and implantable biomedical devices [1–6]. These applications require a highly efficient end-to-end wireless power system that can operate within the bandwidth limitations defined by wireless communication standards and regulations.

For a four-element high-Q MCR wireless power system operating in the over-coupled regime, there are two resonant modes offset by several MHz from the resonant frequency [1]. Prior work has demonstrated wideband frequency tuning techniques that automatically tune the operating frequency to maximize wireless power transfer efficiency [1, 3, 7, 8]. However, a frequency tuning algorithm used to perform maximum power point tracking may not be a viable option because the optimal operating frequency can violate the allowable frequency bandwidths where wireless power systems can operate as defined by wireless communication standards in a given country.

Rather than tuning the operating frequency to achieve maximum wireless power transfer efficiency, an impedance matching network can be used to achieve high efficiency at a single frequency within the narrow regulated bandwidth. Figure 1 shows the system-level block diagram of a wireless power system indicating an input matching network, a set of high-Q MCRs, an output matching network, a rectifier to convert the RF signal into a DC voltage compatible with a specific application, and the corresponding impedance contribution of each block. The impedance Z_{MCR} looking into the MCRs changes as a function of the mutual inductance M_{23} between the transmit (Tx) and receive (Rx) resonators. Additionally, the impedance Z_{RECT} across a full-wave rectifier changes as a function of transferred power. In order to match the varying complex system impedance $Z_{IN,SYS}$

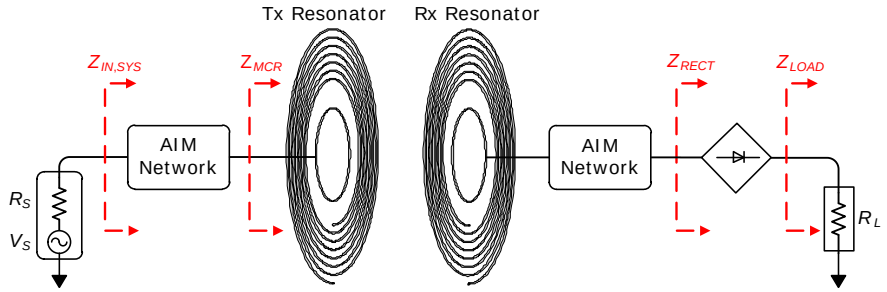

Figure 1: Block diagram of the impedance path for a high-Q MCR wireless power system.

to the source impedance R_S (typically 50 Ω from a power amplifier), an adaptive impedance matching (AIM) network can be used to induce a resonant peak at the specified operating frequency for narrowband wireless power transfer.

In this work, the impedance of each block in the wireless power system is characterized using $ABCD$ transmission matrices. Next, two separate algorithms are proposed to determine the component values of any matching network that will enable maximum wireless power transfer across a set of MCRs at a single transmit frequency. The first technique assumes an ideal matching network and directly calculates the component values of the matching network based on the input impedance Z_{MCR} extracted from measured S-parameter data for the MCRs. The second technique uses a constrained nonlinear optimization algorithm to compute the matching network component values for a lossy matching network that optimize S_{21} for a set of MCRs. Both techniques are validated using a π-match AIM network for a set of MCRs tuned to 13.56 MHz.

Although the analysis presented in this paper can be adapted to any set of MCRs, Figure 2(a) shows the set of MCRs that will be used for both the simulated and experimental inductance (L), tuning capacitance (C), and parasitic resistance (R_p) of the MCRs. These parameters are summarized in Figure 2(b). The resonators are all individually tuned for 13.56 MHz and are optimized for an optimal figure of merit (FOM) by optimizing the loop-coil coupling coefficients k_{12} and k_{34} for the best tradeoff between $|S_{21}|$ and wireless power transfer range according to [1].

2. IMPEDANCE CHARACTERIZATION OF MAGNETICALLY COUPLED RESONATORS

Before selecting an optimal matching network for MCRs, it is desirable to characterize the input impedance to a set of MCRs for a range of coupling coefficients between the resonators. The equivalent circuit diagram for a typical four-element resonant system is shown in Figure 3.

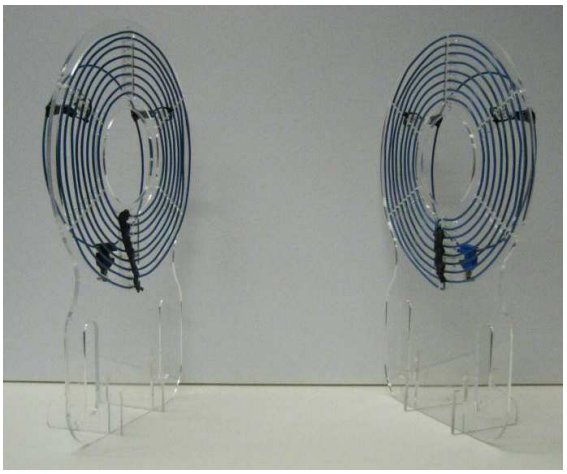

(a)

TRANSMITTER		RECEIVER	
L_1	0.6708 uH	L_4	0.6737 uH
C_1	203.19 pF	C_4	203.6 pF
R_{p1}	0.2627 Ω	R_{p4}	0.2586 Ω
N_1	1	N_4	1
Radius 1	10.25 cm	Radius 4	10.25 cm
R_{source}	50 Ω	R_{load}	50 Ω
Q_1	1.143	Q_4	1.145
F_1	13.63 MHz	F_4	13.58 MHz
K_{12}	0.2798	K_{34}	0.287
Q_2	3129	Q_3	230.29
F_{o2}	13.68 MHz	F_{o3}	13.66 MHz
L_2	17.04 uH	L_3	17.15 uH
C_2	8 pF	C_3	8 pF
R_{p2}	4.66 Ω	R_{p3}	6.36 Ω
N_2	8	N_3	8
Radius 2	14 cm	Radius 3	14 cm

(b)

Figure 2: (a) High-Q MCR resonators used throughout this work, (b) summary of coil parameter values for the MCRs.

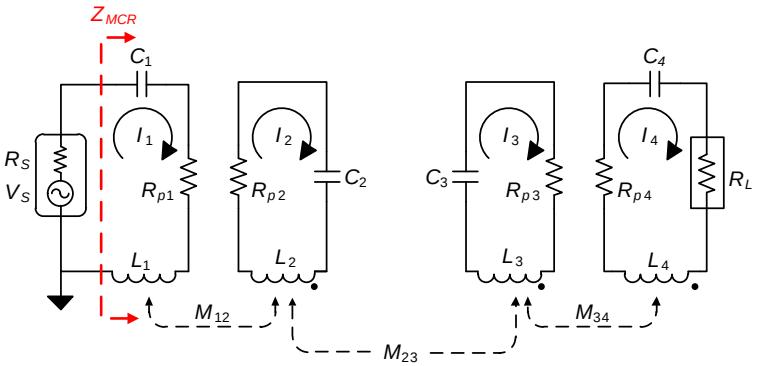

Figure 3: Equivalent circuit diagram of a 4-coil MCR wireless power system.

Flux linkages (Φ_i) and Kirchoff Voltage Loop (KVL) equations are used to solve the loop currents (I_{1-4}) indicated in Figure 3. The flux linkages across each coil are related to the voltage across the two ends of each coil. These flux linkages can also be expressed in terms of the mutual inductance (M_{ij}) between the various coils. The mutual inductance is related to the coupling coefficient k_{ij} between two inductors by (1). The current I_1 supplied by V_S flows through L_1 and produces an oscillating magnetic field. Some of these field lines pass through the other coils to produce a flux Φ_i. These flux linkages can be comprehensively expressed in terms of the mutual and self inductances for the four-element resonant system [9]. Substituting the flux linkage for each coil into the node equations derived from the four KVL equations for the schematic in Figure 3 gives (1).

$$\begin{bmatrix} V_S \\ 0 \\ 0 \\ 0 \end{bmatrix} = \begin{bmatrix} Z_1 & j\omega M_{12} & j\omega M_{13} & j\omega M_{14} \\ j\omega M_{21} & Z_2 & j\omega M_{23} & j\omega M_{24} \\ j\omega M_{31} & j\omega M_{32} & Z_3 & j\omega M_{34} \\ j\omega M_{41} & j\omega M_{42} & j\omega M_{43} & Z_4 \end{bmatrix} \begin{bmatrix} I_1 \\ I_2 \\ I_3 \\ I_4 \end{bmatrix}, \quad k_{ij} = \frac{M_{ij}}{\sqrt{L_i L_j}} \tag{1}$$

After solving for the individual currents, neglecting the parasitic cross-coupling terms ($M_{13} = M_{14} = M_{24} = 0$) and setting $M_{12} = M_{21}$, $M_{23} = M_{32}$ and $M_{34} = M_{43}$, the equivalent input impedance Z_{MCR} can be defined by (2).

$$\begin{aligned} Z_{MCR} &= \frac{V_S}{I_1} - R_S = \frac{M_{12}^2(M_{34}^2\omega^4 + \omega^2 Z_3 Z_4) - (R_S - Z_1)(M_{34}^2\omega^2 Z_2 + M_{23}^2\omega^2 Z_4 + Z_2 Z_3 Z_4)}{M_{34}^2\omega^2 Z_2 + M_{23}^2\omega^2 Z_4 + Z_2 Z_3 Z_4} \\ Z_1 &= R_S + R_{P1} + j\omega L_1 + \frac{1}{j\omega C_1} \\ Z_2 &= R_{P2} + j\omega L_2 + \frac{1}{j\omega C_2} \\ Z_3 &= R_{P3} + j\omega L_3 + \frac{1}{j\omega C_3} \\ Z_4 &= R_L + R_{P4} + j\omega L_4 + \frac{1}{j\omega C_4} \end{aligned} \tag{2}$$

Figure 4 shows the simulated Z_{MCR} plotted against k_{23} at a single frequency of 13.56 MHz for the extracted L, R, C components of the resonators shown in Figure 2. This plot indicates that for strong coupling between the two resonators (over-coupled regime [1]) $|Z_{MCR}| < R_S$ and for weak coupling (under-coupled regime) $|Z_{MCR}| > R_S$. The critical coupling point occurs when $|Z_{MCR}| = R_S = 50\,\Omega$. Therefore, an AIM network must be able to match a load impedance that can be either greater than, less than or equal to the source impedance.

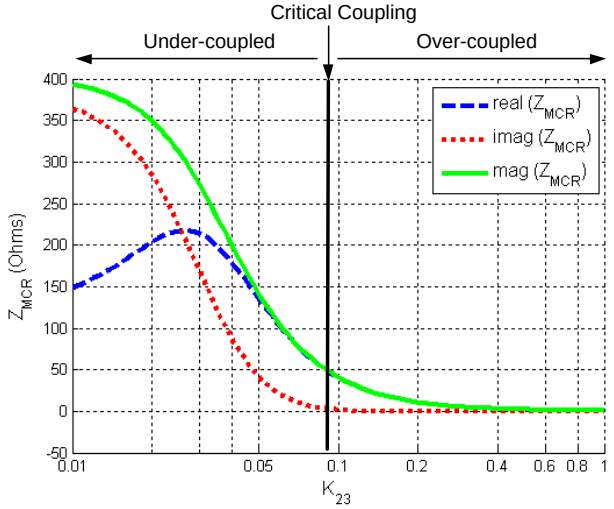

Figure 4: Plot of the real, imaginary, and magnitude components of Z_{MCR} as a function of K_{23}.

3. MATCHING NETWORK COMPONENT SELECTION

To determine the component values of any impedance matching network at a given frequency, the source and load impedances of the matching network must be accurately defined. For the resonant wireless power system shown in Figure 1, the equivalent impedance (Z) matrix can be accurately defined by analyzing each step in the impedance path as a two-port network.

The components in each block can be defined with either ideal components, lossy components, or with extracted scattering (S) parameters from a vector network analyzer (VNA) for the most accurate analysis. For example, an inductor can be modeled as either a lossless component or as a lossy component with a series DC resistance (DCR) based on the parasitic parameters provided by the manufacturer. However, the most accurate parasitic model for an inductor can be extracted by measuring the two-port S-parameters using a VNA and importing these model parameters into a simulation tool.

Similarly for the equivalent impedance of the MCRs: the input impedance for four-element MCRs can be calculated for a given coupling coefficient using (2). However, these theoretical expressions typically neglect parasitic effects such as capacitive cross-coupling and resonator detuning that can significantly reduce efficiency at the resonant frequency for a practical system. Therefore, it is most accurate to extract S-parameters from a VNA for a full range of coupling coefficients and calculate the equivalent input impedance from S_{11} as in (3). Once the impedance characteristics of each block have been defined using these techniques, the algorithms presented in this paper can be implemented to determine the necessary component values of a matching network to match the source impedance R_s to this lumped system impedance $Z_{IN,SYS}$.

$$Z_{in} = R_S \frac{1 + S_{11}(j\omega))}{1 - S_{11}(j\omega))} \tag{3}$$

Throughout this work, a low-pass π-match impedance matching network topology will be used as in Figure 5. In contrast to an L-match topology, the π-match topology enables wideband impedance matching to load impedances that are either greater than, equal to or less than the source impedance. The low-pass π-match topology allows for a fixed inductor value to be placed in the high-current path, and variable source and load capacitor values can control the impedance matching capabilities of the matching network. This switching functionality is preferable because it is easier to implement a parallel bank of switchable capacitors than inductors in series. Additionally, the quality factor (Q_m) of the π-match network provides an extra degree of freedom to achieve wideband or narrowband impedance matching. For strongly coupled MCRs, wideband impedance matching (low Q_m) is desired, but for weak coupling, narrowband impedance matching (high Q_m) is preferable. Refer to Section 4 for an extended analysis of the π-match network implented with a set of MCRs.

3.1. Ideal Conjugate Match Algorithm

Refer to the impedance path in Figure 1 as a reference for this discussion of the matrix transformations for the ideal conjugate match algorithm. For the most accurate modeling, a VNA has been used to extract the S-parameters for a set of MCRs and the rectifier. By converting the S-matrices of the MCRs and the rectifier to $ABCD$ transmission matrices, a single transmission matrix $[ABCD]_{SYS}$ can be defined for the entire system by multiplying together the cascaded $ABCD$ matrices [10, 11]. The $[ABCD]_{SYS}$ matrix is then converted back to an S-matrix from which the equivalent input impedance Z_{MCR} can be defined as in (3).

Now, the component values of the matching network can be selected. For simplicity, the impedance contribution from the rectifier has been neglected and only the real component of Z_{MCR}

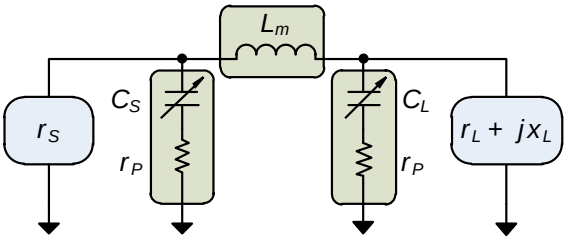

Figure 5: Block diagram of the low pass π-match network.

is used since the imaginary component of Z_{MCR} is negligible in the over-coupled regime as shown in Figure 4. The source impedance r_s seen by the π-match network is equal to R_s and the load impedance $r_l + jx_l$ is equal to $real(Z_{MCR})$. To eliminate the need for a switching circuit in the high-current path, a fixed inductor value L_m in the π-match network is chosen. The source and load capacitors (C_S and C_L) and Q_m of the π-match network can be calculated to provide an accurate impedance match for a specified source and load impedance using (4). By swapping the equations for C_S and C_L and interchanging r_s and r_l, the π-match component values can also be derived for the case when $r_s > r_l$.

$$\left.\begin{aligned} Q_m &= \sqrt{-1 + \frac{r_l(r_l + r_s)}{L_m^2 w_0^2} + \frac{2r_l\sqrt{r_l r_s - L_m^2 w_0^2}}{L_m^2 w_0^2}} \\ C_S &= \frac{\sqrt{-1 + \frac{(1+Q_m^2)r_s}{r_l}}}{r_s w_0} \\ C_L &= \frac{Q_m}{r_l w_0} \end{aligned}\right\} r_s < r_L \tag{4}$$

These expressions are used to define the component values for a π-match AIM network as Z_{MCR} changes as a function of k_{23} for a set of MCRs. From the expression for C_S, the maximum achievable quality factor ($Q_{m,\mathrm{MAX}}$) for a π-match network is determined by (5). The maximum and minimum conditions in (5) account for the additional case when $r_s > r_l$.

$$Q_{m,\mathrm{MAX}} = \sqrt{\frac{\max(r_s, r_l)}{\min(r_s, r_l)} - 1} \tag{5}$$

If Q_m exceeds $Q_{m,\mathrm{MAX}}$ for a given r_s and r_l, then C_S will not be a real number and is not achievable. Therefore, the matching network will not be able to effectively match the source impedance to the load impedance. However, L_m can be increased to reduce Q_m and ensure that the matching network can provide an optimal match for all possible values of r_s and r_l.

The advantage of implementing this algorithm in a wireless power system is that the component values of the AIM network can be directly calculated and selected by a microcontroller unit (MCU). These direct computations can be faster to perform than an optimization routine on an MCU and can be used to quickly define new component values of an AIM network for changing input and output impedances of a wireless power system.

3.2. Parasitic Match Optimization Algorithm

The second algorithm calculates the component values of non-ideal AIM networks placed at both the Tx and Rx sides of MCRs by using extracted S-parameters to define L_m and by modeling C_S and C_L with an equivalent series resistance (ESR). Rather than directly solving for the component values using the calculated source and load impedances of the matching network as in the ideal conjugate match algorithm, the parasitic match algorithm uses constrained nonlinear optimization to compute component values that maximize the magnitude of the system transmission function $S_{21,SYS}$.

By characterizing any type of impedance matching network as a two-port $ABCD$ matrix, extracted S-parameters for inductors and capacitors in the matching network can be used. In the case of the π-match network, extracted S-parameters for the series inductor can be used and converted to an $ABCD$ matrix, and the shunt source and load capacitors can be modeled with an ESR. Then, for a specified inductor, the values of $C_{S1,2}$ and $C_{L1,2}$ are optimally selected to maximize $|S_{21,SYS}|$.

The optimization routine uses the fminsearch function in Matlab. First, $S_{21,SYS}$ is defined at a single frequency as a function of $C_{S1,2}$ and $C_{L1,2}$ using the transmission matrix transformation shown in Figure 6. Next, the fminsearch function computes $C_{S1,2}$ and $C_{L1,2}$ constrained by positive real capacitor values by minimizing the error function (σ) defined in (6).

$$\sigma = \min(1 - |S_{21,SYS}|), \quad 1\,\mathrm{pF} < C_s, \quad C_L < 10\,\mathrm{nF} \tag{6}$$

There are two key benefits of this algorithm over the ideal conjugate match algorithm. First, since all components have been modeled accurately with extracted S-parameters from either the component manufacturer or a VNA, the simulated results accurately match the achievable experimental results as confirmed in Section 4. Second, it is easier than the ideal conjugate matching

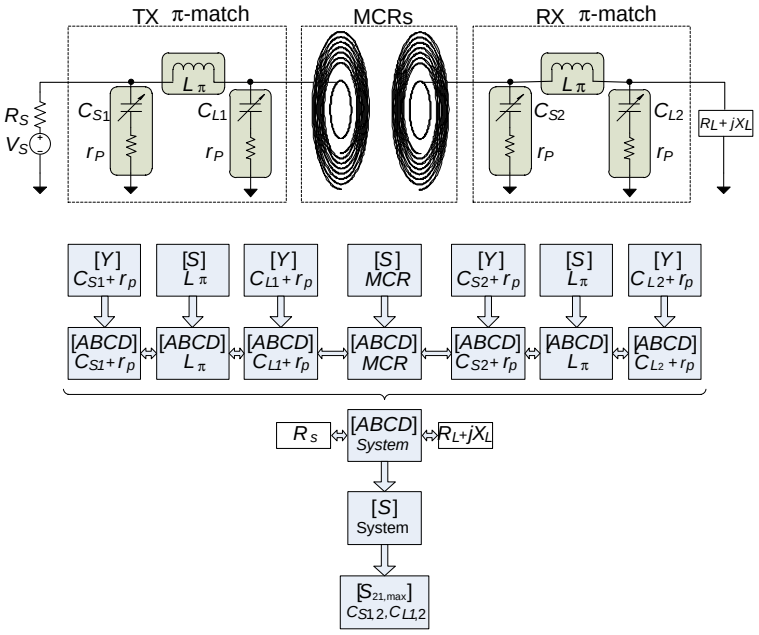

Figure 6: Flow chart of the process used for the parasitic optimization algorithm to extract the shunt capacitor values in the π-match network for an AIM network implemented with a set of high Q MCRs.

algorithm to simulate any impedance matching network topology because the equations for the components in the matching network do not need to be defined for a specific source and load impedance. Rather, the matching network can be easily defined as an $ABCD$ matrix, and after transforming the cascaded $ABCD$ matrices into a single S matrix $[S]_{System}$, the optimization algorithm automatically selects the component values for maximum $|S_{21,SYS}|$. Additionally, the matching network can be placed either at the Tx side only, Rx side only or both sides as in Figure 6 without having to re-calculate the equivalent input impedance, which becomes complicated for a double-sided matching network topology. Section 4 demonstrates that a π-match network at both the input to the Tx resonator and the output of the Rx resonator can achieve a greater $|S_{21,SYS}|$ than a matching network only at the Tx side.

4. MODEL VALIDATIONS AND EXPERIMENTAL RESULTS

A total of 87 S-parameter datasets have been extracted using a VNA for various distances between the Tx and Rx resonators shown in Figure 2(a) ranging from 0.3 cm–40 cm. These model parameters have been used to characterize the MCRs for both the ideal conjugate match and parasitic optimization algorithms presented in Section 3. A 206 nH inductor and switchable capacitors ranging from 1–1000 pF are used in the π-match AIM network. For the ideal conjugate match algorithm, both this inductor and the shunt capacitors have been modeled as ideal, lossless components. For the parasitic optimization algorithm, S-parameters provided by the manufacturer for a 206 nH air-core inductor have been used to model the inductor in the π-match network. The shunt capacitors have been modeled with a 50 mΩ ESR, a standard value for an 0603 package ceramic capacitor in the tens of MHz frequency range.

Figure 7 shows the 3D surface plots of $|S_{21,SYS}|$ versus frequency and distance between the two resonators. Figure 7(a) shows the case without an AIM network: the MCRs are terminated in 50 Ω source and load impedances. This plot demonstrates the frequency splitting effect in the overcoupled region. For a commercial application, this behavior is problematic because the efficiency at the resonant frequency of 13.56 MHz within the regulated frequency band is very low in the overcoupled regime. Figure 7(b) shows how an ideal π-match AIM network with component values selected by the simulated ideal conjugate match algorithm can confine the resonant peaks to a single ridge centered at 13.56 MHz across the entire range of separation distances. Figure 7(c) shows the effect of the simulated parasitic optimization algorithm implemented with the MCRs. For this plot, a π-match AIM network has been placed at both the Tx and Rx resonators. Although there is a significant improvement in efficiency at 13.56 MHz compared to Figure 7(a), this ridge is not as well defined as the ideal case in Figure 7(b) because parasitic components of the matching network

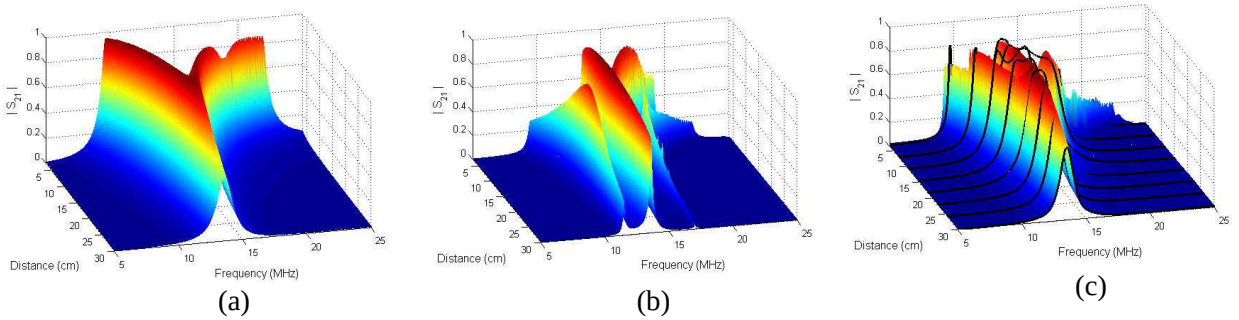

Figure 7: Surface plots of the extracted $|S_{21}|$ for the MCRs with (a) 50 Ω source and load termination impedances, (b) a π-match AIM network at the Tx side corresponding to the simulated ideal conjugate match algorithm, and (c) a π-match AIM network at both the Tx and Rx sides corresponding to the simulated parasitic optimization algorithm (surface plot) with the experimental results overlayed (black lines).

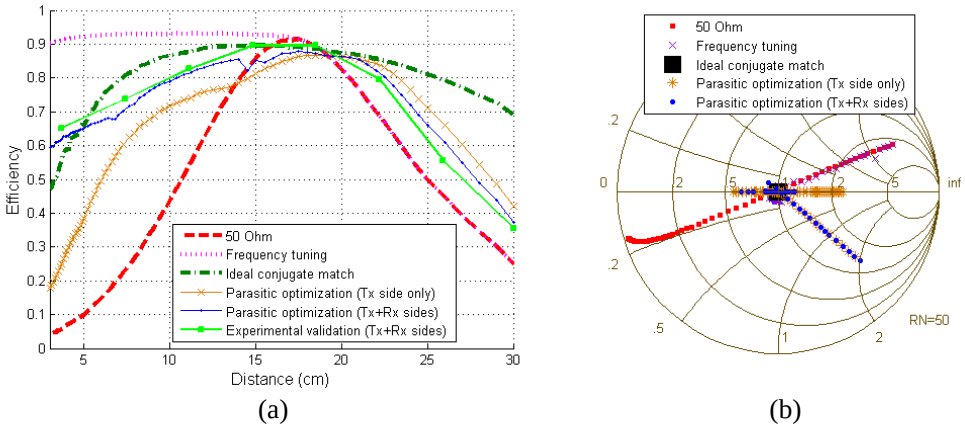

Figure 8: (a) Plot of the simulated and experimental efficiency, or $|S_{21}|^2$, and (b) a Smith chart of the simulated S_{11}.

are included in the simulation. This simulated surface plot is compared to experimental results shown by the black lines in Figure 7(c). The experimental dataset was extracted using a VNA with a π-match network on both sides for eight incremental distances between the resonators. The shunt capacitors are manually switched according to the recommended component values from the parasitic optimization algorithm. This result confirms that the simulated parasitic optimization algorithm accurately models the achievable experimental result.

Figure 8 directly compares the efficiency versus separation distance at a single frequency of 13.56 MHz for all of the simulated analyses and experimental result. Figure 8(a) includes single-frequency results for the MCRs terminated in 50 Ω, an ideal π-match AIM network at the Tx side based on the ideal conjugate match algorithm, a parasitic π-match AIM network at the Tx side as well as at both the Tx and Rx sides based on the parasitic optimization algorithm, and the experimental implementation of the double-sided parasitic optimization algorithm. Figure 8(a) also includes a result for wideband frequency tuning where the operating frequency is selected based on the maximum efficiency points along the low-frequency ridge in Figure 7(a). The AIM networks improve efficiency from the 50 Ω case at a single frequency in both the overcoupled and undercoupled regions, but cannot achieve efficiency as high as the frequency tuning results. Additionally, the S_{11} Smith chart is shown in Figure 8(b) for all of these cases. S_{11} is defined on the Smith chart at 13.56 MHz for each separation distance. The ideal conjugate match algorithm provides a perfect match to the 50 Ω source impedance at the center of the smith chart. The parasitic matching network is able to confine S_{11} towards the center, but cannot provide an accurate match for all distances.

The most problematic scenario occurs for the strongest coupling between the two resonators because the bandwidth is widest for the split resonant modes at this point. An ideal matching network is able to fully recover maximum efficiency at a single frequency for this case. However, the parasitic matching network is incapable of fully recovering maximum efficiency because the load

impedance presented to the matching network by the MCRs for strongest coupling is significantly less than the $50\,\Omega$ source impedance.

5. CONCLUSION

In this paper we demonstrate how an adaptive impedance matching network can be implemented with a set of high-Q MCRs to achieve maximum wireless power transfer efficiency at a single operating frequency. The key contributions of this work are the two algorithms presented that can compute the required component values of an AIM network for an accurate impedance match to both the input and output impedances for any amount of coupling between the MCRs.

We have characterized the input impedance for a four-element MCR system. The first algorithm uses the calculated equivalent input impedance to directly calculate the component values of a π-match AIM network. The second algorithm accounts for a non-ideal matching network by using extracted S-parameters and matrix transformations to define a system S-matrix. Then, an optimization algorithm computes the component values of a matching network that maximize the efficiency of the entire system at a single frequency. Finally, these algorithms are validated with an experimental model of the parasitic optimization algorithm.

REFERENCES

1. Sample, A. P., D. Meyer, and J. R. Smith, "Analysis, experimental results, and range adaptation of magnetically coupled resonators for wireless power transfer," *IEEE Transactions on Industrial Electronics*, Vol. 58, No. 2, 544–554, Feb. 2011.
2. Kurs, A., A. Karalis, R. Moffatt, J. D. Joannopoulos, P. Fisher, and M. Soljacic, "Wireless power transfer via strongly coupled magnetic resonances," *Science*, Vol. 317, No. 5834, 83–86, 2007.
3. Waters, B. H., A. P. Sample, P. Bonde, and J. R. Smith, "Powering a ventricular assist device (VAD) with the free-range resonant electrical energy delivery (FREE-D) system," *Proceedings of the IEEE*, Vol. 100, No. 1, 138–149, Jan. 2012.
4. Low, Z. N., R. Chinga, R. Tseng, and J. Lin, "Design and test of a high-power high-efficiency loosely coupled planar wireless power transfer system," *IEEE Transactions on Industrial Electronics*, Vol. 56, No. 5, 1801–1812, May 2009.
5. Raval, P., D. Kacprzak, and A. P. Hu, "A wireless power transfer system for low power electronics charging applications," *2011 6th Conference on Industrial Electronics and Applications*, 520–525, Jun. 2011.
6. Park, J.-H., B.-C. Park, J.-H. Lee, Y.-H. Ryu, E.-S. Park, and S.-W. Kwon, "Optimum frequency of high Q-factor resonator for magnetic resonance coupling," *2011 41st European Microwave Conference*, 61–63, Oct. 2011.
7. Kim, N. Y., K. Y. Kim, J. Choi, and C. W. Kim, "Adaptive frequency with power-level tracking system for efficient magnetic resonance wireless power transfer," *Electronics Letters*, Vol. 48, No. 8, 452–454, Apr. 2012.
8. Park, J., Y. Tak, Y. Kim, Y. Kim, and S. Nam, "Investigation of adaptive impedance matching methods for near-field wireless power transfer," *IEEE Transactions on Antennas and Propagation*, Vol. 59, No. 5, 1769–1773, May 2011.
9. Cannon, B., J. Hoburg, D. Stancil, and S. Goldstein, "Magnetic resonance coupling as a potential means for wireless power transfer to multiple small receivers," *IEEE Transactions on Power Electronics*, Vol. 24, No. 7, 1819–1825, Jul. 2009.
10. Pozar, F. M., *Microwave Engineering*, Wiley, New York, 2004.
11. Frickey, D. A., "Conversions between S, Z, Y, h, $ABCD$, and T parameters which are valid for complex source and load impedances," *IEEE Transactions on Microwave Theory and Techniques*, Vol. 42, No. 2, 205–211, Feb. 1994.

Analysis of Double Negative Meta-material Asymmetric Planar Slab Waveguide by Transmission Equivalent T-circuit Model

Sanjeev Kumar Raghuwanshi, **Santosh Kumar**, **and Radha Raman Pandey**
Department of Electronics Engineering
Indian School of Mines, Dhanbad, Jharkhand 826004, India

Abstract— The symmetric/asymmetric planar slab waveguide is simplest waveguide structure to be analyzed. These waveguides are used in optical communication systems. In this paper, we have derived the Eigen value equation by using the transmission line (TL) method for the case of Double Negative Meta-material (DNG) slab. The derived results have been exactly matched with the existing results found into the literatures. The unusual behaviour of double negative meta-material is predicted. Dispersion study (b-v graph), mode field profile and power confinement factor are also being discussed at the end.

1. INTRODUCTION

The Usual properties of Meta material waveguide structures may have impact on WDM optical communication systems. The transmission line (TL) method has great application to analyze DNG waveguide structure having arbitrary refractive index profile [1, 2]. There is large number of current research papers on application of TL method of waveguide analysis. The asymmetric waveguide is somewhat tough to analyze due to their asymmetric mode field profile. However the asymmetric waveguide have found certain advantage over the symmetric waveguide structure due to their easiness [3, 4]. In Section 2, we have shown the procedure to derive the Eigen-value equation by TL method followed by double negative meta-material waveguide structure in Section 3. In Section 3, itself, we discussed the results of computation.

2. MAXWELL EQUATIONS AND TRANSMISSION EQUIVALENT T-CIRCUITS

Let consider the simplest planar slab optical waveguide as shown in Fig. 1(a) having refractive index variation in x-direction and direction of wave propagation in $+z$ direction. Consider the following Maxwell equations (time harmonic $e^{j\omega t}$) [4],

$$\begin{cases} \nabla \times E = -\mu_0 \dfrac{\partial H}{\partial t} & (1) \\ \nabla \times H = \varepsilon \dfrac{\partial E}{\partial t} & (2) \end{cases}$$

For the TE mode case propagating in $+z$ direction as shown in Fig. 1(a), having $E_x = 0$, $H_y = 0$ and $E_z = 0$ hence from Eqs. (1) and (2).

$$\frac{\partial E_y}{\partial x} = -\mu_0 j\omega H_z \quad (3)$$

$$\frac{\partial H_z}{\partial x} + j\beta H_x = -j\omega\varepsilon_0 \left\{n(x)\right\}^2 E_y \quad (4)$$

$$\beta E_y = -\omega\mu_0 H_x \quad (5)$$

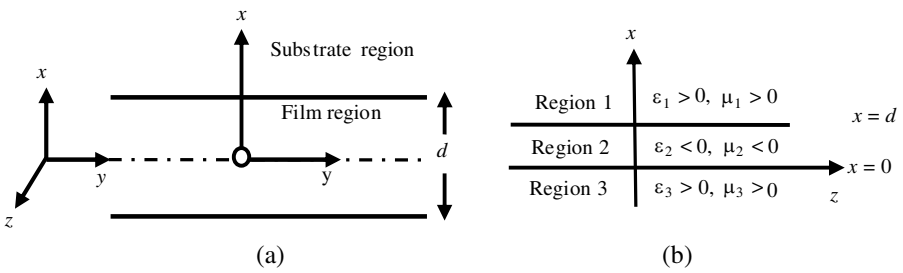

Figure 1: (a) A thin wave guiding element with coordinate. (b) Geometry for an asymmetric double negative meta-material planar slab waveguide.

Let us define new variables as follows [1–3]: $\begin{cases} V = \beta H_z \\ l = \beta E_y = -\omega\mu_0 H_x \end{cases}$. Eq. (4) and Eq. (3) can be written as

$$\frac{\partial V}{\partial x} = -\frac{\gamma^2}{j\omega\mu_0} I \tag{6}$$

$$\begin{cases} \dfrac{\partial l}{\partial x} = -j\omega\mu_0 V & (7) \\ \gamma^2 = \beta^2 - \omega^2\mu_0\varepsilon_0 \left\{n(x)\right\}^2 & (8) \end{cases}$$

The characteristics impedance in Eqs. (6) and (7) is given by

$$Z = \frac{\gamma}{j\omega\mu_0} \tag{9}$$

3. DERIVATION OF EIGEN-VALUE EQUATION AND RESULTS OF CALCULATION FOR DNG ASYMMETRIC PLANAR SLAB DIELECTRIC WAVEGUIDE

In this section, we derive the rigorous and exact Eigen value equation for the waveguide structure as shown in Fig. 1(b) having the refractive index variation [5–7],

$$n(x) = \begin{cases} n_c = \sqrt{\mu_1\varepsilon_1}, & x \geq d \rightarrow \text{Cover Region} — 1 \\ n_f = \sqrt{\mu_2\varepsilon_2}, & 0 \leq x \leq d \rightarrow \text{Film Region} — 2 \\ n_s = \sqrt{\mu_3\varepsilon_3}, & x \leq 0 \rightarrow \text{Substrate Region} — 3 \end{cases} \tag{10}$$

where $n_f \rightarrow \sqrt{(-\mu_2)(-\varepsilon_2)} = -\sqrt{\mu_2\varepsilon_2}$ for the double negative meta-material. Equivalent T network representation in this case can be drawn as shown in Fig. 2, where,

$$\left.\begin{array}{ll} Z_S^F = Z^F \tanh\left(\gamma\frac{d}{2}\right) & Z^F = \dfrac{\gamma}{j\omega\mu_2} = \dfrac{\sqrt{\beta^2 - \kappa_0^2 n_f^2}}{j\omega\mu_2} = \dfrac{j\kappa_2}{j\omega\mu_2} \\ Z_P^F = Z^F \dfrac{1}{\sinh(\gamma d)} \quad \& & Z^s = \dfrac{\sqrt{\beta^2 - \kappa_0^2 n_s^2}}{j\omega\mu_1} = \dfrac{\alpha_1}{j\omega\mu_1} \\ Z^S = -Z^s & \\ Z^C = Z^c & Z^c = \dfrac{\sqrt{\beta^2 - \kappa_0^2 n_c^2}}{j\omega\mu_3} = \dfrac{\alpha_3}{j\omega\mu_3} \end{array}\right\} \tag{11}$$

and also $\kappa_2 = \sqrt{\kappa_0^2 n_f^2 - \beta^2}$, $\alpha_1 = \sqrt{\beta^2 - \kappa_0^2 n_s^2}$, $\alpha_3 = \sqrt{\beta^2 - \kappa_0^2 n_c^2}$ with free space wave number $k_0 = \frac{2\pi}{\lambda_0}$. By using Eq. (11) it can also be shown

$$\begin{cases} Z_S^F = \dfrac{j\kappa_2}{\omega\mu_2} \tan\left(\kappa_2 \dfrac{d}{2}\right) & (12) \\ Z_P^F = \dfrac{\kappa_2}{j\omega\mu_2} \dfrac{1}{\sin(\kappa_2 d)}. & (13) \end{cases}$$

Minus sign in the expression of Z^s is due to limit $x = -\infty$. Finally the Eigen value equation can be derived from the following expression when the impedance seen from either side of terminal A-B in Fig. 2 is same

$$\frac{(Z^C + Z_S^F)Z_P^F}{Z^C + Z_S^F + Z_P^F} + Z_S^F = Z^S. \tag{14}$$

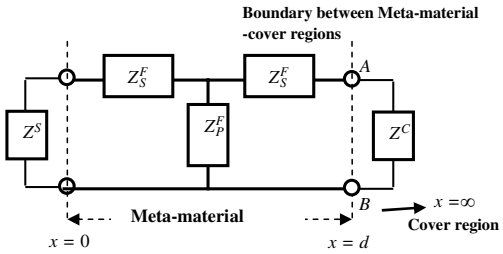

Figure 2: Equivalent T network representation of Meta material asymmetric planar slab waveguide.

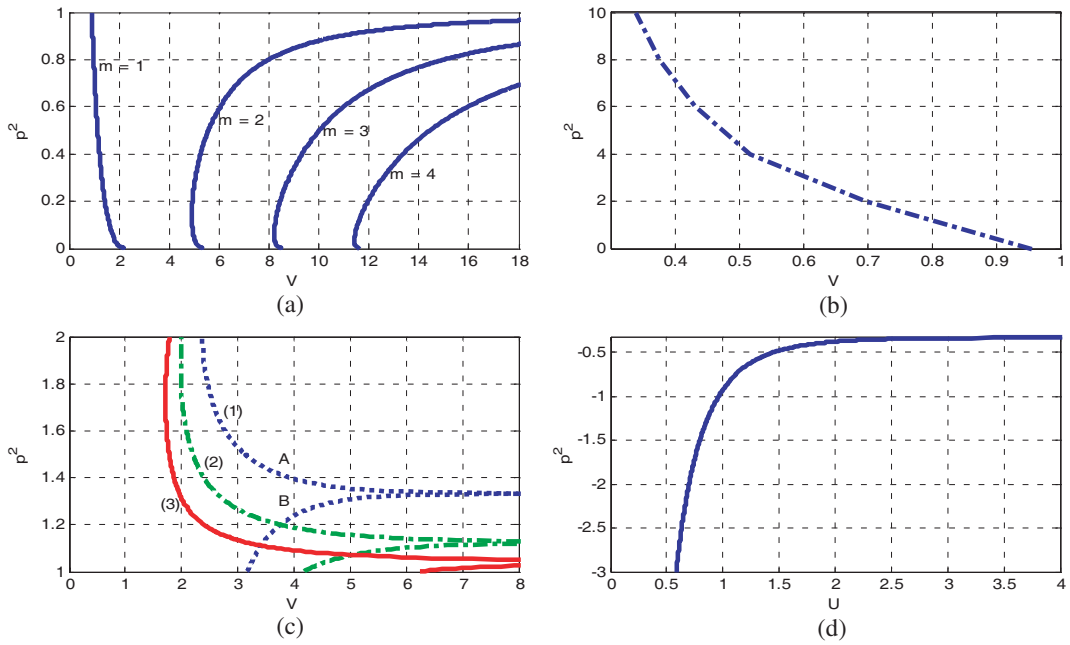

Figure 3: (a) The normalized dispersion curve of TE guided mode with $\varepsilon_1 = 1$, $\mu_1 = 1$, $\varepsilon_2 = -2$, $\mu_2 = -2$, $\varepsilon_3 = 2$, $\mu_3 = 1$, $d = 2\,\text{cm}$. (b) Normalized dispersion curve of the surface wave modes with $\varepsilon_1 = 1$, $\mu_1 = 1$, $\varepsilon_2 = -2$, $\mu_2 = -2$, $\varepsilon_3 = 2$, $\mu_3 = 1$. (c) Normalized dispersion curves of the surface wave modes with $n_c = 1$, $n_f = -2$, $n_s = \sqrt{2}$ where (1) $-\mu_2/\mu_3 = 0.5$, (2) $-\mu_2/\mu_3 = 1/3$, (3) $-\mu_2/\mu_3 = 0.2$. (d) Normalized dispersion relationship of the surface wave modes with $n_c = 1$, $n_f = -\sqrt{2}$, $n_s = 2$, and $-\mu_2/\mu_3 = 2$.

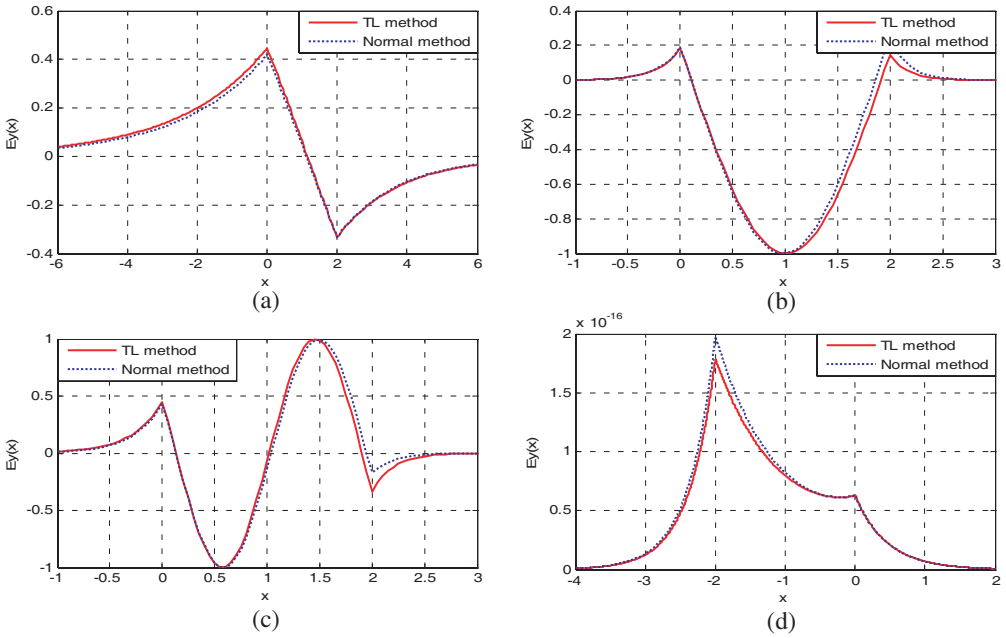

Figure 4: Distribution of amplitudes of electric field components of guided modes, where (a) $V = 1.1363$. (b), (c) $V = 10$. Here m represent the number of intersections between the fields and the x-axis in region 2. (d) The graph represents the distribution of amplitudes of electric field with $n_c = 1$, $n_f = -\sqrt{2}$, $n_s = 2$, and $-\mu_2/\mu_3 = 2$.

Putting the value of Z^C, Z^S, Z_S^F, Z_P^F from Eq. (11) in Eq. (14) and after some algebraic manipulation turns out

$$\kappa_2 d = m\pi + \tan^{-1}\left(\frac{\mu_2\alpha_1}{\mu_1\kappa_2}\right) + \tan^{-1}\left(\frac{\mu_2\alpha_3}{\mu_3\kappa_2}\right) \tag{15}$$

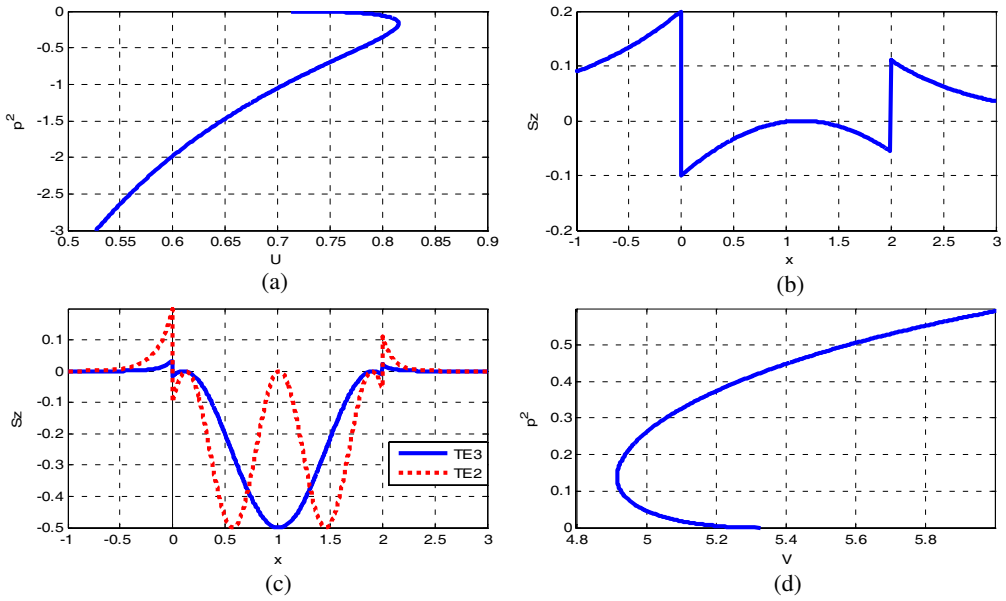

Figure 5: (a) Normalized dispersion relationship of the surface wave modes with $n_1 = 1$, $n_2 = -\sqrt{2}$, $n_3 = 2$, $-\mu_2/\mu_1 = 0.7$ for $-\mu_2/\mu_3 = 0.5$. (b) Distribution of energy flux along the transverse profile of waveguide for a given waveguide parameters, where TE_1: $V = 1.1363$ and (c) the dashed line is TE_2, the real line is TE_3: $V = 10$. (d) Normalized dispersion curve when $m = 2$, $\varepsilon_1 = 1$, $\mu_1 = 1$, $\varepsilon_2 = -2$, $\mu_2 = -2$, $\varepsilon_3 = 2$, $\mu_3 = 1$.

This is an exactly the same Eigen value equation found in literatures [7]. Eq. (15) can be written as

$$V\left(1-p^2\right)^{1/2} = m\pi + \tan^{-1}\left[\frac{\mu_2}{\mu_3}\left(\frac{p^2}{1-p^2}\right)^{1/2}\right] + \tan^{-1}\left[\frac{\mu_2}{\mu_1}\left(\frac{p^2+\Delta}{1-p^2}\right)^{1/2}\right] \tag{16}$$

where $V = k_0 d\sqrt{n_f^2 - n_s^2}$, $p^2 = \frac{N^2-n_s^2}{n_f^2-n_s^2}$, $\Delta = \frac{n_s^2-n_c^2}{n_f^2-n_s^2}$, are the normalization parameters and also $N = \frac{\beta}{k_0}$ where $k_0 = \frac{2\pi}{\lambda}$. Figs. 3, 4 and 5 show the results computed by graphical method followed by back calculation in TL method. In Fig. 5, it is implicit that $S_z = \frac{\beta E_y^2(x)}{2\psi\mu(x)}$. The results are accurate enough when compared with graphical method.

4. CONCLUSION

We have derived and analyzed the electromagnetic properties of DNG asymmetric planar slab waveguide by using TL method. We compare the guidance conditions by using Graphical method. The derivation presented into this paper is useful to the beginners who want to gain inside into TL method. One can easily extended these results to simulate multilayer DNG waveguide structure.

REFERENCES

1. Qian, X. and A. C. Boucouvalas, "Synthesis of symmetric and asymmetric planar optical waveguides," *IET Optoelectron.*, Vol. 1, No. 4, 185–190, 2007.
2. Baccarelli, P., P. Burghignoli, F. Frezza, A. Galli, P. Lampariello, G. Lovat, and S. Simone Paulotto, "Fundamental modal properties of surface waves on meta-material grounded slabs," *IEEE Trans. on Microwave Theory and Tech.*, Vol. 33, No. 4, 1431–1442, 2005.
3. Mahmoud, S. F. and A. J. Viitanen, "Surface wave character on a slab of meta-material with negative permittivity and permeability," *Progress In Electromagnetic Research*, Vol. 51, 127–137, 2005.
4. Raghuwanshi, S. K., "Comparative study of asymmetric versus symmetric planar slab dielectric optical waveguides," *Indian J. of Phys.*, Vol. 84, No. 7, 831–846, 2010.
5. Baccarelli, P., P. Burghignoli, G. Lovat, and S. Paulotto, "Surface-wave suppression in a double-negative metamaterial grounded slab," *IEEE Antennas and Wireless Propagation Letters*, Vol. 2, 260–272, 2003.

6. Raghuwanshi, S. K., V. Kumar, and R. R. Pandey, "Derivation of eigen value equation by using equivalent transmission line method for the case of symmetric/asymmetric planar slab waveguide structure," *Journal of International Academy of Physical Sciences*, Vol. 15, No. 1, 1–14, 2011.
7. Wang, Z. J. and J. F. Dong, "Analysis of guided modes in asymmetric left handed slab waveguides," *Progress In Electromagnetic Research,* Vol. 62, 203–215, 2006.

Reduction of the Staircasing Error in Finite Methods by Using Transformation Media

Mustafa Kuzuoglu[1] and Ozlem Ozgun[2]

[1]Department of Electrical and Electronics Engineering
Middle East Technical University, Ankara, Turkey
[2]Department of Electrical and Electronics Engineering
TED University, Ankara, Turkey

Abstract— This paper presents a design technique for transformation media that aim to reduce staircasing errors occurring in the numerical solution of electromagnetic boundary value problems by finite methods. The main idea is to place transformation media within the computational domain adapted to the Cartesian grid, and to determine the material parameters by mapping the staircase-approximated boundary of the geometry to its original boundary. In this manner, both the staircasing error is reduced, and a uniform and easy-to-generate mesh can be used. This technique also allows the numerical modeling of any arbitrarily-shaped object by using a 'single' mesh and by changing only the constitutive parameters within the transformation media. Several numerical simulations are illustrated in the context of electromagnetic scattering problems.

1. INTRODUCTION

The concept of a 'transformation medium' refers to an artificial medium whose constitutive parameters (i.e., the permittivity, permeability and conductivity) are obtained by means of coordinate transformations. Maxwell's equations preserve their form in the modified coordinate system, but the original material parameters are replaced by anisotropic and spatially-varying constitutive parameters to account for the resulting change in the field behavior after the coordinate transformation. This technique was employed in the literature to design several optical and electromagnetic structures, such as the invisibility cloak, reshapers, miniaturized waveguides, etc. [1–5]. However, most applications of this technique suffer from a lack of physical experiments, and hence, they are indeed living in 'virtual reality'. This is because the material specifications are challenging as a result of the spatially varying material parameters. Our main objective is to utilize specially-designed transformation media (called *software metamaterials*, in order to distinguish them from the metamaterials constructed and used in the physical world), for enhancing the ability of numerical modeling methods in computational electromagnetics.

Although we are interested in several possible designs of software metamaterials in computational electromagnetics, the particular objective of this paper is to achieve reduction of staircasing error in finite methods through the use of anisotropic metamaterials. Most of the numerical techniques (such as finite difference time or frequency methods, finite element method employing rectangular elements) are based on a Cartesian coordinate grid or mesh. However, curved geometries that do not conform to a Cartesian grid can only be modeled by using a staircased approximation of the curved surface. This approximation yields errors due to the inaccurate modeling of the geometry. The proposed approach in this paper constructs transformation media within the computational domain adapted to the Cartesian grid, and obtains the material parameters by mapping the staircase-approximated boundary of the geometry to its original boundary. In other words, an equivalent model that mimics the original problem is created, through the use of transformation media. Hence, this approach reduces the approximation errors without the need for changing simple Cartesian grids. Several numerical results are demonstrated in the context of TM_z electromagnetic scattering problems.

2. DESIGN OF TRANSFORMATION MEDIA

A coordinate transformation technique is presented in order to handle curved geometries by using a Cartesian grid or mesh in finite methods such as the finite element method (FEM) or the finite difference time domain (FDTD) method. The transformation is illustrated in Fig. 1(b), where a circular object with a curved boundary is modeled. The object is placed within a hypothetical metamaterial layer and the region inside the metamaterial layer Ω_{A} is mapped to the region $\tilde{\Omega} =$

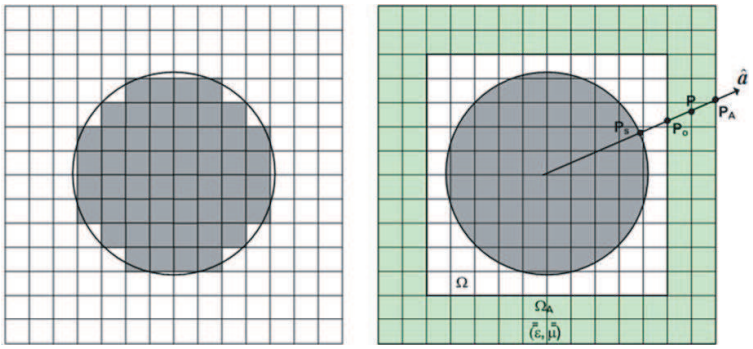

(a) (b)

Figure 1: Coordinate transformation technique for modeling a curved geometry by means of a Cartesian grid: (a) Standard staircased modeling. (b) Modeling with anisotropic metamaterial layer.

$\Omega \cup \Omega_{\mathrm{A}}$ by using the transformation given below:

$$\vec{r} \rightarrow \tilde{\vec{r}} = \mathrm{T}\left(\vec{r}\right) = K\left(\vec{r} - \vec{r}_{\mathrm{o}}\right) + \vec{r}_{\mathrm{s}} \quad \text{where} \quad K = \left\|\vec{r}_{\mathrm{A}} - \vec{r}_{\mathrm{s}}\right\| / \left\|\vec{r}_{\mathrm{A}} - \vec{r}_{\mathrm{o}}\right\| \tag{1}$$

The vectors $\vec{r}$ and $\tilde{\vec{r}}$ are the position vectors of the points P and $\tilde{\mathrm{P}}$ in the original and transformed coordinate systems, respectively. Also, $\vec{r}_{\mathrm{A}}$, $\vec{r}_{\mathrm{o}}$ and $\vec{r}_{\mathrm{s}}$ are the position vectors of the corresponding points. The unit vector $\hat{a}$ is chosen emanating from a point from the innermost domain (such as the center-of-mass point) in the direction of the point P. This transformation achieves a one-to-one correspondence between the boundary of the object and the inner boundary of the metamaterial layer that is conformal to a Cartesian grid. Hence, the curved geometry of the original object can be handled by means of a software metamaterial layer whose boundary is conformal to a Cartesian coordinate system, which implies that a simpler uniform mesh with rectangular elements can be used in the numerical solution.

We note that this technique can be applied to dielectric objects similarly. In this case, $\vec{r}_{\mathrm{s}}$ is set to zero and Ω includes the inner region. When the transformed point falls into the dielectric object, material parameters are computed with respect the dielectric constant of the object. In addition, the boundary conditions that must be imposed on the boundary of the conducting object must be imposed on the inner boundary of the metamaterial region in the equivalent problem. Finally, note that the same mesh can be used for any object of arbitrary shape by simply changing the constitutive parameters of the metamaterial layer computed according to the geometry of the object.

Under the coordinate transformation in (1), the original medium is replaced by an anisotropic medium where the transformed fields satisfy the original forms of Maxwell's equations. In other words, based on the form-invariance property of Maxwell's equations under coordinate transformations, the constitutive tensors of the anisotropic medium are obtained by [6]

$$\bar{\bar{\varepsilon}} = \varepsilon\, \bar{\bar{\Lambda}} \quad \text{and} \quad \bar{\bar{\mu}} = \mu\, \bar{\bar{\Lambda}}, \quad \text{where} \quad \bar{\bar{\Lambda}} = \left(\det \bar{\bar{\mathrm{J}}}\right) \left(\bar{\bar{\mathrm{J}}}^{\mathrm{T}} \cdot \bar{\bar{\mathrm{J}}}\right)^{-1} \tag{2}$$

Here, ε and μ are the permittivity and permeability of the original medium, respectively, and $\bar{\bar{\mathrm{J}}}$ is the Jacobian tensor that is $\bar{\bar{\mathrm{J}}} = \partial\left(\tilde{x}, \tilde{y}, \tilde{z}\right) / \partial\left(x, y, z\right)$ in Cartesian coordinates.

According to the field equivalence principle, the original fields in transformed coordinates, $\vec{E}(\tilde{\vec{r}})$, can be recovered by using the transformed fields in original coordinates, $\tilde{\vec{E}}\left(\vec{r}\right)$, by using the following relation [6]:

$$\vec{E}\left(\vec{r}\right) \rightarrow \tilde{\vec{E}}\left(\vec{r}\right) = \bar{\bar{\mathrm{J}}}^{\mathrm{T}} \cdot \vec{E}\left(\tilde{\vec{r}}\right) \quad \text{and} \quad \vec{H}\left(\vec{r}\right) \rightarrow \tilde{\vec{H}}\left(\vec{r}\right) = \bar{\bar{\mathrm{J}}}^{\mathrm{T}} \cdot \vec{H}\left(\tilde{\vec{r}}\right) \tag{3}$$

This principle of field equivalence is important because it allows us not to lose the near-field information inside the discarded region around the object.

3. NUMERICAL SIMULATIONS

The performance of the proposed technique is tested with simulations performed by our finite element code and finite difference time domain code in the context of TM_z electromagnetic scattering problems.

We first consider the scattering by a circular object whose radius is 1.8λ [$\lambda = 1$ m is wavelength]. In the numerical modeling of this canonical problem via finite methods, the mesh must be fitted to (or refined around) the curved boundary of the object to get accurate results. In Fig. 3(a), the standard finite element solution is shown by using a triangular mesh that is conformal to the boundary. However, if a Cartesian mesh is employed, staircased modeling of the boundary results in errors due to non-conformal mesh. In Fig. 3(b), the solution of the proposed approach is demonstrated which employs a matematerial layer of thickness 1.2λ fitted to the Cartesian grid. The metamaterial layer creates a virtual reality in the sense that Figs. 2(a) and 2(b) must be equivalent and must yield identical field values inside the free-space region (Ω). To confirm our claim, we measure the mean-square percentage difference between the field values of these two simulations as 0.0970%.

Next, we present the results of the simulation performed by the finite difference time domain method for the trapezoidal geometry excited by a sine wave at 3 GHz (see Fig. 3). We plot the field maps of both the equivalent problem employing a metamaterial region and the original problem at different time instants. The original problem is staircased on a "fine" Cartesian grid such that the staircasing error is reduced to a certain value by adjusting the grid size sufficiently small. The mean-square percentage difference between the field values of these two cases is 4.68e-5% (at $n = 800$) and 5.41e-4% (at $n = 1000$).

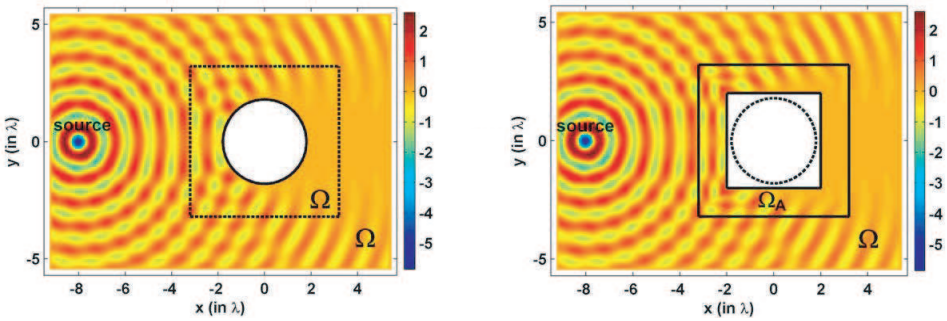

(a) (b)

Figure 2: Finite element simulation of scattering from a circular object: (a) Electric field map in original problem. (b) Electric field map in equivalent problem with metamaterial layer.

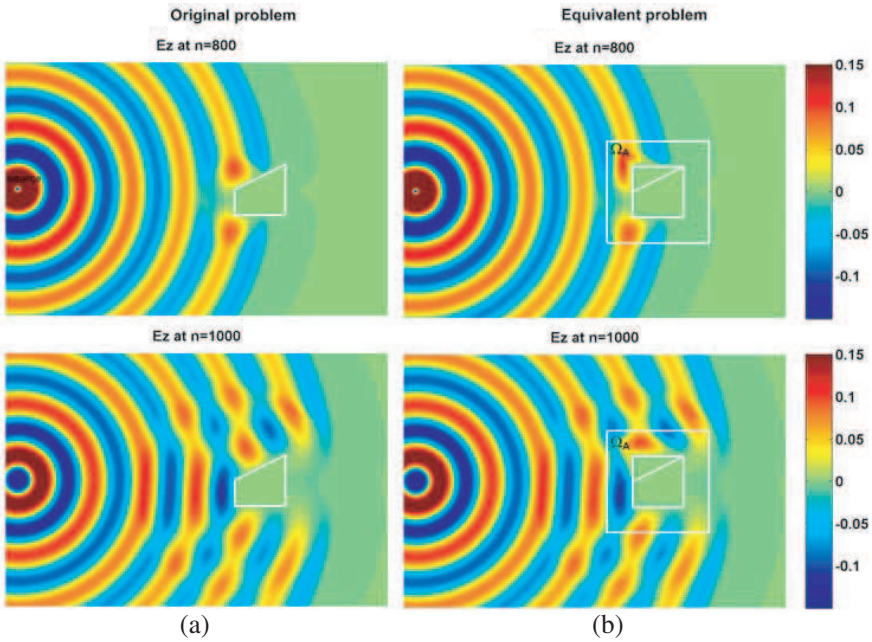

(a) (b)

Figure 3: Finite difference time domain simulation of scattering from a trapezoidal object at different time instants: (a) Solution with fine Cartesian grid. (b) Solution with a matematerial layer.

4. CONCLUSIONS

We have proposed a new coordinate transformation technique for alleviating the staircasing errors in numerical modeling of curved boundaries in finite methods. We have observed good agreements between the analytical formulations and the numerical simulations.

REFERENCES

1. Pendry, J. B., D. Schurig, and D. R. Smith, "Controlling electromagnetic fields," *Science*, Vol. 312, 1780–1782, 2006.
2. Ozgun, O. and M. Kuzuoglu, "Electromagnetic metamorphosis: Reshaping scatterers via conformal anisotropic metamaterial coatings," *Microwave Opt. Technol. Lett.*, Vol. 49, No. 10, 2386–2392, 2007.
3. Ozgun, O. and M. Kuzuoglu, "Utilization of anisotropic metamaterial layers in waveguide miniaturization and transitions," *IEEE Microwave and Wireless Components Letters*, Vol. 17, No. 11, 754–756, 2007.
4. Ozgun, O. and M. Kuzuoglu, "Form-invariance of Maxwell's equations in coordinate transformations: Metamaterials and numerical models," *Metamaterials: Classes, Properties and Applications*, Chapter 3, Nova Science, 2010.
5. Ozgun, O. and M. Kuzuoglu, "Transformation-based metamaterials to eliminate the staircasing error in the finite difference time domain method," *Int. Journal of RF and Microw. Computer-aided Eng.*, Vol. 22, No. 4, 530–540, Jul. 2012.
6. Lindell, I. V., *Methods for Electromagnetic Field Analysis*, Oxford University Press, 1992.

A Thin Wire Method of Moments Scheme Employing King's Green Functions and Sinusoidal Basis Functions

Ö. Zor[1] and B. Polat[2]

[1]Electronics Engineering Department, Uludag University, Bursa, Turkey
[2]Electrical and Electronics Engineering Department, Trakya University, Edirne, Turkey

Abstract— We employ sinusoidal basis functions together with R.W.P. King's analytical Green functions in a Method of Moments formulation of electromagnetic scattering by thin wire mesh structures located over a dielectric ground. The present formulation is an extension of an earlier work by the authors where they have implemented R.W.P. King's Green functions for the first time in literature for the same problem using pulse basis functions. Over a number of numerical tests for canonical structures, it is observed that the results of the present formulation match perfectly with the same solutions provided by the famous open software NEC-2. While the developed codes equally have the ability to read NEC-2 formatted input files, their main advantage lies in the capability to evolve by proper substitutions of Green functions to take into account various terrain features in any scenario.

1. INTRODUCTION

Recently, the present authors have introduced [1] the analytical backbone of a Method of Moments (MoM) code for thin wire mesh geometries located over a dielectric ground with high refractivity, which incorporates the Green functions of R.W.P. King [2] as alternative to a similar role of the extensive numerical/asymptotic libraries of NEC-2 [3]. In the present work these formulations and codes are extended from pulse basis to sinusoidal basis functions by which it is possible to generate the same solutions provided by NEC-2 with perfect accuracy. Since the geometry under consideration and the structure of the electrical field integral equation are essentially the same as in [1], some of the definitions, descriptions, assumptions, field quantities, references, etc. are not repeated in this letter due to size limitation.

2. FORMULATION

We consider regions I ($z > 0$) and II ($z < 0$) free-space and a simple lossy dielectric with constitutive parameters and wave numbers given as (ε_0, μ_0), $k_1 = \omega\sqrt{\mu_0\varepsilon_0}$ and $(\varepsilon_2, \mu_0, \sigma_2)$, $k_2 = \omega\sqrt{\mu_0(\varepsilon_2 + i\sigma_2/\omega)}$, respectively. A time convention $\exp(-i\omega t)$ is assumed and suppressed. The complex refractivity of ground is defined by $N = k_2/k_1 = \sqrt{\varepsilon_r + i\sigma_2/(\omega\varepsilon_0)}$ with $\varepsilon_r = \varepsilon_2/\varepsilon_0$. The high contrast approximation (HCA) $|N|^2 \gg 1$ is already satisfied since in the applications we focus on seawater with $\varepsilon_r \approx 75 - 80$, $\sigma_2 \approx 4 - 5$. For a wire mesh geometry constituting M segments, the sinusoidal current on j-th thin wire segment in MoM formulation is expressed by

$$\vec{I}_j = \hat{z}^j I_j \zeta_j(z^j) = \hat{z}^j I_j \left(A_j + B_j \sin(k_1 z^j) + C_j \cos(k_1 z^j)\right), \quad |z^j| < \ell/2 \tag{1}$$

where the outer and local reference systems and the associated position vectors are depicted in Fig. 1. The procedure followed in determining the coefficients A_j, B_j, C_j according to junction conditions is already provided in [3, pp.10–18] and shall not be repeated here. The unknown coefficients I_j are determined by inverting the linear system of equations $[Z_{mj}][I_j] = [V_m]$, $j, m = 1, \ldots M$. Each element of the impedance matrix constitute direct wave (d), perfect image wave (i) and surface wave (s) components, i.e., $Z_{mj} = Z^d_{mj} + Z^i_{mj} + Z^s_{mj}$, which are calculated from the Green function formulation as follows:

$$Z^d_{mj} = \hat{\ell}_m \cdot \left(\hat{x}^j f^d_{x^j} + \hat{y}^j f^d_{y^j} + \hat{z}^j f^d_{z^j}\right)$$

$$
\begin{aligned}
f^d_{x^j} &= \frac{i\,x^m e^{ikR_1}}{4\pi\omega\varepsilon_0 R_1}\left\{\frac{k_1(z^m-z^{j'})}{(\rho^m)^2}\left(B_j\cos(k_1z^{j'})-C_j\sin(k_1z^{j'})\right)\right.\\
&\quad+\frac{1}{(\rho^m)^2}\left[1-\frac{(z^m-z^{j'})^2(1-ik_1R_1)}{R_1^2}\right]\\
&\quad\left.\times\left(B_j\sin(k_1z^{j'})+C_j\cos(k_1z^{j'})\right)\;+\frac{A_j(1-ik_1R_1)}{R_1^2}\right\}^{\ell/2}_{z^{j'}=-\ell/2}\\
f^d_{y^j} &= \frac{i\,y^m e^{ikR_1}}{4\pi\omega\varepsilon_0 R_1}\left\{\frac{k_1(z^m-z^{j'})}{(\rho^m)^2}\left(B_j\cos(k_1z^{j'})-C_j\sin(k_1z^{j'})\right)\right.\\
&\quad+\frac{1}{(\rho^m)^2}\left[1-\frac{(z^m-z^{j'})^2(1-ik_1R_1)}{R_1^2}\right]\\
&\quad\left.\times\left(B_j\sin(k_1z^{j'})+C_j\cos(k_1z^{j'})\right)+\frac{A_j(1-ik_1R_1)}{R_1^2}\right\}^{\ell/2}_{z^{j'}=-\ell/2}\\
f^d_{z^j} &= \frac{-i}{4\pi\omega\varepsilon_0}\left\{\left[k_1\frac{e^{ikR_1}}{R_1}\;\left(B_j\cos(k_1z^{j'})-C_j\sin(k_1z^{j'})\right)\right.\right.\\
&\quad\left.-\frac{(z^m-z^{j'})(1-ik_1R_1)e^{ikR_1}}{R_1^3}\times\left(B_j\sin(k_1z^{j'})+C_j\cos(k_1z^{j'})\right)\right]^{\ell/2}_{z^{j'}=-\ell/2}\\
&\quad\left.-A_j\left[\frac{(z^m-z^{j'})(1-ik_1R_1)e^{ikR_1}}{R_1^3}\right]^{\ell/2}_{z^{j'}=-\ell/2}-A_jk_1^2\int\limits_{-\ell/2}^{\ell/2}\frac{e^{ikR_1}}{R_1}dz^{j'}\right\}\\
Z^s_{mj} &= i\omega\mu_0\int\limits_{-\ell/2}^{\ell/2}\left[\begin{array}{l}\ell_{mx}t_x^{xs}z_{jx}+\ell_{mx}t_x^{ys}z_{jy}\\+\ell_{mx}t_x^{zs}z_{jz}+\ell_{my}t_y^{xs}z_{jx}\\+\ell_{my}t_y^{ys}z_{jy}+\ell_{my}t_y^{zs}z_{jz}\\+\ell_{mz}t_z^{xs}z_{jx}+\ell_{mz}t_z^{ys}z_{jy}\\+\ell_{mz}t_z^{zs}z_{jz}\end{array}\right]\zeta_j(z^{j'})dz^{j'}
\end{aligned}
$$

Here $\vec{r}_m=(x_m,y_m,z_m)$ denotes the central point and (x_m^I,y_m^I,z_m^I) & $(x_m^{II},y_m^{II},z_m^{II})$, the starting & end points of m-th segment in the presumed direction of current flow. Then its unit tangential vector can be written as $\hat{\ell}_m=\ell_{mx}\hat{x}+\ell_{my}\hat{y}+\ell_{mz}\hat{z}=\left[(x_m^{II}-x_m^I)\hat{x}+(y_m^{II}-y_m^I)\hat{y}+(z_m^{II}-z_m^I)\hat{z}\right]/\ell$, where $\ell=\left[(x_m^{II}-x_m^I)^2+(y_m^{II}-y_m^I)^2+(z_m^{II}-z_m^I)^2\right]^{1/2}$, $\forall m$. We also have $R_1^2(\vec{r}^m,\vec{r}^{j'})\cong(\rho^m)^2+a^2+(z^m-z^{j'})^2$, $(\rho^m)^2=(x^m)^2+(y^m)^2$ and the explicit expressions of the variables t_b^{as}, $a,b=x,y,z$ are already available in [1]. The perfect image wave is the free space radiation field of the image of any segment when the ground $z=0$ is assumed a perfect electrical conductor. Therefore Z^i_{mj} is calculated in a similar manner as Z^d_{mj} with proper change of coordinates and its explicit expression is avoided due to size limitation.

3. NUMERICAL IMPLEMENTATIONS

For a precise comparison of the accuracies of the pulse and sinusoidal basis expansions we consider the same scenarios in [1]. Accordingly, let us consider the crossed wire above planar sea surface ($\varepsilon_r=80$, $\sigma=4\,\mathrm{S/m}$) in Fig. 2 is illuminated by a homogeneous plane wave with incidence angle $\psi=45^\circ$ and unit electrical field amplitude, while $V_m=-\vec{E}^{inc}(\vec{r}_m)\cdot\hat{\ell}_m$. The four arms of the cross are assumed to have the same length 3.33 m while the height of the bottom arm from ground is $h=8\,\mathrm{m}$. In the first set of illustrations in Fig. 3 the operating frequency is taken $f=3\,\mathrm{MHz}$ ($\lambda=100\,\mathrm{m}$) for which each arm length is $\lambda/30$ and $h=2\lambda/25$. In virtue of thin wire approximation the length and the radius of the segments are picked as $\ell=0.5\,\mathrm{m}=\lambda/200\,\mathrm{m}$ and $a=1/40\,\mathrm{m}=\lambda/4000\,\mathrm{m}=\ell/20$. They fall into the range in which the values of the computed fields remain insensitive. Under this parameterisation the total number of segments read 27. We provide the amplitude distributions of currents on the arms of the crossed wire and relative errors calculated by $\%100|(\mathrm{SNEC}^{\texttt{TM}}-CODE)/\mathrm{SNEC}^{\texttt{TM}}|$ with reference to the same results obtained by $\mathrm{SNEC}^{\texttt{TM}}$ [4]. In the second set of illustrations in Fig. 4 we set $f=15\,\mathrm{MHz}$ ($\lambda=20\,\mathrm{m}$) for which the arm length is $\lambda/6$ and $h=2\lambda/5$, while $\ell=0.5\,\mathrm{m}=\lambda/40\,\mathrm{m}$ and $a=1/40\,\mathrm{m}=\lambda/800\,\mathrm{m}=\ell/20$.

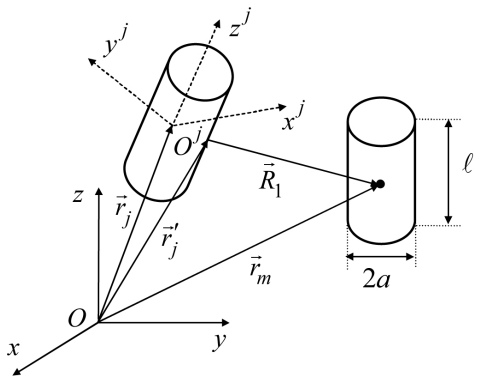

Figure 1: j-th and m-th thin wire segments and position vectors in outer $Oxyz$ and local $O^jx^jy^jz^j$ Cartesian reference systems.

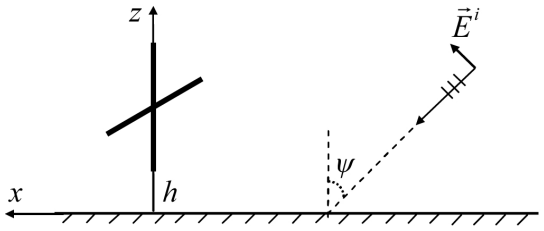

Figure 2: A crossed wire located above planar sea surface and illuminated by a homogeneous plane wave.

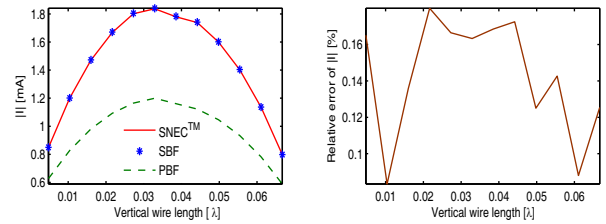

Figure 3: The amplitude distributions of currents on vertical and horizontal arms and relative errors at 3 MHz

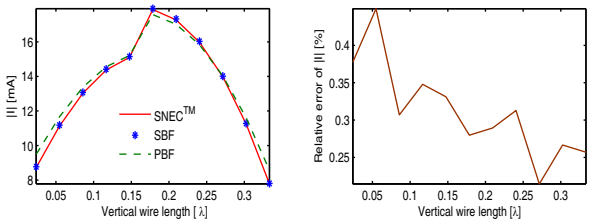

Figure 4: The amplitude distributions of currents on vertical and horizontal arms and relative errors at 15 MHz .

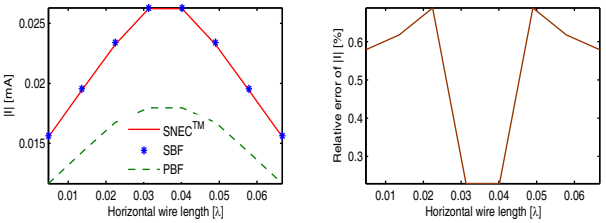

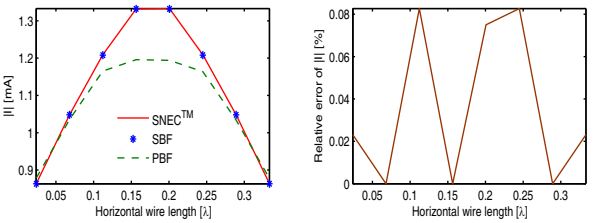

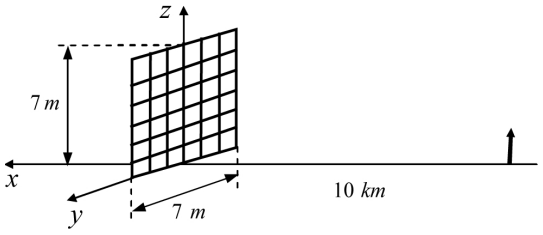

Figure 5: A wire mesh plate illuminated by a monopole residing on planar sea surface.

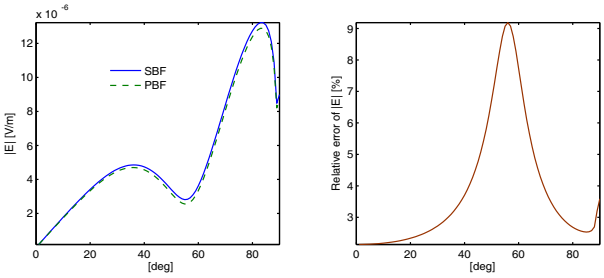

Figure 6: Elevation pattern and relative error for the total scattered field at 30 MHz.

It is observed that the relative error in the calculations using sinusoidal basis functions (SBF) w.r.t. SNEC™ is restricted by 0.6%. We attribute this to indispensable round off errors due to different computational algorithms employed by SNEC™ and MATLAB™. The relative error in phase calculations is observed around 10^{-3}%, which is practically zero.

In the second scenario depicted in Fig. 5 we have a wire mesh plate with side length 7 m and diagonal length $D \cong 10$ m, which is illuminated by a monopole with unit moment at a distance of 10 km.

In Fig. 6, we plot the elevation pattern (Oxz) of the total scattered field at $r = \sqrt{x^2 + z^2} = 10$ km versus $\theta = \tan^{-1}(x/z)$ and the relative error between SBF and PBF (Pulse Basis Function) formulations at 30 MHz ($D \cong \lambda$), which may increase up to 9%.

4. CONCLUSION

Substituing PBF with SBF in MoM investigation provides the advantage of calculating Z^d_{mj}, Z^i_{mj} analytically and the possibility to totally remove the relative error, which is otherwise observed to rise up to 9% in PBF computations. On the other hand there is comparatively more analytical preprocessing in SBF computations in the implementation of the junction conditions. The influence of terrain features can be taken into account by substituting proper range independent Green function available in literature into the MoM scheme (cf. [1] for a wide account). The research is planned to pursue by extending the impedance matrix for dielectric coated mesh structures for stealth applications, which is managed by reformulating the MoM matrix by describing a first order impedance boundary condition on each wire segment. For an analytical demonstration of the validity of the impedance condition on arbitrarily shaped surfaces one may refer to [5].

REFERENCES

1. Zor, Ö. and B. Polat, "An implementation of King's Green functions in thin wire scattering problems," *ACES Journal*, No. 26, 1024–1038, 2011.
2. King, R. W. P., M. Owens, and T. T. Wu, *Lateral electromagnetic Waves: Theory and Applications to Communications, Geophysical Exploration and Remote Sensing*, Springer Verlag, New York, 1992.
3. Burke, G. and A. Poggio, "Numerical electromagnetic code (NEC)-Method of Moments," *Lawrence Livermore Laboratory*, 1981.
4. SuperNec, Poynting Software (Pty) Ltd., South Africa, http://www.supernec.com/.
5. Polat, B., "Approximate boundary conditions on anisotropic sheets," *Progress In Electromagnetics Research B*, Vol. 29, 355–392, 2011.

A Novel Multi-physics and Circuit Co-simulation Algorithm for the Electro-thermal Analysis of Semiconductors and Circuits

J. Q. Chen and X. Chen
College of Electronics and Information Engineering
Sichuan University, Chengdu 610064, China

Abstract— A novel co-simulation algorithm that combines the multi-physics simulation with the circuit simulation for the electro-thermal analysis of circuits with semiconductor devices is proposed. It utilizes a physical model based multi-physics simulation to analyze the semiconductor devices in a circuit, and incorporates the multi-physics simulation into an equivalent-model based circuit simulation to simulate the circuit. As a sample, the proposed algorithm is employed for analyzing the electronic and thermal characteristics of a limiter circuit consisting of commercial PIN diodes with model number mot_bal99lt1. The feasibility and accuracy of the proposed algorithm are certified through comparison with measurements. Besides high-fidelity solutions, the proposed algorithm provides physical mechanisms for better understanding of the behavior of the PIN diode.

1. INTRODUCTION

It is well known that the commonly used method to analysis semiconductor devices and circuits is the circuit simulation, where the complicated and nonlinear characteristics of the semiconductor devices are normally represented by equivalent circuit models [1]. However, equivalent circuit models are not always valid, and may lose their accuracy in some special cases such as high-power, high frequency or ambient temperature variation applications. Moreover, most of those equivalent circuit models are without a direct physical interpretation [1], and thus cannot be easily used to predict the physical effects of the semiconductor devices and circuits.

Another method is the physically-based multi-physics simulation [2]. It does an analysis by building physical models for semiconductor devices, then coupling multiple physical equations (e.g., the electromagnetic, semiconductor transport and thermodynamics equations) to form an equation system and solve the equation system in a numerical approach. Based on physical models rather than equivalent models, it is naturally able to accurately simulate semiconductor devices and circuits under various conditions and is convenient for predicting the physical effects. However, due to solve a set of strongly-coupled nonlinear differential equations, it is computationally expensive [3]. Hence, until now it can only be used to simulate a semiconductor device or a simple circuit consisting of a semiconductor device and a few other elements.

This paper presents a novel multi-physics and circuit co-simulation algorithm. It utilizes a multi-physics simulation method to simulate semiconductor devices in circuits, and then incorporates the multi-physics simulation into an equivalent-model based circuit simulation so that the simulation can be extended to circuits. In this work, the proposed co-simulation algorithm is applied to simulate a limiter circuit consisting of commercial PIN diodes with model number mot_bal99lt1, and a serial of experiments are conducted to validate the proposed algorithm.

2. THE PRINCIPLE OF THE CO-SIMULATION ALGORITHM

2.1. The Multi-physics Simulation for Semiconductor Devices

In principle, the electro-thermal behavior of semiconductors can be described by a multi-physics equation system[4], which includes: the Poisson's Equation (1), the continuity equations for electrons (2) and holes (3), the current relations for electrons (4) and holes (5), the heat flow Equation (7), as well as the equations estimate the relation between the temperature and physical parameters such as the permittivity (8), the intrinsic carrier concentration (9), and the effective mobility of electrons and holes (10). In the equation system, the Poisson's Equation (1) is the simplifications of the Maxwell equations after adopting "lumped" assumption, and the continuity and current Equations (2)–(5) are derive from the Boltzmann transport theory by employing the

drift-diffusion approximation.

$$\nabla^2\varphi = -\frac{q}{\varepsilon}(p-n+N_t), \tag{1}$$

$$\frac{\partial n}{\partial t} = \frac{1}{q}\nabla\cdot\vec{J}_n - R, \tag{2}$$

$$\frac{\partial p}{\partial t} = -\frac{1}{q}\nabla\cdot\vec{J}_p - R, \tag{3}$$

$$\vec{J}_n = \mu_n k_b(T\nabla n + n\nabla T) + q\mu_n n\nabla\varphi, \tag{4}$$

$$\vec{J}_p = -\mu_p k_b(T\nabla p + p\nabla T) + q\mu_p p\nabla\varphi, \tag{5}$$

$$I = (\vec{J}_c + \vec{J}_d)\cdot\vec{A} = (\vec{J}_n + \vec{J}_p + \varepsilon\frac{\partial\vec{E}}{\partial t})\cdot\vec{A} \tag{6}$$

$$\rho c\frac{\partial T}{\partial t} = \nabla\cdot[\kappa(T)\nabla T] + \left(\vec{J}_n + \vec{J}_p + \varepsilon\frac{\partial\vec{E}}{\partial t}\right)\cdot\vec{E}, \tag{7}$$

$$n_i(T) = N_s\exp(-E_g/(2k_bT)), \tag{8}$$

$$\varepsilon(T) = \varepsilon\left[1 + B_\varepsilon\left(T-300\right)\right], \tag{9}$$

$$\mu_T^{n,p} = \mu_0^{n,p}\times\frac{T/T_0}{(1+(E/E_c)^\beta)^{1/\beta}}, \tag{10}$$

where, ε is the permittivity, φ is the electrostatic potential, N_t is doping concentration, n, p are electron and hole density, q is the elementary charge, t is time, $\vec{J}_n$, $\vec{J}_p$ are the electron and hole current density, R is the electro-hole recombination rates, D_n, D_p are the corresponding diffusion coefficients, μ_n, μ_p are the electron and hole mobility, k_b is the Boltzmann constant, $\vec{J}_c$, $\vec{J}_d$ are the conduction and displacement current density, I is the branch current, $\vec{A}$ is the cross-sectional area, $\kappa(T)$ is temperature-dependent thermal conductivity, ρ is the specific mass density, c is the specific heat capacity, T is the temperature, B_ε is Blakemore constant, N_s is the number per unit volume of effectively available states, E_g is the energy gap, μ_0 is the value of mobility at 300 K, E_c is the saturation velocity, and β is the coefficients.

For the set of Equations (1)–(6), as T is a known value, it can be simplified to the solution of an increment equation [5]:

$$\mathbf{A}\Delta\mathbf{y}_{(k-1)} + \mathbf{B}\Delta\mathbf{y}_{(k)} + \mathbf{C}\Delta\mathbf{y}_{(k+1)} = \mathbf{H}_{(k)}, \tag{11}$$

where $y = [\ \varphi \quad n \quad p\ ]^T$, $\Delta y = [\ \Delta\varphi \quad \Delta n \quad \Delta p\ ]^T$, $\mathbf{A}$, $\mathbf{B}$, and $\mathbf{C}$ are 3×3 matrixes, $\mathbf{H}$ is a 3×1 matrix. Similarly, as n, p, and φ are known values, after discretization described in [6], the increment equation of the thermal Equation (7) can be described as:

$$a\Delta y_{(k-1)} + b\Delta y_{(k)} + c\Delta y_{(k+1)}) = h, \tag{12}$$

where $y = [T]$, $\Delta y = [\Delta T]$, a, b, c, and h are the coefficient. Based on the boundary condition, the increment Equations (11), (12) are able to be solved, respectively.

An iterative method as the follows can be used to solve the multi-physical equation system.

1) Initializing the parameters such as the terminal voltages U_j and the ambient temperature T_0.
2) Solving the increment Equation (11) to get the electrical characteristics of the semiconductor.
3) Using the new n, p, and φ to solve the increment Equation (12) to get the thermal characteristics of the semiconductor, and then obtaining the variation of the temperature ΔT_0.
4) Updating the characteristic parameters of semiconductors by employing the above obtained parameters n, p, φ, and T_0, and in this way the electro-thermal effects on semiconductors are considered simultaneously and correlated to each other in the simulation.
5) Repeating the steps 2–4 by using the updated temperature $T_0 + \Delta T_0$ until the convergence criterion, which may be defined as the temperature variation ΔT_0 is less than a preset smaller value, is satisfied.
6) The final results (n, p, φ and T_0) are used to obtain the branch current I_j in the device from (6).

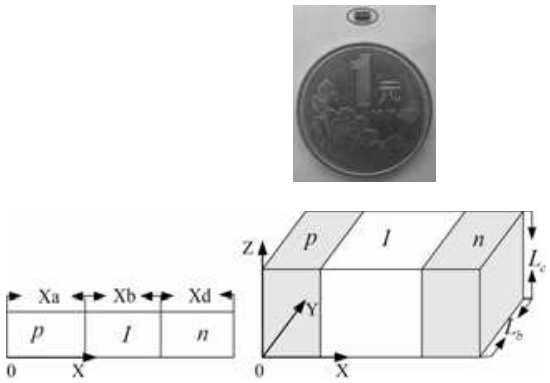

Figure 1: The PIN diode and its physical model.

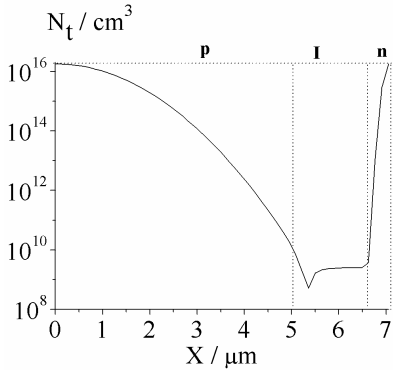

Figure 2: The doping profile of the PIN diode.

2.2. The Multi-physics and Circuit Co-simulation Algorithm

For an element in the circuit, its branch currents are related to the terminal voltages. Assuming a device is located in the jth branch and between the $(k-1)$th and the kth node, it can be described as

$$I_j = \psi(U_k, U_{k-1}). \tag{13}$$

To simplify the simulation and reduce the computation burden, only the crucial and sensitive semiconductors in the circuit are simulated by the above introduced multi-physics simulation. As for other devices, the Equation (13) is derived from their equivalent circuit models.

Based on the method described in the author's previous work [7], for a circuit, its simulation can be simplified to the solution of the iterative equations

$$\mathbf{U}^{n+1} = \mathbf{U}^n - \begin{bmatrix} \frac{\partial f_1^n}{\partial U_1^n} & \cdots & \frac{\partial f_1^n}{\partial I_j^n}\Delta_1 + \frac{\partial f_1^n}{\partial U_{k-1}^n} & \frac{\partial f_1^n}{\partial I_j^n}\Delta_2 + \frac{\partial f_1^n}{\partial U_k^n} \\ \frac{\partial f_2^n}{\partial U_1^n} & \cdots & \frac{\partial f_2^n}{\partial I_j^n}\Delta_1 + \frac{\partial f_2^n}{\partial U_{k-1}^n} & \frac{\partial f_2^n}{\partial I_j^n}\Delta_2 + \frac{\partial f_2^n}{\partial U_k^n} \\ \vdots & \ddots & \vdots & \vdots \\ \frac{\partial f_k^n}{\partial U_1^n} & \cdots & \frac{\partial f_k^n}{\partial I_j^n}\Delta_1 + \frac{\partial f_k^n}{\partial U_{k-1}^n} & \frac{\partial f_k^n}{\partial I_j^n}\Delta_2 + \frac{\partial f_k^n}{\partial U_k^n} \end{bmatrix}^{-1} \mathbf{f}(\mathbf{U}^n), \tag{14}$$

in which $\Delta_1 = \frac{\psi(U_{k-1}^{n\Delta}, U_k^n) - \psi(U_{k-1}^n, U_k^n)}{U_{k-1}^{n\Delta} - U_{k-1}^n}$, $\Delta_2 = \frac{\psi(U_{k-1}^n, U_k^{n\Delta}) - \psi(U_{k-1}^n, U_k^n)}{U_k^{n\Delta} - U_k^n}$, $U_{k-1}^{n\Delta} = U_{k-1}^n + \Delta$, and $U_k^{n\Delta} = U_k^n + \Delta$, where, U_{k-1}^{Δ} and U_k^{Δ} are two trial solutions to approximately calculate the partial derivatives of $I_j\Delta$ is a small constant selected based on experience (such as 1.0×10^{-6}) for a convergent solution. And the iterative procedure is the same as that described in the author's previous work [7].

In the iterative Equation (14), the terms $\psi(U_{k-1}^n, U_k^n)$, $\psi(U_{k-1}^{n\Delta}, U_k^n)$ and $\psi(U_{k-1}^n, U_k^{n\Delta})$ are obtained by multi-physics simulation while the others are derived from the equivalent circuit simulation, In this way, the multi-physics simulation and the circuit simulation are integrated into a unified algorithm.

3. APPLICATIONS OF THE PROPOSED ALGORITHM

A commercial PIN diode with model number mot_bal99lt1 and its physical model are depicted in Figure 1. It is a common practice to extract physical parameters of an electronic device from measured data by using a curve fitting approach [8]. The PIN diode's physical parameters are extracted from a measured DC volt-ampere characteristic curve and as follows: the life time $\tau_p = 5.0 \times 10^{-7}$ s, $\tau_n = 5.0 \times 10^{-7}$ s for p-type and n-type carriers, the thickness of p-layer $X_a = 5.0\,\mu$m, I-layer $X_b = 1.55\,\mu$m, n-layer $X_d = 0.5\,\mu$m, the cross-sectional area $A = 0.7\,\text{cm}^2$, and the doping profile is shown in Figure 2.

As shown in Figure 3, a limiter circuit consisting of two PIN diodes, an AC source with voltage $U_s = 2.5\,$V, two resistors ($R_S = 1\,\text{k}\Omega$ and $R_L = 1\,\text{k}\Omega$), and a capacitor $C_L = 22\,$pF, will be simulated by the proposed co-simulation algorithm as a sample. The simulated results are to be compared with that from measurement using a Tektronix TDS1012 oscillograph. Figure 4 compares the measured and simulated voltage waveform of the limiter's output voltage U_o at 20 MHz and at the ambient temperature $T = 27°$C. From the comparison one observes that the two sets of data

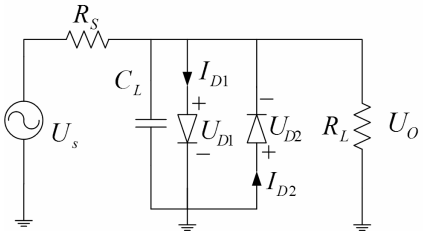

Figure 3: A limiter circuit composed of two PIN diodes.

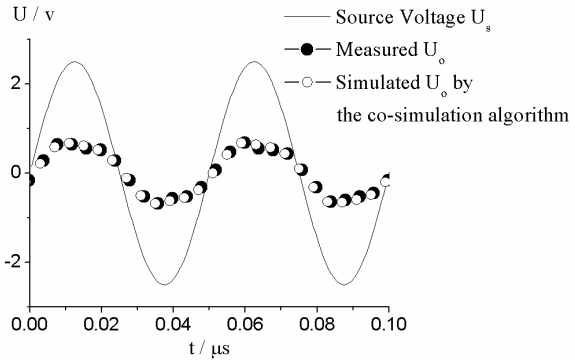

Figure 4: The measured and simulated waveform of U_o at 20 MHz.

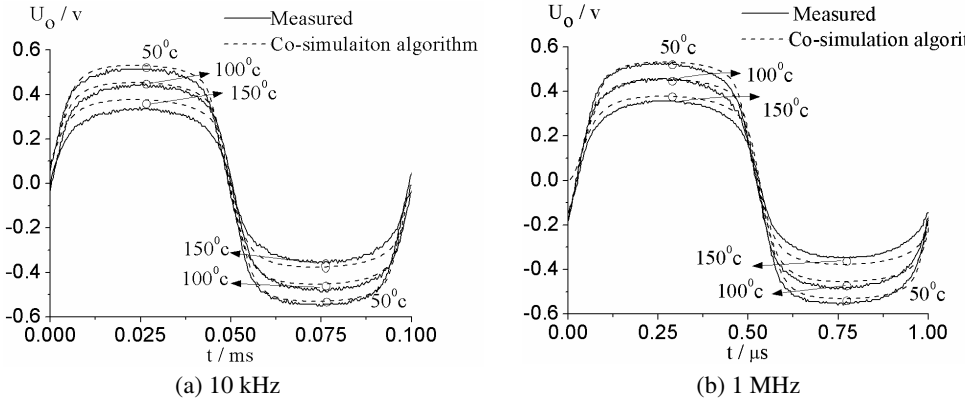

Figure 5: The measured and simulated PIN diode voltage waveforms at different ambient temperature.

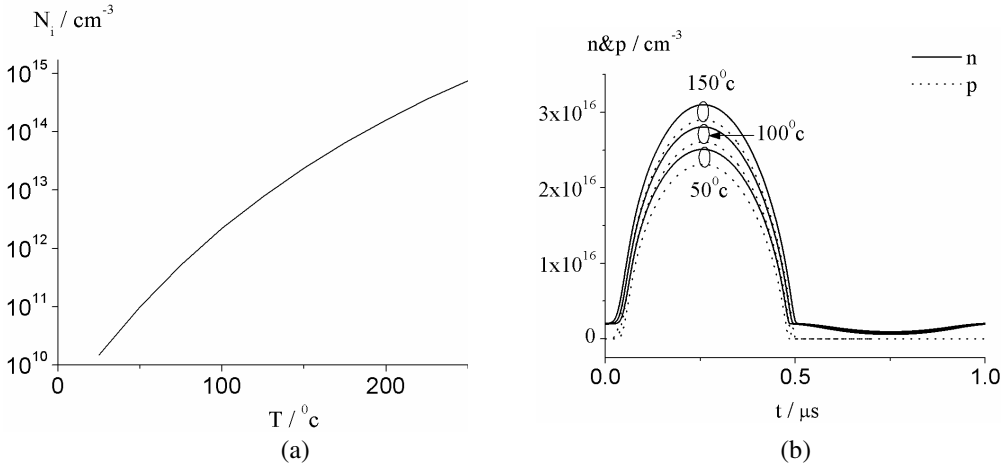

Figure 6: (a) The simulated intrinsic carrier concentration and (b) carrier density of the PIN diode at 1 MHz and at different ambient temperatures, (b) that inside the center I-layer.

are in good agreement, and the output voltage U_o is about 0.65 V when the exciting voltage U_s is 2.5 V, which clearly illustrates the limiting effect of the limiter.

The temperature effect on the PIN diode limiter is simulated, and the results are compared with that measured by a Tektronix TDS1012 oscillograph and a ZTE-202-00AB thermostatic system. As depicted in Figure 5, the simulated and measured results are also in good agreement and the clipping threshold level of the limiter slightly decreases with the increase of the ambient temperature.

The above temperature effect can be clearly and intuitively analyzed by the proposed co-simulation algorithm. As illustrated in Figure 6(a), the simulation of the proposed algorithm estimate that the PIN diode's intrinsic carrier concentration, which is the number of electrons in the conduction band and the number of holes in the valence band per unit volume, increase

with the ambient temperature T. For a PIN diode in the forward voltage period, the increase of the intrinsic carrier concentration leads to the rise in the carrier concentration, which is clearly demonstrated in Figure 6(b). A higher carrier concentration means the PIN diode has a better electrical conductivity and can be in turn-on state even under a smaller positive terminal voltage, which results in the slightly decrease of the diode's clipping threshold. For the limiter, two PIN diodes connect in parallel, always there is one diode being in turn-on state, and thus the slightly decrease of the diode's clipping threshold makes the limiter's clipping threshold to be decreased with the increase of the ambient temperature. It is worth noting that this example demonstrates the proposed multi-physics and circuit co-simulation algorithm is able to provide useful physical pictures of semiconductor devices.

4. CONCLUSIONS

A novel multi-physics co-simulation algorithm is proposed in this paper. This algorithm adopts the multi-physics simulation to analyze the semiconductor devices in a circuit, and incorporates the multi-physics simulation into the circuit simulation to simulate the circuit. The proposed method is employed to simulate a limiter containing commercial semiconductors with model number mot_bal99lt1, and the circuit simulation is validated by comparing its simulation results with the measurement data. Its simulation results agree well with the measurement data. Moreover, the proposed algorithm is capable of depicting useful physical pictures for the analysis of semiconductor devices and circuits. These merits make the proposed algorithm to be a powerful and effective tool for the semiconductor devices and circuits simulation.

REFERENCES

1. Mantooth, H. A. and J. L. Duliere, "A unified diode model for circuit simulation," *IEEE Transactions on Power Electronics*, Vol. 12, No. 5, Sep. 1997.
2. Pokorny, M. and Z. Raida, "Multi-physics model of Gunn diode," *17th International Conference on Microwaves, Radar and Wireless Communications, MIKON 2008*, 4, May 19–21, 2008.
3. Beaussart, S., O. Perrin, M. R. Friscourt, and C. Dalle, "Millimeter-wave pulsed oscillator global modeling by means of electromagnetic, thermal, electrical, and carrier transport physical coupled models," *IEEE Trans. Microwave Theory Tech.*, Vol. 47, 929–934, Jun. 1999.
4. Sze, S. M., *Physics of Semiconductor Devices*, Wiley & Sons, New York, 1981.
5. Kurata, M., "Design considerations of step recovery diodes with the aid of numerical large-signal analysis," *IEEE Trans. Electron Devices*, Vol. 19, No. 11, 1207–1215, 1972.
6. Skibinski, G. and W. Sethares, "Thermal parameter estimation using recursive identification," *IEEE Transactions on Power Electronics*, Vol. 6, No. 2, 228–239, Apr. 1991.
7. Sui, W., *Time-domain Computer Analysis of Nonlinear Hybrid System*, CRC Press, Boca Raton, FL, 2002.
8. Chen, X., J. Q. Chen, K. Huang, and X. B. Xu, "A circuit simulation method based on physical approach for the analysis of Mot_bal99lt1 P-I-N diode circuits," *IEEE Trans. Electron Devices*, Vol. 58, No. 6, Sep. 2011.

Propagation Study of Y-branch Having Inbuilt Optical Splitters and Combiner Using Beam Propagation Method

S. K. Raghuwanshi, S. Kumar, V. Kumar, and D. Chack
Department of Electronics Engineering, Indian School of Mines
Dhanbad, Jharkhand 826004, India

Abstract— The Beam propagation method (BPM) is one of the most power techniques to investigate axially varying waveguides. The single mode optical Y-junction consisting of single mode channel waveguide is a fundamental component for dividing/combining guided light. Beam splitter/combiner sections are a basic element of many optical fiber communication systems often providing a Y-junction by which signals from separate sources can be combined or the received power divided between two channels. Beam propagation methods are used to obtain guided wave characteristics include power loss due to different branching angle. The input field is applied to the branching waveguide and combined after propagating through some distance. The output field is compared with respect to input field for the case of various branching angles. It is expected to high power loss due to wide branching angle. Beam propagation method has been used to estimate the power loss.

1. INTRODUCTION

Optical waveguides are the key elements of photonic devices that perform guiding, coupling, switching, splitting, multiplexing and demultiplexing of optical signals. Passive waveguides, electro-optic components, transmitters, receivers, and driving electronics can be integrated into one chip using planar technology, similar to microelectronics. The explosive growth of optical communication networks, Beam splitters are a basic element of many optical fiber communication systems. We present here theoretical results on channel waveguide switch in the form of Y-junction. The device is consists of a single-mode channel waveguide Y-junction [1–3]. Much theoretical work has been done upon the junction problems. Here, we consider the Y-branch having inbuilt optical beam splitters and combiner as shown in Figure 1. The optical beam splitters and combiner are formed of planar optical waveguides of width w (μm). The junction half-angle is varies ($\theta_2 > \theta_1$). It is divided mainly in two sections first section is splitter, which divides the input power in two parts. Splitter section starts with tapered section. Second section is combiner, which combine the power. Again combiner section ends with tapered section. Splitter and combiner section joined together with a linear waveguide as shown in Figure 1.

In this paper, we describe the Beam Propagation method (BPM) applied to the study of wave propagation in splitter/combiner. We begin by deriving a paraxial form of the Helmholtz equation, known as the Fresnel equation. This equation, valid for paraxial propagation in slowly varying optical structures, is the starting point to develop BPM algorithms [4].

2. BEAM PROPAGATION METHOD: FRESNEL EQUATION

One of the fundamental aspects in integrated optics is the analysis and simulation of electromagnetic wave propagation in photonics devices based on waveguide geometries, including optical waveguides.

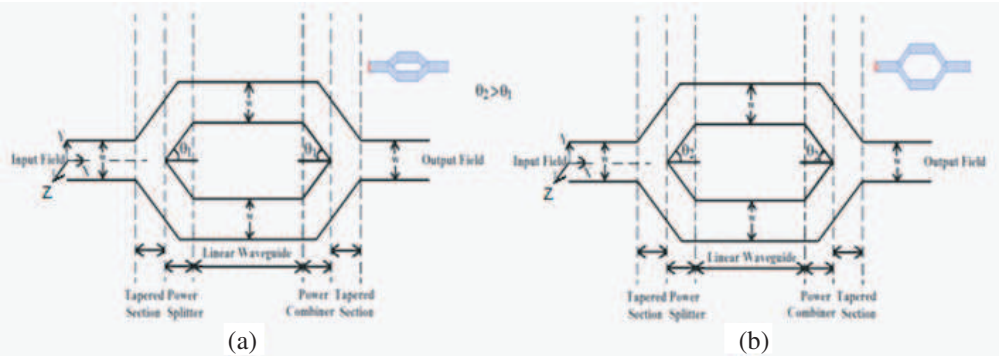

Figure 1: (a), (b) Layout design of Y-branch inbuilt optical beam splitters and combiner.

The problem to be solved is the following: given an arbitrary distribution of refractive index $n(x, y, z)$, and for a given wave field distribution at the input plane at $z = 0$, $E(x, y, z = 0)$, the spatial distribution of light $E(x, y, z)$ at a generic point z must to be found. Figure 1 outlines the problem to a beam splitter/combiner. In this case, the distribution of the refractive index is known, which defines the optical circuit. When a light beam is injected at $z = 0$, the problem is to determine the light intensity distribution at the exit, and in particular, what will be the output light intensity in each of the two branches of the splitter. The problem of light propagation in waveguides with arbitrary geometry is very complicated in general, and it is necessary to make some approximations. In the first place, we will assume a harmonic dependence of the electric and magnetic fields, in the form of monochromatic waves with an angular frequency ω, in such a way that the temporal dependence will be of the form $e^{j\omega t}$. The equation which describes such EM waves is the vectorial Helmholtz equation [5];

$$\nabla^2\mathbf{E}+\left(\frac{\omega}{c}\right)^2 n^2\left(x,y,z\right)\mathbf{E}=0 \tag{1}$$

where $\mathbf{E} = E(x, y, z)$ denotes each of the six cartesian components of the electric and magnetic fields. The refractive index in the domain of interest is given by $n(x, y, z)$, and will be determined by the waveguide geometry having optical fiber, optical beam splitters and combiner, etc.. If the wave propagation is primarily along the positive z-direction, and the refractive index changes slowly along this direction, the field $E(x, y, z)$ can be presented as complex field amplitude $u(x, y, z)$ of slow variation, multiplied by a fast oscillating wave moving in the $+z$ direction (propagation direction):

$$E\left(x,y,z\right)=u\left(x,y,z\right)e^{jKz} \tag{2}$$

where K is a constant which represents the characteristics propagation wave vector, $K = n_0\omega/c$, and n_0 is chosen, for example, as the refractive index of the substrate (or the cover). Substituting the optical field in Helmholtz equation, it follows that;

$$-\frac{\partial^2 u}{\partial z^2}+2jK\frac{\partial u}{\partial z}=\left(\frac{\partial^2}{\partial x^2}+\frac{\partial^2}{\partial y^2}\right)u+\left(k^2-K^2\right)u \tag{3}$$

where $k_0 = \omega/c = 2\pi/\lambda$ denotes the wave vector in the vacuum, and the notation $k(x, y, z) = k_0 n(x, y, z)$ has been introduced to represent the spatial dependence of the wave vector. If we also assume that the optical variation is slow in the propagation direction ("slowly varying envelope approximation, SVEA"), we will have:

$$\left|\frac{\partial^2 u}{\partial z^2}\right|\ll\left|2K\frac{\partial u}{\partial z}\right| \tag{4}$$

In this case, we can ignore the first term on the left-hand side of Eq. (3) with respect to the second one; this approximation is known as parabolic or Fresnel approximation and Eq. (3) leads to;

$$2jK\frac{\partial u}{\partial z}=\left(\frac{\partial^2}{\partial x^2}+\frac{\partial^2}{\partial y^2}\right)u+\left(k^2-K^2\right)u \tag{5}$$

which is known as paraxial equation. It is the starting equation for the description of optical propagation in homogeneous media, and in particular, in waveguide structures. An example is TE propagation in 1D waveguides, where the Fresnel equation reduces to;

$$2jk_0n_0\frac{\partial E_y}{\partial z}=\frac{\partial^2 E_y}{\partial x^2}+k_0^2\left[n^2\left(x,z\right)-n_0^2\right]E_y \tag{6}$$

where E_y is the only non-vanishing components of the electric field associated to TE modes of the 1D waveguide, and where the refractive index is represented by $n(x, z)$. The solution to the Helmholtz equation or the Fresnel equation applied to optical propagation in waveguides is known as the Beam Propagation method (BPM). Two numerical schemes have been proposed in literature to solve the Fresnel equation. In one of them, optical propagation is modeled as a plane wave spectrum in the spatial frequency domain, and the effect of the medium inhomogeneity is interpreted as a correction of the phase in the spatial domain at each propagation step. The use of the

fast Fourier techniques connects the spatial and spectral domains, and this method is therefore called Fast Fourier transform BPM (FFT-BPM). The propagation of EM waves in inhomogeneous media can also be described directly in the spatial domain by a finite difference scheme (FD). This technique allows the simulation of strong guiding structures, and also of structures that vary in the propagation direction. The Beam propagation method which solves the paraxial form of the scalar wave equation in an inhomogeneous medium using the finite difference method is called FD-BPM [6–8].

3. RESULTS AND DISCUSSIONS

In this section, we use the Beam propagation method based on the above formulation in Section 2 to simulate the pulse propagation through Y-branch as shown in Fig. 1. Here core refractive index (n_1= 1.5), cladding refractive index ($n_2 = 1.48$), width of the waveguide ($w = 4\,\mu$m), and operating wavelength of light ($\lambda = 1.55\,\mu$m) are simulation parameters taken for two different angles of Y-junction waveguide. We too calculate the power loss at splitter, combiner and overall power loss in the transmission. Figures 2(a), 2(b), 2(c), and 2(d) show the 2D-plot of optical profile, optical field power versus Y-axis at fix point $X = 800\,\mu$m, optical field power versus X-axis at fix point $Y = 0\,\mu$m and 3-D plot of optical field propagation respectively for layout shown in Figures 1(a) (for the case of $\theta_1 = 2°$). Similarly Figures 2(e), 2(f), 2(g) and 2(h) repeat all the calculations as shown in Figures 2(a)–2(d) for the layout shown in Figure 1(b) (for the case of $\theta_2 = 4°$). It is apparent from the Figure 2 that power loss is substantial at wide angle of Y-branch. Further we have studied the effect of width on field profile as shown in Figure 3. It shows the 2 D-plot of optical field profile and output field power versus Y-axis at fix point $X = 800\,\mu$m for the case of $w = 2.5\,\mu$m and $w = 5\,\mu$m respectively. It reveals that as the width (w) of waveguide increases the power loss increases substantially due to higher order mode conversion effect. Hence by decreasing the width of waveguide, we can compensate the loss due to wide angle of Y-branch. Figure 4 shows the plot of loss versus angle of Y-junction. As angle of Y-junction or splitter increases then loss at the end of waveguide varies. At lower angle losses are minimum but at higher angle (say between 3° to 4°), there is abrupt increase in loss.

Loss at Y-branch having inbuilt optical splitters is more than the Y-branch having inbuilt optical combiner as shown in Figure 4. It is apparent that sign is opposite for splitter power loss versus combiner power loss. It is also apparent that as the angle increases the splitter loss increase up to maximum of $\approx +1.8\,$dB, then it saturates and shows no significant changes with increasing the

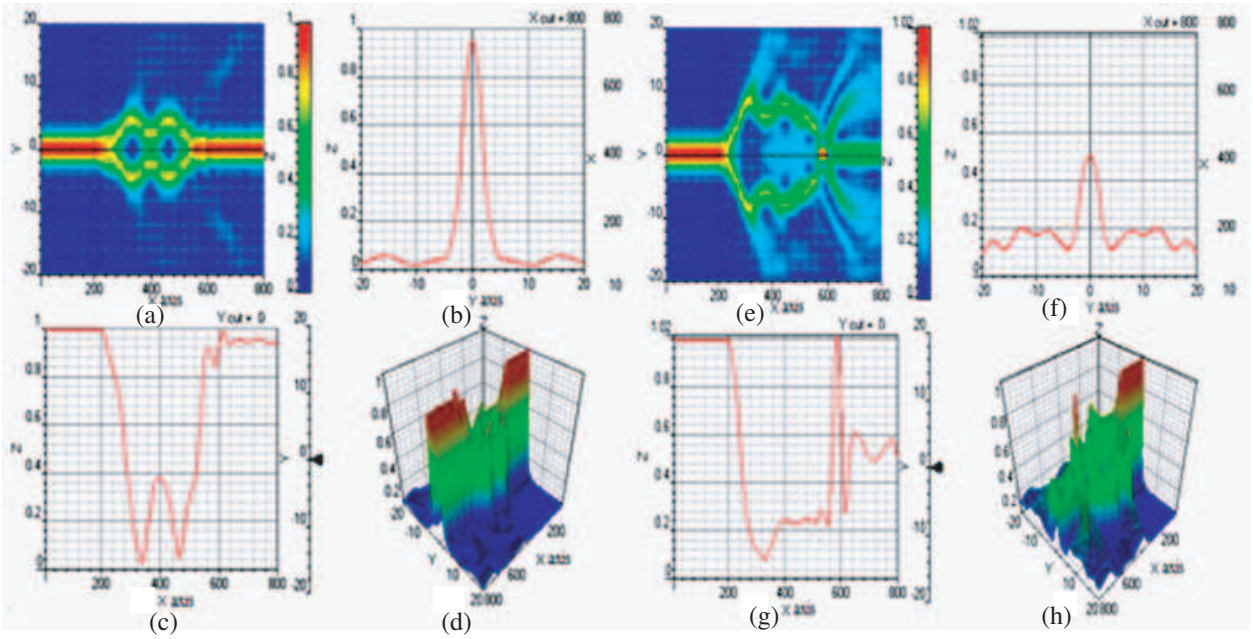

Figure 2: 2-D Plot of optical field propagation, output field profile at fix $X = 800\,\mu$m, output field profile at fix $Y = 0\,\mu$m. and 3-D plot of optical field propagation for the case of (a)–(d) $\theta_1 = 2°$ as shown in Figure 1(a) and for the case of (e)–(h) $\theta_2 = 4°$ as shown in Figure 1(b) respectively.

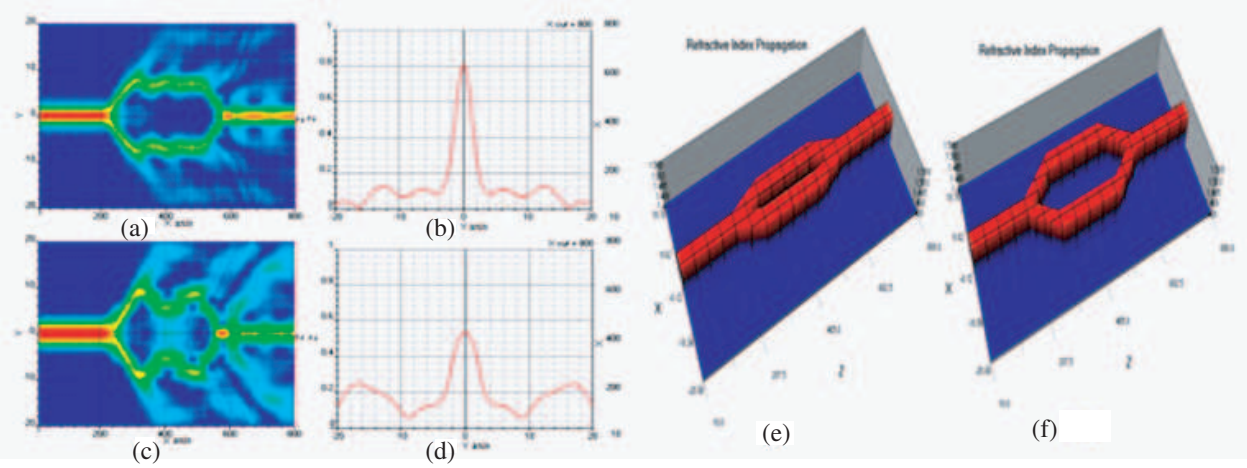

Figure 3: 2-D Plot of optical field profile and output field power at fix point $X = 800\,\mu m$ and $Y = 0\,\mu m$ for the case of (a)–(b) $w = 2.5\,\mu m$ and (c)–(d) $w = 5\,\mu m$ respectively and plot of refractive index profile (e) at $\theta_1 = 2°$ and (f) at $\theta_2 = 4°$.

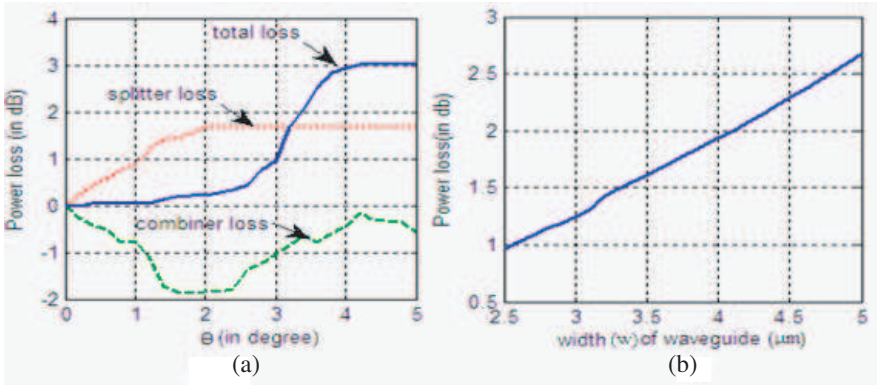

Figure 4: Plot of power loss (dB) versus (a) angle and (b) width of waveguide of Y-junction.

angle. The combiner loss is also increased with angle up to ≈ -1.8dB, and then it decreases. It is concluded that total power loss increases slowly with angle, and then increases drastically with some wide angle. We would also suggest compensating this loss by decreasing the width of the waveguide. Figure 4 shows the variation of power loss with the width of the waveguide. It reveals that power loss increases almost linearly with the width of waveguide. Hence by properly choosing the width of waveguide, one can reduced the effect of wide angle of Y-branch splitter/combiner.

4. CONCLUSION

We have analyzed the Y-branch having inbuilt optical beam splitters and combiner with different branching angle. The power loss found to be more for wide angle. This is due to mode conversion occurred in taper section. Due to this effect light may split into many parts and it may no longer remains guided. These results are found application where to deploy the optical network components. We further observe that power of the guided mode is divided into branching waveguides with relatively small losses when the refractive index difference between the core and the cladding is large. We further show that as the width of waveguide or length of centre waveguide increases total losses increases. Thus we can minimize the losses by reducing the width of waveguide, decreases the length of centre linear waveguide and increasing refractive index difference between the core and the cladding.

REFERENCES

1. Tsutsumi, K., Y. Imada, H. Hirai, and Y. Yuba, "Analysis of single mode optical Y-junctions by the bounded step and bend approximation," *J. Lightwave Technol.*, Vol. 6, 590–600, 1988.

2. Kawano, K. and T. Kitoh, *Introduction to Optical Waveguide Analysis*, John Wiley & Sons, New York, 2001.
3. Sasaki, H. and I. Anderson, "Theoretical and experimental studies on active Y-junctions in optical waveguides," *IEEE J. Quantum. Electron.*, Vol. 14, 883–892, 1978.
4. Raghuwanshi, S. K., S. Talabattula, and A. Selvarajan, "Fourier decomposition of the transverse field for analyzing optical waveguides using beam propagation method," *Journal of Indian Institute of Science*, Vol. 86, 667–680, 2006.
5. Andrew Motes, R., S. A. Shakir, and R. W. Berdine, "An efficient scalar, non-paraxial beam propagation method," *Journal of Lightwave Technology*, Vol. 30, No. 1, 4–8, 2012.
6. Wang, Q., S. He, and L. Wang, "Low-loss Y-branch with a multimode waveguide transition section," *IEEE Photonics Technology Letters*, Vol. 14, No. 8, 2002.
7. Lin, H.-B., J.-Y. Su, R.-S. Cheng, and W.-S. Wang, "Novel optical single-mode asymmetric branches for variable power splitting," *IEEE Journal of Quantum Electronics*, Vol. 35, No. 7, 1999.
8. Rahman, M. S. A., A. N. A. Aziz, A. A. Khairuddin, S. A. C. Aziz, and K. Jumari, "New optical splitter design for application in fibre-to-the home passive optical network using virtual lab platform," *Journal of Computer Science*, Vol. 8, No. 6, 864–871, 2012.

An Efficient Hybrid KA-MoM for Backscattering RCS from Combined Objects by Adaptively Truncating the Size of the Rough Surface

X. Y. Zhang, Z. Li, and Z. W. Liu
School of Information Engineering, East China Jiaotong University, 330013, China

Abstract— A highly efficient hybrid method combining the Kirchhoff approach (KA) and the method of moment (MoM) is proposed for calculating the monostatic RCS of conducting objects above a rough surface. In many engineering applications, the error of the radar cross section (RCS) could be less than 3 dB. Accordingly, the hybrid KA-MoM is able to be further speed up by sacrificing the numerical accuracy. The main difference between the proposed method and the traditional KA-MoM algorithm is the size of the rough surface have been truncated when calculate the interactions between the objects and the rough surface, for depending on the scattering characteristics of the rough surface with various roughness. The adaptive truncation method is used to define the truncated size of the rough surface. By executing the truncation procedure, the memory and the computation time is reduced significantly. The accuracy and efficiency of the proposed method are validated by numerical experiments.

1. INTRODUCTION

The scattering by objects above a rough surface is a typical problem in the study of electromagnetic scattering characteristics of objects and their environments, which is important for target identification and radar design. However, since the multi-interactions between objects and rough surfaces are complicated, analysis of this problem is difficult. In 1990s, numerical methods began to be employed for computing scatterings by arbitrarily shaped targets above a rough surface [1–4]. Due to the restriction of the computer capacity, the most of these attempts are limited to 2D problems. In the recent years, a variety of numerical methods have been proposed for the study of various special models of this kind of 3D problems [5–10]. The calculation of the coupled field from rough surface to object or from object to rough surface is very time consuming, since the size of the rough surface is very large in terms of wavelength, especially at low grazing incident angles. How to truncate the size of the rough surface is the key of solving this problem.

By considering the error of the radar cross section (RCS) could be less than 3 dB in many engineering applications. The adaptive truncation method is used to define the truncated size of the rough surface when only the monostatic scattering is concerned. Based on this, a highly efficient hybrid KA-MoM is proposed in this paper. Different from the traditional hybrid KA-MoM [11], the truncated rough surface interacted with objects is specially chosen at a very small area according to the scattering contribution of the rough surface. Thus the interaction between the objects and the rough surface can be efficiently calculated. The formulation of the method is presented in Section 2. Section 3 performs numerical experiments for investigating accuracy and efficiency of the method. The conclusions are given at last.

2. ROUGH SURFACE TRUNCATION

The roughness of a rough surface is usually described by the root mean square (rms) slope of this rough surface s. For the isotropic Gaussian correlation function ($l_x = l_y = l_c$), s is defined as:

$$s = \sqrt{2}\sigma/l_c \tag{1}$$

where l_c is the correlation length of the rough surface, σ is the rms height. In many cases, the rough surface has the following properties as

$$l_c > \lambda, \quad s < 0.25 \tag{2}$$

For this kind of rough surfaces, the KA is applicable. Numerical experiments show that the scattering by surfaces with the roughness $s < 0.1$ are much stronger at the mirror direction than other directions. However, as the value of the roughness is rising, the characteristic of the scatterings are becoming more complex. For example, the bistatic RCS by the rough surface with the same

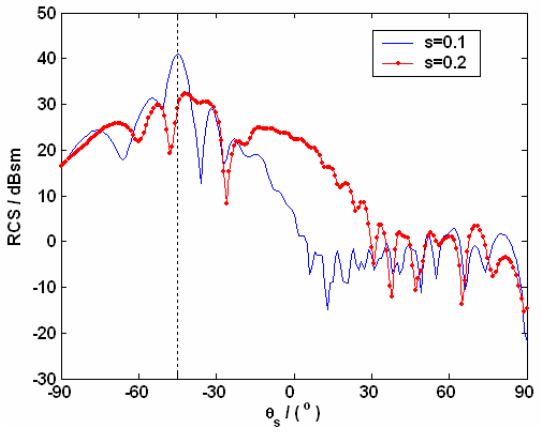

Figure 1: Bistatic RCS of surface-only illuminated by a taper wave.

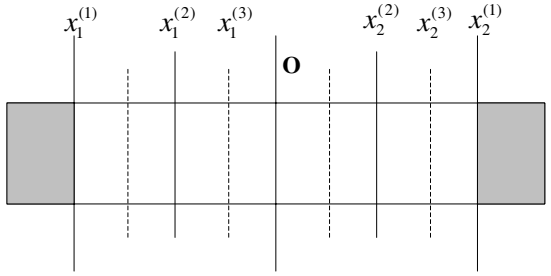

Figure 2: The chosen truncated rough surface.

correlation length as $l_c = 2\lambda$ and different roughness of $s = 0.1$ and $s = 0.2$ are presented in Fig. 1. A taper wave is incident at $\theta_i = 45°$. The illuminated size of the surface is $20 \times 20\lambda^2$.

It can be seen that for the rough surface with $s = 0.1$, the main lobe of the scattered field locates at the mirror of the incidence with narrow beamwidth and high side lobe level. Therefore, the coupled fields from the rough surface to object are mainly contributed by the small size of the projection region of the object according to the mirror direction. The contribution from the areas with $\theta_s > 0°$ could be ignored. On the other hand, for the rough surface with $s = 0.2$, the beamwidth is larger, and the side lobe level is smaller; the coupled fields from the rough surface to object are contributed by a large projection region. In this case, the contribution from the areas with $0° < \theta_s \leq 30°$ couldn't be ignored totally until $\theta_s > 30°$.

In Refs. [12, 13], we have been proposed the truncation method for the smoothly rough surface with $s \leq 0.1$ rough ness. For these methods, the truncation area is defined by an equation which is relative to the scattered angles and the incident angles. Although in most cases, the truncated methods are valid, we still found the phases are inaccuracy, and with the roughness increase, these approaches do not work anymore. In this paper, the adaptively truncation method is utilized to define the proper contribution area.

Figure 2 shows the rough surface truncation method. At the beginning of the RCS calculation, the position of $x_1^{(1)}$, $x_2^{(1)}$ are selected by

$$\begin{cases} x_1^{(1)} = -(h\mathrm{tg}\theta_m + r/\cos\theta_m) \\ x_2^{(1)} = h\mathrm{tg}\theta_m + r/\cos\theta_m \end{cases} \tag{3}$$

where r presents the largest dimension of the object; θ_m is the maximum scattering angles, h is the distance from the center of the object to the rough surface. By performing the Equation (4), the length of $[x_1, x_2]$ is reduced to $[x_1^{(1)},\ x_2^{(1)}]$. If the error of the RCS calculated by the scattering from $[x_1^{(1)},\ x_2^{(1)}]$ is less than 1 dB, the division procedure would be continued. The length of the rough surface will be divided into smaller and smaller size by considering the 80% scattering energy contributions until the total error of the RCS is larger than 3 dB. If the times of the division is 3, the integral region of the rough surface are determined by $L_1 = [x_1^{(3)},\ x_2^{(3)}]$.

It is known that the length in conventional hybrid KA-MoM is as large as [15]

$$L_0 = 16(h\mathrm{tg}\theta_i + r/\cos\theta_i) \tag{4}$$

By comparing L_1 with L_0, L_1 is much smaller especially at low grazing incident angles.

3. NUMERICAL RESULT

To test the validity of this method, the computation of the scattering by a cube ($a = 1.5\lambda$, $h = 3.5\lambda$) above a rough surface is illustrated. The vertical polarized taper wave is incident from $\theta_i \in [0°, 70°]$, $\phi_i = 0°$. The original size of the rough surface is $L_0 \times L_y$ ($L_0 = 450\lambda$, $L_y = 15\lambda$) with $l_c = 2\lambda$,

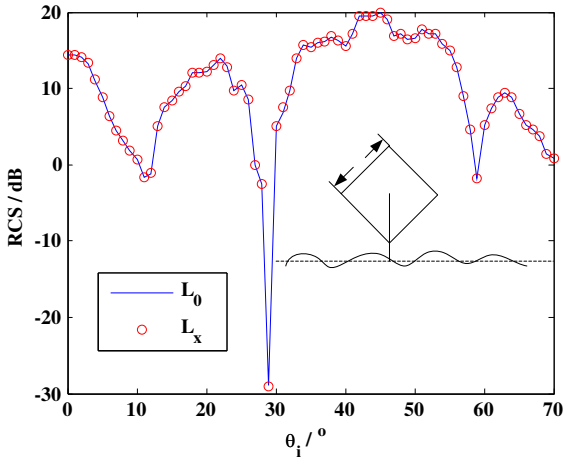

Figure 3: Monostatic RCS of a cube on a rough surfac

$s = 0.15$. By performing the proposed method, the size of the rough surface is reduced to be $L_x \times L_y$. It can be seen from Fig. 3 that the results from our proposed hybrid KA-MoM has a quite good agreement with those from the traditional hybrid KA-MoM. The root mean square error is 0.08 dB. For $\theta_i = 70^\circ$ incidence, the truncated size of the rough surface is reduced to be $14.25 \times 15\lambda^2$, which is smaller 30 times than the original size of the rough surface.

4. CONCLUSIONS

In this paper, an adaptive truncation approach is proposed to determine the size of the rough surface by considering the engineering applications. Based on the truncation, a highly efficient hybrid KA-MoM is proposed by sacrificing the numerical accuracies as the error of the monostatic RCS is limited to 3 dB. By performing the proposed method, the size of the rough surface is significantly reduced. The numerical results show the accuracy and the efficiency of the proposed method.

ACKNOWLEDGMENT

The authors would like to thank the support of National Science Foundation of China (No. 61061002) and the support of East China Jiaotong University Foundation (No. 11XX01).

REFERENCES

1. Wong, P. B., G. L. Tyler, J. E. Baron, et al., "A three-wave FDTD approach to surface scattering with applications to remote sensing of geophysical surfaces," *IEEE Trans. Antennas Propag.*, Vol. 44, No. 4, 504–514, 1996.
2. Pino, M. R., L. Landesa, J. L. Rodriguez, et al., "The generalized forward-backward method for analyzing the scattering from targets on ocean-like rough surfaces," *IEEE Trans. Antennas Propag.*, Vol. 47, No. 6, 961–969, 1999.
3. Wang, X., Y. B. Gan, and L. W. Li, "Electromagnetic scattering by partially buried PEC cylinder at the dielectric rough surface interface: TM case," *IEEE Antennas Wireless Propag. Lett.,* Vol. 2, No. 1, 319–322, 2003.
4. Ye, H. X. and Y. Q. Jin, "Fast iterative approach to difference scattering from the target above a rough surface," *IEEE Trans. Geosci. Remote Sensing*, Vol. 44, No. 1, 108–115, 2006.
5. Geng, N., A. Sullivan, and L. Carin, "Multilevel fast-multipole algorithm for scattering from conducting targets above or embedded in a lossy half space," *IEEE Trans. Geosci. Remote Sensing*, Vol. 38, No. 4, 1561–1573, 2000.
6. Hu, B. and W. C. Chew, "Fast inhomogeneous plane wave algorithm for scattering from objects above the multilayered medium," *IEEE Trans. Geosci. Remote Sensing*, Vol. 39, No. 5, 1028–1038, 2001.
7. Liu, Z. J., R. J. Adams, and L. Carin, "Well-conditioned MLFMA formulation for closed PEC targets in the vicinity of a half space," *IEEE Trans. Antennas Propag.*, Vol. 51, No. 10, 2822–2829, 2003.

8. Lei, K. and Y. Q. Jin, "Numerical simulation of electromagnetic scattering from a 3D target over a randomly rough surface using FDTD method," *Chin. J. Comput. Phys.*, Vol. 24, No. 5, 550–560, 2007.
9. Johnson, J. T. and R. J. Burkholder, "Coupled canonical grid/discrete dipole approach for computing scattering from objects above or below a rough interface," *IEEE Trans. Geosci. Remote Sensing*, Vol. 39, No. 6, 1214–1220, 2001.
10. Johnson, J. T., "A numerical study of scattering from an object above a rough surface," *IEEE Trans. Antennas Propag.*, Vol. 50, No. 10, 1361–1367, 2002.
11. Ye, H. X. and Y. Q. Jin, "A hybrid analytical-numerical algorithm for scattering from a 3-D target above a random rough surface," *Acta Phys. Sin.*, Vol. 57, No. 2, 839–846, 2008.
12. Zhang X. Y. and X. Q. Sheng, "Truncated size of the rough surface for calculating the backscattering RCS from combined objects," *ICMMT*, 2010.
13. Zhang, X. Y. and X. Q. Sheng, "High efficiency hybrid method for monostatic scattering by objects on a rough surface," *IET Microwaves, Antennas & Propagation*, Vol. 4, No. 10, 1597–1604, 2010.

Adaptive Compressed Sampling Method for Fast Comuatation of Monostatic Scattering

Zhiwei Liu[1], **Yueyuan Zhang**[2], **and Xiaoyan Zhang**[1]

[1]School of Information Engineering, East China Jiaotong Unviersity, 330013, China
[2]International School, East China Jiaotong University, 330013, China

Abstract— An adaptive compressed sampling method is proposed to reduce the time requirement for computation of monostatic scattering. The angular samples which would be most informative can be selected optimally by use of the cubic spline interpolation method. Different with our previous work, adaptive sampling is applied to choose the key excitation vectors instead of electric current vectors. Reduction number of multiple excitation vectors can lead to less computation time significantly. Moreover, with low-rank property, the excitation vectors at these sampling angles could be further compressed by singular value decomposition (SVD), resulting in a more efficient adaptive sampling method. The SVD can be replaced by adaptive cross algorithm (ACA) to further reduce the computational complexity. Numerical results demonstrate that this method is efficient for monostatic RCS calculation with high accuracy.

1. INTRODUCTION

Amongst integral formulations, the combined field integral equation (CFIE) is widely used for electromagnetic wave scattering problems as it can handle the most general geometries. The matrix associated with the resulting linear systems is large, dense, complex and non-Hermitian [1]. This difficulty can be circumvented by use of iterative methods, and the required matrix-vector product operation can be efficiently evaluated by multilevel fast multipole algorithm (MLFMA) [2, 3]. The use of MLFMA reduces the memory requirement to $O(N\log N)$ and the computational complexity of per-iteration to $O(N\log N)$.

It is still time-consuming for calculation of monostatic RCS since it requires repeated solution of integral equation at each incident angle. As well known, many interpolation methods are proposed to circumvent this difficult. The model-based parameter estimation (MBPE) technique is presented by Miller and Burke to accurately compute wide band response with a few direct calculations [4, 5]. In the asymptotic waveform evaluation (AWE) technique [6–8], the induced current is expanded in the Taylor series around an angle, and the Padé approximation is used to improve the accuracy. Cubic spline method [9, 10] utilizes the information of C^1-continuous to evaluate the first derivative of the induced current vector instead of solving the large linear equations.

It is noteworthy that selection of sampling points is crucial for interpolation and extrapolation methods. Obviously, non-uniform sampling method shows more flexible and efficient than uniform sampling method. As a result, optimally select those angles that would be most informative will reduce the number of repeated solutions when one must consider for monostatic scattering computations. In [11], an adaptive multi-point AWE method is proposed for a FEM fast frequency sweep. In [9, 10], the cubic-spline based adaptive sampling method is proposed to optimally select the most informative angles in monostatic RCS curve, resulting in an efficient computation of monostatic scattering. In [12], it is reported that multiple excitation vectors or right hand side vectors can be compressed by use of the low rank property. In this paper, the combination of the cubic-spline adaptive sampling and low rank compression is applied to efficient computation of monostatic RCS.

2. ADAPTIVE SAMPLING STRATEGY WITH COMRESSION

The CFIE formulation of electromagnetic wave scattering problems using planar Rao-Wilton-Glisson (RWG) basis functions for surface modeling is presented in [1, 13, 14]. The resulting linear systems from CFIE formulation after Galerkin's testing are briefly outlined as follows:

$$\mathbf{Ax} = \mathbf{b} \tag{1}$$

To solve the above matrix equation by an iterative method, it is time consuming for the computation of monostatic RCS since it requires repeated solution of CFIE at each incident direction. As a result, new methods are required to circumvent this difficulty.

The adaptive strategy with the idea of coarse-to-fine is proposed to generate a set of non-uniform sampling nodes. There are two basic problems that need to be emphasized in this approach. One is how to select the optimal samples and the other is when to stop the process. Take an arbitrary function or curve for example, as shown in Fig. 1. In order to approximation the black curve $f(x)$ with area $[a, b]$, a straightforward idea is to use the line model. The slope of the line is computed by the value of $f(a)$ and $f(b)$. If the black line is C^1-continous, a more accurate method is to use a cubic spline to approximate it [9]. It is named as cubic spline model in this paper. The parameters of cubic spline can be computed by $f(a)$, $f(b)$, $f'(a)$ and $f'(b)$. The first derivatives are evaluated by spline. From the first chart in Fig. 1, it is obvious that cubic spline model is far different with line model. Accordingly, both of the two models are inaccurate and new samples are needed. In the area $[a, b]$, a new sample is defined at the location with largest difference between the two models. Assume c is a new sample, then a new adaptive process will perform in $[a, c]$ and $[c, b]$ which is the same as the process in $[a, b]$. From the second chart of Fig. 1, there is almost no difference between cubic spline model and line model. As a result, no sample is needed to refine the result and the adaptive sampling could be stopped.

In this paper, a new adaptive method is proposed to fast analysis of monostatic scattering. Instead of induced current vectors, the new method is used to select the optimal right hand side vectors. Especially in the implementation of monostatic scattering, the curve of right hand side vectors is very smooth since the excitation is only the function of angle. From (1), the current vectors x can be rewritten as

$$\mathbf{x}(\theta) = \mathbf{A}^{-1}\mathbf{b}(\theta) \tag{2}$$

In order to control the accuracy of the far-field scattering, the Convergence Error (CE) is used for judging whether or not more samples are required. The CE is defined as the relative error between the cubic spline model and the excitation vectors. Since the excitation vectors are computed analytically, it is feasible to ensure the accuracy under the control of the relative error. Generally, when the relatively error is smaller than 0.01, the selected samples could lead to a precise result.

3. NUMERICAL RESULTS

In this section, the result of VFY218 model is presented to demonstrate the accuracy and efficiency of the proposed method for fast calculation of monostatic RCS over wide angular band. The VFY-218 is a well-known model in the field of electromagnetic scattering. The flexible general minimal residual (FGMRES) [18–20] algorithm is applied to solve linear systems. All experiments are conducted on an Intel Core(TM) II Duo with 3.45 GB local memory and run at 2.4 GHz in single precision. The iteration process is terminated when the 2-norm residual error is reduced by 10–3, and the limit of the maximum number of iterations is set as 1000.

In our numerical experiments, the geometry is illuminated by plane wave with the incident pitch angles range from 0 to 180 deg. The frequency is 500 MHz and the azimuth angle is 0 deg. The value of CE is set to be 0.01 in this paper to keep the RCS curve accurate enough. In Fig. 2, the monostatic RCS of VFY-218 is computed by adaptive sampling method. The word "Reference" means results computed by MLFMA without interpolation while "proposed method" means results

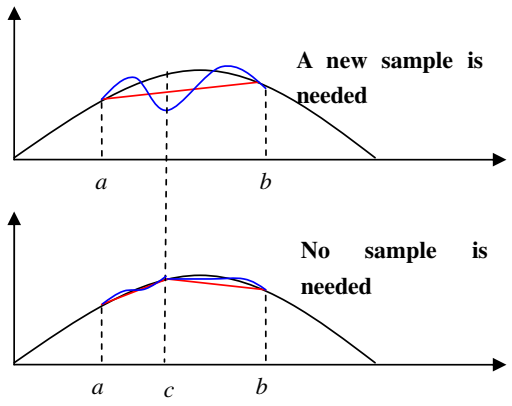

Figure 1: Sketch of adaptive sampling strategy.

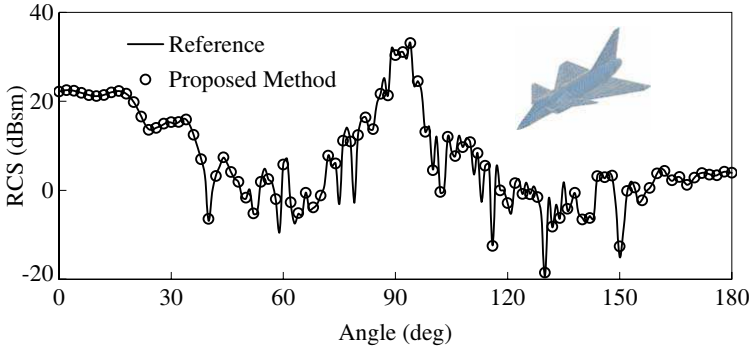

Figure 2: The monostatic RCS results by adaptive sampling method with compression.

computed by proposed method. The CE is set to be 0.01. It is concluded that the proposed method can approximate the RCS curve accurately. For reference results, the total computation time is 106618 s and the number of linear equation solutions is 361 since the space for angle sweep is 0.5 degree. Large time is cost for repeated solution of linear systems. In order to demonstrate the efficiency, the traditional AWE method and adaptive cubic-spline method is applied for comparison. When using the AWE method, uniform samples are used and the order of derivatives is 10. The interval of samples is set to be 12 degree. Accordingly, the number of iterative solutions is 160. When using the adaptive cubic spline method discussed in [9, 10], the sampling vectors is 155. When ACA compression is used, the multiple vectors for these three geometries can be compressed to 73. Consequently, the CPU time is reduced to 28732 s. As a result, our proposed method can be considered as an accurate and efficient method.

4. CONCLUSIONS

In this paper, a novel adaptive sampling framework is proposed for efficient analysis of monostatic scattering. Different from interpolating the electric current, the cubic spline interpolation method is used to approximate the multiple right hand sides on a set of non-uniform sampling angles and the adaptive sampling strategy is employed to generate new sampling points automatically. The most informative angles could be selected by this adaptive procedure. Moreover, applying ACA to compute the eigenvectors of the selected vectors leads to reduction times of iterative solutions of linear systems. Numerical experiments demonstrate that the proposed method is more efficient when compared with the traditional AWE method and adaptive cubic spline method for computing monostatic RCS.

ACKNOWLEDGMENT

The authors would like to thank the support of National Science Foundation of China (No. 61061002) and the support of East China Jiaotong University Foundation (No. 11XX01).

REFERENCES

1. Harrington, R. F., *Field Computation by Moment Methods*, R. E. Krieger, Malabar, Florida, 1968.
2. Chew, W. C., J. M. Jin, E. Michielssen, and J. M. Song, *Fast and Efficient Algorithms in Computational Electro-magnetics*, Artech House, Boston, MA, 2001.
3. Song, J. M., C. C. Lu, and W. C. Chew, "Multilevel fast multipole algorithm for electromagnetic scattering by large complex objects," *IEEE Trans. Antennas Propagat.*, Vol. 45, No. 10, 1488–1493, Oct. 1997.
4. Miller, E. K. and G. J. Burke, "Using model-based parameter estimation to increase the physical interpretability and numerical efficiency of computational electromagnetics," *Computer Physics Communications*, Vol. 68, 43–75, 1991.
5. Miller, E. K., "Model-based parameter estimation in electromagnetics — Part I: Background and theoretical development," *IEEE Antennas Propag. Mag.*, Vol. 40, No. 1, 42–52, Feb. 1998.
6. Erdemli, Y. E., J. Gong, C. J. Reddy, and J. L. Volakis, "Fast RCS pattern fill using AWE technique," *IEEE Trans. Antennas Propagat.*, Vol. 46, No. 11, 1752–1753, Nov. 1998.

7. Slong, R. D., R. Lee, and J. F. Lee, "Multipoint Galerkin asymptotic waveform evaluation for model order reduction of frequency domain FEM electromagnetic radiation problems," *IEEE Trans. Antennas Propagat.*, Vol. 49, No. 10, 1504–1513, Oct. 2001.
8. Wei, X. C., Y. J. Zhang, and E. P. Li, "The Hybridization of fast multipole method with asymptotic waveform evaluation for the fast monostatic RCS computation," *IEEE Trans. Antennas Propagat.*, Vol. 52, No. 2, 605–607, Feb. 2004.
9. Liu, Z. W., R. S. Chen, and J. Q. Chen, "Adaptive sampling cubic-spline interpolation method for efficient calculation of monostatic RCS," *Micro. Opt. Tech. Lett.*, Vol. 50, No. 3, 751–755, Mar. 2008.
10. Liu, Z. W., D. Z. Ding, Z. H. Fan, and R. S. Chen, "Adaptive sampling bicubic spline interpolation method for fast computation of monstatic RCS," *Micro. Opt. Tech. Lett.*, Vol. 50, No. 7, 1851–1857, Jul. 2008.
11. Slone, R. D., J. F. Lee, and R. Lee, "Automating multipoint Galerkin AWE for a FEM fast frequency sweep," *IEEE Trans. Magnetics*, Vol. 38, No. 2, 637–640, Feb. 2002.
12. Peng, Z., M. B. Stephanson, and J. F. Lee, "Fast computation of angular responses of large-scale three-dimensional electromagnetic wave scattering," *IEEE Trans. Antennas Propagat.*, Vol. 58, No. 9, 3004–3012, Sep. 2010.
13. Rao, S. M., D. R. Wilton, and A. W. Glisson, "Electromagnetic scattering by surfaces of arbitrary shape," *IEEE Trans. Antennas Propagat.*, Vol. 30, No. 3, 409–418, 1982.
14. Carvajal, G. K., D. J. Duque, and A. J. Zozaya, "RCS estimation of 3D metallic targets using the moment method and Rao-Wilton-Glisson basis functions," *ACES Journal*, Vol. 24, No. 5, 487–492, Oct. 2009.
15. Shaeffer, J., "Direct solve of electrically large integral equations for problem sizes to 1 M unknowns," *IEEE Trans. Antennas and Propagat.*, Vol. 56, No. 8, 2306–2313, Aug. 2008.
16. Kurz, S., O. Rain, and S. Rjasanow, "The adaptive cross-approximation technique for the 3-D boundary-element method," *IEEE Trans. Magnetics*, Vol. 38, No. 2, 421–424, 2002.
17. Miller, E. K., "Using adaptive estimation to minimize the number of samples needed to develop a pattern to a specified uncertainty," *ACES Journal*, Vol. 17, No. 3, 176–186, Nov. 2002.
18. Chris, R. and H. Anton, *Application of Linear Algebra*, 3rd Edition, John Wiley and Sons, New York, 1984.
19. Saad, Y. and M. Schultz, "GMRES: A generalized minimal residual algorithm for solving nonsymmetric linear systems," *SIAM J. Sci. Stat. Comput.*, Vol. 7, No. 3, 856–869, 1986.
20. Simoncini, V. and D. B. Szyld, "Flexible inner-outer Krylov subspace methods," *SIAM J. Numer. Anal.*, Vol. 40, No. 6, 2219–2239, 2003.
21. Gibson, W. C., *The Method of Moments in Electromagnetics*, Chapman & Hall/CRC, Boca Raton, 2008.

Design of a Wideband RF Front End Based on Multilayer Technology

Christos I. Kolitsidas, Christos S. Lavranos, and George A. Kyriacou
Microwaves Laboratory, Department of Electrical and Computer Engineering
Democritus University of Thrace, Xanthi 67100, Greece

Abstract— A wideband switched beam beamforming network based on an 8×8 Butler matrix is designed. This structure is implemented in a multilayer microstrip slot technology that employs two dielectric layers with common ground plane and coupling slots. Elliptically shaped microstrip hybrids and phase shifters are adopted to realize the required wide bandwidth. The final design of the Butler matrix provides a compact and without any crossovers beamforming network. The Butler matrix outputs feed a tapered slot Vivaldi antenna array that provides operating bandwidth covering the whole desired frequency range of 3.1 to 10.6 GHz.

1. INTRODUCTION

The trend in contemporary wireless communications systems is to develop Ultra Wide Band (UWB) RF components as high speed wireless connectivity has become a daily demand. UWB radio systems are very promising since transmission data rates greater than those on the other WLAN systems can be developed with lower power dissipation. Beamforming networks providing controllable radiation patterns are a solution for wireless applications where high resolution, reduced interference, propagation around obstacles and low cost are design parameters. The most important beamforming networks of common use for multiple beams with linear array are based on the Butler matrix, due to its ability to form a group of orthogonal beams, its reciprocal nature and its design simplicity. The classical realization of Butler matrix, [3] consists of microwave hybrids, crossovers and phase shifters. However, the typical microstrip hybrids and crossovers have a limited bandwidth of maximum 30% to 40% and occupy large space in printed boards. In addition crossovers may also add undesired effects, such as increased insertion loss, mismatched junctions, additional line cross couplings and poor power handling.

In the current study the goal is to successful design wideband Butler matrix (aiming at UWB: Ultra-Wideband) implemented on multilayer microstrip slot technology feeding a wideband vivaldi antenna array. For this purpose elliptically shaped wideband microwave hybrids [8], and phase shifters [9], have been designed in order to implement a Butler matrix in microstrip slot technology with wideband characteristics and provide a compact design that overcomes the problem of the crossovers that appear in conventional designs.

2. RELATED AND PREVIOUS WORK

Our laboratory has extensive experience in the design of Butler matrices. There have been several designs serving different systems but all with a common characteristic: limited bandwidth. Two different Direction of Arrival (DOA) units were developed in our previous effort directed toward the development of smart antennas at the RF-level which support SDMA techniques, e.g., [1, 2]. These systems share the same principles and were based on two different topologies. The first proposed system was based on 4 inputs-4 outputs Butler matrix [1]. The received signal was sampled at the inputs of the Butler matrix by an array comprised of 4 antennas. Depending on the angle of arrival the Butler matrix produces different signals at its outputs. These signals were translated into DC-voltages using crystal detectors. In turn these DC signals are compared with differential amplifiers in order to extract a DC-voltage difference that defines the angle of arrival. The second proposed system was based on the polar phase discriminator approach. The received signal was sampled by two antennas and was processed by four 90° hybrids and four crystal detectors [2]. The space coverage provided by the two DOA developed systems was 120° in azimuth and 60° in the elevation angle. Also based on the same principles two different DOA systems incorporating an 8×8 Butler matrix were developed in order to accomplish full space coverage of 360° in the azimuth plane [4, 5]. Another topology of the Butler matrix has been developed by Kaifas et al. using elliptically shaped hybrids aiming for UMTS applications [6].

This study proposes an extension of the above developed Butler matrices in order to achieve wideband characteristics accompanied with an 8 element tapered slot vivaldi antenna array.

3. THE 8 × 8 BUTLER MATRIX DESIGN

The first stage of this study is to develop an 8×8 UWB Butler matrix. For this purpose microstrip slot technology has been chosen in order to implement the Butler matrix. This technology consists of two microstrip substrates supported by a common ground plane in the middle where appropriate shaped slots are made to accomplish signal coupling between the two sides. Exploiting the multilayer microstrip slot technology a reconfigured Butler matrix block diagram is proposed in Fig. 1, where all crossovers are avoided resulting to a more compact design while keeping its symmetry. Suitable 3 dB UWB directional coupler and phased shifters of elliptical shape have already been introduced in [8, 9] respectively. The elliptically shaped microstrip slot directional coupler and phase shifter layouts that were used to implement the Butler matrix of Fig. 1 are given in Fig. 2. In Fig. 2(b) the cross section of the coupler that consists of three conductor layers is shown, with the middle layer being the common ground plane, interleaved by two dielectric layers. With the aid of the analytical expressions given in [8], the initial dimensions of the elliptical patch and slot where calculated. The microstrip slot coupler was then designed using CST Microwave Studio [7], and the final dimensions are $D_m = 4.8$ mm, $D_l = 7.2$ mm and $D_s = 7.4$ mm. The coupling achieved is 3 ± 1.7 dB at the range of 3.1–4.6 GHz and 3 ± 0.6 dB elsewhere, the return loss at all ports is lower than -20 dB and the phase difference between the ports 2 and 3 is $90° \pm 1.7°$. The design of the phase shifters is similar to the microstrip slot coupler. The phase shifting function is obtained by open circuiting ports 2 and 3 of the microstrip slot coupler, (Fig. 2(c)). Following the design procedure that is stated in [9] the initial values of the three phase shifters were obtained. In turn the phase shifters were designed and optimized using CST Software. The final dimensions for the 67.5° are $D_m = 7$ mm, $D_l = 7$ mm, $D_s = 10.1$ mm, for the 22.5° phase shifter are $D_m = 6.1$ mm, $D_l = 7.3$ mm, $D_s = 8.3$ mm and for the 45° phase shifter are $D_m = 4.8$ mm, $D_l = 7.1$ mm and $D_s = 7.3$ mm. The phase shift is referenced to a microstrip transmission line of the same length as the phase shifter. Rogers RO4003 with $\varepsilon_r = 3.38$ and $h = 0.508$ mm, readily available at our laboratory, is considered as upper or lower substrate.

As a final step of the design procedure all elements were combined together in order to form the layout of the Butler matrix that is presented in Fig. 3. The dark color is the top layer and the light color the bottom layer. The dimensions of the final design are 110 mm × 70 mm which is considerably smaller than ordinary designs including these of our previous work.

The phase shift obtained for the output ports for each possible beam (when different input ports is activated) are $-157.5° \pm 9°$, $-112.5° \pm 8°$, $-67.5° \pm 8°$, $-22.5° \pm 8°$, $157.5° \pm 9°$, $112.5° \pm 8°$, $67.5° \pm 8°$, $22.5° \pm 8°$. The magnitudes of the transmission S-parameters were -10 ± 2.5 dB across the bandwidth which deviates from the ideal of -9 dB. This deviation is due to the fact that the phase shifters introduce some loses when compared to the simple transmission line phase shifters

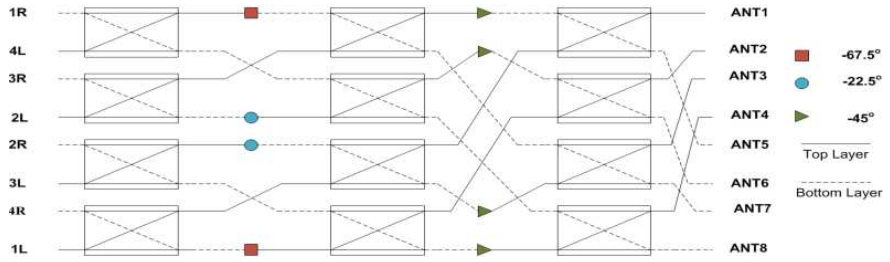

Figure 1: The 8×8 Butler matrix architecture with the multilayer microstrip slot technology configuration.

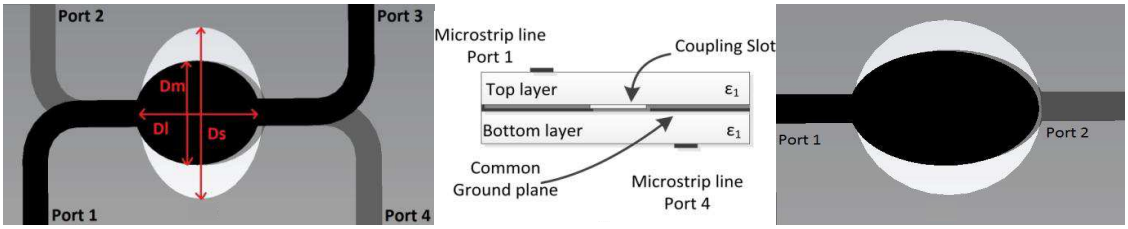

(a) (b) (c)

Figure 2: (a) The microstrip slot coupler, (b) cross section and (c) the phase shifter layout.

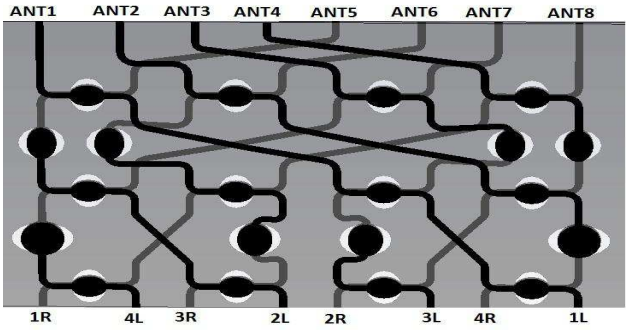

Figure 3: The final layout of the 8×8 Butler matrix.

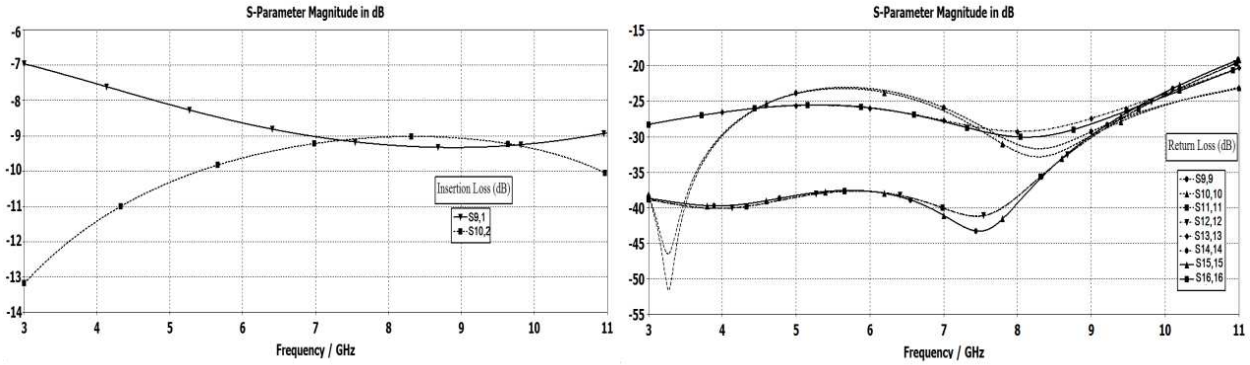

(a) (b)

Figure 4: (a) Simulated insertion loss and (b) return loss of the output ports of the Butler matrix.

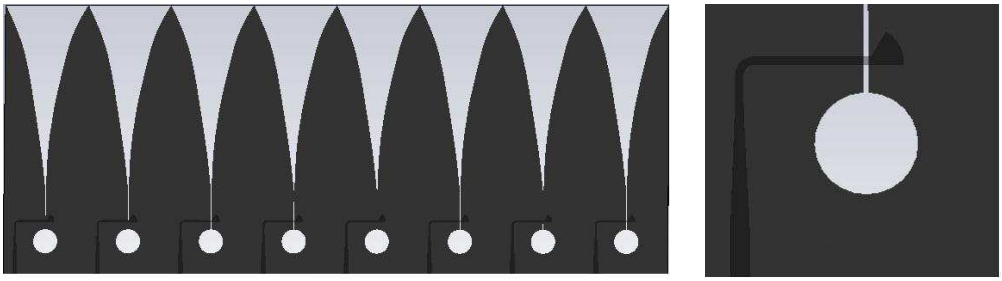

(a) (b)

Figure 5: (a) Vivaldi tapered slot antenna array and (b) the microstrip-fed.

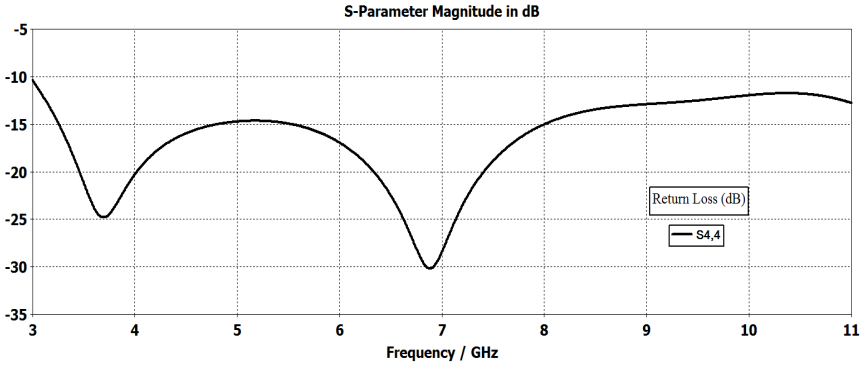

Figure 6: Reflection coefficient at input of the 4th tapered vivaldi slot antenna.

and the maximum deviation is observed at the lower frequencies. The magnitude deviation does not affect considerably the switch beam capacity of the beam forming network.

4. THE VIVALDI ANTENNA ARRAY DESIGN

In order to complete the RF front end a suitable wideband antenna array is in need that will meet the desired characteristics. One of the best candidates that will provide both wideband and directional characteristics is the Vivaldi tapered slot antenna [10]. In the design process of these antenna arrays it is highly important to take into consideration the mutual coupling and utilize it in order to optimize the overall performance of the array. Gaps between the elements of the Vivaldi array causes undesirable resonances that disrupt the wideband performance of the array thus all antenna elements is preferred to be contiguous as shown in Fig. 5(a). The tapered profile is defined by the exponential function $y = 0.25e^{0.05x} - 0.5$. The input power is first transferred from the microstrip line to the slotline by a wideband transition [11], as shown in Fig. 5(b). The slotline of the Vivaldi has a characteristic impedance of $100\,\Omega$ thus a linear tapered impedance transformer was used in order to achieve an input impedance of $50\,\Omega$ at the microstrip input of the antenna. The tapered slot and its ground plane are etched on the bottom layer (Rogers RO4003) while the feeding microstrip line (width $w_{50\,\Omega} = 1.18\,\text{mm}$ and $w_{100\,\Omega} = 0.29\,\text{mm}$) and the wideband matching radial stub (radius of $R_{stub} = 5\,\text{mm}$ and $\theta = 60°$) are printed on the upper substrate. The slot line starts from the circular slot with radius $R_{slot} = 3.5\,\text{mm}$. The tapered slot serves as a wideband impedance transformer and guides the wave to propagate along the slot. Fig. 6 presents the simulated results of the reflection coefficient of the 4th antenna element. The antenna has a good impedance matching (below $-12\,\text{dB}$) over the bandwidth of 3.1–10.6 GHz. The total dimensions of the antenna array are $160\,\text{mm} \times 65\,\text{mm}$.

5. CONCLUSIONS

An Ultra wideband RF front end consisted from an 8×8 Butler matrix and an 8 element vivaldi antenna array was designed. The Butler matrix has been designed using multilayer microstrip slot technology that provided a compact design without using any crossings overcoming the one of the classic problems of the Butler matrix. In order to complete the system an 8 element vivaldi antenna array was designed using tapered slot technology.

ACKNOWLEDGMENT

This work was financially supported by the Greek Ministry of Education, Lifelong Learning and Religious Affairs through the research project THALIS Design Techniques for Digitally Controlled RF-Microwave Structures Appropriate for Software Defined — Cognitive Radio (RF-EIGEN-SDR).

REFERENCES

1. Fakoukakis, F. E., S. G. Diamantis, A. P. Orfanides, and G. A. Kyriacou, "Development of an adaptive and a switched beam smart antenna system for wireless comunications," *Journal of Electromagnetic Waves and Applications*, Vol. 20, No. 3, 399–408, 2006.
2. Fakoukakis, F. E. and G. A. Kyriacou, "SDMA based on RF-beamforming: A switched beam versus a semi-adaptive system," *Journal of the European Microwave Association*, Vol. 2, No. 3, 241–250, 2006.
3. Butler, J. and R. Lowe, "Beam forming matrix simplifies design of electrically scanned antennas," *Electronic Design*, Apr. 1961.
4. Kolitsidas, C. I., F. E. Fakoukakis, D. G. Drogoudis, C. S. Lavranos, and G. A. Kyriacou, "Development of a full 360° azimuth coverage direction of arrival measurement unit," *Proceedings of Mediterranean Microwave Symposium*, 35–39, Damascus, Syria, Oct. 2008.
5. Kolitsidas, C. I., F. E. Fakoukakis, D. G. Drogoudis, M. Chrysomallis, and G. A. Kyriacou, "Angular localization of interfering sources using a butler matrix driven circular array," *Proceedings of EMC Europe Workshop*, 215–218, Athens, Greece, Jun. 2009.
6. Kaifas, T. N. and J. N. Sahalos, "A 4×4 Butler matrix optimized for UMTS applications," *Microwave and Optical Technology Letters*, Vol. 49, No. 3, 585–588, 2007.
7. Microwave Studio 2008, © Computer Simulation Technology CST.
8. Abbosh, A. M. and M. E. Bialkowski, "Design of compact directional couplers for UWB applications," *IEEE Transactions on Microwave Theory and Techniques*, Vol. 55, 189–194, 2007.
9. Abbosh, A. M., "Ultra-wideband phase shifters," *IEEE Transactions on Microwave Theory and Techniques*, 1935–1941, 2007.

10. Gibson, P. J., "The Vivaldi aerial," *Proceedings of the 9th European Microwave Conf.*, 101–105, 1979.
11. Schuppert, B., "Microstrip/slotline transitions: Modeling and experimental investigation," *IEEE Transactions on Microwave Theory and Techniques*, Vol. 36, No. 8, 1272–1282, Aug. 1988.

The Casimir Force for Arbitrary Three-dimensional Objects with Low Frequency Methods

P. R. Atkins[1], **W. C. Chew**[1], **Q. I. Dai**[2], **and W. E. I. Sha**[2]

[1]University of Illinois, Urbana, IL, USA
[2]University of Hong Kong, Pok Fu Lam, Hong Kong, China

Abstract—There has been much progress in recent years in the simulation of Casimir forces between various objects. Current methods have allowed traditional computational electromagnetic solvers to be used to find the Casimir forces in arbitrary threedimensional objects. The underlying theory to these approaches requires knowledge and manipulation of advanced quantum field theory or quantum statistical physics. We present a means of deriving the Casimir force using the method of moments via the argument principle that presents a simplified derivation and greater freedom in the representation of the moment matrix.

1. INTRODUCTION

The ability to model the bulk effect of molecular forces has become increasingly desired with the development of microand nanoelectromechanical systems (MEMS and NEMS). Improved modeling of the static and dynamic behaviors of such MEMS devices involves the accurate evaluation of the molecular and electrodynamic forces. To this end, a simple and robust method of calculating the Casimir force has been developed based around a recent method developed by Reid, Rodriguez, White and Johnson (RRWJ) [1–3]. This method allows for the use of traditional computational electromagnetic (CEM) solvers such as the method of moments (MoM) to find the Casimir force for arbitrary three-dimensional objects of arbitrary medium. However, this method has only been derived for the traditional MoM matrix problem which suffers from such limitations as low frequency breakdown and mesh density breakdown.

To alleviate these limitations and to further broaden the flexibility of the algorithm, we propose a new method of deriving the Casimir force using the argument principle. With the advantages of the new derivation we can provide a means of calculating the Casimir force that is free of the low frequency breakdown and offers greater freedom in the choice of the CEM formulation to address other shortcomings of traditional solvers.

2. PROPOSED METHOD

Focusing upon the perfect electrically conducting (PEC) problem, the RRWJ method derives an expression for the Casimir energy as [2, 4],

$$\mathcal{E} = \frac{\hbar c}{2\pi} \int_0^\infty d\kappa \ln \frac{\det \bar{\mathbf{M}}(\kappa)}{\det \bar{\mathbf{M}}_\infty(\kappa)} \tag{1}$$

where we now use an imaginary frequency dyadic Green's function by applying what is called the Wick rotation,

$$\bar{\mathbf{G}}_\kappa(\mathbf{r}, \mathbf{r}') = \left[\bar{\mathbf{I}} + \frac{\nabla\nabla'}{\kappa^2}\right] \frac{e^{-\kappa|\mathbf{r}-\mathbf{r}'|}}{4\pi|\mathbf{r}-\mathbf{r}'|} \tag{2}$$

and the elements of the matrix $\bar{\mathbf{M}}$,

$$[\bar{\mathbf{M}}]_{ij} = \iint \mathbf{f}_i(\mathbf{r}) \cdot \bar{\mathbf{G}}_\kappa(\mathbf{r}, \mathbf{r}') \cdot \mathbf{f}_j(\mathbf{r}') d\mathbf{r}' d\mathbf{r} \tag{3}$$

are of the same as the matrix elements of the MoM impedance matrix with $\mathbf{f(r)}$ being the chosen basis functions. The method used to derive Equation (1) follows a framework that assumed a specific action for the path integral and properties of the matrix $\bar{\mathbf{M}}$. Attempts to modify the resulting impedance matrix used in Equation (1) requires one to start over with a new path integral formulation. Deriviations using EFIE [2], PMCHWT [3, 5], and scattering matrices [6] all required starting over with a new path integral formulation and working it out to the end. Instead of attempting to rederive a new path integral formula for different solvers where a method like the

low frequency Augmented-Electric Field Integral Equation (AEFIE) [7] cannot be used as a direct replacement for $\bar{\mathbf{M}}$ in the RRWJ derivation, a simpler approach can be taken by making use of the argument principle.

It starts by noting that the Casimir force results from the relative perturbation of the quantum vacuum fields by the objects in question. The objects force the fluctuating vacuum fields to conform to the appropriate boundary conditions and in doing so change the energy density of the vacuum. The perturbation in the energy density due to the relative position of scatterers gives rise to the Casimir force. The calculation of the Casimir force on an object can be done by first calculating the Casimir energy (the normalized energy of the fluctuating fields) and taking the gradient of the energy with respect to the displacement of the object in question. If one can determine the eigenfrequencies of the field configurations that can satisfy the geometry's boundary conditions then the unnormalized energy of the fluctuating fields can be found via [8, 9]

$$\mathcal{E} = \sum_{\omega} \frac{1}{2}\hbar\omega \tag{4}$$

Normally the above pertains only to cases where the vacuum is located within a finite space, like a PEC cavity since the modes of an open problem are generally continuous. This can be addressed by first finding the energy when the scatterers are confined within a finite PEC cavity, in which case the modes are discretized, and then generalizing the result by finding the energy in the limit of the cavity growing to infinite size. Previous derivations of the Casimir force have made use of the argument principle to find the eigenmodes of the vacuum fields to define the energy density [9–12]. Assuming that there is some dispersion equation that describes the eigenmodes of the problem, the Casimir energy can be calculated by the argument principle. This is done by first noting that the argument principle states that

$$\frac{1}{2\pi i}\oint \phi(\omega)\frac{d}{d\omega}\ln f(\omega)d\omega = \sum_{i}\phi(\omega_0,\, i) - \sum_{j}\phi(\omega_\infty,\, j) \tag{5}$$

where ω_0, i are the zeros and ω_∞, j are the poles of the function $f(\omega)$ inside the contour of integration. Noting that the Casimir energy of a geometry is given by Equation (4), we can relate the Casimir energy with the contour integral from above by allowing the function $f(\omega)$ to evaluate to zero at the eigenfrequencies and ω_0, i to be the energy of the eigenmodes as defined by Equation (4). This is done by choosing a contour that runs along the imaginary frequency axis and encloses the right hand side of the complex frequency plane. The path integration that deviates from the imaginary axis evaluates to zero via Jordan's Lemma. Thus, using integration by parts and describing the integration along the imaginary axis via $\omega = ic\kappa$, we find

$$\mathcal{E} = \frac{\hbar c}{2\pi}\int_0^\infty d\kappa \ln\frac{f(ic\kappa)}{f_{norm}(ic\kappa)} \tag{6}$$

where the zeros of $f(\omega)$ correspond to the eigenmodes of the structure and $f_{norm}(\omega)$ is a normalization of $f(\omega)$ that is taken as the geometry when the objects are infinitely separated. The theoretical problem is then to find some function $f(\omega)$ that evaluates to zero at the natural frequencies of our Casimir geometry. This has previously been done using a closed form equation for the dispersion relations of the system however it can also be generalized to matrix approximations of the system.

The traditional EFIE for PEC objects is derived using the fact that the fields arising from currents induced on the surface of a PEC must cancel any excitation fields that are present. The resulting matrix equation is

$$\bar{\mathbf{Z}}\cdot\mathbf{J} = \mathbf{V} \tag{7}$$

where $\bar{\mathbf{Z}}$ is the matrix representation of the non-Wick rotated Green's operator, $\mathbf{J}$ is the vector representation of the current $\mathbf{J(r)}$, and $\mathbf{V}$ is the vector representation of the exciting fields. As previously stated, the eigenmodes of the quantum vacuum are those where the fluctuating fields can conform themselves to the boundary conditions of the geometry. In other words, the eigenmodes exist where we can have currents on the surface of the objects without the need of any excitation fields. These natural modes automatically satisfy the geometry's boundary conditions, and in the case of the EFIE matrix equation, they also satisfy the relation,

$$\bar{\mathbf{Z}}\cdot\mathbf{J} = \mathbf{0} \tag{8}$$

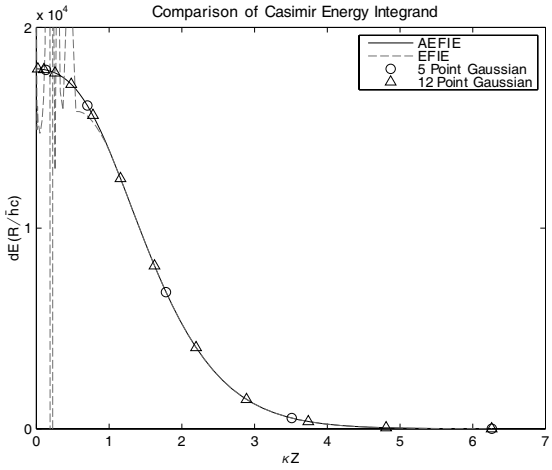

Figure 1: Comparison of the integrand for the Casimir Energy integral for the EFIE and A-EFIE formulations using single precision.

We can then conclude that $f = \det\bar{\mathbf{Z}} = 0$ for the natural frequencies. Using this new function for our argument principle's Casimir energy, applying the Wick rotation, and normalizing the energy with the energy of the problem when the objects are infinitely separated, we rederive Equation (1).

Two objections can be noted by the fact that the EFIE MoM problem assumes an open space. First, the modes of the open problem are continuous, and, second, due to the Sommerfeld radiation condition in the Green's operator the resulting modes are complex. The former point can be addressed by again assuming that the problem starts out confined to a finite PEC cavity which will approach the open problem by expanding the volume of the cavity to infinity. The effects of the cavity reflections can be incorporated into the Green's function and the overall matrix problem remains unchanged. In addition, an infinitesimal loss needs to be introduced into the cavity Green's function to allow for the Sommerfeld radiation condition to come out in the limit of the cavity to infinity. This changes the cavity Green's function into the retarded Green's function. The enclosed problem has discrete modes that can be summed up using the argument principle as described above. The resulting energy will become the Casimir energy in taking the limit of the volume of the PEC cavity to infinity, in which case the infinitesimally lossy cavity Green's function becomes the normal free-space Green's function.

However, the Green's function's infinitesimal loss factor turns the eigenfrequencies into complex numbers. One would expect the summation of the complex eigenmodes to result in a complex number but the result can be shown to still be real by the fact that the system is treated at imaginary frequencies. Under purely imaginary frequencies, the Kramers-Kronig relation states that the permittivity and permeability become real [13], resulting in a purely real dyadic Green's function and an associated purely real integrand. The physicality of using these complex eigenmodes to calculate the energy has been addressed in recent work which showed that the energy of the electromagnetic fields can still be expressed as the summation over the vacuum energies of the modes using imaginary frequencies despite the fact that the system was lossy [14, 15].

To demonstrate the flexibility of this approach, a low frequency method like the A-EFIE that would not be compatible with previous derivations is used to calculate the Casimir energy and force. It can be shown that the A-EFIE impedance matrix, which will be called $\bar{\mathbf{Z}}_A$, will have the same function $f(\omega) = \det\bar{\mathbf{Z}}_A = 0$ at the eigenfrequencies of the geometry per the above arguments. The A-EFIE impedance matrix can be then used as a direct replacement for the EFIE impedance matrix. Thus, the Casimir energy becomes,

$$\mathcal{E} = \frac{\hbar c}{2\pi}\int_0^\infty d\kappa \ln\frac{\det\bar{\mathbf{Z}}_A(\kappa)}{\det\bar{\mathbf{Z}}_{A,\infty}(\kappa)} \tag{9}$$

Using the sum of the eigenvalues as a means to find the determinants, the integrand of the Casimir energy can be calculated. It was seen that using A-EFIE results in a more accurate low frequency energy spectrum than using EFIE. While in general, double precision can give satisfactory results, Figure 1 shows that the A-EFIE and EFIE results for the Casimir energy start to depart from each other as the frequency drops when using single precision for the case of two PEC spheres.

The deviation in the calculated integration is a result of the location of the Gaussian points but the error in the EFIE result can be greater than 100% while the A-EFIE remains in agreement to almost single precision when compared with the double precision results. Similar results can be found for the Casimir force integrand and for the comparison between the total calculated Casimir force.

3. CONCLUSION

This paper presents an alternative derivation for the Casimir energy and force that has been derived using the RRWJ method. This new derivation presents a simple procedure that can be used to easily adapt different CEM methods to overcome the difficulties when using traditional solvers like EFIE. As we have shown, the importance of the low frequency content of the integrand can give rise to erroneous results when relaxing the computational precision due to low frequency breakdown and this can be addressed through the use of the low frequency A-EFIE. Future work will focus around providing extended functionality to dielectric objects and even allowing for new physical representations using the Equivalence Principle Algorithm (EPA) [16]. In the EPA, the problem is described using scattering and translation operators and their matrix representations. This results in a new formulation that is based around different physical representations of the problem. The result is one that is conceptually similar as previous work [6], but once again avoids the complicated and strict derivation.

REFERENCES

1. Emig, T., N. Graham, R. L. Jaffe, and M. Kardar, "Casimir forces between arbitrary compact objects," *Phys. Rev. Lett.*, Vol. 99, 2007.
2. Reid, M. T. H., A. W. Rodriguez, J. White, and S. G. Johnson, "Efficient computation of casimir interactions between arbitrary 3d objects," *Phys. Rev. Lett.*, Vol. 103, 2009.
3. Reid, M. T. H., J. White, and S. G. Johnson, "Computation of casimir interactions between arbitrary three-dimensional objects with arbitrary material properties," *Phys. Rev. A*, Vol. 84, 2011.
4. Li, H. and M. Kardar, "Fluctuation-induced forces between rough surfaces," *Phys. Rev. Lett.*, Vol. 67, No. 23, 3275–3278, 1991.
5. Poggio, A. J. and E. K. Miller, *Integral Equation Solutions of Three Dimensional Scattering Problems*, Permagon Press, Elmsford, NY, 1973.
6. Rahi, S. J., T. Emig, N. Graham, R. L. Jaffe, and M. Kardar, "Scattering theory approach to electrodynamic casimir forces," *Phys. Rev. D*, Vol. 80, No. 8, 085021, 2009.
7. Qian, Z.-G. and W. C. Chew, "Fast full-wave surface integral equation solver for multiscale structure modeling," *IEEE Trans. Antennas Propag.*, Vol. 57, 3594–3601, November 2009.
8. Milonni, P. W., *The Quantum Vacuum: An Introduction to Quantum Electrodynamics*, Academic Press, San Diego, CA, 1994.
9. Barash, Y. S. and V. L. Ginzburg, "Electromagnetic fluctuations in matter and molecular (van-der-waals) forces between them," *Sov. Phys. Usp.*, Vol. 18, No. 5, 305–322, 1975.
10. Langbein, D., "The macroscopic theory of van der waals attraction," *Solid State Comm.*, Vol. 12, 853–855, 1973.
11. Schram, K., "On the macroscopic theory of retarded van der waals forces," *Phys. Lett. A*, Vol. 43, No. 3, 282–284, 1973.
12. Lambrecht, A. and V. N. Marachevsky, "New geometries in the casimir effect: Dielectric gratings," *J. Phys. Conf. Ser.*, Vol. 161, 1–8, 2009.
13. Chew, W. C., *Waves and Fields in Inhomogeneous Media*, IEEE Press, New York, 1995.
14. Rosa, F. S. S., D. A. R. Dalvit, and P. Milonni, "Electromagnetic energy, absorption, and casimir forces: Uniform dielectric media in thermal equilibrium," *Phys. Rev. A*, Vol. 81, 033812, 2010.
15. Rosa, F. S. S., D. A. R. Dalvit, and P. Milonni, "Electromagnetic energy, absorption, and casimir forces. II. Inhomogeneous dielectric media," *Phys. Rev. A*, Vol. 84, 053813, 2011.
16. Li, M.-K., W. C. Chew, and L. J. Jiang, "A domain decomposition scheme based on equivalence theorem," *Microwave and Opt. Tech. Lett.*, Vol. 48, No. 9, 1853–1857, 2006.

Radio Frequency Identification Devices (RFID) in Prevention of Medication Errors: A Review

M. D. Marcos[1], **S. de Miguel**[2], **and V. Ramos**[2]

[1]Agency Laín Entralgo for Education and Health Research, Regional Ministry of Health, Madrid, Spain
[2]Health Institute Carlos III, Telemedicine and e-Health Research Unit, Madrid, Spain

Abstract— Pervasive healthcare has been widely approved to be the next generation form of healthcare, in which distributed, patient-centric and self-managed care is emphasized compared to the traditional hospitalized, staff-centric and professional managed care. Poor compliance for medication has become a well-known problem all around the world. It is defined as the patients lack of compliance to follow the prescription (dosage, schedule, etc.) from physicians. Non-compliance for regimens causes worsening of disease, death and increase of healthcare costs. One of the technological options are low-cost information gathering and dissemination devices, such as sensors and RFID tags that facilitate fast-paced interactions among the objects themselves as well as the objects and persons in any place and at any time. For some years now the RFID technology has been considered a very promising option to solve that healthcare problem. Consequently, this work aims to expose the technological advances produced from 2001 to 2011 and which factors might explain both the RFID penetration rate in healthcare and RFID successes on preventing medical errors.

1. INTRODUCTION

The integration of RFID with other pervasive computing technologies such as communications protocols and wireless sensor networks is leading to further innovative applications in the telemedicine area [1], particularly for ubiquitous persistent monitoring of elderly or disabled people, as well as for patient follow-up during rehabilitation phase that have to self-manage their medication. Poor compliance for medication has become a well-known problem all around the world [2]. It is defined as the patients lack of compliance to follow the prescription (dosage, schedule, etc.) from physicians. Non-compliance for regimens causes worsening of disease, death and increase of healthcare costs.

Medication errors have been the focus of several studies since 2000 when the USA Medicine Institute reported on their quantity and severe side effects [3, 4]. For some years now the RFID technology has been considered a very promising option to solve that healthcare problem but both its ratio of penetration as well as their real effectiveness remain unknown [5]. Consequently, this work aims to review the technological advances produced from 2001 to 2011 which have been based on radiofrequency identification in order to preserve the Patients five Rights in administering medications — 1. Right patient. 2. Right time and frequency of administration. 3. Right dose. 4. Right route of administration and finally. 5. Right drug.

2. METHODS AND MATERIAL

2.1. Search Strategy

Both automatic and manual searches have been carried out on conference proceedings and other engineering journals included in IEEExplore to identify relevant articles published between 2001 and 2011.

The keywords used in searching articles for effective results were a combination of RFID or radiofrequency identification and also patient safety or medication error with 55 papers as result.

A second search using RFID or radiofrequency identification plus the single word medication give 53 papers more. After eliminating both duplicates and other inaccurate results, there were 75 papers finally taken into account.

2.2. Data Synthesis

Two authors independently reviewed the selected papers in order to classify them into one of the following categories at least:

(a) Id: Identification (patients or health professionals).
(b) It: Information technology which includes two subcategories B.1. Information management (Im) and B.2. Communication systems (Cs).

(c) Ta: Asset tracking.

(d) Nm: New Materials.

(e) Aal: Ambient assisted living which illustrates more complex scenarios including patients homes.

A more careful reading of the summaries showed that selected papers not always matched with the focus of this review. Papers located using search engines contained the words we are looking for but not always were they in the proper context. Search engines usually work using orthographical criteria and not semantic one and this is a great weakness in automated searches. As a consequence, only 23 papers were specifically dedicated to preventing the negative effects of medication errors and all of them were selected for an entire reading. However, about 31 more described systems, platforms or workflows developed with other aims but which could be used to avoid medication errors in the future.

3. RESULTS

From 2001, the number of papers which incorporate RFID technology to manage medication error seemed to have increased significantly, as Figure 1 shows.

These 75 papers were classified into the six categories we have proposed attending the year of publication, as Figure 2 shows.

However, a more careful reading showed, as it is written above, that although papers mention this subject (medication errors), in fact they are not dedicated to avoid them. As Figure 4 shows, there is a category which is gaining importance and attracting the interest of researchers, the Ambient Assisted Living, characterized more complex scenarios, where RFID tags and readers are combined with sensors for working together in a wireless network, finally connected via Internet to remote information repositories of data and software. Reducing hospital admissions and length of stay is a main objective in order to save economical and human resources, as well as to improve patients quality of live. However, most of these outpatients are elderly or have temporary or permanent disability, and many have no caregivers to help them. Then, they are solely responsible for ensuring their own five Rights in administering medications and technological advances can be very useful to fulfill that goal. Then, from 2007 and especially in 2010 and 2011, the number of papers dedicated to ambient assisted living in patients home has been increased and they show that RFID technology can provide useful information.

4. DISCUSSION

On the whole, the evaluation of the methodological quality of studies has been a very difficult task because of the heterogeneity of the papers included in the review. This is due to the fact that there is a lack of published papers in the first two years considered, as is showed in Figure 1. Most of the papers included only partially cover the subject matter. The research performed for this document clearly demonstrates the high number of publications during the recent years on this

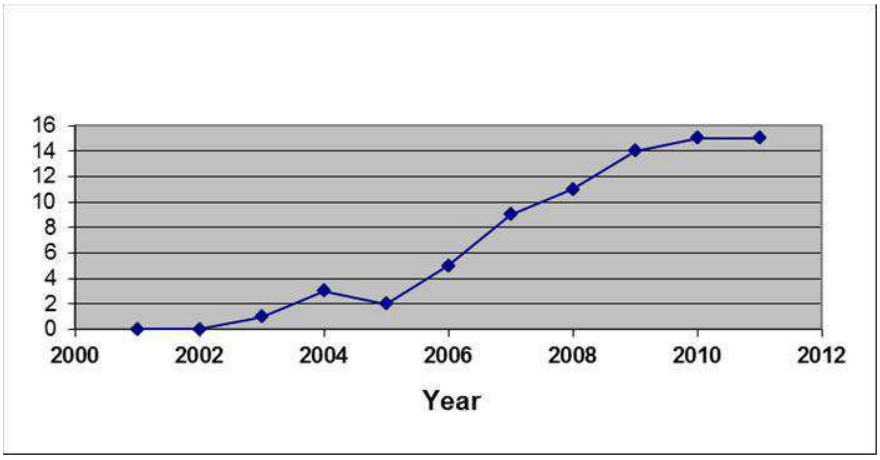

Figure 1: RFID technology to manage medication error from 2001 to 2012 (Npapers: 75).

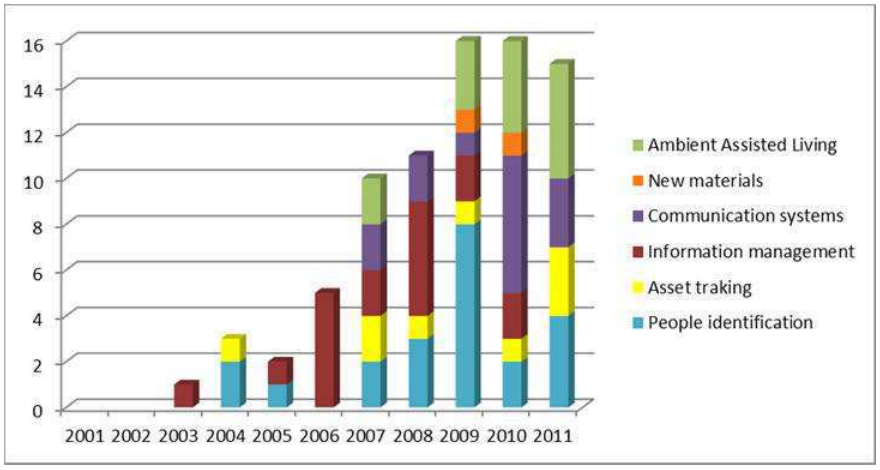

Figure 2: RFID applications areas in terms of functionality (Npapers: 75).

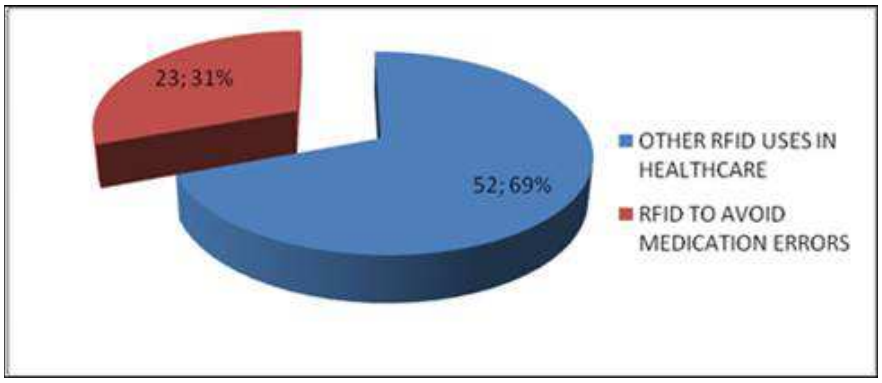

Figure 3: Papers that use RFID to avoid medication errors (Npapers 75).

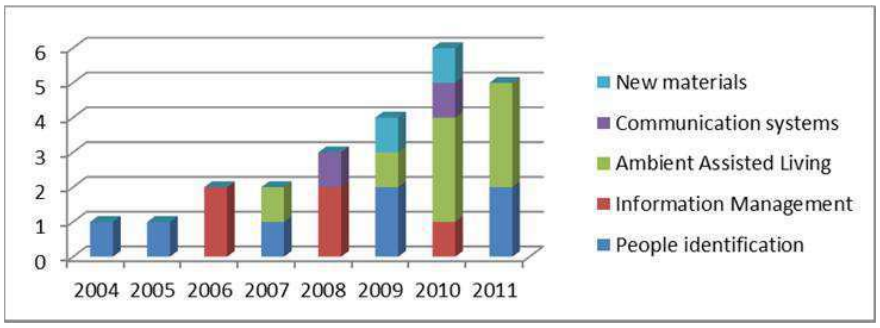

Figure 4: RFID applications areas in terms of functionality (Npapers: 23).

subject. However, despite the large number of studies found, there is a lack of publications evaluating effectiveness of RFID and most of the studies only cover technological issues. Regarding the effectiveness of RFID and radiofrequency identification systems in patients safety and medication errors prevention, the scarcity of studies is evident and it can be observed in Figure 3. The absence of homogeneous criteria among authors to choose keywords to describe their papers may have an undesirable consequence: an indeterminate number of papers may have been omitted by search engines. To confirm the usefulness of RFID technology in preventing medication errors there is much still to do. Among other things, it should improve the quality and reliability of the signal, and there are some works that address current limitations of antennas.

Because most of the papers are technological, this research will continue with the evaluation of other data base like Pubmed, Embase + Medline, Health Systems Evidence, etc., in order to identify additional relevant studies which exemplify the penetration of these technologies in real

work flows.

5. CONCLUSIONS

Pervasive healthcare has been widely approved to be the next generation form of healthcare, in which distributed, patient-centric and self-managed care is emphasized comparing to the traditional hospitalized, staff-centric and professional managed care. The integration of RFID with other pervasive computing technologies such as communications protocols and wireless sensor networks is leading to further innovative applications in the tele-medicine area, particularly for ubiquitous persistent monitoring of elderly or disabled people, as well as for patient follow-up during rehabilitation phase that have to self-manage their medication.

Poor compliance for medication has become a well-known problem all around the world. It is defined as the patients lack of compliance to follow the prescription (dosage, schedule, etc.) from physicians. Non-compliance for regimens causes worsening of disease, death and increase of healthcare costs. In this context, Ambient Assisted Living (AAL) where objects are being capable of identifying, locating, sensing and connecting and thus leading to new forms of communication between people and things and things themselves, offers new possibilities to support outpatients in their daily routine to allow an independent and safe lifestyle without caregivers. Developing real smart objects have to be the next step, including ingestible or subcutaneous sensor tags.

ACKNOWLEDGMENT

Financial support of this research was partially provided by the research grant DGPY 1301/08.

REFERENCES

1. European Commission Information Society and Media, "Internet of things in 2020: Roadmap for the future," Infso D.4 Networked Entreprise & RFID, Infso G.2 Micro & Nanosystems, Working Group RFID of the ETP EPoSS., 2008.
2. National Community Pharmacists Association, "Take as directed: A prescription not followed," Research Conducted by the Polling Company, 2006.
3. Kohn, L. T., J. M. Corrigan, and M. S. Donaldson, "To err is human: Building a safer health system," National Academy Press, Committee on Health Care in America, Institute of Medicine, Washington, DC, 1999.
4. Aspden, P., J. A. Wolcott, J. Lyle Bootman, and L. R. Cronenwett, "Preventing medication errors," National Academy Press, Committee on Identifying and Preventing Medication Errors, Institute of Medicine, Washington, DC, 2007.
5. Vilamovska, A. M., E. Hatziandreu, H. R. Schindler, C. van Oranje-Nassau, H. de Vries, and J. Krapels, "Study on the requirements and options for RFID application in healthcare — Identifying areas for radio frecuency identification deployment in healthcare delivery," A Review of Relevant Literature, Rand Corporation, 2009.

Analysis of Electromagnetic Compatibility of Wireless Ambient Assisted Living Devices

S. de Miguel[1], **J. García**[1], **D. Rubio**[2], **O. Suarez**[2], **and V. Ramos**[1]

[1]Health Institute Carlos III, Telemedicine and e-Health Research Unit, Madrid, Spain
[2]General Direction of Telecommunications and Information Technologies
Electromagnetic Compatibility Services, Madrid, Spain

Abstract— There are no previous studies about the influence of the use of social alarms in the electromagnetic (EM) environment. Two models of social alarm devices were chosen from among the most used in telecare monitoring activities. After obtaining the radiation pattern and determining the direction maximum radiation, the Equivalent Isotropically Radiated Power (EIRP) and the power density were calculated for each of the tested models. The results recorded were compared with the levels set by the national and international regulations to analyse the exposure to EM fields of people using and in the proximity of social alarm devices in assisted environments.

1. INTRODUCTION

Social alarm devices are used to assist patients, elderly and disabled people in distress situations, with the possibility of the inclusion of many types of conventional alarms (gas, smoke, flood, etc.). Environments equipped with such wireless, sensitive and responsive devices are referred to as being Ambient Assisted Living (AAL).

The increasing average age of people and the consequent rise of chronic diseases will result in a dramatic growth of the need for assistance and healthcare within the years to come. There is an increasing demand for outpatient care accessibility, maintaining and restoring health, as well as maximizing the independence of patients [1]. Social alarms devices provide direct benefits when applied in healthcare environments. The special implication of these devices with welfare and safety requirements involves a special interest in its operating conditions as well as in promoting correct habits of usage. The use of such devices and transmission sources based on short range wireless technologies involves the increase of the levels of electromagnetic (EM) fields in residential environments.

For some years now the short range technology has been considered a very promising option to cope with healthcare monitoring challenges. Some models of social alarm devices are based on a wide range of wireless technologies (RFID, UWB, NFC, WLAN, etc.). Specific architectures of short range technologies have been adapted for medical applications (ZigBee Health Care and Bluetooth Health Device Profile). Other type of social alarm devices operate in its own working frequency, from 869.2 to 869.25 MHz in accordance with European standards (2011/829/EU: Commission Implementing Decision of 8 December 2011 amending Decision 2006/771/EC on harmonisation of the radio spectrum for use by short-range devices).

People using or in the proximity of short range devices (SRD) are exposed to radio signal emitted from them. Laboratory measurements have been carried out to characterize and analyze the RF emissions of the selected devices. The objectives were to establish the radiation pattern (angular distribution of electric field strength around each type of device), identify the orientation at which the electric field is maximum, and calculate the power density and the Equivalent Isotropically Radiated power (EIRP) for each of the tested devices.

2. METHODS AND MATERIAL

For this work, two models of social alarm devices were chosen from among the most used in telecare monitoring activities. These devices, Tunstall AMIE+ (device 1) and Neat Atom (device 2), are shown in Figure 1. Their working frequency is 869.21 MHz.

The measurements were performed in a semianechoic chamber, shown in Figure 2. The room has dimensions of 9.76 m × 6.71 m × 6.10 m, the walls are lined with a foam based radiofrequency absorber material (RANTEC Ferrosorb300) specified to have a reflection/absorption coefficient of −18 dB at the frequency of 869.21 MHz.

All of the measurements during this work were made in the far field region with respect to the sources. At 869.21 MHz, the wavelength is about 34 cm, which means the reactive near field

(a) (b)

Figure 1: Selected models of social alarms devices: (a) Tunstall AMIE+. (b) Neat atom.

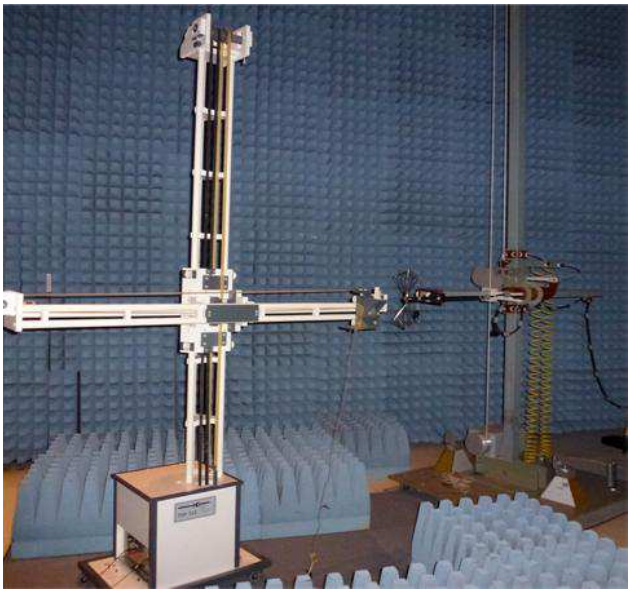

Figure 2: Measuring antenna and positioners required for the E-field measurements inside the anechoic chamber.

extends to around 5.5 cm from the source (based on the usual $\lambda/2\pi$ criterion, where λ is the wavelength). The antennas of the social alarm devices are no more than around 5 cm in size, and they are integrated inside the casing device. Hence, the radiating near field extends no further than around 1.5 cm at 869.21 MHz (based on the usual $2D^2/\lambda$ criterion, where D is the maximum source dimension).

The devices under test were mounted on a manual positioning device with a EMCO 1060 motor, allowing the device to be rotated and permitting the measuring antenna to sample the radiation pattern at any angle.

All the measurements were performed in vertical and horizontal polarizations, a positioner with a EMCO 1051 motor allows the changes of the position of the measuring antenna.

After obtaining the radiation pattern, the position of each tested device at which the electric field strength is maximum was fixed. In that position the electric field strength was measured as a function of distance in horizontal and vertical polarization in the far field region in steps of 10 cm, from 0.2 m to 1.7 m. The positioning device used to determain the distances was a FSM 016, with an HD10 controller to move it automatically.

The measurements were carried out with an EMI Test Receiver ESIB26, Rhode & Schwartz with a frequency range of 20 Hz–26.5 GHz, and the measuring antenna is a VBAA-9144 Schwarzbeck biconical antenna with a frequency range of 80 MHz–1 GHz.

The EMI test receiver calculates the electric field strength taking into account the antenna factor and the cable attenuation, according to the following equation [2]:

$$E = V + AF + ATT \tag{1}$$

where E is the electric field strength (dBμV/m), V is the measured voltage (dBμV), AF is the antenna factor (dBm^{-1}), and ATT is the cable attenuation (dB).

After obtaining the horizontal and vertical components, the total field strength was calculated.

The power density was derived using the following equation:

$$S = \frac{E^2}{377} \tag{2}$$

where the unit of S is W/m^2 and E has now been converted to linear units.

The EIRP of each tested device was calculated for comparison with the emission limit of 16.4 mW set by standard regulations [3, 4].

EIRP is the power that would have to be emitted if the antenna were isotropic in order to produce a power density equal to that observed in the direction of maximum gain of the actual antenna. The EIRP is obtained from the power density as follows:

$$EIRP = 4\pi r^2 S_{\max}(r) \tag{3}$$

where EIRP is in units of W, r is the distance to the antenna in meters, and $S_{\max}(r)$ is the maximum power density measured at each distance in W/m^2.

The EIRP was calculated using the maximum measurement of power density, so the measurements of the electric field strength were realized in the direction of maximum radiation.

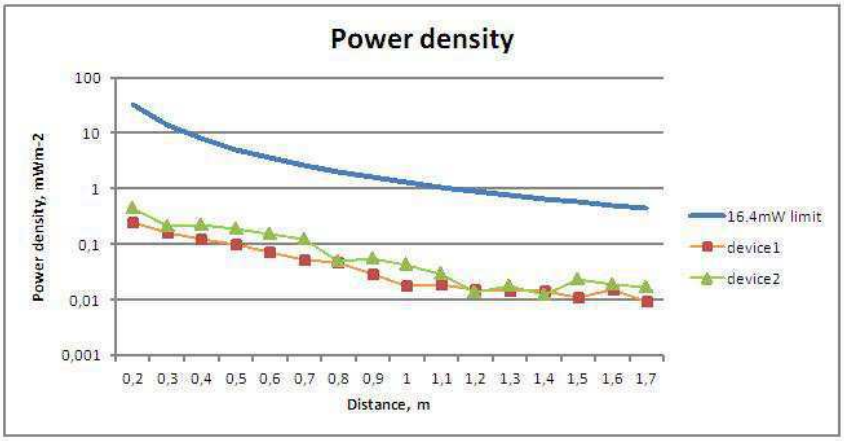

Figure 3: Variation of power density and the *EIRP* limit as a function of distance for two social alarm devices.

Table 1: Maximum electric field strength (E), power density (S), and *EIRP* for the tested devices.

	Device 2			**Device 1**		
Distance (m)	***E* (mV/m)**	***S* (mW/m^2)**	***EIRP* (mW)**	***E* (mV/m)**	***S* (mW/m^2)**	***EIRP* (mW)**
0.2	310.662	0.256	0.129	419.038	0.466	0.234
0.3	249.879	0.166	0.187	283.527	0.213	0.241
0.4	219.518	0.128	0.257	289.373	0.222	0.447
0.5	196.383	0.102	0.321	267.815	0.190	0.598
0.6	164.764	0.072	0.326	243.292	0.157	0.710
0.7	142.712	0.054	0.333	215.788	0.124	0.761
0.8	134.910	0.048	0.388	138.447	0.051	0.409
0.9	105.952	0.030	0.303	146.854	0.057	0.582
1	83.361	0.018	0.232	125.115	0.042	0.522
1.1	85.096	0.019	0.292	104.006	0.029	0.436
1.2	76.252	0.015	0.279	72.701	0.014	0.254
1.3	73.644	0.014	0.306	83.463	0.018	0.392
1.4	73.285	0.014	0.351	68.100	0.012	0.303
1.5	64.293	0.011	0.310	94.780	0.024	0.674
1.6	75.860	0.015	0.491	84.643	0.019	0.611
1.7	59.532	0.009	0.341	81.043	0.017	0.633

3. RESULTS

Figure 3 shows the variation of the power density as a function of the distance for the test devices operating at 869.21 MHz. The power density calculated from an EIRP equal to 16.4 mW limit is shown for comparison. The ordinate axis is represented in logarithmic scale to improve the comparison between the obtained results and the set limit of 16.4 mW.

Overall, the power density plots calculated from maximum electric field strength as a function of distance broadly follow the expected inverse-square dependence on the distance.

Table 1 shows the values of the maximum electric field strength (E), power density (S), and *EIRP* as a function of the distance for each of the devices under test.

4. CONCLUSIONS

This paper intends to address the EM environment actually present in homes regarding the assessment for potential safe use of social alarm devices. The main finding of this study is that the electric field strength and the EIRP around social alarm devices are well within the guidelines set by the ICNIRP and the thresholds set by standard regulations.

All the field strengths recorded in this study are well bellow the corresponding ICNIRP reference level of 40 V/m defined for the general public at the working frequency [5]. It means E field level in healthcare environment at home is apparently safe according with the health and safety requirements regarding the exposure of patients, professionals and general public for protecting against possible health effects from nonionizing radiation.

The recorded values of EIRP are well below the level that would be expected based on 16.4 mW, set by the national and international regulations: Commission Implementing Decision of 8 December 2011 amending Decision 2006/771/EC on harmonisation of the radio spectrum for use by short-range devices (2011/829/EU) [3], and the Spanish National Table of Spectrum Location (ITC/332/2010) [4], so the tested social alarm devices operate in safe conditions under the set limits of EIRP.

ACKNOWLEDGMENT

This work has been realized thanks to the help of the Electromagnetic Compatibility Laboratory of the General Direction of Telecommunications and Information.

REFERENCES

1. Carranza, N., V. Ramos, F. G. Lizana, et al., "A literature review of transmission effectiveness and electromagnetic compatibility in home telemedicine environments to evaluate safety and security," *Telemed. J. e-Health*, Vol. 16, No. 7, 530–541, 2010.
2. NPL, "A guide to power flux density and field strength measurement," National Physical Laboratory, The Institute of Measurement and Control, Middlesex, London, UK, 2004.
3. 2011/829/EU, "Commission implementing decision of 8 December 2011 amending decision 2006/771/EC on harmonisation of the radio spectrum for use by short-range devices," *Official Journal of the European Union*, 2011.
4. ITC/332/2010, Order of 12 February 2011, Which Approves the National Table of Spectrum Allocation, 2011.
5. ICNIRP, "Guidelines for limiting exposure to protection time-varying electric, magnetic and electromagnetic fields (up to 300 GHz)," International Commission on Non-Ionizing Radiation, 1998.

A Thorough Analysis of SAR Evaluation in Human Head Models

A. O. Rodrigues and J. A. Ramirez
Universidade Federal de Minas Gerais, Belo Horizonte, Minas Gerais, Brazil

Abstract— This paper presents a thorough evaluation of the specific absorption rate (SAR) in the human head due to mobile telephones operating at 900 MHz, 1.8 GHz, 2.1 GHz and 2.4 GHz. The evaluation is performed using two complimentary approaches: measurements and computational simulations. The measurements were performed using a DASY 4 system in two models of the human head: a at and a homogeneous head model. The numerical simulations were carried out using the finite-difference time-domain (FDTD) method for two models of the human head: a homogeneous and a heterogeneous head model, the latter is composed of 17 different materials. All SAR measurements are in agreement with the IEEE Std1528. The numerical results for the homogeneous head model resulted in maximum differences in the $SAR_{1\,g}$ of 2.6% for 900 MHz, 8.5% for 1.8 GHz and 11.8% for 2.1 GHz, in comparison with the IEEE Std1528, values that are in agreement with the literature. The simulations of a commercial mobile telephone operating with power of 23.44 mW (13.7 dBm) at 2.1 GHz, and at 2.4 GHz, in the heterogeneous head model, resulted in the worst case the maximum $SAR_{1\,g}$ of 1.06 W/kg and 1.27 W/kg, respectively, at the fat region of the head; values that are smaller than 1.6 W/kg/1 g indicated by the IEEE guidelines.

1. INTRODUCTION

In the past fifteen years, the rapid and widespread adoption of wireless devices by our society, particularly cellular telephones, has raised public concern on whether the proximity of the cellular phone to the human head may cause any adverse health effects.

In order to evaluate these effects, dosimetry is used to determine the amount of power in various parts of the body exposed to the electromagnetic fields. The effects of this power deposition are quantified in the specific absorption rate (SAR) and have been used to define guidelines and limits for exposure [1, 2]. These standards have often served as basis for regulations in several countries. To assess if a device is within the limits defined by the guidelines, the dosimetry of fields can be performed using two complimentary methods: a) measurements; and computational simulations.

There have been some contributions on the calculation of the specific absorption rate (SAR) in the human head [3, 4], amongst others, and the implications of the new relaxed IEEE safety standard [5]. Recent studies have been concerned with the new frequencies used in telephones, specifically 2.1 GHz for the 3G generation and the fact that mobile phones and other wireless devices now also operate in 2.4 GHz [6].

It is recognized that the head model may lead to uncertainties in the SAR calculations, due to:

1. The number of tissues: the use of homogeneous models has been shown to result in an overestimation of approximately 30% for the 1 g averaged SAR [7].
2. Resolution of the model: it has a direct impact on the calculated peak SAR, as it is a result of the electric field in each point of the domain. A smaller resolution tends to provide higher peak SAR values.
3. Presence of the pinna: it has been shown that it results in a smaller value of SAR [8]. That is a consequence of two facts: the distance of the model from the antenna is larger for models with pinna; and the distribution of the SAR is more concentrated in models without pinna.

In terms of SAR measurements, the IEEE Std 1528 [8] is the main reference for electromagnetic fields in the range 300 MHz–3 GHz. It uses the definition: $SAR = \sigma|E|^2/\rho$, where σ is the electrical conductivity, $|E|$ is the rms magnitude of the electric field and ρ is the mass density of the medium. The current state-of-the-art indicates that the E-field measurement is carried out by scanning within a thin anatomically phantom shell filled with a tissue equivalent liquid, typically using a multi-axis robot to position a miniature probe.

In this paper we present a thorough analysis of the SAR induced in the human head due to the use of cellular telephones. Particular emphasis is given to comparisons of the numerical results between the homogeneous and heterogeneous head models.

Table 1: Dielectric property measurements.

Frequency	Value	IEEE Std 1528 [8]		Measured
		Acceptable	Desired	
900 MHz	ε_R [-]	39.4 to 43.6	41.5	41.6
	σ [S/m]	0.92 to 1.02	0.97	0.99
1.8 GHz	ε_R [-]	38 to 42	40.0	38.11
	σ [S/m]	1.33 to 1.47	1.40	1.43

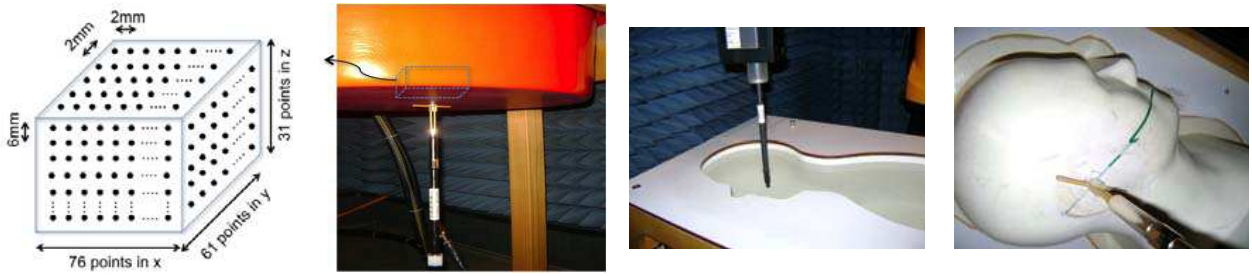

(a) (b) (c) (d)

Figure 1: Measurement grid and scanning setup.

2. MATERIALS AND METHODS

This section is organized in two parts. The first part describes how the SAR is measured and the second how it is calculated using the finite difference time domain method. In both methods, the SAR is normally evaluated over a 1 g or 10 g of tissue [8]. The maximum values allowed for exposure for the general public are 1.6 W/kg/1 g (head) and 4 W/kg/10 g (members), respectively [1].

2.1. SAR Measurements

All measurements were performed at the CPqD, Brazil, using a DASY4 Systems provided by SPEAG, following [8]: 1) Setup and calibration of the probe, the phantom, verification of the dielectric parameters and system validation; 2) Configuration of the devices to verify the operating conditions; 3) Positioning of the device with respect to the phantom; 4) Scanning procedures for determination of the peak spatial-average SAR locations and values; 5) Applicability of the test procedure for testing to an individual device.

Setup of dielectric properties The dielectric parameters of the liquid were verified before and after each measurement and the temperature of the liquid was monitored at all times, resulting the values presented in Table 1.

Measurements of the power irradiated were performed to validate the source of electromagnetic fields, resulting in a total irradiated power of 16 dBm. In order to compare $\mathrm{SAR}_{1\,\mathrm{g}}$ and $\mathrm{SAR}_{10\,\mathrm{g}}$ with [8], a conversion was performed to calculate the equivalent values for a radiated power of 1 W.

Positioning of the device and scanning procedures Figure 1(a) shows the measurement grid used, which is composed by 76 points in x, 126 points in y and 31 points in z, spaced by 2 mm in x and y directions, and 6 mm in z direction, respectively. The center of the grid was set at the peak SAR point defined by a pre-scan. This grid was used for the at and homogeneous phantoms at 900 MHz and 1.8 GHz. Figure 1(b) shows the at phantom with the dipole in detail. Figures 1(c) and (d) illustrate details of the dipole adjustment in the homogeneous model.

2.2. Numerical Simulations

There are six steps to perform the numerical calculation of $\mathrm{SAR}_{1\,\mathrm{g}}$ and $\mathrm{SAR}_{10\,\mathrm{g}}$: 1) First, the physical models must be constructed to represent the domain; 2) The next step is to define the electromagnetic source; 3) Using a numeric method, the electric ($\vec{E}$) and magnetic fields ($\vec{H}$) are calculated in each point of the domain; 4) Once steady state is reached, the maximum value of electric field ($|E|$) is calculated for each point of the domain; 5) Then, the SAR is calculated in each point of the domain. The cell where the maximum value of SAR occurs is the Peak SAR cell; 6) Finally, two cubes are defined around the Peak SAR cell, one with 1 g mass and one with 10 g mass. All values of SAR in the cells inside that cube are added and this value is divided by the number of cells, obtaining the average SAR in 1 g and 10 g.

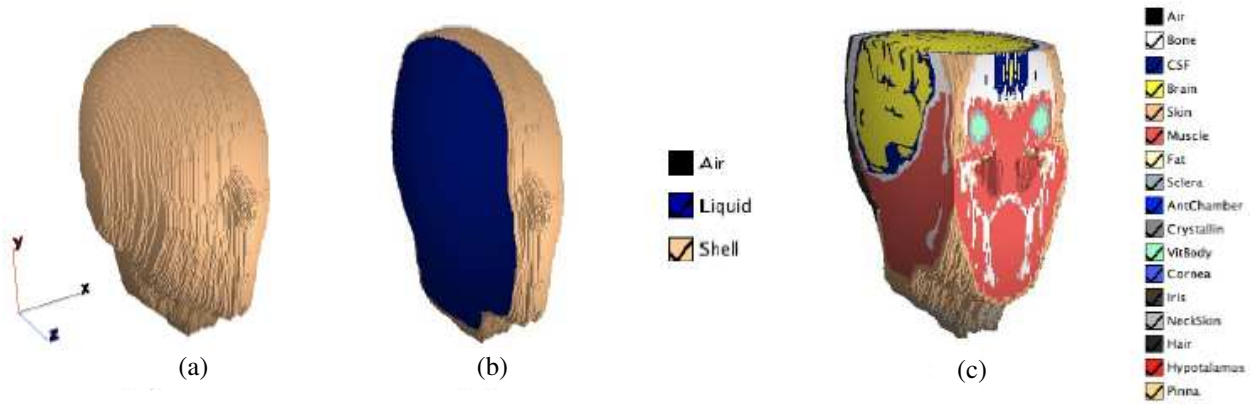

Figure 2: (a) Head model. (b) Homogenous model. (c) Heterogeneous model (cuts to show the internal tissues).

Table 2: SAR measurements.

Model	SAR [W/kg]	900 MHz			1.8 GHz		
		Std1528	FDTD	Error (%)	Std 1528	FDTD	Error (%)
Flat	1 g	10.8	10.24	5.2	38.1	37.8	0.5
	10 g	6.9	6.62	4.1	19.8	19.66	0.7
Homog.	1 g	10.8	10.38	3.9	38.1	37.64	1.2
	10 g	6.9	6.74	2.4	19.8	20.05	1.3

2.2.1. Numerical Head Models

Three models were implemented. The flat phantom is composed of air, a 2 mm plastic shell, internal liquid, dimensions and physical properties as suggested by the IEEE Std 1528 [8]. The homogeneous and heterogeneous head models have a resolution of 1.15 mm × 1.52 mm × 1.34 mm in x, y and z directions, respectively, and are composed of 296 cells in x, 188 cells in y and 296 cells in z, resulting in 16.47 million cubic cells and a total size of 34 cm × 28.6 cm × 39.7 cm. The physical properties of the homogeneous and heterogeneous models can be found at [8, 9]. Figure 2 illustrates the homogeneous and heterogeneous head models.

2.2.2. Electromagnetic Field Source

The source of the electromagnetic fields is a half wavelength dipole for 900 MHz, 1.8 GHz, 2.1 GHz and 2.4 GHz, with a radiated power (P_r) of 1 W as defined by [8]. This dipole was located parallel to the y axis, the gap was located in the center of the ear of the phantom in the x and y directions. The dipole has a separation of $s = 15$ mm (900 MHz) or $s = 10$ mm (1.8 GHz, 2.1 GHz and 2.4 GHz) from the liquid inside the phantom. The source was implemented as a thin dipole as presented in [11]. A commercial cellular phone operating at 900 MHz, 1.8 GHz, 2.1 GHz and 2.4 GHz with a power of 23.44 mW (13.7 dBm) was also considered.

2.2.3. Electromagnetic Field Calculation

The electric ($\vec{E}$) and magnetic fields ($\vec{H}$) are calculated in each point of the domain using the finite-difference time-domain method (FDTD), further details can be found in [10, 11].

2.2.4. Maximum Electric Field and Peak SAR

After the electromagnetic fields reach steady state, the maximum value of electric field ($|E|$) for each point of the domain is calculated. Taking the maximum value of electric field (E_0), the SAR is calculated using conductivity $\text{SAR} = \sigma|E|^2/\rho$, where ($\sigma$) and ($\rho$) are the conductivity and density of each point.

2.2.5. Calculation of 1 g and 10 g of SAR

To calculate SAR averaged in 1 g and 10 g, two different methods were investigated: a) IEEE Std 95.3 [12] that specifies that the SAR must be averaged using a 1 g and a 10 g cube that contains the peak SAR; and b) making the cube grow continuously until the needed tissue mass is obtained (1 g or 10 g).

Table 3: FDTD SAR simulation — flat and homogeneous head models.

Model	SAR	900 MHz			1.8 GHz			2.1 GHz		
	[W/kg]	Std1528	FDTD	Error (%)	Std 1528	FDTD	Error (%)	Std 1528	FDTD	Error (%)
Flat	1 g	10.8	11.2	3.2	38.1	38.2	0.3	44.0	43.0	2.2
	10 g	6.9	7.3	5.1	19.8	20.6	4.0	21.9	22.2	1.5
Homog.	1 g	10.8	10.5	2.6	38.1	34.8	8.5	44.0	44.0	11.8
	10 g	6.9	6.9	0.2	19.8	20.9	5.4	21.9	22.8	4.2

Table 4: FDTD SAR simulation — heterogeneous head model.

Tissues	SAR [W/kg]							
	900 MHz		1.8 GHz		2.1 GHz		2.4 GHz	
	1 g	10 g	1 g	10 g	1 g	10 g	1 g	10 g
CSF	0.03	0.02	0.05	0.04	0.04	0.02	0.06	0.04
Brain	0.15	0.09	0.12	0.06	0.13	0.05	0.11	0.02
Skin	0.06	0.04	0.05	0.04	0.06	0.03	0.04	0.02
Muscle	0.16	0.09	0.09	0.24	0.58	0.26	0.68	0.26
Fat	0.24	0.13	0.75	0.31	1.06	0.31	1.27	0.34
Eye	0.01	0.00	0.01	0.00	0.01	0.00	0.01	0.00
Hypot.	0.03	0.02	0.03	0.02	0.02	0.01	0.02	0.01

3. RESULTS

3.1. SAR Measurements

The measured values for 900 MHz and 1.8 GHz, given in Table 2, are in good agreement with the IEEE Std 1528 [8], presenting a maximum error of 5.2% for $SAR_{1\,g}$ in at phantom at 900 MHz and 1.3% for the $SAR_{10\,g}$ in homogeneous phantom at 1.8 GHz. Considering the good agreement, these results will be used to validate part of the simulation results.

3.2. FDTD Simulations

3.2.1. Flat and Homogeneous Head Model

Table 3 shows the SAR numerical results for the at phantom and the homogeneous head model. The numerical results for the at phantom are in good agreement with the values of IEEE Std 1528 [8], with a maximum error of 5.1% and 4.0% for the $SAR_{10\,g}$ at 900 MHz and at 1.8 GHz, and 2.2% for the for $SAR_{1\,g}$ at 2.1 GHz. In terms of the homogeneous model, there are maximum errors of 2.6%, 8.5% and 11.8% for the $SAR_{1\,g}$ at 900 MHz, 1.8 GHz and 2.1 GHz, respectively, which are in good agreement with the literature. Considering the good agreement, the FDTD code will be used to evaluate the SAR due to a modern cellular phone in a heterogeneous head model.

3.2.2. Heterogeneous Head Model

Table 4 shows the SAR numerical results for heterogeneous head model. In this case the cellular phone is operating at the four frequencies studied with a power of 23.44 mW (13.7 dBm), which is similar to commercial phones. In the worst case, the maximum SAR is 1.27 W/kg for 1 g at the fat region for 2.4 GHz; a value that is smaller than 1.6 W/kg/1 g indicated by the IEEE guidelines.

4. CONCLUSION

The paper has presented a thorough analysis of the SAR induced in the human head due to cellular phones. The numerical results of the homogeneous head model are in very good agreement with the measurements, indicating that numerical simulations can be used as an useful tool to evaluate the SAR in the human head. In addition, the homogeneous model yielded a more conservative estimation of the SAR when compared to the heterogeneous model. The numerical simulation of a commercial cellular phone in the heterogeneous model — a more realistic representation of the human head — resulted in SAR values that are smaller than 1.6 W/kg/1 g in all tissues of the head.

ACKNOWLEDGMENT

This work was supported by the National Council for Scientific and Technological Development — CNPq, Brazil, under grant: 306.910/2006-3, and by The State of Minas Gerais Research Foundation — FAPEMIG, Brazil, under grants: TEC 251/09 and Pronex APQ 01075/09.

REFERENCES

1. IEEE C95.1, *IEEE Standard for Safety Levels with Respect to Human Exposure to Radio Frequency Electromagnetic Fields, 3 kHz to 300 GHz*, IEEE, USA, 2005.
2. ICNIRP, "Guidelines for limiting exposure to time-varying electric, magnetic, and electromagnetic fields (up to 300 GHz)," *Health Phys.*, Vol. 74, No. 4, 494–522, 1998.
3. Gandhi, O. P., G. Lazzi, and C. M. Furse, "Electromagnetic absorption in the human head and neck for mobile telephones at 835 and 1900 MHz," *IEEE Trans. on Microw. Theory and Tech.*, Vol. 44, No. 10, 1884–1897, 1996.
4. Bernardi, P., M. Cavagnaro, S. Pisa, and E. Piuzzi, "Specific absorption rate and temperature increases in the head of a cellular-phone user," *IEEE Trans. on Microw. Theory and Tech.*, Vol. 48, No. 7, 1118–1126, 2000.
5. Li, Q.-X. and O. P. Gandhi, "Thermal implications of the new relaxed IEEE RF safety standard for head exposures to cellular telephones at 835 and 1900 MHz," *IEEE Trans. on Microw. Theory and Tech.*, Vol. 54, No. 7, 3146–3154, 2006.
6. Sabbah, A. I., N. I. Dib, and M. A. Al-Nimr, "Evaluation of specific absorption rate and temperature elevation in a multi-layered human head model exposed to radio frequency radiation using the finite-difference time domain method," *IET Microw. Antennas Prop.*, Vol. 5, No. 9, 1073–1080, 2011.
7. Furse, C., D. A. Christensen, and C. H. Durney, *Basic Introduction to Electromagnetics*, CRC Press, Boca Raton, FL, USA, 2009.
8. IEEE STD 1528, *IEEE Recommended Practice for Determining the Peak Spatial Average Specific Absorption Rate (SAR) in the Human Head from Wireless Communications Devices: Measurements Techniques*, IEEE, USA, 2003.
9. Rodrigues, A. O., J. J. Viana, and J. A. Ramirez,"A head model for the calculation of SAR and temperature rise induced by cellular phones," *IEEE Trans. on Magn.*, Vol. 44, No. 6, 1446–1449, 2008.
10. Taflove, A. and S. Hagness, *Computational Electrodynamics — The Finite Difference Time Domain Method*, Artech House, Norwood, MA, USA, 2005.
11. Elsherbeni, A. and V. Demir, *The Finite Difference Time Domain Method for Electromagnetics: with Matlab Simulations*, SciTech Pub., Raleigh, NC, USA, 2009.
12. IEEE C95.3, *IEEE Recommended Practice for Measurements and Computations of Radio Frequency Electromagnetic Fields with Respect to Human Exposure to Such Fields, 100 kHz–300 GHz*, IEEE, USA, 2006.

An *in vitro* Study of Apoptosis in Pancreatic Cancer Cells by High-intensity Nanosecond Pulses

N. Pausawasdi[1], V. Sirivatanauksorn[2], C. Srisawat[2], and P. Kirawanich[3]

[1]Department of Internal Medicine, Faculty of Medicine Siriraj Hospital
Mahidol University, Bangkoknoi, Bangkok 10700, Thailand
[2]Department of Biochemistry, Faculty of Medicine Siriraj Hospital
Mahidol University, Bangkoknoi, Bangkok 10700, Thailand
[3]Electrical Engineering Department, Mahidol University
Salaya, Nakhon Pathom 73170, Thailand

Abstract— This paper reports the unique apoptotic responses of human pancreatic cancer cells (Panc-I) induced by nsPEF systems. In vitro experiments were carried out using laboratory-assembled apparatus, serving the cells with 10-ns and 500-ns high-intensity pulses. Our data suggested that the apoptotic effects of nsPEF on Panc-I cells are pulse characteristics dependent. In addition, both long pulse duration and post treatment period are required to initiate the apoptosis demonstrated by a maximal increase in activation of caspases-3/7 activities of 50% ($p < 0.05$) at 24 h after 500-ns nsPEF treatment. The slow progression rate of apoptosis induced by nsPEF appears to be a unique property of Panc-I cells when compared to other mammalian cells. nsPEF-induced apoptosis in Panc-I cells may involve multiple mechanisms but at least in part due to intrinsic pathway and activation of caspase signaling.

1. INTRODUCTION

Pancreatic cancer is known for treatment resistance owing to its ability to develop anti-apoptotic mechanisms. Regardless of advanced researches in the pathogenesis and treatment, this disease remains a challenging problem given its poor overall survival rate. Apoptosis, in general, can be activated through two pathways. The first pathway is mitochondria dependent, known as intrinsic pathway. It is triggered by cellular stress, cytotoxic agents, and growth factor deprivation that result in an increase in mitochondrial outer membrane permeability and release of apoptotic factors including cyctochrome c, Apaf-1 and caspase-9 into the cytoplasm. The other is called extrinsic pathway mediated by death receptors, which belong to the tumor necrosis factor (TNF) super family including the TNF-, FAS-(APO-1, CD95) and TRAIL-(TNF-related apoptosis inducing ligand) receptors. Both pathways finally activate the executioner caspases-3/6. Basically, in type I cells, the activation of caspase 8 is independent of mitochondria. In contrast, type II cell apoptotic pathways are mediated through the release of cytochrome c from mitochondria and caspase-9 activation, which lead to cell failure via activation of caspase-3. It is known that deregulation and evasion of the apoptosis are not unusual mechanisms in pancreatic cancer. Highly efficient techniques, therefore, are required in order to improve the prognosis of this disease [1].

In recent years, nanosecond second pulsed electric field (nsPEF) is emerging as a new application for cellular apoptosis induction. It has been employed to serve as an alternative tool for activation of apoptosis in a variety of cancer cell lines. Thus, we examined whether nsPEF can provoke apoptosis in pancreatic cancer cells, which are known to develop anti-apoptotic mechanisms [2]. We report here the use of high-intensity electrical pulses in nanosecond regime as an intracellular electro-manipulation agent for induction of apoptosis in pancreatic cancer cells through the demonstration of caspase activity. The key apparatus to corporate nsPEF effect on pancreatic cancer cells is a pulse forming circuit, which generates the ultrashort, high-intensity pulses [3–5].

2. MATERIALS AND METHOD

Two different pulse forming circuits were assembled in our facility to serve the load with 10-ns and 500-ns high-voltage electrical pulses shown in Fig. 1. The load is the treatment chamber filled with pancreatic cancer cell line in a buffer solution. The treatment chamber is a 1-mm commercial electroporation cuvette (VWR Scientific Products, West Chester, PA, USA) that can offer homogeneous electric fields across the entire active region.

Human pancreatic cells, Panc-I [6] were used for our experiments. The Panc-I cells were grown in Chang medium® C (Irvine Scientific, Santa Ana, CA, USA) and incubated at 37°C with 5%CO_2–95%O_2 condition. To prepare cells for nsPEF treatment, they were tripsinized with 0.25% trypsin.

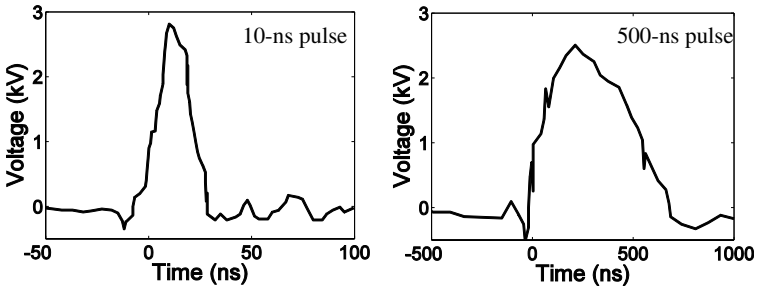

Figure 1: Temporal waveforms of 10-ns and 500-ns high-voltage pulses.

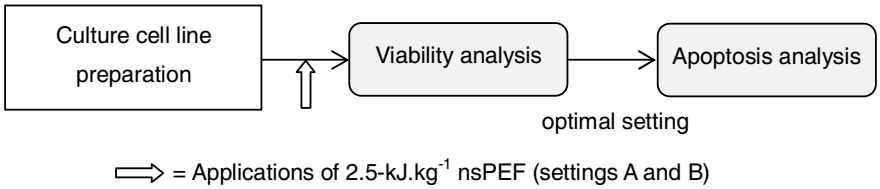

Figure 2: Flow diagram of the entire sequence of *in vitro* cellular apoptosis studies by means of intracellular electro-manipulation.

After trypsinization, the cells were washed with PBS 3 times before resuspended in PBS with the final concentration of 3–6 $\times$ 10^5 cells/ml.

The outline of *in vitro* nsPEF experiments is detailed in Fig. 2 with treatment settings, i.e., A and B. All settings were arranged with different pulse conditions (amplitude, durations, and pulse numbers) to account for the same specific energy of 2.5 kJ $\cdot$ kg^{-1}. That is, setting A was carried out with 50 pulses while only 3 pulses were assigned for setting B. For each setting, a total volume of 125 µl of cell suspension was added to a pre-sterilized, disposable 1-mm electroporation cuvette and 100 µl was used as a control. After nsPEF treatment, 100 µL of the treated cells was transferred into a microcentrifuge tube and spun down at 5000 rpm. The supernatant was removed and the cell pellet was resuspended with Chang medium® C to make the final cell concentration of $\sim 7.5 \times 10^4$ cells/mL before plating 100 µl of the cell suspension to each well of a 96-well FluoroNunc™ black culture plate (Thermo Scientific, Lafayette, CO, USA). The same protocol was applied to the control group.

To determine cell viability, CellTiter-Blue® Cell Viability Assay (Promega Corporation, Wisconsin, USA) was used. We carried on cell viability assay at 0, 6, and 24 hr with 20 µl of CellTiter-Blue reagent directly added to each well at each time point and cells were incubated for 1 h at 37°C. Each assay was performed in duplicate. After incubation, the fluorescent signal proportional to the number of viable cells was measured using a Synergy™ HT Multi-Mode Microplate Reader (Bio-Tek Instruments, Winooski, VT, USA) at $545 \pm 40_{\mathrm{Ex}}/590 \pm 25_{\mathrm{Em}}$ (in nm) with the sensitivity of 50.

The assessment of caspase activity was done using Apo-ONE® Homogeneous Caspase-3/7 Assay (Promega Corporation, Wisconsin, USA). 50 µl of the diluted reagent was added to each well and cells were incubated for 1 h at 37°C. Each assay was performed in duplicate. The fluorescent signal proportional to the number of viable cells was measured using a Synergy™ HT Multi-Mode Microplate Reader at ($485 \pm 20_{\mathrm{Ex}}/530 \pm 25_{\mathrm{Em}}$).

Data are presented as means $\pm$ standard error (SE). Mann-Whitney U test was used for statistical analysis. The p value less than 0.05 was considered statistically significant.

3. RESULTS AND DISCUSSION

Initially, the effect of nsPEF on cell death was evaluated using viability assay. Fig. 3 shows the average percentage of pancreatic cancer cell viability after treatment with both nsPEF settings A and B compared to control group. The viability tests were performed at 1 and 24 h. It was observed that delivering 3 pulses of 500-ns duration (setting B) significantly induced cell death at 24 h ($p = 0.02$), demonstrated by viability rate of nearly 50%, but not at 1 h. Setting A, meanwhile, was found to have some effects without statistically significant results at both time points.

We performed follow-up experiments with the use of setting B in which the caspase activity was

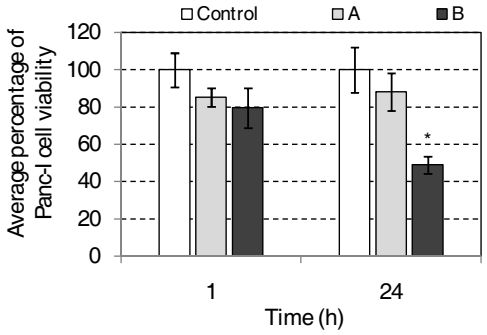

Figure 3: Average rates of pancreatic cancer cells viability at 1 and 24 h after the treatments for settings A and B compared to the control group. The asterisk $*$ indicates statistical significance ($p = 0.02$).

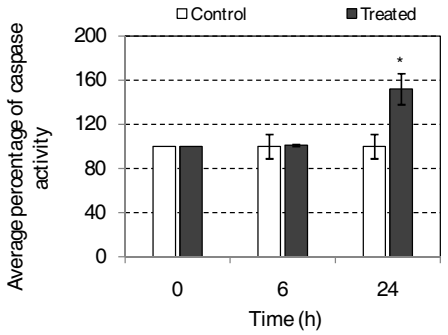

Figure 4: Average caspase activity observed at 0, 6 and 24 h after the treatment. The asterisk $*$ indicates statistical significance ($p < 0.05$).

assessed to evaluate whether the induction of cell death by nsPEF involved apoptotic pathway. The apoptosis assessments were performed at 0, 6, 24 h. Fig. 4 shows that there were no differences of caspase activity among treated and untreated group at 0 and 6 h. However, average caspases-3/7 activities increased significantly by 50% compared with control at 24 h ($p < 0.05$).

nsPEF treatments to induce apoptosis in pancreatic cancer cells with the longest pulse duration at 24 h have shown the most effective results. They underline the significance of both pulse characteristics and incubation time after the treatment. Basically, the nsPEF technique has been shown to rapidly induce apoptosis within few minutes after treatment in typical mammalian cells [7, 8]. This, however, may not apply to pancreatic cancer cells. The apoptosis induction by nsPEF in pancreatic cancer cells may involve multiple mechanisms but at least in part due to intrinsic pathway and caspase activation.

4. CONCLUSIONS

The slow progression rate of apoptosis induced by nsPEF appears to be a unique property of Panc-I cells when compared to other mammalian cells. The apoptotic responses of pancreatic cancer cells to pulsed electric fields are complex and unique partly due to the crosstalk between extrinsic and intrinsic pathways occurring in this particular cell type. nsPEF-induced apoptosis in Panc-I cells may involve multiple mechanisms but at least in part due to intrinsic pathway and activation of caspase signaling. In addition to a need for observing the cell apoptotic responses by other types of pulses, further studies to define the sites of action in the complex apoptotic pathways are suggested.

ACKNOWLEDGMENT

The authors would like to thank The Medical Association of Thailand for the full financial support.

REFERENCES

1. Hamacher, R., R. M. Schmid, D. Saur, and G. Schneider, "Apoptotic pathways in pancreatic ductal adenocarcinoma," *Mol. Cancer*, Vol. 7, 64, 2008.
2. Li, X., A. B. Roginsky, X.-Z. Ding, C. Woodward, P. Collin, R. A. Newman, R. H. Bell, Jr., and T. E. Adrian, "Review of the apoptosis pathways in pancreatic cancer and the anti-apoptotic effects of the novel sea cucumber compound, Frondoside A," *Annals of the New York Academy of Sciences*, Vol. 1138, 181–198, 2008.
3. Behrend, M., A. Kuthi, X. Gu, P. T. Vernier, L. Marcu, C. M. Craft, and M. A. Gundersen, "Pulse generators for pulsed electric field exposure of biological cells and tissues," *IEEE Trans. Dielectr. Electr. Insul.*, Vol. 10, 820–825, 2003.
4. Nuccitelli, R., U. Pliquett, X. Chen, W. Ford, R. J. Swanson, S. J. Beebe, J. F. Kolb, and K. H. Schoenbach, "Nanosecond pulsed electric fields cause melanomas to self-destruct," *Biochem. Biophys. Res. Commun.*, Vol. 310, 286–295, 2003.
5. Kuthi, A., T. Vernier, X. Gu, and M. A. Gundersen, "Compact nanosecond pulse generator for cell electroperturbation experiments," *Proceedings of the 2002 International Power Modulator Conference and High Voltage Workshop*, Hollywood, CA, Jun. 30–Jul. 3, 2002.

6. Lieber, M., J. Mazzetta, W. Nelson-Rees, M. Kaplan, and G. Todaro, "Establishment of a continuous tumor-cell line (panc-1) from a human carcinoma of the exocrine pancreas," *Int. J. Cancer.*, Vol. 15, 741–747, 1975.
7. Ford, W. E., W. Ren, P. F. Blackmore, K. H. Schoenbach, and S. J. Beebe, "Nanosecond pulsed electric fields stimulate apoptosis without release of pro-apoptotic factors from mitochondria in B16f10 melanoma," *Arch. Biochem. Biophys.*, Vol. 497, 82–89, 2010.
8. Hall, E. H., K. H. Schoenbach, and S. J. Beebe, "Nanosecond pulsed electric fields induce apoptosis in p53-wildtype and p53-null HCT116 colon carcinoma cells," *Apoptosis*, Vol. 12, 1721–1731, 2007.

Enhanced Microwave Transmission and Magnetophotonic Response in One-Dimensional Magnetophotonic Crystals

K. Smith and A. A. Chabanov
Department of Physics and Astronomy, University of Texas at San Antonio
San Antonio, Texas 78249, USA

Abstract— We report microwave transmission studies of one-dimensional magnetophotonic layered structures incorporating a cobalt layer. When placing the cobalt layer at the node of the localized mode at the defect in periodic structure, a significant enhancement (up to 3 orders of magnitude) of microwave transmission is observed, whereas the magnetophotonic response strongly depends on the quality of the deposited cobalt film.

1. INTRODUCTION

Magnetic materials are of great importance to microwave engineering [1] and photonics [2] due to their nonreciprocal properties such as Faraday and Kerr effects. They are utilized in various microwave and optical components, including isolators, circulators, phase shifters, modulators, etc. One of the approaches to miniaturizing magnetooptic elements exploits one-dimensional (1D) magnetophotonic crystals [3–5], that are periodic stacks of layers with a component being a ferrite or ferromagnet, in which nonreciprocal properties can be significantly enhanced. Experiments [5] have already demonstrated enhancement of Faraday and Kerr rotation in magnetophotonic crystals composed of a ferrite layer sandwiched between two Brag reflectors. The enhancement, however, was accompanied by a significant decrease in respective transmission and reflection due to losses in the magnetic layer. For example, in a study of optical transmission and Faraday rotation in a 1D magnetophotonic crystal containing a thin Cobalt layer of the variable thickness, d, the transmission nearly vanished for $d > 50\,\text{nm}$ [6], thus emphasizing the fact that many magnetic materials exhibiting strong magnetophotonic responses have been ignored due to their high losses in spectral ranges of interest.

On the other hand, it was recently shown that absorption of lossy components in 1D photonic crystals can be greatly suppressed [7, 8]. The absorption suppression mechanism is due to a highly nonuniform electromagnetic field distribution inside the photonic crystal. For example, at the transmission resonance, the electromagnetic field in the photonic crystal is nearly a standing wave, in which the nodes of the electric field coincide with the antinodes of the magnetic field and vice versa (Fig. 1). When lossy (e.g., metallic) components dominated by the permittivity tensor are positioned at the nodes of the electric field, their absorption is greatly suppressed [8]. The desired nonreciprocal properties of the components, in order to be enhanced in the magnetophotonic crystal, should then be dominated by the magnetic permeability tensor. In ferromagnets this is the case at microwave and far infrared frequencies.

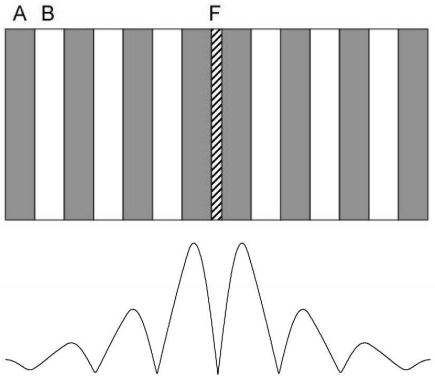

Figure 1: Magnetophotonic structure under study (upper panel) and spatial distribution of the localized mode electric field amplitude (lower panel) utilized to suppress conductivity losses of the cobalt layer F.

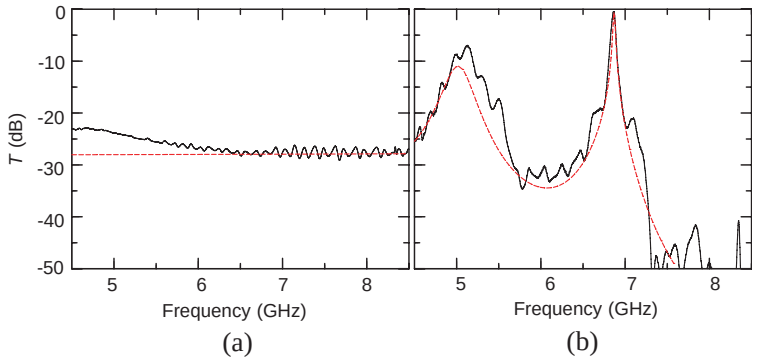

Figure 2: (a) Microwave transmission through a stand alone 275-nm cobalt layer and magnetophotonic structure of Fig. 1(b); no magnetic field. The red line indicates transfer matrix calculations.

In this work, we report microwave transmission measurements in a cobalt film incorporated into a 1D photonic crystal. We show that cobalt reflection and electromagnetic losses are greatly suppressed, when placing the cobalt layer at the node of the localized mode at the defect in periodic structure, in agrement with transfer matrix calculations. We also show that magnetophotonic properties of cobalt depend on the quality of the deposited cobalt film and can be controlled with magnetic field.

2. EXPERIMENTAL SETUP

The magnetophotonic structure under study was organized as the following. A unit cell of 1D photonic crystal consisted of two dielectric layers, alumina (A) and air (B), of dielectric constants, $\epsilon_A = 10$ and $\epsilon_B = 1$, respectively. The dielectric layers had the same thickness of 4.0 ± 0.1 mm and magnetic permeability $\mu = 1$. The initial structure had $N = 7$ unit cells. An additional layer A was added to the right end, and the middle layer B was removed to create a defect at the center. A cobalt film of thickness $d = 275$ nm was RF sputtered on a glass substrate of thickness 500 µm and inserted at the center of the defect, as depicted in the upper panel of Fig. 1. The microwave field transmission measurements were carried out over the frequency range of 4.5–8.5 GHz with the use of a network vector analyzer and a pair of linearly polarized horn antennas positioned in front and behind the structure. In order to measure magnetophotonic response of the structure, it was placed in the bore of a DC magnet with magnetic field oriented perpendicular to the structure. The magnet bore was furnished and capped with microwave absorber.

3. RESULTS AND DISCUSSION

Microwave transmission measurements were first carried out without magnetic field. The stand alone cobalt layer transmission is shown in the left panel of Fig. 2. At microwave frequencies, the dielectric permittivity of cobalt can be assumed to be purely imaginary, $\epsilon \approx i4\pi\sigma/\omega$, where σ is the electrical conductivity and ω is the angular frequency. The transmittance of a cobalt layer of thickness d can be approximated by, $T \approx (2\pi\sigma d/c)^{-2}$, where c is the speed of light. The comparison to the measured transmission brings the conductivity of the cobalt film, $\sigma \approx 4.2 \times 10^{15}$ s^{-1}. The transmission through the photonic structure of Fig. 1 is shown in the right panel of Fig. 2, which proves strong absorption suppression. The defect in the periodic structure produces a localized electromagnetic state at $f_0 \approx 6.9$ GHz in the spectral band gap. At the transmission resonance frequency, the microwave transmission is nearly 3 orders of magnitude the transmission through the stand alone cobalt layer.

When an external magnetic field was applied, the transmission spectra of Fig. 2 and the microwave absorption suppression did not change noticeably, except we were able to observe a small dip (~ 0.03 dB) in the relative transmission, with the dip frequency depending on the magnetic field (Fig. 3). The dip was identified as the ferromagnetic resonance (FMR) of the cobalt film. The FMR frequency was found to increase linearly with the magnetic field (Fig. 3), to match closely with the Kittel's formula for the frequency of the FMR in magnetic field, $f_0 \sim \gamma H_0$, where H_0 is the internal magnetic field and γ the gyromagnetic ratio. The fit of the data in Fig. 3 yielded $\gamma = 24.4 \pm 0.2$ GHz/T for the cobalt film.

The presence of the FMR is a magnetophotonic response of the cobalt layer. However, Faraday rotation induced by the cobalt film could not be reliably measured due to its small value and uncertainty of microwave polarization measurements. The weak magnetophotonic response of the

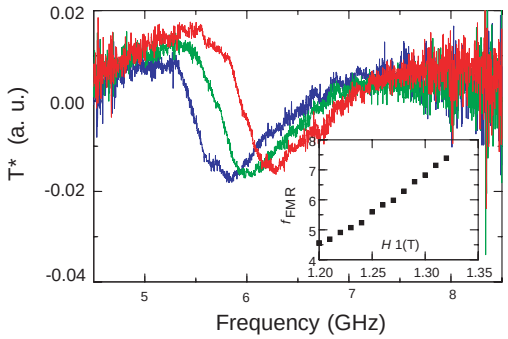

Figure 3: Microwave transmission through the magnetophotonic structure of Fig. 1 in magnetic field $H =$ 1.26 T (blue), 1.27 T (green) and 1.28 T (red), normalized by the transmission of Fig. 2(b). The dip in transmission indicates FMR. Inset: FMR frequency in GHz versus applied magnetic field.

photonic structure measured can be explained by the following factors. The homogeneity of the magnetic field across the cobalt film was $\sim 2\%$, which explains the broadening of the FMR line in Fig. 3. More importantly, the cobalt film had a random polycrystalline structure, as was confirmed in XRD measurements. Because magnetophotonic response of the cobalt film, including Faraday rotation, strongly depends on the orientation of the magnetoanisotropy axis, it was smeared and nonreciprocal properties were reduced due to random polycrystalline orientation of the film.

4. CONCLUSION

In conclusion, lossy magnetic layers incorporated in 1D photonic crystals can be utilized for achieving strong magnetophotonic response. By placing the magnetic layer at the node of the electric field in the photonic crystal, electromagnetic losses can be dramatically suppressed, while magnetophotonic response significantly enhanced at resonance with the localized mode at the defect in the periodic structure. We performed microwave studies of a 1D magnetophotonic layered structure incorporating a cobalt layer and observed significant enhancement (up to 3 orders of magnitude) of microwave transmission, as compared to a stand alone cobalt layer. At the same time, the magnetophotonic response was found strongly dependent on the quality of the deposited cobalt film and therefore can be significantly improved by using epitaxial or highly textured cobalt films. Our work suggests that lossy magnetic materials may have important photonics applications and lead to a new generation of magnetophotonic devices.

ACKNOWLEDGMENT

We are grateful to Ilya Vitebskiy for illuminating discussions. This research was supported by NSF-NIRT Grant No. ECCS-0709323. A portion of this work was performed at the National High Magnetic Field Laboratory, supported by NSF and the State of Florida.

REFERENCES

1. Pozar, D. A., *Microwave Engineering*, John Wiley, New York, 1998.
2. Zvezdin, A. K. and V. A. Kotov, *Modern Magnetooptics and Magnetooptical Materials*, Taylor & Francis, New York, 1997.
3. Inoue, M., K. Arai, T. Fujii, and M. Abe, "Magnetooptical properties of one-dimensional photonic crystals composed of magnetic and dielectric layers," *J. Appl. Phys.*, Vol. 83, 6768–6770, 1998.
4. Sakaguchi, S. and N. Sugimoto, "Transmission properties of multilayer films composed of magnetooptical and dielectric materials," *J. Lightwave Technol.*, Vol. 17, 1087–1092, 1999.
5. Inoue, M., K. Arai, T. Fujii, and M. Abe, "One-dimensional magnetophotonic crystals," *J. Appl. Phys.*, Vol. 85, 5768–5770, 1999.
6. Hamon, T., S. Buil, E. Popova, P. R. Dahoo, and N. Keller, "Investigation of a one-dimensional magnetophotonic crystal for the study of ultrathin magnetic layer," *J. Phys. D*, Vol. 39, 1012–1017, 2006.
7. Figotin, A. and I. Vitebskiy, "Absorption suppression in photonic crystals," *Phys. Rev. B*, Vol. 77, 104421, 2008.

8. Smith, K. and A. A. Chabanov, "Enhanced transmission and nonreciprocal properties of a ferromagnetic metal layer in one-dimensional photonic crystal," *Integr Ferroelectr*, Vol. 131, 66–71, 2011.

Scattering of Waves: Imperfect Coupling and Absorption or Amplification

R. A. Méndez-Sánchez[1], **A. M. Martínez-Argüello**[1, 2], **G. Báez**[3], **and M. Martínez-Mares**[2]

[1]Instituto de Ciencias Físicas, Universidad Nacional Autónoma de México
A. P. 48-3, Cuernavaca Mor. 62210, México
[2]Departamento de Física, Universidad Autónoma Metropolitana-Iztapalapa
A. P. 55-534, Distrito Federal 09340, Mexico
[3]Departamento de Ciencias Básicas, Universidad Autónoma Metropolitana-Azcapotzalco
A. P. 21-267, Distrito Federal 04000, Mexico

Abstract— A panorama on the scattering of waves of absorbing (amplifying) systems, in which imperfect coupling to the incoming and outgoing channels is also present, is given. The theoretical calculations for the nonunitary scattering matrix are also discussed from a perspective of two different theoretical frameworks. From one side, we discuss simple quantum mechanical systems with local and global absorption (amplification), in the presence of direct reflections. In the one channel case, the movement of the nonunitary scattering matrix on the Argand plane is discussed for two cases: the first one consists of a complex delta potential and the second one consists of a real delta with an imaginary constant potential. The probability distribution of the nonunitary scattering matrix is given by the nonunitary Poisson kernel. From the other side, we consider complex scattering of microwaves by chaotic and disordered systems with global absorption (amplification) and imperfect coupling. The result for one and several channels is discussed in terms of the Poisson kernel squared. The theoretical Random Matrix Theory predictions are supported by different numerical and experimental results, with an agreement of several orders of magnitude.

1. INTRODUCTION

Scattering of waves by classical systems has been of interest in the recent years (see for instance Refs. [1–4] and references therein). One of the main reasons is that they are classical analogs of quantum systems, with some advantages like the easy control of external parameters [5, 6]. However, a cost to be paid is the existence of power losses that comes from the absorption of energy in the system walls [7, 8]. Therefore, a lot of work have been done in order to investigate the effect of the absorption in the scattering properties [1–4, 7–9]. On the other hand, the phenomenon of amplification has been also of interest from theoretical and experimental points of view [10, 11], as happens in optics, where the interplay between gains and chaos is investigated [12].

In most of the cases the absorption or amplification is in volume, it takes place at any point in the interior of the system, as happens in microwave cavities or microcavity lasers [7, 12]. Recently, it has been proposed that absorption can be controlled by attaching absorbing patches in the inner walls of the system [13]. In a previous work, we analyzed the scattering matrix of a simple system with local absorption or amplification [10]. Currently, local absorption has being considered to study the quasimodes in chaotic cavities [14]; local amplification has been used to amplify scar modes [11]. Moreover, classical wave systems with both, local absorption and amplification, are very useful tools to simulate quantum systems with $\mathcal{PT}$-symmetry, systems described by non-Hermitian Hamiltonians with invariance under joint parity ($\mathcal{P}$) and time-reversal ($\mathcal{T}$) [15].

It is well known that an imperfect coupling of the antennas that feed a system with global or local absorption, affects the scattering properties, and hence the transport or waves [10, 16]. It is due to direct reflection that give rise to a prompt response in the system. Therefore, it is also expected that the prompt responses affect the scattering properties in the presence of gains [10]. Prompt responses or direct processes make that the scattering matrix has a probability density, or a statistical distribution in a stationary random process, that is given by a nonunitary version of the Poisson kernel [10], or the Poisson kernel squared in the stationary random process [16].

In this paper, a panorama of what is known about scattering of waves in the presence of absorption or amplification and imperfect coupling is given. In next section we consider simple examples of local and volume absorption with direct reflections. In Section 3, we give an overview of absorbing chaotic systems with imperfect coupling. Finally, we conclude in Section 4.

2. DIRECT PROCESSES AND ABSORPTION OR AMPLIFICATION IN 1D

2.1. Local Absorption or Amplification

As a first example we consider a one-dimensional cavity that is formed by a Dirac delta potential in front of an impenetrable barrier at a distance a. The intensity of the delta potential is chosen to be a complex number to simulate absorption or amplification located at $x = a$. Therefore, the potential of this one-dimensional problem is

$$V(x) = \begin{cases} \infty, & x < 0 \\ (u \mp iv)\,\delta(x-a), & x > 0 \end{cases}, \tag{1}$$

where u and v are positive constants; the minus (plus) sign corresponds to absorption (amplification).

The outgoing plane wave amplitude is related to the incoming one by the 1×1 scattering matrix, which is given by [10]

$$\tilde{S} = \sqrt{R}\, e^{i\theta} = -\frac{[\sin ka + (k/\tilde{\alpha})\cos ka] + i(k/\tilde{\alpha})\sin ka}{[\sin ka + (k/\tilde{\alpha})\cos ka] - i(k/\tilde{\alpha})\sin ka}, \tag{2}$$

where $\tilde{\alpha} = 2m(u \pm iv)/\hbar^2$ and $k = \sqrt{2mE/\hbar^2}$; θ is twice the phase shift plus π and $R = \tilde{S}^{\dagger}\tilde{S}$ is the reflection coefficient; $R < 1$ for absorption and $R > 1$ for amplification. When $v = 0$, $\tilde{\alpha} = 2mu/\hbar^2$ and the unitary case is recovered ($R = 1$).

In Fig. 1, we show the movement of $\tilde{S}$ in the Argand plane when ka is varied from 10^3 to complete 35 resonances. As we can see it describes a circle of radius $\sqrt{R_0} < 1$ ($\sqrt{R_0} > 1$) for absorption (amplification), displaced along the real axis. This circle touch the unitary one in the point $R = 1$ and $\theta = \pi$ where the delta potential is totally transparent because the wave function has a node just in the position of the delta potential.

The scattering matrix $\tilde{S}' = \sqrt{R'}\, e^{i\theta'}$ that is viewed from the center of the circle can be obtained from $\tilde{S}$ by the translation

$$\tilde{S}' = \tilde{S} + \left(1 - \sqrt{R_0}\right). \tag{3}$$

What it is very interesting here is that the probability distribution of $\tilde{S}'$ is given by [10]

$$p'\left(\tilde{S}'\right) = q'\left(\theta'\right)\,\delta\left(R' - R_0\right) = \frac{1}{2\pi}\frac{R' - \left|\overline{\tilde{S}'}\right|^2}{\left|\tilde{S}' - \overline{\tilde{S}'}\right|^2}\,\delta\left(R' - R_0\right), \tag{4}$$

where $q'(\theta')$ is the nonunitary version of the Poisson kernel, with $\overline{\tilde{S}'}$ the energy average of $\tilde{S}'$, which is taken from the numerical experiment and gives a measure of the direct processes (see Fig. 1).

2.2. Volume Absorption or Amplification

Volume absorption or amplification in one dimension can be simulated by a complex constant potential between an impenetrable barrier and a Dirac delta potential which intensity is purely real

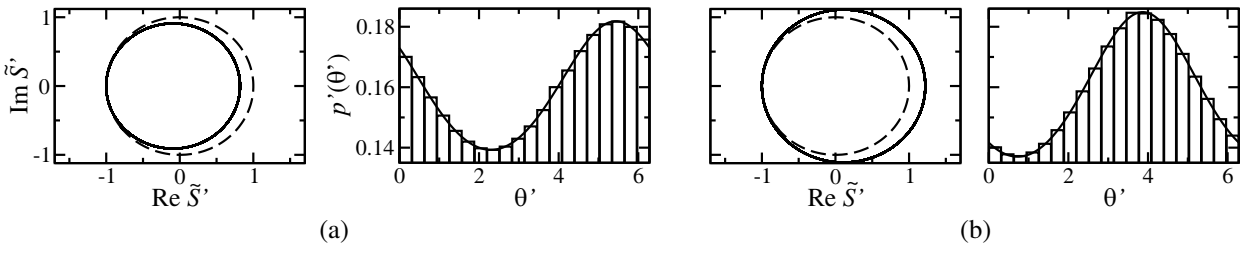

Figure 1: In presence of *local* (a) absorption, or (b) amplification, the motion of $\tilde{S}'$ describes a circle of radius $\sqrt{R_0} < 1$, or $\sqrt{R_0} > 1$, displaced along the real axis with respect to the origin of the unitary circle obtained in absence of absorption, or amplification. The probability density of $\tilde{S}'$ is given by the nonunitary Poisson kernel. Here, $ua = va = 10^3$ and $R_0 \approx 0.91$. Adapted from Ref. [10].

and positive. That is,

$$\mathrm{Re}\, V(x) = \begin{cases} \infty, & x < 0 \\ u\,\delta(x-a), & x > 0 \end{cases}, \qquad \mathrm{Im}\, V(x) = \pm i\, V_0, \quad 0 < x < a \tag{5}$$

where V_0 and u are positive constants. As before, the plus sign in (5) corresponds to amplification while the minus sign to absorption.

In this case, the scattering matrix associated to the cavity is also 1×1 and it is given by

$$\tilde{S} = \sqrt{R}\, e^{i\theta} = -\frac{\left[\sin \tilde{k}a + (\tilde{k}/\alpha)\cos \tilde{k}a\right] + i(k/\alpha)\sin \tilde{k}a}{\left[\sin \tilde{k}a + (\tilde{k}/\alpha)\cos \tilde{k}a\right] - i(k/\alpha)\sin \tilde{k}a}, \tag{6}$$

where $\alpha = 2mu/\hbar^2$ and

$$\tilde{k} = \sqrt{\frac{1}{2}k^2 + \frac{1}{2}\sqrt{k^4 + W^4}} \pm i\sqrt{-\frac{1}{2}k^2 + \frac{1}{2}\sqrt{k^4 + W^4}}, \tag{7}$$

with $k = \sqrt{2mE/\hbar^2}$ and $W = \sqrt{2mV_0/\hbar^2}$; the plus sign correspond to absorption and the minus sign to amplification. Note that for $W = 0$, Eq. (7) reduces to k and Eq. (6) reduces to the unitary case. Therefore, W gives a measure of the absorption or amplification strength.

In Fig. 2, we present the results for the numerical experiment for $ua = 10^3$ and $Wa = 50$. As for the local case, $\tilde{S}$ is nonunitary and the reflection coefficient R oscillates and increases (absorption) or decreases (amplification) with ka, as can be seen in panels (c) and (d) of this figure. The $\tilde{S}$-matrix describes an spiral in the Argand plane and as a consequence stationarity is not fulfilled. For high enough energies we can assume stationarity such that the motion of $\tilde{S}$ describes almost a circle displaced along the imaginary axis with respect to the unitary circle, as can be seen in panels (a) and (b) of Fig. 2. The numerical simulation is done for ka in the range from 10000 to 10110, where there are 35 resonances.

From the center of this circle the scattering matrix is $\tilde{S}' = \sqrt{R'}e^{i\theta'}$, where we can assume that the reflection coefficient R' is almost constant, $R' = R_0$. In panels (e) and (f) of this figure we compare the distribution of the phase θ' obtained from the numerical experiment with the Poisson kernel given by $q'(\theta')$ of Eq. (4), where the only relevant parameters are R_0 and $\overline{\tilde{S}'}$, both obtained from the experiment. The excellent agreement show that also in the global case the phase is distributed according to Poisson kernel.

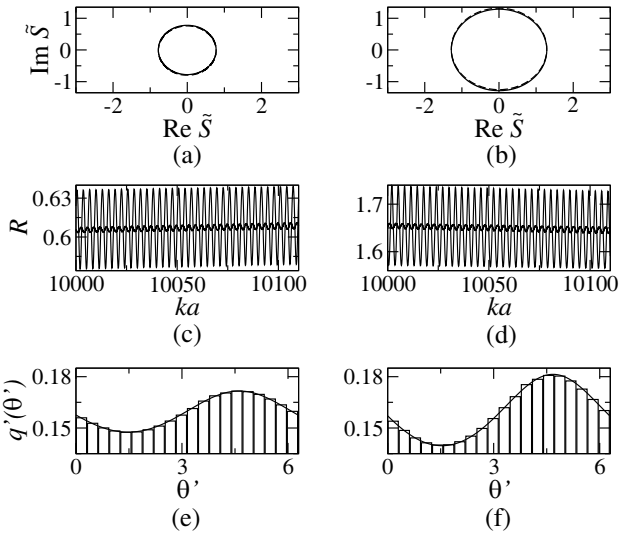

Figure 2: In presence of *volume* (a), (c), (e) absorption or (b), (d), (f) amplification, the motion of $\tilde{S}'$ describes a circle of radius $\sqrt{R_0} < 1$, or $\sqrt{R_0} > 1$, displaced along the imaginary axis with respect to the origin of the unitary circle obtained in the absence of absorption, or amplification. Here, also, it seems that the probability density of $\tilde{S}'$ is given by the nonunitary Poisson kernel. Here, $ua = 10^3$ and $Wa = 50$ and $R_0 \approx 0.91$.

3. ABSORBING CHAOTIC CAVITIES WITH IMPERFECT COUPLING

In a classical chaotic cavity the scattering matrix $\tilde{S}_0$ that describes it is a subunitary one that is a member of an ensemble of scattering matrices. The statistical distribution of this ensemble is very well explained by Random Matrix Theory in the absence of direct processes [3]. However, in the presence of such processes a phenomenological model was implemented such that the scattering matrix $\tilde{S}$, for a system with direct processes, can be obtained from $\tilde{S}_0$ [6]. In the one channel case, $\tilde{S} = \sqrt{R}\, e^{i\theta}$, $\tilde{S}_0 = \sqrt{R_0}\, e^{i\theta_0}$, and their relation is given by

$$\tilde{S} = -\sqrt{1-T_a} + \sqrt{T_a}\frac{1}{1-\tilde{S}_0\sqrt{1-T_a}}\tilde{S}_0\sqrt{T_a}, \tag{8}$$

where T_a is the coupling of the antenna to the cavity. This transformation is of the form

$$\tilde{S} = \left\langle \tilde{S} \right\rangle + \tilde{S}_{\text{fluc}}, \tag{9}$$

where S_{fluc} is the fluctuating part and $\langle \tilde{S} \rangle = -\sqrt{1-T_a}$ is the ensemble average that quantifies the direct processes which are obtained from the experimental data; therefore, the coupling can be quantified through $T_a = 1 - |\langle \tilde{S} \rangle|^2$.

The absorption strength is quantified by a parameter γ which is implicit in the statistical distribution of $\tilde{S}_0$ and can be calculated through the average of the reflection coefficient. Through our model, the statistical distribution of $\tilde{S}$ can be obtained from the one of $\tilde{S}_0$, which is known from Random Matrix Theory results. That is [16],

$$p^{(\beta)}_{\langle \tilde{S} \rangle}\left(\tilde{S}\right) = \frac{1}{2\pi}\left(\frac{1-\left\langle \tilde{S} \right\rangle^2}{\left|1-\tilde{S}\left\langle \tilde{S} \right\rangle\right|^2}\right)^2 p_0^{(\beta)}\left(R_0\left(\tilde{S}\right)\right), \tag{10}$$

where $\beta = 1(2)$ in the presence (absence) of time reversal invariance. It was show that [4]

$$\langle R \rangle_\beta = 1 - T_a + T_a^2 \sum_{n=1}^{\infty} (1-T_a)^{(n-1)} \langle R_0^n \rangle_\beta, \tag{11}$$

which is a very complicated calculation. However, we can present two cases of interest, strong and weak absorption limits and introduce the correct criterion for them, namely [4]

$$\langle R \rangle_\beta \approx \begin{cases} 1-T_a, & \gamma \gg T_a, \quad \text{strong absorption} \\ 1-\gamma & \gamma \ll T_a, \quad \text{weak absorption} \end{cases}. \tag{12}$$

It is important to notice that the first factor on the right hand side of this equation is the Poisson kernel squared, such that the direct processes affect the distribution of $\tilde{S}$. In Fig. 3, we show the comparison between the theoretical prediction with experimental observation for the distribution of θ. The agreement is excellent.

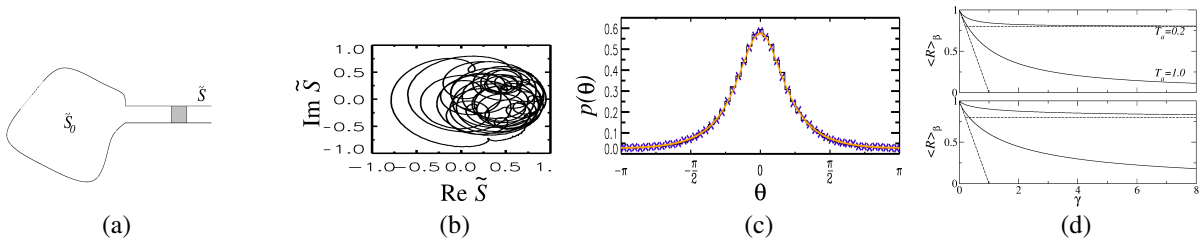

Figure 3: (a) Model for imperfect coupling. (b) Experimental results for $\tilde{S}$ in microwave cavities ($T_a = 0.754$). (c) Distribution of θ, when $T_a = 0.754$ and $\gamma = 2.42$, agrees with the prediction of Poisson kernel squared. (d) Average of R for $\beta = 1$, 2, where the limits of weak and strong absorption are shown. Adapted from Refs. [2, 4].

4. CONCLUSION

We gave a panorama on the scattering of waves by systems with local and global absorption or amplification, in presence of direct processes. We present theoretical calculations for simple quantum mechanical systems in the local and global cases. The subunitary scattering matrix that describe the system moves on a non-unitary circle in the Argand plane, which is displaced from the origin. In both cases the scattering matrix satisfies the Poisson kernel distribution in its non-unitary version. In chaotic systems with global absorption and imperfect coupling the Poisson kernel squared describes the statistical distribution of the sub-unitary scattering matrix.

ACKNOWLEDGMENT

This work was supported under projects DGAPA PAPIIT-IN111311, CONACYT 79613 and PROMEP UAM-PTC-183 No. 47510197.

REFERENCES

1. Méndez-Sánchez, R. A., U. Kuhl, M. Barth, C. H. Lewenkopf, and H.-J. Stöckmann, "Distribution of reflection coefficients in absorbing chaotic microwave cavities," *Phys. Rev. Lett.*, Vol. 91, No. 17, 174102-1–174102-4, 2003.
2. Kuhl, U., H.-J. Stöckmann, and R. Weaver, "Classical wave experiments on chaotic scattering," *J. Phys. A: Math. Gen.*, Vol. 38, No. 49, 10433–10463, 2005.
3. Fyodorov, Y. V., D. V. Savin, and H.-J. Sommers, "Scattering, reflection and impedance of waves in chaotic and disordered systems with absorption," *J. Phys. A: Math. Gen.*, Vol. 38, No. 49, 10731–10760, 2005.
4. Báez, G., M. Martínez-Mares, and R. A. Méndez-Sánchez, "Absorption strength in absorbing chaotic cavities," *Phys. Rev. E*, Vol. 78, No. 3, 036208-1–036208-7, 2008.
5. Arcos, E., G. Báez, P. Cuatláyol, M. L. H. Prian, R. A. Méndez-Sánchez, and H. Hernández-Saldaña, "Vibrating soap films: An analog for quantum chaos on billiards," *Am. J. Phys.*, Vol. 66, No. 7, 601–607, 1998.
6. Gutiérrez, L., A. Díaz-de-Anda, J. Flores, R. A. Méndez-Sánchez, G. Monsivais, and A. Morales, "Classical analogs of a diatomic chain," *AIP Conference Proceedings*, Vol. 1319, 73–81, 2010.
7. Doron, E., U. Smilansky, and A. Frenkel, "Experimental demonstration of chaotic scatterin of microwaves," *Phys. Rev. Lett.*, Vol. 65, No. 25, 3072–3075, 1990.
8. Fyodorov, Y. V., "Induced vs spontaneous breakdown of S-matrix unitarity: Probability of no return in quantum chaotic and disordered systems," *JETP Lett.*, Vol. 78, No. 4, 250–254, 2003.
9. Schanze, H., H.-J. Stöckman, M. Martínez-Mares, and C. H. Lewenkopf, "Universal transport properties of open microwave cavities with and without time-reversal symmetry," *Phys. Rev. E*, Vol. 71, No. 1, 016223-1–016223-12, 2005.
10. Martínez-Argüello, A. M., R. A. Méndez-Sánchez, and M. Martínez-Mares, "Wave systems with direct processes and localizaed losses or gains: The non-unitary poisson kernel," *Phys. Rev. E*, in Press.
11. Michel, C., S. Tscu, V. Doya, P. Aschiéri, W. Blanc, O. Legrand, and F. Mortessagne, "Experimental phase-space-based optical amplification of scar modes," *Phys. Rev. E*, Vol. 85, No. 4, 047201-1–047201-4, 2012.
12. Harayama, T., P. Davis, and K. S. Ikeda, "Stable oscillations of a spatially chaotic wave function in a microstadium laser," *Phys. Rev. Lett.*, Vol. 90, No. 6, 063901-1–063901-4, 2003.
13. Martínez-Mares, M. and P. A. Mello, "Statistical wave scattering through classically chaotic cavities in the presence of surface absorption," *Phys. Rev. E*, Vol. 72, No. 2, 026224-1–026224-6, 2005.
14. Xeridat, O., C. Poli, O. Legrand, F. Mortessagne, and P. Sebbah, "Quasimodes of a chaotic elastic cavity with increasing local losses," *Phys. Rev. E*, Vol. 80, No. 3, 035201-1(R)–035201-4(R), 2009.
15. Schomerus, H., "Quantum noise and self-sustained radiation of PT-symmetric systems," *Phys. Rev. Lett.*, Vol. 104, No. 23, 0233601-1–0233601-4, 2010.
16. Kuhl, U., M. Martínez-Mares, R. A. Méndez-Sánchez, and H.-J. Stöckmann, "Direct processes in chaotic microwave cavities in the presence of absorption," *Phys. Rev. Lett.*, Vol. 94, No. 14, 144101-1–144101-4, 2005.

A Novel Retrodirective Array by Removing Band Pass Filter

Shahrokh Jam and Mohsen Kalantari
Shiraz University of Technology, Shiraz, Iran

Abstract— Usually, in heterodyne Retrodirective Array (RDA), for mixing RF and LO signals, a nonlinear component is used. Result of this mixing is generation of harmonics of RF frequency (f_{RF}). In other side, a BPF couples the LO into the mixer at f_{LO} frequency, also, it isolates LO to mixer at f_{RF}. In this paper, BPF is replaced with configuration of two $\lambda/4$ length transmission lines. With replacement of BPF with this configuration, no considerable changes occur in diode voltage signal and power harmonics which incident to antenna port in this novel structure. With this change, a RDA is designed with less complexity and is fabricated smaller and lighter.

1. INTRODUCTION

In recent years, design and fabrication of devices with directed beam forming capability have attracted much attention [1]. Beam forming decreases interference (between waves), increases quality of communication, and causes that a communication be more secure. RDA and Smart Antenna are two methods for achievement of a device with beam forming property. RDAs have the characteristic of reflecting an incident wave toward the source direction without any prior information on the source location. Also, RDAs have shown much potential for use in many applications; automatic pointing and tracking systems, microwave tracking beacons, transponder, radar, RFID, solar power satellite (SPS) network and complex communication systems [1].

RDAs are achieved in three methods: right corner, Vanatta array and Heterodyne array. A Right corner consists of two (infinite) metal plates, that joint together in one edge, and angle between them is 90°. When a wave propagates toward a right corner, it reflects back toward transmitted source, after two reflections from each surface of right corner [1]. A Vanatta array consists of multi antennas and a network. The network consists of transmission lines, and its functionality is connection of each two antennas that located in conjugated places. The connection of two antennas causes that the output currents (of antennas ports), swap between them [2].

Generally, RDA design is based on heterodyne array method. Heterodyne RDA was proposed by C. Y. Pon in 1964. He proposed that phase of output signal of each antenna ports (RF signal) is reversed and then, signal returned to antenna (Figure 1). For phase reversion, he proposed that RF signal mixed with LO signal which its frequency is twice of RF frequency ($f_{LO} = 2f_{RF}$) [3]. When RF signal mixed with LO signal, two signals are produced. One of them has a frequency equal to f_{RF} and its phase is reverse of phase of RF signal (IF signal). Frequency of the second signal is equal to triple of f_{RF}, and, its phase is equal to phase of RF signal [1, 3]. Therefore, in heterodyne RDA design, designers need a LO which its frequency is twice of f_{RF}. Also, they must design a mixer to produce IF signal with mixing RF signal with LO signal.

In heterodyne RDA, a BPF is placed between mixer and LO. Ideally, It connects LO and mixer at f_{LO}, and separate them in other frequencies, to suppress of signals from mixer to LO (except at f_{LO}).

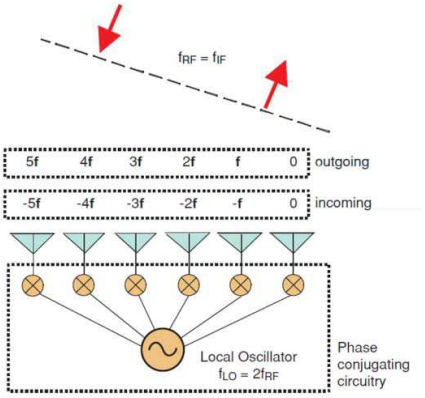

Figure 1: Heterodyne RDA (Pon RDA) [4].

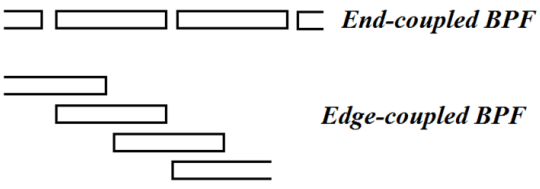

Figure 2: End-coupled and Edge-coupled BPF.

In the next sections, we discuss about role of BPF in heterodyne RDA. Then, we replace this BPF with two parts of transmission lines, and omit BPF from heterodyne RDA structure. Finally, for implementation of the new idea, three RDA structures are simulated by AWR 2008, and voltage signal at diode node and power harmonics which present at antenna port are demonstrated for three cases.

2. THE ROLE OF BPF IN RDA STRUCTURES

It's well known that in a circuit with nonlinear elements, the harmonics of fundamental frequency are generated [5]. Usually, in heterodyne RDA, a nonlinear component is used to mix RF and LO signals. Result of this mixing, is generation of many harmonics. Each of these harmonics is equal to $mf_{RF} + nf_{LO}$ (m and n are integer numbers). Because f_{LO} is twice of f_{RF}, then $mf_{RF} + nf_{LO}$ is a harmonic of f_{RF}.

For suppression these harmonics, a cascade filter is usually used between LO and mixer. In other words, the role of BPF in heterodyne RDA is rejection of all harmonics of f_{RF} except $2f_{RF}$.

At microwave frequencies, a BPF is realized by various methods, such as End-coupled BPF and Edge-coupled BPF methods [6] (Figure 2). The cascade filter increases size and cost of structure, and yields additional Insertion Loss (IL). In addition to this disadvantages, some disadvantages occur in usage of microwave filters; for example, parallel coupled microstrip line have been used as the main coupling component in Edge-coupled BPF design, which it causes that this filter has spurious pass band. The first spurious pass band of this filter appears at twice the basic pass band frequency [7].

For removing the cascade filter, several new technologies have been studied recently. A photonic Bandgap (PBG) structure, a Defected Ground Structure (DGS) and Compact Microstrip Reso-

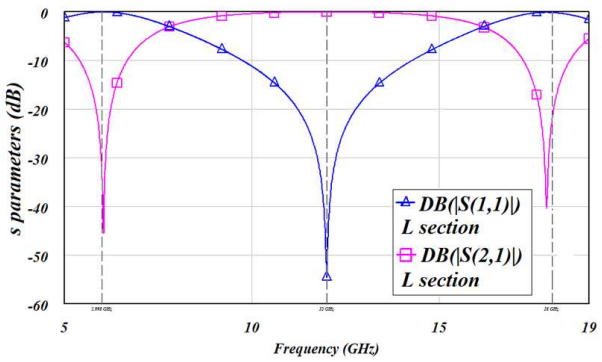

Figure 3: $|s_{11}|$ (△) and $|s_{21}|$ (□) for L-section (in dB).

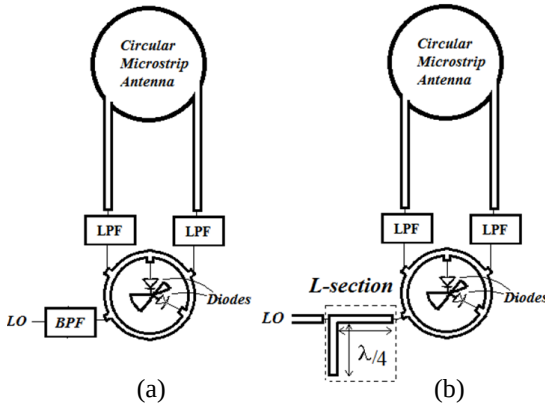

Figure 4: First heterodyne RDA, with (a) BPF and (b) L-section.

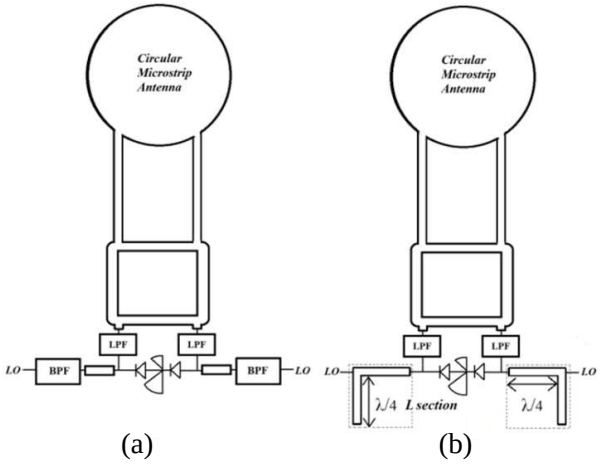

Figure 5: Second heterodyne RDA, with (a) BPF and (b) L-section.

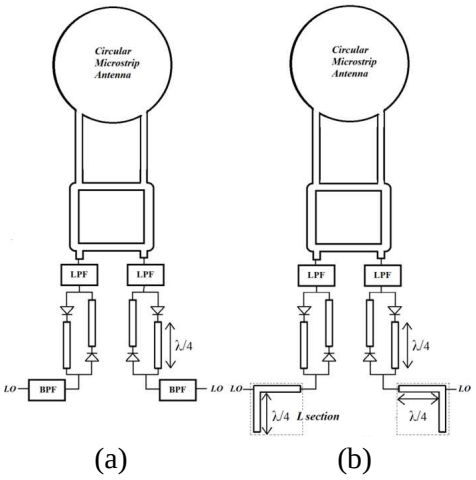

Figure 6: The third heterodyne RDA, with (a) BPF and (b) L-section.

nant Cavity (CMRC) are some of techniques that are used to reject spurious harmonics. Besides harmonic suppression in these methods, some difficulties occurs when designers use them [8, 9].

3. REPLACEMENT OF BPF WITH TWO PARTS OF TRANSMISSION LINE

We try to replace BPF with two quarter wavelength transmission lines. One of them is located between LO and mixer, and the second one is used as an open stub which is connected to the connection of first transmission line and LO. In present paper, this configuration of two transmission lines is called L-section.

Input impedance of the open stub (with length of $\lambda/4$) is zero at odd harmonics of f_{RF} and infinite at even harmonics of f_{RF}.

$$Z_{open\ stub} = \frac{Z_0}{j\tan(\beta l)} = \begin{cases} 0 & \beta l = (2k+1)\pi/2 \\ \infty & \beta l = k\pi \end{cases} \quad (1)$$

Based on this note, at odd harmonics of f_{RF}, input impedance of L-section is infinite from port 1, and at even harmonics of f_{RF}, port 1 is connected to port 2 with a $\lambda/4$ length transmission line. In other words, L-section isolates port 2 from port 1 at odd harmonics of f_{RF} and connects port 2 to port 1 at even harmonics of f_{RF}.

$|s_{21}|$ and $|s_{11}|$ for L-section, which is designed at 6 GHz are shown in Figure 3. $|s_{21}|$ is approximately zero and one at odd and even harmonics of f_{RF}, respectively. This behavior is the same as what happens for a BPF that is realized by parallel coupled microstrip line at harmonics of $2f_{RF}$.

In other view, Figure 3 is similar to a Band Stop Filter (BSF) graph, with a difference that this graph has multi center frequencies. In this case, these center frequencies are odd harmonics of f_{RF} [10]. Therefore, L-section rejects odd harmonics of f_{RF} that are generated in mixer.

Generally, in heterodyne RDA, harmonics of f_{RF} are generated at mixer, and a BPF is placed between LO and mixer, to block all harmonics of f_{RF} except $2f_{RF}$. Therefore, we can say that the role of BPF is harmonic rejection. As mention before, BPFs which are realized at microwave frequencies, have the spurious pass bands (out of desired pass band). Also, L-section can reject odd harmonics of f_{RF}, but it can't reject even harmonics of f_{RF}. Then, these two structures are the same behavior in heterodyne RDA when each of them is placed between LO and mixer.

For implementation of this idea, we use three RDAs.

The first one is a RDA that is introduced in [10] (Figure 4(a)). This structure consists of a circular microstrip antenna with two ports that connect to two ports of a ratrace coupler. The proposed structure is similar to a single balanced rat_race mixer, when LO and IF signals are interchanged [10]. Two mixer diodes are placed at two remaining ports of coupler. Placing the LO port in the longer section of the ring at a 6 GHz quarter wave from either port 1 or 4, so the other ports can be formed to feed the diodes with equal power (Figure 4(a)). The mixer employed (SMS7621) mixer diodes [10].

Each element in second structure consists of a circular microstrip antenna with two ports that connect to two ports of a branch_line coupler. Two diodes (SMS7621) are connected to other ports of coupler through a LPF. LO is connected to each of diodes with a BPF [11] (Figure 5(a)).

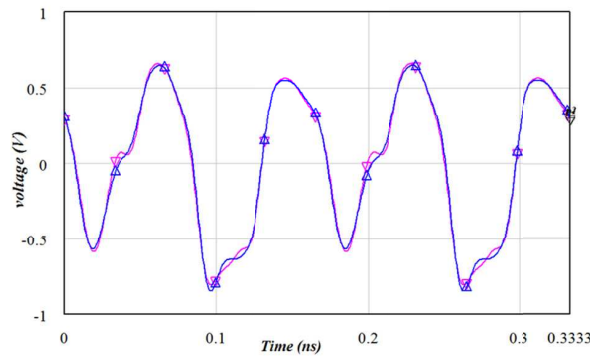

Figure 7: Voltage signal at the connection of diode to coupler, (▽) RDA with BPF, (△) RDA with L-section.

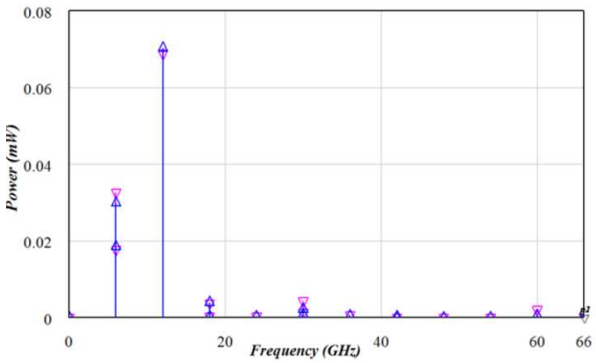

Figure 8: Power harmonics which incident to antenna port, (▽) RDA with BPF, (△) RDA with L-section.

Also, the third structure consists of a circular microstrip antenna with two ports that they connect to two ports of a branch_line coupler (Figure 6(a)). Two dual channel phase conjugators are connected to other ports of coupler through a LPF. Each of phase conjugators contains two ports, one for the LO and the other for RF/IF port. The channels are identical except position of the 90° phase delay line (at the RF frequency). Beside this, two diodes (SMS7621) are mounted in opposite directions. Since the f_{LO} is twice that of the f_{RF}, no power coupled to branch_line coupler at f_{LO}, providing good LO isolation [12] (Figure 6(a)). The board which is used in two cases, is RT/Duroid 5870, with its height is equal to 31 mil, and its ε_r and $\tan\delta$ are 2.33 and 0.0012, respectively. These RDAs are designed for receive and transmit wave at 6 GHz.

Now, we remove BPFs from these structures and insert L-section in them as Figures 4(b), 5(b) and 6(b).

4. SIMULATION

As mention before, three RDA strucrures are considered, each one is simulated in two cases, when BPF is placed between LO and mixer and when the BPF is replaced with L-section. In these cases, diode voltages and power harmonics which incident to antenna ports are demonstrated in two cases.

A. For first structure is shown in Figure 4:

Figure 7 shows voltage signals at connection of one of diodes to coupler, in two cases. In this structure, the conversion loss is approximately 6.5 dB at 6 GHz. The LO power is 10 dBm. Power harmonics that incident into antenna ports are shown in Figure 8.

B. For second structure is shown in Figure 5:

Figure 9 shows voltage signals at connection of one of diodes to coupler when BPF and when L-section are placed between LO and mixer. In this structure, the conversion loss is approximately 6 dB at 6 GHz. The LO power is 10 dBm. Power harmonics which incident to antenna ports are shown in Figure 10.

C. For third structure is shown in Figure 6:

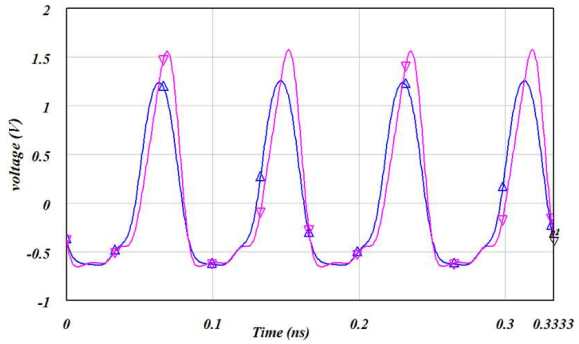

Figure 9: Voltage signal at the connection of one of diodes, (▽) RDA with BPF, (△) RDA with L-section.

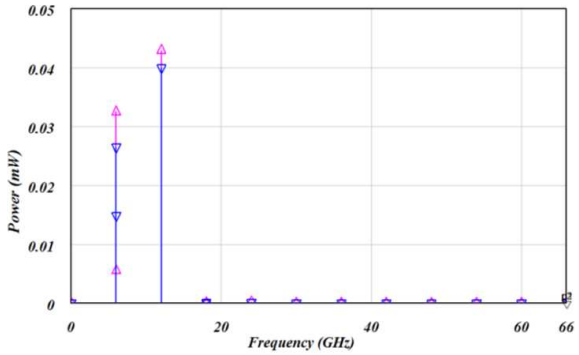

Figure 10: Power harmonics which incident to antenna port, (△) RDA with BPF, (▽) RDA with L-section.

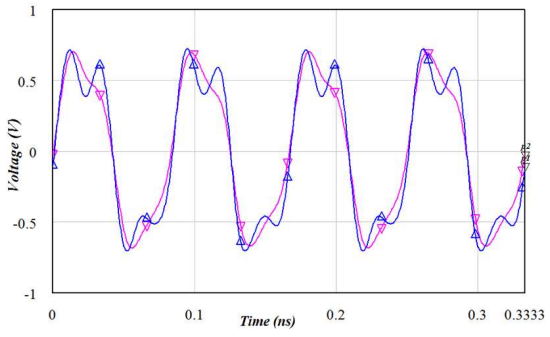

Figure 11: Voltage signals at the connection of diode, (△) RDA with BPF, (▽) RDA without BPF.

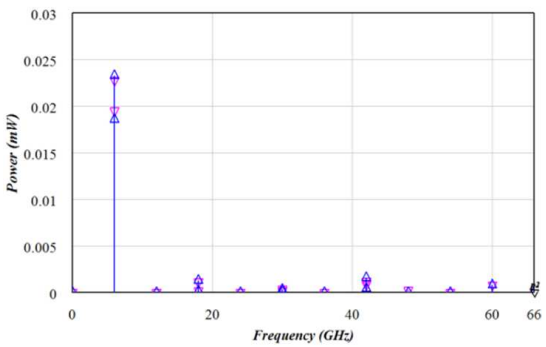

Figure 12: Power harmonics which incident to antenna port, (▽) RDA with BPF, (△) RDA with L-section.

The third structure is shown in Figure 6. Same as before structures, diode voltages are shown in Figure 11. In this structure, the conversion loss is approximately 7 dB at 6 GHz. The LO power is 10 dBm. Power harmonics which incident to antenna ports, are shown in Figure 12.

Voltage signal at diode node and Power harmonics which incident to antenna ports, are approximately equal, in three structures. Also, conversion losses in two cases (when BPF/L-section is placed between LO and mixer) are the same for three RDA structure. It means that replacement of BPF with L-section in heterodyne RDA does not affect to functionality of RDA mixer.

5. CONCLUSIONS

In present paper, BPF is replaced with two parts of transmission line (L-section). One of these transmission lines is located between LO and mixer and the other one connects to connection of LO and the first transmission line, in parallel mode. With this replacement, heterodyne RDA structure is fabricated smaller and lighter, and it is designed with less complexity, whilst no changes occur in signals at different nodes of circuit.

REFERENCES

1. Guo, Y. C., X. W. Shi, and L. Chen, "Retrodirective array technology," *Progress In Electromagnetics Research B*, Vol. 5, 153–167, 2008.
2. Van Atta, L. C., "Electromagnetic Reflector," U.S.Patent, No. 2908002, 1959.
3. Pon, C. Y., "Retrodirective array using the heterodyne technique," *IEEE Transaction on Antennas and Propagation*, 176–180, March 1964.
4. Leong, K. M. K. H., R. Y. Miyamoto, and T. Itoh, "Moving forward in retrodirective antenna arrays," *IEEE Potentials*, Vol. 22, 16–21, 2003.
5. Dehbashi, R., Z. Atlasbaf, and K. Forooraghi, "New compact size microstrip antennas with harmonics rejection," *IEEE Antennas and Wireless Propagation Letters*, Vol. 5, 395–398, 2006.
6. Edwards, T. C. and M. B. Steer, *Foundation of Interconnect and Microstrip Design,* 3rd edition, John Wiley & Sons, 2000.
7. Marimuthu, J., S. Member, and M. Esa, "Wide band and harmonic suppression method of parallel coupled microstrip bandpass filter using centered single groove," *Proceedings of the 2007 IEEE International Conference on Telecommunications*, 622–626, Malaysia, 2007.
8. Xiao, S., Z. Shao, Y. Zhang, M. T. Zhou, V. D. Hoang, and M. Fujise, "Microstrip antenna with compact coplanar harmonic suppression structure," *Antennas and Propagation Society International Symposium 2006*, 643–646, 2006.
9. Xiao, S., L. Jiang, B. Z. Wang, and J. Wang, "A millimeter wave microstrip antenna array with harmonics suppression elements," *Global Symposium on Millimeter Waves Proceeding*, 407–410, 2008.
10. Pobanz, C. W. and T. Itoh, "A conformal retrodirective array for radar applications using a heterodyne phased scattering element," *IEEE MTT-S International Microwave Symposium Digest,* 905–908, May 1995.
11. Diego, A. D., J. A. Garcia, and A. Mediavilla, "A retrodirective array using unbiased subharmonic resistive mixers," *IEEE MTT-S Digest*, 1249–1252, 2004.
12. Miyamoto, R. Y., Y. Qian, and T. Itoh, "Phase conjugator for active retrodirective array applications," *Electronic Letters*, Vol. 6, No. 1, 4–5, 2000.
13. Pozar, D. M., *Microwave Engineering*, Addison-Wesley Publishing Company, 1990.
14. Maas, S. A., *Nonlinear Microwave and RF Circuits*, 2nd Edition, Artech House Publishers, 2003.
15. Maas, S. A., *Microwave Mixers*, Artech House, 1986.
16. Zhang, J. and A. Raisanen, "A new model of step recovery diode for CAD," *IEEE MTT-S Digest*, 1459–1462, 1995.
17. Liao, S. Y., *Microwave Circuit Analysis and Amplifier Design,* Prentice Hall International Inc., 1987.

Mobile Phone EMC Deterioration Due to Different Realistic Usage Patterns

S. I. Yahya Al-Mously
School of Computer Engineering, Koya University, Koya, Iraq

Abstract— This paper presents in details the effects of different realistic usage patterns on the EMC, that represented by the antenna total efficiency (η_{tot}) and the total isotropic sensitivity (*TIS*), of different mobile phone handsets, where a commercial FDTD-based EM solver is used to solve Maxwell's equations. Different semi-realistic mobile phone handset models operating in the GSM900, GSM1800, and UMTS/IMT-2000 bands are simulated to achieve the available commercial models, whereas, a heterogeneous MRI-based CAD model is used to simulate the mobile phone user's head. The results achieved in this paper showed that certain realistic usage patterns during a call could dramatically affect the mobile phone antenna specifications, i.e., η_{tot}, and *TIS*, and consequently deteriorate its EMC.

1. INTRODUCTION

While moving towards a ubiquitous society where anyone can get information from anywhere at any time, antennas are becoming a key component for cellular handsets and other portable wireless devices. Users of portable wireless devices want such devices to be of small volume, light weight, and low cost. With the huge progress in very large scale integration (VLSI) technology, this dream has become a reality in the past two decades. All that imposed a big challenge to engineers in keeping the mobile phone handset compatible electromagnetically.

From a more technical point of view, the user's body, head and hand, have an impact on the mobile handset. The tissue of the user represents a large dielectric and lossy material distribution in the near field of a radiator. It is obvious, therefore, that all antenna parameters, such as impedance, radiation characteristic, radiation efficiency and total isotropic sensitivity (*TIS*), will be affected by the properties of the tissue. Moreover, the effect can differ with respect to the individual habits of the user in placing his hand around the mobile handset or attaching the handset to the head. Optimized user interaction, therefore, becomes a technical performance parameter of cellular mobile phones. The electromagnetic interaction between mobile phone antenna and human body was investigated extensively in the previous literatures, where a review of the most published articles in this field can be found in [1], whereas, the Electromagnetic Compatibility (EMC) of mobile phone antennas are studied by few authors [2, 3].

The EMC of a cellular handset is defined as its ability to function properly in its intended electromagnetic environment and without introducing excessive electromagnetic energy that may interfere with other devices. This paper investigated the mobile phone EMC, that represented in terms of total efficiency (η_{tot}) and *TIS* deterioration due to different realistic usage patterns, where both η_{tot} and *TIS* are computed due to different handhold and handset positions.

2. MOBILE PHONE ANTENNA EFFICINCY AND TIS

2.1. Antenna Total Efficiency (η_{tot})

The efficiency of a handset antenna is the ratio of the total power radiated by the antenna to the forward power available at its terminals (or those of its associated matching network). The antenna efficiency is a parameter which takes into account the amount of losses at the terminals of the antenna and within the structure of the antenna. These losses are: reflections because of mismatch between the transmitter and the antenna, and I^2R losses (conduction and dielectric). Hence the total antenna efficiency can be written as:

$$\eta_{\text{tot}} = \eta_{\text{mis}} \cdot \eta_{\text{c}} \cdot \eta_{\text{d}} \tag{1}$$

where: η_{tot} = total efficiency, $\eta_{\text{mis}} = (1 - |\Gamma|^2)$ mismatch efficiency, Γ = reflection coefficient, η_{c} = conduction efficiency, and η_{d} = dielectric efficiency. Since η_{c} and η_{d} are difficult to separate, they are lumped together to form the η_{rad} efficiency which is given as [4]:

$$\eta_{\text{rad}} = \eta_{\text{c}} \cdot \eta_{\text{d}} \cdot \frac{R_r}{R_r + R_L} \tag{2}$$

η_{rad} is called as the antenna radiation efficiency, and is defined as the ratio of the power delivered to the radiation resistance R_r, to the power delivered to R_r and loss resistance R_L. Efficiency may be measured either in passive or active modes. In active measurements, it is difficult to determine the forward power, so the better active parameter is a measurement of the total radiated power (TRP) — which is what matters in network performance.

In the typical operating situation, a mobile terminal is located in very close proximity to the user. When RF radiation is emitted from a mobile terminal held next to a human, a portion is radiated away into the surrounding air, and body tissues absorb another portion. When a mobile terminal is located in a traditional talk position, mostly head and hand regions absorb RF radiation. Thus, the handset efficiency deteriorated drastically in realistic usage patterns [5, 6].

2.2. Total Isotropic Sensitivity (*TIS*)

The sensitivity is defined as being the input signal power that gives rise to a specific frame error rate or residual bit error rate. The sensitivity is sampled in orthogonal polarizations at points spread over a surface surrounding the handset [7]. The *TIS* is a measure of the handset receiving performance, where both *TIS* and *TRP* together determine the effectiveness of the handset as a piece of radio equipment, in particular the maximum range at which the handset can operate from the base station with some given level of performance [7]. As compared with the normal receiver sensitivity in the GSM-family, a typical specification for the *TIS* is around 10-dB higher in talk position [8]. The *TIS* can be measured in a reverberation chamber with a definition formula given in [9]. The sensitivity of a commercially available GSM900 phone in receiving mode could be measured in a reverberation chamber for different handset setups (in free space and against head phantom) [10].

3. NUMERICAL COMPUTATIONS

The Finite-Difference Time-Domain (FDTD) method proposed by Yee in 1966 [11] is a direct solution of Maxwell's curl equations in the time domain. Maxwell's curl equations are discretized using a 2nd order finite-difference approximation both in space and in time in an equidistantly spaced mesh [12], where a FDTD-based EM solver, SEMCAD X, is used to simulate the handheld next to head in different position at different frequencies, and solve Maxwell's equations.

3.1. Modeling of Mobile Phone Handset

Three groups of twelve single-band handset models are designed and simulated to find out the available commercial models design as follow:

1. Candy-bar type handset with left-side external antenna (model-A),
2. Candy-bar type handset with upper internal patch antenna (model-B),
3. Clamshell type handset with left-side external antenna (model-C),
4. Clamshell type handset with upper internal patch antenna (model-D).

The first group of the designed handsets is working at 900 MHz to cover the GSM-900 band, the second group is working at 1800 MHz to cover the GSM-1800 band, and the third group is working at 2025 MHz to cover the UMTS-IMT 2000 band. In this paper, the adopted external antenna is a short whip, top-loaded with a small cylinder [6], whereas, the internal antenna is a shorted microstrip patch antenna [6]. Fig. 1 shows the adopted handset models close to head at different positions.

3.2. Human-hand Model

A homogeneous hand model consisting of three tissues (skin, muscle, and bone) [5, 6, 13] is designed with two common different holding positions referred as hand1 and hand2. Hand1 is gripping the lower part of the handset, whereas, hand2 is gripping the upper part of the handset. The proposed hand-holds represent the two possible extreme cases.

3.3. Human-head Model

The user's head is simulated using an MRI-based anatomically correct model, High-Resolution European Female Head (HR-EFH), available with SPEAG [12]. The electrical properties and densities of tissues are given in [6].

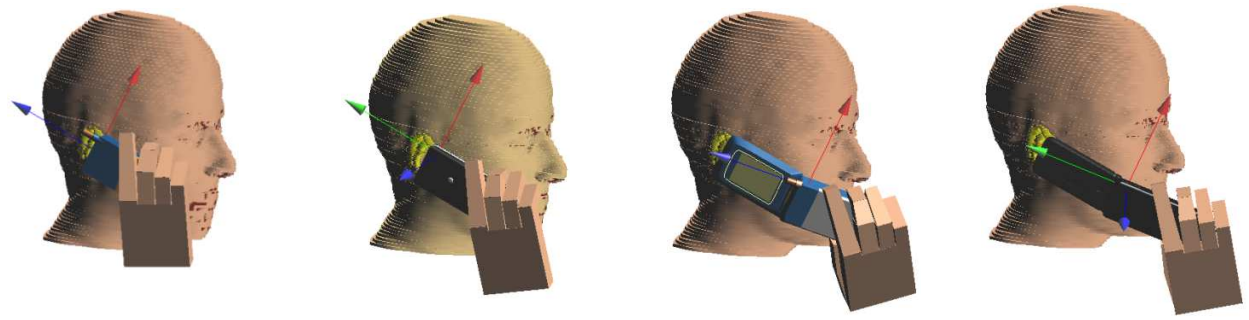

(a) Model-A, Hand1 (b) Model-B, hand1 (c) Model-C, hand1 (d) Model-D, hand1

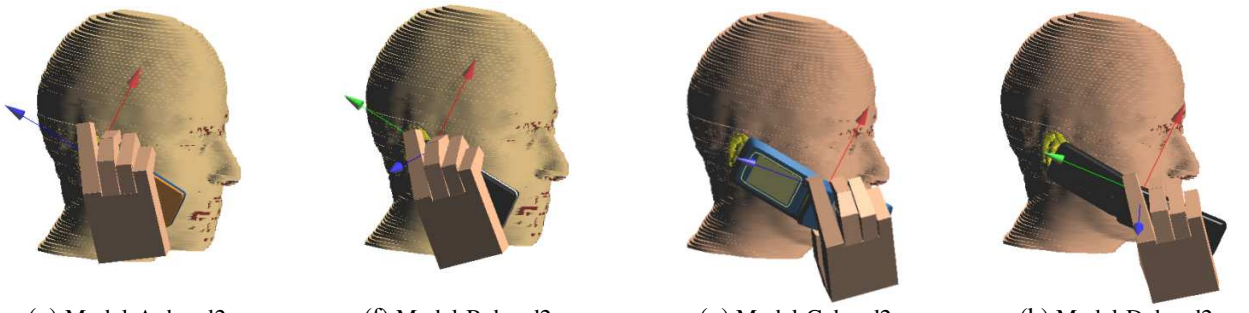

(e) Model-A, hand2 (f) Model-B, hand2 (g) Model-C, hand2 (h) Model-D, hand2

Figure 1: Handset models-A, B, C, and D in close proximity to HR-EFH gripped by hand at different positions, i.e., hand1 and hand2.

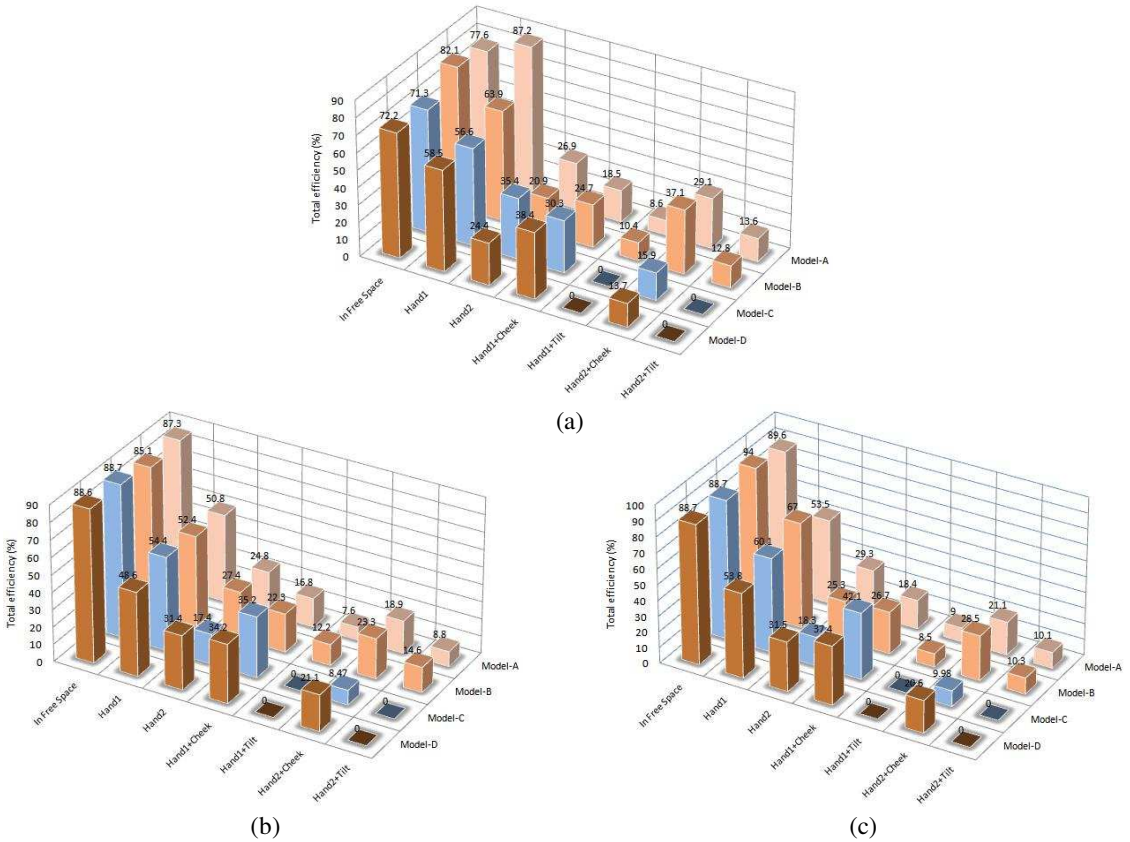

(a) (b) (c)

Figure 2: 3D-bar representation of the handset models total efficiency at different positions operating at; (a) 900 MHz, (b) 1800 MHz, and (c) 2025 MHz.

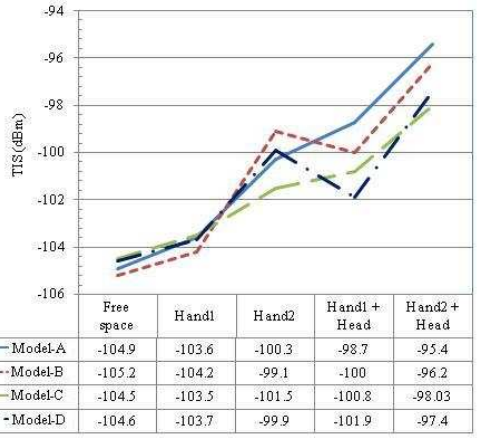

	Free space	Hand1	Hand2	Hand1 + Head	Hand2 + Head
Model-A	-104.9	-103.6	-100.3	-98.7	-95.4
Model-B	-105.2	-104.2	-99.1	-100	-96.2
Model-C	-104.5	-103.5	-101.5	-100.8	-98.03
Model-D	-104.6	-103.7	-99.9	-101.9	-97.4

(a)

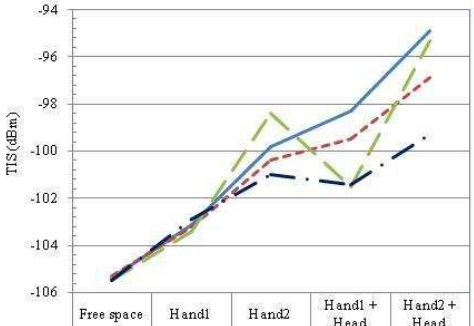

	Free space	Hand1	Hand2	Hand1 + Head	Hand2 + Head
Model-A	-105.4	-103.1	-99.8	-98.3	-94.9
Model-B	-105.3	-103.2	-100.4	-99.5	-96.9
Model-C	-105.5	-103.4	-98.4	-101.5	-95.3
Model-D	-105.5	-102.9	-101	-101.4	-99.3

(b)

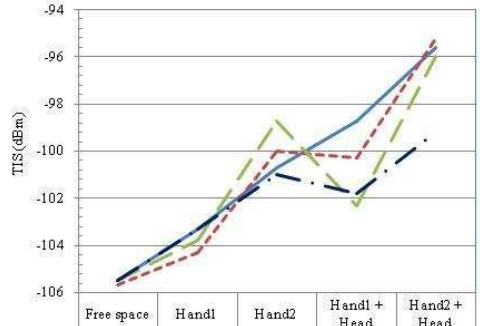

	Free space	Hand1	Hand2	Hand1 + Head	Hand2 + Head
Model-A	-105.5	-103.3	-100.7	-98.7	-95.6
Model-B	-105.7	-104.3	-100	-100.3	-95.2
Model-C	-105.5	-103.8	-98.7	-102.3	-96
Model-D	-105.5	-103.3	-101	-101.8	-99.2

(c)

Figure 3: *TIS* versus handset setup for the different adopted models at cheek-position operating at: (a) 900 MHz, (b) 1800 MHz, and (c) 2025 MHz.

4. SIMULATION RESULTS

Figure 2 demonstrates the η_{tot} values of the twelve adopted mobile phone handset antennas versus realistic usage patterns, i.e., in free space, in hand1, in hand2, in hand1+*cheek*, in hand2+*cheek*, in hand1+*tilt*, and in hand2+*tilt*, whereas, Fig. 3 demonstrates the *TIS* values of the adopted handsets versus different realistic usage patterns with *check*-position only. As shown in these figures, holding the mobile phone handset next to head may dramatically deteriorate both η_{tot} and *TIS*.

At 900 MHz operating frequency, a maximum deterioration was noticed for the handset model-A, where 89% decrease in the η_{tot} value while holding the handset with hand1 at *tilt*-position, whereas, 9.5 dBm increase in the *TIS* while holding the handset with hand2 at *cheek*-position. The same scenario for handset model-A was noticed at 1800 MHz operating frequency, where more than 91% decrease in the η_{tot} value while holding the handset with hand1 at tilt-position, whereas, 10.5 dBm increase in the *TIS* while holding the handset with hand2 at *cheek*-position. At 2025 MHz operating frequency, a maximum deterioration was noticed for the handset model-B, where 91% decrease in the η_{tot} value while holding the handset with hand1 at *tilt*-position, whereas, 10.5 dBm increase in the *TIS* while holding the handset with hand2 at *cheek*-position. The *TIS* values during a call are agreed with those given in [5].

It is obvious that the candy-bar type handset, i.e., model-A, is more affected by the vicinity of the user's head whereas, the clamshell type handset, i.e., model-C and model-D, is less affected by the vicinity of the user's head. It should be noticed that for the clamshell type and due to its shape, only a *cheek*-position was considered. This is why the η_{tot} of clamshell at *tilt*-position appears equal to zero in Fig. 2. According to the results shown in both Fig. 2 and Fig. 3, the handset antenna matching parameters and the handset EMC may include the presence of hand and head during the design process, with an acceptable EMC in free space. This will insure less handset EMC deterioration while making a call and deposits less SAR in the user's tissues.

5. CONCLUSIONS

The results achieved in this paper showed that certain realistic usage patterns during a call could dramatically affect the mobile phone antenna specifications, i.e., total efficiency, and total isotropic sensitivity, and consequently deteriorate its electromagnetic compatibility. This electromagnetic compatibility deterioration may, firstly: disables the mobile phone handset to function properly in its intended electromagnetic environment, and secondly: push the mobile phone handset to introduce excessive electromagnetic energy to keep a successful electromagnetic connection with the cellular base-station. The later may increase the specific absorption rate (SAR) in the user's head. Thus, the realistic usage pattern should be considered while the mobile phone designed and assembled by the manufacturer.

The manufacturer may involve both the human head and handhold dielectric properties while designing and attaching the antenna to PCB of the prototype mobile phone handset and calculating the final electromagnetic specifications, i.e., antenna total efficiency and total isotropic sensitivity.

REFERENCES

1. Al-Mously, S. I., "Design and performance enhancement of cellular handset antennas and assessment of their EM interaction with a human," School of Applied Sciences and Engineering, Academy of Graduate Studies, Tripoli, Libya, 2009.
2. Su, C. M., K. L. Wong, C. L. Tang, and S. H. Yeh, "EMC internal patch antenna for UMTS operation in a mobile device," *IEEE Transaction on Antennas Propagation,* Vol. 53, 3836–3839, Nov. 2005.
3. Su, C. M., C. H. Wu, K. L. Wong, S. H. Yeh, and C. L. Tang, "User's hand effects on EMC internal GSM/DCS dual-band mobile phone antenna," *Microwave and Optical Technology Letters*, Vol. 48, No. 8, 1563–1569, Aug. 2006.
4. Balanis, C. A., *Antenna Theory: Analysis and Design*, John Wiley and Sons, 1997.
5. Al-Mously S. I. and M. M. Abousetta, "A study of the hand-hold impact on the EM interaction of a cellular handset and a human head," *International Journal of Electronics, Circuits, and Systems (IJECS),* Vol. 2, No. 2, 91–95, Spring, 2008.
6. Al-Mously, S. I. and M. M. Abousetta, "Anticipated impact of hand-hold position on the electromagnetic interaction of different antenna types/positions and a human in cellular communications," *International Journal of Antennas and Propagation (IJAP)*, Vol. 2008, Article ID 102759, 22 pages, 2008.
7. Chen, Z. N., *Antennas For Portable Devices*, John Wiley & Sons, Ltd, Chichaster, 2007.
8. Lindberg, P., "Wideband active and passive antenna solutions for handheld terminals," Ph.D. Thesis, 266, Faculty of Science and Technology, Uppsala University, Uppsala, Sweden, 2007.
9. Orlenius, C., P.-S. Kildal, and G. Poilasne, "Measurements of total isotropic sensitivity and average fading sensitivity of CDMA phones in reverberation chamber," *Proceedings of the IEEE Antennas and Propagation Society International Symposium,* Vol. 1A, 409–412, Washington DC, USA, Jul. 2005
10. Orlenius, C., N. Serafimov, and P.-S. Kildal, "Procedure for measuring radiation efficiency in downlink band for active mobile phones in a reverberation chamber," *Proceedings of the IEEE Antennas and Propagation Society International Symposium (AP-S 2003)*, Vol. 4, 731–734, Columbus, Ohio, USA, Jun. 2003
11. Yee, K. S., "Numerical solution of initial boundary value problems involving Maxwell's equations in isotropic media," *IEEE Transaction on Antennas and Propagation*, Vol. 14, No. 3, 302–307, 1966.
12. SEMCAD X Reference Manual, *SEMCAD Simulation Platform for Electromagnetic Compatibility, Antenna Design and Dosimetry*, SPEAG, http://www.semcad.com.
13. Al-Mously, S. I. and M. M. Abousetta, "Effect of the hand-hold position on the EM interaction of clamshell-type handsets and a human," *PIERS Proceedings*, 1727–1731, Moscow, Russia, Aug. 18–21, 2009.

A Parametric Study and Design of the Balanced Antipodal Vivaldi Antenna (BAVA)

A. R. Bayat and R. Mirzakhani
International Imam Khomeini University (IKIU), Qazvin, Iran

Abstract— Now days the ultra wide band antenna (UWB) is widely used in different applications such as microwave imaging, wireless communications, ground penetrating radars, remote sensing and phased arrays. Since then the Vivaldi antenna is a suitable candidate for this applications. This antenna has 3 main categories: 1- Co-planar Vivaldi antenna, 2- Antipodal Vivaldi antenna and 3- Balanced Antipodal Vivaldi antenna (BAVA). The BAVA has great advantages over the other types of antennas, as well as better radiation characteristics, wider bandwidth and better return loss characteristics. In this paper a parametric study and design of the balanced antipodal Vivaldi antenna (BAVA) has been taken with the aim of using them as elements of wideband phased arrays. The study reported here was performed in the 1–20 GHz by using commercial electromagnetic simulation software ANSOFT HFSS. The BAVA is constructed using RT/duroid 6002 (Rogers Corporation CT. USA) which has relative permittivity of 2.94. The simulation showed that the return loss is better than −10 dB within the bands. This antenna is suitable for imaging radar or tissue scanning applications.

1. INTRODUCTION

The Vivaldi antenna was first introduced by Gibson in "The Vivaldi aerial" [1]. Since then, it is widely used in different applications such as microwave imaging, wireless communications and ground penetrating radars. The Vivaldi antenna, nowadays, has three main categories: The coplanar Vivaldi antenna which is introduced by Gibson, the antipodal Vivaldi antenna [2] and balanced antipodal Vivaldi antenna [3]. These categories, in general, have the exponentially tapered flares. In all of them, traveling wave propagate on the inner edges of the flares which is the main mechanism for radiation. So, exponentially tapered flare is the unique specific feature of this work which

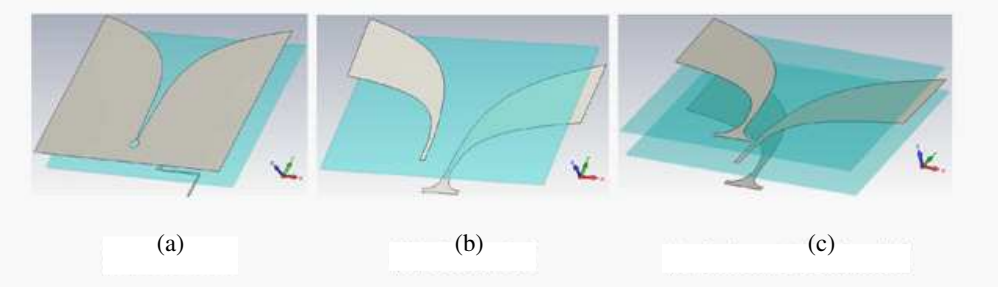

Figure 1: Three structures of the Vivaldi antenna. (a) Coplanar. (b) Antipodal. (c) Balanced antipodal.

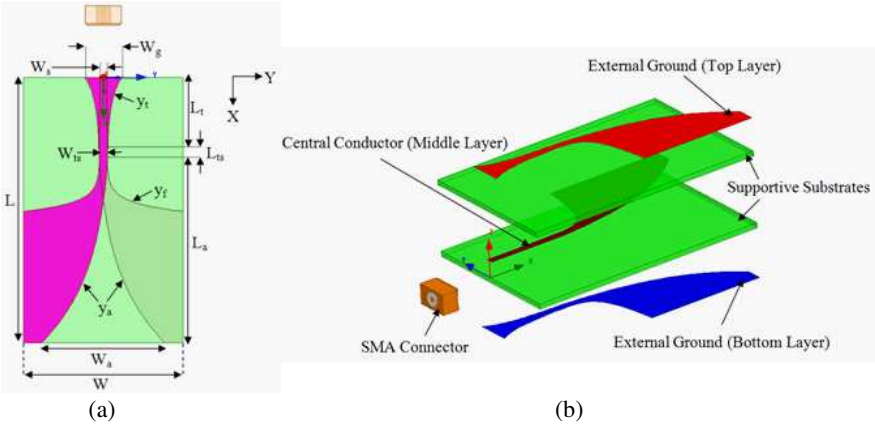

Figure 2: (a) Geometry and dimensions of the BAVA. (b) Exploded view of designed BAVA.

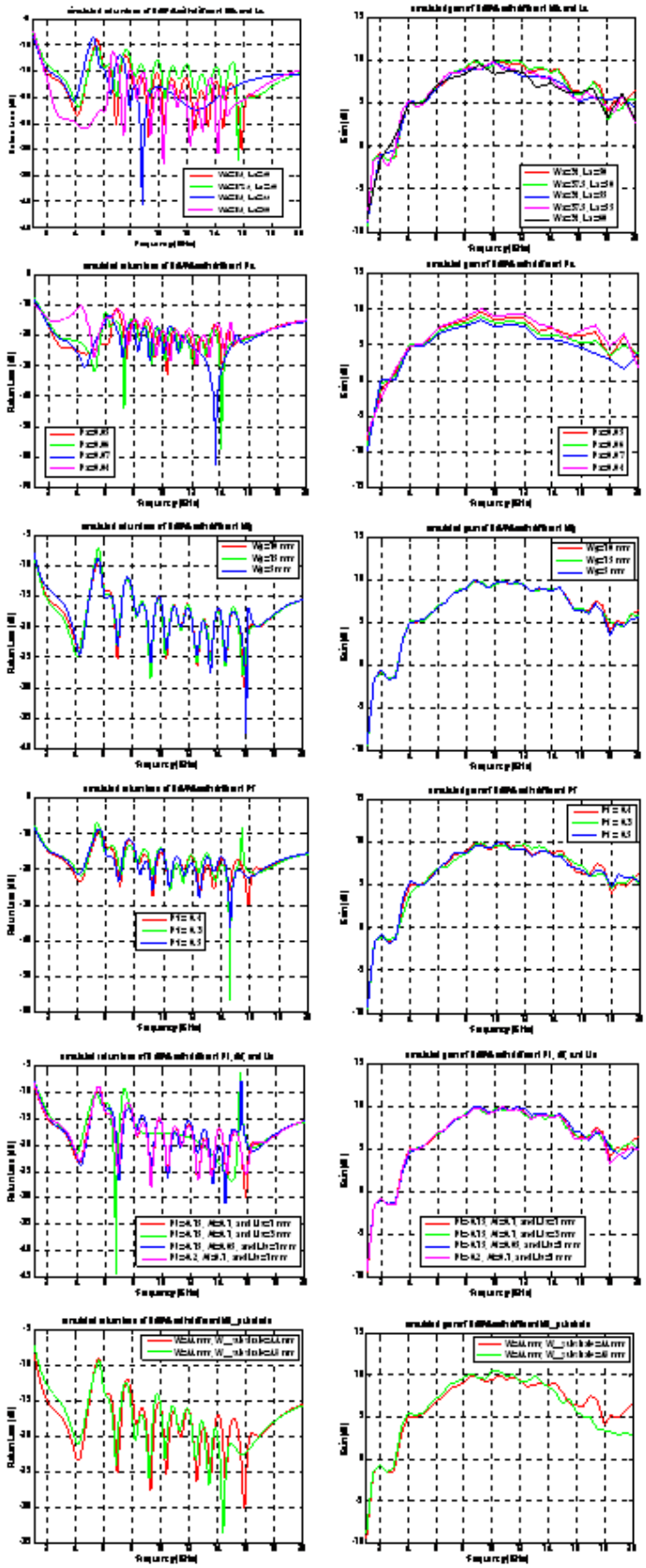

Figure 3: The variation of return loss and gain of BAVA with different parameters.

makes the antenna operates over a broad frequency bands. Similar to bow-tie antenna, Vivaldi antenna can be manufactured reasonably cheap using PCB technology. In coplanar Vivaldi antenna, the oldest form of Vivaldi, two radiator planes are on the same side of the dielectric sheet. This structure has been shown in Figure 1(a). The antenna can be fed by aperture coupling from the other side as depicted in this figure. There is another feeding circuit using broadband balloon which is not convenient in many designs due to the length of these balloons and the complexity they might add to the structure.

The antipodal Vivaldi antenna (Figure 1(b)) is proposed to solve the feeding in coplanar ones. In this type of Vivaldi antenna one of the layers is printed on top and the other one which is tapered in opposite direction is printed on the bottom of the dielectric substrate sheet. This antenna can be fed easily by soldering the connector to the two sides of the sheet. The impedance matching of conventional 50 Ω line has been done by the transition between twin parallel strip-line to micro-strip line. The antipodal Vivaldi antenna, however, increase the cross-polarized radiation which is not suitable for radar applications. This can be improved by balanced antipodal structure of Vivaldi antenna, Figure 1(c). In balanced antipodal Vivaldi antenna, another dielectric sheet has been added on top of the antipodal structure and a metal plate just like the one in the bottom of the antenna has been printed on top of the newly added sheet [4].

2. ANTENNA DESIGN

The antenna consists of three copper layers; the two external layers are connected to the feeding line ground planes and the central layer is connected to the signal conductor of the feeding line (Figure 2). The copper layers are supported by two dielectric substrates on each side of the antenna. The feed is a gradual transition between a strip-line to a tri-strip transmission line (TL). The conductor width increases linearly while the ground width decreases exponentially to keep constant impedance along the transition [5]. The tri-strip TL extends for a short distance and then the grounds and conductor start to flare in opposite directions with exponential curvatures to create the antenna aperture [5].

The geometry parameters are presented in Figure 2: W, L and T are the overall width, length and thickness respectively, W_s and W_g are the width of the strip-line and corresponding ground plane width, W_{ts} is the width of the transmission line tri-strip, W_a defines the actual aperture width, L_t, L_{ts} and L_a correspond to the transition, tri-strip TL and aperture length respectively. The dielectric thicknesses are defined by T for the supportive substrates. Finally, the exponential curves for the transition, flare and aperture (Y_t, Y_f, Y_a) are defined by the following equation:

$$y_i = \pm\left(A_i \times e^{P_i \times (x - B_i)} + C_i\right) \quad i:\ a,\ f, \text{ and } t \tag{1}$$

where, A is the scaling factor, P the exponential rate, B the shifting value and C the offset. These parameters are defined for each curve in Table 1.

3. DESIGN AND PARAMETRIC STUDY

The study shows that dielectric with permittivity slightly higher than the surrounding environment ($\varepsilon_r = 2.5$) produces superior radiation behavior while the thickness of the supportive substrate (T) does not significantly influence the antenna performance. Once the dielectric material has been selected, the influence of increasing the aperture variables W, W_a and P_a has been investigated. Increasing the aperture or total width improves the S_{11} performance but usually degrades the other metrics. A small exponential rate (P_a) is preferred which actually translates to a longer aperture. The flare parameters A_f and P_f influence the matching. A sharp flare curve increases the end-fire radiation but at the expense of degrading the S_{11} performance. The transition dimensions W_g, W_s and W_{ts} are defined to provide TLs with 50 Ohms characteristic impedance at both ends. P_t is selected to get the best transmission coefficient (S_{21}).

Table 1: Exponential curves parameters [5].

Curve	A	P	B	C
Y_t	$\frac{W_{ts}-W_g}{2\times(e^{P_t \times L_t}-1)}$	P_t	0	$\frac{W_g}{2} - A_t$
Y_f	A_f	P_f	$L_t + L_{ts}$	$\frac{W_{ts}}{2} - A_f$
Y_a	$\frac{W_{ts}-W_g}{2\times(e^{P_t \times L_t}-1)}$	p_a	$L_t + L_{ts}$	$-\frac{W_{ts}}{2} - A_a$

The selected dielectric is RT/duroid® 6002 from Rogers Corporation which has a relative permittivity of 2.94. The thickness T is chosen to be 1.524 mm. The lengths are listed here: $L = 74$ mm, $L_t = 23$ mm, $L_{ts} = 1$ mm, $L_a = 50$ mm. Finally the remaining parameters are: $W = 44$ mm, $W_a = 34$ mm, $W_g = 10$, $W_s = 2$ mm, $W_{ts} = 2.24$ mm, $P_t = -0.15$, $P_f = 0.4$, $P_a = 0.05$ and $A_f = 0.1$.

4. FINAL DESIGN AND SIMULATION

The lengths were already defined but are listed here again: $L = 84$ mm, $L_t = 23$ mm, $L_{ts} = 1$ mm, $L_a = 60$ mm, $W = 44$ mm, $W_a = 34$ mm, $W_g = 10$, $W_s = 2$ mm, $W_{ts} = 2.24$ mm, $P_t = -0.15$ mm, $P_f = 0.4$ mm, $P_a = 0.05$ mm, $A_f = 0.1$ mm, $B_a = 24$ mm, $A_a = 0.00095$ mm, $C_a = -2.0694$ mm, $C_f = 1.02$ mm, $A_t = 0.004$ mm and $C_t = 0.993$ mm. The simulation is done by ANSOFT HFSS

Figure 4: The H-plane and E-plane radiation pattern of BAVA from 1 to 20 GHz.

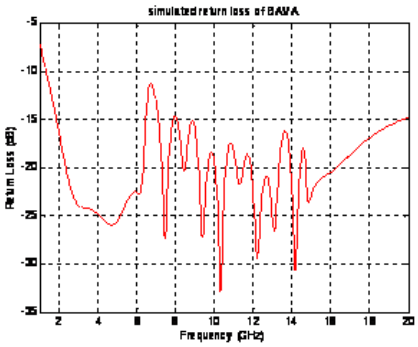

Figure 5: Simulated return loss of BAVA.

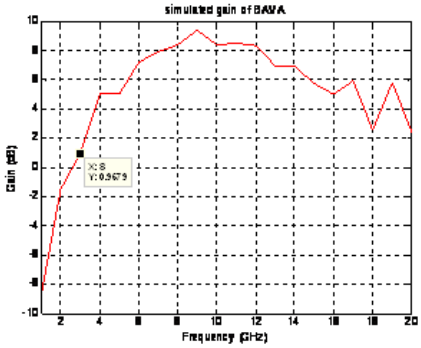

Figure 6: Simulated gain of BAVA.

V.13.0. For this design, S_{11} is below -10 dB above 1 GHz, as shown in Figure 5 and the gain up to more than 9 dB as shown in Figure 6. The radiation patterns in H-plane and E-plane are shown in Figure 4.

5. CONCLUSIONS

This paper presents the design and detailed results of the Balanced Antipodal Vivaldi Antenna with the selection of RT/Duriod 6002 substrate material. This antenna is showing remarkable performance over the entire frequency range between 1–20 GHz with high gain up to more than 9.5 dB and very low Cross polarization. This antenna can be used as an element in phased arrays for wide band wide angle scanning because of its wide beam width in both the planes and also providing wide bandwidth.

ACKNOWLEDGMENT

The authors would like to gratefully acknowledge Imam Khomeini International University for providing the facilities and financial support.

REFERENCES

1. Gibson, P. J., "The Vivaldi aerial," *9th European Microwave Conference*, 101–105, 1979.
2. Gazit, E., "Improved design of the Vivaldi antenna," *Proceeding of Institute of Electrical Engineering*, Vol. 135, No. 2, 89–92, 1988.
3. Langly, J., P. Hall, and P. Newham, "Novel ultrawide-bandwidth Vivaldi antenna with low crosspolarisation," *Electronics Letters*, Vol. 29, No. 23, 2004–2005, 1993.
4. Azodi, H., "UWB air-coupled antenna for ground peneterating radar," Thesis Submitted for Degree of Master of Science in Electrical Engineering, Delft University of Technology, 2009–2010.
5. Bourqui, J., M. Okoniewski, and E. C. Fear, "Balanced antipodal Vivaldi antenna for breast cancer detection," *Proc. 2nd Eur. Conference Antenna Propagation*, 1–5, Edinburgh, U.K., Nov. 2007.

Study of Performance Improvement on the Design of Compact SRR Embedded Microstrip Low Pass Filter

S. Suganthi[1], **S. Raghavan**[2], **and D. Kumar**[3]

[1]Shri Angalamman College of Engineering and Technology, Trichy, India
[2]National Institute of Technology, Trichy, India
[3]Periyar Maniammai University, Thanjavur, India

Abstract— This paper proposes a design of a Chebyshev type microstrip low pass filter (LPF) loaded with an array of split ring resonator (SRR) as an additional plane between ground and filter sections for superior performance. Metamaterials (MTM) are the artificial materials engineered to exhibit double negative (DNG) properties that are not found in nature. Such a material gains its properties from its structure rather than its chemical composition. Many researchers have introduced various MTM structures such as spiral resonator, split ring resonator, complementary slip ring resonators, omega, S structures etc., in recent years in that category. The advantage of MTM is its compact size with ability to provide improved performance. Firstly the conventional microstrip LPF was designed at 2 GHz. The novel SRR consisting of new V shaped structures was designed and verified separately for the existence of its μ negative and ε negative properties using a separate coding written in MATLAB for Nicolson-Ross-Wier (NRW) method. Finally the already designed LPF was loaded with the verified metamaterial structure and simulated. For the design and simulation, HFSS 3D simulation tool was used. On comparison it is observed that the SRR loaded low pass filter provides improved performance over the conventional type.

1. INTRODUCTION

A miniature size better performing low pass filters are of great demand in the applications of microwave circuits. Though the low pass filters [1] designed using microstrip technology provides low profile, improvement in the filter characteristics are still investigated intensively with different alternatives [2]. Recently metamaterials (MTM) play important role in the performance improvement [3] of microstrip components such as antennas, filters etc.. Russian Scientist Victor Vesselago in 1967 first introduced the MTM concept in theories during 1967. Later the use and applications of these materials in the field of microwaves have been under investigation vigorously since year 2000 after a silent period of roughly around 30 years when the work on slip ring resonators (SRR) proving the negative μ and ε was first reported by B. Pendry et al., in 2000. MTMs are artificial materials obtained from their physical structures and not from their chemical composition. They are attracting researchers because of their negative medium properties which influence the performances. The effective medium thus prepared are recognized as negative refractive index (NRI) medium, left handed metametarial (LH MTM), double negative medium (DNG), single negative medium(SNG), epsilon negative medium (ENG), mu negative medium (MNG), all [4] depending on the negativeness of dielectric permittivity and magnetic permeability of the new artificial substrate. There are mainly resonator and transmission line approaches for preparing the artificial substrates. Researchers have been contributed a variety of SRR and CSRR structures [6–9] for such investigations. The SRR or CSRR embedded on or in the substrate disturbs [10] the shield current distribution in the ground plane and changes the properties of inductor and capacitor. The proposed microstrip low pass filter is based on resonator approach. This makes use of a novel SRR consisting of V shaped metallic structures arranged to form an array on a plane embedded between the filter on the top and the ground at the bottom giving rise to change in the effective inductance and capacitance of the mictrostrip line laid as filter. The filter properties are influenced by the presence of the embedded MTM and also the gap distance between the unit cells. The difference between the conventional grounded filter and the SRR embedded and grounded filter is visible from the characteristics shown in Figure 2.

2. CONVENTIONAL MICROSTRIP LOW PASS FILTER DESIGN

The conventional LPF of order three has been designed using the empirical formulae found in literatures [1, 2, 6, 8]. This paper considers the design aspects of third order Chebyshev type low

pass T section filter. The simplified design steps involved in this filter are described in Equations from (1) to (12).

$$Ripple \quad r = 1 + a_m^2 T_n^2\left(\omega'\right) \tag{1}$$

where for stop band attenuation

$$T_n^2\left(\omega'\right) = 1 \tag{2}$$

for stop band attenuation r_{pba} at f_s,

$$T_n^2(\omega') = \cosh^2\left(n\cosh^{-1}\,\omega'_s\right) \tag{3}$$

$$\omega'_s = \omega_s/\omega_c \tag{4}$$

$$\frac{W}{h} = \frac{8\ e^A}{e^{2A}\ -2} \tag{5}$$

where

$$A = \frac{Z_o}{6}\left[\frac{\varepsilon_r+1}{2}\right]^{1/2} + \frac{\varepsilon_r-1}{\varepsilon_r+1}\left[0.23+\frac{0.11}{\varepsilon_r}\right] \tag{6}$$

The characteristic impedance Z_0 is essentially considered to be 50 ohms for matching conditions and ε_r is the relative permittivity of the substrate material. Depending on whether $W/h < 1$ or $W/h \geq 1$, one can choose the appropriate formula for the determination of the effective medium property.

If $W/h\ <\ 1$, then the following Equations (7) and (8) may be chosen

$$\varepsilon_{eff} = \left[\frac{\varepsilon_r+1}{2}\right] + \left[\frac{\varepsilon_r-1}{2}\right]\left[\left(1+\frac{12h}{W}\right)^{-\frac{1}{2}} + 0.04\left(1-\frac{W}{h}\right)\right]^2 \tag{7}$$

$$Z_0 = \frac{60}{\sqrt{\varepsilon_{eff}}}\ln\left[\left(\frac{8h}{W}\right)+0.25\left(\frac{W}{h}\right)\right] \tag{8}$$

If $W/h \geq 1$, then the following Equations (9) and (10) may be used

$$\varepsilon_{eff} = \left[\frac{\varepsilon_r+1}{2}\right] + \left[\frac{\varepsilon_r-1}{2}\right]\left[1+\frac{12h}{W}\right]^{-1/2} \tag{9}$$

$$Z_0 = \left[\frac{377}{\sqrt{\varepsilon_{eff}}}\right]\left[\frac{W}{h}+1.393+\left(\frac{2}{3}\right)\ln\left(\frac{W}{h}+1.444\right)\ \right]^{-1} \tag{10}$$

For the inductor, $Z_0 = Z_{0L} = 100$ ohms and for the capacitor $Z_0 = Z_{0C} = 20$ ohms may be used with reference to the Wheeler's curve found in literature [2]. Similarly the transmission line length, the width and length of inductor and capacitor can be calculated. The transmission line length can be taken to be multiples of $\frac{\lambda_{g0}}{4}$. Moreover for pass band ripple of 0.5 dB the g values are $g_o = 1.0000,\ g_1 = 1.\ 5963,\ g_2 = 1.0969,\ g_3 = 1.5963$ and $g_4 = 1.0000$. If any other ripple value is planned then the appropriate g values can be obtained from the table in literature and in [2, 3]. The other parameters can be calculated using the equations listed below:

The free space wave length

$$\lambda_o = c/f_c \tag{11}$$

The wave length through transmission line

$$\lambda_{go} = \frac{\lambda_0}{\sqrt{\varepsilon_{effTx}}} \tag{12}$$

The transmission line length

$$L_{Tx} = \ \lambda_{g0}/8 \tag{13}$$

The wavelength through the inductor

$$\lambda_{gL} = \lambda_0/\sqrt{\varepsilon_{effL}} \tag{14}$$

The wavelength through the capacitor

$$\lambda_{gC} = \lambda_0/\sqrt{\varepsilon_{effC}} \tag{15}$$

For T section filter the following formulae may be used:

Length of inductor

$$\beta L_{\ L1,L3} = L_{1,3}\frac{Z_0}{Z_{0L}} \quad \text{where} \quad \beta = 2\pi/\lambda_{gL} \tag{16}$$

where

$$L_1 = L_3 = (Z_0/g_0)\ (\Omega_c/2\pi f_c)\ g_1 \tag{17}$$

Length of capacitor

$$\beta L_{c2} = C_2\frac{Z_{0L}}{Z_0} \quad \text{where } \beta = 2\pi/\lambda gc \tag{18}$$

where

$$C_2 = (g_0/Z_0)\ (\Omega_c/2\pi f_c)\ g_2 \tag{19}$$

The roll-off rate [6] for the LPF is given by

$$\xi = \frac{\alpha_{\max} - \alpha_{\min}}{f_s - f_c} \tag{20}$$

where ξ is in dB/GHz and $\alpha_{\max}$ and $\alpha_{\min}$ are the attenuation points corresponding to f_s and f_c respectively. The input parameters considered for the design are the cut-off frequency f_c, the stop band frequency f_s, the stop band attenuation r_{sba}, the pass band ripple level r_{pba}, the dielectric permittivity of the substrate ε_r the thickness of the substrate h and the characteristic impedance for matching Z_O.

3. DESIGN AND SIMULATION

3.1. Conventional Filter Synthesis

The conventional filter synthesis was carried out using procedure outlined in equations from (1) to (20) and inputting the specified set of data $f_c = 2\,\text{GHz},\ f_s = 4\,\text{GHz},\ r_{sba} = 25\,\text{dB},\ r_{pba} = 0.5\,\text{dB},$ $\varepsilon_r = 4.4$, $h = 1.6\,\text{mm}$, $L_{Tx} = \frac{\lambda_{g0}}{8}$ and $Z_o = 50\,\Omega$, and the dimensions are as indicated in the Table 1. The corresponding filter section is shown in the inset in Figure 2(b). For the design and simulation the HFSS software is used. Simulations are performed for both the conventional T section filter as well as novel V shaped SRR embedded third order LPF. The filter components are designed using copper conductor on a double side printed $FR4$ substrate of thickness 1.6 mm and permittivity 4.4 with dimensions (47.54 mm × 20.3 mm). The ground plane is laid at the bottom of the substrate.

3.2. Metamaterial Preparation and Negative Medium Verification

The proposed SRR type metamaterial preparation is based on the V shaped structures. The unit cell and the array structures are shown in Figure 1. This structure is embedded as copper strips between filter section and ground at 0.8 mm inside the FR4 substrate of 1.6 thickness. After creating the said MTM structure, the PE (perfect electric) boundary on two sides of x-axis, PM (perfect magnetic) boundary on two sides of z-axis and in the rest sides of y-axis the waveports 1 and 2 should be set up appropriately and then simulated with appropriate sweep frequency range. The S-parameters thus obtained will have $S_{11},\ S_{21},\ S_{12}$ and S_{22} since there are two ports.

These are complex numbers having real and imaginary parts. The negative medium properties can then be determined by making use of any one of the appropriate parameter retrieval procedures. There are four popular methods [5] such as Nicolson-Ross-Wier (NRW), NIST iteration

Table 1: Conventional T section filter dimensions.

Filter	Z_o	Z_{oL}	Z_{oC}	λ_{go}	λ_{gL}	λ_{gC}	W_{Tx}
T sec	50	99.78	18.43	82.39	88.99	77.36	3.06
Filter	W_{OL}	W_{OC}	L_{Tx}	L_{C2}	L_{L1}	L_{L3}	-
T sec	0.7008	12.256	10.3	4.98	10.98	10.98	-

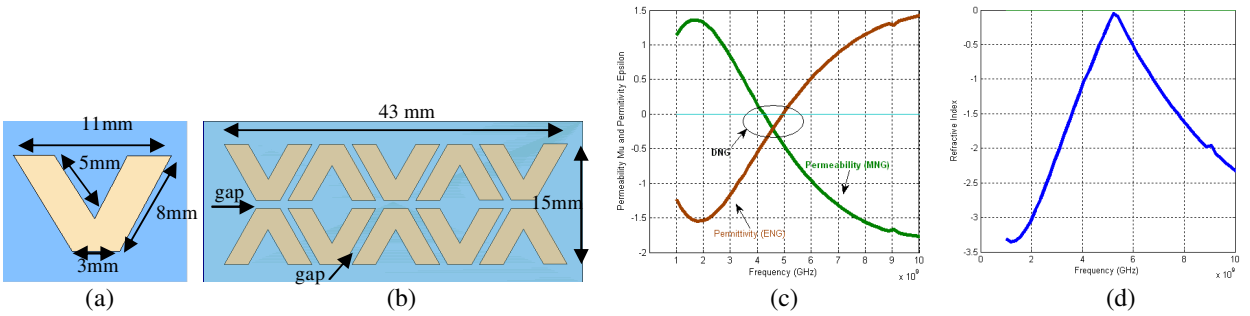

Figure 1: Proposed SRR structures and S-parameter retrieval for negative medium properties. (a) Single unit structure. (b) Array of V structures placed underneath the filter sections. (c) Permeability and permittivity of the MTM medium. (d) Refractive index.

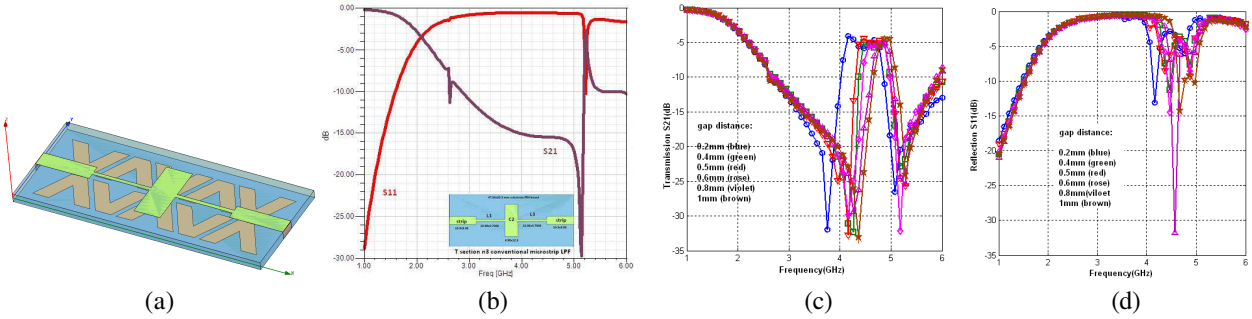

Figure 2: Simulated outputs. (a) View of Metamaterial loaded LPF. (b) Reflection and transmission loss of conventional LPF (Inset: LPF structure). (c) Transmission loss of MTM LPF for various gap distances. (d) Reflection loss of MTM LPF for various gap distances.

technique, new non-iterative technique (NNIT) and short circuit techniques (SCT) available for the negative medium property verification. The selection of the retrieval technique is based on the some constraints such as the measured S-parameters, length of the substrate, the required dielectric properties, time involved in the conversion process and the accuracy of the obtained results. The SCT is suitable for one port measurement hence has the possibility of determining relative permittivity only. In NIST iteration and NNIT methods, ε_r can only be determined and μ_r is treated as unity only. In this paper, the NRW method is adapted as it can give both medium properties, simple, involves fewer steps and less time consuming, straight forward and makes use of one set of reflection and transmission S-parameters only. The permittivity and permeability of the medium are related to S-parameters by the Equations from (21) to (22) as given below.

$$\varepsilon_r = \frac{2}{jkoh}\frac{1-V1}{1+V1} \tag{21}$$

$$\mu_r = \frac{2}{jk_0h}\frac{1-V_2}{1+V_2} \tag{22}$$

where

$$V_1 = S_{21} + S_{11} \tag{23}$$

$$V_2 = S_{21} - S_{11} \tag{24}$$

and

$$n = \sqrt{\varepsilon_r \mu_r} \tag{25}$$

where k_0 is a wave number equivalent to $2\pi/\lambda_0$, h is the thickness of the substrate and V_1 and V_2 are terms representing the composite of S_{11} and S_{21}. The term k_0h is expected to be very much less than unity for meeting the condition that the structure of MTM must be smaller in size [9]. The calculation of refractive index can also be done using the formulae listed in [6]. Using the S-parameters data obtained from the simulation, in the Equations from (21) to (25) for verification

of negative medium, the properties ε_r, μ_r and refractive index n are obtained and also drawn as a function of frequency.

3.3. MTM Loaded LPF Simulation

The MTM is inserted between the filter and the ground as shown in Figure 2(a). The filter is set up for a sweep frequency of 2 GHz in a sweep range of 1 to 6 GHz with lumped port input fed to two ports and simulated to obtain the filer properties.

4. RESULTS AND DISCUSSIONS

The Figure 1(c) shows the dominating negative epsilon medium upto 4.2 GHz and dominating negative mu medium after 5 GHz. The double negative property is noticed between 4.2–5 GHz range. The Figure 1(d) indicates the negativeness of the refractive index of the artificially prepared substrate medium. From the literature [4] it is already experienced that the ENG and MNG media aids in improving the performance due to good coupling between strips.

The simulated S-parameters of the conventional LPF as a function of frequency are shown in Figure 2(b). The inset indicates the filter structure. The reflection loss is −28 dB initially at 1 GHz and raises uniformly as the frequency increases. It remains high after 3 GHz and continues upto 6 GHz. However, the transmission curve is nearly flat in the passband and it starts decreasing after the cut-off frequency of 2 GHz corresponding to −3 dB. It reaches −15 dB only at 4.4 GHz and again it rises. Hence this filter is able to provide a poor roll-off rate only because this curve does not even cross −15 dB whereas the specification planned is 25 dB in the stop band at 4 GHz which is not achieved by this filter. The Figure 2(c) shows the transmission (S_{21}) values of the metamaterial loaded LPF for various gap distances between adjacent V structures. The transmission band is flat without any ripples and the cut-off frequency occurs at 1.95 GHz corresponding to −3 dB and then decreases to nearly around −34 dB for all the gap distances. However, for each gap distance reduction from 1 mm to 0.2 mm, it is seen that the stop band frequency reduces and hence improving to good roll-off rate. This rate is low for 1 mm gap distance and becomes appreciably lower when it is 0.2 mm. The 25 dB attenuation point is reached at 3.6 GHz whereas for the rest of the gap distances, it occurs after 4 GHz only. Similarly the reflection characteristics curves for various gap distances are shown in Figure 2(d). As the distance decreases the reflection loss remains varying between −18 dB and −20 dB initially and then rises uniformly. Also in the stop band, this S_{11} is better for the gap distance of 0.2 mm when compared to other values. Hence, as the gap between the MTM structures reduces, more coupling takes place between strip lines and yielding better performance of the filtering action when compared to the conventional filter.

5. CONCLUSION

This paper reported the results of an effort of improving the performance of a third order Chebyshev conventional T section microstrip low pass filter using metamaterial array structure in the substrate. The novel V shaped metamaterial structure as a SRR array was laid as performance improving cover between filter section and conventional ground layer. Better transmission and reflection characteristics have been obtained without compromising the size. The roll-off rate of 13.33 dB/GHz has been achieved with the proposed filter whereas in the conventional filter this was observed to be 7.096 dB/GHz only. The advantage of this filter considers improved and fast roll-off, good reflection and transmission loss in the pass and stop bands. The future work is to investigate the possibility of practical implementation of this metamaterial filter structure and test its real performance. The characteristic changes with respect to change in position of the V shaped SRR array inside the substrate can also be analyzed in terms of filter performance.

ACKNOWLEDGMENT

The author[1] acknowledges the technical support and expertise extended by the authors[2&3] for carrying out this work.

REFERENCES

1. Pozar, D. M., *Microwave Engineering*, John Wiley & Sons, Inc., 2006.
2. Hong, J.-S. G. and M. J. Lancaster, *Microstrip Filters for RF/Microwave Applications*, 1st Edition, John Wiley & Sons Inc., 2001.
3. Radonic, V., B. Jokanovic, and V. Crnojevic-Bengin, "Different approaches to the design of metamaterials," *Microwave Review*, 1–7, 2007.

4. Ekmekci, E. and G. Turhan-Sayan, "Comparative investigation of resonance characteristics and electrical size of the double sided SRR, BC-SRR and conventional SRR type metamaterials for varying substrate parameters," *Progress In Electromagnetics Research B*, Vol. 12, 35–62, 2009.
5. Rohde and Schwarz, "Measurement of dielectric material properties," Application Note, RAC0607-0019, Application Center Asia/Pacific, 2006.
6. Sahu, S., R. K. Mishra, and D. R. Poddar, "Compact metamaterial low-pass filter," *Journal of Electromagnetic Analysis and Applications*, Vol. 3, 399–405, 2011.
7. Kumar, D. and A. De, "Compact low pass filter design for L-band application," *Journal of Electromagnetic Analysis and Applications*, Vol. 3, 115–117, 2011.
8. Li, J. L., S. W. Qu, and Q. Xue, "Compact microstrip low pass filter with sharp roll-off and wide stop band," *Electronic Letters*, Vol. 45, No. 2, 2009.
9. Tang, C.-W. and S.-C. Yang, "Employing complementary split ring resonators for the wide stopband microstrip lowpass filter design," *Microwave and Optical Technology Lett.*, Vol. 52, No. 11, 2010.
10. Ahn, D., J.-S. Park, C.-S. Kim, J. Kim, Y. Qian, and T. Itoh, "A design of the low-pass filter using the novel microstrip defected ground structure," *IEEE Microwave Theory and Techniques*, Vol. 49, No. 1, 86–93, 2001.

Optimized Design of Microstrip Low Pass Filter with ANN for Performance Improvement

S. Suganthi[1], **S. Raghavan**[2], **and D. Kumar**[3]

[1]Shri Angalamman College of Engineering and Technology, Trichy, India
[2]National Institute of Technology, Trichy, India
[3]Periyar Maniammai University, Thanjavur, India

Abstract— A compact artificial neural network (ANN) trained Chebyshev type microstrip low pass filter has been proposed in this paper. Micrstrip filters always find an important place in many microwave applications. They are most widely preferred for selecting or confining the microwave signals within specified spectral ranges. The challenges on the microwave filters with requirements such as improved performance, miniature size, lighter weight, and lower cost are ever increasing with the emerging applications of wireless communications. The microstrip type filters play vital role at microwave frequencies because of these features. The conventional and ANN trained filters were designed using HFSS simulation tool. The design and analysis of microstrip low pass filter at cut-off frequency of 2 GHz on a FR4 substrate was initially performed using HFSS and then the necessary filter design parameters were trained with an ANN optimization technique using MATLAB. The performance comparison of the conventional filter designed was executed with the ANN model. The best possible design dimensions of the filter could be obtained with the ANN and the reflection (S_{11}) and transmission (S_{21}) properties were obtained in a satisfactory level.

1. INTRODUCTION

Microstrip filters gain attracting popularity among researchers because their day to day improvement in designs and their needs in many microwave systems including satellite communication [1, 2]. Depending on the need and application either Butterworth or Chebyshev type of filter with either low pass, high pass, band pass or band stop filter configurations [3] can be used. The conventional low pass filters can be synthesized using equivalent circuit model [2]. However, this type of synthesis methods suffer from some limitations such as mathematical complexity and time consuming computational efforts in determining the best possible designs. This paper provides an artificial neural networks (ANN) based low pass filter design for a 2 GHz cut-off frequency. The improvement in the filter design is made possible with the help of ANN [4, 5]. The artificial neural networks are proposed because they offer a fast and fairly accurate design before going for fabrication. There are different kinds of ANN used [6] in the recent years for overcoming limitations found in synthesis and analysis of microstrip components. ANNs are crude model of many engineering systems describing the analogy of neural structure of the brain. In terms of technical perspective they are viewed as parallel information computing systems consisting of large number of interconnected processing systems called neurons, working together to provide a solution to complicated variables based problems. The attracting feature of ANN is that it possesses the ability to learn through trainings and provide best decision [7]. To learn the neuron, two main learning schemes such as supervised learning and unsupervised learning are available. In the supervised learning an external supervisor called output set corresponding to the input set are provided. However, in the unsupervised learning there is no such defined output set to compare with the obtained outputs set after training. Hence, it needs some kind of regularities to make decisions. Generally, for decision making after applying the learning algorithm various activation functions [8] are used. The various inputs given to the neuron are processed with the weights of some neuro-cells. Finally the output from the neuro model is compared with the fixed threshold set of values by using any of the activation functions and decision is made for the best. Hence, they are found described as yield prediction and optimization [9] methods in microstrip based components designs. In this paper back propagation algorithm (BPA) is used to train the data set. Many ANN models adapt supervised learning since it is a popular learning algorithm and has the ability to classify the input data patterns and relate with the output patterns and provide accuracy. It mainly compares the outputs produced from the neural network with the specified outputs and then the error in the calculation is back propagated to the network for making a modification in the weights.

2. CONVENTIONAL MICROSTRIP LOW PASS FILTER DESIGN

From the equivalent circuit model found in literatures [2, 3] the conventional microstrip low pass filter can be designed. This paper considers the design aspects of third order Chebyshev type low pass Pi section filter. The simplified design steps involved in this filter synthesis are described in Equations from 1 to 20.

$$Ripple\ r = 1 + a_m^2 T_n^2\left(\omega'\right) \tag{1}$$

where for stop band attenuation

$$T_n^2(\omega') = 1 \tag{2}$$

and for stop band attenuation r_{pba} at f_s,

$$T_n^2(\omega') = \cosh^2(n\cosh^{-1}\omega'_s) \tag{3}$$

$$\omega'_s = \omega_s/\omega_c \tag{4}$$

$$\frac{W}{h} = \frac{8e^A}{e^{2A}-2} \tag{5}$$

where

$$A = \frac{Z_o}{6}\left[\frac{\varepsilon_r+1}{2}\right]^{1/2} + \frac{\varepsilon_r-1}{\varepsilon_r+1}\left[0.23+\frac{0.11}{\varepsilon_r}\right] \tag{6}$$

The characteristic impedance Z_0 is essentially considered to be 50 ohms for matching conditions and ε_r is the relative permittivity of the substrate material. Depending on whether $W/h < 1$ or $W/h \geq 1$, one can choose the appropriate formula for the determination of the effective medium property.

If $W/h < 1$, then the following Equations (7) and (8) may be chosen

$$\varepsilon_{eff} = \left[\frac{\varepsilon_r+1}{2}\right] + \left[\frac{\varepsilon_r-1}{2}\right]\left[\left(1+\frac{12h}{W}\right)^{-\frac{1}{2}} + 0.04\left(1-\frac{W}{h}\right)\right]^2 \tag{7}$$

$$Z_o = \frac{60}{\sqrt{\varepsilon_{eff}}}\ln\left[\left(\frac{8h}{W}\right)+0.25\left(\frac{W}{h}\right)\right] \tag{8}$$

If $W/h \geq 1$, then the following Equations (9) and (10) may be used

$$\varepsilon_{eff} = \left[\frac{\varepsilon_r+1}{2}\right] + \left[\frac{\varepsilon_r-1}{2}\right]\left[1+\frac{12h}{W}\right]^{-1/2} \tag{9}$$

$$Z_o = \left[\frac{377}{\sqrt{\varepsilon_{eff}}}\right]\left[\frac{W}{h}+1.393+\left(\frac{2}{3}\right)\ln\left(\frac{W}{h}+1.444\right)\right]^{-1} \tag{10}$$

For the inductor, $Z_0 = Z_{0L} = 100$ ohms and for the capacitor $Z_0 = Z_{0C} = 20$ ohms may be used with reference to the Wheeler's curve found in literature [11]. The strip width may assume the notations W_{Tx}, W_{OL} and W_{OC} corresponding to transmission line, inductor and capacitor respectively. The transmission line length can be taken to be multiples of $\frac{\lambda_{go}}{4}$. Moreover for pass band ripple of 0.5 dB the g values are $g_o = 1.0000$, $g_1 = 1.5963$, $g_2 = 1.0969$, $g_3 = 1.5963$ and $g_4 = 1.0000$. For any other ripple value or for any change in the order of the filter, the appropriate g values can be obtained from the table in literature and in [2, 3].

The free space wave length

$$\lambda_o = c/f_c \tag{11}$$

where $c = 3 \times 10\text{^}100$ mm/sec.

The wave length through transmission line

$$\lambda_{go} = \frac{\lambda_o}{\sqrt{\varepsilon_{effTx}}} \tag{12}$$

The transmission line (strip) length

$$L_{Tx} = \lambda_{go}/8 \tag{13}$$

The wavelength through the inductor

$$\lambda_{gL} = \lambda_o / \sqrt{\varepsilon_{effL}} \tag{14}$$

The wavelength through the capacitor

$$\lambda_{gC} = \lambda_o / \sqrt{\varepsilon_{effC}} \tag{15}$$

For third order Pi section filter the following formulae may be used:
Length of inductor strip

$$\beta L_{L2} = L_2 \frac{Z_o}{Z_{oL}} \quad \text{where} \quad \beta = 2\pi/\lambda_{gL} \tag{16}$$

$$\text{where } L_2 = \left(\frac{Z_o}{g_0}\right)\left(\frac{\Omega_c}{2\pi f_c}\right) g_2 \quad \text{and} \quad \Omega_c = 1 \tag{17}$$

Length of capacitor strip

$$\beta L_{C1,C3} = C_{1,3} Z_{oL}/Z_o \quad \text{where} \quad \beta = 2\pi/\lambda_{gC} \tag{18}$$

$$\text{where } C_1 = C_3 = \left(\frac{g_0}{Z_o}\right)\left(\frac{\Omega_c}{2\pi f_c}\right) g_1 \quad \text{and} \quad \Omega_c = 1 \tag{19}$$

The roll-off rate corresponding to LPF is given by

$$\xi = \frac{\alpha_{\max} - \alpha_{\min}}{f_s - f_c} \tag{20}$$

where $\alpha_{\max}$ and $\alpha_{\min}$ are the attenuation points corresponding to f_s and f_c respectively.

The input parameters considered for the design are the cut-off frequency f_c the stop band frequency f_s the stop band attenuation r_{sba} the pass band ripple level r_{pba} the dielectric permittivity of the substrate ε_r the thickness of the substrate h and the characteristic impedance for matching Z_O. Similarly the hidden output parameters expected to be calculated are the characteristic impedance of the transmission line Z_O, the characteristic impedance of the inductor Z_{OL}, the characteristic impedance of the capacitor Z_{OC}, the wavelength through the transmission line λ_{go}, the wavelength through the inductor λ_{gL}, and the wavelength through the capacitor λ_{gC}. The microstrip dimensions of main feed line, L and C components are W_{Tx}, W_{OL}, W_{OC}, L_{Tx}, L_{L2}, L_{LC1}, L_{LC3} which are calculated from the knowledge of the input data set as well as the six hidden output parameters Z_o, Z_{oL}, Z_{oC}, λ_{go}, λ_{gL}, and λ_{gC}. For the selected input data $f_c = 2\,\text{GHz}$, $f_s = 4\,\text{GHz}$, $r_{sba} = 20\,\text{dB}$, $r_{pba} = 0.5\,\text{dB}$, $\varepsilon_r = 4.4$, $h = 1.6\,\text{mm}$, $L_{Tx} = \frac{\lambda_o}{8}$ and $Z_o = 50\,\Omega$, the conventional filter calculations are made and the dimensions are as indicated in the Table 1. The corresponding filter section is shown in the inset in Figure 2(a).

3. NEURAL NETWORK MODEL

3.1. ANN Input, Ranges and Output Data Set

Recent research on ANN applications imply that the ANNs are knowledge based [9, 10] structures which combine the existing empirical formulae and equivalent circuit models with the networks for providing optimum results. For fixing an accurate model for the problem defined it is necessary to have a sufficient number (k) of neurons. However, it depends on the degree of non-linearity and dimensionality involved in the synthesis. For highly non-linear components, the number of neurons required is more. Hence adaptive processes are also used which can add or discard neurons as per the necessity at the time of training [10]. The number (m) of input parameters set (x) planned for the design of proposed filter and the number (n) of output parameters set (y) expected are seven. This is represented in Equations (21) and (22).

$$x = \{f_c, f_s, r_{sba}, r_{pba}, \varepsilon_r, h, Z_o\} \tag{21}$$

$$y = \{W_{TX}, W_{OL}, W_{OC}, L_{Tx}, L_{L2}, L_{LC1}, L_{LC3}\} \tag{22}$$

For conventional filter the output depends on the input set as defined by the empirical formulae listed from Equations (1) to (20).

$$y = f(x) \tag{23}$$

However, for ANN training a weight parameter associated with the interconnections in the neural network must be included. The training for data set is decided based on the actual relationship between the input and output parameters. Thus, Equation (23) becomes modified as below (Equation (24))

$$y = f(x, w) \tag{24}$$

3.2. ANN Model

The BPA based ANN model used in this paper is shown in Figure 1. The complete coding has been developed in MATLAB using ANN tool box. There are three layers- input layer, output layer and hidden neuron layer. However in the hidden layer, the input data or output data is not directly associated but through the actual as well as the weighted functions relationship as mentioned in Equation (24).

3.3. The Data Range

The data range in conventional and ANN model are shown below. This ANN is applied for design accuracy of the filter and hence the S parameters which describe the filter characteristics are simulated using HFSS simulator. The input data range for ANN is given by

$$f_c = 2\,\text{GHz}\,(1:0.1:2\,\text{GHz}), \quad f_s = 4\,\text{GHz}\,(2.8:0.1:4.5\,\text{GHz}), \quad r_{sba} = (20:2:40\,\text{dB})$$
$$r_{pba} = 0.5\,\text{dB}\,(0.1, 0.2, 0.5\,\text{dB}), \quad \varepsilon_r = 4.4 \quad h = 1.6\,\text{mm}, \quad L_{Tx} = \left(\frac{\lambda_o}{8}, \frac{\lambda_o}{16}, \frac{\lambda_o}{32}\right) \text{ and } Z_o = 50\Omega$$

3.4. Synthesized Filter Dimensions

The synthesized filter dimensions (impedance in ohms, wavelengths, lengths and widths in millimeter) are listed in Table 1.

4. HFSS SIMULATION

Both the conventional as well as ANN designed filter parameters are taken to HFSS software where the simulations are performed. The filter components are drawn using copper conductor on a double side printed $FR4$ substrate ($42.63\,\text{mm} \times 16.3\,\text{mm}$) of thickness 1.6 mm and permittivity 4.4. The ground plane is laid at the bottom of the substrate. The filter is set up for a sweep frequency of 2 GHz in a sweep range of 1 to 6 GHz with lumped port input fed to two ports and simulated.

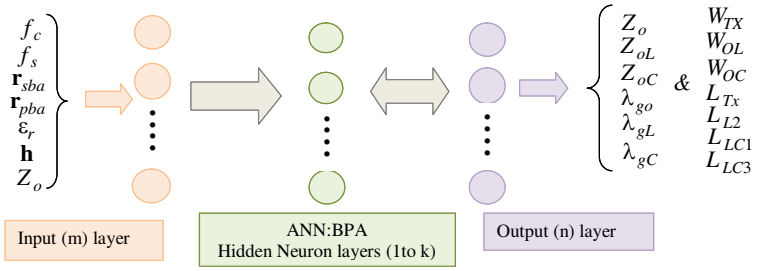

Figure 1: ANN model for microstrip low pass filter design.

Table 1: Synthesized Pi section filter dimensions.

Filter	Z_o	Z_{oL}	Z_{oC}	λ_{go}	λ_{gL}	λ_{gC}	W_{Tx}
Conv	50	99.78	18.43	82.39	88.99	77.36	3.06
ANN	50.088	103.4861	18.4452	81	84.9	76.2	3.059
Filter	W_{OL}	W_{OC}	L_{Tx}	L_{L2}	L_{C1}	L_{C3}	
Conv	0.7088	12.256	10.3	7.55	7.24	7.24	
ANN	0.7092	12.2428	2.5745	10.099	7.079	7.079	

5. RESULTS AND DISCUSSIONS

5.1. Simulation Results and Discussion

The simulated S parameters of the conventional LPF as a function of frequency are shown in Figure 2(a). The reflection loss S_{11} value lies well below -10 dB with a deep upto -31 dB at 1.43 GHz indicating a good matching at the port. From the transmission properties it can be found that the passband ripple varying between -1 and -4 dB and a roll off takes place after cut-off frequency (1.9 GHz) and is found as 14.16. At 3 GHz the attenuation is -20 dB. A transition of -15 dB per 1 GHz is noticed in the stopband after 1.9 GHz. Though, there is an increase in attenuation after 3 GHz, the insertion loss is not sufficient and appreciable after f_s.

The S parameters obtained for ANN trained filter are shown in Figures 2(b) and (c). In Figure 2(b), the reflection loss quantities are compared with various strip lengths $L_{Tx} = (\frac{\lambda_{go}}{8}, \frac{\lambda_{go}}{16}, \frac{\lambda g_o}{32}, \frac{\lambda g_o}{64})$ as per ANN outputs. For $\frac{\lambda_{go}}{8}$ the reflection (S_{11}) parameter is well upto -45 dB but there is dip in attenuation noticed at 2.6 GHz in the stop band. Similarly the attenuation for other two consecutive strip lengths are found providing reflection loss of around -30 dB but there is dip noticed at 3.6 GHz and 4.4 GHz respectively. However, the $\frac{\lambda g_o}{64}$ length strip provides a constant stop band attenuation in addition to sufficient passband reflection level. In Figure 2(c), the insertion loss characteristics for the said four strip lengths are shown. The stop band insertion loss is appreciably good for $\frac{\lambda g_o}{64}$ when compared to other three strip lengths. Insertion loss of upto -68 dB is provided by this structure. A sharp transition occurs after cut-off frequency and a roll-off rate of 12.14 is also achieved. Also the maximum stopband attenuation occurs well within 4.2 GHz in advance when compared to the specified maximum value in the input data. This remains comparatively better than that of the conventional filter. There is a downshift in frequencies in S_{11} and S_{21} corresponding various strip lengths in the increasing order. The S_{22} and S_{12} parameters appear same as S_{11} and S_{21} and hence they are not shown here.

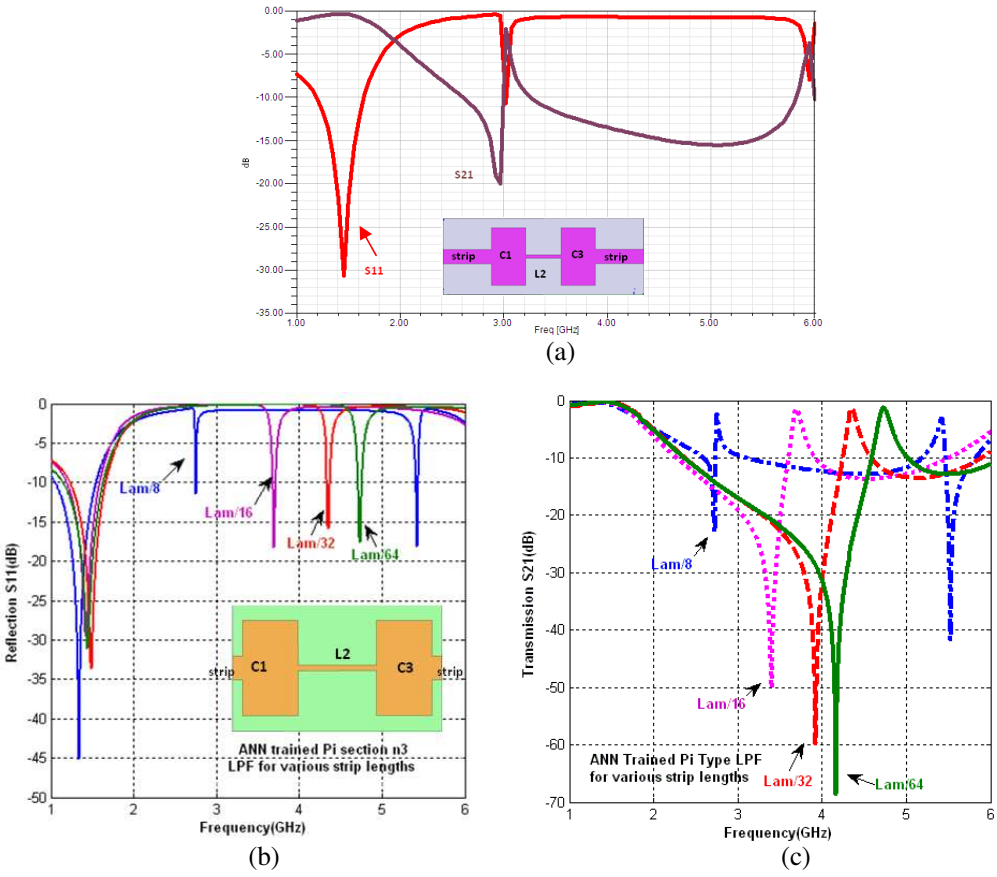

Figure 2: Simulated results of S_{11} and S_{21} (Inset: Filter structures). (a) Conventional filter. (b) ANN trained filter output for S_{11}. (c) ANN trained filter output for S_{21}.

5.2. Comparison of the Characteristic Parameters of the Proposed Filter

The filter parameters designed from conventional method and from the artificial neural networks are compared and produced in Table 1. It lists the values of conventional filter elements obtained using Equations from 1 to 19 for the stated input data. The size of the substrate board is $0.517\lambda_{go} \times 0.197\lambda_{go}$ in the conventional filter. The ANN trained optimum dimensions for better reflection and transmission properties are different from the calculated ones. The transmission strip length is also very small compared to that of the conventional filter. Hence the size of the substrate board is $0.295\lambda_{go} \times 0.197\lambda_{go}$ showing size reduction possibility with ANN approach. From the comparison is found that the ANN has produced optimized dimensions using best possible combinations of the supplied input data set.

6. CONCULSION

The application of artificial neural networks in the design of microstrip low pass filter is verified in this paper. The optimum method of synthesis of microstrip filter low pass filter has been performed using back propagation algorithm based ANN model. The designed filter has been simulated for both conventional as well as ANN trained data sets separately and then compared. From the simulated results it is evident that the design accuracy can be achieved using artificial neural networks. A filter size reduction has also been achieved considerably with the help of ANN. The future work is to fabricate the filters and then evaluate the experimental performance.

ACKNOWLEDGMENT

The author[1] acknowledges the technical and software support provided by author[2&3] for developing this paper.

REFERENCES

1. Swanson, Jr., D. G. and W. J. R. Hoefer, *Microwave Circuit Modeling Using Electromagnetic Field Simulation*, Artech House Inc., London, 2003.
2. Hong, J.-S. G. and M. J. Lancaster, *Microstrip Filters for RF/Microwave Applications*, 1st Edition, John Wiley & Sons Inc., 2001.
3. Pozar, D. M., *Microwave Engineering*, John Wiley & Sons, Inc., 2006.
4. Callan, R., *The Essence of Neural Networks*, Prentice Hall Europe, 1999.
5. Sri Ramakrishna, K., J. Lakshmi Narayana, and L. Pradeep Reddy, "Performance evaluation of ANN models for the analysis of microstrip low pass filter," *ICGST AIML Journal*, Vol. 9, No. 1, 9–18, 2009.
6. Kushwah, V. S., F. M. Sharma, and G. S. Tomar, "Analysis and design of microstrip high pass filter using artificial neural network," *International Journal of Computer Information Systems and Industrial Management Applications*, Vol. 3, 347–354, 2011.
7. Thiruvalar Selvan, P. and S. Raghavan, "Multilayer perceptron neural analysis of edge coupled conductor backed edge coupled coplanar waveguides," *PIER B*, Vol. 17, 169–185, 2009.
8. Malik, P. K., V. Vishnoi, and S. Pundir, "Hardware design of equilateral triangular microstrip antenna using artificial neural networks," *Technia — International Journal of Computing Science and Communication Technologies*, Vol. 3, No. 2, 642–645, Jan. 2011.
9. Kabir, H., Y. Wang, M. Yu, and Q. J. Zhang, "Applications of artificial neural network techniques in microwave filter modeling, optimization and design," *PIERS Online*, Vol. 3, No. 7, 1131–1135, 2007.
10. Zhang, Q.-J., K. C. Gupta, and V. K. Devadhaktuni, "Artificial neural networks for RF and microwave design — From theory to practice," *IEEE MTT,* Vol. 51, No. 4, 1339–1350, 2003.
11. Gupta, K. C., R. Garg, and P. Bhartia, *Microstrip Lines and Slotlines*, 2nd Edition, 1996.